Technische Universität München
TUM School of Natural Sciences

Investigation on crystal structure - band structure relationships of ternary alkali metal pnictidotrielates and -tetrelates

Sabine G. Zeitz

Vollständiger Abdruck der von der TUM School of Natural Sciences der Technischen Universität München zur Erlangung einer

Doktorin der Naturwissenschaften (Dr. rer. nat.)

genehmigten Dissertation.

Vorsitz: Prof. Dr. Tom Nilges

Prüfende der Dissertation:

1. Prof. Dr. Thomas F. Fässler
2. Prof. Dr. Antti Karttunen

Die Dissertation wurde am 07.11.2024 bei der Technischen Universität München eingereicht und durch die TUM School of Natural Sciences am 25.11. 2024 angenommen.

"A week of camp life is worth six months of theoretical teaching in the meeting room."

Sir Robert Stevenson Smith Baden-Powell, Lord of Gilwell

Danksagung

Zunächst einmal möchte ich mich bei Professor Dr. Thomas Fässler bedanken, dass ich meine Promotion an seinem Lehrstuhl durchführen durfte. Besonders dafür, dass ich eigenverantwortlich mit drei Praktikanten zusammen von berechenbaren Alkalitriel- und tetrelpnictogeniden die Bandstruktur aufklären durfte, und damit den Grundstein zu meiner Dissertation legen konnte. Auch möchte ich mich für die zusätzlichen Themen bedanken, von denen einige weitere Ergebnisse geliefert haben.
Vielen Dank an unsere Lehrstuhlsekretärin Manuela, die immer helfen konnte, wenn man nicht weiter wusste und einen gekonnt und mit lächeln durch die Untiefen der TUM-Bürokratie geführt hat
Des weiteren möchte ich mich bei allen aktuellen und ehemaligen Kolleg*innen bedanken, für die tolle Atmosphäre in den Büros und beim Mittagessen, die die Motivation im Promotionsalltag hoch gehalten haben. Im speziellen danke an Viktor, fürs Kristall lösen, Samuel fürs DSC messen, Dominik für die Ramanspektren, Maria für die EDX-Messungen, Vincent für die Denkanstöße, wenn sich ein Problem mal nicht so leicht hat lösen lassen und Alex und Manuel für die Hilfe beim Rietvelden. Auch ein großes Dankeschön an meinen 5 Forschungspraktikant*inn, die mich bei der Forschung und teilweise später als HiWis unterstützt haben, vor allem euch beiden Hanna und Yulia. Danke für eure Hilfe im Forschungspraktikum, im Labor und das wir so gute Freunde geworden sind. Ich bin mir sicher, ihr könnt die Eldritch-Monster auch ohne mich besiegen. Viel Erfolg bei eurer Promotion!
Professor Antti Karttunen möchte ich besonders für die Einführung in die DFT-Rechnungen danken, den herzlichen Empfang in Helsinki, die Hilfe bei Problemen und den Diskussionen zu unklaren Ergebnissen. Ich freue mich schon auf die Post-Doc Zeit.
Abschließend noch ein Dank an meine Freunde und Familie, ohne die die Promotion nicht möglich gewesen wäre: Danke an meine Eltern für die finanzielle Unterstützung während dem Studium und Zeit in Amerika. Danke Oma Maria und Oma Irmgard, dass ich während den Ferien und im Urlaub immer bei euch willkommen war. Auch wenn er es nie mitbekommen hat: Danke Opa Werner, dass du mein Interesse an Chemie geweckt hast und für deine Bücher, die mich durch das Studium begleitet haben. Ich wünschte ich hätte mit dir über all die Kuriositäten in der Chemie diskutieren können. Danke an meine Freunde vom Stamm St. Michael Perlach für die vielen coolen Sommerlager, Wochenenden und Aktionen, die ich mitgestalten könnte und ein guter Freizeitausgleich waren (außer dem Jamboree in Südkorea). Danke dir Thomas für die tolle Zeit als Büropartner, die vielen Film- und Serienabende, (Brett)Spielrunden und dass du als mein Mentor übernommen hast.

Abstract

Semiconductors have lost of different applications, such as photovoltaic systems, light emitting diodes and thermoelectric components, but for all of them an intelligent ans efficient material design and optimisation process is required, although sometimes the state of the art is not the most efficient system. Most commercially available solar cells for example are silicon based, although the electronic structure with its indirect band gap has only a low degree of efficiency in terms of the total amount of energy harvested from sun light. Therefore research is focused on finding (new) materials with direct band gaps, which then can be tuned for better performance. To make this field of research more efficient it would be beneficial to know how different properties of the crystal structure and composition influence the electronic structure and even better to know how the crystal has to be built for optimum performance.

Therefore in this work the electronic structure of all ternary compounds, which were suitable for calculation, of the system A_xTr/Tt_yPn_z (A = Li-Cs, Tr = Al-In, Tt = Si-Sn, Pn = P-Bi) were analyzed by means of quantum chemical methods, with a hybrid-correlation functional after Perdew, Burke and Ernzerhof (DFT-PBE0) and Gaussian type triple ζ-valence + polarization (triels, tetrels and pnictogens) or split valence and polarization level basis sets. The compounds can be described as Zintl phases comprising polyanionic *TrPn* and *TtPn* substructures. As common motif most structures are formed by the connection of *TrPn4* or *TtPn4* tetradera. 56 of all calculated 143 compounds show direct, 17 pseudo-direct, 68 indirect band gaps and two are metallic. With these compounds as data set several properties are investigated regarding their influence on the occurrence of direct band gaps and size of the gaps. For the latter the electronegativity difference between the triel/tetrel and pnictogen has the most influence. The size of the band gap decreases from phosphides to arsenides and antimonides by about 0.5 eV each for compounds within the same family. As for molecules which show larger HOMO-LUMO gaps for more covalent bonds, the band gap of the phosphides is larger due to the better overlap with the triel/tetrel orbitals and thus more covalent bonds, which a Mulliken population analysis revels between them.

The nature of the band gaps is influenced by different parameters which occur simultaneously, which were investigated in more detail for specific compound families, classified by their atom ratio. On one hand have compounds with the same crystal structure mostly the same kind of band gap, but Sn and In compounds on the other might show direct band gaps,

even if their Ga/Ge analogue structures have indirect band gaps. This could be caused by an increased repulsion of neighbouring In/Sn atoms, leading to higher energies for their anti-bonding interactions or their chosen basis set that accounts for scalable relativistic effects. The data set also shows that direct band gaps are favoured by three-dimensional polyanionic sub-structures and Li compounds with isolated $TrTtPn_4$ tetrahedra.

Lastly were two Zintl compounds studied in more detail to compare the influence of composition and structure on specific band gaps. $Na_{13}Sn_{26-x}Bi_{1+x}$ with x = 0-2 has a three-dimensional open Sn framework hosting Bi guest atoms. Calculations reveal that the additional charge of the Bi guest atoms is not located at the isolated Bi position but rather distributed over the whole Sn network. The size of the indirect band gap remains mostly the same for modelled structures with x = 0 and x= 2. Calculations on the different polymorphs of $CaSi_2$ and β-$CaGe_2$ reveal their anisotropic metallic behaviour similar to graphite. It is shown that α-$CaGe_2$ is a meta stable phase, probably stabilized during synthesis by indium impurities. Further on are mixed $CaSi_{2-x}Ge_x$ compounds synthesised revealing a statistical mixture on all Si/Ge positions over the entire composition range of x = 0-2. Models with homoatomic and mixed Si/Ge layers are calculated showing that their band structures are almost identical to the parent compounds.

Zusammenfassung

Halbleiter besitzen eine Vielzahl von Anwendungen, so etwa in Photovoltaik Anlagen, Licht emittierenden Dioden oder thermoelektrischen Bauteilen. Allen gemeinsam ist ein intelligenter und effizienter Materialentwicklungsprozess, auch wenn der aktuelle Stand der Technik nicht immer das effizienteste System ist. So etwas basieren kommerziell erwerbliche Solarzellen meist aus Silizium, obwohl es durch seine indirekte Bandlücke nicht das beste Material ist, um den gesamten Energiebereich der Sonne einzufangen, sind sie dennoch der kommerzielle Standrad. Nicht zuletzt deswegen ist die Forschung bemüht (neue) Materialien mit direkten Bandlücken zu finden und zu verbessern um die Effizienz in Bezug auf die gewonnene Energie zu verbessern. Um die schneller an gut Ergebnisse zu kommen, wäre es deswegen hilfreich zu wissen, wie sich verschiedene Eigenschaften der Kristallstruktur und Zusammensetzung auf die elektronische Struktur auswirken, oder noch besser, zu wissen, welche Kristallstruktur vorhanden sein muss, um die besten Ergebnisse zu erzielen.

Deshalb befasst sich diese Arbeit mit der Untersuchung der elektronischen Struktur aller, zum Rechnen geeigneten, Verbindungen des Systems A_xTr/Tt_yPn_z (A = Li-Cs, Tr = Al-In, Tt = Si-Sn, Pn = P-Bi) mithilfe quantum-chemischer Methoden basierend auf einem hybrid-Korrelations- und Austauschfunktional nach Perdew, Burke und Ernzerhof und triple ζ-Valenz + Polarisations (Triele, Tetrele und Pnictogene) oder split-Valenz und Polarisations Basis Sets. Alle Verbindungen können als Zintl phasen mit polianionischen *TrPn* oder *TtPn* Teilstrukturen beschrieben werden. Die meisten Verbindungen sind aus *TrPn4* oder *TtPn4* Tetraeder als gemeinsames Strukturmotiv aufgebaut. 56 aller gerechneten 143 Verbindungen haben direkte, 17 weitere pseudo-direkte und 68 indirekte Bandlücken, zwei sind metallisch. Mit diesen Verbindungen als Datenset kann untersucht werden wie sich verschiedene Eigenschaften auf das Auftreten direkter Bandlücken und allgemein der Größe der Lücke auswirken. Letztere wird vor allem durch die Elektronegativitätsdifferenz zwischen Triel/Tetrel und Pnictogen beeinflusst. Zudem nimmt die Größe der Bandlücke von Phosphiden über die Arsenide zu den Antimoniden um jeweils ca. 0.5 eV bei vergleichbaren Verbindungen. Eine Mulliken Population Analyse zeigt, dass zwischen Phosphor und dem Triel/Tetrel ein vergleichsweise besserer Überlapp der Orbitale vorhanden ist, was die kovalenten Bindungen stärker macht und ähnlich wie bei Molekülen, deren HOMO-LUMO Lücke mit steigender Kovalenz zunimmt, zu größeren Bandlücken führt.

Die Art der Bandlücke wird von verschiedenen Parametern gleichzeitig beeinflusst, die im

Detail für verschiedene Verbindungsklassen, eingeteilt nach Zusammensetzung, untersucht wurden. Einerseits scheinen Verbindungen mit der gleichen Kristallstruktur auch die gleiche Art der Bandlücke zu haben, aber andererseits zeigen Sn und In Verbindungen auch dann direkte Bandlücken, wenn ihre Ga/Ge Analoga indirekte Bandlücken besitzen. Diese könnten auf eine stärkere Abstoßung benachbarter In/Sn Atome zurückzuführen sein, die ihre antibindenden Wechselwirkungen zu höheren Energie verschiebt oder an den verwendeten In/Sn Basissätzen, die skalierbare relativistische Effekte berücksichtigen. Im Datenset lassen sich ebenfalls Anzeichen dafür finden, dass direkte Bandlücken von dreidimensionalen Polyanionischen Teilstrukturen und Li Verbindungen mit isolierten $TrTtPn_4$ Tetraedern bevorzugt wird.

Zum Schluss wurden zwei Zintl Phasen im Detail untersucht um den Einfluss der Zusammensetzung und Struktur auf spezifische Bandlücken zu untersuchen. $Na_{13}Sn_{26-x}Bi_{1+x}$ mit x = 0-2 besitzt ein dreidimensionales, offenes Sn Netzwerk, das Bi Gastatome beinhaltet. Rechnungen zeigen, dass die zusätzliche Ladung des Bi Gastatoms nicht etwa auf der isolierten Bi Position liegt, sondern über das gesamte Sn Netzwerk verteilt wird. Die Größe der indirekten Bandlücke bleibt für die beiden modellierten Extremfälle mit $x = 0$ und $x = 2$ nahezu gleich. Für die verschiedenen $CaSi_2$ Isomeren und β-$CaGe_2$ wurde ein anisotropes, metallisches Verhalten gefunden, dass dem von Graphit ähnelt. Außerdem wurde gezeigt das α-$CaGe_2$ eine metastabile Verbindung ist, die vermutlich durch Indium Verunreinigungen während der Synthese stabilisiert wird. Des Weiteren wurden gemischte $CaSi_{2-x}Ge_x$ Verbindungen synthetisiert, die zeigen das sich über den gesamten Bereich x = 0-2 Si und Ge statistisch auf allen Positionen mischen. Die elektronische Struktur von Modelle mit homoatomaren oder gemischten Si/Ge Schichten unterscheidet sich kaum von denen ihrer Randverbindungen.

Declaration

This work has been written as publication-based thesis. Peer-reviewed articles published in journals as well as supporting information and manuscripts are provided in chapter 5, contribution of co-authors is given in Tabelle 2.3. Introduction, some theoretical background and relevance of this topic are presented in chapter 1. Experimental and computational procedures are described in chapter 2, chapter 3 summarizes all results and their discussion on the general and detailed trends of the investigated compound class. Chapter 4 contains the overall summary and conclusion. The Appendix contains additional information on the calculations, crystal structure, band structure, Mulliken overlap population tables and Mulliken charges for all investigated compounds.

The research summarized in the dissertation was carried out at the chair of inorganic chemistry with focus on novel materials, school of natural science, at the Technical University Munich between April 2020 and September 2024.

List of abbreviations

A	Alkali metal: Li, Na, K, Rb, Cs
BXDS	Canadian Brockhouse X-ray Diffraction and Scattering
CBM	conduction band minimum
cif	crystallographic information file
CLS	Canadian Light Source
COHP	crystal orbital hamilton population
COOP	crystal orbital overlap population
DFT	density functional theory
DOS	density of states
DSC	differential scanning calorimetry
ECP	effective core potential
FWHM	full width at half maximum
ICSD	inorganic crystal structure database
Pn	Pnictogen: P, As, Sb, Bi
ppm	parts per million
pT	triangular planar coordination
PXRD	powder x-ray diffraction
SCXRD	single crystal x-ray diffraction
SVP	split valence+polarization
T_d	$Tt/TrPn_4$ tetrahedra
Tm	Transition metal
Tr	Triel: Al, Ga, In
Tt	Tetrel: Si, Ge, Sn
TZVP	triple-ζ-valence+polarization
VBM	valence band minimum
WHE	high energy wiggler beamline

Contents

1 Introduction

Semiconductors are incredibly versatile in their applications, such as light-emitting diodes (LEDs), transistors, thermoelectrics, solar cells and many more. They all require intelligent material design, which can include specific requirements for the material texture, composition or a very precisely tuned band gap.[1–5] The latter is particularly important for solar cells, where the band gap should be around 1.1 eV for a maximum in energy conversion efficiency.[6, 7] Today, the standard material for solar cells is silicon, although its indirect band gap is suboptimal and therefore the efficiency is rather low.[8, 9] Recent research has therefore focused on finding new materials, studying their electronic properties and, if promising, tuning them to achieve maximum efficiency.[10, 11]

Materials with direct band gaps are particularly sought after because their properties are favourable for energy conversion. For the material to interact with light, the minimum energy of the incoming photons must be equal to the band gap. If the band gap is direct, an electron is excited from the valence band, more precisely from the valence band maximum (VBM), to a conduction band state. If the energy of the photon is equal to the energy of the VBM it will get excited to the conduction band minimum (CBM). For a direct band gap, the symmetry of the states at VBM and CBM must have the same symmetry (Abbildung 1.1 left). An electron-hole pair is formed, which upon recombination can release the stored energy. In solar cells this energy can be harvested to produce electricity, while the excitation by electricity is used to emit the stored energy as light in LEDs. The general process of interaction between light and indirect band gap materials is the same, but since valence band maximum and conduction band minimum are located on different k-points and therefore have different quasi-momenta, this process must be accompanied by a phonon (lattice vibration), which cannot be provided by the photon itself (Abbildung 1.1 right). This makes indirect transitions less attractive for optoelectronic applications.[12]

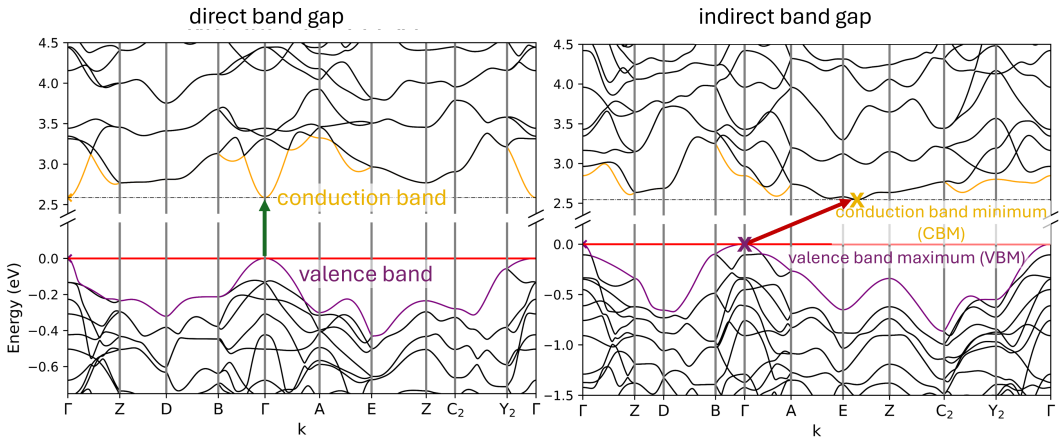

Figure 1.1: Examples of band structures with direct (left) and indirect band gap (right).

To make the process of designing new materials for such applications more effective, it would be useful to be able to predict the size and kind of a band gap, just by looking at the crystal structure. Such crystal structure-band structure relationships could also help to design materials for very specific applications.
However, since semiconducting materials can be divided into a large number of different classes, basic research should first focus on a class of compounds that is easy to understand, yet diverse in its different structures and strictly separated from other classes of compounds. Zintl compounds are the perfect candidate because their many different structures of the polyanions can be easily understood by the bonding preferences of the main group elements.

1.1 Zintl Compounds

Zintl compounds, named after Eduard Zintl, are intermetallic compounds consisting of an alkali or alkaline-earth metal and a p-block metal or non metal from group 13 to 16. They are either poor conductors or semiconductors with small band gaps, are often brittle and are characterized by a mix of covalent and ionic chemical bonds.[13–15] They can be divided into ionic and intermetallic Zintl compounds by the (hypothetical) Zintl boundary between group 13 and 14, which also characterises the chemical bonding situation for these compounds to some extent.
Due to the difference in electronegativity, the valence electrons of the alkali(ne-earth) metal are transferred to the p-block metal or non metal for which the anionic substructure can therefore be easily determined using the Zintl-Klemm concept, also known as 8-N rule, with N = number of valence electrons. With the charge of the polyanion the number of bonds for

each anion is determined that need to be formed to achieve an electron octet. Thereafter the structure of the anionic network can be determined, which is often similar to the covalent networks of the group 13 to 16 elemental crystal structures.
For example in NaSi (Na_4Si_4), Si has a formal charge of -1 due to the electron transferred from Na. With 8-5 = 3 bonds, each Si has to form three bonds with neighbouring Si atoms. Thus the Si^- anions form isolated $Si_4{}^{4-}$ tetrahedra, analogous to the structure of elemental white phosphorus as shown in Abbildung 1.2.[16–18]

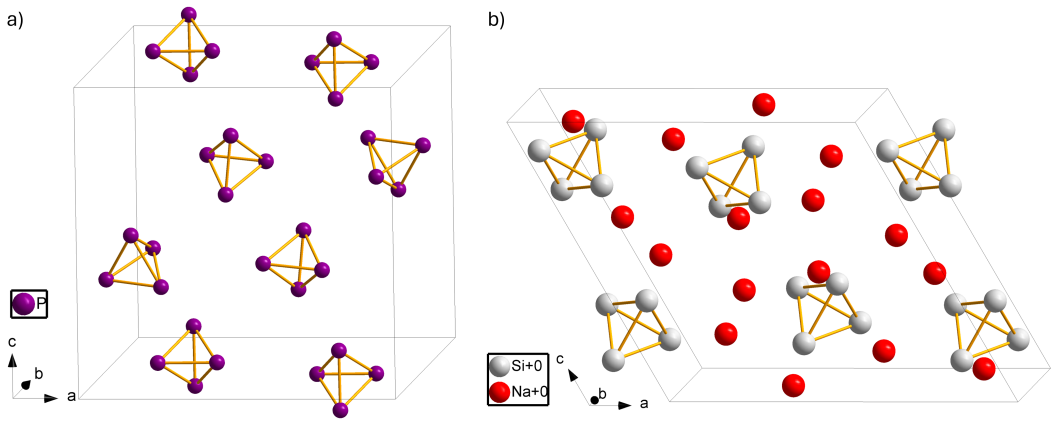

Figure 1.2: Example for the similarity of the a) crystal structure of elemental white phosphorus (γ-P_4) and b) structure of NaSi determined by the 8-N rule.

Zintl compounds comprising polyhedral clusters may be used in solution based chemistry, where the Zintl compounds, synthesized in solid state reactions, are dissolved in different organic solvents with the alkali metal cations often being complexed by crown ethers. The structure of these polyhedral anions can also be predicted using the polyhedral skeletal electron pair theory, also known as Wade-Mingos rules.[19, 20] These anionic clusters can be used for many different follow-up reactions, such as cluster extensions or catalysis.[21–24]
Although the Zintl-Klemm concept and Wade-Mingos rules are a powerful tool to determine the polyanionic structures of Zintl compounds, they are limited in their prediction, if (multiple) isomers for the same bonding situation are possible. One example are compounds of the A_3TrPn_2 system, with A = alkali metal, Tr = Al-In, Pn = P-Bi, which show a large number of isomeric polyanions that form structures reaching from discrete molecular like units to three-dimensional networks. Although their exact structure prediction is more challenging, the large variety of possible structures makes Zintl compounds an even better class of materials for studying crystal structure-property relationships. In particular, different isomers with the same bonding situation can help to separate such effects from influences on the band

structure arising from other properties.

1.2 Dimensionality and Connectivity of Zintl Compounds

The A_3TrPn_2 system mentioned above is a good example for the diversity of structures adapted by Zintl phases. There are three main properties that can be used to classify the different isomers present, namely the basic building unit of the polyanionic structure, their connectivity among each other and the dimension of the resulting (poly)anionic network. One way to classify the connectivity of tetrahedral building units is the Liebau nomenclature.[25] But since it is mostly used in describing the connection of tetrahedra in silicates, here the number of bonds and shared tetrahedra vertices combined with the dimension of the repeating unit is used to describe the (poly)anionic network.

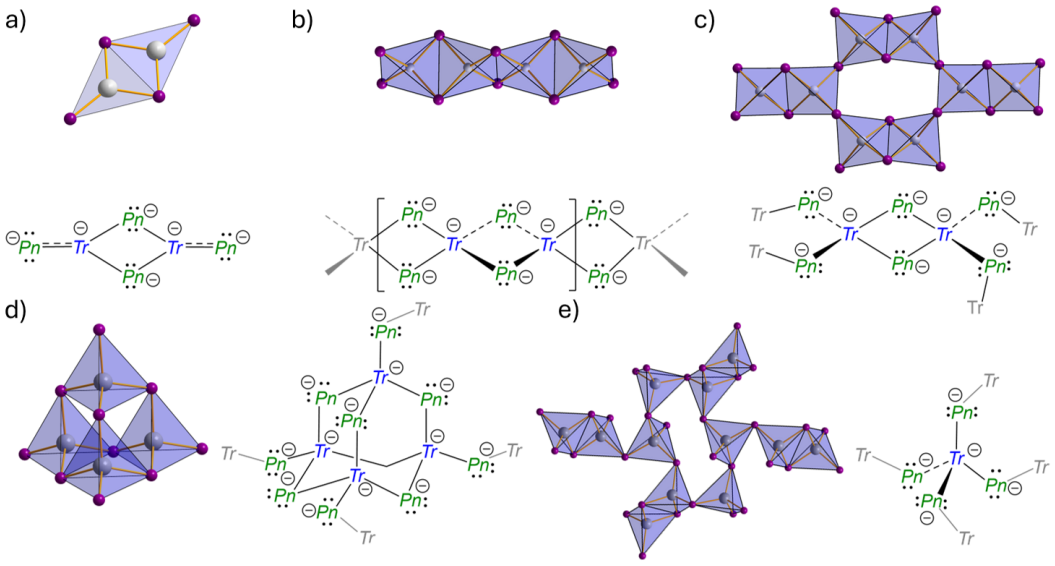

Figure 1.3: Different structures (coordination polyhedra and Lewis formula) present in the A_3TrPn_2 system with a) the zero-dimensional, b) one-dimensional, c) two-dimensional, d) only corner-sharing three-dimensional and e) corner- and edge-sharing three-dimensional isomer.[26]

As stated by the Zintl-Klemm concept, the alkali metal atoms transfer their electron to the $TrPn_2$ unit which then forms (4b-Tr^-) and (2b-Pn^-), where nb = n-fold bonding, Tr = triel, Pn = pnictogen. Although this is only one possible distribution of the electrons,

its the most likely since with this atom connectivity the basic building unit of either the carbonate analogue triangular planar *TrPn*$_3$ or the tetrahedral *TrPn*$_4$ unit, with the trial atom four-fold bonded within the pnictogen tetrahedron can be formed, which are the most common building blocks for these Zintl compounds. To further achieve the octet for each pnictogen atom the tetrahedral building units are either connected via vertices and/or shared edges. Based on this five different isomers with different dimensions have been observed: zero-dimensional, molecular like *Tr2Pn4*$_6^-$ units (Abbildung 1.3a), one-dimensional chains of edge-sharing tetrahedra ($^1_\infty[TrPn_{4/2}]^{3-}$, Abbildung 1.3b), two-dimensional layers of edge- and corner-sharing tetrahedra ($^2_\infty[TrPn_{4/2}]^{3-}$, Abbildung 1.3c) and two isomers building three-dimensional networks, one with adamantane-like T_4 super tetrahedra ($^3_\infty[TrPn_{4/2}]^{3-}$, Abbildung 1.3d) by solely corner-sharing tetrahedra, the other with a more complex network, with additional edge-sharing tetrahedra ($^3_\infty[TrPn_{4/2}]^{3-}$, Abbildung 1.3e). For some compounds in this system, even two different isomers are present in the unit cell.[26–31]

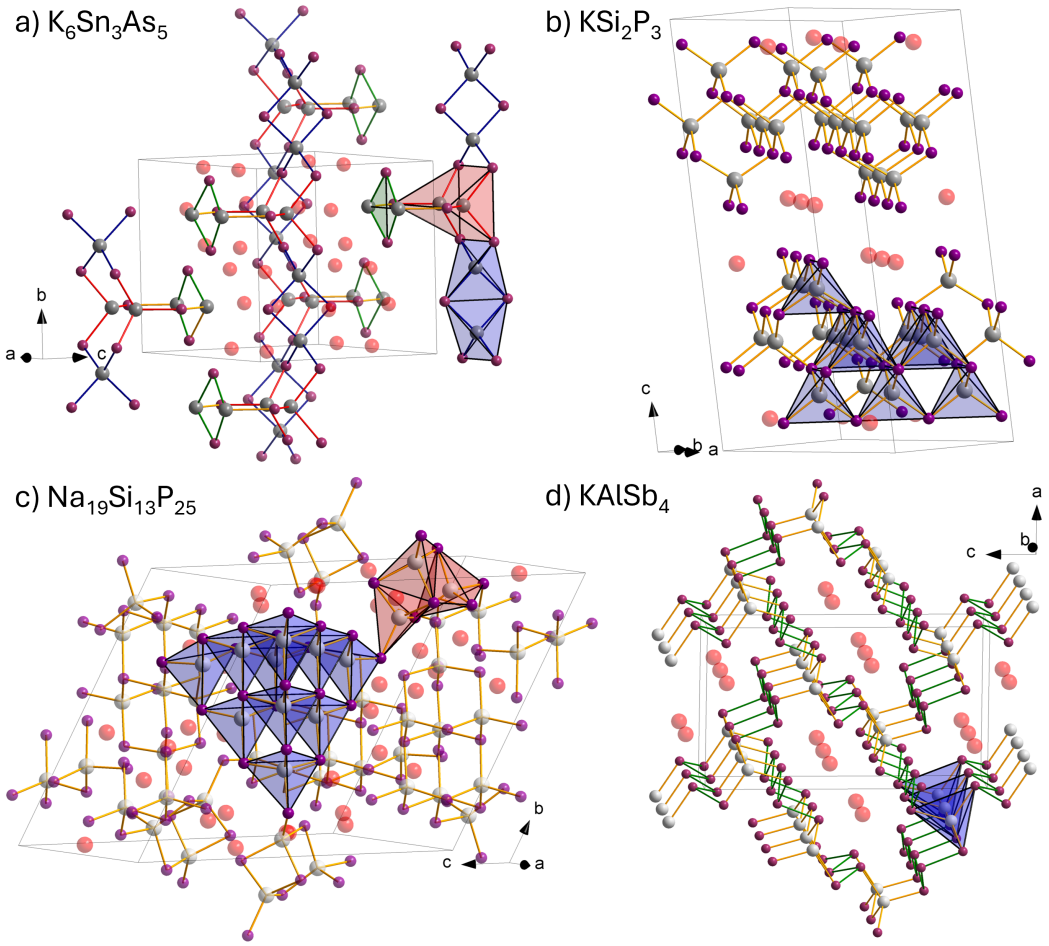

Figure 1.4: Crystal structures of a) $K_6Sn_3As_5$, b) KSi_2P_3, c) $Na_{19}Si_{13}P_{25}$ and d) $KAlSb_4$ with the polyhedra of the main structural motive marked.In all structures alkali metals, triel/tetrel and pnictogens are depicted in red, grey and purple respectively.

These rather simple structural motives are just a fraction of the various Zintl compounds know up to date. Other than the (rather simple) structural motives shown beforehand, many (more complex) crystal structures have been reported. For some additional building blocks, like the Sn-Sn dumbbell centred trigonal prisms and square planar Sn_2As_2 units can be found, for example in $K_6Sn_3As_5$ (Abbildung 1.4a), which form complex one-dimensional chains.[32] For others the connectivity of the $Tr/TrPn_4$ tetrahedra is more diverse, leading to, for example, the more complex two- and three-dimensional structures of KSi_2P_3 and $Na_{19}Si_{13}P_{25}$ as shown in Abbildung 1.4b and c, respectively.[33, 34] Lower dimensional structural motives are also quite often connected via additional *Tr-Tr/Tt-Tt* or *Pn-Pn* bonds or atoms, forming higher dimensional and more complex structures such as $KAlSb_4$ (shown in Abbildung 1.4d), where bridging Sb atoms connect the one-dimensional $AlSb_4$ tetrahedra to a

three-dimensional network.[35]

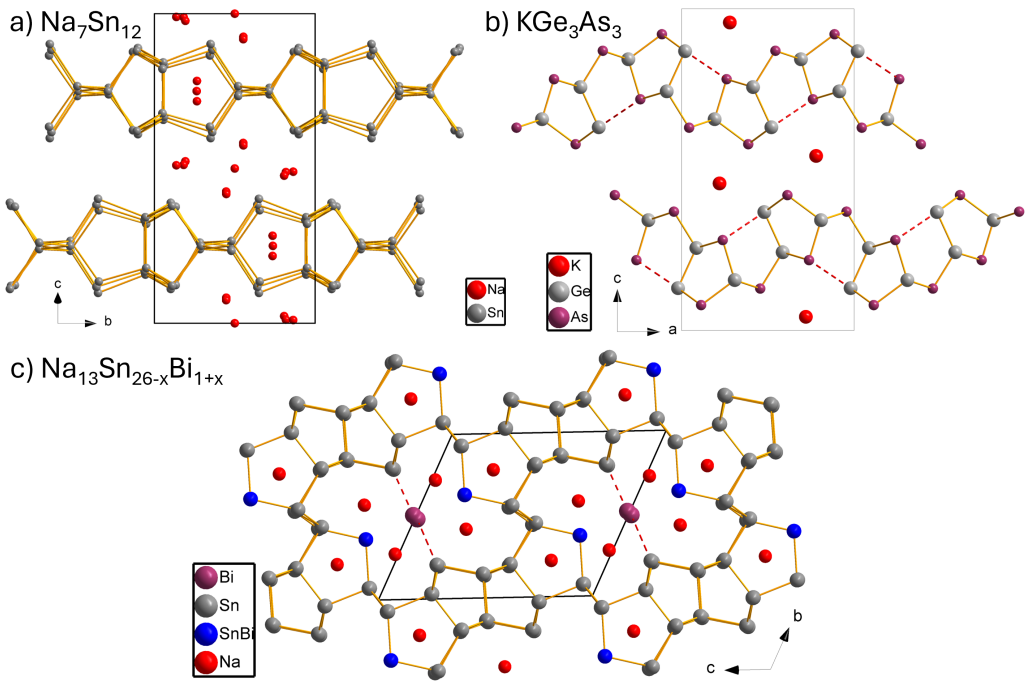

Figure 1.5: Side view of the Crystal structures of a) Na_7Sn_{12}, b) KGe_3As_3, with the long Ge-As interaction of 3.5 Å marked in red, and c) $Na_{13}Sn_{26-x}Bi_{1+x}$.

Other Zintl compounds show even more complex structures, which still can be explained by the Zintl-Klemm concept. Many anionic sub-structures build open frameworks of different dimensions, that are not build by the "classic", e.g. tetrahedral, building units. Na_7Sn_{12} for example forms Sn_5 five-membered rings which are connected to two-dimensional layers (Abbildung 1.5a). [36] The same five-membered clusters, although Sn and Ge are mixed, can be found in KGe_3As_3 (Abbildung 1.5b). They also form two-dimensional layers with bridging As atoms. Interestingly, while for Na_7Sn_{12} the 3.1 Å long distance between two Sn atoms is considered bonding, the long 3.5 Å distances in KGe_3As_3 are not, since they are not necessary to achieve the electron octet. Otherwise additional five-membered, slightly larger clusters, would be formed, leading to layers of edge-sharing clusters.[37] Three-dimensional open framework structures are also found, incorporating again the same five-atom-clusters, as seen for $Na_{13}Sn_{26-x}Bi_{1+x}$, which forms a complex three-dimensional framework with large cavities, in which isolated Bi^{1+x} are located as guest atoms (Abbildung 1.5c).

1.3 Outline of this work

As shown, Zintl compounds are perfect to investigate possible crystal structure - band structure relations, due to the large diversity in crystal structures present. But since there are so many different compounds, that range from binaries to quaternaries, investigations should start with a defined sub-set. Such a set of compounds should consist of a defined number of mutual atoms, for example alkali metal compounds, but none with alkaline-earth metals, have a large number of different structures, with different isomers for the same nominal composition, and should be dividable in even smaller sub-sets with similar compounds, to compare and expand findings.
Since ternary $A_x Tr/Tt_y Pn_z$ Zintl phases show a large variety of possible zero- to three dimensional polyanion structures, with most stoichiometric sub-system having more than one isomer, they are an ideal system for the investigation of correlations between crystal and band structure. Especially identifying properties that influence the occurrence of direct band gaps would be beneficial for an efficient and smart design of highly functional materials in the future. Therefore, all structures of the compounds of the system available in the Inorganic Crystal Structure Database (ICSD), which are suitable for quantum chemical calculation, were optimized and their harmonic frequencies at Γ-point calculated. For each compound band structure and density of states were calculated and a Mulliken population analysis conducted. With this the nature and size of the band gap could be determined for the whole data set. Each compound was further classified by different crystal structure parameters, such as space group and anionic substructure, as well as chemical properties, such as composition and electronegativity of the structure's atoms.
These properties were correlated against the band gap size, for direct and indirect band gaps, and investigated regarding possible trends. The results were further analysed by having a more detailed look at different sub-systems which are limited to specific stoichiometries. Whenever possible the top valence and lowest conduction bands were analysed in more detail, to get a better understanding, which properties are able to influence their shape and thus the kind of and band gap. Since some of the systems are related, for example the triel $A_3 TrPn_3$ and tetrel $A_2 TtPn_2$ systems, their results can be compared to understand, whether effects observed are limited to certain sub-systems or applicable to the whole data set. Therefore, the data presented in the first half of Kapitel 3 is often supplemented by additional structure predictions on the remaining, not yet synthesized compounds of the systems.
Lastly two Zintl compounds were picked to be investigated in more detail. The first one, $Na_{13}Sn_{25.72}Bi_{1.27}$, was picked, since calculations reveal that it shows a phase broadening of

$Na_{13}Sn_{26-x}Bi_{1+x}$, with x = 0-2. The second compound is $CaSi_2$ for which, together with $CaGe_2$, the different polymorphs are energetically compared and possible Si-Ge-mixed compounds modelled. Further on it is shown how a small change in the chemical surrounding, that also includes the coordination of the electropositive Ca atom, has a huge impact on the band structure and electronic properties. Since no $Ca_Si1\text{-}xGe_x$ compounds were reported, the solid solution was also investigated experimentally.

2 Experimental

2.1 Synthesis Methods

2.1.1 Starting Materials

All starting materials were handled and stored in an argon filled glove box (MBraun, $O_2 <$ 1.5 ppm and $H_2O <$ 2 ppm, argon purity 4.8, supplier Westfalen AG). Silicon and germanium were ground into a fine powder by mechanical alloying (Unterabschnitt 2.1.3) and oxide layers on alkali and earth alkali metals were cut off before synthesis.

Table 2.1: Supplier and purity of starting materials.

Element	Purity (%)	shape	Supplier
(Bi) Bismuth	99.999	pieces	ChemPur
(Ca) Calcium	99.5	pieces	Alfa Aeser
(Ge) Germanium	99.999	pieces	Evochem
(K) Potassium	98	chunks	Merck
(Li) Lithium	99	rods	Rockwood Lithium
(Na) Sodium	99	chunks	Chempur
(P) Phosphorus	97	powder	Sigma Aldrich
(Si) Silicon	99.9	balls	Wacker
(Sn) Tin	99.9	powder	Merck
	99.9	pieces	Onyxmed

2.1.2 Ampoule Preparation

Niobium ampoules for synthesis were cut from niobium tubes (10 mm diameter with 0.5 mm wall thickness) into 30 mm to 40 mm long pieces and slightly widened at the ends to ensure that caps fit accurately. Caps for the ampoules (0.5 mm thickness, punched from Nb sheets) were cleaned together with the ampoules in an ultrasonic bath, where they were sonicated for 15 min each in acetic acid, water and lastly acetone. They were dried in a drying cabinet

for 1 h.
Bottom caps were attached by arc welding. After sample weighting the ampoule was sealed airtight by squeezing the open end flat and subsequent arc welding.

2.1.3 Mechanical Alloying

Fine powders of Si and Ge were prepared before synthesis by mechanical alloying in Retsch PM100 planetary ball mill. 25 g to 30 g Si/Ge are weighted into an 80 mL WC jar with 25 balls with a diameter of 1 mm. The jar is closed within an argon filled glove box. The milling program was set with the following parameters: rotational speed of 250 rpm, duration of 6 h with resting periods of 3 min every 5 min.

2.1.4 Arc-Furnace Synthesis of $CaSi_{2-x}Ge_x$

Samples of the nominal composition $CaSi_{2-x}Ge_x$ were prepared for x = 0, 0.5, 1, 1.5, and 2 in an Argon filled glove box. Accordingly, stoichiometric amounts of Ca, Si and/or Ge were weighed. Pellets with Ca chunks embedded in the Si and/or Ge powder were pressed in a hydraulic press (*Specac*) with a pressure of 2 t. The pellet was consecutively melted, in a water-cooled copper heart, with an arc furnace (MAM-1, *Edmund Bühler GmbH*). The regulus was then ground in an agate mortar, pressed into a pellet again and molten twice in the arc furnace to get a phase pure product.

2.1.5 High Temperature Synthesis

For the synthesis the previously prepared Nb-ampoules were put in silica tubes which were evacuated ($<10 \times 10^{-3}$ mbar) and flushed with argon three times to prevent ampoule oxidation by residual air. The tubes then are vertically put in a tube furnace with resistance heating (HTM Reetz LOBA 1200-40-600). Depending on the compound an appropriate temperature program was chosen for synthesis, programmed by an Eurotherm 2416 controller. The first heating step was chosen so that all reactants and possible (binary) first reaction products are in a liquid state. This temperature is normally held for a couple of hours to ensure a homogenic distribution of the elements. Afterwards the reactive mixture is cooled either directly to room temperature or slowly to an intermediate temperature, for single crystal growth.
Reaction products are then isolated by opening the ampoules inside the glove box and are stored in small mostly air tight sample containers.

2.2 Characterization

2.2.1 Powder X-Ray Diffraction

For powder X-ray diffraction (PXRD) measurements, the sample was ground in an agate mortar and sealed in a 0.3 mm glass capillary. PXRD measurements were performed at room temperature on a Stoe Stadi P diffractometer equipped with a Ge(111) monochromator for Cu $K_{\alpha 1}$ radiation ($\lambda = 1.540\,56$ Å, $2\,2\theta$ to $90\,2\theta$) and a MYTHEN DCS 1K detector (Dectris). For compounds containing Sn an identical diffractometer equipped with a Mo $K_{\alpha 1}$ radiation source ($\lambda = 0.710\,73$ Å), $2\,2\theta(\mathrm{deg})$ to $50\,2\theta(\mathrm{deg})$) was used.
Short measurements, used for phase analysis, were measured for 15 min with a step size of 0.015 and 3 s per step. Measurements for Rietveld-refinements were measured for 12 h with a step size of 0.015 and 12 s per step.
The raw powder data was processed with the software package WinXPOW.[38]

2.2.2 Rietveld Refinement

Structure refinements by the Rietveld method of both laboratory and synchrotron X-ray diffraction data were conducted using the Fullprof programme package.[39] Starting models of the atomic positions were taken from literature data of compounds with the same crystal structures, while the cell parameters wee refined using the Werner indexing algorithm of the software WinXPow. [38] Profiles were fitted using the Thompson Cox Hastings profile function. The Cagliotti parameters (*U, V, W*), corresponding to the respective instrumental resolution as well as peak shape asymmetries and zero shifts were determined beforehand by a full refinement of externally measured LaB_6 standards. For the structure determination sample displacement, cell parameters, microstrain and size parameters, atomic positions occupations and thermal displacement parameters were freely refined. The background was corrected using interpolating background points.

2.2.3 Single Crystal X-Ray Diffraction

The single crystal X-ray diffraction (SCXRD) measurement was performed on a Stoe Stadivari diffractometer equipped with a micro source (GENIX, Mo $K_{\alpha 1}$ radiation, $\lambda = 0.710\,73$ Å) and a PILATUS 300 K detector (Dectris) at 150 K K. Single crystals were sealed in a 0.3 mm glass capillary in an argon-filled glove box.

The structure was solved by Direct Methods (SHELXS) and refined by full-matrix least-squares calculations against F^2 (SHELXL).[40, 41] Data reduction and multi-scan absorption correction were carried out with the X-AREA (version 1.88, Stoe) and the STOE LANA (version 1.77.1, Stoe) software packages, respectively.[42]

2.2.4 Synchrotron Powder X-Ray Diffraction

Powder X-ray diffraction patterns for the $CaSi_{2-x}Ge_x$ samples were collected using the Canadian Brockhouse X-ray Diffraction and Scattering (BXDS) high energy wiggler beamline (WHE) at the Canadian Light Source (CLS).[43] WHE employs a Si (111) side bounce Laue monochromator and data sets were collected using a photon energy of ~30.3 keV (calibrated wavelength, $\lambda = 0.408\,67$ Å) and a sample-detector distance of ~496.4 mm. Two-dimensional (2D) diffraction patterns were collected on a Perkin Elmer XRD 1621 CN3 EHS detector with an active area of 409.6 mm x 409.6 mm, and a pixel size of 200 µm^2.
The 2D PXRD patterns were calibrated and integrated using the GSASII software package.[44] The sample-detector distance, detector offset and detector tilt were calibrated using an image from a lanthanum hexaboride (LaB_6) standard reference material (NIST SRM 660a LaB_6) and the calibration parameters were applied to all patterns prior to integration.[45] After calibration, the 2D patterns were integrated to obtain standard point detector powder diffraction patterns.
For the measurement, polycrystalline powders were sealed within glass capillaries (ø0.5 mm, 0.01 mm wall thickness).

2.2.5 Differential Scanning Calorimetry

For thermal analysis, small samples of reaction products are sealed in a niobium ampoule and measured on a differential scanning calorimetry (DSC) machine (Netzsch, DSC 404 Pegasus) under a constant gas flow of 75 mL min^{-1}. The samples are heated to 500 °C to 1000 °C (depending on the range where signals are expected) and cooled to 100°C twice at a rate of 5 K min^{-1}. Results are plotted and evaluated by a self-written python script.

2.2.6 Raman Spectroscopy

Raman spectra of the bulk material of were measured using an inVia Raman microscope (Renishaw, RE04), equipped with a CCD detector. The powdered sample was sealed into a 0.5 mm glass capillary and irradiated with a 785 nm laser beam for 1 s at 1 % laser power using

a microscope equipped with a 50-fold magnifying objective and a grating with 1800 line/mm. For the final spectra 100 single measurements were averaged. The software WiRe 4.2 (build 5037, Renishaw 2002) was used for data recording.[46]

2.3 Computational Methods and Visualisation

2.3.1 Level of Theory

All calculations were done with the program Crystal17, which can perform *ab initio* calculations of ground state energy, energy gradients, electronic wave functions and properties of periodic systems.[47, 48] The dimensionality of the periodic systems range from molecules to three dimensional crystal structures, for which the fundamental approximation is made by single particle wave functions, built by linear combinations of Bloch functions defined as local functions (atomic orbitals). For the atomic orbitals, Gaussian type functions with *s, p, sp, d, f* and *g* symmetry are used (further called basis sets).
For all calculations basis sets were provided by literature, with varying level. For all atoms, except for the alkali metals, Gaussian-Type triple ζ-valence + polarization level basis sets were used (TZVP), which were derived from the molecular Karlsruhe basis sets. To reduce the cost of calculations for the alkali metals, only split valence and polarization level basis sets (SVP) were used, since this basis set size is suitable enough to the describe the influence of the, mostly ionic, interactions of the alkali metals with their neighbouring atoms. For heavier atoms, to slightly reduce computation time and take scalar relativistic effects into account, an effective core potential (ECP)for the inner shells (all but the last two electron shells) was applied.

Crystal17 has Hartree-Fock and different (hybrid) density functional methods build-in, but for all calculations a hybrid exchange-correlation functional after Perdew, Burke, and Ernzerhof (DFT-PBE0) was used.[63] This method has proven to be a good compromise between accuracy and computation time, and was used in previous works for the calculations of band gaps in the discussed material class.
For the evaluation of Coulomb and exchange integrals (TOLINTEG), tight tolerance factors of 8, 8, 8, 8, 16 were used for all calculations. The reciprocal space of compounds was sampled using Monkhorst-Pack-type *k*-point grids. For all calculations, as a rule of thumb, the k-mesh (SHRINK) was chosen such that the real space primitive cell edge times the SHRINK factor is at least 30 Å, which has been proven to be a good compromise between

Table 2.2: Basis set sources and Level of theory for each atom. Basis sets, that include an effective core potential are marked with ECP.

Element	basis set size		Element	basis set size		Element	basis set size	
Li	SVP	[49]	B	TZVP	[50]	P	TZVP	[51]
Na	SVP	[52]	Al	TZVP	[49]	As	TZVP	[53]
Na	TZVP	[54]	Ga	TZVP	[55]	Sb	TZVP, ECP	[53]
K	SVP	[52]	In	TZVP, ECP	[56]	Bi	TZVP, ECP	[57]
Rb	SVP, ECP	[58]	Si	TZVP	[59]	Ta	TZVP	[60]
Cs	SVP, ECP	[52]	Ge	TZVP	[61]			
			Sn	TZVP, ECP	[62]			

accuracy and computational cost. For some calculations denser k-meshes were used, for example if the Fermi-Level was not calculated precise enough and the top valence band was intersected thereby.

2.3.2 Crystal Structure Optimization

For all calculations the input geometry was taken from experimental data provided by the Inorganic Crystal Structure Database (ICSD).[64] The information on cell parameters and atomic positions were extracted by the cif2cry tool and cross-checked with the crystallographic information file (cif). For each compound the unit cell generated by the Crystal17 program and the published cell were controlled, to make sure all atomic positions were transferred from the original cif. For some compounds an origin shift thus had to be applied, to match the published structure. For compounds with split or mixed crystallographic atom positions, ordered models were created by lowering the symmetry or, if atomic positions were not fully occupied, by combining two or more positions into an averaged one or rounding some occupations up to 1, to match the sum formula of the compounds. After optimization cell parameters of the calculation are compared to the published experimental cell parameters. If larger deviations occur, they often arise from anisotropy within the crystal structure, such as layered structural motives with weak interactions between layers, or large errors on the experimental cell parameters.

The experimental and optimized crystal structures are also compared to see if larger deviations in atomic positions occur. Therefore original and optimized atomic positions are combined in one cif file and looked at with the crystal structure visualization program Diamond.[65] Here most atoms show only small deviations to their original position, only alkali metals sometimes "wander" a bit from there original position. But this is within the expected range, considering their large distances to the *Tr/Tt-Pn* structure and presumably ionic interactions.
For each compound harmonic frequencies were calculated at the Γ-point to check whether the optimized crystal structure is a true local minimum on the potential energy surface. If no imaginary frequencies are found, this is deemed to be true. If imaginary frequencies occur, the optimized crystal structure is distorted along the largest such frequency. The resulting structure, sometimes with lower symmetry, is optimized again. This is repeated until all imaginary frequencies vanish.

2.3.3 Electronic Properties Calculation

Electronic properties calculated for each compound include the band structure, density of states, crystal orbital Hamilton population and a Mulliken population analysis.

Band Structure The Brillouin Zone paths used for band structure calculations are provided by the web service *SeeK-path*.[66] For most compounds the path provided was directly used, while for the rest some corrections have been made. Three cases mainly occurred: For space groups, where the coordinates of the *k*-points depend on the cell parameters, the proposed shrinking factor is often too large for the input, therefore the coordinates were adapted to a shrinking factor of 1000. The second correction occurred, if two *k*-points are too close to each other such that the number of data points calculated between them is very small. These paths were then excluded from the calculation, since no information could be obtained from them. This sometimes lead to a rearrangement of the order of *k*-points, to reduce the number of jumps. The last case occurred for compounds, which show a doubled *k*-path with additional points for systems, that do not have time reversal symmetry, which does not apply to our systems. The second half of theses *k*-paths was therefore not calculated.
The total number of data points calculated along the path equals 100 data points per step, which are automatically arranged according to the length of the path. The standard number of bands plotted includes 20 bands below and above the band gap, but was adjusted for comparability and if bands showed a very large or very low dispersion.

Density of Sates (DOS) For the density of states the number of points for which the eigenvectors are calculated is quadrupled (doubled if the original k-mesh had to be doubled) for a more accurate DOS and determining the Fermi-Level. The energy range of the DOS is the same as for the band structure and a total of 800 to 1000 data points are calculated fo each projection. 12 Legendre polynomials are used for the Fourier-Legendre technique to expand the DOS. Multiple options for the projection of the DOS are given, for example atom, crystallographic position or orbital projected DOS. The first is usually applied to see the energy ranges for which the different elements show their states. The other projections are used, if additional information on the distribution of states is needed.

Crystal Orbital Hamilton Population (COHP) The COHP gives an insight on how much interaction between the different atoms is present. The "standard" calculation includes the interaction for all heteroatomic interactions, namely between *A*-*Tr*/*A*-*Tt*, *A*-*Pn* and *Tr*-*Pn*/*Tt*-*Pn* (with *A* = alkali metal, *Tr* = triel, *Tt* = tetrel, *Pn* = pnictogen), for which all atomic positions of each atom are selected. They can also be reduced to, for example, atomic interactions for which chemical bonds are formed. The number of interacting atomic positions is then reduced accordingly. Also a look into orbital specific interactions is possible. If the interaction of atoms of the same Wyckoff position need to be investigated, they must not include interactions between atoms of the same atomic number, since they give no reasonable results.

Mulliken Population Analysis A Mulliken analysis is mainly used to get an insight on two properties. On one hand Mulliken charges can be determined which give an insight on the charge distribution within the unit cell. The Mulliken charge is determined by the difference of electrons in the basis set minus the number of electrons located at the atomic position. On the other hand overlap populations can be calculated, which give an insight on the strength of interaction between neighbouring atoms.[67] If the overlap is larger than 0.2 (value was chosen empirically) and the distance small enough, chemical bonds can be assigned to the interaction. Small overlap populations are interpreted as mostly ionic interactions and negative values as repulsion of adjacent atoms.

2.3.4 Calculation of Theoretical Raman Spectra

Using the results of the frequency calculation, theoretical Raman spectra can be calculated. Therefore an analytical coupled perturbed Hartree-Fock/Kohn-Sham scheme (CPHF/CPKS) is used. The full width at half maximum (FWHM) is set to $8\,\mathrm{cm}^{-1}$ and the pseudo-Voigt broadening to 50:50 Gaussian:Lorenzian. The laser wavelength is set to 785 nm, which is the same as at the measurement device. To assign signals in the spectrum to vibrations of the lattice, the software Jmol is used for visualizing of the theoretical vibration modes.[68] To account for the overestimation of the theoretical Raman at high wave-numbers, the wave-numbers are scaled by a factor 0.95.

2.3.5 Overview of Python Scripts for Data Visualisation

To visualize the calculated data different plotting functions were written in Python, which are listed below with a short description of the arguments available to customize the plots.

Band Structure and Density of States The function takes the band structure .BAND and density of states .DOSS files generated by Crystal17 as input and plots them next to each other. The *k*-path used for calculation, the upper and lower energy range for the band structure and DOS, labels and plotting colours for the projected DOS curves, the plot's title and the path for saving the graphic have to be set as arguments. Optional arguments include a scaling factor for the x-axis of the DOS, options to mark the top valence band and lowest conduction band, as well as the valence band maximum (VBM) and conduction band minimum (CBM), and an option to cut off the y-axis within the energy range of the band gap or to zoom into the band structure in a separate plot. Additional options for the saved plot are setting the resolution and file type. The function calculates the minimal difference between valence and conduction bands (band gap size) as well as the transition at Γ and prints them in the console, for the number of the specified top valence band. The Fermi-Level as well as the top of the band gap are marked by a red line and a grey dashed line, respectively. If the energy range for the band structure and DOS are different, the function automatically marks the range plotted for the DOS in the band structure. If the argument for a second zoom into the band structure is set, an additional plot is attached on the left side, again with a highlight of the plotted section.

Crystal Orbital Hamilton Population (COHP) This function can plot the COHP/COOP data calculated. As arguments the labels for the projected COHPs/COOPs, their colours and

the energy range for the plot have to be set. The "set-mode" refers to the kind of data that is to be plotted (e.g. COHP, COOP, DOSS) and sets the x-axis label. If a minus is added the x-axis is inverted. Optional arguments include setting a title, a limit for the x-axis and to add a dashed line at the top of the band gap. For saving the plot, additional arguments include setting the resolution, file type and folder, where the plot is saved. The Fermi-Level is marked by a red line automatically.

Mulliken Population Analysis This script extracts information provided by a Mulliken population analysis and saves it as a LaTeX-table and/or simple data file. Arguments to set are the folder, where the Mulliken population analysis data from CRYSTAL are stored, as well as its file name. By default, only the overlap populations are extracted. Optional arguments include adding the name of the compound, a filename and folder for the output, to change the caption and labels of the LaTeX-tables and options to also extract the Mulliken charges or to reduce the overlap population data by skipping duplicates. If charges are to be extracted, the elements and their number of electrons in the basis set have to be specified.
To support the functions above a small function to format (simple) chemical formulas was written. All other data or measurement plots used in the thesis are also programmed with python.

2.4 Contribution of Co-Authors

The following table contains all papers and manuscripts

Table 2.3: Contribution of Co-Authors for each paper/manuscript.

Electronic Structure Analysis of the $A_{10}Tt_2P_6$ System (A = Li Cs; Tt = Si, Ge, Sn) and Synthesis of the Direct Band Gap Semiconductor $K_{10}Sn_2P_6$ [69]	
Viktor Hlukhyy	Solution of the single crystal
Hanna Antoniuk	Primary synthesis of the compound and preliminary DFT calculations
Large Number of Direct or Pseudo-Direct Band Gap Semiconductors among A_3TrPn_2 Compounds with A = Li, Na, K, Rb, Cs; Tr = Al, Ga, In; Pn = P, As [26]	
Yulia Kusnetsova	Preliminary DFT calculations and ChemDraw schemes
Electronic structure analysis of the $A_2Tr/TtPn_2$ system with A = Li-Cs; Tr = Al-In; Tt = Si-Sn; Pn = P-Sb	
Zoe Listmann	Preliminary DFT calculations
Electronic structure analysis of A_6TrPn_3 compounds with A = Rb, Ca; Tr = Al, Ga, In and Pn = As, Sb	
Hanna Antoniuk	Preliminary DFT calculations
Electronic structure analysis of the ATt_3Pn_3 system with A = Li-Cs; Tr = Al-In; Tt = Si-Sn; Pn = P-Sb	
Yulia Kusnetsova	Preliminary DFT calculations
Electronic structure analysis of compounds of $A_2Tr_2Pn_3$ compounds with A = Na Cs; Tr = Al, Ga, In; Pn = As, Sb	
Zoe Listmann	Preliminary DFT calculations
Electronic property calculation of $ASnPn$ compounds with A = Na, K and Pn = P, As, Sb	
	no contributions
Open Sn Framework Structure Hosting Bi Guest atoms – Synthesis, Crystal and Electronic Structure of $Na_{13}Sn_{26}Bi$	
Marina Boyko	Synthesis and refinement of the published single crystal
Simeon Ponou	Synthesis, powder diffraction and solution of the first single crystal
Viktor Hlukhyy	Helped with solution and refinement of the single crystals
$CaSi_{2-x}Ge_x$, solid solution and analysis of ordered structure	
Alexander Mutschke	Fine-tuning of the Rietveld refinements
Contributions as Co-author:	
$Na_3Ge_2P_3$: A Zintl Phase Featuring [$P_3Ge-GeP_3$] Dimers as Building Blocks	
[70]	DFT calculations (incl. analysis and discussion)
Synthesis, Structure and Physical Properties of the Sodium-Rich Phosphidogermanate Na_8GeP_4	
[71]	DFT calculations (incl. analysis and discussion)
Direct Band Gap Semiconductors with Two- and Three-Dimensional Triel-Phosphide Frameworks (Triel=Al, Ga, In)	
[72]	DFT calculations (incl. analysis and discussion)
Synthesis, Crystal structure, electronic structure, and Raman spectra of $Li_4Sr_2SiP_4$	
[73]	DFT calculations (incl. analysis and discussion)
Aliovalent substitution in phosphide-based materials – Crystal structures of $Na_{10}AlTaP_6$ and Na_3GaP_2 featuring edge-sharing EP_4 tetrahedra (E = Al/Ta and Ga)	
[74]	DFT calculations (incl. analysis and discussion)

3 Results and Discussion

3.1 Analysis of Crystal Structure - Band Structure Relationships

3.1.1 Data Set and Parameter Overview

In the Inorganic Crystal Structure Database (ICSD) contains about 200 crystal structures of Zintl phases of the A_xTr/Tt_yPn_z system (with A = Li-Cs, Tr = B-Al, Tt = Si-Sn, Pn = P-Bi). Among those, compounds with mixed or not fully occupied positions were not considered for the calculations, as were compounds, where the calculations could not be completed within a reasonable time with the given computational infrastructure, due to too large unit cells with low symmetry. Thus for 143 compounds band structure, density of states (DOS), and crystal orbital Hamilton populations (COHPs) for specific interatomic interactions within certain compound systems were calculated. Subsequently crystal structure optimisation and frequency calculations were performed.
For these compounds as "data set", different chemical and crystal structure specific properties were investigated regarding their influence on the band structure, band gap (size and kind) and DOS. The investigated chemical properties include the elemental and stoichiometric composition, electronegativity differences, Mulliken partial charges and overlap populations of neighbouring atoms. As for aspects of the crystal structure, the influence of the symmetry (space group) and the (poly)anionic substructure (dimension and connectivity) were studied. The following sections summarize the collected data and give an overview of trends observed. Detailed information on each compound's crystal structure, calculated band structures and DOS, as well as tables obtained by the Mulliken population analysis, can be found in the Appendix under each compound's stoichiometry.
The following plots will all use the same colour code for direct (green), indirect (red) and pseudo-direct (purple) band gaps and the same symbols for the data points, depending on the alkali metal: △ Li, □ Na, ○ K, ◊ Rb and ☆ Cs.

3.1.2 Influence of the Composition

141 of all 143 calculated compounds are semiconductors with band gaps spanning from 3.39 eV (K_3BP_2) to 0.44 eV (Na_3InBi_2). Only two compounds, namely $NaSn_2As_2$ and $NaGe_6As_6$, show metallic characteristics. Tabelle 3.1 gives an overview of the distribution of direct, indirect and pseudo-direct band gaps by incorporated elements in absolute and relative numbers.

Table 3.1: Overview of the distribution of direct, indirect and pseudo-direct band gaps by composition with absolute numbers and in percent.

	absolute numbers				percent		
Element	direct	indirect	pseudo-direct	sum	direct / %	indirect / %	pseudo-direct / %
Li	19	6	1	26	**73.1**	23.1	3.8
Na	11	22	5	38	28.9	**57.9**	13.2
K	14	19	2	35	40.0	54.3	5.7
Rb	8	10	0	18	44.4	55.6	0.0
Cs	4	11	**9**	24	16.7	45.8	37.5
	56	68	17	141			
B	0	7	0	7	0	100	0
Al	10	8	3	21	47.6	38.1	14.3
Ga	7	11	5	23	30.4	47.8	21.7
In	14	4	4	22	**63.6**	18.2	18.2
	31	30	12	73			
Si	6	14	1	21	28.6	**66.7**	4.8
Ge	4	14	2	20	20.0	**70.0**	10.0
Sn	12	10	3	25	48.0	40.0	12.0
	22	38	6	66			
P	28	25	4	57	49.1	43.9	7.0
As	14	28	5	47	29.8	**59.6**	10.6
Sb	12	14	7	33	36.4	42.4	21.2
Bi	2	1	1	4	50.0	25.0	25.0
	56	68	17	141			

The type of band gap is calculated in the output of the density of states calculation, which assigns direct or indirect band gaps to all semiconducting compounds. The result is compared

with the band gap shown in the band structure diagram, and in most cases they coincide. Pseudo-direct band gaps are assigned if the band gap at Γ is less than 0.02 eV larger than the assigned indirect band gap. This threshold was chosen empirically. They are also referred to as case one pseudo-direct band gaps below. The second case of pseudo-direct gaps are compounds, for which the valence band maximum and conduction band minimum are close to each other on the same *k*-path and therefore an almost direct transition between valence and conduction band is possible. For the data set only the first case of pseudo-direct band gaps were assigned, if not noted otherwise.
Looking closer at the band gap distribution in Tabelle 3.1, some values seem to stand out, so they are marked in bold. While the distribution of direct and indirect band gaps is almost equal among K and Rb compounds, Li compounds show more direct and Na compounds more indirect band gaps, with 73.1 % and 57.9 % each. Furthermore, a total of 9 Cs compounds show a pseudo-direct band gap, which is with 37.5 % of all Cs compounds, twice the amount of all other elements. As for the triel and tetrel atoms, In compounds seem to show more direct and Si and Ge more indirect band gaps with 63.6 %, 66.7 % and 70.0 %, respectively. For the pnictogen only As shows with 59.6 % more indirect band gaps. Finally, as a general trend, the occurrence of pseudo-direct band gaps seems to increase for heavier elements.

Abbildung 3.1 gives an overview of the band gaps of all calculated compounds, sorted by alkali metal. Each column is further subdivided by the pnictogen atom present. From the range of the band gaps for each alkali metal it can be seen, that the band gap ranges decreases significantly from phosphides to antimonides. For example, comparing compounds that have the same stoichiometry and elements but differ in their pnictogen, the band gaps for phosphides are about 0.5 eV larger than the corresponding arsenides and about 1 eV larger than the antimonides. Excluding the boron compounds, a similar trend can be seen for the alkali metals, where Li compounds have the largest band gaps and Rb and Cs compounds the smallest, but the absolute differences are smaller.

In Abbildung 3.2 all calculated band gaps are plotted against their composition. At first sight, ignoring possible different crystal structures for each composition, compounds with an 8-1-4/9-1-4/7-1-4, 1-1-4 and 3-1-2 *A-Tr/Tt-Pn* composition seem to have more direct band gaps, whereas 6-1-3, 2-1-2 and 1-3-3 have more indirect band gaps. The remaining compositions show no preferred band gap type. Looking closer at the different crystal structure types in each group, that show more direct band gaps, the 8-1-4/9-1-4/7-1-4 and 1-1-4 groups are very similar. For the latter, one structure type is present. There are ten different crystal

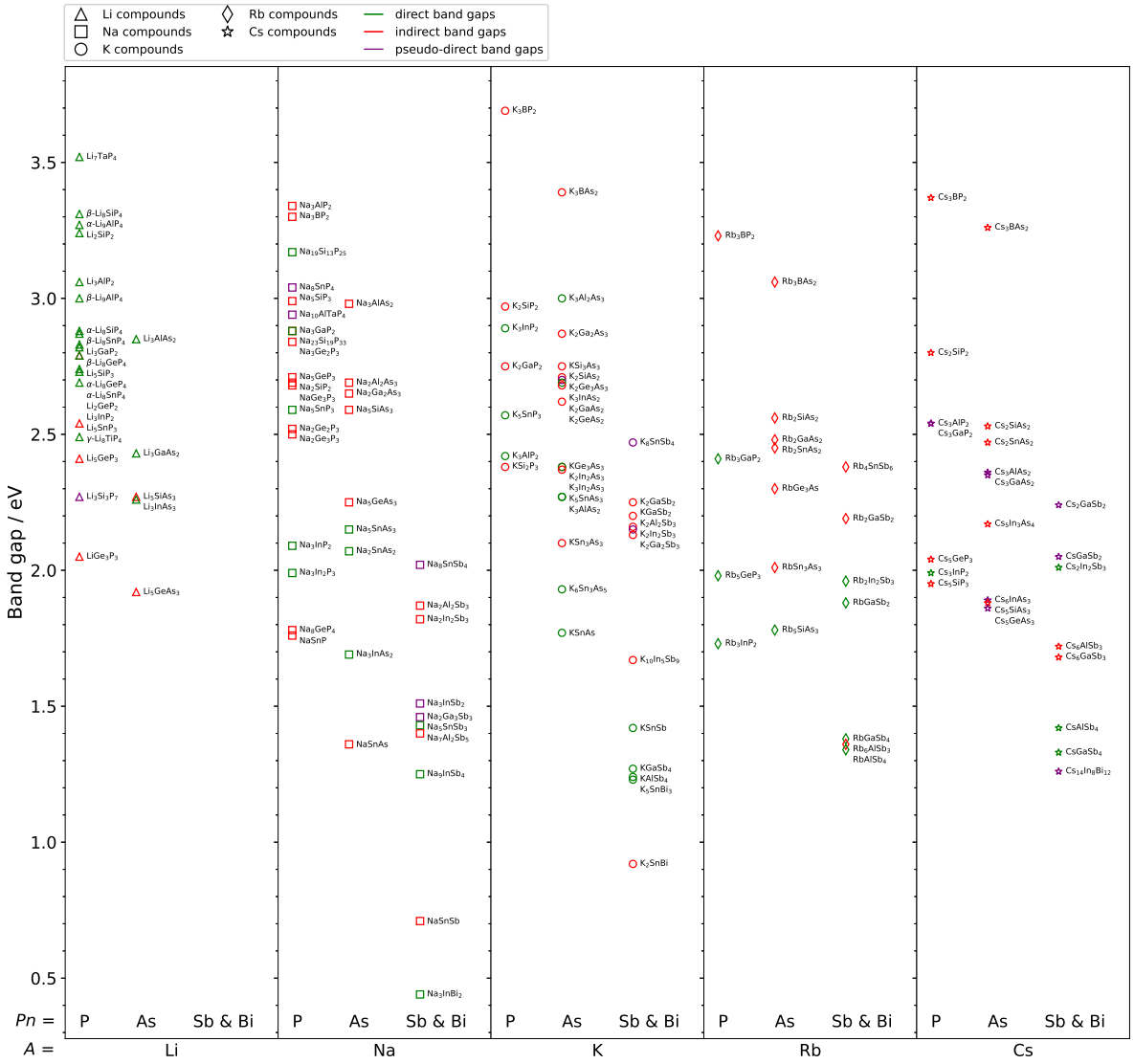

Figure 3.1: Band gaps plotted against the alkali metal and pnictogen present.

structures for the 3-1-2 composition, but indirect band gaps have only been calculated for two of them. This suggests that either the composition or the crystal structure may be an important factor in determining the nature of the band gap. Certainly, one expects that the symmetry and thus the crystal structure determines the nature of the band gap, however there are other systems such as the 1-1-1 compounds, for which indirect band gaps are calculated only for Na compounds, and the 5-1-3 system, for which direct and indirect band gaps are found for both structure types. These observations consequently indicate an influence of the elements in the compounds on the band gap nature. Therefore, the relationship between structure type and direct/indirect band gaps will be discussed later for selected compositions

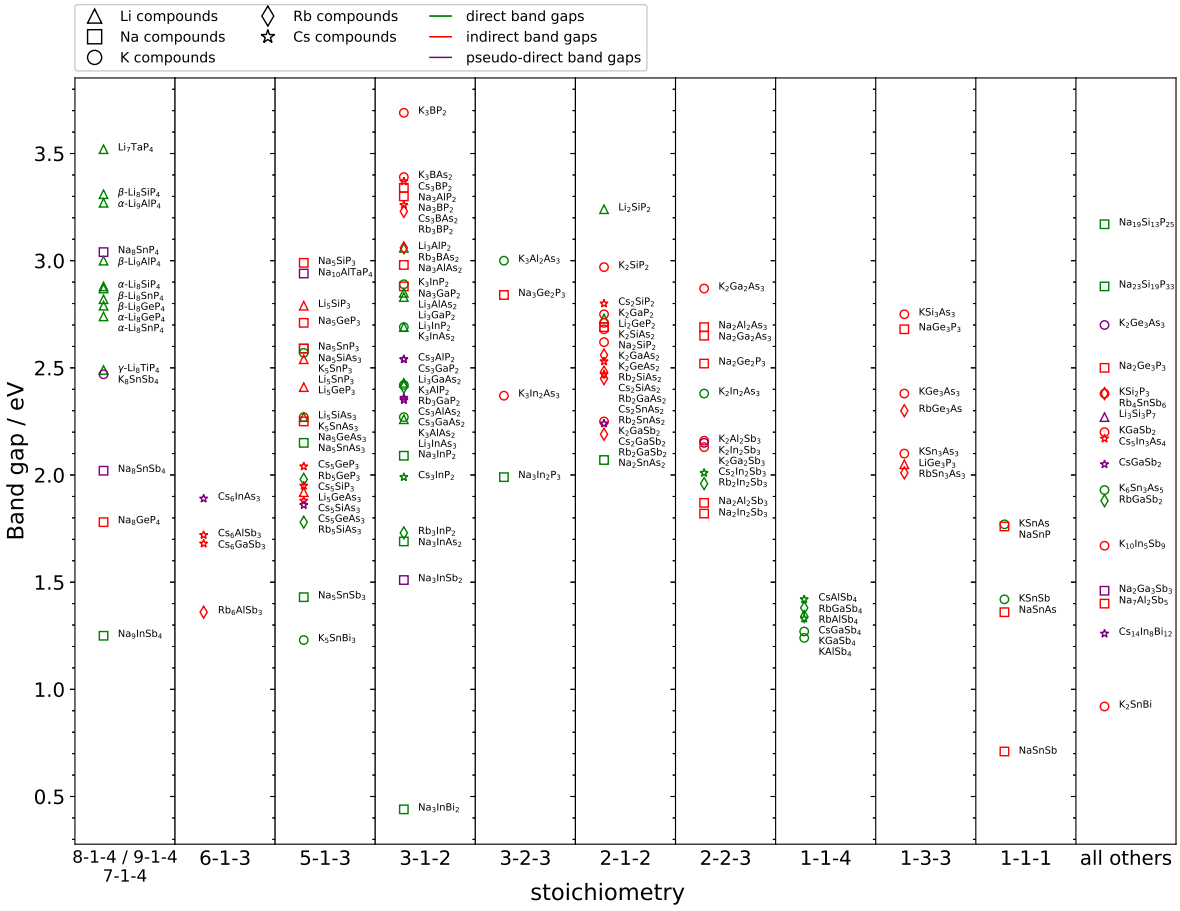

Figure 3.2: All calculated compounds with the band gaps plotted against the composition.

later on.

Lastly Abbildung 3.3 shows the dependence of the band gap on the mole fraction of each atom. The mole fractions of the alkali metal and tetrel show no real trend, but for the triel and pnictogen one could interpret, that the phosphide band gaps decrease and the arsenide and antimonide gaps increase with the an increasing amount of them. However, since the band gaps for one composition are already spread over a large interval as shown above, this trend should not be taken as more than a rough estimate.

To sum up the influence of the (atomic) composition on the occurrence of direct, indirect and pseudo-direct band gaps the following trends could be observed. On one hand, direct band gaps are preferred for certain elements, but they also depend on composition and crystal structure type. Two examples are given by the Li and Na compounds: For Li almost three fourths of the compounds show a direct band gap, and half of them have the same structure

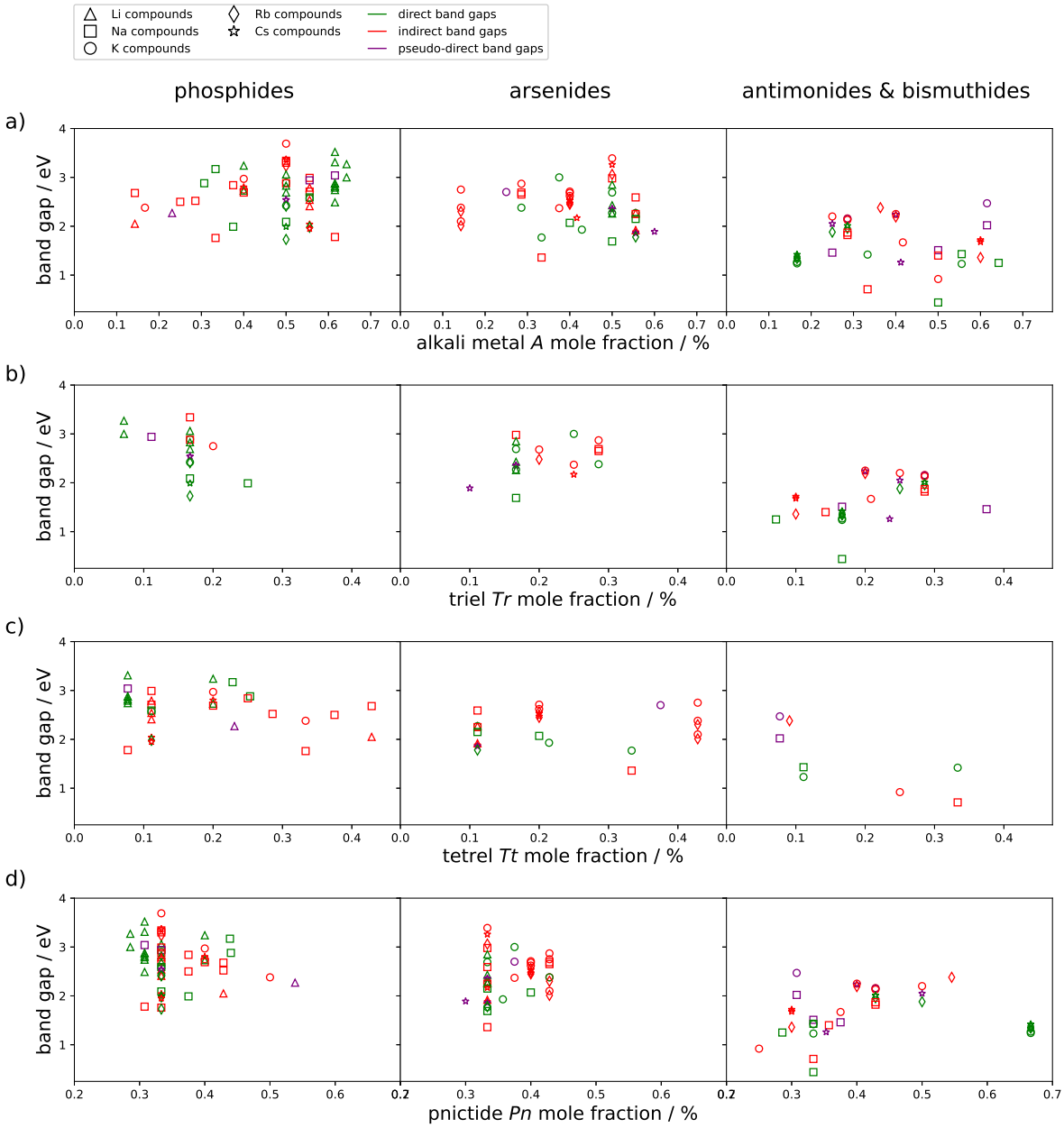

Figure 3.3: a), b), c) and d), show band gap dependence on the mole fraction of the alkali metal, triel, tetrel and pnictogen, respectively. Each subplot is further divided by the pnictogen present.

type. This is in favour that the structure type has a large influence on the nature of band gap. Na compounds on the other hand show more indirect band gaps that also occur, if the compounds have the same composition and structure type as other elemental combinations. One example are the K compounds within the 1-1-1 and 3-1-2 systems, that have direct band gaps, while their corresponding Na compounds have indirect and gaps. This suggests, that

certain elements might have an influence on the nature of the band gap. The occurrence of pseudo-direct band gaps further on increases with the presence of heavier atoms, especially at the alkali metal position. Here no real dependence on any crystal structure type is observed. The size of the band gap seems to be mainly influenced by the elemental composition. The pnictogen atom seems to have the largest influence, since comparable compounds differ about 0.5 eV in band gap size. This is also represented by the mole fraction of the different atom classes, where mainly triel and pnictogen atoms seem to have an effect. The ratio of the elements of a given combination and structure type seem to have only a limited influence on the band gap size, since the gaps within a given element combination span over a wide range and, with minor exceptions, follow the trends discussed for the elemental combination.

3.1.3 Influence of the Crystal Structure

As a first and pretty easy approach the influence of the crystal structure's space groups is investigated. Therefore in Abbildung 3.4 all band gaps are plotted against their crystal structure's space group number, grouped in their respective crystal system, to get a quick insight on possible relationships.
At first sight, the number of compounds crystallising in monoclinic and orthorhombic crystal system is striking, accounting for more than two thirds of all compounds. This coincides with the general distribution of space groups among the inorganic crystal structures recorded in the ICSD data base.[75] Looking at the distribution of direct and indirect band gaps, triclinic, tetragonal and cubic crystal systems seem to strongly generate direct band gaps. For the compounds adapting cubic crystal systems, this can be explained by them having very similar crystal structures and compositions (all have compositions of 7-, 8- or 9-1-4). For the monoclinic and tetragonal crystal systems, there are at least 3 different structure types and compositions present. This could hint for this compound family towards some kind of correlation between space group and band gap, but as a number of 143 compounds is still small for a data set, it should not be treated as more than a hunch.

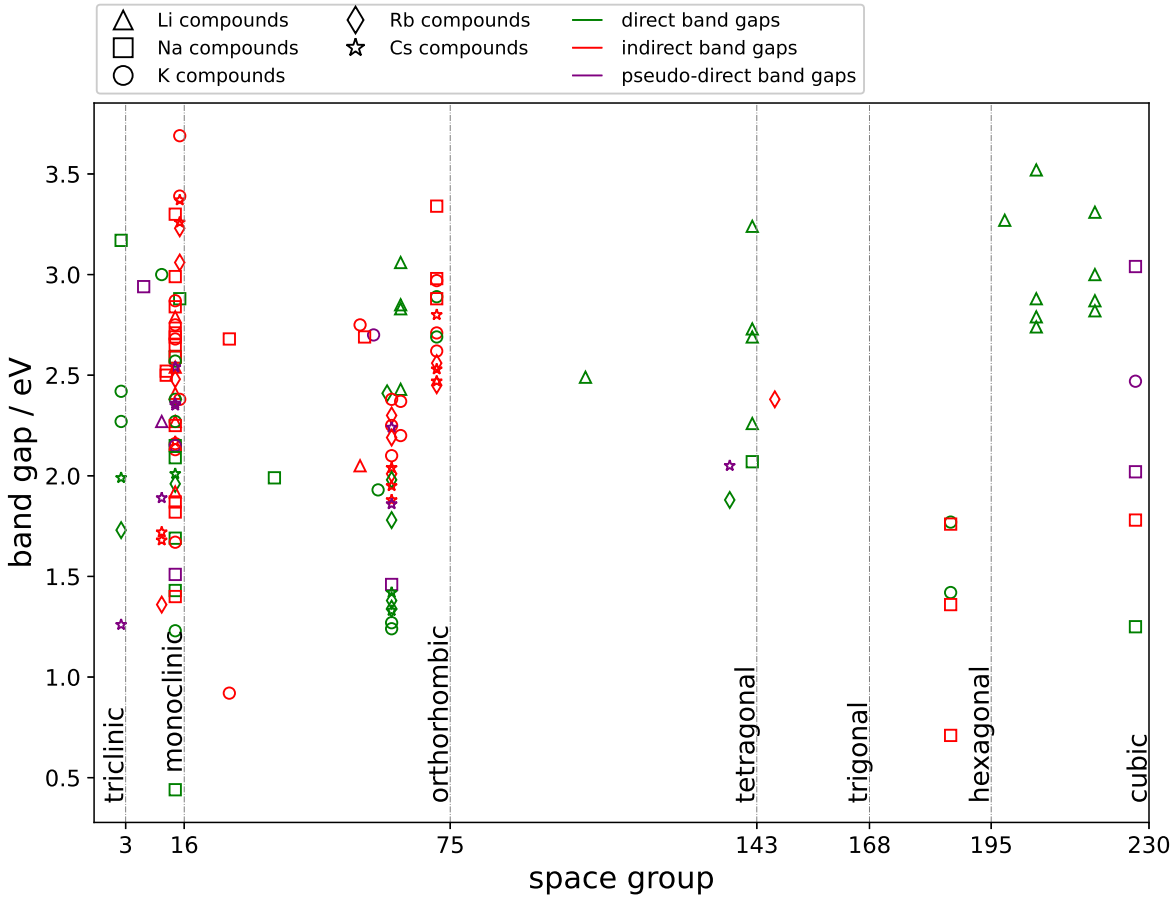

Figure 3.4: Band gaps plotted against their respective crystal structure's space group.

To gain more insight into how the crystal structure influences the size and nature of the band gap, all compounds were further classified by their (poly)anionic substructure. The alkali metal cations and their positions within the structure are not further investigated here, since they are considered to be just electron donors according to the Zintl-Klemm concept and therefore mostly seen as positive point charges in a first approach.[13] For a more detailed discussion on their influence, see the crystal structure specific discussions in the sections below.

Abbildung 3.5 shows the band gap plotted against the dimension of the anionic substructure, represented by 0D for molecule like units, 1D for one-dimensional chains, 2D for two-dimensional layered and 3D for three-dimensional structures, with further differentiation by the structural motive, tetrahedra (T_d) or planar triangles (pT). Compounds which show two different dimensions within their structure are shown in both columns. Three-dimensional structures stand out, as they all have direct or pseudo-direct band gaps. The same holds for the two-dimensional structures with planar triangular building units, that all have indirect

band gaps. The latter compounds crystallise all in the same structure type, so this correlation should rather be attributed to possible correlations attributed to the structure type. For the three-dimensional tetrahedral structures several different crystal structures can be found, so this may be more than a coincidence.

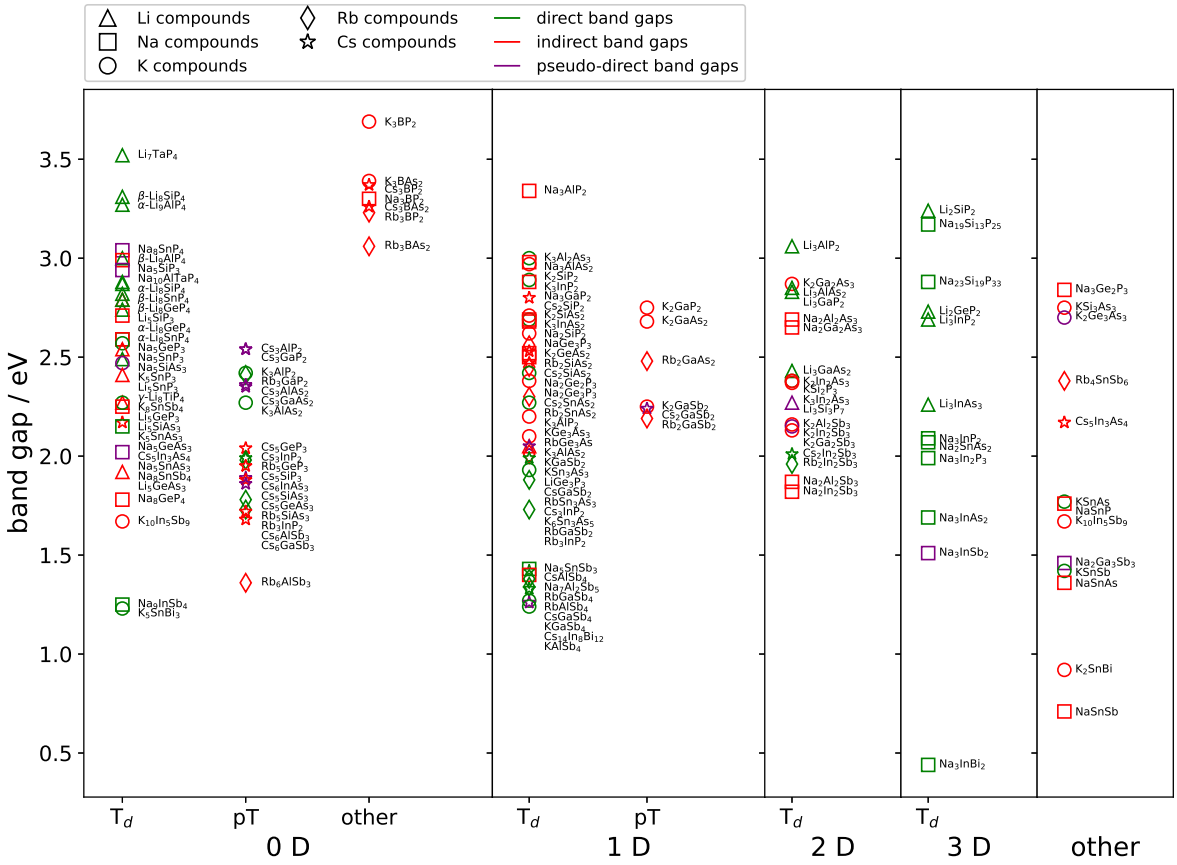

Figure 3.5: Band gap plotted against the dimensionality of the anionic substructure. 0D, 1D, 2D and 3D stand for zero-, one-, two- and three dimensional connection of the two main structural motives of (connected) tetrahedra (T_d) or triangular planar coordination (pT).

Looking in more detail at the column for one-dimensional structures with chains of edge- or vertex-sharing tetrahedra, they reveal a trend for a separation in compounds with indirect and direct band gaps, with the latter having smaller gaps. For the zero dimensional compounds with isolated $Tr/TtPn_4$ tetrahedra or trigonal planar $Tr/TtPn_3$ units, there also seems to be a split as well, but this time the compounds with direct band gaps are larger. The zero-dimensional compounds labelled "other" are all boron compounds that crystallise in two very similar structure types, so they all have large indirect band gaps.

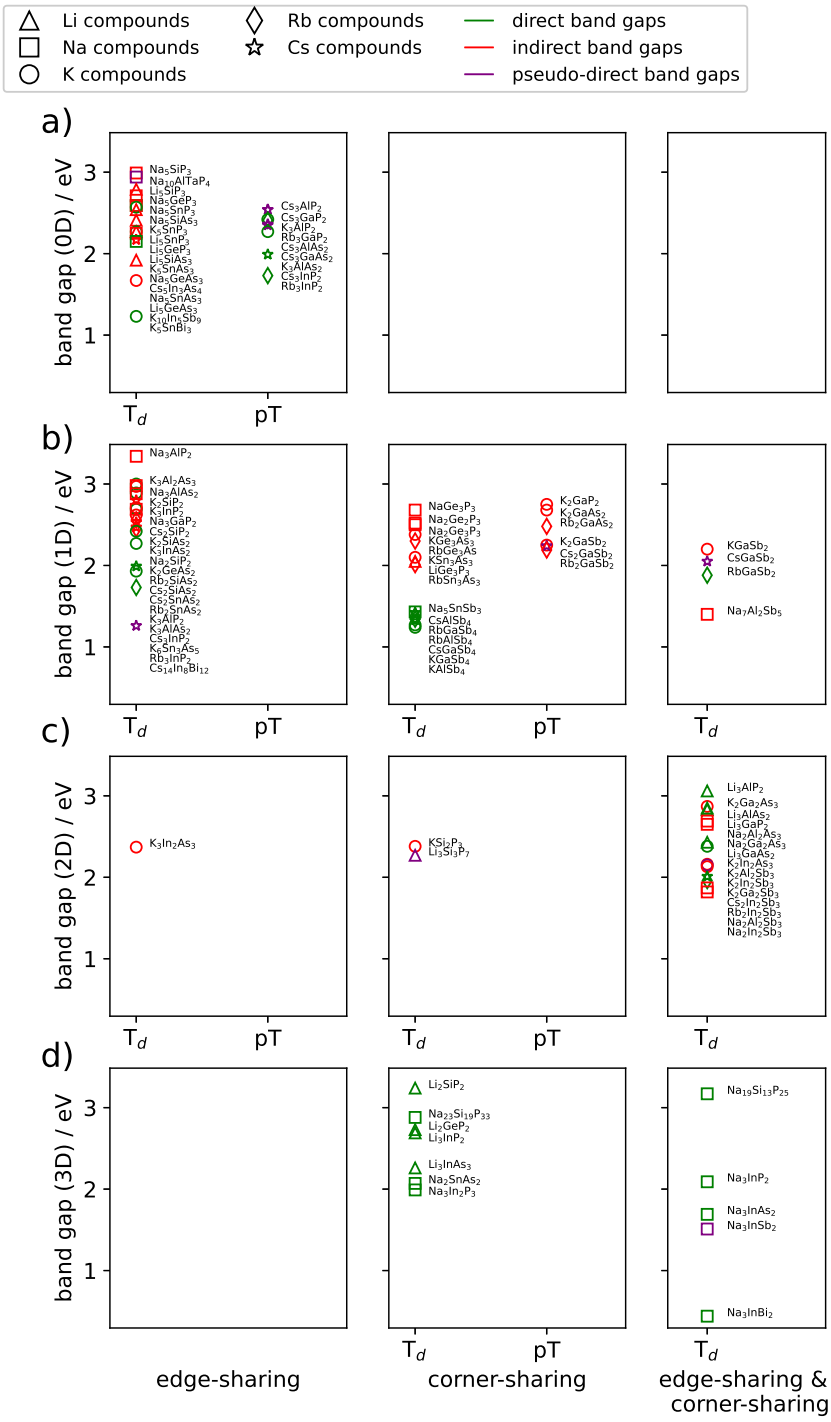

Figure 3.6: Band gap plotted against the kind of connectivity of the tetrahedral (T_d) or trigonal planar structural motif. a), b), c) and d) represent a zero-, one-, two- or three-dimensional connectivity, respectively.

To further classify the crystal structures, they were labelled according to the connectivity in the anionic substructure. Therefore, in Abbildung 3.6 the band gap is plotted against the tetrahedral and trigonal planar structure motives, but with subplots divided by solely edge- and corner-sharing or a combination of both. Since no zero-dimensional corner-sharing or mixed corner- and edge-sharing compounds, as well as three-dimensional pure edge-sharing structures are known, these subplots remain empty. Again compounds with two different substructures are plotted in both subplots.
For the zero-dimensional edge-sharing compounds with tetrahedral building blocks, direct band gaps are exclusive to Sn compounds with their gaps distributed over a wide energy range. This is in favour for the hypothesis, that the nature of the element influences the occurrence of direct band gaps for crystal structures for which several examples of other homologue elements show preferably indirect band gaps. The edge-sharing trigonal planar structures all show direct or pseudo-direct band gaps. Since some of these compounds also show a second structural motive (one dimensional chains of edge-sharing tetrahedra), for which also indirect band gaps could be obtained, this could hint, that substructures can influence the kind of gap, but more data is needed, to get a closer look into proper trends.
For the one-dimensional structures with exclusively corner- or edge-sharing connectivity of the tetrahedral substructure, indirect band gaps seem to be smaller than direct band gaps. For the edge-sharing structures, there are still some K compounds with band gaps between 2 eV and 3 eV, but for corner sharing structures, there is a clear gap between direct and indirect band gaps. For structures with corner-sharing triangular planar units, only indirect band gaps have been calculated, but since the values are in the same range as the tetrahedral structures, there could be a split between them and hypothetical direct band gap compounds as well.
For the two-dimensional structures, no real separation between direct and indirect band gaps could be observed for mixed corner and edge-sharing connectivities. For structures with exclusively edge- or vertex-sharing connectivities, only limited data is available. The three-dimensional structures show the above mentioned trend of direct or pseudo-direct band gaps. Since there are only Li and Na compounds known, calculations and experiments on K, Rb and Cs compounds would be a great addition to the data set, to see if this trends persists.

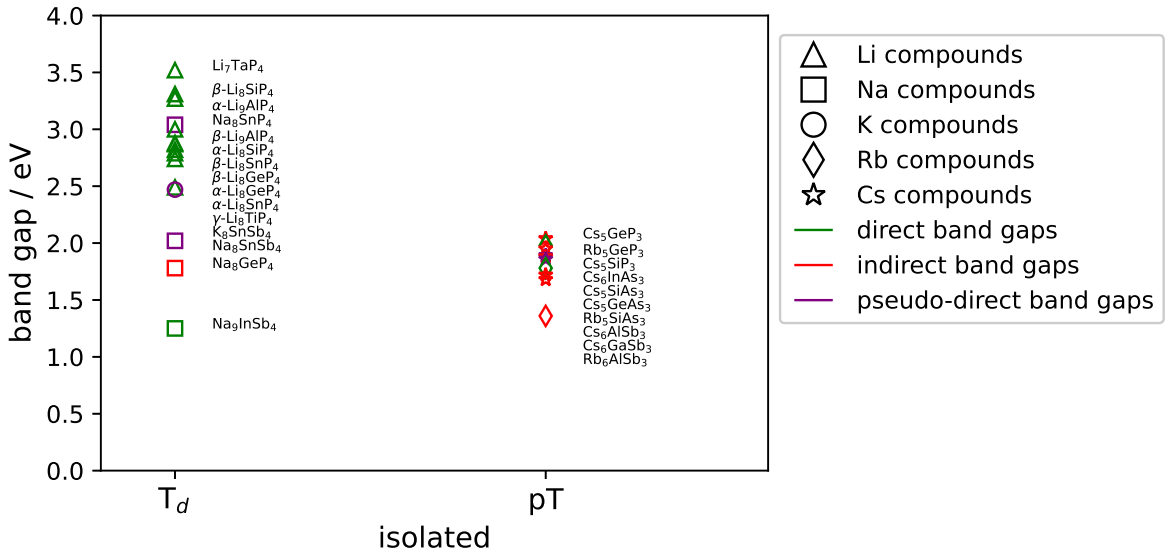

Figure 3.7: Band gap plotted against the tetrahedral (T_d) or trigonal planar (pT) structural motif for the zero-dimensional structures.

Lastly Abbildung 3.7 features all compounds that show isolated $Tr/TtPn_4$ tetrahedra or $Tr/TtPn_3$ triangular planar units. For the former the band gaps are mostly direct, for the latter indirect. Additionally, the observed range of the band gaps is smaller and lower in energy for triangular planar structures and only compounds with Rb or Cs are present, while tetrahedra occur for Li, Na and K compounds. Looking back at Abbildung 3.6, a general trend can be observed that planar triangles as coordination polyhedra are only present for compounds with the heavier K to Cs alkali metals, while tetrahedral structural motifs are present for all alkali metals. This is discussed in more detail for the different stoichiometric compound systems in their respective sections, but the general trend suggests that compounds with the heavier alkali metals prefer less restricted triangular planar structural motives. As an explanation one might consider, that the heavier cations are too large to fit in between the more complex anionic substructures, which are often build by a cubic or hexagonal closed packing of phosphorus with limited size of their tetrahedral or octahedral voids, and thus prefer the more flexible and simple structures with $Tr/TtPn_3$ units.

To summarize the trends, all calculated three-dimensional compounds show direct- or pseudo-direct band gaps. For two-dimensional structures no clear trends could be found, while for one-dimensional compounds, indirect band gaps are larger than direct gaps for a pure edge- or corner-sharing connectivity. For zero-dimensional structures that form edge-sharing dimers, tetrahedral structures are more likely to have indirect band gaps, while trigonal planar

structures are more likely to have direct band gaps. This is reversed, if the structure motives are isolated $Tr/TtPn_4$ or $Tr/TtPn_3$ units. The latter is exclusive to compounds with K, Rb or Cs as alkali metals, while structures with (connected) $Tr/TtPn_4$ tetrahedra can be found for all alkali metals.

3.1.4 Influence of the Electronegativity of the Constituting Elements

Since the last sections dealt with aspects of the composition and crystal structure, this section will focus on the influence of the chemical properties on the nature and size of the band gap. Since compounds with large electronegativity differences are often associated with insulators, such as salts, a link between band structure, especially the band gap size, and electronegativity difference seems likely. Thus Abbildung 3.8 shows the electronegativity differences between the different elements in A_xTr/Tt_yPn_z compounds are plotted against the band gap. The electronegativity values, according to the Pauling scaler, used for these calculations can be found in Tabelle B.1.
Although for each element combination many different band gaps were obtained, each subplot shows a more or less clear trend. For Abbildung 3.8 c) to e) that show the difference between alkali metal - pnictogen, triel - pnictogen and tetrel - pnictogen, an increased band gap is be observed for larger electronegativity differences. The boron compounds are an exception though, since they are located at much higher band gaps than the other triel compounds. Excluding them the trend shows that large electronegativity differences correspond with large band gaps as expected. The opposite is true for subplots a) and b). For the alkali metal and triel difference the boron compounds, which are the seven data points at the top right corner of Abbildung 3.8a, are again an exception with larger band gaps. For the K/Rb-Ga and K/Rb-In compounds, the band gaps seem to be stagnant, while they seem to slightly increase again for K/Rb-Sn to K/Rb-Ge compounds. Since there is an increase in electronegativity for Ga and Ge, going down the periodic table, due to the filled d-orbitals, they appear at higher ΔEN.

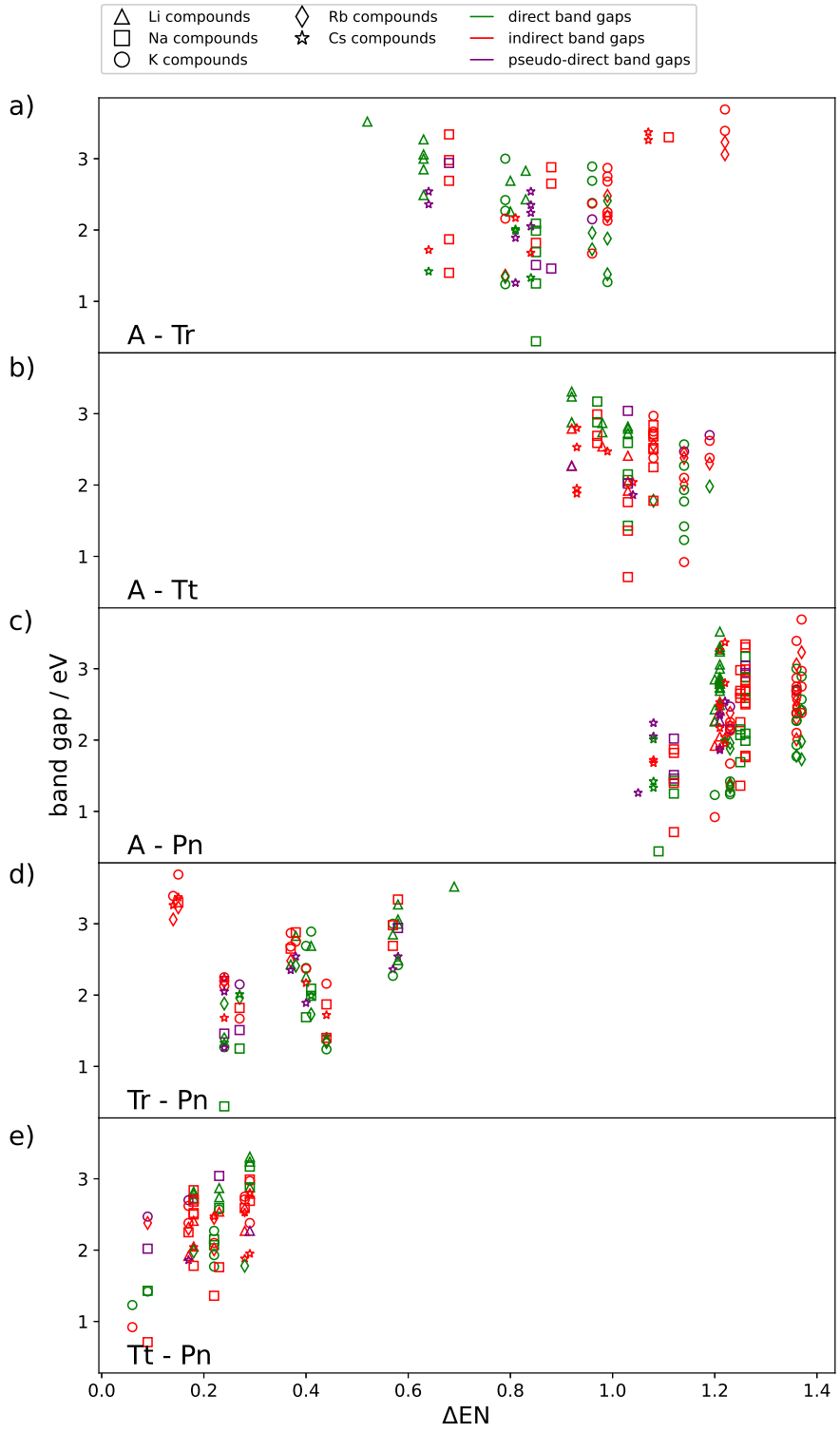

Figure 3.8: Electronegativity difference ΔEN between two elements each plotted against the band gap. a) alkali metal - triel, b) alkali metal - tetrel, c) alkali metal - pnictogen, d) triel - pnictogen, e) tetrel - pnictogen.

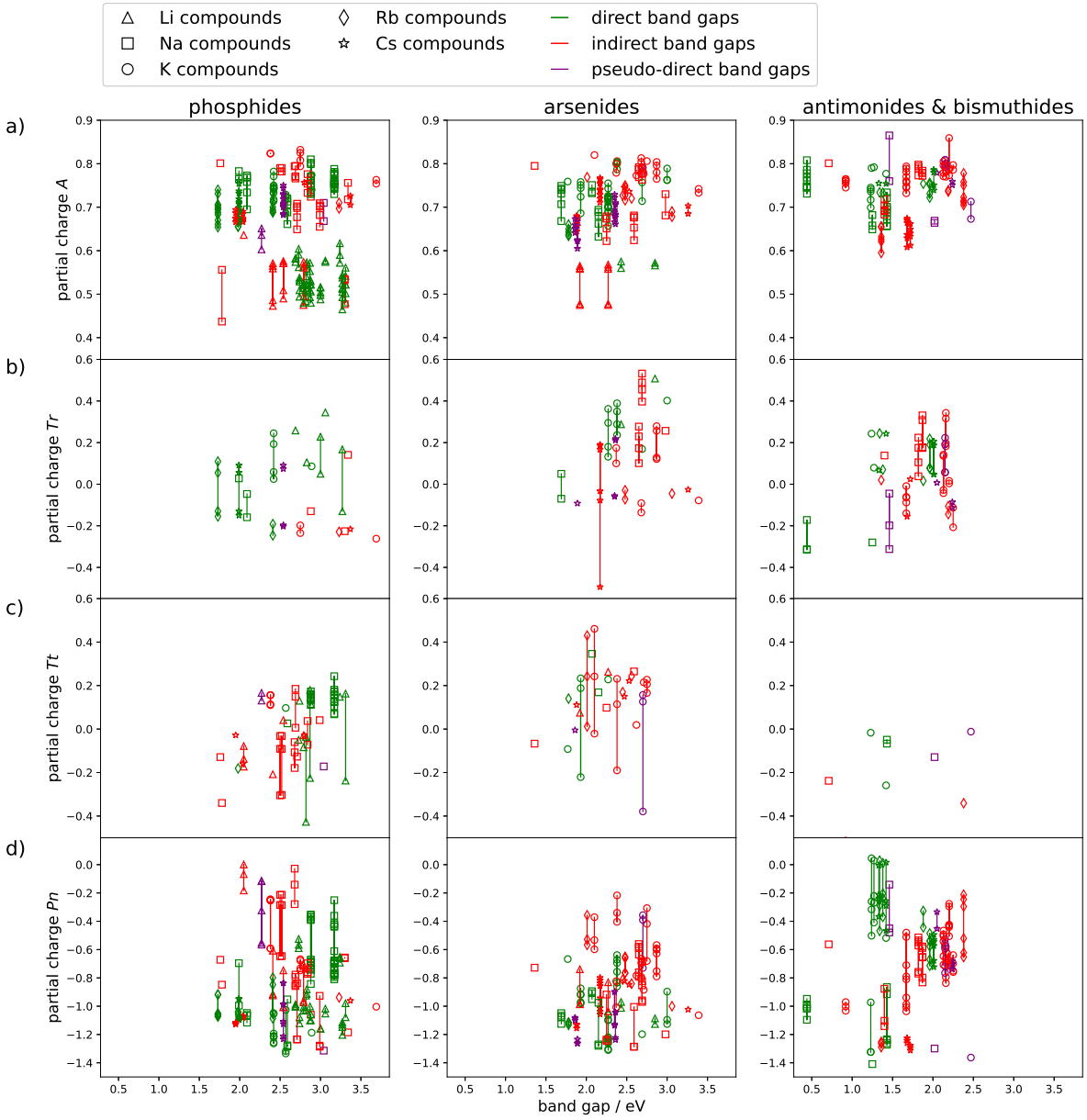

Figure 3.9: Partial charges calculated for each atomic position plotted against the band gap. The subplots a), b), c) and d) show values fo alkali metals, triels, tetrels and pnictogens, respectively. If for one atom different crystallographic positions are occupied, their values are connected by a line.

The electronic donor-acceptor situation within the Zintl-compound can be divided by two factors: On one hand there are the cationic alkali metals, that donate their electron to the anionic *Tr/Tt-Pn* network. Since within the network polar *Tr/Tt-Pn* bonds are present, the pnictogen receives an additional formal negative charge. This is in line with the general trend, that with larger electronegativity difference to the pnictogen the band gap increases. Lower

band gaps occur with an increased *A*-*Tr*/*A*-*Tt*-ΔEN. As for the increase in band gaps for Ga and Ge compounds, the atom size may play a role. Since larger atoms are more diffuse and have weaker (thus less covalent) bonds, the band gaps might decrease more compared to compounds with smaller atoms and more covalent bonds.
To get an insight on the charge distribution, the Mulliken partial charges for each atomic position are calculated and plotted against the band gap in Abbildung 3.9. If an atom occupies more than one crystallographic position, they are connected by a vertical line. The compounds are subdivided by phosphides, arsenides and antimonides/bismuthides. For the alkali metals it can be seen, that the Mulliken charges of Li are about 0.2 lower than the other alkali metals, which is in agreement with findings in molecular chemistry that bonding to Li atoms always has a strong covalent contribution. The alkali metal's general trend shows a slight increase of the partial charge with the band gap. This could be interpreted that more electron density is being transferred to the anionic substructure, in which then more polarized bonds may be present and thus larger band gaps occur. For the triels and tetrels no real trend can be seen. For phosphidotetrelates, there could be a hint towards an increasing band gap for higher charges, but more data is required to confirm this. The pnictogens however, show some trends towards increased band gaps with higher partial charges. This is more prominent for arsenides, antimonides and bismuthides than phosphides.

Summarising the trends from electronegativity differences and partial charges, ΔEN between alkali metals, triels and tetrels and the pnictogens shows the clearest trend. Here large differences coincide with large bang gaps, which can be explained by more polar bonds and easier electron transfer from the alkali metal to the pnictogen. This is affirmed by the trend of larger band gaps found for compounds with high alkali metal and pnictogen Mulliken charges, although not as clearly represented by the data for the latter. With an increase of the electronegativity difference between the alkali metal and the triel/tetrel, the band gaps decrease. Here the bond polarity decreases with increasing electronegativity of the triel/tetrel and thus smaller band gaps are obtained. This trend is slightly disturbed by the increased electronegativity for Ga and Ge, where the atom size might play a roll in slightly increasing the band gap. Mulliken partial charges for triels and tetrels show no clear trend backing up this hypothesis.

3.1.5 Influence of the Overlap Population and Bonding Situation

As a further parameter possibly influencing the band gap, the overlap population between neighbouring atoms is investigated. The value gives an insight on the strength of interaction

between two atoms, that are covalently connected.[67] Therefore the overlap population of different heteroatomic interactions, which were limited to distances of about 5 Å, are plotted against the band gap.

Since most compounds are formed by a cubic or hexagonal closed packing of the pnictogen, in which the triel/tetrel and alkali metal occupy different octahedral and tetrahedral voids, distances between alkali metals and triels/tetrels are larger than their distance to neighbouring pnictogens. As few overlap populations with distances below 5 Å, and thus non-zero overlap populations, were obtained, it is not possible to discuss trends for them.

The anionic substructure of most compounds is formed by either $Tr/TtPn_4$ tetrahedra or $Tr/TtPn_3$ triangular planar units, that form molecular units or complex up to three-dimensional networks, for which bonds are assumed to be formed between Tt/Tt and Pn. In Abbildung 3.10 all corresponding overlap populations can be seen, again plotted against the band gap. Most values of the overlap population are larger than $0.2\,e^-$, confirming strong bonding interactions within the atoms of the anionic substructure. This is fully in line with the 8-N rule emphasizing covalent bonds between the atoms of the polyanionic substructure. In analogy to larger HOMO-LUMO gaps in molecules, increase stronger covalent interactions the band gap, but compounds with double bonds do not posses larger band than other compounds with the same elemental composition.

The Li-*Tr*-P compounds and two Na-*Tr*-P separate from the remaining trielphosphides with larger band gaps, but band gaps still increase. Especially high Tr/Tt-Pn overlap populations can be found for Rb and Cs compounds, reaching values of up to $0.5\,e^-$. These interactions coincide with compounds that form partial double bonds, which can be assigned to the largest overlap populations.

In Abbildung 3.11 the values for all alkali metal pnictogen interactions can be seen. The compounds are sorted by triel/tetrel and pnictogen, in columns and rows respectively. Alkali metals are known to not form covalent bonds to neighbouring atoms, thus as expected their overlap population with neighbouring atoms is in general small, which is in agreement with the salt-like description of their interactions as introduced in the Zintl-Klemm concept. Although do compounds with Li, and a few with Na, show, in contrast to other compounds of the heavier alkali metal atoms, non-zero overlaps with their neighbours. As seen earlier, the Li compounds also show the lowest Mulliken partial charges, which could be interpreted as donor-acceptor interactions between A and Pn, where the electron is not completely transferred, whereas the Na to Cs compounds seem to transfer most valence electrons and then show only weak ion-like interactions. Other than that, no correlation can be seen between the overlap population and the band gap.

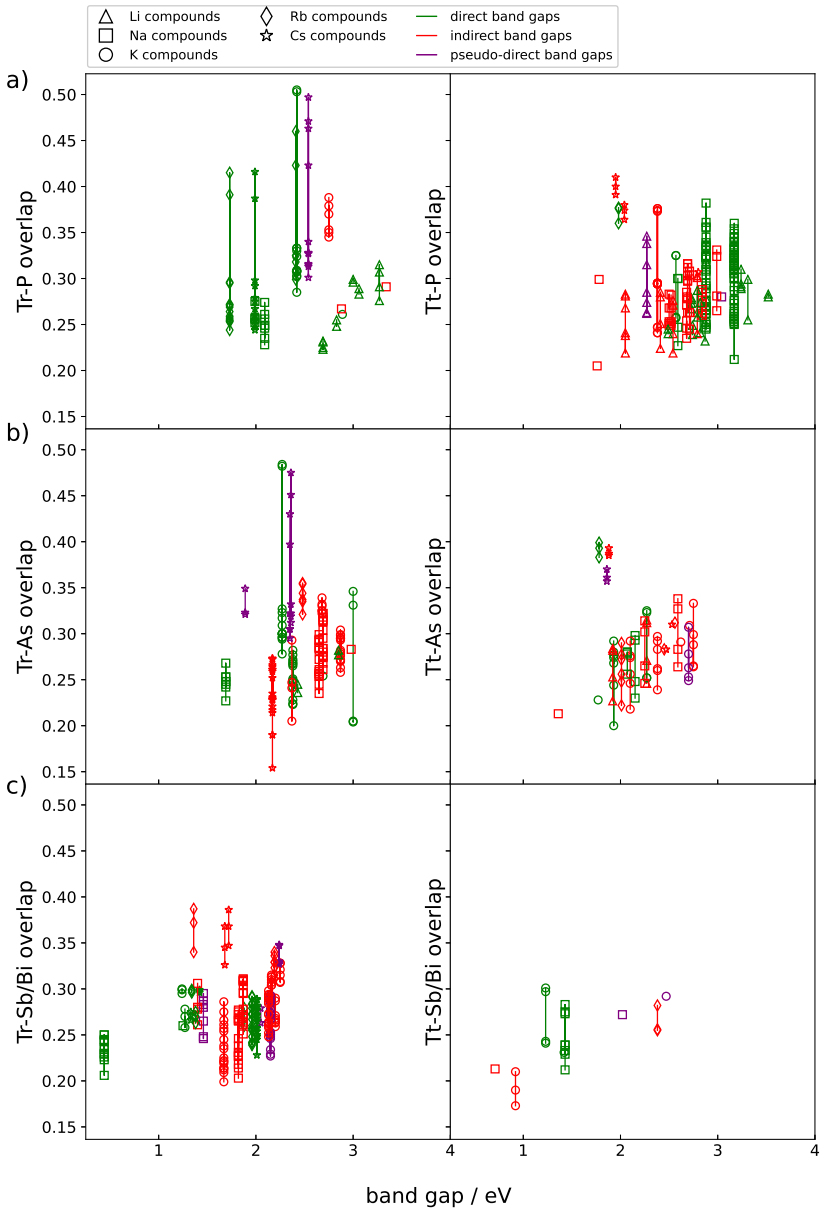

Figure 3.10: Mulliken overlap population (e^-) of triel/tetrel-pnictogen interactions plotted against the band gap. a), b), and c), show specifically Tr/Tt-P, Tr/Tt-As and Tr/Tt-Sb/A-Bi interactions, respectively. The subplots are further divided by triel (left) and tetrel (right) compounds.

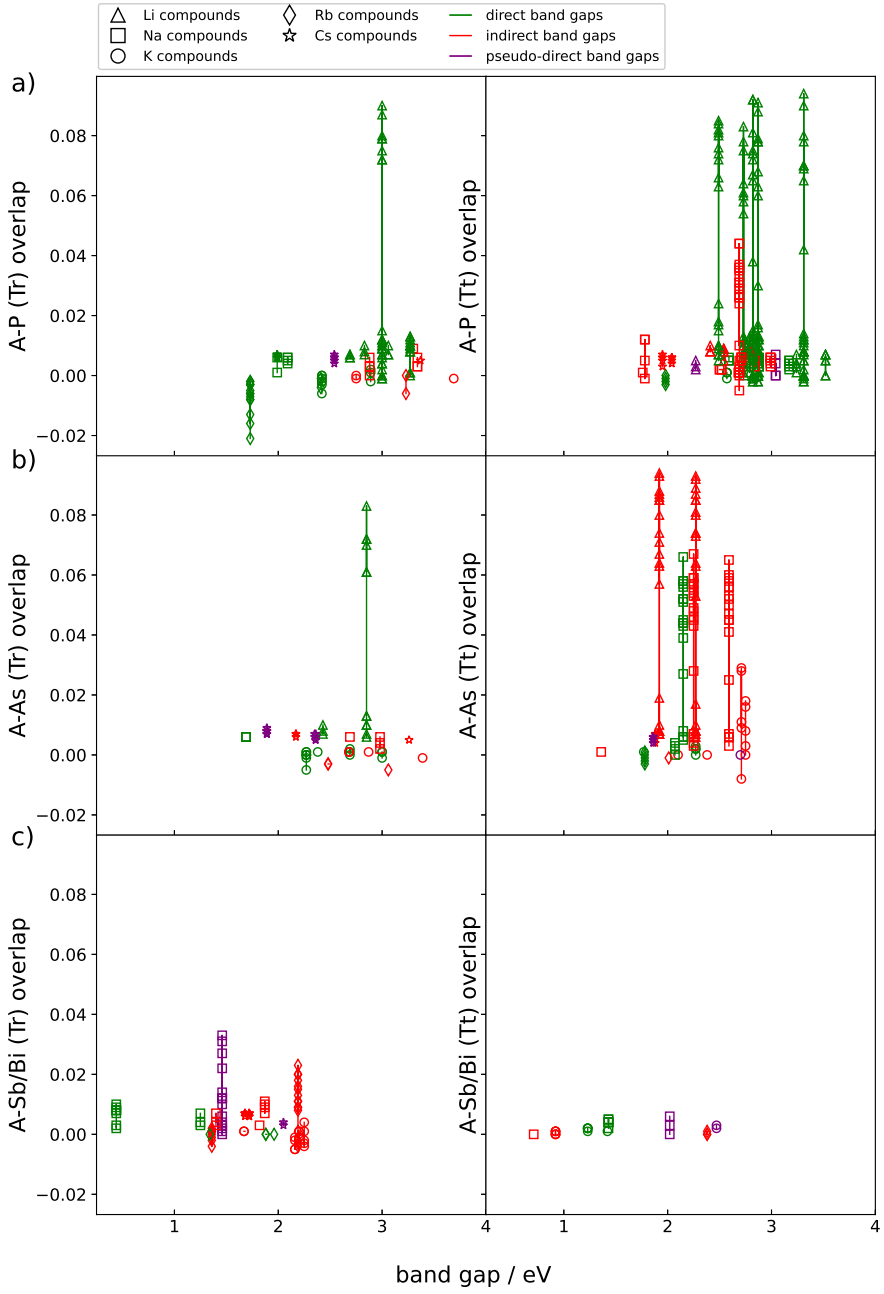

Figure 3.11: Overlap population of alkali metal pnictogen interactions plotted against the band gap. a), b), and c), show specifically A-P, A-As and A-Sb/A-Bi interactions, respectively. The subplots are further divided by triel (left) and tetrel (right) compounds.

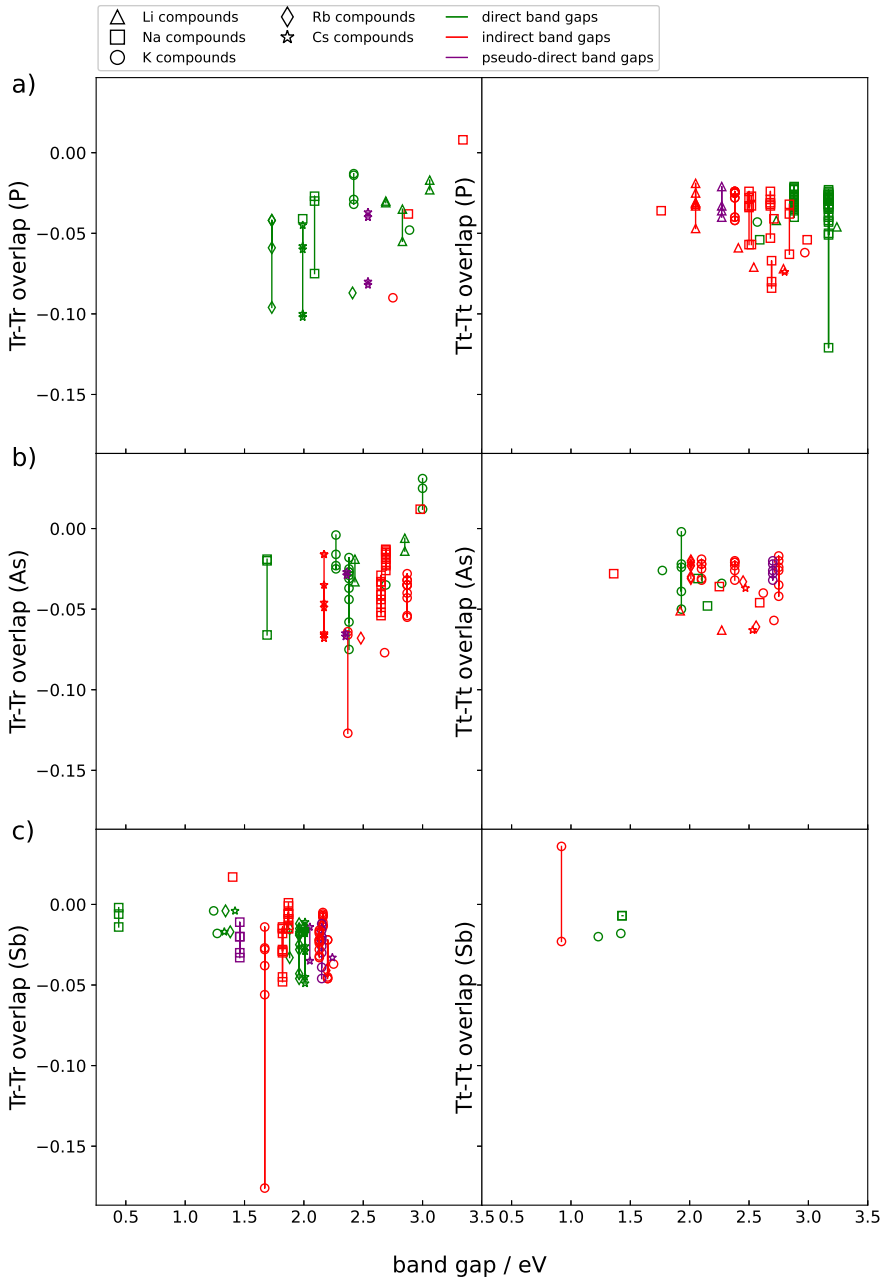

Figure 3.12: Mulliken overlap population (e^-) of triel-triel/tetrel-tetrel interactions plotted against the band gap. The subplots are further divided by triel (left) and tetrel (right) compounds. a), b), and c), show interactions in phosphides, arsenides and antimonides/bismuthides, respectively.

Lastly, discussed in more detail below, the influence of the triel-triel/tetrel-tetrel overlap population, between for example two neighbouring triel occupied tetrahedral voids, was investigated. The plot can be seen in Abbildung 3.12. Here all overlap populations, which

can be assigned to *Tr-Tr/Tt-Tt* bonds were cut off, to specifically look at the far-range interaction between them.
The values of the overlap population are mostly negative, which represents a small repulsion of the neighbouring atoms. For the phosphides interestingly most compounds with triel-triel antibonding interactions have direct band gaps which are increasing with larger overlap, while the ones with tetrel-tetrel interaction have mostly indirect band gaps, for which the trend is decreasing. For compounds in the 3-1-2 system, this trend is further discussed later. While the As compounds somewhat show a similar trend, Sb and Bi compounds do not reproduce these trends, probably due to less data.

Summarising the influence of the overlap population on the band gap, two main trends are found. On one hand do strong (single) bonds between *Tr/Tt* and *Pn* result in larger band gaps, as well as less repulsion between triels in phosphidotrielates. In molecules a strong orbital overlap results in a larger HOMO-LUMO gap between ground and excited states, thus similar effects could be present. On the other hand seem large repulsions in phosphidotetrelates lead to a decreasing band gaps. At least for phosphides this repulsion may also influence which kind of band gap is formed, but more data is needed.

3.1.6 Conclusion on Trends within the Data Set

With the data set of 141 ternary $A_x Tr/Tt_y Pn_z$ Zintl-compounds, some general trends for band gap sizes and nature thereof could be identified. Main influences on the size is the elemental composition, where larger atoms decrease the band gap, mostly at the pnictogen position. This is backed up by smaller values for the Mulliken overlap population between the triel/tetrel and pnictogen atoms, since larger atoms form in general weaker covalent bonds. Further on, does a large electronegativity difference and a good overlap between the triel/tetrel and pnictogen increase the band gap. Lastly could the nature of the band gap also slightly influence the gap size, since indirect band gaps tend to be larger than direct band gaps, if they are based on a similar anionic substructure. Which kind of gap is present seems to be influenced by the composition (elements and atomic ratios), as it was pointed out for the Li compounds or compounds of the 3-1-2 system that both mostly show direct band gaps. Heavier atoms on the other hand seem to increase the occurrence of pseudo-direct band gaps, mostly caused by a flattening of the top valence bands. Further on does it seem like three dimensional anionic substructures, for which unfortunately only Li and Na compounds are known, only show (pseudo-)direct gaps. The same can be found for triclinic,

tetragonal and cubic crystal structures.
Although 141 compounds might sound like a lot, it is only a small fraction of all Zintl-compounds known. Therefore, the trends presented should only be treated as a first investigation. There seem to be a lot of factors influencing the calculated band gap at the same time. For example the occurrence of direct band gaps for cubic compounds could also be seen as a systematic error, since most of the presented compounds have a very similar structure. A next step to identifying possible systematic errors should be modelling compounds in (all) different structure types of for example one stoichiometry and comparing the results to experimental data. This would lead to a larger, in a sense also more complete, data set. Then each of the trends can be compared in each subsystem, as well as in the whole set to see, how the different variables influence each other.
To go a step further the trends identified here also need to be investigated in a larger context, for example by expanding the data set to binary Zintl-compounds or by investigating oxide systems with the same criteria. Therefore, it may be necessary to explore possible implementations of automatic computational routines or neural networks for data analysis to keep track of the data and manage the huge computational workload.

3.2 Detailed Investigation of Selected Compound Classes

By looking at the whole A_xTr/Tt_yPn_z system, although some trends on the occurrence of direct band gaps, regarding atomic or structural properties can be found, it becomes also clear, that most of these properties are interconnected and could lead to biased assumptions. The stoichiometry was chosen as the main factor to pick sub-sets of the data, since here the influence of the composition is limited to different elemental combinations rather than different molar fractions. Especially systems, for which many different compounds are known in literature are ideal. Here two systems stand out particularly, namely the A_5TtPn_3 and A_3TrPn_2 systems. The former is especially useful to investigate the influence of the atomic composition, since the crystal structures incorporate only two simple structure motives. The latter, on the other hand, shows a large variety of different structure types, which range from simple molecular anions to three-dimensional polyanionic structures, that allow a closer look on property relationships arising from the "crystallographic composition".
Furthermore can results of the investigations be rounded off by comparing the findings of the two main systems with other, similar compounds, which were studied themselves more thoroughly, such as the A_6TrPn_3 and A_2TtPn_2 systems, which are the respective triel and tetrel compounds of the initial model systems. Additional systems that were investigated include the ASnPn system, due to its correspondence of direct and indirect band gaps for certain alkali metals, the A_2TrPn_2 and ATt_3Pn_3 systems, with additional Pn-Pn bonds, and the $A_2Tr_2Pn_3$ system, with Tr-Tr bonds.
The following sections summarize and compare results from the investigations on each of these subsystem. A more detailed analysis can be found in the respective published papers and manuscripts found in Kapitel 5.

3.2.1 In-depth Investigation on the Influence of the Composition on the Electronic Structure

List of publications and manuscripts to chapter 3.2.1.:

> **see 5.1:** Sabine Zeitz, Hanna Antoniuk, Viktor Hlukhyy, T. F. Fässler, Electronic Structure Analysis of the $A_{10}Tt_2P_6$ System (A = Li Cs; Tt = Si, Ge, Sn) and Synthesis of the Direct Band Gap Semiconductor $K_{10}Sn_2P$, *Chemistry — A European Journal* **2024**, *30*, e202400002.
>
> **see 5.2:** Sabine Zeitz, Hanna Antoniuk, Thomas F. Fässler, Electronic structure analysis of A_6TrPn_3 compounds with A = Rb, Cs; Tr = Al, Ga, In and Pn = As, Sb, *manuscript for publication*.

A_5TtPn_3 compounds - Influence of the Elemental Composition

Compounds with the composition A_5TtP_3 (A = Li-Cs, Tt = Si-Sn) are an ideal model system to investigate the influence of the elemental composition on the nature and size of the band gap, since for all compounds of this family only two, simple, isomeric crystal structures are known in literature. There are clear preferences for one of the two observed crystal structures depending on the alkali metal: Li and Na compounds show edge-sharing $Tt_2P_6^{10-}$ double tetrahedra (dimer structure), which can be seen as the dimers of the carbonate like triangular planar TtP_3^{5-} units found for the Rb and Cs compounds (monomer structure). Both structures are shown in Abbildung 3.13.[76–83]

All compounds were calculated in both structure types, to identify possible phase transitions, predict the structure for, in literature, unknown compounds and analyse the electronic structure for both. The differences of the Gibbs free enthalpy obtained by frequency calculations at different temperatures are shown in Abbildung 3.14. All Li compounds and Na_5SnP_3 show lower enthalpies for the dimer structure, while all Rb and Cs compounds, as well as K_5SiP_3 and K_5GeP_3 prefer the monomer structure. Na_5SiP_3, Na_5GeP_3 and K_5SnP_3 show a phase transition from dimer to monomer structure at higher temperatures. The predicted and experimentally determined structures are in good agreement for all known compounds. Due to limited space within the tetrahedral and octahedral voids of the P cubic closed packing of the dimer structure, it might be unfavourable for the larger Rb^+/Cs^+ cations, resulting in larger energies and enthalpies. For Sn compounds the dimer structure is preferred, which can be explained by the double bond rule, which states, that atoms of higher periods prefer

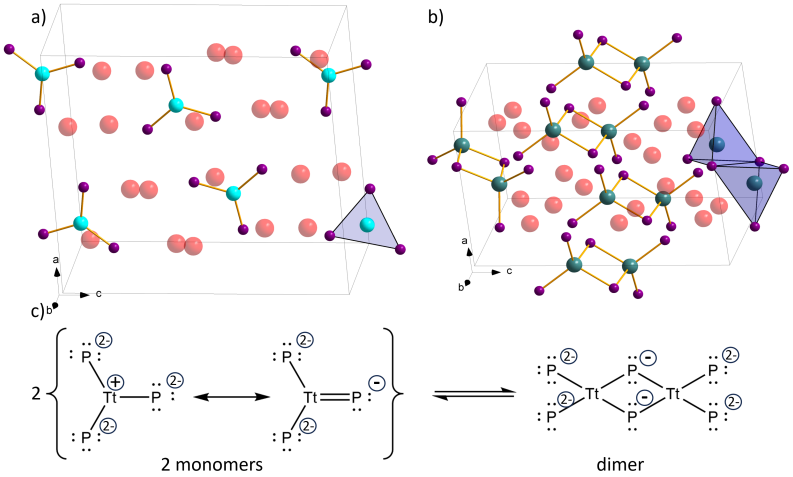

Figure 3.13: Representations of the two possible crystal structure types. a) comprising monomeric, triangular planar TtP_3^{5-} and b) $Tt_2P_6^{10-}$ edge-sharing double tetrahedra. c) Resonance structures of monomeric TtP_3^{5-} and equilibrium forming the dimeric $Tt_2P_6^{10-}$ unit. Alkali metals, tetrel and pnictogen are shown red, turquoise and purple, respectively.

multiple single over double bonds, which would be present in the monomer structure.[84]

The experimentally unknown K_5SnP_3 was synthesized from the elements in niobium ampoules at 650 °C. It showed the predicted dimer structure.

For all calculated compounds band structure, density of states (DOS) and crystal orbital Hamilton population (COHP) were calculated. The band gap size is found to be mainly determined by the electronegativity difference (ΔEN) between the tetrel atoms and phosphorus, as the band gap decreases from Si to Ge and increases again for Sn compounds. This in line with trends proposed by Abbildung 3.8, for which the band gap increases with larger ΔEN. Sn compounds that break the trend by showing a smaller band gap than the corresponding Ge compounds, the band gap switches from indirect to direct, which might cause this anomaly. This would also fit well with the observation, that direct band gaps of similar compounds seem to be smaller than indirect gaps.
From the experimentally know structures three have a direct band gap, Na_5SnP_3 (dimer), K_5SnP_3 (dimer) and Rb_5GeP_3 (monomer), as well as three predicted compounds, Na_5SiP_3 (monomer), Rb_5SiP_3 (monomer) and Rb_5SnP_3 (monomer). Cs_5SnP_3 (monomer) shows a pseudo-direct band gap, all other compounds have an indirect band gap. There is no corre-

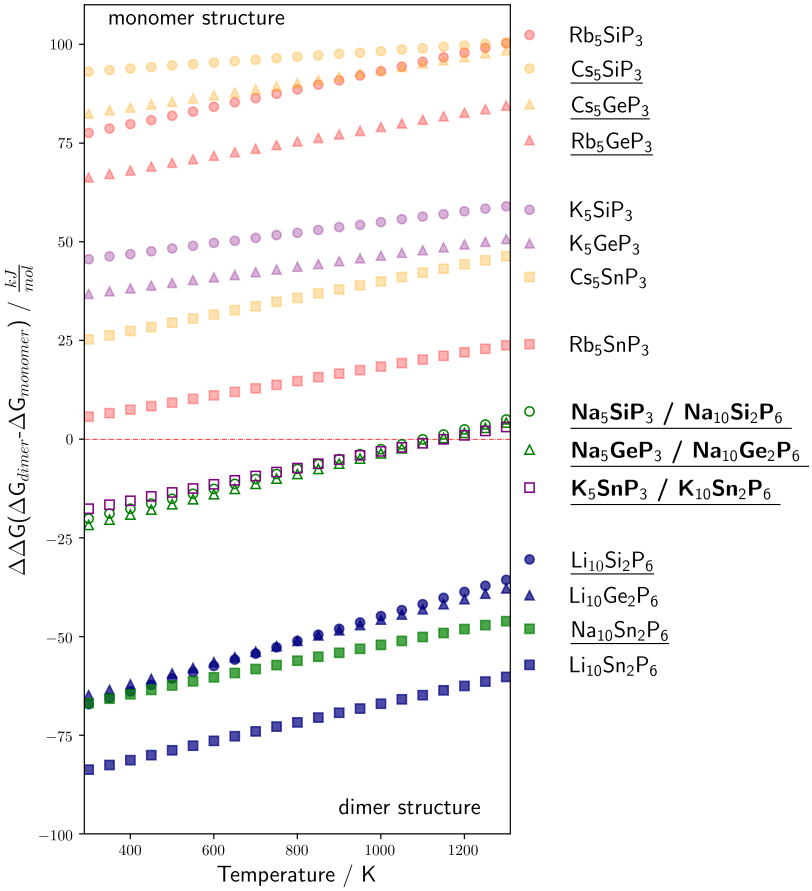

Figure 3.14: Gibbs Gibbs enthalpy differences for all calculated structure models depending on the temperature. Below the zero line the dimer phase is more stable, above the monomer. Phases marked in bold font in the legend show a phase transition. Experimentally known phases are underlined.

lation between the structure type and the nature of the band gap, but direct gaps seem to be especially prominent for Sn and Rb compounds. For all compounds with a direct gap the transition between valence band maximum (VBM) and conduction band minimum (CBM) is located at Γ. A closer look at the Fermi-Level of compounds with the VBM at other *k*-points reveals, that they have a large(r) number of alkali metal states, which could be the reason for the rise in energy of the top valence band at these points. This can be seen in Abbildung 3.15 and Abbildung 3.16, where a lot Cs/Na states close to the Fermi-Level are present, which does not seem to be limited to the structure type, since it can be found for both. For all compounds which have the VBM at Γ the alkali metal projected DOS falls back to zero right below the Fermi-Level.

To see if there is some interaction between the alkali metal and the anionic Sn-P substruc-

ture, a crystal orbital Hamilton population (COHP) has been calculated for all hetero atomic interactions. The general trend shows, that for heavier alkali metals the interaction with P increases, especially for the dimer structure, probably due to the large alkali metal being confined in "small" tetrahedral and octahedral voids. Thus it can be assumed, that these states are primarily of non-bonding nature, but become anti-bonding if the alkali metal atoms are close to their neighbours.

Apart from that, there is not much interaction between the atoms for the top valence bands, although there are many phosphorus states present in the density of states. Therefore, most of these states seem to be of non-bonding nature and probably belong to the phosphorus lone pairs.

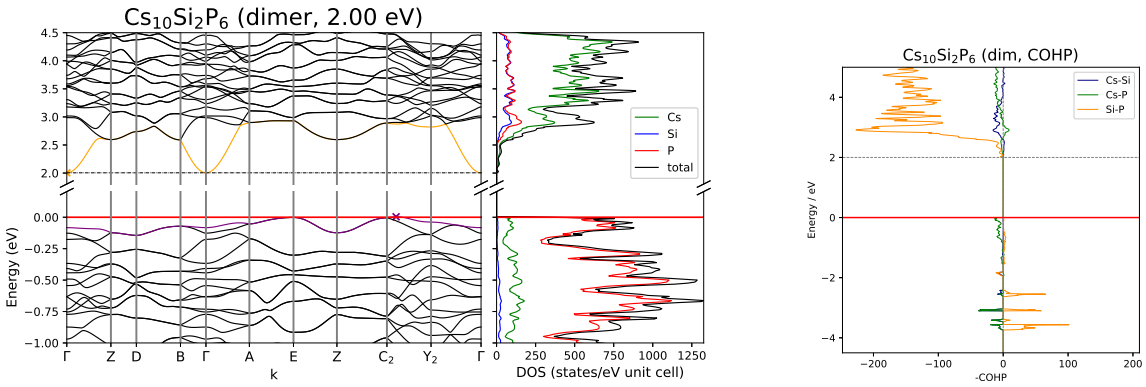

Figure 3.15: Band structure and DOS of Cs_5SiP_3 (dimer structure) and COHP of Cs-Si, Cs-P and Si-P interactions.

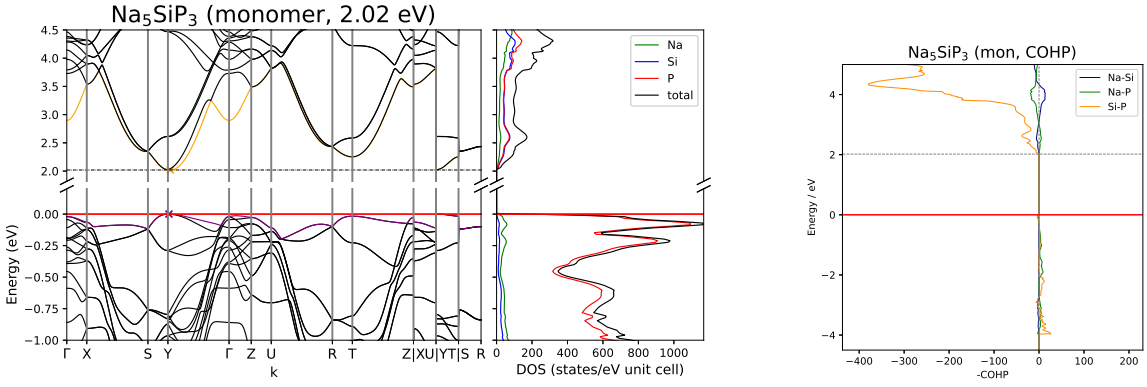

Figure 3.16: Band structure and DOS of Na_5SiP_3 (monomer structure) and COHP of Na-Si, Na-P and Si-P interactions.

Comparing these results to calculations of the experimentally known arsenides, the same trends can be found. Compounds with Li, Na and K prefer the dimer structure, while Rb and Cs crystallize within the monomer structure.[80, 85–88] Compounds with Sn (Na_5SnAs_3, K_5SnAs_3) or Rb (Rb_5SiAs_3) show direct band gaps, while Cs_5GeAs_3 shows a pseudo-direct band gap. All remaining compounds have indirect band gaps. The band gap sizes for the arsenides are about 0.5 eV smaller than the phosphides, which fits into the trends discussed above.
As mentioned in the first chapter, there are certain peculiarities regarding the preference of direct band gaps for different atoms. There, this observation correlated with many of those compounds showing the same crystal structure, which lead to the question whether this trend could be biased. Since for the A_5TtPn_3 compounds there is still some correlation for Sn and Rb compounds and direct band gaps, although the majority of the compounds (both dimer and monomer structures) show indirect band gaps, there might be some small influence on the nature of the band gap by the elemental composition.

Comparison to A_6TrPn_3 compounds

Compounds of the A_6TrPn_3 class (A = Rb, Cs; Tr = Al-In; Pn = As, Sb) posses the same carbonate analogue triangular planar $TrPn_3^{6-}$ units as $TtPn_3^{5-}$ in the A_5TtPn_3 class (Abbildung A.25). In contrast to the A_5TtPn_3 system, no crystal structure similar to the dimer structure is know. A total number of eight compounds are experimentally known, but for Na_6GaP_3, K_6InP_3, Na_6GaAs_3 and K_6InAs_3 no calculations are possible, as the crystal structures have several underoccupied crystallographic positions.[89–96] For Na and K compounds in the A_5TtP_3 system the dimer structure type is predicted to be lower in energy, but surprisingly no such structure type exists for this system.
All A_6TrPn_3 compounds with A = Rb, Cs; Tr = Al-In; Pn = As, Sb, were calculated. The input geometry was either taken from or modelled based on experimental data. Only Cs_6InAs_3 shows a pseudo-direct, all other compounds indirect band gaps. As for A_5TtPn_3 compounds mainly Sn compounds show direct band gaps, the difference between indirect and direct band gap at Γ is significantly smaller for all In compounds.
The size of the band gaps is not as dependent on the electronegativity difference between the triel and pnictogen as in other families, therefore the differences between arsenides and antimonides are only small. For the A_6TrPn_3 compounds the decreasing band gaps between Rb and Cs compounds is more prominent, with the Cs compounds having about 0.5 eV smaller gaps. As the electronegativities of Rb and Cs are almost the same, the difference and the gap size could be due to a better separation of the anionic units for the Cs compounds due

to the larger size.

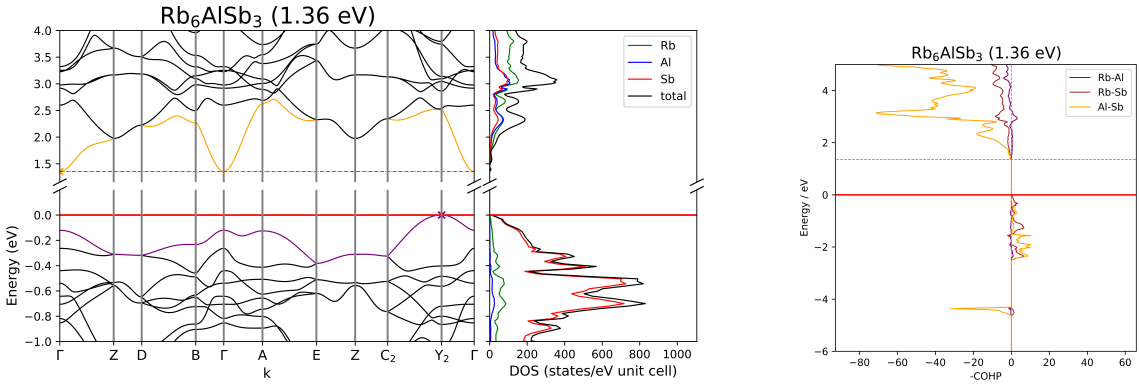

Figure 3.17: Band structure and DOS of Rb_6AlSb_3 and COHP of Rb-Al, Rb-Sb and Al-Sb interactions.

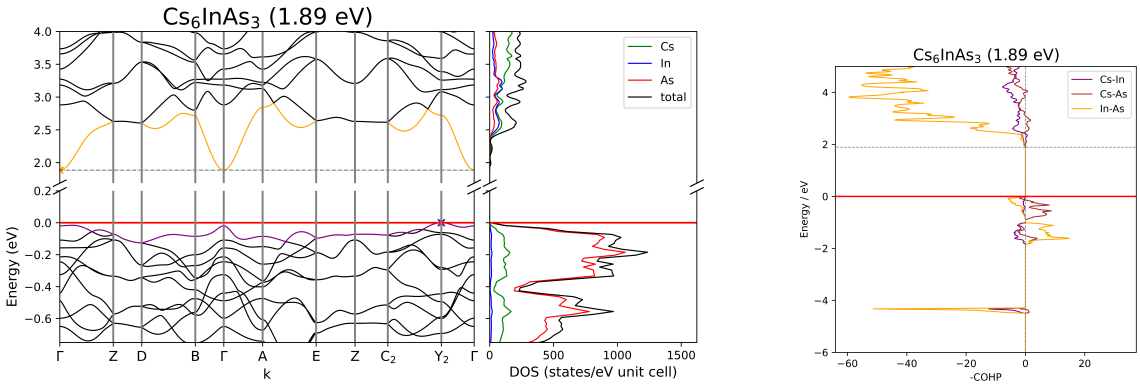

Figure 3.18: Band structure and DOS of Cs_6InAs_3 and COHP of Cs-In, Cs-As and In-As interactions.

In Abbildung A.26 and Abbildung A.27 band structures, density of states (DOS) and crystal orbital Hamilton population (COHP) of Rb_6AlSb_3 and Cs_6InAs_3 are shown, respectively. As seen in those two figures, like Rb_6AlSb_3, all compounds with an indirect band gap have the valence band maximum (VBM) at Y_2, while Cs_6InAs_3 has it at Γ. The conduction band minimum (CBM) is at Γ for all compounds. The additional alkali metal states, that were present for all compounds were the VBM was not located at Γ in the A_5TtPn_3 system, can be found here as well, but with a lower amount of states. For Cs_6InAs_3 the alkali metal projected DOS falls back to zero at the Fermi-Level, while all other compounds still have some states left at 0 eV. Other than that, all compounds show mostly pnictogen states for

the valence bands and a mix of states from all atoms in the conduction bands. A closer look at the COHP gives more insight into the electronic structure close to the Fermi-Level. For all compounds only few interactions can be found below the Fermi-Level, thus most states present in the pnictogen projected DOS can probably be attributed to non-bonding states, similar to the A_5TtPn_3 system. Additionally, most compounds show few *Tr-Pn* interactions as well as some *A-Pn* interactions right below the Fermi-Level, with most of them of bonding nature. For Cs_6InAs_3 although, there are In-As as well as some Cs-As anti-bonding interactions at the Fermi-Level. The latter switch to bonding interactions at energies where the top valence band maximum at Y_2 is located. For the other In compounds some anti-bonding In-*Pn* interactions can be found at energies, where their top valence band is at Γ.
One explanation could be that the In-*Pn* double bonds states are at especially high energies, due to the double bond rule, leading to an elevated top valence band at Γ. Since a VBM at Y_2 is the norm in this system, while for the A_5TtPn_3 system it was mostly at Γ and the additional interactions with the alkali metal atoms also lead to higher energies for the top valence band at other *k*-points, this could be some common trend for all A_xTr/Tt_yPn_z compounds.
The CBM is exclusively at Γ for triel compounds, but appears at different *k*-points for the tetrel compounds. At the edge of the band gap top tetrelates show according to the COHP a small increase in *Tt*-P interactions, while the trielates show no interactions. One explanation might be, that the polarity of the *Tr-Pn* bonds is larger than the *Tt-Pn* bonds, which could result in a smaller splitting of the respective states in the tetrel compounds, lowering them in energy. But since DFT methods only estimate the nature of excited states rather than actually calculating them, post-DFT methods are needed to get more insight on this matter. At this point, this should only be taken as a hint that further investigation of this matter could lead to interesting results.

3.2.2 In-depth Investigation on the Influence of the Crystal Structure on the Electronic Structure

List of publications and manuscripts to chapter 3.2.2.:

> **see 5.3:** Sabine Zeitz, Yulia Kuznetsova, and T. F. Fässler, Large Number of Direct or Pseudo-Direct Band Gap Semiconductors among A_3TrPn_2 Compounds with A = Li, Na, K, Rb, Cs; *Tr* = Al, Ga, In; *Pn* = P, As, *Molecules* **2024**, *29*, 4087.

Tassilo M. F. Restle, Sabine Zeitz, Philip M. Stanley, Antti J. Karttunen, Jan Meyer, Gabriele Raudaschl-Sieber, Wilhelm Klein, Thomas F. Fässler, Direct Band Gap Semiconductors with Two- and Three-Dimensional Triel-Phosphide Frameworks (Triel=Al, Ga, In), *Chemistry — A European Journal* **2023**, *30*, e202304097. [97]

see 5.4: Sabine Zeitz, Zoe Listmann, Thomas F. Fässler, Electronic structure analysis of the $A_2TrTtPn_2$ system with A = Li-Cs; Tr = Al-In; Tt = Si-Sn; Pn = P-Sb, *manuscript for publication*.

see 5.5: Sabine Zeitz, Thomas F. Fässler, Electronic property calculation of ASnPn compounds with A = Na, K and Pn = P, As, Sb, *manuscript for publication*.

A_3TrPn_2 compounds - Influence of Different Isomers

The A_3TrPn_2 class (with A = Li-Cs; Tr = Al-In; Pn = P, As) is chosen as a "model"-system, due to the known variety in crystal structures. There are eight different types, with "zero"-dimensional $Tr_2Pn_4^{6-}$ edge-sharing triangular planar units (**A, B**), mixed zero- and one-dimensional structures, that additionally include chains of edge-sharing tetrahedra (**C, D**) to the molecular units, pure one-dimensional structures with SiS_2-type edge-sharing tetrahedra chains (**E**), two-dimensional layered structures of corner- and edge-sharing tetrahedra (**F**) and three-dimensional networks of super tetrahedra (**G**) or corner- and edge-sharing tetrahedra (**H**), as shown in Abbildung 3.19. For further information on the crystal structures please refer to Abschnitt A.3.[27–31, 74, 98–110] Since also for each dimension at least two different compounds are known, this system can give a first insight on the influence of the crystal structure on nature and size of the band gap.
There is a clear trend that the preferred structure types with higher and lower dimensions appear for small (Li, Na, K) and large (Rb,Cs) alkali metals, respectively. This is similar to the A_5TtPn_3 system, since the two- and three-dimensional structures are primarily build by cubic or hexagonal closed packings of the pnictogen, that have "small" tetrahedral and octahedral voids for the alkali metal to occupy. Therefore, the large Rb and Cs compounds prefer the "less restricted" zero- (and mixed with one-) dimensional crystal structure types.

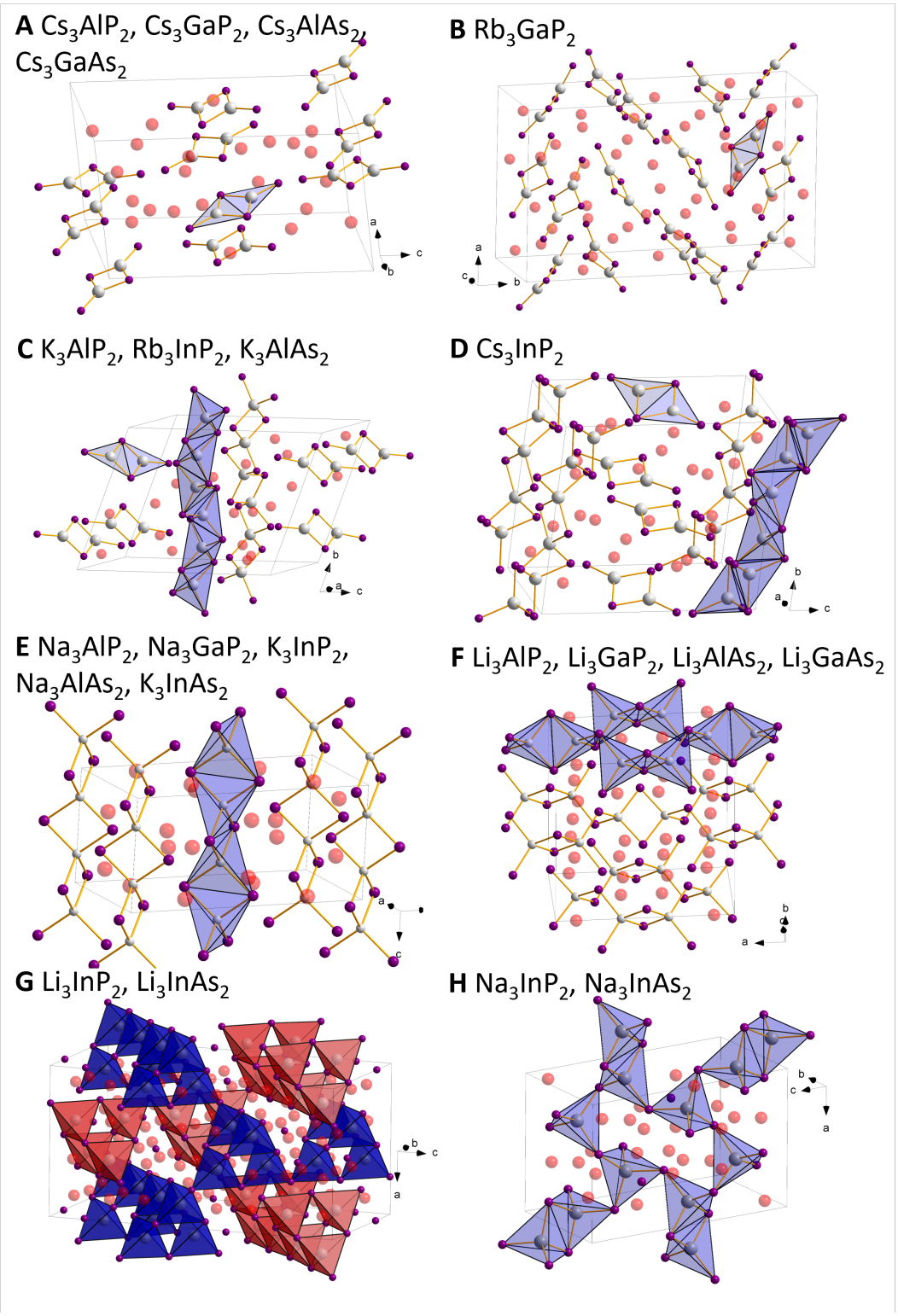

Figure 3.19: Crystal structures present in the A_3TrP_2 system. For a more detailed description see Abschnitt A.3 in the appendix. Alkali metals, triel and pnictogen are shown red, turquoise and purple, respectively.

To complete the system, for all eight experimentally unknown phosphide and arsenide crystal structures different possible structures were calculated and the lowest Gibbs enthalpy structure determined. Surprisingly all but three compounds, namely Na_3AlP_2, Na_3GaP_2 and Na_3AlAs_2, show a direct or pseudo-direct band gap. Although all indirect band gap compounds share the same structure type, not all compounds of this type show an indirect band gap, since K_3InP_2 and K_3InAs_2 both have a direct band gap. This is on one hand in contrast to the previous system, where no clear trend was found regarding the occurrence of direct band gaps for certain crystal structures, but on the other in line, since compounds with large *Tt*/*Tr* atoms here also show different band gaps the corresponding smaller atoms.
The band gap size is determined by two factors, the electronegativity difference between the pnictogen and triel atoms and the dimension of the crystal structure. Due to the primary trend, most arsenides show band gaps about 0.5 eV smaller, due to the smaller overlap of the As orbitals with its neighbouring atoms. For compounds that break this trend, different crystal structures are present for the arsenide and phosphide. If the same structures would be present, there would be no exceptions from the first trend. As for compounds with the same pnictogen, the band gaps decrease with a decreasing *Tr-Pn* electronegativity difference, as shown in Abbildung 3.8.
The decrease of the band gap with lower dimension of the structure might be a follow up trend arising from the heavier alkali metal's preferred dimensionality. The band gap for triel compounds decreases with an increasing electronegativity difference between the alkali metal and triel (Abbildung 3.8). Additionally these compounds also crystallize in structures with lower dimensionality, which shows the same trend.

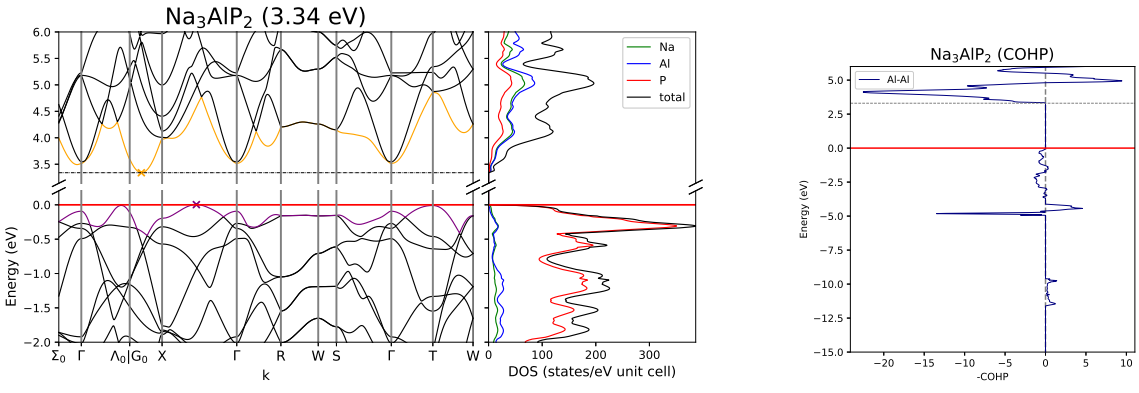

Figure 3.20: Band structure and DOS of Na_3AlP_2 and COHP of neighbouring Al-Al interactions.

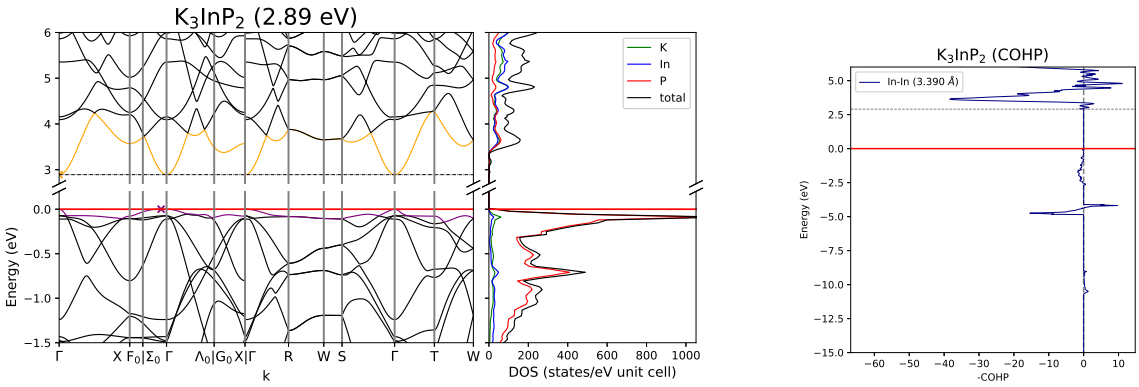

Figure 3.21: Band structure and DOS of K_3InP_2 and COHP of neighbouring In-In interactions.

All compounds with direct band gaps show transitions at Γ, like most compounds so far. Since for structure type **E** direct, as well as indirect band gaps were calculated, their band structures might give some insight on what property leads to that switch. Abbildung 3.20 and Abbildung 3.21 show band structures, density of states and crystal orbital Hamilton population for Na_3AlP_2, with an indirect and K_3InP_2 with a direct band gap. For Na_3AlP_2 the valence band minimum additional Na states can be found in the projected DOS close to the Fermi-Level. The conduction band minimum for Na_3AlP_2 is located between G_0 and X, while K_3InP_2 has it at Γ. At the band gap top in the *Tr-Tr* projected COHP, compounds with indirect band gaps show a sharp increase in anti-bonding *Tr-Tr* interactions, while compounds with direct band gaps show no or only few interactions here. Therefore the *Tr-Tr* interaction might be one of the factor influencing the CBM position. This might be accompanying or causing the trend that heavier triel or tetrel compounds often change the nature of the band gap. Nonetheless the crystal structure seems to be the main factor in this system, deciding which type of band gap is present.

Comparison to A_2TtPn_2 compounds

A_2TtPn_2 correspond to equivalent tetrel analogues, with the same total number of valence electrons. A_2TtPn_2 compounds, with A = Li-Cs, Tt = Si-Sn, Pn =P, As, possess two main structure motives, identical to A_3TrPn_2. For the Li compounds, as in Na_2SnAs_2, a three-dimensional system of corner-sharing super-tetrahedra can be found. The remaining compounds show one-dimensional crystal structures with the same SiS_2 like linear chains of edge-sharing tetrahedra as structure type **E** of the triel compounds.[111–116]

Interestingly, all compounds with super-tetrahedra show direct band gaps, and all compounds with one-dimensional chains indirect gaps, although there is no switch to direct gaps for the Sn compounds as for the triel system. Nonetheless, the general trend for the correlation of certain structures and direct/indirect band gaps is the same for both systems, especially since the main structural motives are identical. This strengthens the hypothesis, that the crystal structure to some extent can influence the type of band gap.
The band gap size for the one-dimensional structure type follows the trend of lower band gaps for smaller electronegativity differences, except for Na_2SiP_2, which has a slightly lower band gap. For the three-dimensional compounds the band gaps are slightly lower than expected (except Li_2SiP_2), which could be explained by the direct band gaps. As seen in Abbildung 3.6 compounds with direct band gaps show smaller gaps for lower dimensions, compared to the respective indirect band gap compounds.

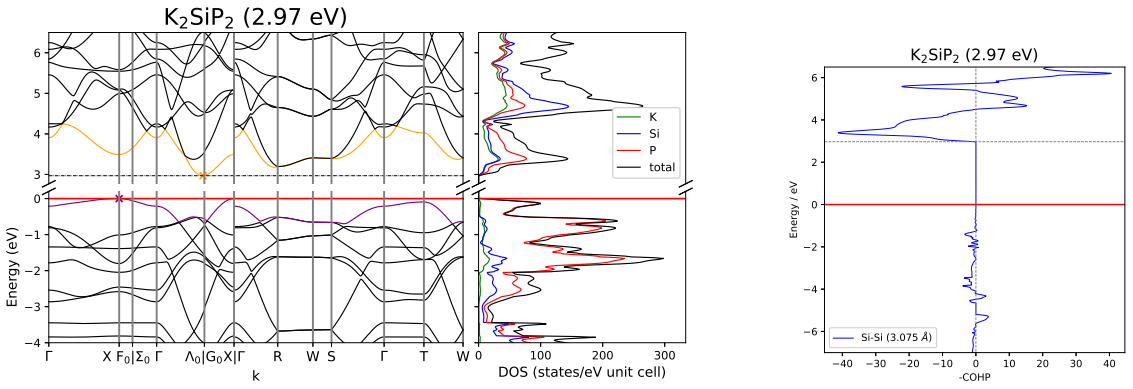

Figure 3.22: Band structure and DOS of K_2SiP_2 and COHP of neighbouring Si-Si interactions.

Except Na_2SiP_2, show A_2TtPn_2 compounds the VBM at X, which probably is caused by additional alkali metal states close to the Fermi-Level as seen in all previous systems. Most *Pn* states present in the top valence bands belong to non-bonding interactions. The band structures, density of dates and crystal orbital Hamilton population of K_2SiP_2 and Rb_2SnAs_2 are shown in Abbildung 3.22 and Abbildung 3.23, respectively. The conduction band minimum is located at G_0 for K_2SiP_2 and at Γ for Rb_2SnAs_2. The *Tt-Tt* interaction projected COHP of K_2SiP_2 shows the same sharp increase in Si-Si interactions at the band gap top as the A_3TrPn_2 indirect band gap compounds. For Rb_2SnAs_2 these interactions are at higher energies and the overall shape is similar to K_3InP_2 (Abbildung 3.21).
Therefore the *Tr-Tr*/*Tt-Tt* interactions and their influence on the band gap have to be dis-

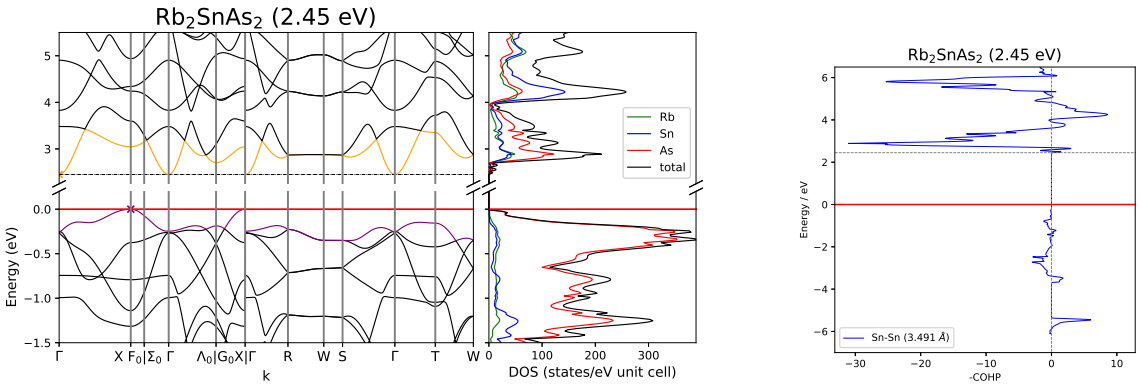

Figure 3.23: Band structure and DOS of Rb_2SnAs_2 and COHP of neighbouring Sn-Sn interactions.

cussed in more detail. On one hand this sharp increase of states in the projected COHP is peculiar, since it can be seen for different, although similar, systems. On the other hand, as mentioned, are DFT calculations limited in the accuracy to describe excited states (conduction bands) and post-DFT methods are needed for a better insight on those. Nonetheless, since these interactions occur regularly, even if they arise from an "error" or inaccuracy of the calculation, their systematic occurrence is suspicious, and thus should be kept in mind for further research.

Another possibility might be, that the different CBM positions are caused by relativistic effects. One hint towards this is, that the CBM position at other *k*-points is mostly found for compounds with lighter triel or tetrel atoms, while for the respective Sn and In compounds it is mostly located at Γ. Since the basis sets of Sn and In contain a core potential, which considers certain relativistic effects, this might also be able to cause the different CBM position, or be the reason for the energy shift in *Tr-Tr*/*Tt-Tt* interactions.

Comparison to *A*Sn*Pn* compounds

The *A*Sn*Pn* compounds with *A* = Na, K and *Pn* = P-Sb have a layered crystal structure consisting of grey arsenic like layers of chair conformed six-membered rings with alternating Sn and *Pn* atoms (see Abbildung A.95 for a more detailed description). Four compounds are known experimentally with this type of structure, KSnP and NaSnSb were calculated as well.[32, 117–119]

Smaller band gaps from phosphides to antimonides correlate with the electronegativity difference between Sn and the pnictogen atoms. Additionally the gaps of NaSnAs and NaSnSb

are smaller than the respective K compounds, probably due to the lower electronegativity of K. This would be in line with Abbildung 3.8, where an increased difference in alkali metal-pnictogen electronegativity increases the band gap.

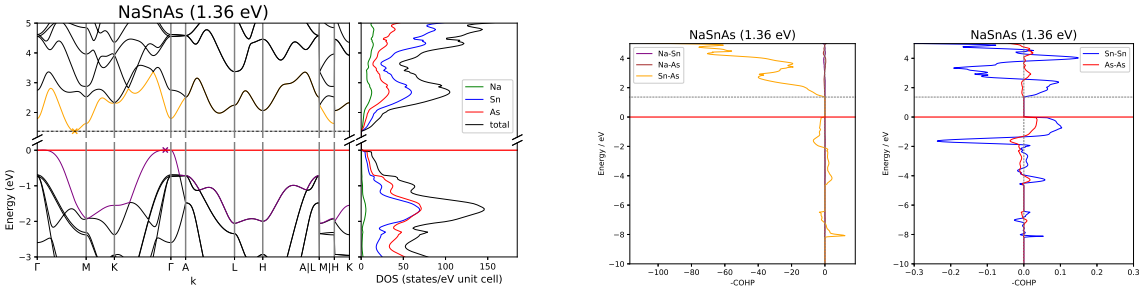

Figure 3.24: Band structure and DOS of NaSnAs and COHP of neighbouring heteroatomic, Sn-Sn and As-As interactions.

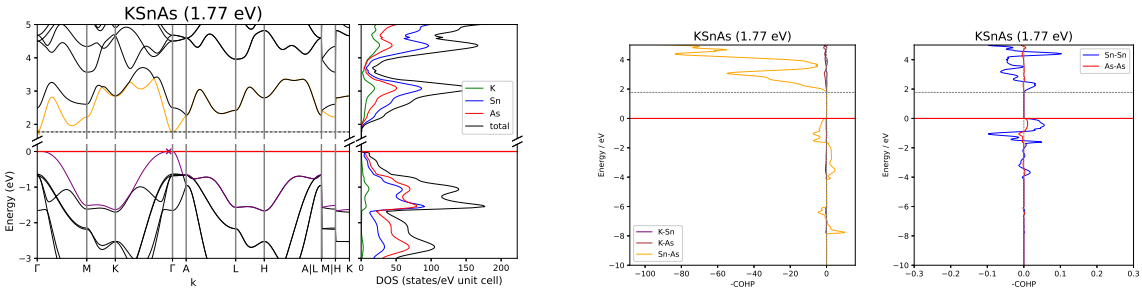

Figure 3.25: Band structure and DOS of KSnAs and COHP of neighbouring heteroatomic, Sn-Sn and As-As interactions.

There is a clear split between indirect and direct band gaps for Na and K compounds, respectively (Abbildung 3.24 and Abbildung 3.25). For the valence bands, in contrast to other systems, a lot more Sn states are present, which to some extend show anti-bonding interactions with the *Pn* atoms close to the Fermi-Level. There might also be some non-bonding states of the Sn and *Pn* atoms, since the Sn-*Pn* interactions are rather small compared to the conduction bands, but the amount of states in the projected DOS is roughly the same. All valence band maxima are located at Γ and therefore, no additional alkali metal states can be observed at the Fermi-Level.

A closer look at the Sn-Sn and *Pn*-*Pn* interaction projected COHP reveals weak bonding interactions for both at the Fermi-Level, although they are slightly stronger for the Na compounds. For the conduction bands the Na compounds also show stronger Sn-Sn interactions

than the K compounds, but the sharp edge in anti-bonding interactions above the band gap is not present as for other systems, here they are of bonding nature. NaSnSb shows a similar small edge in bonding interactions, but for the other Na compounds its more of a steep increase. The K compounds also have an increase in bonding Sn-Sn interactions, but it is less steep. Therefore the Sn-Sn interaction might influence the CBM position slightly, but not to the same extend as in other systems. Here some additional influence might arise from the *Pn-Pn* interaction, which is anti-bonding for the Na and zero for the K compounds. But since they are small as well, this is more something to keep in mind, than a potential cause.

3.2.3 Investigation on the Influence of Additional *Tr-Tr/Tt-Tt/Pn-Pn* Bonds on the Electronic Structure

List of publications and manuscripts to chapter 3.2.3.:

> **see 5.6:** Sabine Zeitz, Yulia Kuznetsova, Thomas F. Fässler, Electronic structure analysis of the ATt_3Pn_3 system with A = Li-Cs; Tr = Al-In; Tt = Si-Sn; Pn = P-Sb, *manuscript for publication*.
>
> **see 5.7:** Sabine Zeitz, Zoe Listmann, Thomas F. Fässler, Electronic structure analysis of $A_2Tr_2Pn_3$ compounds with A = Na Cs; Tr = Al, Ga, In; Pn = As, Sb, *manuscript for publication*.

Since the *Tr-Tr/Tt-Tt* interactions seem to play a role in deciding whether compounds have a direct or indirect band gap, a closer look at systems containing *Tr-Tr* or *Tt-Tt* bonds may reveal some interesting insights. The same would be interesting for additional *Pn-Pn* bonds, so the following chapter gives some insights into how the electronic structures differ for compound systems, that have these additional *Tr-Tr/Tt-Tt* or *Pn-Pn* bonds.

ATt_3Pn_3 Compounds - Influence of Mixed Tetrahedra

Compounds of the ATt_3Pn_3 system with A = Li-Rb; Tt = Si-Sn; Pn = P, As incorporate the "normal" $TtPn_4$ as well as mixed Tt_2Pn_3 tetrahedra, that form layered crystal structures (Abbildung 3.26, refer to Abschnitt A.6 for further description of the crystal structures). [37, 120–122] Within these layers *Tt-Tt* bonds are present in mixed or interpenetrating tetrahedra, which could give some insight on the influence of *Tt-Tt* interactions on the band gap.

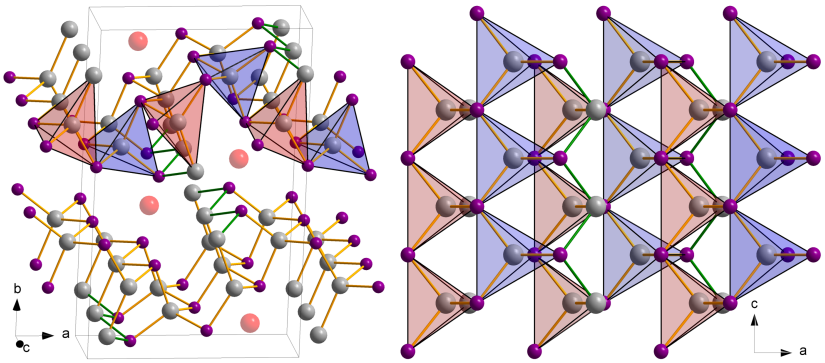

Figure 3.26: Crystal structure of $LiGe_3P_3$. Right: Unit cell, left: top view on one layer. Li, Ge and P are shown in red, grey and purple, respectively, the additional Ge-Ge bonds in the layer are marked in green.

Like in other systems the structure types, even though they are similar, have a large influence on the band gap. For compounds with the same structure type, the usual trends of decreasing gaps with larger electronegativity differences are found. All compounds have indirect band gaps, but most of them could be classified as case two pseudo-direct, since their valence band maximum and conduction band minimum are close on the *k*-path. The band structure, density of states and crystal orbital Hamilton population of $RbGe_3As_3$ are shown in Abbildung 3.27.

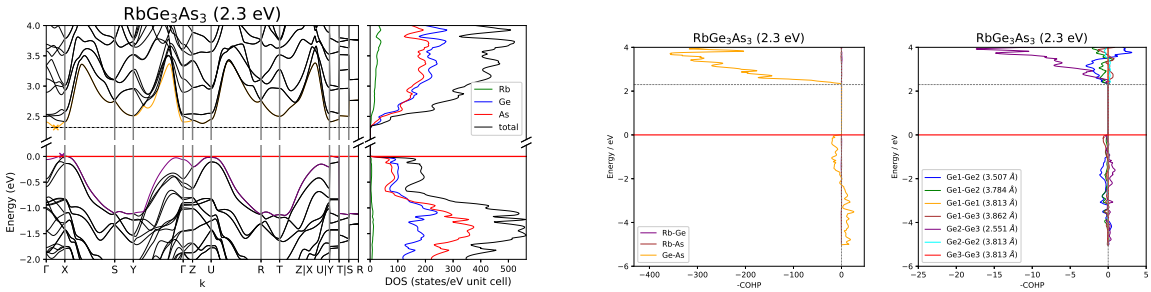

Figure 3.27: Band structure and DOS of $RbGe_3As_3$ and COHP of neighbouring heteroatomic Ge-Ge interactions.

The density of states shows many more tetrel element states at the Fermi-Level and no alkali metal states, so the VBM position does not seems to be affected by the alkali metal in this system. The COHP reveals anti-bonding interactions close to the Fermi-Level for the *Tt-Pn* and *Tt-Tt* interactions, which can be attributed to the interactions of the *Tt-Tt* bonds. The only exception is KSi_3As_3, which has a large amount of *Tt-Tt* bonding interactions at 0 eV, probably due to the different structure type. All compounds also show a small edge of

Tt-*Tt* and *Tt*-*Pn* anti-bonding interactions above the band gap, which becomes smaller if the actual CBM is close to Γ.
From this it seems that the additional *Tt*-*Tt* bonds lead to a change in states at the Fermi-Level, similar to the *A*Sn*Pn* system, where the different structural motive also increased the number of *Tt* states at the Fermi-Level. There are no clear trends on what might decide the position of VBM and CBM, but it seems like the *Tt*-*Tt* bonds do play a role. As for possible relativistic effects, Sn compounds show a very flat band around Γ, compared to the other tetrel compounds, which show a clear minimum in the first conduction band, accompanied by some sort of small maximum in the *Tt*-*Tt* and *Tt*-*Pn* projected COHP.

A_2TtPn_2 compounds - Influence of Bridging *Pn* Atoms

Alongside the A_2TtPn_2 system discussed above, there are also triel compounds with the same stoichiometry forming the A_2GaPn_2 system with A = K-Cs and Pn = P-Sb. Their crystal structures consists of one-dimensional chains of triangular planar units of $GaPn_3$, which are connected via corner-sharing and additional *Pn*-*Pn* bonds (Abbildung 3.28, refer to Abschnitt A.4 for a more detailed description).[123–128] All compounds show an indirect band gap, except for Cs_2GaSb_2 which has a type two pseudo-direct band gap, where valence band maximum and conduction band minimum are close on the *k*-path. The size of the band gap follows the usual trend with decreasing gaps from phosphides to antimonides.

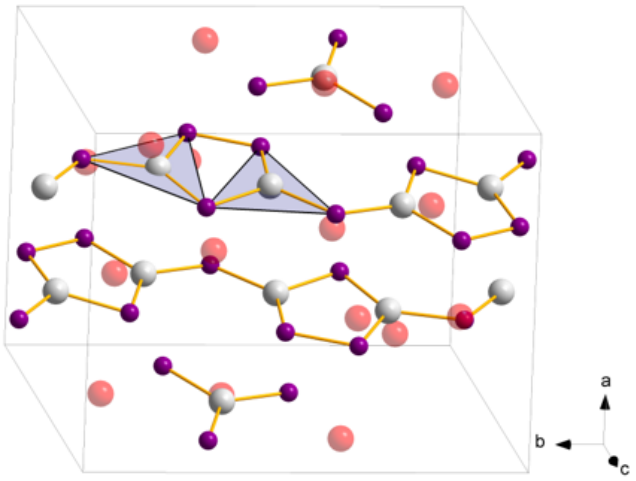

Figure 3.28: Crystal structure of K_2GaP_2.

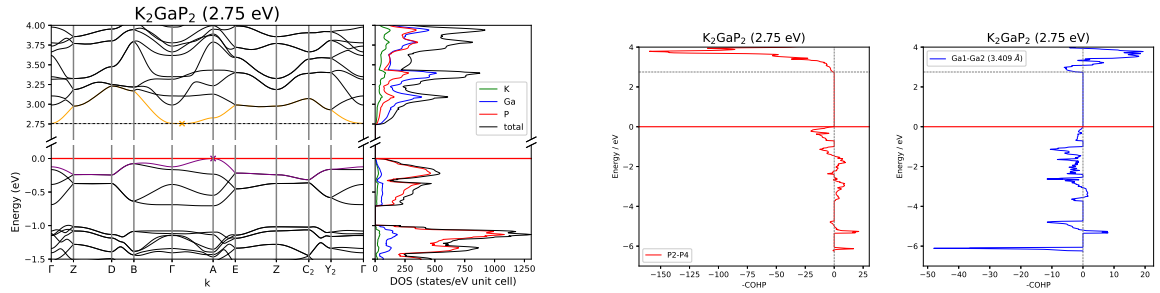

Figure 3.29: Band structure and DOS of K_2GaP_2 and COHP of bonding P-P and neighbouring Ga-Ga interactions.

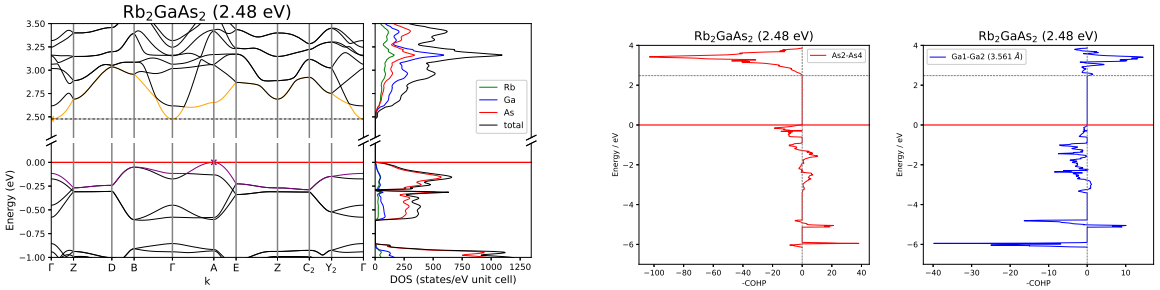

Figure 3.30: Band structure and DOS of Rb_2GaAs_2 and COHP of bonding As-As and neighbouring Ga-Ga interactions.

For all compounds the valence band maximum is located at either A or between Γ and one of its adjacent points, with a very flat top valence band on this path (Abbildung 3.29 and Abbildung 3.30). For all compounds the VBM is accompanied by some additional alkali metal states, especially if the top valence band shows a low dispersion. In the COHP, like most other systems, there is not much interaction of the gallium and pnictogen atoms with the alkali metal, therefore these states could be of non-bonding nature. The COHP projected on the additional *Pn-Pn* bonds reveals *Pn-Pn* anti-bonding interactions for all compounds close to the Fermi-Level, which could also be responsible for the VBM position.

The CBM is always located at or around Γ, again with some compounds, e.g. K_2GaP_2, showing a very flat band. Interestingly, the Ga-Ga projected COHP shows the same sharp increase in Ga-Ga interactions above the band gap, similar to the compounds of the tetrel system with the same stoichiometry. Additionally this steep increase becomes smaller, if the band is less flat at Γ and is absent for Rb_2GaAs_2, which has a sharp CBM. In the same interval the *Pn-Pn* bond projected COHP is identical for all compounds, with a slow increase in interactions. Therefore, it could be assumed that in this system *Pn-Pn* bonds influence the valence bands and might decide, where the maximum is located in addition to the alkali

metal's influence. For the conduction bands no significant influence of the *Pn-Pn* bonds can be found, since they are mainly influenced by the *Tr-Tr* interactions identified in other systems.

$A_2Tr_2Pn_3$ compounds - Comprising Pn-Pn bonds within the Layered Structure

The $A_2Tr_2Pn_3$ compounds, with A = Na-Cs, Tr = Al-In and Pn = As, Sb, build a second system, with additional *Pn-Pn* bonds, this time between $TrPn_4$ tetrahedra in layered structures. The layers consist of corner and edge-sharing $TrPn_4$ tetrahedra, for a detailed description please refer to Abschnitt A.9.[128–138]

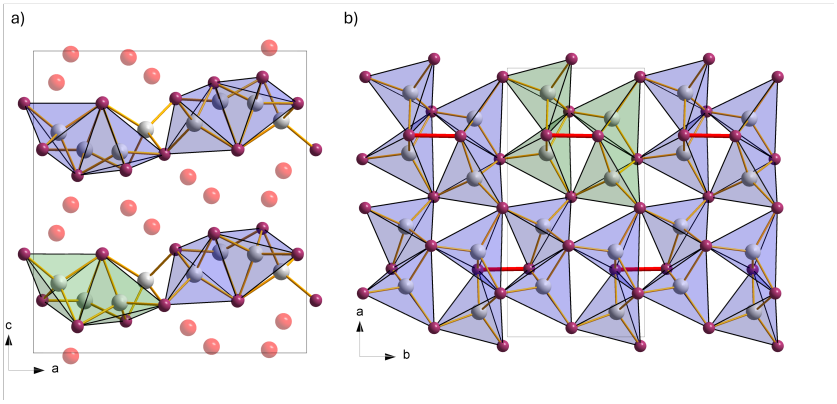

Figure 3.31: a) Crystal structure of the $A_2Tr_2Pn_3$ compounds with alkali metal, triel and pnictogen shown in red, grey and purple, respectively. b) Top-view one layer with the additional *Pn-Pn* bond marked in red.

For this system most compounds show an indirect band gap, but $K_2In_2As_3$, $Rb_2In_2Sb_3$ and Cs_2In_2Sb have direct and K_2InSb_3 has a pseudo-direct band gap, which are all but one indium compound. $Na_2Al_2As_3$ could also be categorized as type two pseudo-direct band gap since valence and maximum and conduction band minimum are close on the *k*-path. The $A_2Tr_3Pn_3$ system shows the largest difference of band gaps between arsenides and antimonides, with up to 0.7 eV compared to about 0.5 eV for other systems. For compounds that only differ by the triel atom, only for $K_2Ga_2As_3$ and $K_2In_2As_3$ a noticeable difference can be found for the band gap size, which might be due to the direct band gap. The band gaps within the arsenides and antimonides each, decreases for heavier alkali metals which is also a trend observed for other systems.

Most compounds, like $K_2In_2As_3$ show a very flat top valence band between B and Γ, therefore

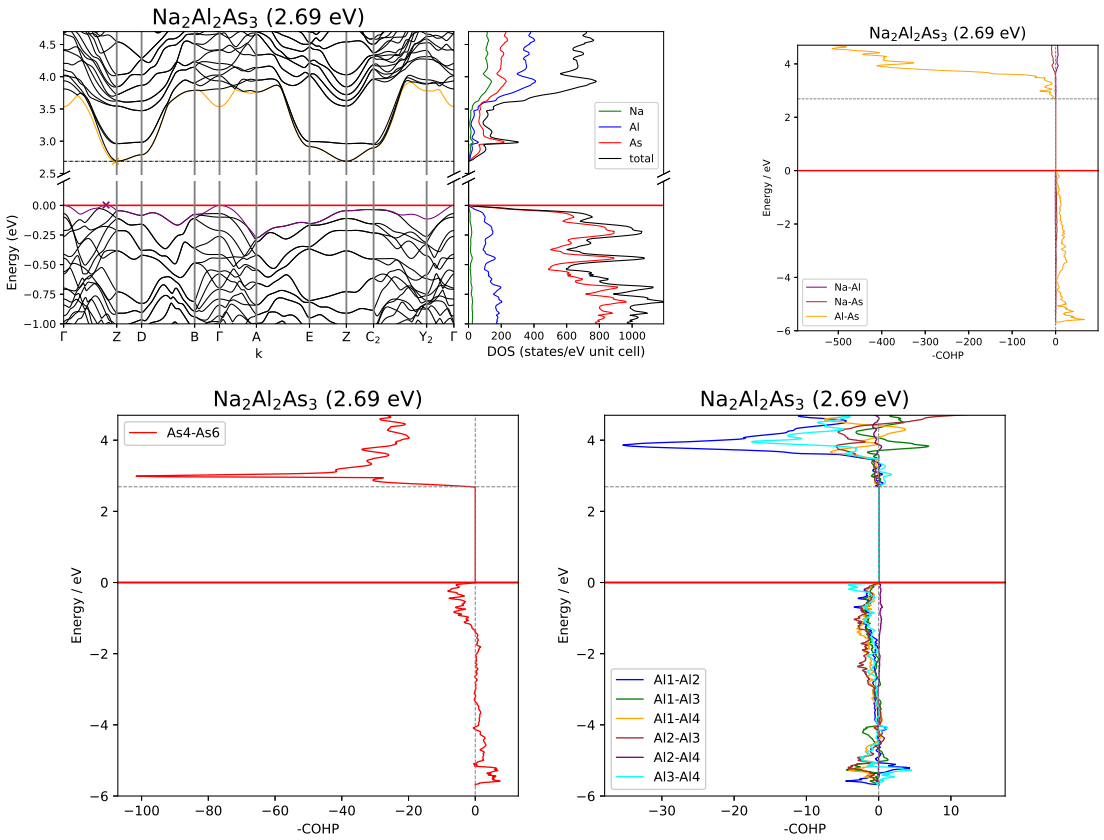

Figure 3.32: Band structure and DOS of $Na_2Al_2As_3$ and COHP of heteroatomic, bonding As-As and neighbouring Al-Al interactions.

many transitions are possible (Abbildung 3.32 and Abbildung 3.33). Here the DOS shows a small, detached maximum in *Tr* and *Pn* states at the Fermi-Level, but zero contribution from the alkali metals. In the same energy range the heteroatomic COHP shows little to no interaction between *Tr* and *Pn*, while the homoatomic *Tr*-*Tr* or *Pn*-*Pn* COHP show anti-bonding interactions, which might be responsible for the lifted top valence band between Γ and B. Similar to the A_2Ga*Pn*$_2$ compounds, the *Pn* states below the Fermi-Level belong (partially) to *Pn*-*Pn* anti-bonding interactions.

The In compounds have the CBM located at Γ, while indirect band gap compounds have them at Z, accompanied by a sharp increase in *Pn*-*Pn* interactions, instead of *Tr*-*Tr* interactions found in other compounds classes. These interactions are absent for In compounds. Since this effect is found for both arsenides and antimonides, it might not be caused by scalable relativistic effects, because only the Sb basis set accounts for them. The bond lengths of all As-As and Sb-Sb bonds are also very similar, thus, the rise in energy of the *Pn*-*Pn* anti-bonding interactions remains unclear.

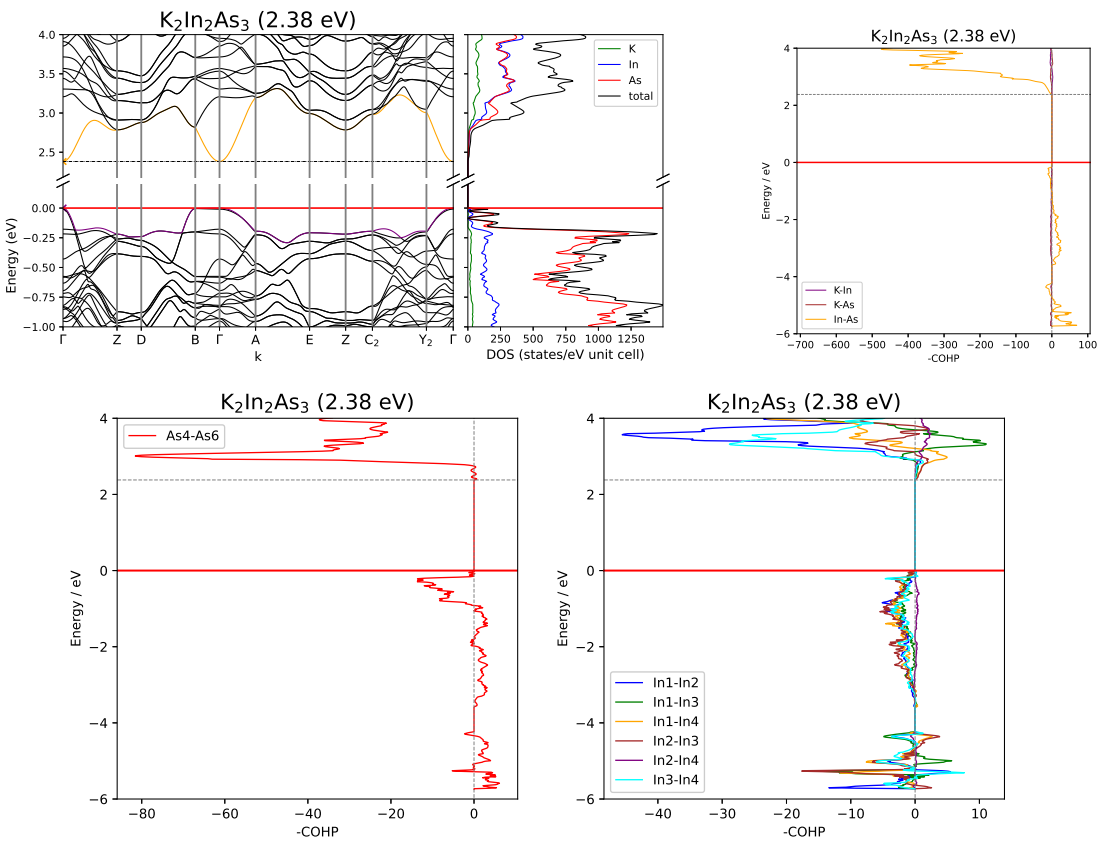

Figure 3.33: Band structure and DOS of $K_2In_2As_3$ and COHP of heteroatomic, bonding As-As and neighbouring In-In interactions.

3.2.4 Conclusions on Trends within the Compound Families

All results obtained from a more detailed study of several model systems, show that the basic electronic structure of all A_xTr/Tt_yPn_z compounds is very similar, but differ in the details. The band gap size primarily dependents on the electronegativity difference between the triel/tetrel and pnictogen, with the size decreasing from phosphides to antimonides, due to the less effective orbital overlap for larger pnictogen atoms with their neighbouring atoms. Aside from that, other factors influence the band gap size, such as the electronegativity difference between the alkali metal and the other atoms (A_5TtPn_2) or the crystal structure type(ATt_3Pn_3). Also do both effects act cooperatively or the alkali metal metals influences the type of structure build, like for the A_3TrPn_2 compounds. Therefore, each structure family has to be analysed separately for each trend to understand the fine differences between the band gap sizes.

Whether compounds have a direct or indirect band gap, as seen in the first chapter of the

discussion, depends on many factors and none of them seems to stand out. Looking closer at the different systems, the crystal structure seems to play an important role in each of them. In most systems compounds with the same structure tend to have the same nature of band gap, but not all different structures of one system. Additionally, the compounds with the heavier triel or tetrel atoms can break the trend, especially if the structure type mainly has indirect gaps.

Most compounds with a direct band gap show the respective transition at the Γ point, only few have them at other *k*-points. The top valence bands of most compounds with the maximum at Γ consist of mostly non-bonding pnictogen states. The top band can be lifted at several *k*-points by additional, presumably non-bonding, alkali metal states at the Fermi-Level, as well as additional *Pn*-*Pn* or *Tt*-*Tt* bonds, which result in anti-bonding interactions close to the Fermi-Level. All bonding interactions between *Tr*/*Tt* and *Pn* are at lower energies and thus, have not much influence on the states around the band gap. Therefore, the interactions of the alkali metals with their neighbouring atoms should be investigated more, to better understand, which effects lead to these non-bonding states.

The conduction bands primarily consist of triel/tetrel-pnictogen anti-bonding interactions. For systems with additional *Pn*-*Pn* or *Tt*-*Tt* bonds, their anti-bonding interactions add to the conduction bands. For compounds where the triel or tetrel atoms are close enough to interact with their neighbours of the same atom type, *Tr*-*Tr* or *Tt*-*Tt* interactions can be found above the band gap as well, although they are rather weak, since the distances are larger than the *Tr*/*Tt*-*Pn* bond lengths. Nonetheless in most systems, especially A_3TrPn_2 and A_2TtPn_2, they seem to have some influence on the position of the conduction band minimum. Often, if the minimum is not located at Γ, the *Tr*-*Tr*/*Tt*-*Tt* interactions show a sharp increase above the band gap, while compounds with the minimum at Γ have no or slightly bonding interactions. These interactions are especially often absent for Sn and In compounds, which then show the aforementioned trend of forming a different type of gap or are the only compounds within their system to have the CBM at Γ.

But this result has to be interpreted carefully. Since DFT methods are not ideal for calculating excited states and therefore conduction bands, this trend could be seen as a kind of calculation error, since the neighbouring *Tr*-*Tr*/*Tt*-*Tt* interactions are electrostatic interactions rather than the classical orbital interactions used to describe chemical bonds. However, since this trend can be found in different systems this would be, if at all treated as an error, rather a systematic than a statistic error. Another explanation could be, since *Tr*-*Tr*/*Tt*-*Tt* interactions are often absent or at higher energies for Sn and In compounds, that relativistic effects play a role for them. For Sn and In the basis sets have a core potential included for

the inner shells, and therefore some of these relativistic effects are taken into account in the calculation. For Ga and Ge new basis sets with core potentials could be used in calculations and results compared to the trends presented here.

3.3 Additional Calculations on Specific Compounds

List of publications to chapter 3.3.:

see 5.8: S. Zeitz, M. Boyko, S. Ponou, V. Hlukhyy, T.F. Fässler, Open Sn Framework Structure Hosting Bi Guest atoms – Synthesis, Crystal and Electronic Structure of $Na_{13}Sn_{26}Bi$, *manuscript for publication*.

see 5.9: S. Zeitz, A. Mutschke, T.F. Fässler, $CaSi_{2-x}Ge_x$, solid solution and analysis of ordered structures, *manuscript for publication*.

For the reason of comparison, the influence of composition and structure on the occurrence of specific band gaps is exemplarily extended to two compounds that either show a three-dimensional network with a small contribution of another component to the network or in which the atoms in the anionic network might mix over the entire composition range. Thus in this section the exemplary Zintl phases $Na_{13}Sn_{26-x}Bi_{1+x}$ and $CaSi_{2-x}Ge_x$ are presented, their (electronic) structures discussed and the influence of the previously found trends identified.

3.3.1 $Na_{13}Sn_{26-x}Bi_{1+x}$ (x = 0-2) - an Open Sn Framework Structure Hosting Bi Guest atoms

$Na_{13}Sn_{26-x}Bi_{1+x}$ is a Zintl compound comprising a complex open framework build by Sn atoms. It has been synthesized before by a reaction of the elements in a Na:Sn:Bi 5:12:1 ratio at 270 °C.[139, 140] All single crystals obtained from this compound show a composition of $Na_{13}Sn_{25.72}Bi_{1.27}$. It is the first reported compound in the Na-Sn-Bi system. The refined structure with 90 % probability ellipsoids is shown in Abbildung 3.34. The compound crystallizes in the triclinic space group $P\bar{1}$ (no. 2).

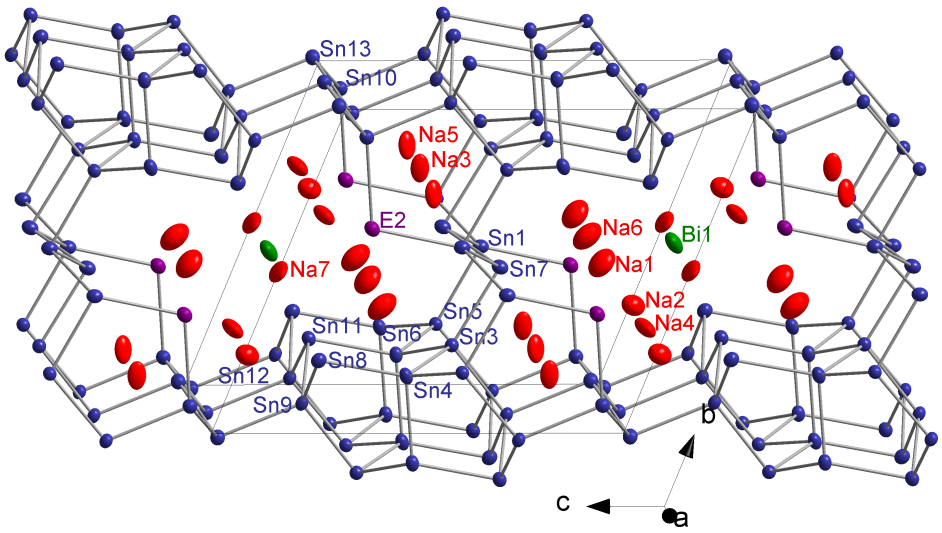

Figure 3.34: Crystal structure of $Na_{13}Sn_{25.72}Bi_{1.27}$. Na, Sn and Bi are shown in red, blue and green, respectively, the mixed Sn/Bi position E2 in purple. All ellipsoids are shown with a 90 % probability.

The three-dimensional open framework is build by 12 Sn atoms and one mixed Sn/Bi position E2 (Sn 86.4 %, Bi 13.6 %), which form two different cages I and II, that build tetramers consisting of cages I-II-II-I. Four such fragments are connected to form large cavities, which together with cage II, host the Na atoms. The isolated Bi atom is locate on a split position in the centre of the cavity. With interatomic distances between the Sn atoms of 2.822 Å to 2.947 Å covalent interactions are anticipated. The resulting bonding situations is as follows: Sn7, Sn8, Sn11 and Sn13 are three-, Sn1, Sn3, Sn4, Sn5, Sn6, Sn9, Sn10 and Sn12 – four-fold-bonded to neighbouring atoms. The same holds for the mixed E2 position with the neighbouring Sn1 and Sn10 position, since the distances of 2.965 Å and 2.985 Å are still in the range for covalent bonds and thus can be accounted for as two-fold bonded. The Bi split position has a distance of 3.145 Å and 3.455 Å to its neighbouring Sn11 position which therefore only weakly interacts with the framework.

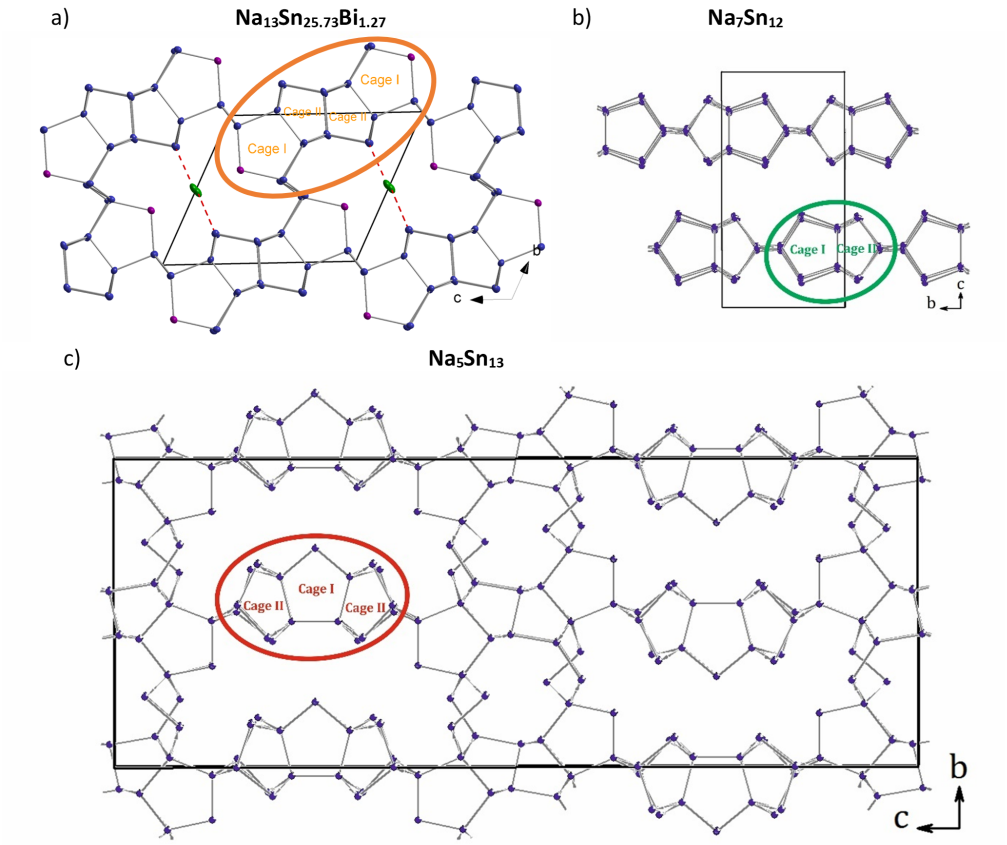

Figure 3.35: Comparison between the crystal structures of a) $Na_{13}Sn_{25.72}Bi_{1.27}$, b) Na_7Sn_{12} and c) Na_5Sn_{13} with cages I and II marked.

The crystal structure is related to Na_7Sn_{12} and Na_5Sn_{13} where the same two cages I and II can be found. While one cage I and II each are connected to form layers in Na_7Sn_{12}, a trimer of cages II-I-II is build which form with other fragments a three-dimensional network (see Abbildung 3.35).[36, 141]

To understand the bonding situation in $Na_{13}Sn_{25.72}Bi_{1.27}$, two boundary cases were analysed, where the E2 position is either fully occupied by Sn (case 1) or Bi (case 2). For the first case, with a nominal composition of $Na_{13}Sn_{26}Bi$ the anionic framework is built by $[(2b\text{-}Sn^{2-})_2(3b\text{-}Sn^{-})_8(4b\text{-}Sn^{0})_{16}]$, where n$b$ equals the number of bonds, and holds a total charge of -12. For a charge balanced compound and 13 Na^+ counterions the isolated Bi has to hold a negative charge of -1, resulting in $(Na^+)_{13}[(0b\text{-}Bi^{1-})_1(2b\text{-}Sn^{2-})_2(3b\text{-}Sn^{-})_8(4b\text{-}Sn^{0})_{16}]$. For the second case, with Bi occupying the E2 position, the composition $Na_{13}Sn_{24}Bi_3$ leads to the following electron count for the framework: $[(2b\text{-}Bi^{-})_2(3b\text{-}Sn^{-})_8(4b\text{-}Sn^{0})_{16}]$ and an overall charge of the polyanion of -10. According to the same 13 Na+ counterions the isolated Bi

atom has to hold a charge of -3 according to $(Na^{+})_{13}[(2b\text{-}Bi^{-})_{2}(3b\text{-}Sn^{-})_{8}(4b\text{-}Sn^{0})_{16}]$.
For the composition obtained via SC-XRD measurements of $Na_{13}Sn_{25.72}Bi_{1.27}$ the E2 position is occupied by 86.4 % Sn and 13.6 %. Therefore, combining the occupation with both modelled boundary cases an average sum formula can be formed, resulting in:
$(Na^{+})_{13}[(0b\text{-}Bi^{-})_{0.864}(0b\text{-}Bi^{3-})_{0.136}(2b\text{-}Bi^{-})_{0.272}(2b\text{-}Sn^{2-})_{1.728}(3b\text{-}Sn^{-})_{8}(4b\text{-}Sn^{0})_{16}]$.
This suggests that the isolated Bi guest atom can take up the surplus of electrons originating from the mixed position.
For both modelled boundary cases, $Na_{13}Sn_{26}Bi$ and $Na_{13}Sn_{24}Bi_{3}$ a structure optimization was calculated and band structure and density of states are shown in Abbildung 3.36. Both are indirect semiconductors with band gaps of about 0.6 eV. The overall shape of the bands is similar, but the two models differ in the dispersion of the top valence band and first conduction band. For $Na_{13}Sn_{26}Bi$ the first conduction band (1) has a dispersion of around 0.5 eV, while the top valence band (2) is comparably flat. In $Na_{13}Sn_{24}Bi_{3}$ this is inverted with the conduction band (3) being flat and the top valence band (4) having a 0.5 eV dispersion. Since the latter has 2 additional, considering a rigid band model, the Fermi-Level should be shifted, resulting in a conducting state. But this is not the case, since instead an additional band is added below the Fermi-Level, since Bi has an additional occupied p-orbital.
This can be seen in the DOS as well. While both models show, that Sn atoms have the highest contribution, is the contribution of Bi to the top valence and first conduction band negligible in $Na_{13}Sn_{26}Bi$, but almost a third in $Na_{13}Sn_{24}Bi_{3}$. Resolving the Bi states by their atomic position reveals, that this large contribution originates from the two-bonded Bi2 position, which due to their negative charge and non-bonding electron pairs appear as, energetically, highest occupied states.

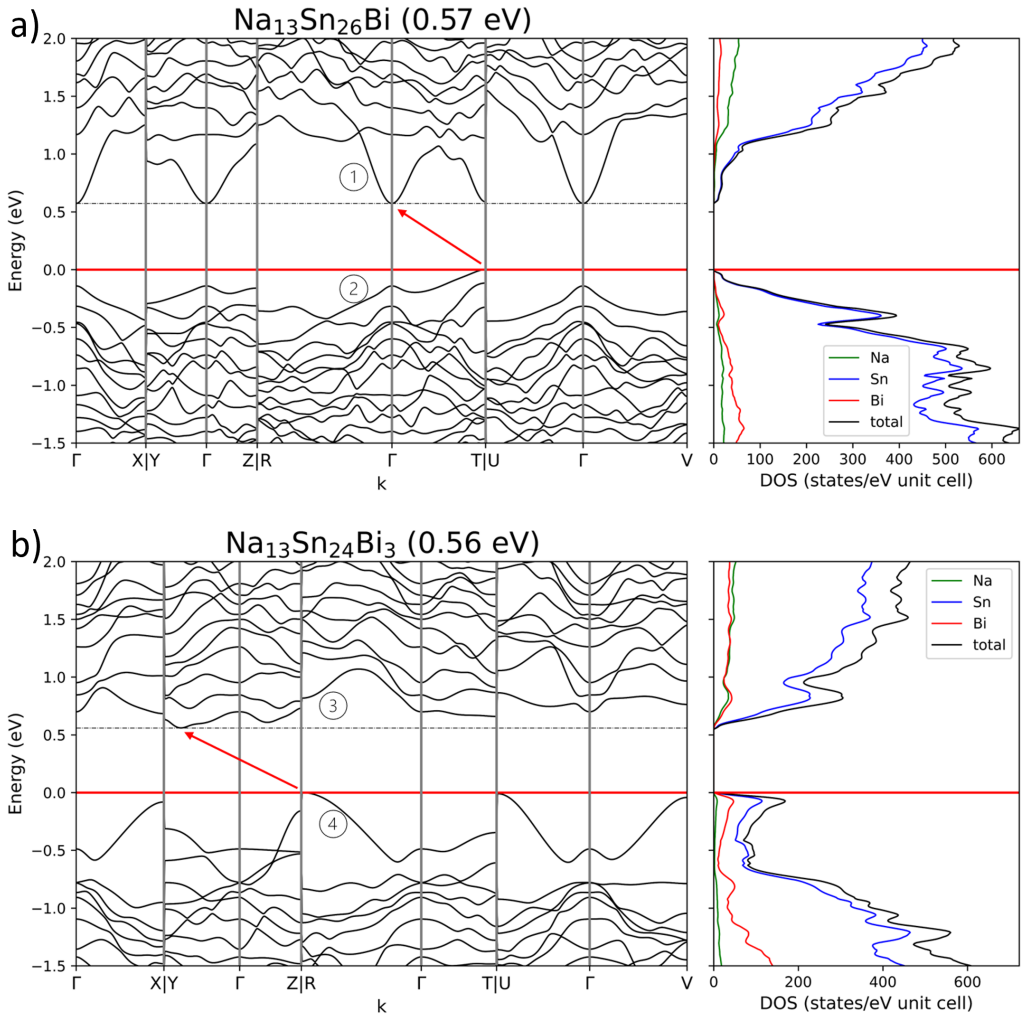

Figure 3.36: Band structures and density of states of a) $Na_{13}Sn_{26}Bi$ and b) $Na_{13}Sn_{24}Bi_3$.

Applying a Mulliken population analysis and assigning covalent bonds to overlap populations over $0.2\,e^-$ leads to the same three-dimensional framework described above. The isolated Bi1 atom shows a decreased overlap of about $0.084\,e^-$ ($0.094\,e^-$ for $Na_{13}Sn_{24}Bi_3$) with its neighbouring Sn11 atom, which can be considered as a weak interactions but not a covalent bond. All Na atoms show only weak interactions, that can be interpreted as ionic, which are in line with the Zintl-Klemm concept, stating that they act as mere electron donors.[14, 15] The Mulliken partial charges are also mostly in line with the proposed charges for $Na_{13}Sn_{26}Bi$. Na atoms show positive charges of about 0.8, while all Sn atoms have charges between 0 and -0.6. 3*b*-Sn, 2*b*-Sn and 4*b*-Sn atoms with proposed charges of -1, -2, and 0 show higher charges of -0.6 to -0.2, -1.1 and 0, respectively. The isolated Bi has a Mulliken partial charge

of -1.1, which hints also for a higher formal negative charge than the proposed -1.
For $Na_{13}Sn_{24}Bi_3$ the overall charge distribution is identical, even though a higher charge is expected for the Bi1 position, since the formal charge is appointed to -3. Interestingly is the charge with a value -1.05 even smaller than in $Na_{13}Sn_{26}Bi$. Therefore it is implied, that the excess charge, arising from the mixed position, is rather distributed over the whole three-dimensional framework, than located on Bi1.

In summary, is the reported compound an interesting example how a semiconducting Zintl phase retains its properties despite being non-electron precise, with respect to the 8-N rule. The experimentally observed composition is always $Na_{13}Sn_{25.73}Bi_{1.27}$, with powder diffraction and single crystals showing, within standard deviations, always the same lattice parameters. This can be explained with the compound's host-guest nature, in which the guest atom Bi1 can slightly change the oxidation state without changing the stiff Sn network. The crystal structure is similar to the two binary Zintl compounds Na_7Sn_{12} and Na_5Sn_{13} incorporating the same cages as building blocks. The band structure is remarkably flexible in shifting bands at the Fermi level retaining the band gap.

3.3.2 Investigation on $CaSi_2$ and $CaGe_2$ Allotropes and Mixed $CaSi_{2-x}Ge_x$ Compounds

$CaSi_2$ and $CaGe_2$ are iso-structural classical examples of Zintl compounds, for which the anionic sub-structure can be described with the Zintl-Klemm concept. Ca atoms act as an electron donor, transferring both valence electrons to Si/Ge, resulting in Si^-/Ge^-, which form grey As like layers of chair conformed edge-sharing layers of six-membered rings. Within the unit cell layers of Si/Ge and Ca are alternating, with different stacking orders depending on the isomer (Abbildung 3.37). For both $CaSi_2$ and $CaGe_2$ synthesis from the elements in an arc-furnace leads to the formation of types **A** and **E**, respectively, which are also known as $CaSi_2$-type or *hR*6 (**A**) and β-$CaGe_2$ type (**E**).[142, 143] Other $CaSi_2$ isomers can be obtained by synthesis under (hydrogen) pressure, α-$CaGe_2$ by Indium flux synthesis. [143–146]

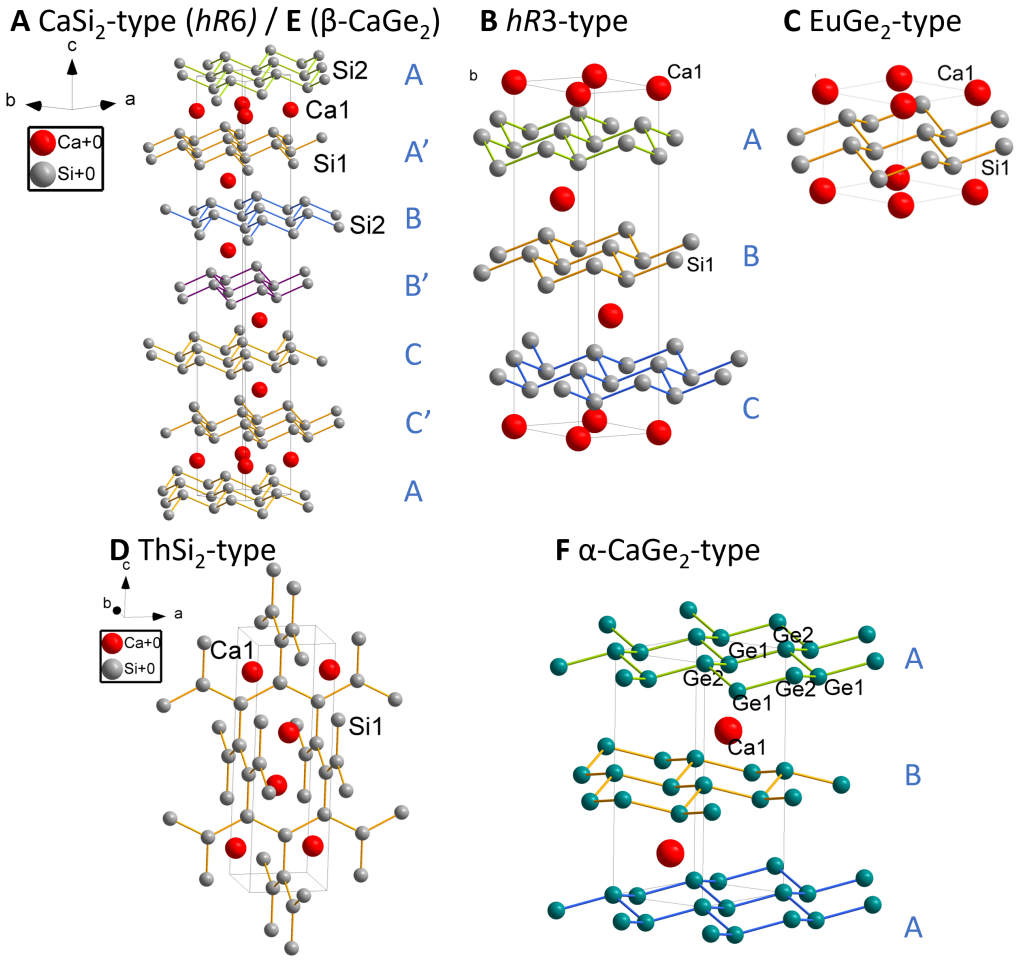

Figure 3.37: Overview of different structure types of $CaSi_2$ and $CaGe_2$. Ca, Si and Ge are shown in red, grey and green, respectively. Above each unit cell the structure type and reference name are written in black. The stacking order of certain structure types are marked in blue letters.

Each isomer structure was optimized. All optimized cell parameters are in good agreement with the experimental ones, except for some larger deviations of the c-parameters, probably caused by the layered nature and thus anisotropy of the crystal structure. To compare the stability of the isomers energy and Gibbs free enthalpy were calculated (Tabelle 3.2.). To show that the crystal structures of $CaSi_2$ (type **A**) and β-$CaGe_2$ (type **E**) are equivalent, models based on the respective other experimental data with switched atoms were calculated as well. As expected from the experiments structures **C** and **D**, which are only accessible at high pressures show larger energies and enthalpies, while the $CaSi_2$-type has the lowest energy. **B** might have a slightly lower energy, due to the less complex stacking order.

For the two $CaGe_2$ polymorphs, the experimentally feasible β-type is by far the more stable isomer. The frequency calculation for α-$GaGe_2$ revealed one negative frequency, therefore the structure was re-optimized in a lower $Cmc2_1$ (no. 36) symmetry. **F'** has now the lowest energy of all $CaGe_2$ polymorphs, which also might be caused by the less complex stacking order. **F'** further on shows the same octahedral coordination of the Ca^{2+} cations as in β-$CaGe_2$, showing that the structures of both polymorphs can be transformed into each other. It also implies, that α-$CaGe_2$ might be only accessible via In-flux, because the structure is stabilized by some minor In impurities.
As for the comparison between $CaSi_2$ in β-$CaGe_2$ structure an vice versa, the energy differences to the original structure types are negligible, which shows that both structure types are indeed the same.

Table 3.2: Energetic comparison of different $CaSi_2$ and $CaGe_2$ polymorphs. The compound with the lowest energy (E/Z) and Gibbs free enthalpy (G/Z) respectively were set as 0. All other ΔE and ΔG values are calculated relative to them.

			E/Z (AU):	ΔE (kJ mol^{-1})	G/Z (AU)	ΔG (kJ mol^{-1})
$CaSi_2$	$CaSi_2$-type	**A**	-1256.2234	0	-1256.2216	0
	$EuGe_2$-type	**C**	-1256.2201	8.8	-1256.2176	10.5
	$hr3$-type	**B**	-1256.2251	-4.3	-1256.2222	-1.7
	$ThSi_2$-type	**D**	-1256.2171	16.6	-1256.2161	14.4
	β-$CaGe_2$-type	**E**	-1256.2234	0.0	-1256.2216	0.0
$CaGe_2$	β-type	**E**	-4831.0136	0	-4831.0146	0
	α-type	**F**	-4830.9811	170.6	-4830.9811	176.0
	$CaSi_2$-type	**A**	-4831.0136	0.0	-4831.0146	0.0
	α'-type (gr.36)	**F'**	-4831.0145	-4.5	-4831.0155	-4.7

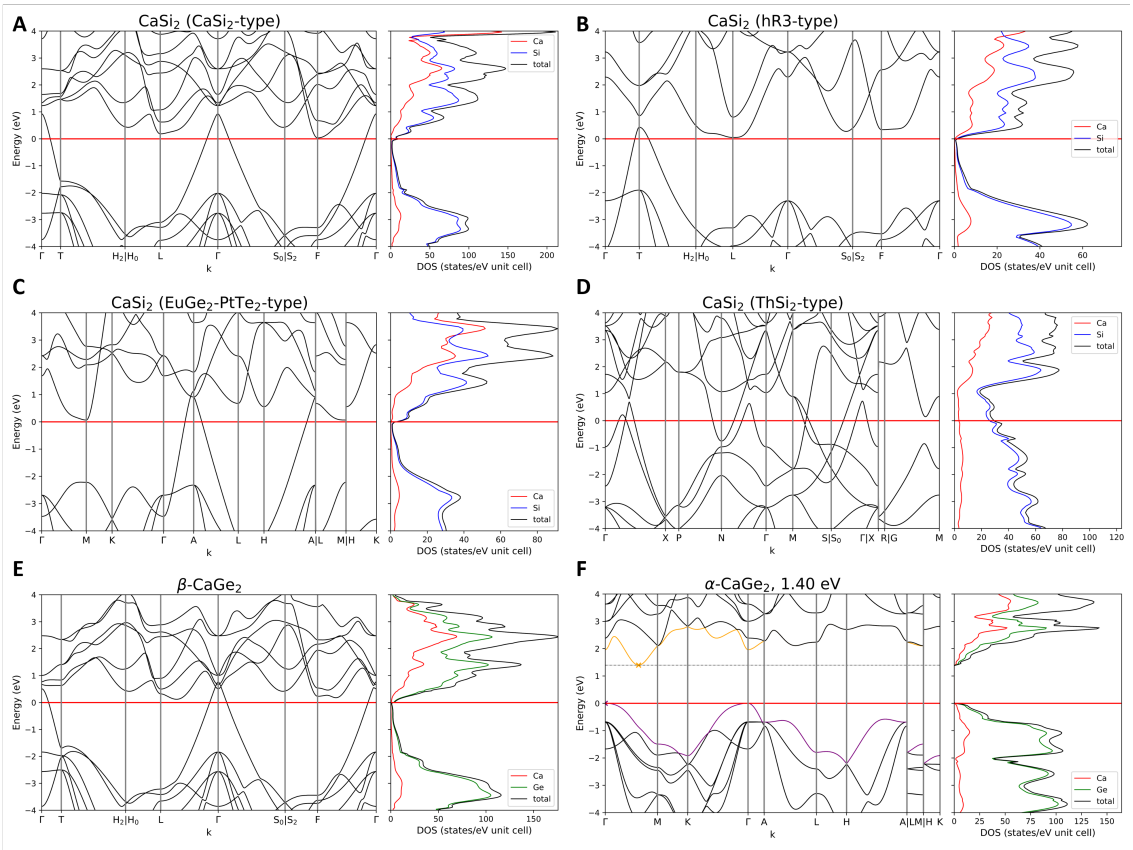

Figure 3.38: Band structures and density of states for all polymorphs **A** to **F** of $CaSi_2$ and $CaGe_2$. Only α-$CaGe_2$ shows an indirect band gap of 1.40 eV.

For all polymorphs band structure and density of states were calculated (Abbildung 3.38). All but α-$CaGe_2$ show a anisotropic metallic band structure with large dispersions for both conduction and valence bands. The conducting behaviour can be interpreted, similar to graphite, as conducting within the Si/Ge layers, but isolating perpendicular to the layers.[147] Interestingly, does α-$CaGe_2$ show semi-conducting behaviour, which goes back to conducting upon structure re-optimization. This behaviour is linked to the occurrence of some Ca states around the band gap in α-$CaGe_2$, which are absent for the other polymorphs. They might arise from a smaller Ca-Si distance, compared to the other polymorphs, resulting in more interaction between them. This could hint, that only the chemical environment of Ca^{2+} is determining, whether compounds in this system are conducting or not. This behaviour is similar to the alkali metal compounds in the A_xTr/Tt_yPn_z system, where indirect band gaps were often linked to some alkali metal states close to the Fermi-Level. Therefore the influence of the alkali and earth alkali metal basis sets on the electronic structure calculations has to be investigated further.

To compare the influence of the Si/Ge occupation of specific atom sites on the electronic band structure, ordered models resembling a mixed CaSiGe phase based on the models of the binary phases were calculated and analysed. Since α-$CaGe_2$ has been found to be a semi-conductor, ordered models based on this phase were calculated as well.

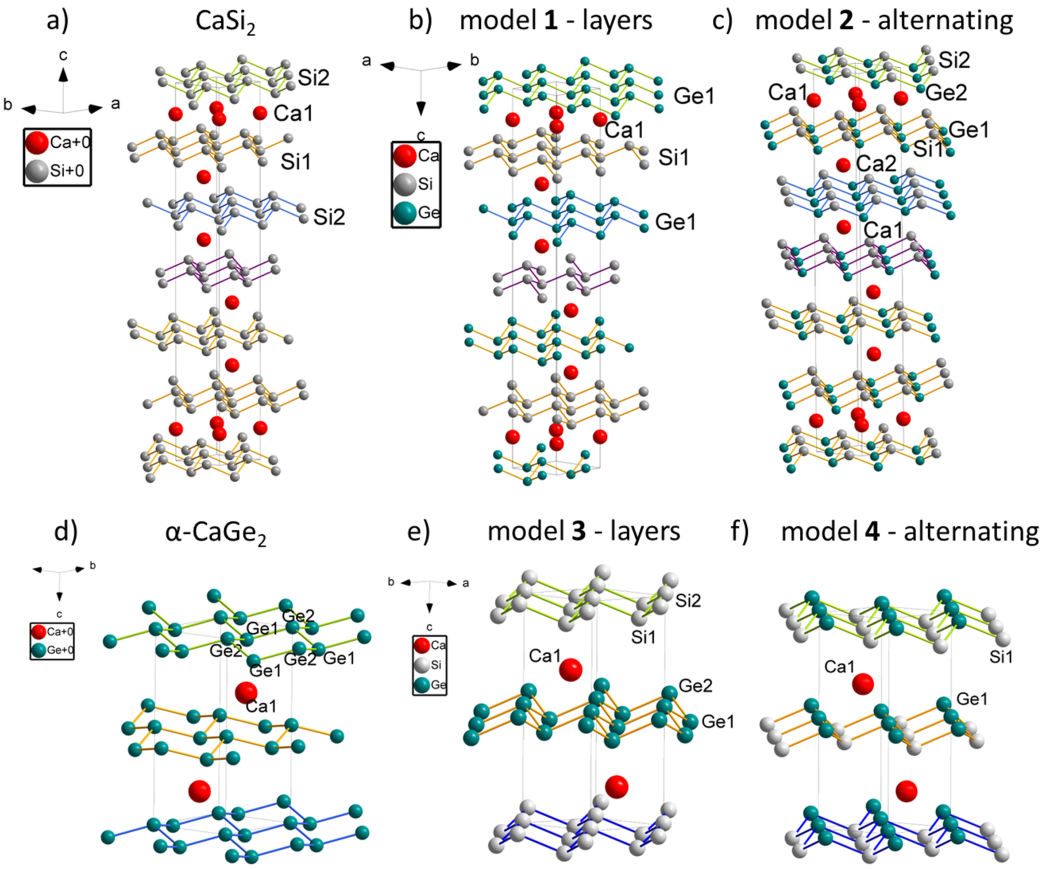

Figure 3.39: Created ordered models based on the $CaSi_2$ structure type shown in a). b) Layered structure model **1** with alternating Si and Ge nets along the c-direction obtained without reducing the symmetry, c) symmetry reduction to group 160 ($R3m$) allowing for two-dimensional Si—Ge nets with alternating Si and Ge atoms in structure model **2**. Created ordered models based on the α-$CaGe_2$ structure type shown in d). e) Layered structure model **3** with alternating Si and Ge nets along the c-direction obtained by reducing the symmetry to group 156 ($P3m1$), f) two dimensional Si—Ge nets with alternating Si and Ge atoms in structure model **4**, obtained without reducing the symmetry.

The crystal structures of all ordered models are shown in Abbildung 3.39. For model **1**, originating from the $CaSi_2$ structure, Si1 is retained, while the second silicon position is

Table 3.3: Distances and dihedral angles of the different ordered models of CaSiGe. The dihedral angle describes the angles between the centre square plane of the six-membered ring and the triangular tip.

parent comp.		Model		$d_{Si\text{-}Si}$ (Å)	$d_{Ge\text{-}Ge}$ (Å)	∡ Si-layer (°)	∡ Ge-layer (°)
$CaSi_2$	A	layers	1	2.4649	2.4913	64.117	67.323
β-$CaGe_2$	E		1	2.4675	2.4937	64.165	67.327
α-$CaGe_2$	F		3	2.4609	2.5128	60.435	67.042
$CaSi_2$	A	layer (VV)	1'	2.4351	2.5189	59.838	70.167
β-$CaGe_2$	E		1'	2.4331	2.518	59.429	70.032
α-$CaGe_2$	F		3'	2.4609	2.5128	60.463	67.064
				$d_{Si1\text{-}Ge1}$ (Å)	$d_{Si2\text{-}Ge2}$ (Å)	∡ Si1-layer (°)	∡ Si2-layer (°)
$CaSi_2$	A	alternating	2	2.4929	2.4644	67.115	63.622
β-$CaGe_2$	E		2	2.4929	2.4641	67.086	63.562
α-$CaGe_2$	F		4	2.4847		63.268	
$CaSi_2$	A	alternating (VV)	2'	2.4931	2.4643	67.101	63.579
β-$CaGe_2$	E		2'	2.4928	2.4644	67.129	63.668
α-$CaGe_2$	F		4'	2.4895		64.195	

changed to Ge, forming alternating Si and Ge layers (Abbildung 3.39b). For model **2** with alternating Si and Ge within the six membered rings, the Si1 and Si2 *6c-Wyckoff* positions are spit into two *3a* positions each upon symmetry reduction to group 160 (Abbildung 3.39c). The same models were build with Si and Ge positions switched (marked with VV). For the models based on α-$CaGe_2$, the layered model **3** is created by lowering the symmetry to space group 156, such that the 2a and 2b *Wyckoff*-positions are split and homoatomic layers can be formed (Abbildung 3.39e). For the alternating model **4** the symmetry is retained and Ge1 position changed to Si (Abbildung 3.39f). The same models **1'** to **4'** were build with Si and Ge positions swapped.

Tabelle 3.3 gives an overview of the bond lengths within and dihedral angles of the six-membered rings for each optimized CaSiGe ordered model. For the layered models, as expected, are the Si-Si bonds slightly smaller than the Ge-Ge bonds, but since the size of the six-membered rings within each layer has to be the same when seen from above, the larger Ge layers show a larger dihedral angle. For the mixed CaSiGe models an average bond length between Si and Ge can be found and small differences in the dihedral angles.

The energies and enthalpies of all calculated models **1** and **2** are all very similar with the largest difference being about 5 kJ mol^{-1}. Comparing them to the obtained bond lengths, the energy differences are smaller if the Ge-Ge bond is longer, probably due to less strain in the Ge six-membered rings. Since the mixed layer models have average bond lengths and angles they show a medium energy difference. The differences to the models **3** and **4** are about 90 kJ mol^{-1}, due to the imaginary frequencies that arise during the calculation.

As for the stability of the ordered models compared to the parent compounds the energies and enthalpies can be compared according to the following reaction:

$$\frac{1}{2}\,\mathrm{CaSi_2} + \frac{1}{2}\,\mathrm{CaGe_2} \longrightarrow \mathrm{CaSiGe} \tag{3.1}$$

with the energies of the educt side being set to 0. The ordered models all show a slightly larger energy with differences of up to $5\,\mathrm{kJ\,mol^{-1}}$. Since the reaction does not take possible entropic effects of the (statistical) Si/Ge mixing into account and the energies differences are negligible small, mixed compounds should still form easily.
Like their parent compounds do all models **1** and **2** show anisotropic, metallic band structures, while models **3** and **4** are semi-conductors.

Synchrotron p-XRD measurements of solid solutions of $CaSi_2$ and $CaGe_2$ synthesised in an arc furnace from stoichiometric mixtures of the elements with the nominal formula of $CaSi_{2-x}Ge_x$, with x = 0, 0.5, 1, 1.5 and 2 confirm the statistical mixing of Si and Ge within the layers. The cell parameters of the parent compounds are in good agreement with literature.[142, 143] Cell parameters plotted against the refined composition are shown in Abbildung 3.40.

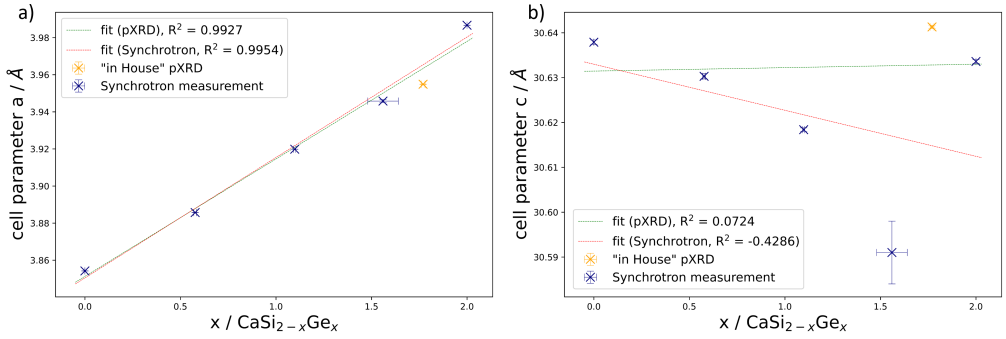

Figure 3.40: Cell parameter a and c plotted against the composition. Synchrotron measurements and the additional pXRD sample are marked in blue and yellow respectively. The linear regression of the synchrotron measurements is shown in red, while the green one incorporates the pXRD sample for x = 1.5 instead.

Two linear regressions were fitted with the data, one for all synchrotron measurements and one switching the x = 1.5 measurement with a refined in house p-XRD measurement, since the synchrotron sample partially decomposed during measurement. Cell parameter a evidently follows Vegard's law and except for the decomposed sample all points show negligible

errors, represented by error bars and the coefficient of determination R^2 which is close to 1 for both fits. For the c parameter the Vegard's law seems not to apply. All c parameters are within a range of 0.05 Å and seem to be smaller for mixed $CaSi_{2-x}Ge_x$. The replacement pXRD sample shows the largest and the synchrotron measurement the smallest c. This could hint that there is no direct dependence of the c parameter on the composition, but it might be influenced by the synthesis. Since the layers of $CaSi_2$ and $CaGe_2$ have in general distances of about 5 Å between each other and thus only interact weakly, this gives them a larger scope in movement at higher temperatures and in combination with the abrupt cooling of the arc furnace might result in the not Vegard-like behaviour.

4 Conclusion

Electron precise Zintl compounds of the A_xTr/Tt_yPn_z system, with A = Li, Na, K, Rb, Cs, Tr = Al, Ga, In, Tt = Si, Ge, Sn and Pn = P, As, Sb, have been proven to be an ideal model system for the investigation of crystal structure band structure relations. Due to their large variety of structural motives and their connectivity the influence of different crystal structure parameters as well as chemical properties could be investigated. By looking at the whole data set, the electronegativity seems to be the main factor influencing the size of the band gap, especially the difference between triel/tetrel and pnictogen. The band gaps for arsenides decrease due to their less effective orbital overlap with neighbouring atoms. Smaller influence of the band gap has the electronegativity of the alkali metal or the dimension of the crystal structure type, although if investigated in more detail, the occurrence of certain crystal structures is also differently favoured by certain alkali metals. This leads to the conclusion, that the different properties might be closer dependent on each other than they look at first glance. To differentiate the influences of certain properties one needs to investigate the (stoichiometric) sub-systems.

The occurrence of direct band gaps seems to be linked to different properties. Since on one hand all compounds with three-dimensional polyanionic networks show direct band gaps and on the other most compounds within one system that have the same crystal structure also show the same kind of band gap, could the crystal structure play an important role in influencing the band gap. More detailed investigations revealed, that most direct band gaps have $\Gamma \rightarrow \Gamma$ transitions. Additional, non-bonding alkali metal states or Pn-Pn/Tt-Tt interactions close to the Fermi-Level might be responsible for valence band maxima at different *k*-points, since most compounds with the valence band maximum at Γ show mostly Pn non-bonding states at E_F. For the conduction band minimum Tr-Tr or Tt-Tt interactions right above the band gap are often present, if the minimum is not located at Γ. Up to this point their there are two possibilities as to where thy originate from. They could be an artefact of the calculation itself, since the methods used are limited in the prediction of excited states. Further on, since the indirect band gaps often change to direct band gaps for compounds that show the same crystal structure, but account for some relativistic effects with their basis sets, the

level of theory of the elemental basis sets could also play a role. Otherwise is the effect of the Tr-Tr/Tt-Tt interaction present in different (stoichiometric) systems, such that if they are simply an error it would rather be a systematic error. Therefore interactions between neighbouring triel or tetrel atoms could be responsible for the conduction band minimum at other *k*-points and simply at higher energies for Sn and In compounds, which then show direct band gaps.

Lastly did more detailed research an specific compounds revealed that small changes in the crystal structure can have a large influence on the electronic structure. For the Zintl compound $Na_{13}Sn_{26-x}Bi_{1+x}$ with x between 0 and 2, switching one Sn atoms with Bi, lead to a drastic change in shape for the top valence band as well as first conduction band. For the $Na_{13}Sn_{26}Bi$ model the first conduction band shows a large dispersion, while the additional Bi states in $Na_{13}Sn_{24}Bi_3$ are located close to the Fermi-Level, increasing the dispersion of the top valence band. Interestingly did the and gap size not change at all between the two models. A Mulliken population analysis was able to verify most formal charges imposed by the Zintl-Klemm concept for both models, since the surplus of electrons might be delocalised over the whole Sn network instead of localised at the isolated Bi position.

Investigations on the different polymorphs of $CaSi_2$ and $CaGe_2$ revealed, that the influence of the (earth) alkali metal on the electronic structure should be studied further. Here a small difference in coordination of the Ca^{2+} cation leads in α-$CaGe_2$ to semi-conducting properties, while β-$CaGe_2$ is a metal. Re-optimization of α-$CaGe_2$, due to imaginary frequencies, lead to a structure similar to β-$CaGe_2$ and metallic properties. This could also explain why the α-phase is only experimentally feasible via In-flux synthesis, since In impurities might stabilize the structure.

Future research should focus on two aspects: On one hand expanding the data set by on one hand calculating more (Zintl) compounds such as earth alkali metal based pnictidotrielates and -tetrelates. Additionally modelling of the experimentally unknown compounds is necessary to complete research on the sub-systems and specify the trends identified. On the other hand should the influence of the (earth) alkali metal on the band structure calculations be investigated as well as the level of theory. Here more accurate (TZVP) basis sets for the (earth) alkali metals and incorporation of core potentials for the lighter Ga, Ge and As atoms could be a good starting point. Calculations with post-DFT methods should also be explored to give a more accurate insight on excited states and which properties could have an effect on them.

5 Publications and Manuscripts

This dissertation is written as a publication-based thesis (see Declaration). In this chapter all publications as well as manuscripts for publications are included.

5.1 Electronic Structure Analysis of the $A_{10}Tt_2P_6$ System (A = Li Cs; Tt = Si, Ge, Sn) and Synthesis of the Direct Band Gap Semiconductor $K_{10}Sn_2P_6$

Sabine Zeitz, Hanna Antoniuk, Viktor Hlukhyy, and T. F. Fässler

published in

Chemistry — A European Journal **2024**, *30*, e202400002

Check for updates

Chemistry–A European Journal

Research Article
doi.org/10.1002/chem.202400002

Chemistry Europe
European Chemical Societies Publishing

www.chemeurj.org

Electronic Structure Analysis of the $A_{10}Tt_2P_6$ System (A = Li–Cs; Tt = Si, Ge, Sn) and Synthesis of the Direct Band Gap Semiconductor $K_{10}Sn_2P_6$

Sabine Zeitz,[a] Hanna Antoniuk,[a] Viktor Hlukhyy,[a] and T. F. Fässler[a]

Investigating the relationship between atomic and electronic structures is a powerful tool to screen the wide variety of Zintl phases for interesting (opto−)electronic properties. To get an insight in such relations, the $A_{10}Tt_2P_6$ system (A = Li–Cs; Tt = Si–Sn) was picked as model system to analyse the influence of structural motives, combination of elements and their properties on type and width of the band gaps. Those compounds comprise two interesting structural motives of their anions, which are either monomeric trigonal planar TtP_3^{5-} units which are isostructural to CO_3^{2-} or $[Tt_2P_6]^{10-}$ dimers which correspond to two edge-sharing TtP_4 tetrahedra. The $A_{10}Tt_2P_6$ compounds were structurally optimized for both polymorphs and subsequent frequency analysis, band structure as well as density of states calculations were performed. The Gibbs free energies were compared to determine temperature dependent stability, where $Na_{10}Si_2P_6$, $Na_{10}Ge_2P_6$ and $K_{10}Sn_2P_6$ were found to be candidates for a high temperature phase transition between the two polymorphs. Additionally, the unknown, but predicted compound $K_{10}Sn_2P_6$ was synthesized and characterized by single crystal and powder x-ray diffraction. It crystalizes in the monoclinic space group $P\,2_1/n$ and incorporates $[Sn_2P_6]^{10-}$ edge sharing double tetrahedra. It was determined to be a direct band gap semiconductor with a band gap of 2.57 eV.

Introduction

While for many ternary alkali-metal phosphidotetrelates the ionic conductivity was intensively investigated, their electronic structures were merely briefly mentioned.[1–5] Recently interesting electronic properties such as direct band gaps, which make these compounds interesting candidates for electronic applications, have been reported.[6] The class of alkali-metal phosphidotetrelates, comprises many representatives and thus forms a good basis for the search of structure property relationships which may lead to an insight on why direct band gaps occur in some phases. Such criteria, if proven true, could also be used to screen and optimize materials for further application processes such as band gap tuning. To find such relations, a variety of crystal structure characteristics and their influence on the electronic structure can be investigated and if possible be traced back to bonding situation, structural motives, elemental composition, and the elemental properties such as electronegativity. Keeping them in mind it becomes evident that for first principles investigations a good model system, for which a large variety of existing archetypes and possible allotropes is known, must be chosen.

Compounds of the composition $A_{10}Tt_2P_6$ (with A = Li, Na, K, Rb and Cs, Tt = Si, Ge, Sn) are interesting candidates, since many representatives are known, and they show rather different but simple structural motives. All are electron precise compounds according to the Zintl concept. Thus, the influence of different structural motives despite the same composition and the influence of a homologue series on the electronic structure can be investigated. The compounds of the composition $A_{10}Tt_2P_6$ form three structure types. $Li_{10}Si_2P_6$ and $Na_{10}Tt_2P_6$ compounds crystalize in the monoclinic space group $P2_1/n$ containing units of two edge-sharing tetrahedra $[Tt_2P_6]^{10-}$ (Tt = Si, Ge, Sn) further on referred to as "dimer structure type" and depicted with sum formulae containing the 10:2:6 stoichiometry (Figure 1b).[7,8,2] In contrast $Li_{10}Ge_2P_6$ and $Li_{10}Sn_2P_6$ crystalize in the cubic space group $Fm\bar{3}m$ in which according to the CaF_2 structure type, the P atoms form a cubic closest packing (ccp) with Tt and Na atoms appearing disordered over all tetrahedral voids.[9] The known compounds with heavier alkali metals, Rb_5GeP_3, Cs_5SiP_3 and Cs_5GeP_3 crystallize in the *Pnma* space group. The structural motive changes from edge-sharing tetrahedra to monomeric trigonal planar TtP_3^{5-} (Tt = Si, Ge) units that are isostructural to CO_3^{2-}.[10,11] This structure is further on referenced to "monomer structure type" and given stoichiometries of 5:1:3 in sum formulae (Figure 1a).

Additionally, and most interestingly, no representatives of the potassium-analogues $K_{10}Tt_2P_6$ have been reported. Those are of particular interest since they are at the borderline between existing Na and Rb compounds, thus both structure types are possible and thus also phase transitions between them might energetically be reasonable. Modelling them could lead to the prediction of new compounds and give a deeper insight on factors influencing the structure formation. In

[a] S. Zeitz, H. Antoniuk, V. Hlukhyy, T. F. Fässler
School of Natural Science, Technical University of Munich, Chair of Inorganic Chemistry with Focus on Novel Materials, Lichtenbergstraße 4, D-85747 Garching, Germany

Supporting information for this article is available on the WWW under https://doi.org/10.1002/chem.202400002

Chemistry–A European Journal
Research Article
doi.org/10.1002/chem.202400002
Chemistry Europe
European Chemical Societies Publishing

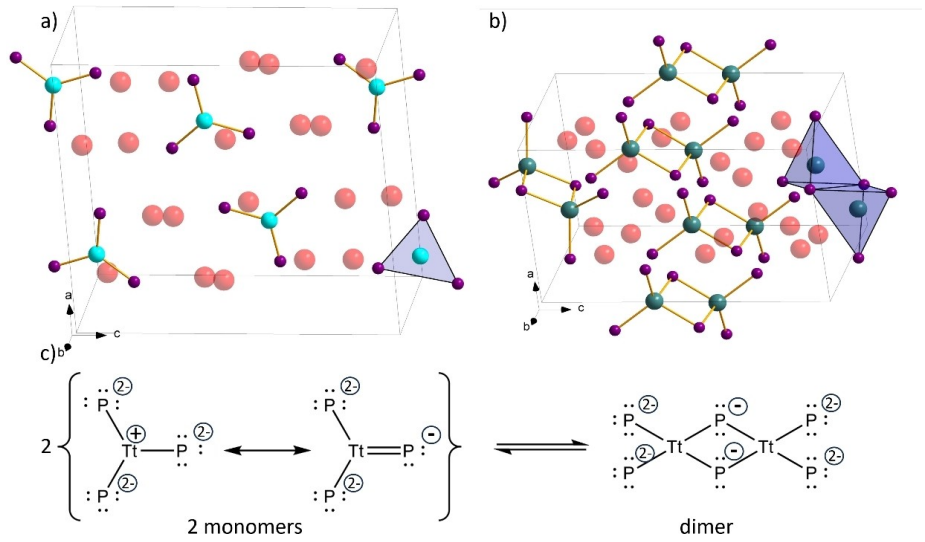

Figure 1. Representation of two possible structure types for compounds with the composition $A_{10}Tt_2P_6$, a) comprising monomeric TtP_3^{5-} and b) dimeric $Tt_2P_6^{10-}$ units with A = Li–Cs shown as red, Tt = Si, Ge, Sn shown as blue or green, as well as P atoms shown as purple spheres. c) Resonance structures of monomeric TtP_3^{5-} and equilibrium forming the dimeric $Tt_2P_6^{10-}$ unit.

general, the K-*Tt*-P is scarcely explored, and only two compounds are known. K_2SiP_2 consists of SiS_2 analogue 2D chains of edge sharing tetrahedra and KSi_2P_3 of corner sharing 3D networks of tetrahedra resulting in T5 super tetrahedra.[12,13] For Ge and Sn no ternary compounds are known. Modelling the K_5TtP_3 compounds through quantum chemical calculations can thus lead to the prediction and if experiments are successful discovery of new compounds.

In this paper, an investigation regarding possible transitions between the dimer and monomer structures (Figure 1c) by calculating the Gibbs free enthalpy was conducted and predicted also structures of unknown compounds. For all presented compounds band structure and density of states were calculated using CRYSTAL17. In consequence we synthesized the new compound $K_{10}Sn_2P_6$ and found that it indeed crystalizes in the Na_5GeP_3 structure type. The structure was determined by single crystal and powder X-ray diffraction.

Experimental

Synthesis

$K_{10}Sn_2P_6$ was synthesised by reaction of the elements with an excess of phosphorus. Therefore, elemental K (Merck, 98%), Sn (Merck, 99.9%) and P (Sigma Aldrich, 97%) were sealed in a Niobium ampule with a stoichiometry of 5:1:4. The mixture was heated up to 650 °C with a rate of 2 K·min^{-1} in an evacuated silica tube in a vertical resistance furnace (HTM Reetz LOBA 1200-40-600, Eurotherm 2416 controller). After 72 h the tube furnace was turned off and the ampule cooled naturally to room temperature. The isolated product of $K_{10}Sn_2P_6$ is a grey-black powder with flat, plated crystals and is air and moisture sensitive. The compound can be synthesized almost phase pure, since only minor reflections of an unknown impurity can be found in the powder X-ray diffractogram (Figure 2). For single crystal growth the ampule was cooled with a rate of 0.1 K·min^{-1}.

Single crystal structure determination

Shiny black, plate-like single crystal of $K_{10}Sn_2P_6$ was sealed in a 0.3 mm glass capillary in argon-filled glove box. The single crystal X-ray diffraction (SCXRD) measurement was performed on a Stoe Stadivari diffractometer equipped with a micro source (GENIX, Mo K_α radiation, λ = 0.71073 Å) and a PILATUS 300 K detector (Dectris) at 150 K. The structure was solved by Direct Methods (SHELXS) and refined by full-matrix least-squares calculations against F^2 (SHELXL).[14,15] Data reduction and multi-scan absorption correction were carried out with the X-AREA (version 1.88, Stoe) and the STOE LANA (version 1.77.1, Stoe) software packages, respectively.[16] Crystallographic data and selected data and details of the structure refinement for $K_{10}Sn_2P_6$ are listed in Table S1 (Supporting Information). Deposition Number 2310244 contains the supplementary crystallographic data for this paper. These data are provided free of charge by the joint Cambridge Crystallographic Data Centre and Fachinformationszentrum Karlsruhe.

Powder X-ray diffraction

For powder X-ray diffraction (PXRD) measurements, the sample was ground in an agate mortar and sealed in a 0.3 mm glass capillary. PXRD measurements were performed at room temperature on a Stoe Stadi P diffractometer equipped with a Ge(111) monochromator for Cu $K_{\alpha1}$ radiation (λ = 1.54056 Å) and a MYTHEN DCS 1 K detector (Dectris). The raw powder data was processed with the software package WinXPOW.[17]

Chemistry–A European Journal
Research Article
doi.org/10.1002/chem.202400002
Chemistry Europe
European Chemical Societies Publishing

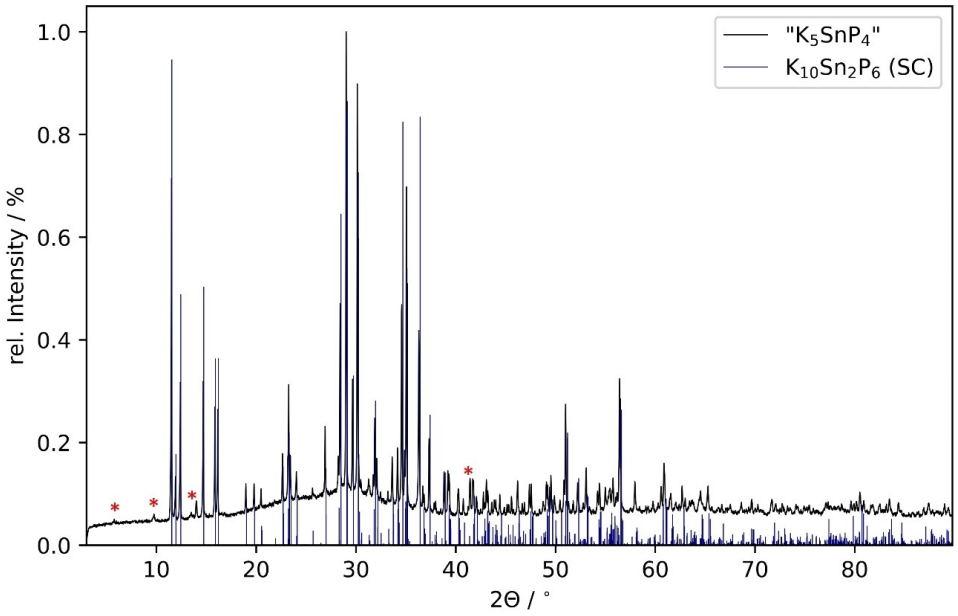

Figure 2. Powder XRD pattern of $K_{10}Sn_2P_6$. The theoretical pattern (blue, $K_{10}Sn_2P_6$ (SC)) was derived from a single crystal measurement at 150 K, the experimental pattern (black) was obtained from a "K_5SnP_4" weighted in stoichiometry. Minor, unknown reflections of an impurity are marked with red asterisks.

Differential scanning calorimetry (DSC)

For thermal analysis, $K_{10}Sn_2P_6$ was sealed in a niobium ampoule and measured on a differential scanning calorimetry (DSC) machine (Netzsch, DSC 404 Pegasus) under a constant gas flow of 75 mL·min^{-1}. The sample was heated to 700 °C and cooled to 100 °C twice at a rate of 5 K·min^{-1}.

Electronic structure calculations

The computational studies of all compounds in the $A_{10}Tt_2P_6$ system (with A = Li, Na, K, Rb, Cs and Tt = Si, Ge, Sn) were performed using the CRYSTAL17 program package and hybrid density functional methods.[18,19] A hybrid exchange-correlation functional after Perdew, Burke, and Ernzerhof (DFT-PBE0) was used.[20] Localized, Gaussian-Type triple ζ-valence + polarization level basis sets were used for Si, Ge, Sn and P and split valence + polarization level basis sets for Li, Na, K, Rb and Cs. The basis sets were derived from the molecular Karlsruhe basis sets.[21—23,6,24,25] For the evaluation of the Coulomb and exchange integrals (TOLINTEG), tight tolerance factors of 8, 8, 8, 8, 16 were used for all calculations. The reciprocal space of all dimer structure models was sampled with 5×5×2 and all monomer structure models with 2×5×2 Monkhorst-Pack-type *k*-point grids. The starting geometries were taken from experimental data whenever possible. All other models were derived from them by atom replacements. Both, lattice parameters and atomic positions were fully optimized within the constraints imposed by the space symmetry. Further on all optimized structures were confirmed to be true local minima by means of harmonic frequency calculations at Γ-point. Electronic band structures and density of states (DOS) were calculated. The Brillouin Zone paths of Γ-Z-D-B-Γ-A-E-Z-C_2-Y_2-Γ for all dimer structures and Γ-X-S-Y-Γ-Z-U-R-T-Z|X-U|Y-T|S-R for all monomer structures were provided by the web service *SeeK-path*.[26]

Results and Discussion

Stability analysis of $A_{10}Tt_2P_6$ compounds

We found that the $A_{10}Tt_2P_6$ system represents a good model to understand the influence of the structure type and nature of elements on the electronic structure in more detail. Since many experimental crystal structures are known the experimental data allows a good insight on the accuracy of the calculations. We chose this series to investigate the temperature dependence of the stability of the two polymorphs and to see the influence of the structure type (symmetry) on the type of band gap as well as the influence of the size of the alkali metal on the size of the band gap. This knowledge is a prerequisite for band gap tuning. For the calculations two of the three existing structure types were picked, the monoclinic structure type (space group $P2_1/n$) comprising edge-sharing double tetrahedra (dimer structure type) that appears for $Li_{10}Si_2P_6$, $Na_{10}Si_2P_6$, $Na_{10}Ge_2P_6$, $Na_{10}Sn_2P_6$ (Figure 1b) and the orthorhombic structure type (space group *Pnma*) comprising carbonate-analogue trigonal planar units (monomer structure type) as found in Rb_5GeP_4, Cs_5SiP_3, and Cs_5GeP_3 (Figure 1a). The cubic $Fm\bar{3}m$ structure type observed for $Li_{10}Ge_2P_6$ and $Li_{10}Sn_2P_6$ reveals a more complex situation since atoms show a mixed occupancy in the tetrahedral voids, thus a direct comparison between the two other more related structures is out of the scope of the

Chemistry–A European Journal
Research Article
doi.org/10.1002/chem.202400002
Chemistry Europe
European Chemical Societies Publishing

investigation here. The dimer structure can also be traced back to a distorted hexagonal closed packing (hcp) of P atoms in which *Tt* atoms occupy two edge sharing tetrahedral voids whereas alkali metal atoms occupy all octahedral voids and remaining cations are found in remaining tetrahedral voids.

For all calculations starting geometries were taken from experimental data, if possible, otherwise, models were created by substituting homologue atoms. All deviations between experimental and optimized cell parameters can be found in the Supporting Information Table S5. All deviations are below 5% except for the cell parameters *a* of the monomeric phases which deviate about 10% and might originate from anisotropy of the crystal structure. For all structural models, geometry optimizations, frequencies, band structure and density of states were calculated.

From the results of the frequency calculation at the Γ-point the temperature dependence of the Gibbs free Enthalpy ΔG for each dimer and monomer structure model was calculated. Subsequently, the difference in enthalpy between both models, ΔΔG, was calculated and plotted versus temperature for each compound (Figure 3). Consequently, points below the zero line implicate that the dimer structure is more stable than the monomer. If for one compound the ΔΔG versus temperature line crosses the zero line upon temperature increase, a phase transition seems reasonable. However thermodynamic considerations might be always hindered by kinetics reasons, which especially applies for transitions in the solid state. All values of ΔΔG can be found in the Supporting Information Table S7.

For our system this leads to the following energetical order of the stability of the structures: All Li derivatives and $Na_{10}Sn_2P_6$ are thermodynamically favoured in the dimer structure over the whole temperature range. This is in good agreement with the experimental findings as $Li_{10}Si_2P_6$ and $Na_{10}Si_2P_6$ are only known in that structure type.[2,8,7] For $Li_{10}Ge_2P_6$ and $Li_{10}Sn_2P_6$ the cubic phase has been observed revealing a ccp of P atoms with Li and Tt atoms are disordered in tetrahedral voids. This structure is related to the dimeric structure type with connected TtP_4 tetrahedra.[2] As pointed out above this structure type was not included here. For all Rb and Cs compounds, K_5SiP_3 and K_5GeP_3 the monomer phase is more stable (all points are above the zero line), which is for the known compounds again in good agreement with literature.[10,11] This leaves $Na_{10}Si_2P_6$, $Na_{10}Ge_2P_6$ and $K_{10}Sn_2P_6$ crossing the zero line as possible candidates for a phase transition from the dimer to the monomer structure at high temperatures. In this calculation the transition temperature is predicted to be around 1050 K for all three compounds. Up to this point for the Na compounds no phase transition was reported. For the new title compound $K_{10}Sn_2P_6$ (so far) only the dimer structure was synthesized which is in accordance with the prediction of the energy comparison that the dimer structure is more stable at lower temperatures.

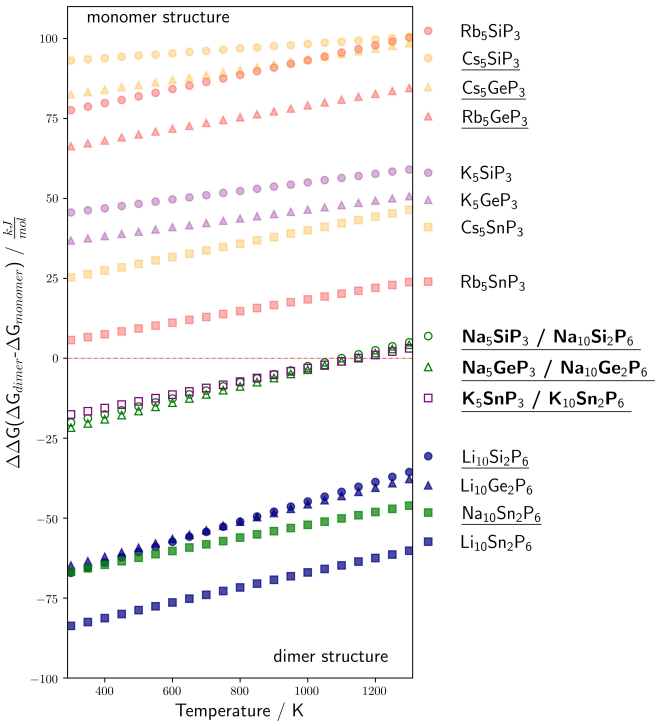

Figure 3. Gibbs enthalpy differences for all calculated structure models in dependency of the temperature. Below the zero line the dimer phase is more stable, above the monomer. Phases marked in bold font in the legend show a phase transition. Experimentally known phases are underlined.

Chemistry–A European Journal
Research Article
doi.org/10.1002/chem.202400002
Chemistry Europe
European Chemical Societies Publishing

Another trend that can be seen in Figure 3 is that the overall difference in stability for the tin compound is always lower than the corresponding Si and Ge compounds. This leads to Rb_5SnP_3 having a difference of only 5.7 kJ/mol between the two structure types at 300 K. This could hint towards an incredibly low transition temperature and thus making the compound another candidate for having two polymorphs. Unfortunately, there again is no experimental data since the compound is still unknown and although performing multiple experiments it has not yet been synthesized.

Interestingly only three compounds show the possibility to undergo a phase transition at elevated temperatures under the formation of monomers (Figure 3). This results is nicely in accordance with the double bond rule, originally developed for molecules, which states that, atoms of higher periods prefer multiple single bonds in complex structural motifs over double bonds.[27] On one hand, for all experimentally observed compounds (Rb_5GeP_4, Cs_5SiP_3 and Cs_5GeP_3) only Si and Ge compounds form the monomer structure with the carbonate analogue units that are stabilized by *Tt*-P double bonds. On the other hand, the two experimentally known Sn compounds – $K_{10}Sn_2P_6$ and $Na_{10}Sn_2P_6$ – crystallize with dimer structure comprising exclusively *Tt-P* single bonds (Figure 1c). Further on, the monomer structures of Sn derivatives are less stable than the corresponding Si and Ge compounds.

The role of the alkali metal counter ions is less clear, but the size effect may play an important role. To form the dimer structure, the occupation of two neighbouring tetrahedral voids of the (distorted) closed packing of P atoms must occur as pointed out before. Rb^+ and Cs^+ ions might be too large to allow the P atoms to form a close atom arrangement since they do not fit into the remaining tetrahedral voids formed by the P atoms. In addition, the larger Rb^+ and Cs^+ ions may also favour a better separation of the monomeric anions.

Interestingly, no K derivatives were reported yet, therefore synthesis of all three derivatives $K_{10}Tt_2P_6$ for *Tt* = Si, Ge, and Sn was tried, but only the dimer structure for Tt = Sn was found. According to the arguments given above, K^+ ions might still be capable to fit in tetrahedral voids in case of the larger Sn atoms widening the P atom arrangement, but not for Si and Ge. In addition, the size of K^+ seems not to be sufficient for separating the higher number of discrete TtP_3^{5-} anions.

Synthesis and Crystal Structure of $K_{10}Sn_2P_6$

The compound was synthesized by reaction from the elements in sealed niobium ampoules at 650 °C. The best results were obtained by a slight excess of phosphorus otherwise unreacted potassium was found in the product.

Single crystals suitable for X-ray structure determination were obtained directly from the reaction product (Table 1). $K_{10}Sn_2P_6$ crystallizes in the monoclinic group $P2_1/n$ (no. 14) in the Na_5GeP_3 structures type.[7] It contains edge sharing double tetrahedra consisting of $[Sn_2P_6]^{10-}$ units and isolated K^+ atoms which leads to a charge-balanced Zintl phase. The structure obtained from single crystal X-ray structure determination at 150 K is represented in Figure 4 with all atoms shown as ellipsoids at 95% probability. Crystallographic information is given in Table 1 and the Supporting Information Tables S1 to S4. All atoms are located on 4e Wyckoff positions and are fully occupied (Table 2). As mentioned for previous compounds of this structure type, the P atoms form a distorted hexagonal packing with partially occupied tetrahedral voids.[3] Since the unit cell harbours 3 P atoms per stoichiometric unit, with Z = 4, a total of 12 octahedral and 24 tetrahedral voids result. All octahedral voids are filled with atoms K3 to K5, while 50% of the tetrahedral voids are filled by Sn, K1 and K2.

Table 1. Crystallographic data and selected details of the structure refinement of $K_{10}Sn_2P_6$.

Formula	K_5SnP_3
Formula weight ($g \cdot mol^{-1}$)	407.1
Space group	$P2_1/n$ (no. 14)
Z	4
Unit cell parameters (Å)	$a = 8.9431(4)$ $b = 8.0941(3)$ $c = 14.7833(7)$ $\beta = 90.107(4)^\circ$
Volume ($Å^3$)	1070.11(8)
$D_{calc.}$ ($g \cdot cm^{-3}$)	2.527
Abs. Coeff. (mm^{-1})	4.706
Temperature (K)	150
Reflections collected	5176 ($R_\sigma = 0.027$)
Unique reflections	3894 ($R_{int} = 0.0386$)
Data/parameter	5176/82
GOF on F^2	1.035
R_1, wR_2 ($I > 2\,\sigma(I)$)	0.030, 0.054
R_1, wR_2 (*all data*)	0.052, 0.059
Largest diff. peak/hole ($e \cdot Å^{-3}$)	1.24/-2.68

The anion forms covalent Sn–P bonds with typical bond elongation observed in anions (2.535(1)–2.618(1) Å) if compared to the covalent radii of Sn and P typical Sn–P single bond lengths of 2.5 Å.[28] The longest bond occurs between Sn1–P1 which is still in the range of bond lengths that occur in other related Sn compounds.[9,29] The distance between two neighbouring Sn atoms is 3.3198 Å which is 0.5 Å longer than elemental Sn, thus no bond is assumed between them.[28] Within the tetrahedra the smallest P–Sn–P bond angle is 92.39(2)° for P1–Sn1–P1 which is considerably smaller than the remaining angles that range from 111.02(2)° to 114.33(2)°. Due to the smaller P1–Sn1–P1 angles, the edge sharing tetrahedra appear elongated along the Sn–Sn axis.

According to the calculations as pointed out before, $K_{10}Sn_2P_6$ might undergo a phase transition at elevated temperatures. DSC shows an exothermal signal offset around 550 °C by heating the sample from room temperature and an endothermal at around 500 °C by cooling (see Figure S2) indicating a reversible process. A sample of $K_{10}Sn_2P_6$ was quenched at 550 °C however no crystalline product could be detected. A PXRD recorded after the DSC measurement reveals that neither

Chemistry–A European Journal
Research Article
doi.org/10.1002/chem.202400002
Chemistry Europe
European Chemical Societies Publishing

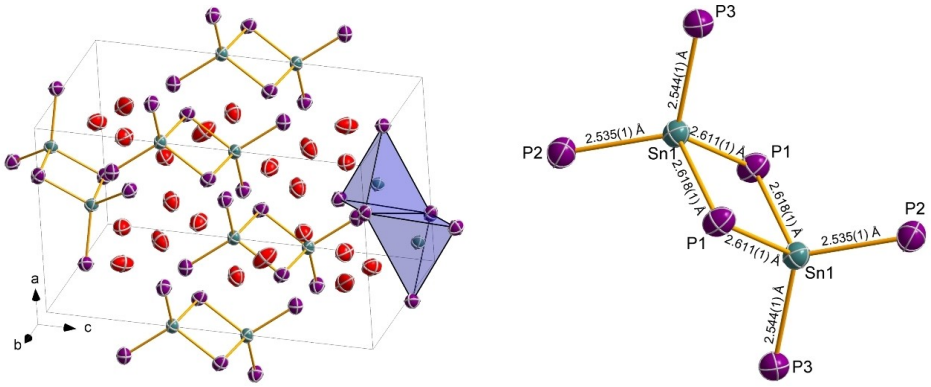

Figure 4. Left side: Crystal structure of $K_{10}Sn_2P_6$ with ellipsoids at 95% probability with K in red, Sn in green and P in purple. One double tetrahedral $[Sn_2P_6]^{10-}$ is marked in blue. Right side: bond lengths within the double tetrahedra unit.

Table 2. Atomic coordinates and equivalent isotropic displacement parameters (Å^2) for of $K_{10}Sn_2P_6$.

Atom	Wyck.	$U_{eq.}$	x/a	y/b	z/c
Sn1	4e	0.01028(4)	0.07488(2)	0.13743(2)	0.41479(2)
K1	4e	0.0199(1)	0.07853(7)	0.16625(7)	0.75880(4)
K2	4e	0.0203(1)	0.58175(7)	0.32604(7)	0.57928(4)
K3	4e	0.0193(1)	0.68629(7)	0.00401(7)	0.40826(4)
K4	4e	0.0211(1)	0.80664(7)	0.51174(7)	0.74099(4)
K5	4e	0.0242(1)	0.16327(7)	0.48212(7)	0.57753(5)
P1	4e	0.0129(1)	0.92386(7)	0.18358(7)	0.56368(4)
P2	4e	0.0140(1)	-0.07431(7)	0.22253(8)	0.27642(4)
P3	4e	0.0135(1)	0.33918(7)	0.25338(8)	0.42007(4)

$K_{10}Sn_2P_6$ nor K_5SnP_3 is present. Since we used excess P for the reaction, the DTA signal may arise from phosphorus polymorphs or a reversible decomposition reaction.

Electronic structure analysis of $K_{10}Sn_2P_6$

To calculate the electronic properties cell parameters and all atomic positions of $K_{10}Sn_2P_6$ were optimized. Differences between experimental and optimized lattice parameters are smaller than 0.4% and no imaginary frequencies at the Γ-point were found. Thus, band structure and density of states (DOS) of $K_{10}Sn_2P_6$ were calculated and are represented Figure 5. The compound has a direct band gap of 2.57 eV with the transition at Γ-point. The valence bands appear as flat bands at the Fermi-Level. In contrast the energetically lower valence bands show considerably more dispersion than the other bands. Additionally, the lowest conduction band is pulled down from the rest of the bands at the Γ-point with the conduction band minimum (CBM) being about 0.5 eV lower than the rest of the conduction bands. Looking at the density of states for the valence bands, orbitals of the P atoms have the highest contribution followed by small contributions from K and Sn atoms. In the conduction bands at higher energy, considerably more Sn atom contribution is observed.

Further on a Mulliken analysis was conducted to get an insight on the overlap population which, to a certain extent, describes the bonding situation.[30] For K there are only overlap populations below 0.04 for adjacent P atoms, which corresponds with a weak ionic interaction between the atoms and supports the salt-like description according to the Zintl-type approach (see Supporting Information Table S6). The Sn–P interactions of the double tetrahedra rise to 0.325 and 0.257 which confirms bonding interactions. As for the Sn–Sn interaction the overlap population gives a value of −0.043 which can be interpreted as slight repulsion between the metal centres within the double tetrahedra leading to an elongation of the tetrahedra along the Sn–Sn axis as described above.

To investigate the influence of the crystal structure and thus the symmetry on the electronic structure the hypothetical monomer structure of K_5SnP_3 was calculated using the experimental data of Rb_5GeP_3 as basis for the model.[10] Band structure and density of states are represented in Figure 6. The monomer structure has an indirect band gap of 2.24 eV with transition from Γ to Y, thus the band gap is smaller than for the dimer structure. As for the dimer structure the valence bands around the Fermin Level are flat, but bands with higher

Chemistry–A European Journal
Research Article
doi.org/10.1002/chem.202400002
Chemistry Europe
European Chemical Societies Publishing

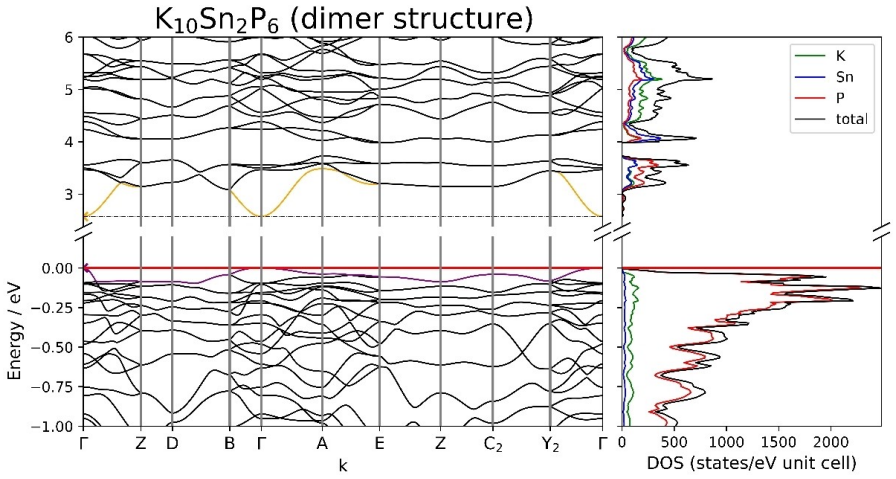

Figure 5. Band structure and density of states (DOS) diagrams of $K_{10}Sn_2P_6$ calculated based on the single crystal structure revealing a direct band gap of 2.57 eV.

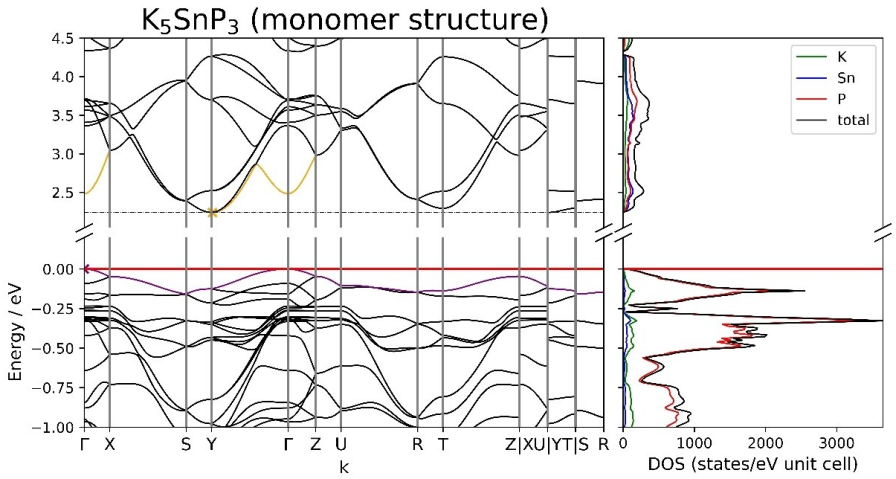

Figure 6. Band structure and density of states of modelled monomer K_5SnP_3. It is an indirect band gap semiconductor with an indirect band gap of 2.24 eV.

dispersion are found at lower energies. The CBM is at the Y k-point and the bands at Γ are about 0.25 eV higher in energy which causes the indirect band gap in contrast to Figure 5. As for the density of states the valence bands are mostly made up by P states and some minor contributions of K and Sn. In the first few conduction bands, P and Sn atoms contribute almost equally, above 3.5 eV the P atom contribution increases. K has only minor contributions at all.

Since the two polymorphs of K_5SnP_3 have different types of band gaps, one might expect that different structural motives and thus the crystal structure (symmetry) might have some influence on this. Upon zooming into the band structure above the Fermi level for the dimer structure the energetically lower bands contain more K and P states than the monomer structure, where Sn atoms have the highest contribution. This leads to the assumption that the contribution of the alkali metal has an influence on the band gap.

Further on a crystal orbital Hamilton overlap (COHP) was calculated for both compounds, which are displayed in Figure 7 b) and c). For both polymorphs the COHP shows only minor interactions just below the Fermi-Level down to −1 eV although many P atom states are present in the DOS (Figure 7 a) & c)). Therefore, these states can be assigned to nonbonding lone pairs of P atoms, which are thus the highest occupied states. Further down bonding interactions between Sn and P arise, again for both polymorphs, which can be attributed to the covalent bonds described above for both structural motives. The interactions of Sn and P with K are only minor over the whole energy range and thus represent rather ionic interactions

Chemistry–A European Journal
Research Article
doi.org/10.1002/chem.202400002
Chemistry Europe
European Chemical Societies Publishing

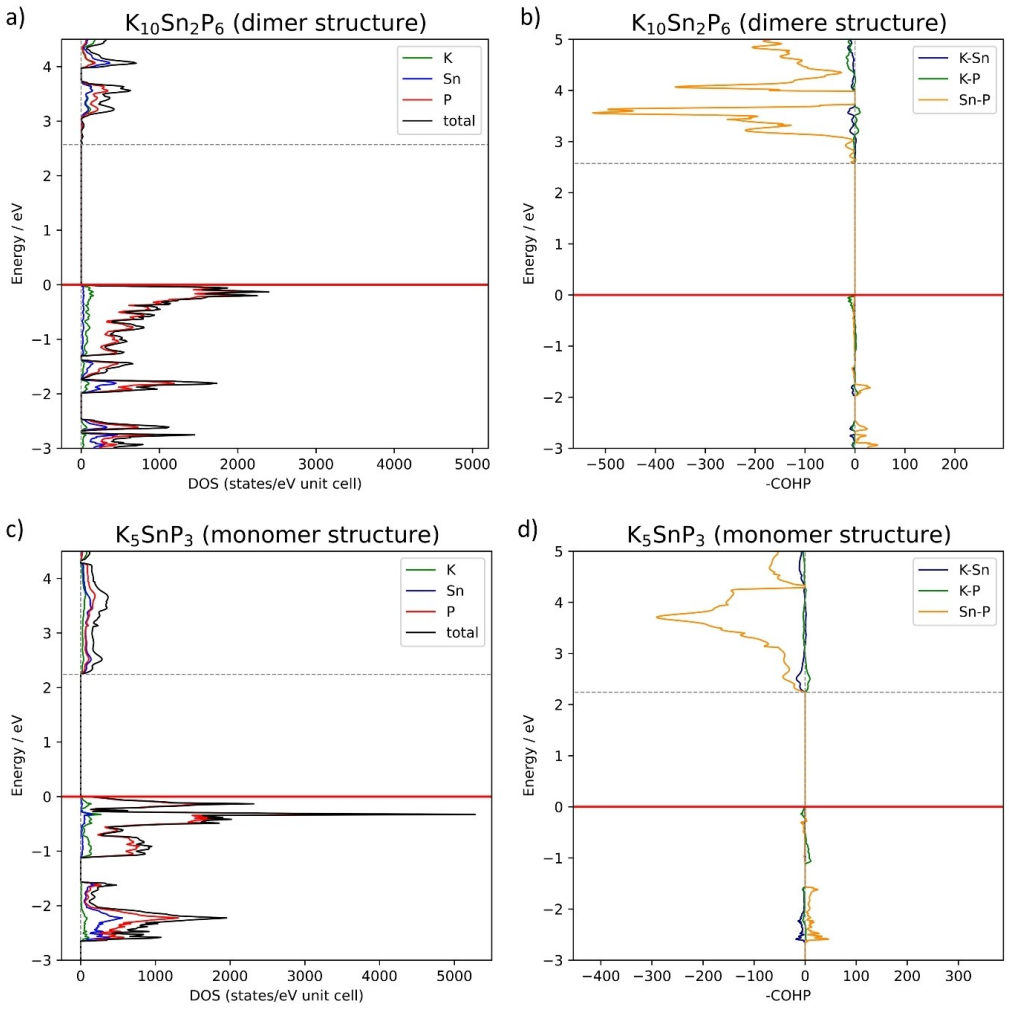

Figure 7. a) Density of states with atom contributions and b) Crystal orbital Hamilton population of the dimer structure $K_{10}Sn_2P_6$, c) Density of states with atom contribution and d) Crystal orbital Hamilton population of the monomer structure K_5SnP_3 in the range +4.5 to −3 eV. The dashed line below the conduction bands represents the lowest energy level of the conduction band.

between them, while the strong interactions between Sn and P confirm the chemical bonding situation.

Above the Fermi-Level, the COHP differs for the two polymorphs. For the dimer only minor interactions can be found at about 0.5 eV above the band gap, while the monomer structure has a significant number of Sn–P interactions. This is due to the low lying π^*-orbitals of the carbonate analogue SnP_3^{5-} unit which make up these antibonding interactions in the COHP. Since the dimer structure does not have any π-interactions there are no interactions present within that energy range. Further above both polymorphs show strong anti-bonding Sn–P interactions.

Systematic investigation of the electronic structure analysis of $A_{10}Tt_2P_6$ series

By calculating all possible compounds in each of the two structure types, information on how the band structure can be influenced by different element combinations for the same structure type and by the structural motive for similar element combinations could be achieved. All resulting band structures, DOS and COHP plots are given in the Supporting Information Figures S6 to S35. The calculated band gap widths and types are collected in Table 3 and Table 4. For the band gaps we observe the following trends: For the dimer structures, the band gap decreases from Si to Ge and increases from Ge to Sn compounds. The only exceptions are $Na_{10}Sn_2P_6$ and $K_{10}Sn_2P_6$ for which the band gap slightly decreases as well. This trend

Chemistry–A European Journal | Research Article doi.org/10.1002/chem.202400002 | Chemistry Europe European Chemical Societies Publishing

Table 3. Band gaps for the monoclinic phases in eV. Direct band gaps and experimentally known structures are marked with (d) and (*), respectively.

$A_{10}Tt_2P_6$ (dimer)	Li	Na	K	Rb	Cs
Si	2.79 (*)	2.99 (*)	2.73	1.91	2.00
Ge	2.40	2.71 (*)	2.60	1.86	1.93
Sn	2.54	2.58 (*,d)	2.57 (*,d)	1.98	2.00

Table 4. Band gaps for the orthorhombic phases in eV. Direct band gaps, pseudo direct band gaps, and experimentally known structures are marked with (d), (pd) and (*), respectively.

A_5TtP_3 (monomer)	Li	Na	K	Rb	Cs
Si	1.20	2.02 (d)	2.17	1.94 (d)	1.95 (*)
Ge	1.17	1.84	2.19	1.98 (*,d)	2.04 (*)
Sn	1.36	1.71	2.24	2.00 (d)	2.09 (pd)

correlates with the difference in electronegativity between the *Tt* and P atoms. From Si to Ge, the electronegativity difference decreases, which correlates the observed smaller band gaps,[31] and the electronegativity difference increases for Sn which leads to a larger band gap. Interestingly, for the two Sn compounds that do not follow this trend, a switch to a direct band gap is observed. This hints to a slightly different electronic situation lifting the valence band maximum (VBM) at Γ-point. Looking closer at the density of states whenever the VBM is located at the Γ-point, there are less contribution of the alkali metals to the DOS, if compared to compounds where the top valence band is closer to the Fermi-Level. There is also more alkali metal contribution to the DOS at the at the conduction band minimum (CBM). Overall, the changes in the band gaps from Si to Sn are more pronounced for the lighter alkali metal homologues. For the monomer structures, the trend in band gap size changes is similar and again the Sn derivative Na_5SnP_3 does not follow this trend. For the K, Rb and Cs compounds the trend is again less pronounced leading to almost equal band gaps. The COHP curves follow the trend as discussed for $K_{10}Sn_2P_6$ and K_5SnP_3 above in more detail.

In summary, direct band gaps appear independent of the crystal symmetry, and are observed in both structure types. As a general trend, direct band gaps at Γ are favoured by compounds that have only little or no alkali metal orbital contribution at the VBM. Thus, the influence of the alkali metal on the electronic structure is an important factor.

Conclusions

By computational analysis of the compound family A_5TtP_3. For A = Li–Cs and Tt = Si to Sn) we found that for known lighter alkali metal atoms A = Li to K the dimer structure $A_{10}Tt_2P_6$ is stabilized at lower temperatures over the monomer structure A_5TtP_3. For the Na and K derivatives a phase transition to the monomer structure is predicted at high temperatures. For A = Li and Na the calculated stabilities of the dimer structures are in accordance with the experimentally observed structures. Since the K homologues were not reported we synthesized $K_{10}Sn_2P_6$ and found, also in accordance with theory, the dimer structure. Comparable reaction conditions did not lead to the formation of one of the polymorphs for Tt = Si and Ge. Due to the decomposition of $K_{10}Sn_2P_6$ above 550 °C the predicted phase transition at 770 °C could not be observed. Also, in accordance with the experimentally observed structures, we find for all heavier alkali metal homologues, the monomer structure as the thermodynamically more stable phase. With respect to the appearance of direct and indirect band gaps we found that the structure type or with other words the symmetry of the crystals does not play any role. In general, we find for all monomeric compounds a higher dispersion among the valence and conduction bands, which is in line with a partial double bond formation between the atoms of the carbonate analogue monomer TtP_3^{5-} anion. We also find no direct influence of the nature of the *Tt* element. As a general trend, direct band gaps at Γ are favoured by compounds that have only little or no alkali metal orbital contribution at the VBM. Thus, the influence of the alkali metal on the electronic structure is an important factor.

Both discussed structural motives are also known for other lithium– and sodium phosphidotetrelates, so trends identified can be further investigated in future studies by expanding the number of compounds to be analysed.[32–40]

Acknowledgements

We thank TUM.solar in the context of the Bavarian Collaborative Research Project *Solar Technologies Go Hybrid* (SolTech) supported by the Bavarian State Ministry of Science and the Artsand the Bavarian Ministry of Economic Affairs, Regional Development, and Energy within the project *Industrialisierbarkeit von Festkörperelektrolytzellen*. The authors thank Prof. Antti Karttunen for solving problems with CRYSTAL17 as well as input on the discussion of unclear findings. Open Access funding enabled and organized by Projekt DEAL.

Conflict of Interests

The authors declare no conflict of interest.

Data Availability Statement

The data that support the findings of this study are available in the supplementary material of this article.

Keywords: Zintl phase · Direct Band Gap · Structure prediction · Semiconductor · Phase Transition

[1] H. Eickhoff, W. Klein, L. Toffoletti, G. Raudaschl-Sieber, T. F. Fässler, *Z. Anorg. Allg. Chem.* **2022**, *10*, 648.

Chemistry–A European Journal
Research Article
doi.org/10.1002/chem.202400002
Chemistry Europe
European Chemical Societies Publishing

[2] H. Eickhoff, L. Toffoletti, W. Klein, G. Raudaschl-Sieber, T. F. Fässler, *Inorg. Chem.* **2017**, *56*, 6688.
[3] T. M. F. Restle, S. Zeitz, J. Meyer, W. Klein, G. Raudaschl-Sieber, A. J. Karttunen, T. F. Fässler, *Z. Anorg. Allg. Chem.* **2021**, *647*, 1804.
[4] A. Haffner, A.-K. Hatz, O. E. O. Zeman, C. Hoch, B. V. Lotsch, D. Johrendt, *Angew. Chem. Int. Ed. Engl.* **2021**, *60*, 13641.
[5] A. Haffner, A.-K. Hatz, I. Moudrakovski, B. V. Lotsch, D. Johrendt, *Angew. Chem.* **2018**, *130*, 6263.
[6] T. M. F. Restle, J. V. Dums, G. Raudaschl-Sieber, T. F. Fässler, *Chem.* **2020**, *26*, 6812.
[7] B. Eisenmann, M. Somer, *Z. Naturforsch. B* **1985**, *40*, 886.
[8] B. Eisenmann, J. Klein, *Z. Kristallogr. Cryst. Mater.* **1991**, *197*, 269.
[9] S. Strangmüller, D. Müller, G. Raudaschl-Sieber, H. Kirchhain, L. van Wüllen, T. F. Fässler, *Chem.* **2022**, *28*, e202104219.
[10] B. Eisenmann, J. Klein, M. Somer, *Z. Kristallogr. Cryst. Mater.* **1991**, *197*, 263.
[11] B. Eisenmann, J. Klein, M. Somer, *Angew. Chem.* **1990**, *102*, 92.
[12] B. Eisenmann, M. Somer, *Z. Naturforsch. B* **1984**, *39*, 736.
[13] K. Feng, L. Kang, W. Yin, W. Hao, Z. Lin, J. Yao, Y. Wu, *J. Solid State Chem.* **2013**, *205*, 129.
[14] G. M. Sheldrick, *SHELXS-2014. program for crystal structure solution*, University of Goettingen, Goettingen, **2014**.
[15] G. M. Sheldrick, *SHELXL-2014. Program for the refinement of crystal structures*, University of Goettingen, Goettingen, **2014**.
[16] J. Koziskova, F. Hahn, J. Richter, J. Kozísek, *Acta Chim. Slov.* **2016**, *9*, 136.
[17] *WinXPOW*, STOE & Cie GmbH, Darmstadt, Germany, **2011**.
[18] CRYSTAL17, R. Dovesi, V. R. Saunders, C. Roetti, R. Orlando, C. M. Zicovich-Wilson, F. Pascale, B. Civalleri, K. Doll, N. M. Harrison, I. J. Bush **2017**.
[19] R. Dovesi, A. Erba, R. Orlando, C. M. Zicovich-Wilson, B. Civalleri, L. Maschio, M. Rérat, S. Casassa, J. Baima, S. Salustro et al., *Wiley Interdiscip. Rev.: Comput. Mol. Sci.* **2018**, *8*, 1360.
[20] J. P. Perdew, W. Yang, K. Burke, Z. Yang, E. K. U. Gross, M. Scheffler, G. E. Scuseria, T. M. Henderson, I. Y. Zhang, A. Ruzsinszky, et al., *Proc. Natl. Acad. Sci. USA* **2017**, *114*, 2801.
[21] A. J. Karttunen, T. F. Fässler, *Chem.* **2014**, *20*, 6693.
[22] A. J. Karttunen, T. F. Fässler, M. Linnolahti, T. A. Pakkanen, *Inorg. Chem.* **2011**, *50*, 1733.
[23] B. Scheibe, S. I. Ivlev, A. J. Karttunen, F. Kraus, *Eur. J. Inorg. Chem.* **2020**, *2020*, 1319.
[24] L. M. Scherf, A. J. Karttunen, O. Pecher, P. C. M. M. Magusin, C. P. Grey, T. F. Fässler, *Angew. Chem. Int. Ed. Engl.* **2016**, *55*, 1075.
[25] R. E. Stene, B. Scheibe, A. J. Karttunen, W. Petry, F. Kraus, *Eur. J. Inorg. Chem.* **2019**, *2019*, 3672.
[26] Y. Hinuma, G. Pizzi, Y. Kumagai, F. Oba, I. Tanaka, *Comput. Mater. Sci.* **2017**, *128*, 140.
[27] P. P. Power, *Chem. Rev.* **1999**, *99*, 3463.
[28] P. Pyykkö, M. Atsumi, *Chem.* **2009**, *15*, 186.
[29] B. Eisenmann, J. Klein, *Z. Naturforsch. B* **1988**, *43*, 1156.
[30] A. E. Reed, R. B. Weinstock, F. Weinhold, *J. Chem. Phys.* **1985**, *83*, 735.
[31] A. F. Holleman, *Lehrbuch der anorganischen Chemie*, Walter de Gruyter GmbH & Co KG, **2019**.
[32] A. Adam, H.-U. Schuster, *Z. Naturforsch. B* **1990**, *45*, 559.
[33] B. Eisenmann, J. Klein, M. Somer, *Z. Kristallogr. Cryst. Mater.* **1991**, *197*, 273.
[34] J. Klein, B. Eisenmann, *Z. Kristallogr. Cryst. Mater.* **1991**, *196*, 213.
[35] K. Mayer, J. V. Dums, W. Klein, T. F. Fässler, *Angew. Chem. Int. Ed. Engl.* **2017**, *56*, 15159.
[36] K. Beuthert, F. Pan, L. Guggolz, R. J. Wilson, J. Hempelmann, R. Dronskowski, S. Dehnen, *Angew. Chem. Int. Ed.* **2022**, *64*, e202207232.
[37] B. Eisenmann, J. Klein, M. Somer, B. Eisenmann, J. Klein, M. Somer, *Z. Kristallogr. Cryst. Mater.* **1991**, *197*, 267.
[38] B. Eisenmann, J. Klein, *Z. Kristallogr. Cryst. Mater.* **1991**, *197*, 265.
[39] R. Juza, W. Schulz, *Z. Anorg. Allg. Chem.* **1954**, *275*, 65.
[40] B. Eisenmann, U. Rössler, *Z. Kristallogr. New Cryst. Struct.* **2000**, *215*, 347.

Manuscript received: January 1, 2024
Accepted manuscript online: February 6, 2024
Version of record online: March 5, 2024

5.2 Electronic structure analysis of A_6TrPn_3 compounds with A = Rb, Cs; Tr = Al, Ga, In and Pn = As, Sb

Sabine Zeitz, Hanna Antoniuk, Thomas F. Fässler

Manuscript for publication

Electronic structure analysis of A_6TrPn_3 compounds with A = Rb, Ca; Tr = Al, Ga, In and Pn = As, Sb

Sabine Zeitz[a], Hanna Antoniuk[a], Thomas F. Fässler[a]

Abstract

Compounds with the composition A_6TrPn_3 (*A* = Rb, Cs; *Tr* = Al, Ga, In; *Pn* = As, Sb) are good model system to investigate the influence of the elemental composition on the size and kind of band gaps. The crystal structure incorporates CO_3^{2-} analogue triangular planar $[TrPn_3]^{6-}$ units, which offer to study the influence of various parameters on the band gap due to their simple, yet unique structure. Therefore, the crystal structure four experimentally known compounds as well as eight modelled compounds was optimized with a PBE0/TZVP level of theory. For all compounds band structure, density of states and crystal orbital Hamilton populations were calculated. While Cs_6InAs_3 has a direct band gap, all other compounds show indirect band gaps, which are caused by a shift of the valence band maximum. This shift was identified to be caused by a decrease of energy of *Tr*-*Pn* anti-bonding states, which might arise form partial double bonds. The size of the band gap was found to depend on the pnictogen and alkali metal present, with the latter having less influence. The bonding situation imposed by the crystal structure was confirmed by a Mulliken analysis. Further on many trends were found, which are similar to compounds of the analogue tetrelates, deepening the knowledge on crystal structure band structure relations.

Introduction

Highly specialised materials have become increasingly important in the development of our information-based society over the last few decades. Semiconductors, due to their various applications such as light emitting diodes (LEDs), transistors, thermoelectrics and solar cells, are among the most researched classes of compounds.[1–5] For the latter, bandgap tunability is of particular importance to find new materials to achieve the much debated transition from fossil to renewable energy. In order to optimize the material design process, it would therefore be beneficial to be able to predict the electronic properties simply by knowing the crystal structure, both to determine whether newly discovered materials are of interest in specific applications, and to efficiently design the structure of new materials by systematic modification of their crystal

structure. It is therefore necessary to study, in simple model systems, the relationships between the crystal structure and the band structure.

Within the A_6TrPn_3 system, with A = Na – Cs, Tr = Al – In and Pn = P – Sb, eight different compounds have been found so far in two very simple structure types. Na_6GaP_3, Na_6InAs_3, K_6InP_3 and K_6InAs_3 crystallize in space group $P\bar{1}$ (no. 2) in the K_6InAs_3 structure type.[6–9] The Rb and Cs compounds Cs_6InAs_3, Rb_6AlSb_3, Cs_6GaSb_3 and Cs_6InSb_3 crystallize in space group $P\,2_1/m$ (no. 11) in the Cs_6InAs_3 structure type.[10–13] While both structure types show the same structural motive for the *Tr*-*Pn* substructure, the K_6InAs_3 structure type has multiple underoccupied alkali metal positions in contrast to the Cs_6InAs_3 structure type where all atomic positions are fully occupied.

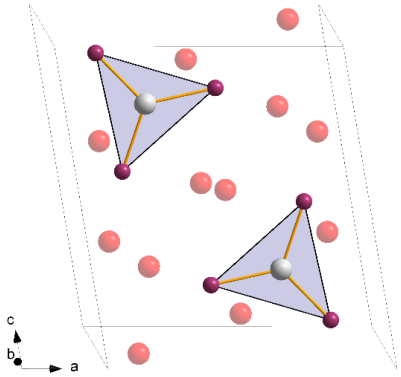

Figure 1. Crystal structure of the Cs_6InAs_3 structure type. The alkali metal , triel and pnictogen are red, grey, and purple coloured, respectively.

Figure 1 shows the unit cell of Cs_6InAs_3 with the anionic substructure motive of triangular planar $[TrPn_3]^{6-}$ units within the ac-plane, which are analogue to CO_3^{2-}. The alkali metal atoms are situated in between these units and are quite isolated within the structure, since their distance to neighbouring atoms is larger than 3.5 Å for each compound. Between *Tr* and *Pn* (covalent) bonds of about 2.6 Å can be found.

Since all compounds of the 6-1-3 system are electron precise Zintl compounds, the theoretical charges can be determined easily. The alkali metals transfer their valence electron to the $TrPn_3$ units and thus have partial charges of +1. Within the triangular planar units, (1b)-*Pn* and (3b)-*Tr* are present with partial charges of -1 and 0, respectively (nb = n-fold bonded).

Electronic structure calculations

The computational studies of all compounds in the A_6TrPn_3 system (with A = Rb, Cs; Tr = Al, Ga, In and Pn = As, Sb) were performed using the CRYSTAL17 program package and hybrid density functional methods.[14][15] A hybrid exchange-correlation functional after Perdew, Burke, and

Ernzerhof (DFT-PBE0) was used, [16] Localized, Gaussian-Type triple ζ-valence + polarization level basis sets were used for Al, Ga, In, As and Sb and split valence + polarization level basis sets for Rb and Cs. The basis sets were derived from the molecular Karlsruhe basis sets.[17–22] For the evaluation of Coulomb and exchange integrals (TOLINTEG), tight tolerance factors of 8, 8, 8, 8, 16 were used for all calculations. The reciprocal space of all calculations was sampled with 6×10×6 Monkhorst-Pack-type *k*-point grids. The starting geometries were taken from experimental data whenever possible. For the unknown compounds models based on adjacent structures by atom replacement were derived. Both lattice parameters and atomic positions were fully optimized within the constraints imposed by the space group symmetry. Further on all optimized structures were confirmed to be true local minima by means of harmonic frequency calculations at Γ-point. For all compounds and models electronic band structures, density of states (DOS) and heteroatomic crystal orbital Hamilton populations (COHP) were calculated. The Brillouin Zone paths were provided by the web service *SeeK-path* and a list can be found in the SI.[23]

Calculation results:

Table 1. Optimized crystal structure parameters for all calculated compounds. For each compound, the first line shows experimental (exp.), the second calculated (calc.) cell parameters and the third the percentual difference (Δ). The transition refers to the position of the valence band maximum and conduction band minimum of the band structure.

	a / Å	b / Å	c / Å	β / °	band gap / EV		transition
Rb_6AlSb_3 (exp.)	10.624	6.260	12.377	100.7	1.36	indirect	Y2 -> Γ
(calc.)	10.599	6.273	12.279	100.8			
Δ / %	-0.23	0.20	-0.80	0.07			
Cs_6AlSb_3	10.845	6.507	12.707	100.95	1.72	indirect	-"-
	10.927	6.504	12.624	101.19			
	0.75	-0.04	-0.66	0.24			
Cs_6GaSb_3	10.858	6.490	12.729	101.1	1.68	indirect	-"-
	10.923	6.492	12.641	101.3			
	0.60	0.03	-0.70	0.19			
Cs_6InAs_3	10.469	6.356	12.208	101.3	1.89	pseudo-direct	Γ -> Γ
	10.574	6.343	12.177	101.4			
	0.99	-0.21	-0.25	0.16			

From all eight experimentally known compounds of the 6-1-3 system, only the Rb and Cs compounds have fully occupied crystallographic positions for all atoms. Therefore, experimental data of these four was used as input geometry for their respective calculations. For them cell parameters and atomic positions were optimized. The maximum deviation between experimental

and calculated cell parameters is about 1 % and frequency calculations revealed no imaginary frequencies, thus the optimized structures were proven to be true local minima. Subsequently band structure, density of states (DOS) and crystal orbital Hamilton population were calculated as well as a Mullikan analysis. All cell parameters (experimental and calculated), their deviations, band gaps and transitions can be found in Table 1.

Since four compounds are a small number to get an insight on trends regarding size and kind of band gap, for all remaining Rb and Cs arsenides and antimonides models based on the known crystal structures were created by atom switching. For them all cell parameters and atom positions were optimized as well and harmonic frequencies calculated. The resulting cell parameters can be found in Table S2 in the Supporting information. For Cs_6InSb_3 two imaginary frequencies of -22.7237 cm^{-1} and -15.3517 cm^{-1} were found. Therefore, this structure was distorted along the first frequency and re-optimized in space group 4. Upon further absence of negative frequencies band structure, density of states and crystal orbital Hamilton population were calculated for all compounds. For Cs_6InSb_3 the model in space group 4 and the original model showed the same band structure and band gap as well as a very similar shape of the density of states and crystal orbital Hamilton population.

Table 2. Calculated band gaps for all Rb/Cs_6*Tr*As/Sb_3 compounds in eV. Calculations based on experimental data are printed in bold letters.

A-Tr-Pn	**Rb-As**	**Cs-As**	**Rb-Sb**	**Cs-Sb**
Al	1.37	1.89	**1.36**	**1.72**
Ga	1.37	1.87	1.32	**1.68**
In	1.43	**1.89 (pd)**	1.39	1.71

In Table 2 all calculated band gaps can be found. In the similar 5-1-3 system the band gaps were mainly influenced by the *Tt* atom (*Tt* = Si, Ge, Sn) and its electronegativity difference with P.[24] For the 6-1-3 compounds, this trend is not reproduced, as can be seen for the band gaps of compounds which only differ by their triel atom which differ by a maximum of 0.07 eV. Here the band gap is more influenced by the alkali metal present, thus the more electronegative Cs leads to larger band gaps for its compounds compared to Rb.[25] In this system it strikes further out, that all Sb compounds show smaller band gaps than their respective As counterparts, although the difference is rather small for the Rb compounds. This implies that the overall electronegativity difference between the alkali metal and pnictogen determines the size of the band gap.

Band structure and DOS:

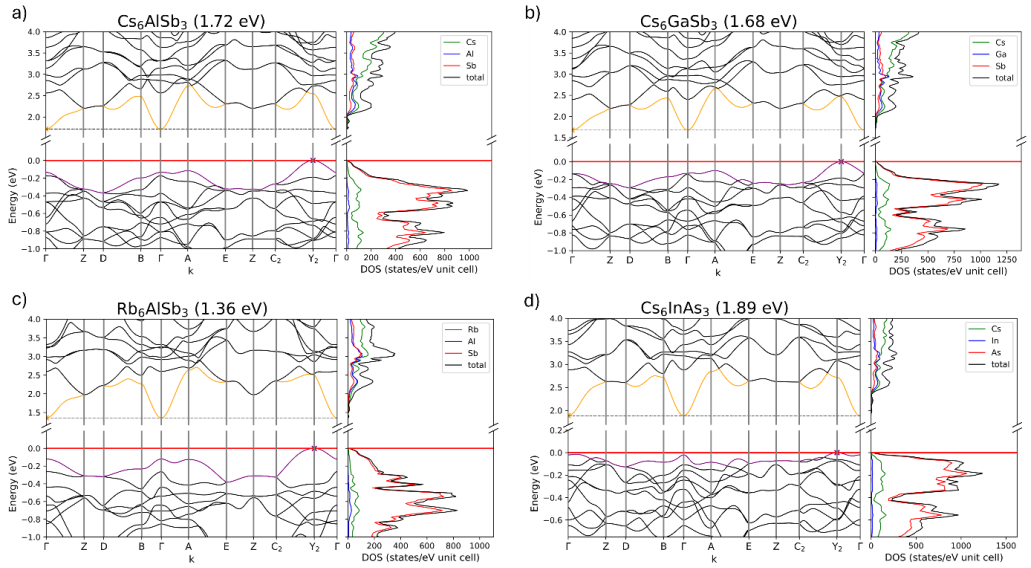

Figure 2. Band structure and density of states of a) Cs_6AlSb_3, b) Cs_6GaSb_3, c) Rb_6AlSb_3 and d) Cs_6InAs_3 with band gaps of 1.72 eV, 1.68 eV, 1.36 eV and 1.89 eV, respectively. All but Cs6InAs3 show indirect band gaps.

Figure 2. shows the calculated band structures for Cs_6AlSb_3, Cs_6GaSb_3, Rb_6AlSb_3 and Cs_6InAs_3. While the three former compounds have an indirect band gap, the latter one shows a pseudo-direct band gap, since the difference between direct and indirect band gap is only 0.02 eV. The overall shape of the band structure is very similar for all compounds (experimentally feasible and theoretical alike): The valence bands of Rb_6AlSb_3 show more dispersion than the Cs compounds depicted, which suggests that the electron density is more localized for these Cs compounds. The same can be found for all predicted compounds, where the dispersion of the Rb compounds is always slightly larger than the Cs compounds. The valence band maximum (VBM) is located at Y_2 for all compounds, while the conduction band minimum (CBM) is at Γ. Most compounds show a difference of up to 0.1 eV between the indirect transition Y_2 -> Γ compared to the direct Γ -> Γ transition, but for all In compounds this gap is considerably smaller than the other compounds. For Cs_6InAs_3 the difference becomes smaller than 0.02 eV thus a pseudo-direct band gap can be assumed.

The DOS is again similar for all compounds. The valence band mostly consist of As/Sb states with minor contributions of the Tr and alkali metal. For the conduction bands up to about 3 eV all atoms contribute equally for all compounds. At higher energies the alkali metal contribution increases and shows most states. In previous works a shift of the VBM was linked to an increase in alkali metal states right below the band gap, which could be seen as an increase in states in the DOS.[24] In this system, no such states can be seen at the Fermi-Level. Although the alkali metal projected

DOS curve in Cs_6InAs_3 shows more states between -0.2 eV and the Fermi-Level, right below 0 eV there is still a sharp edge cutting down the alkali metal contribution to zero at the VBM. Since the top valence band itself is rather flat compared to the other compounds, the increase in alkali metal states should be attributed to other k-points than Γ. Another interesting feature of the DOS is, that for most compounds the top two valence bands show no triel contribution at all, which can be seen especially for Rb_6AlAs_3.

Mullikan analysis

To get a better insight on the bonding situation of the 6-1-3 compounds a Mullikan analysis was conducted for each compound. All obtained Mulliken charges and overlap populations can be found in the SI. According to the Zintl concept, the alkali metal transfers its valence electron to *Pn* since it has the highest electronegativity, resulting in (1b)Pn^{2-} while the *Tr* stays uncharged. Consequently $[TrPn_3]^{6-}$ units are formed, which are isostructural to CO_3^{2-}. These theoretical charges are found in the Mulliken analysis as well. All alkali metals show Mulliken charges of about 0.6, *Pn* atoms of about -1.3. The difference to the theoretical charge of *Pn* can be explained by partial double bonds formed in the $[TrPn_3]^{6-}$ units through possible back-bonds from the *Pn* atoms. The *Tr* atoms differ slightly: while Al has a positive Mulliken charge of up to 0.16, Ga and In show slightly negative charges of about -0.1. Here Ga atoms always show a larger negative charge than In. This is caused by the partial double bonds on one hand and the decreasing electronegativity difference on the other. Although for Al double bonds can are formed the easiest, the electronegativity difference between Al and *Pn* (ΔEN) is also the largest and thus the charge is slightly positive, since the pnictogen attracts the electron density in the polar bond. For Ga ΔEN is the smallest and double bonds are still be formed to an extent, thus the largest negative charges are found, In is the most reluctant to form double bonds, since it prefers multiple single bonds and thus has a lower negative charge.[26,25]

Fuher on the overlap population was calculated to get an insight on the bonding situation. With values of around 0.36 it can be assumed that rather strong bonds, potentially partial double bonds, are formed between *Tr* and *Pn*. Again, the reluctance to form double bonds between In and *Pn* can be seen, since they have the lowest overlap population, although their atomic radii match the best. Al on the other hand has the largest overlap with *Pn*. The alkali metal shows only weak interactions with its surrounding *Tr* and *Pn* atoms, thus they probably only show ionic interactions.

COHP:

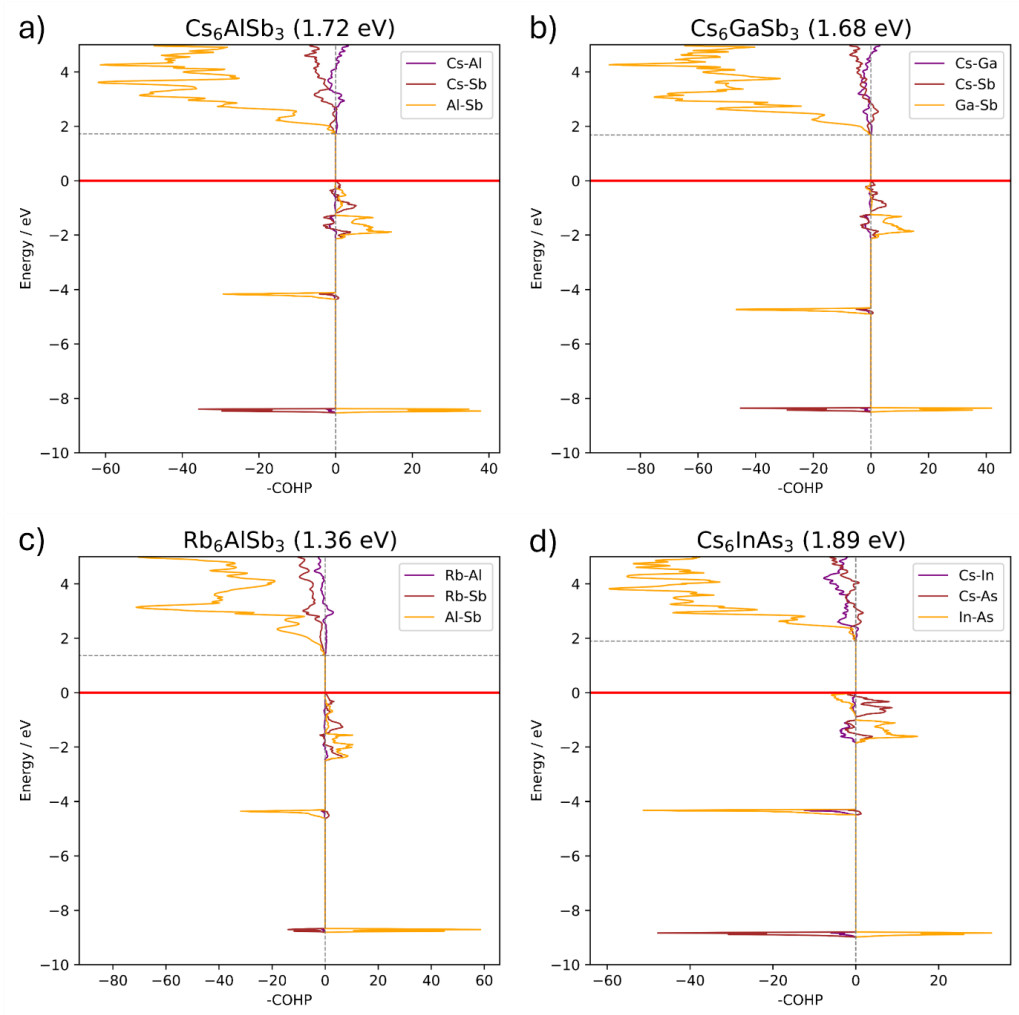

Figure 3. Crystal orbital Hamilton population of a) Cs_6AlSb_3, b) Cs_6GaSb_3, c) Rb_6AlSb_3 and d) Cs_6InAs_3.

To get further insight one the nature of the interatomic interactions a crystal orbital Hamilton interaction (COHP) was calculated for all heteroatomic interactions. The valence bands span over the interval of 0 to about -2 eV. Although for all compounds there are mostly *Pn* states present in the DOS, only few interactions can be seen. Therefore, these states could result mostly from non-bonding sates, such as the *Pn* lone pairs. For all compounds *Tr-Pn* anti-bonding states are present at -4 eV and bonding states at -9 eV, which are accompanied by anti-bonding alkali metal-*Pn* interactions. The conduction bands primarily consist of *Tr-Pn* anti-bonding states for all compounds.

The COHP of Cs_6InAs_3 differs from the other compounds at the Fermi-Level since more In-As anti-bonding interactions are present. There are also more Cs-As bonding states present, but where

the Cs DOS curve falls ack to zero, the projected COHP curve switches to anti-bonding interactions right below the Fermi-Level. Thus, these bonding interactions probably arise from other k-points than Γ and can be attributed to the flat part of the top valence band. For the other In compounds these states can also be found, but are at slightly lower energies which is in line with the larger difference of direct and indirect band gap. Cs_6InAs_3 is the only compound that shows a pseudo-direct band gap, for which these In-As anti-bonding interactions could be the reason. A possible explanation could be that the partial double bonds are, although rather weak, unfavourable. Therefore, the states are located right below the Fermi-Level, where other compounds mostly show the states of the *Pn* lone pairs.

Comparison to 5-1-3 compounds

Since the 6-1-3 Rb and Cs triel compounds show a very similar crystal structure to the Rb and Cs tetrel compounds found in the 5-1-3 system, a comparison between the findings in both systems might give a deeper insight on possible crystal structure band structure relations. For the tetrel compounds two, isomeric structure types were found, one dimeric with edge-sharing $[Tt_2P_6]^{10-}$ double tetrahedra and one monomeric with $[TtP_3]^{5-}$ CO_3^{2-} analogue units, while for the trielates only the monomeric structural motif was found.[24] In the 5-1-3 system a clear energetic separation of both structure types by involved alkali metal was found with the latter structure only present for Rb and Cs compounds. Although the discussed compounds in this paper are also limited to Rb and Cs compounds, there are K and Na compounds published with the same anionic unit. This raises two questions: Is there some, to the 5-1-3 system, analogue dimeric structure and since Na and K compounds are known, is there some factor stabilizing this monomeric structure? One explanation might be the number of valence electrons of the *Tr* and *Tt* compounds. Since *Tr* atoms within a dimeric $[Tr_2Pn_6]^{12-}$ would have a partial charge of -1, this might cause some instability, compared to the neutrally charged *Tr* in $[TrPn_3]^{6-}$ units. This might stabilize the Na and K compounds found, but to get an idea on this matter, further calculations with a dimeric model need to be done. Another factor for stabilizing compounds with different alkali metals could be the pnictogen present in the compound, since here arsenides and antimonides were investigated, while in the 5-1-3 system phosphides were in the spotlight. The larger radii of As and Sb could influence the preferred crystal structure similar to the influence by the alkali metal size, thus an investigation of the phosphides within this system could give further valuable insights.

For both systems the band structures and densities of states are similar regarding the position of the VBM or uplifted bands at other k-points by additional alkali metal states and the top valence bands being assigned to mostly *Pn* non-bonding states, possibly lone pairs. Further on does the

dispersion of the band decrease for compounds with heavier elements, especially on the alkali metal side, leading to the formation of pseudo-direct band gaps. One main difference between the two compounds is that for the tetrelates the CBM is often positioned at another k-point compared to the trielates, where the CBM is always located at Γ. Upon closer look at the edge of the band gap top in the COHP, the tetrelates all show at least a small edge in Tt-P states, while the trielates are all zero right above the gap with a slow increase in *Tr*-*Pn* states for higher energies. One explanation might be that the polarity of the *Tr*-*Pn* bonds is larger than the *Tt*-*Pn* bonds, which could result in a smaller splitting of the respective states in the latter compounds, lowering them in energy.

Conclusion

For the experimentally feasible Rb and Cs compounds of the 6-1-3 system, crystal structures, based on experimentally, data were fully optimized and band structures, density of states and crystal orbital Hamilton populations calculated. The remaining Rb/Cs arsenides and antimonides were modelled based on the existing crystal structures by switching atoms in the unit cell and subsequently optimizing the structure. All but one compound, namely Cs_6InAs_3 which has a pseudo-direct band gap, were found to be indirect band gap semiconductors.

The size of the band gap was found to be mainly dependent on the pnictogen and alkali metal present, with differences of up to 0.5 eV between arsenides and antimonides. As for the shift of the valence band maximum from Γ to Y_2 lower lying *Tr*-*Pn* interactions, compared to Cs_6InAs_3, were identified, which might be caused by partial double bonds that lower these states in energy. As for previous studies, additional alkali metal states were identified, which can lift the top valence band at different k-points.[24] All results were compared with monomeric structure type of the A_5TtP_3 system (*A* = Li-Cs and *Tt* = Si, Ge, Sn) for which similar results were obtained.

Further research should focus on one hand on the Li, Na and K compounds of this system as well as all phosphides, to see how trends of the band gap change for these compounds and to complete the investigation of the system. Modelling compounds based on the dimeric structure type in the 5-1-3 system could further deepen the understanding of this system and by investigating the energetics of both compounds, could lead to the prediction of new compounds. Experimental research should focus on the synthesis of the predicted compounds. One could also consider investigating mixed $A_{6-x}Tr_{1-x}Tt_xPn_3$ compounds since due to the similar crystal structure new materials with tuneable band gaps could be discovered.

References

[1] H. Hosono, *Journal of Non-Crystalline Solids* **2006**, *352*, 851.
[2] K. S. Kazunori Sato, H. K.-Y. Hiroshi Katayama-Yoshida, *Jpn. J. Appl. Phys.* **2000**, *39*, L555.
[3] A. Mehta, A. Mishra, S. Basu, N. P. Shetti, K. R. Reddy, T. A. Saleh, T. M. Aminabhavi, *Journal of environmental management* **2019**, *250*, 109486.
[4] T. Todorov, T. Gershon, O. Gunawan, Y. S. Lee, C. Sturdevant, L.-Y. Chang, S. Guha, *Advanced Energy Materials* **2015**, *5*.
[5] J. Wan, X. Xu, G. Zhang, Y. Li, K. Feng, Q. Peng, *Energy Environ. Sci.* **2017**, *10*, 1739.
[6] W. Blase, G. Cordier, M. Somer, *Zeitschrift für Kristallographie - Crystalline Materials* **1991**, *195*, 121.
[7] W. Blase, G. Cordier, M. Somer, *Zeitschrift für Kristallographie - Crystalline Materials* **1993**, *206*, 141.
[8] W. Blase, G. Cordier, M. Somer, *Zeitschrift für Kristallographie - Crystalline Materials* **1993**, *206*, 145.
[9] W. Blase, G. Cordier, M. Somer, *Zeitschrift für Kristallographie - Crystalline Materials* **1993**, *206*, 143.
[10] W. Blase, G. Cordier, M. Somer, *Zeitschrift für Kristallographie - Crystalline Materials* **1991**, *195*, 117.
[11] W. Blase, G. Cordier, M. Somer, *Zeitschrift für Kristallographie* **1992**, *199*, 279.
[12] G. Cordier, W. Blase, *Zeitschrift für Kristallographie - Crystalline Materials* **1992**, *199*, 277.
[13] H. G. von Schnering, M. Somer, K. Peters, W. Blase, G. Cordier, *Zeitschrift für Kristallographie - Crystalline Materials* **1990**, *193*, 283.
[14] R. Dovesi, V. R. Saunders, C. Roetti, R. Orlando, C. M. Zicovich-Wilson, F. Pascale, B. Civalleri, K. Doll, N. M. Harrison, I. J. Bush **2017**.
[15] R. Dovesi, A. Erba, R. Orlando, C. M. Zicovich-Wilson, B. Civalleri, L. Maschio, M. Rérat, S. Casassa, J. Baima, S. Salustro et al., *Wiley Interdiscip. Rev.: Comput. Mol. Sci.* **2018**, *8*.
[16] J. P. Perdew, W. Yang, K. Burke, Z. Yang, E. K. U. Gross, M. Scheffler, G. E. Scuseria, T. M. Henderson, I. Y. Zhang, A. Ruzsinszky et al., *Proc. Natl. Acad. Sci. U. S. A.* **2017**, *114*, 2801.
[17] T. M. F. Restle, J. V. Dums, G. Raudaschl-Sieber, T. F. Fässler, *Chem.* **2020**, *26*, 6812.
[18] T. M. F. Restle, S. Zeitz, J. Meyer, W. Klein, G. Raudaschl-Sieber, A. J. Karttunen, T. F. Fässler, *Zeitschrift anorg allge chemie* **2021**, *647*, 1804.
[19] T. M. F. Restle, S. Zeitz, P. M. Stanley, A. J. Karttunen, J. Meyer, G. Raudaschl-Sieber, W. Klein, T. F. Fässler, *Chem.* **2024**, *30*, e202304097.
[20] B. Scheibe, S. I. Ivlev, A. J. Karttunen, F. Kraus, *Eur. J. Inorg. Chem.* **2020**, *2020*, 1319.
[21] B. Scheibe, A. J. Karttunen, F. Weigend, F. Kraus, *Chem.* **2021**, *27*, 2381.
[22] R. E. Stene, B. Scheibe, A. J. Karttunen, W. Petry, F. Kraus, *Eur. J. Inorg. Chem.* **2019**, *2019*, 3672.
[23] Y. Hinuma, G. Pizzi, Y. Kumagai, F. Oba, I. Tanaka, *Comput. Mater. Sci.* **2017**, *128*, 140.
[24] S. Zeitz, H. Antoniuk, V. Hlukhyy, T. F. Fässler, *Chem.* **2024**, *30*, e202400002.
[25] A. F. Holleman, *Lehrbuch der anorganischen Chemie*, Walter de Gruyter GmbH & Co KG, **2019**.
[26] P. P. Power, *Chem. Rev.* **1999**, *99*, 3463.

5.3 Large Number of Direct or Pseudo-Direct Band Gap Semiconductors among A_3TrPn_2 Compounds with *A* = Li, Na, K, Rb, Cs; *Tr* = Al, Ga, In; *Pn* = P, As

Sabine Zeitz, Yulia Kuznetsova, and T. F. Fässler

published in

Molecules **2024**, *29*, 4087

molecules

MDPI

Article

Large Number of Direct or Pseudo-Direct Band Gap Semiconductors among A_3TrPn_2 Compounds with A = Li, Na, K, Rb, Cs; Tr = Al, Ga, In; Pn = P, As

Sabine Zeitz, Yulia Kuznetsova and Thomas F. Fässler *

Chair of Inorganic Chemistry with Focus on Novel Materials, School of Natural Science, Technical University of Munich, Lichtenbergstraße 4, D-85747 Garching, Germany; sabine.zeitz@tum.de (S.Z.); yulia.kuznetsova@tum.de (Y.K.)
* Correspondence: thomas.faessler@lrz.tum.de

Abstract: Due to the high impact of semiconductors with respect to many applications for electronics and energy transformation, the search for new compounds and a deep understanding of the structure–property relationship in such materials has a high priority. Electron-precise Zintl compounds of the composition A_3TrPn_2 (A = Li − Cs, Tr = Al − In, Pn = P, As) have been reported for 22 possible element combinations and show a large variety of different crystal structures comprising zero-, one-, two- and three-dimensional polyanionic substructures. From Li to Cs, the compounds systematically lower the complexity of the anionic structure. For an insight into possible crystal–structure band–structure relations for all compounds (experimentally known or predicted), their band structures, density of states and crystal orbital Hamilton populations were calculated on a basis of DFT/PBE0 and SVP/TZVP basis sets. All but three (Na_3AlP_2, Na_3GaP_2 and Na_3AlAs_2) compounds show direct or pseudo-direct band gaps. Indirect band gaps seem to be linked to one specific structure type, but only for Al and Ga compounds. Arsenides show smaller band gaps than phosphides due to weaker Tr-As bonds. The bonding situation was confirmed by a Mullikan analysis, and most states close to the Fermi level were assigned to non-bonding orbitals.

Keywords: Zintl phase; direct band gap; structure prediction; semiconductor; DFT calculation

Citation: Zeitz, S.; Kuznetsova, Y.; Fässler, T.F. Large Number of Direct or Pseudo-Direct Band Gap Semiconductors among A_3TrPn_2 Compounds with A = Li, Na, K, Rb, Cs; Tr = Al, Ga, In; Pn = P, As. *Molecules* **2024**, *29*, 4087. https://doi.org/10.3390/molecules29174087

Academic Editors: Andrea Bencini and Vito Lippolis

Received: 15 July 2024
Revised: 23 August 2024
Accepted: 26 August 2024
Published: 28 August 2024

1. Introduction

Semiconductors have a variety of applications, like solar cells, LEDs, laser applications, etc., which are essential for the continuous evolution of our modern society. As their applications become more diverse and complex, efficient band gap engineering is becoming increasingly important in the design of new and highly specialised materials [1–3]. When searching for compounds that allow a correlation between their atomic structure and the nature of their constituent elements with their properties, compound classes that have several or many representatives are particularly useful for determining the relevant parameters [4,5].

The $Ga_xAl_{1-x}As$ and $In_xGa_{1-x}As$ compound family are exemplary compounds where a simple variety in the composition leads to highly tuneable band gaps [6–10]. However, besides these well-defined examples, concepts for more complex compound families are missing; thus, exploring possible crystal–structure band–structure relations is key for the future of intelligent and efficient material design. In a previous study, we reported that, for a certain series of compounds, the nature and size of their band gaps were not solely dependent on the crystal structure and composition of the elements. In more detail, the electron-precise Zintl-phase A_5TtP_3 or $A_{10}Tt_2P_6$ system (A = Li − Cs; Tt = Si − Sn) occurs with two different isomers for the anionic subunits—either carbonate analogue TtP_3^{5-} monomers with a partial Tt-P double bond character or $Tt_2P_6^{10-}$ dimers with exclusively single bonds, respectively, (Scheme 1). We found for all compounds with monomeric units

a higher dispersion within the valence and conduction bands, which is in line with a partial double bond formation between the atoms of the carbonate analogue monomer TtP_3^{5-} anion. We also found no direct influence of the nature of the *Tt* element on the band gap. As a general trend, we found that direct band gaps at Γ are favoured in compounds with only little or no alkali metal orbital contribution at the valence band maximum, which suggests that the influence of the alkali metal on the electronic structure is an important factor [11].

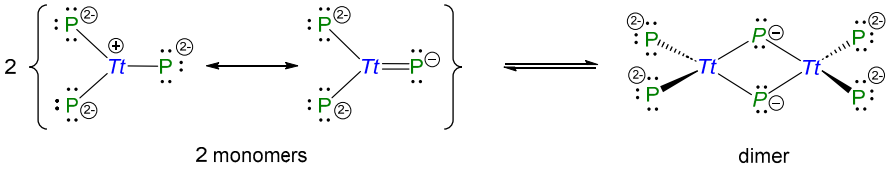

Scheme 1. Polyanions in compounds of the composition A_5TtP_3 and $A_{10}Tt_2P_6$ (A = Li − Cs; Tt = Si − Sn).

With this new insight, it becomes evident that the matter at hand needs to be further investigated for a more diverse system, where the variety of compounds present is greater and the influence of the alkali metal on the crystal and band structure can be further studied. We report here on our investigation of a class of compounds with a large number of representatives, namely the Zintl phases with the composition A_3TrPn_2 (*A* = Li − Cs, *Tr* = Al, Ga, In; *Pn* = P, As). They were chosen since there are 22 experimentally achievable compounds, within seven different structure types. Although many of the compounds within the system were characterised in the 1990s, their electronic structures were only scarcely investigated for selected compounds [12–14]. An overview of the crystal structures known up to date is shown in Table 1 and Scheme 2. According to the Zintl–Klemm concept, the alkali metals transfer their valence electron to the anionic substructure of the triel and pnictogen, thus allowing various covalent one-, two- or three-dimensional structural motifs of edge- or corner-sharing $TrPn_4$-tetrahedra, as well as a "zero"-dimensional triangular planar coordination of the triel atom for compounds of the heavier alkali metals.

Table 1. Overview of the crystallographic details of the 3-1-2 compounds. Cell parameters given in the first line and second line are of experimental and calculated origin, respectively. The third line shows the deviation in %. If only one line is presented, the data refer to the predicted crystal structure discussed below.

Compound	a	b	c	α	β	γ	Space Group	No.	Crystal System	Connectivity
structure type F										
Li_3AlP_2	11.5138	11.7634	5.8202				*Cmce*	64	orthorhombic	2D
	11.5388	11.7560	5.8267							
	0.22	−0.06	0.11							
Li_3GaP_2	11.5839	11.7809	5.8129				*Cmce*	64	orthorhombic	2D
	11.5910	11.7834	5.8289							
	0.06	0.02	0.27							
Li_3AlAs_2	11.894	12.150	6.005				*Cmce*	64	orthorhombic	2D
	11.932	12.139	6.011							
	0.32	−0.09	0.11							
Li_3GaAs_2	11.9626	12.1629	5.9984				*Cmce*	64	orthorhombic	2D
	11.9959	12.1610	6.0145							
	0.28	−0.02	0.27							
structure type G										
Li_3InP_2	12.0065		23.9165				$I4_1/acd$	142	tetragonal	3D
	12.0407		23.9862							
	0.28		0.29							
Li_3InAs_2	12.388		24.6587				$I4_1/acd$	142	tetragonal	3D
	12.409		24.7284							
	0.17		0.28							

Molecules **2024**, *29*, 4087

Table 1. *Cont.*

Compound	a	b	c	α	β	γ	Space Group	No.	Crystal System	Connectivity
structure type E										
Na_3AlP_2	13.176	6.764	6.065				*Ibam*	72	orthorhombic	2D
	13.261	6.468	6.008							
	0.64	−4.57	−0.94							
Na_3GaP_2	13.081	6.728	6.211				*Ibam*	72	orthorhombic	2D
	13.304	6.339	6.123							
	1.68	−6.13	−1.44							
K_3InP_2	14.489	7.658	6.816				*Ibam*	72	orthorhombic	2D
	14.523	7.499	6.781							
	0.23	−2.12	−0.52							
Na_3AlAs_2	13.604	6.895	6.227				*Ibam*	72	orthorhombic	2D
	13.741	6.458	6.187							
	1.00	−6.77	−0.64							
K_3InAs_3	7.821	14.759	6.936				*Ibam*	72	orthorhombic	2D
	7.613	14.817	6.964							
	−2.73	0.39	0.40							
Cs_3InAs_2	15.745	8.469	7.247				*Ibam*	72	orthorhombic	2D
structure type H										
Na_3InP_2	9.401	7.371	15.358		92.4		$P2_1/c$	14	monoclinic	3D
	9.342	7.277	15.236		92.6					
	−0.63	−1.30	−0.80		0.22					
Na_3InAs_2	9.677	7.547	15.731		92.6		$P2_1/c$	14	monoclinic	3D
	9.624	7.439	15.611		92.9					
	−0.55	−1.45	−0.77		0.29					
Na_3GaAs_2	9.301	7.296	15.199		92.3		$P2_1/c$	14	monoclinic	3D
structure type C										
K_3AlP_2	8.871	11.879	15.280	72.47	73.35	71.62	$P\bar{1}$	2	triclinic	1D + 0D
	8.822	11.767	15.140	72.94	73.45	72.40				
	−0.55	−0.95	−0.92	0.65	0.14	1.07				
Rb_3InP_2	9.397	12.500	15.927	97.16	107.00	106.72	$P\bar{1}$	2	triclinic	1D + 0D
	9.462	12.556	15.935	96.87	107.40	106.18				
	0.69	0.45	0.05	−0.30	0.38	−0.51				
K_3AlAs_2	9.062	12.164	15.570	72.40	73.05	71.63	$P\bar{1}$	2	triclinic	1D + 0D
	8.969	12.070	15.508	72.69	73.27	72.16				
	−1.03	−0.78	−0.40	0.40	0.30	0.74				
structure type D										
Cs_3InP_2	9.662	12.884	15.840	81.1	81.6	70.7	$P\bar{1}$	2	triclinic	1D + 0D
	9.750	12.922	15.843	80.6	81.6	71.2				
	0.90	0.29	0.02	−0.57	0.01	0.81				
structure type B										
Rb_3GaP_2	14.634	24.893	9.163				*Pbca*	61	orthorhombic	0D
	14.930	24.905	9.115							
	1.99	0.05	−0.53							
K_3GaP_2	14.496	23.634	8.740				*Pbca*	61	orthorhombic	0D
Rb_3AlP_2	14.880	24.961	9.140				*Pbca*	61	orthorhombic	0D
K_3GaAs_2	14.777	24.100	8.938				*Pbca*	61	orthorhombic	0D
Rb_3AlAs_2	15.175	25.440	9.343				*Pbca*	61	orthorhombic	0D
Rb_3GaAs_2	15.232	25.375	9.315				*Pbca*	61	orthorhombic	0D
structure type A										
Cs_3AlP_2	11.233	8.641	18.986		100.056		$P2_1/c$	14	monoclinic	0D
	11.253	8.684	19.181		100.912					
	0.17	0.50	1.02		0.85					
Cs_3GaP_2	11.173	8.661	18.939		99.64		$P2_1/c$	14	monoclinic	0D
	11.241	8.672	19.173		100.77					
	0.60	0.12	1.22		1.13					
Cs_3AlAs_2	11.458	8.831	19.453		99.68		$P2_1/c$	14	monoclinic	0D
	11.427	8.844	19.578		100.31					
	−0.27	0.14	0.64		0.63					
Cs_3GaAs_2	11.371	8.857	19.460		99.225		$P2_1/c$	14	monoclinic	0D
	11.413	8.836	19.571		100.180					
	0.37	−0.25	0.57		0.95					
Rb_3InAs_2	12.074	8.179	18.868		101.1		$P2_1/c$	14	monoclinic	0D

Molecules **2024**, *29*, 4087

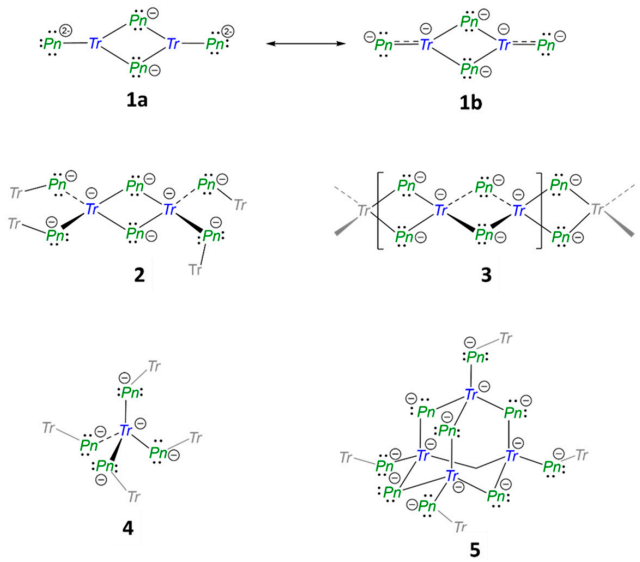

Scheme 2. Lewis valence structures of the various building units in A_3TrPn_2 Zintl phases. Mesomere valence formulae **1a** and **1b** of the "zero"-dimensional $[Tr_2Pn_4]^{6-}$ unit of two edge-sharing triangular planar units. The dimeric $[Tr_2Pn_4]^{6-}$ unit **2** and the one-dimensional $^1_\infty[TrPn_{4/2}]^{3-}$ string **3** of edge-sharing tetrahedra, a $TrPn_4$ tetrahedra **4** and the adamantane type subunit **5**. Further connecting atoms are represented in grey colour without formal charges.

Here, we report on the structural relationship of the 22 experimentally known compounds and their electronic properties by calculating their band structures, density of states (DOS) and crystal orbital Hamilton population (COHP). The influence of the crystal structure and elemental composition on the nature and size of the band gaps is analysed. Further on, eight crystal structures for compounds with new element combinations were predicted and their electronic structures investigated. An overview of the similarities and differences between these structures is given.

2. Results and Discussion

2.1. Structural Relationship of Compounds with Composition A_3TrPn_2 (A = Li − Cs, Tr = Al − In, Pn = P, As)

The Zintl phases A_3TrPn_2 (*A* = Li − Cs, *Tr* = Al, Ga, In, *Pn* = P, As) possess a unique variety of structures due to the covalent bonding of two *Pn* atoms by one *Tr* atom, resulting in the same charge of the polyanions. Depending on the alkali metal triel/pnictide element combination, the anionic substructures adopt different dimensions, ranging from isolated molecular anions ("zero"-dimensional) up to three-dimensional networks. Representatives of the different structure types are shown in Figure 1.

Compounds with the largest alkali metals such as Cs_3AlP_2, Cs_3GaP_2, Cs_3AlAs_2, Cs_3GaAs_2 and Rb_3GaP_2 form "discrete" molecular polyanions. Whereas all Cs compounds crystalise in space group *Pbca* (no. 61, Figure 1A), Rb_3GaP_2 shows a lower monoclinic symmetry with space group $P2_1/c$ (no. 14, Figure 1B). These structures will be referred to as structure types **A** and **B**, respectively [15–19]. Despite the different symmetry of the crystals, both structure types contain the same edge-sharing triangular planar $[Tr_2Pn_4]^{6-}$ polyanion, made up by two $(3b\text{-}Tr)^0$, two $(2b\text{-}Pn)^-$ and two $(1b\text{-}Pn)^{2-}$ atoms (nb = n-fold bonded). In order to achieve an electron octet for all atoms, resonance structures with a *Tr-Pn* double bond are required (Scheme 2, **1b**), resulting in four $(2b\text{-}Pn)^-$ and two $(4b\text{-}Tr)^{1-}$. Similarly, TtP_3 units have been observed in the A_5TtP_3 (*A* = Li − Cs, *Tt* = Si − Sn) system, where $[CO_3]^{2-}$ isosteric $[TtP_3]^{5-}$ units with a double bond character occur due to the higher amount of alkali metal [11]. The main difference between Rb_3GaP_2 and the Cs compounds

Molecules **2024**, *29*, 4087

is that the triangular dimers in Rb_3GaP_2 show a slightly bent structure, with a dihedral angle of 14.6(1)° between the two edge-sharing triangular planar $TrPn_3$, compared to a perfectly planar arrangement for the Cs compounds.

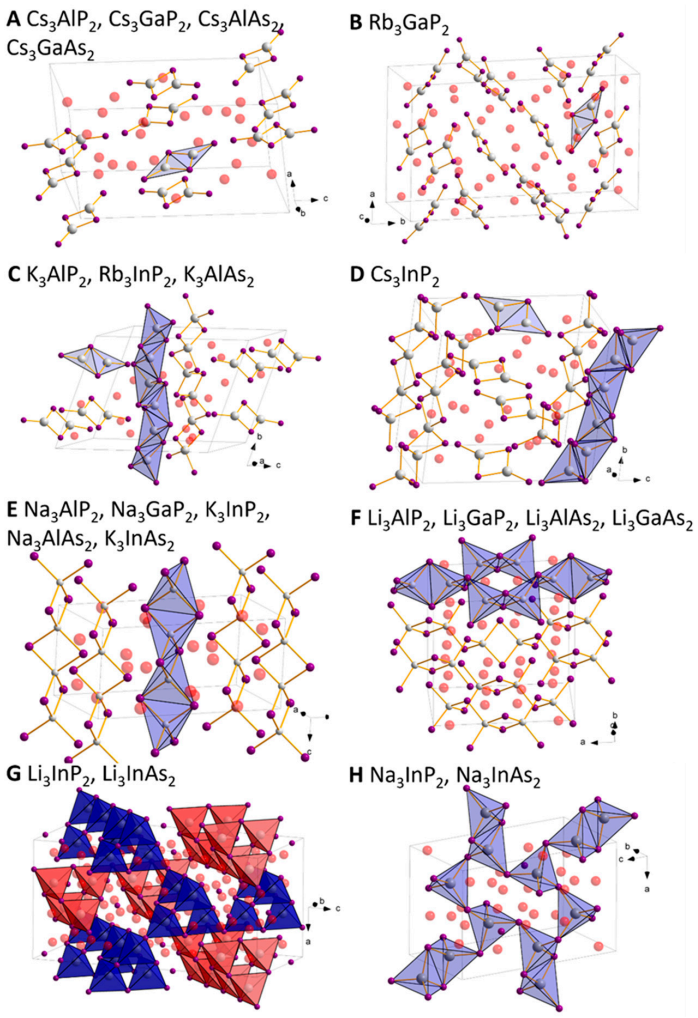

Figure 1. Overview of all known structure types within the A_3TrPn_2 system (with A = Li − Cs, Tr = Al, Ga, In, Pn = P, As). The respective structure types (denoted as (**A**–**H**) in the picture) are used to reference the structures. For all structures, the alkali metal A is depicted in red, the pnictide Pn in purple and the triel element Tr in grey.

K_3AlP_2, Rb_3InP_2 and K_3AlAs_2 form a structure type with two different polyanions and crystalise in space group $P\bar{1}$ (no. 2). They contain the molecular, triangular planar ("zero-dimensional") $[Al_2Pn_4]^{6-}$/$[In_2P_4]^{6-}$ unit (Scheme 2, **1a** and **1b**) that has been described above, and a linear one-dimensional substructure with tetrahedrally coordinated Tr atoms (Scheme 2, **3**). The InP_4 tetrahedra are edge-sharing, forming one-dimensional chains along the b-axis (Figure 1C), referred to as structure type **C** [20–22]. The chains contain exclusively $(2b\text{-}Pn)^-$ and $(4b\text{-}Tr)^-$, and the recurring unit can thus be formulated as $^1_\infty[TrPn_{4/2}]^{3-}$. The two subunits are separated from each other through alkali metal atoms. Cs_3InP_2 shows in general the same structural motifs and crystallises in the same space group, but the one-dimensional chains and triangular planar units have a slightly different arrangement

in the unit cell (Figure 1D) [23]. Here, the dimeric units of $[In_2P_4]^{6-}$ have a planar structure, whilst the dihedral angles of 3.60(8)°, 4.0(2)° and 6.60(5)° in K_3AlP_2, Rb_3InP_2 and K_3AlAs_2, respectively, lead to a slightly bent conformation. This type is henceforth referred to as structure **D**.

The Na compounds, Na_3AlP_2 and Na_3GaP_2, Na_3AlAs_2, as well as K_3InP_2 and K_3InAs_2, are all isostructural and crystallise in space group *Ibam* (no. 72) [24–28]. They consist solely of one-dimensional chains of edge sharing tetrahedra $^1_\infty[TrPn_{4/2}]^{3-}$ along the c-axis (**3**, SiS_2-type analogue) (Figure 1E). The structure is henceforth referred to as structure type **E** [29].

Li_3AlP_2, Li_3GaP_2, Li_3AlAs_2 and Li_3GaAs_2 crystallise in space group *Cmca* (no. 64) and consist exclusively of dimers of edge-sharing $TrPn_4$ tetrahedra. The Tr_2Pn_6 dimers (Scheme 2, **2**) are further connected by their vertices to neighbouring units of the same type, with the *Pn*-*Pn* vector of each edge-sharing tetrahedra dimer alternating in perpendicular directions with respect to each other, thus forming two-dimensional layers (Figure 1F), henceforth referred to as structure type **F** [12,30,31]. Consequently, the two-dimensional polyanion $^2_\infty[TrPn_{4/2}]^{3-}$ exclusively consists of (4b-*Tr*)$^-$ and (2b-*Pn*)$^-$, resulting in the same bonding situation as structure type **E**.

Li_3InP_2 and Li_3InAs_2, in contrast, form a three-dimensional structure with exclusively vertex-sharing $TrPn_4$ tetrahedra in space group $I4_1/acd$ (no. 142) [31,32]. Four $TrPn_4$ tetrahedra form an adamantane-type $[In_4Pn_{10}]$ "super tetrahedra" (Scheme 2). These units are further connected via their "outer vertices" to neighbouring super-tetrahedra to build a three-dimensional polyanion $^3_\infty[TrPn_{4/2}]^{3-}$. The structure can be understood as a hierarchical variant of the diamond structure by replacing C atoms with adamantane-type units. Since each *Tr* and *Pn* atom remains four- and two-fold bonded, the same charge as in structures **E** and **F** results. Two such independent three-dimensional networks of tetrahedra (Figure 1G), referred to as structure type **G**, interpenetrate each other without any bonds formed between the two subunits.

Lastly, for Na_3InP_2 and Na_3InAs_2 an alternative three-dimensional connection of the InP_4 tetrahedra is present [33,34]. These compounds crystallise in space group $P2_1/c$ (no. 14). Here In_2Pn_6 dimers of edge-sharing tetrahedra and $InPn_4$ tetrahedra (Scheme 2, **2** and **4**, respectively) are connected via common *Pn* atoms. Since each Pn_4Tr-tetrahedron is either corner- or edge-sharing with its neighbours, all *Pn* atoms are (2b-*Pn*)$^-$, while In atoms remain four-fold bonded (4b-In)$^-$, and the same overall charge of the polyanion $^3_\infty[TrPn_{4/2}]^{3-}$ results (Figure 1H, referred to as structure type **H**).

Thus, all structure types presented can be considered as constitutional isomers of compounds with the composition A_3TrPn_2, since the bonding situation of the *Pn* and *Tr* atoms is the same, but their connection leads to a variety of zero-, one-, two-, and three-dimensional polyanions.

2.2. Crystal Structure Optimisation of the Known Compounds

Using the experimental crystal structures as starting models, all existing compounds of the A_3TrPn_2 system were structurally optimised with subsequent frequency calculations. All but one experimentally observed structure were proven to be true local minima. For Cs_3InP_2, one imaginary frequency at -12.7551 cm^{-1} was found, and thus, upon distortion along that frequency, a new optimisation in P 1 symmetry was conducted. This structure was then proven to be a true local minimum by the absence of further imaginary frequencies. However, the reduction in the symmetry did not lead to significant structural differences and did not change the band structure or density of states (DOS) at all.

Table 1 shows an overview of all experimental and calculated cell parameters for all existing compounds. They are in good agreement, with deviations below 2%, but for structure type **E**, the calculated cell parameter b can be up to 6.5% smaller than the experimental reference. This could be due to the anisotropy of the structure, with the one-dimensional chains being aligned along the c-axis. Thus, only the alkali metal "connects" them along b. Since the interactions between the chains are only weak, this parameter

might shrink more compared to the other cell parameters, for the structure optimisation at 0 K.

2.3. Structure Predictions for Unknown A_3TrPn_2 Phosphides and Arsenides

The crystal structures of K_3GaP_2 Rb_3AlP_2, Na_3GaAs_2, K_3GaAs_2, Rb_3AlAs_2, Rb_3GaAs_2, Rb_3InAs_2 and Cs_3InAs_2 have not yet been reported. In order to make a theoretical prediction of the stability of the possible structure types, models were constructed based on the crystal structures of experimentally feasible P and As compounds as described above, containing either alkali, triel or pnictide atoms of the previous or next period. For example, for K_3GaP_2, models based on Rb_3GaP_2, K_3AlP_2 and Na_3GaP_2 with structure types **B**, **C** and **E**, respectively, were used, since these are the experimentally feasible compounds with the lighter or heavier alkali metal (Na_3GaP_2 and Rb_3GaP_2, respectively) or triel element (K_3AlP_2). From their experimental crystal structures, models were created for K_3GaP_2, optimised and the subsequent frequency, band structure, density of states (DOS) and crystal orbital Hamilton population (COHP) calculated. After optimisation and frequency calculation, the energy per unit cell and Gibbs free enthalpy can be obtained, respectively, and compared between each compound. Results for all structure predictions can be found in Tables 2 and S3 in the Supporting Information, where the differences (ΔΔE and ΔΔG) were referenced to the lowest energy ΔE and Gibbs free enthalpy ΔG for each compound.

Table 2. Energy comparison of different possible structures for all unknown phosphides and arsenides. The structure type in the second column refers to the crystal structures shown in Figure 1. The energetically most stable structure was set to 0, marked with bold letters. If the most stable structure differs for ΔΔE and ΔΔG, they are additionally marked in italics. The type of band gap is denoted as follows: dir. = direct, indir. = indirect, p-dir. = pseudo-direct band gap (where the indirect band gap is less than 0.03 eV smaller than the direct).

	Structure Type	ΔΔE (kJ/mol)	ΔΔG (kJ/mol)	Band Gap (eV)
K_3GaP_2	**B**	0	0	2.98 (dir.)
	C	6.01	8.24	2.41 (dir.)
	E	18.15	25.72	3.12 (p-dir.)
Rb_3AlP_2	**B**	0	0	2.44 (dir.)
	C	4.32	6.39	1.85 (dir.)
	A	6.21	5.87	2.37 (p-dir.)
Na_3GaAs_2	**H**	0	0	2.03 (dir.)
	F	17.02	20.09	2.30 (dir.)
	E	11.423	11.415	2.39 (indir.)
K_3GaAs_2	**B**	0	0	2.79 (dir.)
	C	5.41	7.22	2.17 (dir.)
	E	14.48	22.09	2.96 (indir.)
Rb_3AlAs_2	**B**	0	0	2.26 (dir.)
	C	3.44	4.88	1.73 (dir.)
	A	7.29	7.11	2.18 (dir.)
Rb_3GaAs_2	**B**	0	0	2.23 (dir.)
	A	7.94	7.44	2.15 (indir.)
	C	13.53	14.80	1.67 (dir.)
Rb_3InAs_2	***C***	0	0.34	1.57 (dir.)
	A	1.00	0	1.86 (indir.)
	E	4.19	11.86	1.96 (indir.)
Cs_3InAs_2	**E**	0	0	2.24 (dir.)
	D	3.26	6.32	1.81 (dir.)
	A	7.09	7.01	2.15 (dir.)
	E	9.78	20.42	2.07 (indir.)

Thus, the predicted structures are as follows: For K_3GaP_2, R_3AlP_2, K_3GaAs_2, Rb_3GaAs_2 and Cs_3InAs_2, structure type **B** with its trigonal planar dimer units has the lowest energy and Gibbs free enthalpy and is therefore considered to be the most stable. The lowest energy for Na_3GaAs_2 corresponds to structure type **H**, with its three-dimensional network of corner and edge-sharing tetrahedra. For Rb_3InAs_2, two structure types are possible, since the lowest energy could be obtained for structure **C**, while the mixed zero- and one-dimensional structure and the lowest Gibbs free enthalpy could be obtained for structure type **A**. This could be an indication of a possible phase transition from structure **C** to **A** for an increased reaction temperature and subsequent quenching.

Since all the computed energy and enthalpy differences are small, phase transitions between these predicted structures might occur. For example, the difference for Rb_3AlP_2 between the favoured type **B** and type **A** is only 6.21 kJ/mol. Although higher than the difference to structure **C**, this difference decreases for the Gibbs free enthalpy, which—in contrast to the bare minimum energy calculated at 0 K—includes the influence of the temperature for the optimised structure. In the case of Rb_3AlP_2, the decrease in $\Delta\Delta G$ for structure type **A**, compared to the energy difference, hints towards the existence of a high-temperature phase. The same trend is found for type **E** Na_3GaAs_2, type **A** Rb_3AlAs_2 and type **A** Cs_3InAs_2, which therefore could also be candidates for high-temperature phase transitions.

The general trend in dimensionality of the anionic sublattice shows that larger alkali metal atoms prefer a lower dimensionality, but larger triel atoms (mostly In) prefer a higher dimensionality. These trends can be seen, for example, in the Li-Al and Li-Ga phosphides and antimonides, which all crystallise in the two-dimensional structure **F**, while their corresponding In compounds crystallise in the three-dimensional structures **G** and **H**. Furthermore, all Rb and Cs compounds crystallise in structures containing only edge-sharing triangular planar dimers, type **A** and **B**, except Cs_3InP_2, Rb_3InP_2 and Rb_3InAs_2 (based on energy comparison), which crystallise in structures **C** or **D**, containing additional one-dimensional substructures. The remaining Na and K compounds crystallise in the one-dimensional or one- and zero-dimensional structure types **E** and **C**, except for the predicted structures of K_3GaP_2, K_3GaAs_2 and Na_3GaAs_2 which prefer structure types **B** and **H**, respectively. Comparing the structures of each phosphide–antimonide pair, almost all show the same structure, except for Na_3GaP_2/Na_3GaAs_2 and Cs_3InP_2/Cs_2InAs_2.

From these trends, it seems clear that the size of the atoms is the main factor determining which crystal structure is formed. More complex structures, formed through connections of $TrPn_4$-tetrahedra, allow only for smaller voids, where Li and Na ions fit best. The larger cations K, Rb and Cs are more space demanding, and may not fit in these voids. Instead, less complex anionic substructures with a more flexible anion arrangement are formed (such as monomeric units) into which the larger cations fit better. The second trend of the more complex structures for In compounds, can also be explained by the larger size of the In atoms. Larger atoms widen the polyanionic network, resulting in larger voids for the cations. Al and Ga cannot widen the structure enough; thus, the simpler polyanionic structures **A** and **B** are formed for the Rb and Cs compounds.

2.4. Electronic Structure Analysis

2.4.1. Size of the Band Gap

For all compounds and predicted structures, the band structure and the density of states (DOS) were calculated. Plots for all structures can be found in the SI, and all band gap sizes and band gap types are listed in Table 3. If an indirect band gap is less than 0.03 eV smaller than the smallest direct band gap, the gap is denoted as a pseudo-direct band gap. As an interesting fact, we found that 27 compounds reveal a direct or pseudo-direct band gap and only Na_3AlP_2, Na_3GaP_2 and Na_3AlAs_2 possess indirect band gaps.

Molecules **2024**, *29*, 4087

Table 3. Structure types and band gaps for all A_3TrPn_2 compounds. Direct band gaps are marked with, "dir.", indirect band gaps with "indir." and compounds where the direct and indirect band gap only have a small difference (<0.03 eV) are labelled as "pseudo-direct", abbreviated as "p-dir.". Italicised cells represent the previously predicted compounds. For Rb_3InAs_2, both possible structures with their band gaps are included.

A_3TrP_2	Li	Na	K	Rb	Cs
Al	**F**, 3.06 eV, dir.	**E**, 3.34 eV, indir.	**C**, 2.42 eV, dir.	***B***, *2.44 eV*, *dir.*	**A**, 2.54 eV, p-dir.
Ga	**F**, 2.83 eV, dir.	**E**, 2.88 eV, indir.	***B***, *2.98 eV*, *dir.*	**B**, 2.41 eV, p-dir.	**A**, 2.54 eV, p-dir.
In	**G**, 2.69 eV, dir.	**H**, 2.09 eV, dir.	**E**, 2.89 eV, dir.	**C**, 1.73 eV, dir.	**D**, 1.99 eV, dir.
A_3TrAs_2	Li	Na	K	Rb	Cs
Al	**F**, 2.85 eV, dir.	**E**, 2.98 eV, indir.	**C**, 2.27 eV, dir.	***B***, *2.26 eV*, *dir.*	**A**, 2.26 eV, p-dir.
Ga	**F**, 2.43 eV, dir.	***H***, *2.03 eV*, *dir.*	***B***, *2.79 eV*, *dir.*	***B***, *2.23 eV*, *dir.*	**A**, 2.35 eV, p-dir.
In	**G**, 2.26 eV, dir.	**H**, 1.69 eV, dir.	**E**, 2.69 eV, dir.	***C***, *1.57eV*, *dir.* ***A***, *1.86 eV*, *indir.*	***B***, *2.24 eV*, *dir.*

The width of the band gaps is decreasing for all heavier triels, including the most stable predicted structures of the eight unknown compounds, except for K_3AlP_2 and K_3AlAs_2, which have much smaller band gaps than their heavier homologues with Ga and In. Since these structures possess $[Al_2P_4]^{6-}$ dimeric units, which incorporate partial double bonds (Scheme 2), in contrast to structures with solely tetrahedral structural motifs, smaller band gaps are expected. This is indeed found for all structures incorporating this motif, including the predicted compounds, which also show especially small band gaps for compounds with structure type **C**. For Cs_3GaAs_2, the electronegativity difference could explain the slight increase in the band gap, since Ga has a higher electronegativity [35].

As for the comparison between the band gaps of phosphides and arsenides, the latter have, in general, gaps that are about 0.2 to 0.4 eV smaller than the corresponding phosphides. This observation correlates with the idea that for the larger As atoms, the orbital overlap with their neighbouring atoms is less effective, which leads in molecules to a smaller HOMO-LUMO separation. However, three compounds do not follow this trend, namely Na_3GaPn_2, for which the As compound shows a much smaller band gap, as well as Cs_3InPn_2 and Rb_3InPn_2 (lower enthalpy structure), for which the As compounds have a larger band gap. Interestingly, this coincides with the set of compounds for which the structure type of the phosphide and arsenide are different, which raises the question as to whether the structure type also has an influence on the size of the band gap. A closer look at the difference between the calculated bad gaps for the predicted structures confirms this hypothesis, since the band gaps for the different structure types of, for example, Na_3GaAs_2 range from 2.03 eV (**H**) to 2.39 eV (**E**).

By taking a closer look at the band gap size distribution over the different dimensionalities of structure types **A** to **H**, the band gap is on one hand increasing with the dimension of the anionic structure and on the other decreasing with the occurrence of edge-sharing tetrahedra as an anionic structural motif. Therefore, the lowest band gaps are obtained for structure types **C** and **D**, with a zero- and one-dimensional structure, followed by types **A** and **B** (pure zero-dimensional triangular planar units), type **E** (only one-dimensional), types **F** and **H** (two- and three-dimensional) and lastly type **G** (three-dimensional structure without edge-sharing tetrahedra). This could explain the larger band gaps for the As compound of Cs_3InPn_2 and Rb_3InPn_2, since they crystallise with molecular anions (zero-dimensional structures). If they were to adopt the same structure type as their corresponding P compounds, the band gaps of the As compounds would follow the trend of having lower gaps.

All band structures and DOS plots are available in the SI. Among the 30 compounds, we chose 4 examples to show the characteristics of the various band structures. Li_3AlP_2 and Cs_3AlP_2, with structure type **F** and **A**, respectively, shown in Figure 2, correspond to compounds with direct and pseudo-direct band gaps. Na_3AlP_2 and K_3InlP_2, shown in

Molecules **2024**, *29*, 4087

Figure 3, are an example where both structures adapt the same structure type **E** but have indirect and direct band gaps, respectively.

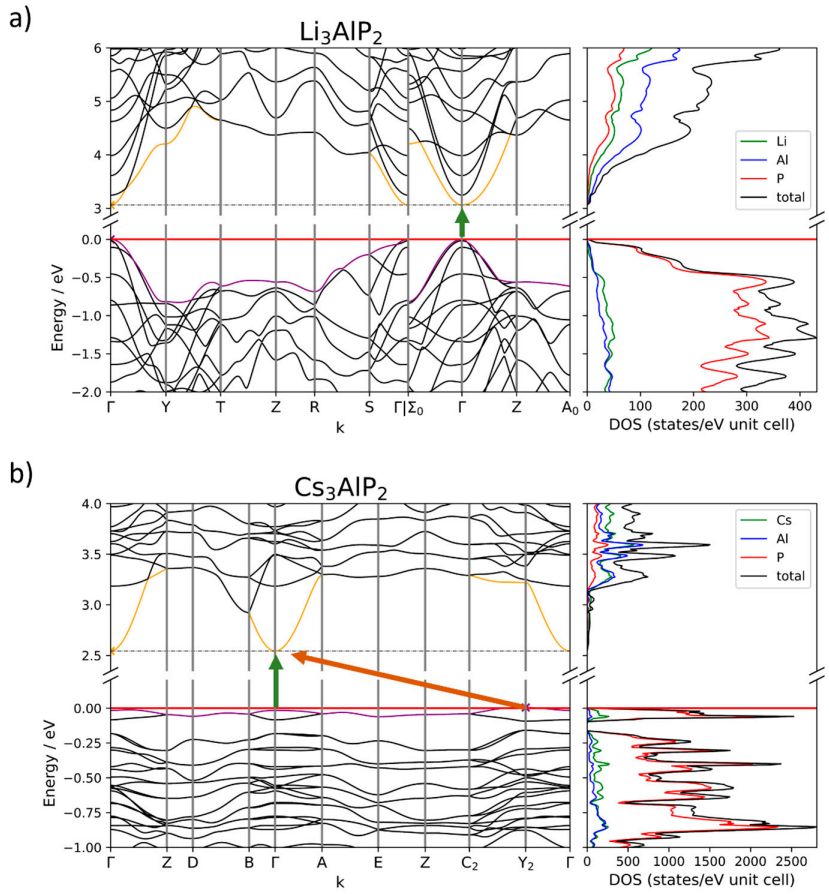

Figure 2. (**a**) Band structure and density of states of Li_3AlP_2 (type **F**) with a direct band gap of 3.06 eV green arrow); (**b**) band structure and density of states of Cs_3AlP_2 (type **A**) with a pseudo-direct band gap of 2.54 eV (green arrow) and an indirect band gap of 2.56 eV (orange arrow).

The dispersion of the bands varies for the different structure types **A** and **F**. As for type **F**, all structure types with two- or three-dimensional polyanions (types **E**–**H**, Figure 2a) show a large band dispersion (especially in the area of the filled band region below E_F), whereas structures that incorporate "discrete" edge-sharing triangular planar dimers (types **A**–**D**, Figure 2b) have bands with a small dispersion (flat bands). As a consequence, all Cs compounds show an increased occurrence of pseudo-direct band gaps as they adopt structure types **A**, **C**, and **D**. Since especially the top valence band is very flat at the Fermi level, multiple transitions similar in energy are possible and pseudo-direct band gaps arise. As an example, the band structure of Cs_3AlP_2, with two possible transitions, is shown in Figure 2b. The direct band gap at Γ (green transition) is only 0.02 eV larger than the indirect transition $Y_2 \rightarrow \Gamma$ (orange arrow). The low dispersion of the bands is a result of the rather localised electron density within the anionic–molecular $[Tr_2Pn_4]^{6-}$ units that are fully separated by alkali metal ions, while extended edge- or corner-sharing tetrahedra structural motifs result in a farther-distributed electron density along the two- or three-dimensional network, resulting in more disperse bands.

Molecules **2024**, *29*, 4087

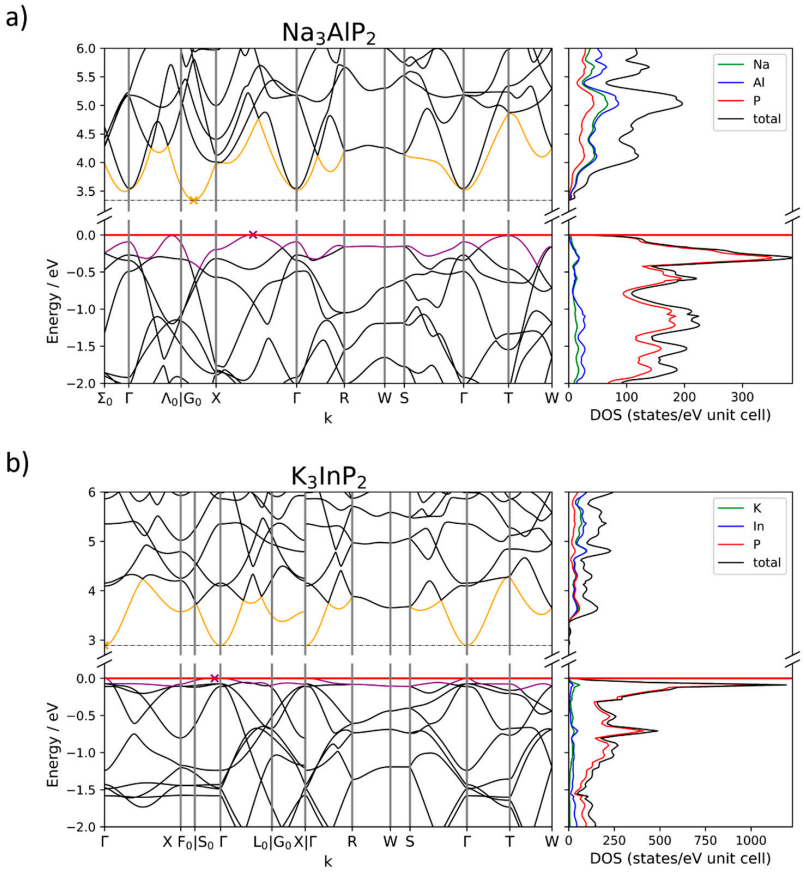

Figure 3. (**a**) Band structure and density of states of Na_3AlP_2 (type **E**) with an indirect band gap of 3.34 eV; (**b**) band structure and density of states of K_3InP_2 (type **E**) with a direct band gap of 2.89 eV.

2.4.2. Band Structures and DOS

The DOS looks similar for all A_3TrPn_2 compounds: the valence bands contain mostly *Pn* states with minor contributions of the alkali and triel elements. Around the Fermi level of compounds with flat bands, an increase in alkali metal states can be observed. The lower conduction bands for most compounds contain mostly states of the triel, followed by pnictide and alkali metal states. This is not the case for Na_3AlP_2, Na_3GaP_2, Na_3AlAs_2 and K_3InP_2, where all elements contribute equally to the DOS. For higher bands, the most contributing element either changes, or all elements contribute equally.

All direct and pseudo-direct band gaps are located at Γ. Only three compounds, Na_3AlP_2 (Figure 3a), Na_3GaP_2 (Figure S29, SI) and Na_3AlAs_2 (Figure S37, SI), have an indirect band gap. For Na_3AlP_2, the valence band minimum (VBM) appears—in contrast to, for example, K_3InP_2 (Figure 3b)—not at Γ but on the path from Γ to X. At the same time, the lowest conduction band gets pushed up at Γ such that the conduction band minimum (CBM) lies between G_0 and X (Figure 3a). Na_3GaP_2 again has the VBM at Γ while the CBM remains at the same position (Figure S29). A closer look at the DOS shows that, in contrast to all direct band gap compounds at the Fermi level, additional alkali metal states are present in indirect band gap compounds, leading to changes in the VBM. An increase in alkali metal states is also observed for compounds with very flat valence bands at the Fermi level.

Molecules **2024**, *29*, 4087

The same can be seen for the conduction bands, which are pushed up in Na_3AlP_2, Na_3GaP_2 and Na_3AlAs_2 at Γ. In the DOS, it can be seen that there are more Na states present. The Li compounds and Na_3InP_2/Na_3InAs_2 have mainly triel states, followed by small contributions of Li/Na and P/As. Compounds with the heavier alkali metals also have more alkali metal states around the CBM, although they are at or close to Γ, so the mere existence of these states should not prevent the occurrence of direct gaps. This suggests that the interaction of the alkali metal with itself or adjacent triel and pnictide atoms could be a determining factor for the occurrence of direct and indirect band gaps.

A Mulliken analysis was conducted for all compounds, as well as all predicted compounds, determining the atom's Mulliken charges and the overlap population between neighbouring atoms (see SI). Mulliken charges represent trends in the charge distribution based on the calculated wave function, but do not reproduce the full expected ionic charges or formal charges that occur in representations of Lewis formulae. In all compounds with two-fold bonded *Pn* atoms, P and As atoms have a Mulliken charge of about −1. For those compounds that contain both one- and two-fold bonded Pn atoms (1b and 2b, respectively), the 1b-Pn have up to 0.2 higher negative charges, thus reflecting the trend of the bonding situation as shown in Scheme 2. All alkali metals show Mulliken charges, which are increasing for Na and K from about 0.56 to 0.75, but decrease again for Rb and Cs to around 0.70. Overall, the expected positive charge of the alkali metal is reflected in those numbers.

With respect to chemical bonding, triel elements can on the one hand be treated as Tr^{3+} according to an ionic description and, on the other hand, with a formal charge of −1 or 0, according to a covalent description applying the octet rule, for the tetrahedral and triangular planar coordination, respectively. The Mulliken charges calculated for the triel atoms are between −0.3 and +0.5. The values represent a mostly polar covalent description of the charge, and the Mulliken charge of the triel element decreases for compounds with smaller electronegativity differences. Therefore, Al compounds show the highest charges. On the other hand, a trend for between three- and four-fold-bonded structure motifs can be found for each triel atom, since the atoms which are tetrahedrally coordinated show larger Mulliken charges than the triangular planar ones, due to the higher number of polar bonds formed.

Values larger than 0.2 for the overlap population indicate bonding triel–atom *Pn* interactions, which are in line with the bonds assigned based on the interatomic distances described in the crystal structures. Further on, the highest overlap populations are found for *Tr*-*Pn* bonds, which form partial double bonds within the dimeric triangular planar units in structures **A** to **D** (see Scheme 2). Here, for example, the Al-P overlap in K_3AlP_2 is about 0.5, which strongly hints towards a higher bond order. Since the absolute value of the overlap population for these partial double bonds decreases for Ga-*Pn* and In-*Pn*, the validation of the double bond rule, namely that heavier elements are less favoured for double bond formation, is stated. Since the probability of forming (partial) double bonds decreases with the atomic number within a group, Ga and In show less overlap population for these atomic interactions [36].

Between alkali metals and *Pn*, as well as alkali metals and triel, only negligible interactions are found. For the interactions between two neighbouring triel elements, negative values were obtained for the overlap population, which suggests that atoms in adjacent (edge-sharing) tetrahedra and triangular planar units have no attractive, but a slightly repelling, interaction. This is more distinct for compounds of the heavier triel atoms, due to their increase in size, as well as structures with edge-sharing tetrahedra. As a consequence, the distance between adjacent triel atoms is smaller. The same negative overlap, and thus repulsion, can be found for the long-distance interaction between the next but one *Pn* atoms.

For all compounds, a crystal orbital Hamilton population (COHP) was calculated for all heteroatomic interactions, as well as the triel–triel interaction(s). For the latter, as well as the extra plots of the *Tr*-*Pn* interactions, they were reduced to the interactions of only neighbouring (and thus, for *Tr*-*Pn*, between bonding) atoms. A selection of these

Molecules **2024**, *29*, 4087

COHP plots can be found in Figure 4. In general, as seen in Figure 4a, there are only few interactions from 0 eV until about −3 eV in the COHP, although a lot of states are present in the DOS, especially for *Pn*. Therefore, in this energy range, mainly the states of Pn lone pairs contribute to the DOS.

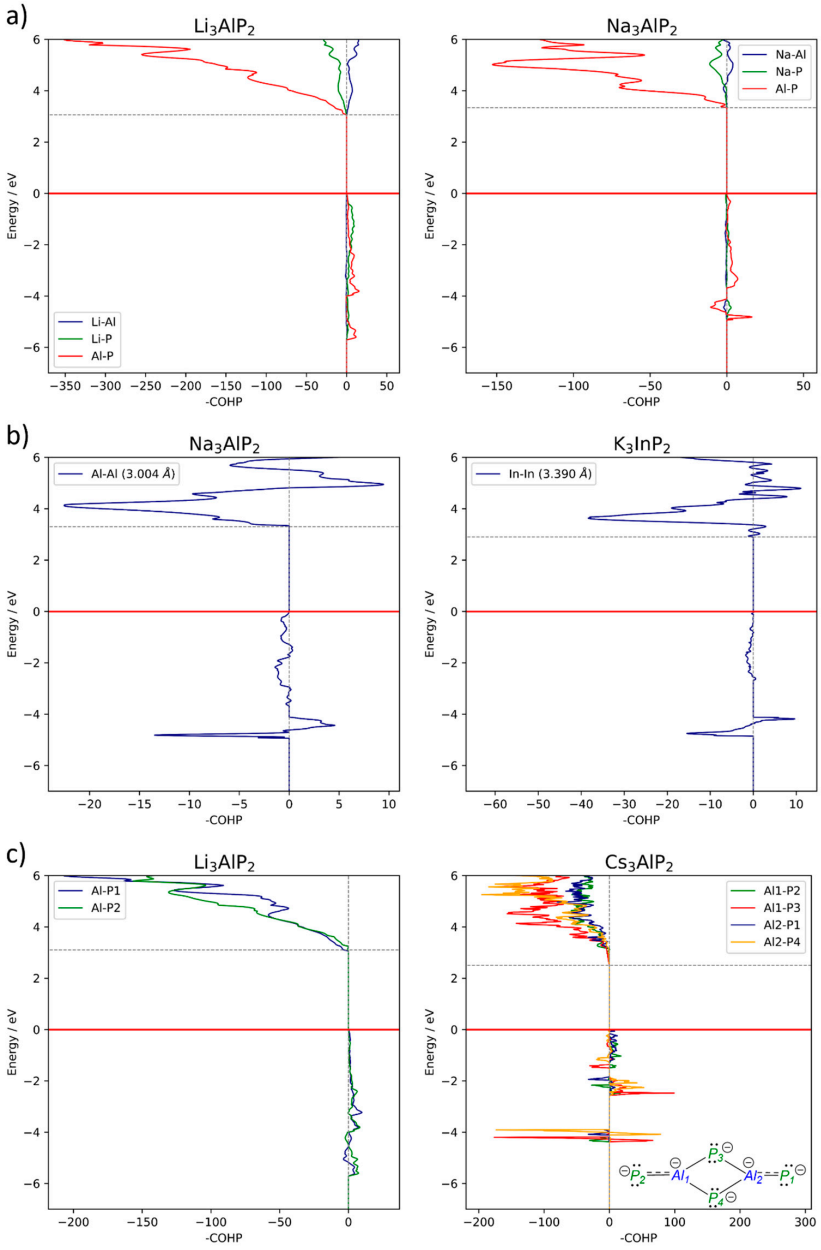

Figure 4. (**a**) COHP for all heteroatomic interactions in Li_3AlP_2 and Na_3AlP_2. (**b**) COHP for Tr-Tr interactions for Na_3AlP_2 and K_3InP_2. (**c**) Al-P bond projected COHP for Li_3AlP_2 and Cs_3AlP_2. For all plots, the red line represents the Fermi level at 0 eV and the grey, dashed line the top of the band gap. For Cs_3AlP_2, the atomic positions in the projected DOS refer to the assigned positions in the scheme.

For Na_3AlPn_2 and Na_3GaP_2 the projected COHP of the heteroatomic interactions shows two peculiar features. Below the Fermi level, there occur, compared to the other compounds, low values for the Na-*Tr* and Na-*Pn* interactions. The higher number of states observe in the DOS hints at additional Na electron density close to the Fermi level, which was deemed to be responsible for the position of the valence band maximum (VBM) and thus the indirect band gap, as pointed out above. Since the interactions with Na are small, the additional states are thus attributed to non-bonding Na states (see SI). Secondly, the COHP of the Al-Al interactions (Figure 4b, left) shows a sharp increase in states at the band gap top. These interactions between the triel atoms might be responsible for the position of the conduction band minimum (CBM) at another *k*-point than Γ, since they are not present in K_3InP_2 (Figure 4b, right), which also crystalises in the same structure type, but has a direct band gap (at Γ). The stronger In-In interactions, which are also represented by a stronger negative overlap population in the Mulliken analysis, could lead to an increase in energy for these interactions and thus an absence of them above the band gap.

Comparing the COHP of *Tr*-*Tr* interactions of structure type **E** with all other compounds, interactions between the triel atoms are absent or have a similar shape as K_3InP_2, for which they change between bonding and anti-bonding interactions above the Fermi level. Since all these compounds also show direct band gaps, the strength of the *Tr*-*Tr* interaction might be able to influence the position of the CBM. To gain more insight into this hypothesis, calculations with post-DFT methods have to be conducted, since the level of theory present is limited in the accuracy of describing excited states. Further on, relativistic effects might play a role, since within structure type **E** the switch to direct band gaps occurs only for In compounds. Since the In basis set accounts for some relativistic effects by a core potential, which the Al and Ga basis sets do not, the direct band gap could also arise from the chosen level of theory.

Lastly, all compounds that contain $[Tr_2Pn_4]^{6-}$ units show another interesting feature in the "bond" projected COHP of *Tr*-*Pn* interactions. Figure 4c (left) shows that for Li_3AlP_2, the COHP, calculated for interactions of Al-P bonds, no significant difference between the different bonds can be found, since all Al-P bonds are single bonds. Therefore, the shape of the projected COHPs is the same. For Cs_3AlP_2 (Figure 4c, right), due to the partial double bond for the terminal P atoms P1 and P2, their interactions can be found directly below the Fermi level, since these π-bonds are high in energy. The bonding interactions for the bridging P atoms, P3 and P4, are lower in energy (at about −2 eV) due to the single bonds.

3. Methods

The computational studies of all compounds in the A_3TrP_3 system (with *A* = Li − Cs and *Tr* = Al, Ga, In) were performed using the CRYSTAL17 program package and hybrid density functional methods [37,38]. A hybrid exchange–correlation functional after Perdew, Burke, and Ernzerhof (DFT-PBE0) was used, ref. [39] Localised, Gaussian-type triple ζ-valence + polarisation level basis sets were used for Al, Ga, In and P and split valence + polarisation level basis sets for Li, Na, K, Rb and Cs. The basis sets were derived from the molecular Karlsruhe basis sets [12,28,40–42]. For the evaluation of the Coulomb and exchange integrals (TOLINTEG), tight tolerance factors of 8, 8, 8, 8, 16 were used for all calculations. The reciprocal space of all calculations was sampled with Monkhorst–Pack-type *k*-point grids; their respective sizes can be found in the SI. The starting geometries were taken from experimental data whenever possible. For the unknown compounds, models based on adjacent structures by atom replacement were derived. Both the lattice parameters and atomic positions were fully optimised within the constraints imposed by the space group symmetry. Further on, all optimised structures were confirmed to be true local minima by means of harmonic frequency calculations at the Γ-point. For all compounds and models, electronic band structures and density of states (DOS) were calculated. The Brillouin Zone paths were provided by the web service *SeeK-path* and a list can be found in the SI [43].

4. Conclusions

In this paper, band structures and density of states for all 30 A_3TrPn_2 compounds with A = Li, Na, K, Rb, Cs; Tr = Al, Ga, In; Pn = P, As, a family of electron-precise Zintl phases, were presented. A total of 27 out of 30 compounds show direct or pseudo-direct band gaps. Na_3AlP_2, Na_3AlAs_2 and Na_3GaP_2 possess an indirect band gap. For the compounds with indirect band gaps, the conduction band minimum (CBM) and valence band maximum (VBM) are not located at Γ (as for the other compounds). The position of the VBM is probably caused by an increase in (non-bonding) Na states right below the Fermi level. The position of the CBM could be influenced by the strength of the *Tr*-*Tr* interaction above the band gap as well as relativistic effects, which are partially accounted for in the calculation by the In basis set. The width of the band gap was discussed, based on the structure as well the composition of the compound. Arsenides, as well as compounds with lower-dimensional anionic substructures, show lower band gaps, due to less interatomic overlap within the structure or between the atoms.

The bonding situation imposed by the crystal structure was confirmed by a Mulliken analysis, where bonds between the triel and *Pn* atoms were found. For the triangular planar Tr_2Pn_4 building units, partial double bonds for the lighter triels were identified, as well as being excluded for the compounds with the heavier element In according to the double bond rule. Insights into atomic interactions, by calculation of the COHP, further described the electronic situation of the compounds.

For confirmation as well as to expand the correlations found, experiments on synthesising the predicted compounds need to be conducted. Experimentally known compounds should also be screened for possible phase transitions to gain an even deeper insight into the system. Calculations and structure predictions could also to be extended to antimonides and bismuthides to see how they affect the appearance of direct band gaps, since both basis sets take relativistic effects into account with a core potential [44–47]. Calculations should also be expanded to compounds in the A_2TtPn_2 system (with A = Li−Cs, Tt = Si−Sn, Pn = P, As), which is the equivalent tetrel system, and therefore their crystal structures are closely related [48–52].

Further on, post-DFT calculations are needed to investigate all the effects found for conduction bands, as they provide a more accurate description for excited states [53,54].

Supplementary Materials: The following supporting information can be downloaded at: https://www.mdpi.com/article/10.3390/molecules29174087/s1. Additional Information on DFT calculations; Structure types A–H; Structure predictions; References [12,15–28,30–34,55] are cited in Supplementary Materials.

Author Contributions: Writing—original draft preparation, visualisation, S.Z.; data curation, S.Z. and Y.K.; validation, S.Z. and T.F.F.; conceptualisation, writing—review and editing, supervision, project administration, funding acquisition T.F.F. All authors have read and agreed to the published version of the manuscript.

Funding: This project received financial support from the Bavarian State Ministry of Education, Science and the Arts under the program "Solar Technologies go Hybrid".

Institutional Review Board Statement: Not applicable.

Informed Consent Statement: Not applicable.

Data Availability Statement: Data are contained within the article and Supplementary Materials.

Acknowledgments: The authors thank Antti Karttunen for solving problems with CRYSTAL17 as well as input on the discussion of unclear findings.

Conflicts of Interest: The authors declare no conflicts of interest. The funders had no role in the collection, analyses, or interpretation of data or the writing of the manuscript.

References

1. Prasanna, R.; Gold-Parker, A.; Leijtens, T.; Conings, B.; Babayigit, A.; Boyen, H.-G.; Toney, M.F.; McGehee, M.D. Band Gap Tuning via Lattice Contraction and Octahedral Tilting in Perovskite Materials for Photovoltaics. *J. Am. Chem. Soc.* **2017**, *139*, 11117–11124. [CrossRef]
2. Ning, C.-Z.; Dou, L.; Yang, P. Bandgap engineering in semiconductor alloy nanomaterials with widely tunable compositions. *Nat. Rev. Mater.* **2017**, *2*, 17070. [CrossRef]
3. Unger, E.L.; Kegelmann, L.; Suchan, K.; Sörell, D.; Korte, L.; Albrecht, S. Roadmap and roadblocks for the band gap tunability of metal halide perovskites. *J. Mater. Chem. A* **2017**, *5*, 11401–11409. [CrossRef]
4. Johrendt, D. Structure–property relationships of iron arsenide superconductors. *J. Mater. Chem.* **2011**, *21*, 13726. [CrossRef]
5. Kovnir, K.A.; Shevelkov, A.V. Semiconducting clathrates: Synthesis, structure and properties. *Russ. Chem. Rev.* **2004**, *73*, 923–938. [CrossRef]
6. Pearsall, T. $Ga_{0.47}In_{0.53}As$: A ternary semiconductor for photodetector applications. *IEEE J. Quantum Electron.* **1980**, *16*, 709–720. [CrossRef]
7. Smith, A.M.; Nie, S. Semiconductor nanocrystals: Structure, properties, and band gap engineering. *Acc. Chem. Res.* **2010**, *43*, 190–200. [CrossRef]
8. Freundlich, A.; Guillemoles, J.-F. (Eds.) *Physics, Simulation, and Photonic Engineering of Photovoltaic Devices II*; SPIE OPTO: San Francisco, CA, USA, 2013.
9. Kechiantz, A.; Afanasev, A. Tuning up the performance of GaAs-based solar cells by inelastic scattering on quantum dots and doping of $Al_yGa_{1-y}Sb$ type-II dots and $Al_xGa_{1-x}As$ spacers between dots. In *Physics, Simulation, and Photonic Engineering of Photovoltaic Devices II*; SPIE: Bellingham, WA, USA, 2013; Volume 8620, pp. 377–385.
10. Wu, T.Y.; Pearson, G.L. Phase diagram, crystal growth, and band structure of $In_xGa_{1-x}As$. *J. Phys. Chem. Solids* **1972**, *33*, 409–415. [CrossRef]
11. Zeitz, S.; Antoniuk, H.; Hlukhyy, V.; Fässler, T.F. Electronic Structure Analysis of the $A_{10}Tt_2P_6$ System (A = Li-Cs; Tt = Si, Ge, Sn) and Synthesis of the Direct Band Gap Semiconductor $K_{10}Sn_2P_6$. *Chemistry* **2024**, *30*, e202400002. [CrossRef]
12. Restle, T.M.F.; Dums, J.V.; Raudaschl-Sieber, G.; Fässler, T.F. Synthesis, Structure, Solid-State NMR Spectroscopy, and Electronic Structures of the Phosphidotrielates Li_3AlP_2 and Li_3GaP_2. *Chem.-Eur. J.* **2020**, *26*, 6812–6819. [CrossRef]
13. Kuriyama, K.; Anzawa, J.; Kushida, K. Growth and band gap of the filled tetrahedral semiconductor Li_3AlP_2. *J. Cryst. Growth* **2008**, *310*, 2298–2300. [CrossRef]
14. Restle, T.M.F.; Zeitz, S.; Stanley, P.M.; Karttunen, A.J.; Meyer, J.; Raudaschl-Sieber, G.; Klein, W.; Fässler, T.F. Direct Band Gap Semiconductors with Two- and Three-Dimensional Triel-Phosphide Frameworks (Triel=Al, Ga, In). *Chemistry* **2024**, *30*, e202304097. [CrossRef]
15. Somer, M.; Walz, L.; Thiery, D.; von Schnering, H.G. Crystal structure of caesium di-μ-phosphido-bis- (phosphidoaluminate), $Cs_6(Al_2P_4)$. *Z. Kristallogr.-Cryst. Mater.* **1990**, *193*, 303–304. [CrossRef]
16. Somer, M.; Thiery, D.; Hartweg, M.; Walz, L.; Peters, K.; von Schnering, H.G. Crystal structure of caesium di-μ-phosphido-bis(phosphidogallate), $Cs_6(Ga_2P_4)$. *Z. Kristallogr.-Cryst. Mater.* **1990**, *193*, 287–288. [CrossRef]
17. Somer, M.; Peters, K.; Thiery, D.; von Schnering, H.G. Crystal structure of trirubidium diphosphidogallate, Rb_3GaP_2. *Z. Kristallogr.* **1990**, *192*, 271–272. [CrossRef]
18. Somer, M.; Thiery, D.; Hartweg, M.; Walz, L.; Popp, T.; Peters, K.; von Schnering, H.G. Crystal structure of tricaesium diarsenidoaluminate, Cs_3AlAs_2. *Z. Kristallogr.* **1990**, *192*, 269–270. [CrossRef]
19. Somer, M.; Peters, K.; Popp, T.; von Schnering, H.G. Crystal structure of tricaesium diarsenidogallate, Cs_3GaAs_2. *Z. Kristallogr.-Cryst. Mater.* **1990**, *192*, 273–274. [CrossRef]
20. Somer, M.; Walz, L.; Peters, K.; von Schnering, H.G. Crystal structure of potassium catena-di-μ- phosphidoaluminate di-μ-phosphido-bis (phosphidoaluminate), $K_{12}(AlP_2)_2(Al_2P_4)$. *Z. Kristallogr.-Cryst. Mater.* **1990**, *193*, 301–302. [CrossRef]
21. Somer, M.; Carrillo-Cabrera, W.; Peters, E.M.; Peters, K.; von Schnering, H.G. Crystal structure of rubidium cα/ˆ/2α-di-μ-phosphìdoindate di-μ-phosphi-do-bis (phosphidoindate), Rhuˆ InPilz [IπιPα]. *Z. Kristallogr.-New Cryst. Struct.* **1998**, *213*, 5–6. [CrossRef]
22. von Schnering, H.G.; Somer, M.; Walz, L.; Peters, K.; Cordier, G.; Blase, W. Crystal structure of potassium catena-di- μ arsenidoaluminate di-μ -arsenido-bis(arsenidoaluminate), $K_{12}(AlAs_2)_2(Al_2As_4)$. *Z. Kristallogr.-Cryst. Mater.* **1990**, *193*, 299–300. [CrossRef]
23. Blase, W.; Cordier, G.; Somer, M. Crystal structure of caesium catena-di-μ-phosphidoindate di-μ-phosphido-bis (phosphidoindate), $Cs_{12}(InP_2)_2(In_2P_4)$. *Z. Kristallogr.-Cryst. Mater.* **1991**, *195*, 123–124.
24. Somer, M.; Carrillo-Cabrera, W.; Peters, K.; Peters, E.M.; von Schnering, H.G. Crystal structure of trisodium catena-di-μ-phosphidoaluminate, Na_3AlP_2. *Z. Kristallogr.-Cryst. Mater.* **1995**, *210*, 777. [CrossRef]
25. Blase, W.; Cordier, G.; Somer, M. Crystal structure of tripotassium catena-di-μ-phosphido-indate, K_3InP_2. *Z. Kristallogr.-Cryst. Mater.* **1991**, *195*, 109–110. [CrossRef]
26. Boyko, M.; Hlukhyy, V.; Fässler, T.F. $K_7In_4As_6$ and K_3InAs_2-Two more Zintl phases showing the rich variety of In-As polyanion structures. *Z. Anorg. Allg. Chem.* **2023**, *649*, e202300164. [CrossRef]

27. Cordier, G.; Ochmann, H. Na_3AlAs_2, eine Zintlphase mit SiS_2-isosterer Anionenteilstruktur. *Z. Naturforsch. B J. Chem. Sci.* **1988**, *43*, 1538–1540.
28. Restle, T.M.F.; Zeitz, S.; Meyer, J.; Klein, W.; Raudaschl-Sieber, G.; Karttunen, A.J.; Fässler, T.F. Aliovalent substitution in phosphide-based materials–Crystal structures of $Na_{10}AlTaP_6$ and Na_3GaP_2 featuring edge-sharing EP_4 tetrahedra (E = Al/Ta and Ga). *Z. Anorg. Allg. Chem.* **2021**, *647*, 1804–1814. [CrossRef]
29. Büssem, W.; Fischer, H.; Gruner, E. Die struktur des siliciumdisulfids. *Naturwissenschaften* **1935**, *23*, 740. [CrossRef]
30. Juza, R.; Schulz, W. Herstellung und Eigenschaften der Verbindungen Li_3AlP_2 und Li_3AlAs_2. *Z. Anorg. Allg. Chem.* **1952**, *269*, 1–12. [CrossRef]
31. Wegner, F.; Kamm, F.; Pielnhofer, F.; Pfitzner, A. Li_3TrAs_2 (Tr =Al, Ga, In)–Derivatives of the antifluorite type structure, conductivities and electronic structures. *Z. Anorg. Allg. Chem.* **2023**, *649*, e202200330. [CrossRef]
32. Restle, T.M.F.; Deringer, V.L.; Meyer, J.; Raudaschl-Sieber, G.; Fässler, T.F. Supertetrahedral polyanionic network in the first lithium phosphidoindate Li_3InP_2-structural similarity to Li_2SiP_2 and Li_2GeP_2 and dissimilarity to Li_3AlP_2 and Li_3GaP_2. *Chem. Sci.* **2020**, *12*, 1278–1285. [CrossRef]
33. Blase, W.; Cordier, G.; Somer, M. Crystal structure of trisodium tecto-diphosphidoindate, Na_3InP_2. *Z. Kristallogr.-Cryst. Mater.* **1991**, *195*, 119–120. [CrossRef]
34. Cordier, G.; Ochmann, H. Crystal structure of trisodium tecto-diarsenidoindate, Na_3InAs_2. *Z. Kristallogr.-Cryst. Mater.* **1991**, *195*, 105–106. [CrossRef]
35. Holleman, A.F. *Lehrbuch der Anorganischen Chemie*; Walter de Gruyter GmbH & Co. KG: Berlin, Germany, 2019; ISBN 3110838176.
36. Power, P.P. pi-Bonding and the Lone Pair Effect in Multiple Bonds between Heavier Main Group Elements. *Chem. Rev.* **1999**, *99*, 3463–3504. [CrossRef]
37. Dovesi, R.; Saunders, V.R.; Roetti, C.; Orlando, R.; Zicovich-Wilson, C.M.; Pascale, F.; Civalleri, B.; Doll, K.; Harrison, N.M.; Bush, I.J. CRYSTAL17 User's Manual. University of Turin: Turin, Italy, 2017. Available online: https://iris.unito.it/bitstream/2318/1709158/1/crystal17.pdf (accessed on 14 July 2024).
38. Dovesi, R.; Erba, A.; Orlando, R.; Zicovich-Wilson, C.M.; Civalleri, B.; Maschio, L.; Rérat, M.; Casassa, S.; Baima, J.; Salustro, S.; et al. Quantum-mechanical condensed matter simulations with CRYSTAL. *Wiley Interdiscip. Rev. Comput. Mol. Sci.* **2018**, *8*, e1360. [CrossRef]
39. Perdew, J.P.; Yang, W.; Burke, K.; Yang, Z.; Gross, E.K.U.; Scheffler, M.; Scuseria, G.E.; Henderson, T.M.; Zhang, I.Y.; Ruzsinszky, A.; et al. Understanding band gaps of solids in generalized Kohn-Sham theory. *Proc. Natl. Acad. Sci. USA* **2017**, *114*, 2801–2806. [CrossRef] [PubMed]
40. Stene, R.E.; Scheibe, B.; Karttunen, A.J.; Petry, W.; Kraus, F. Lewis Acidic Behavior of $MoOF_4$ towards the Alkali Metal Fluorides in Anhydrous Hydrogen Fluoride Solutions. *Eur. J. Inorg. Chem.* **2019**, *2019*, 3672–3682. [CrossRef]
41. Scheibe, B.; Ivlev, S.I.; Karttunen, A.J.; Kraus, F. Synthesis and Characterization of the Tetrafluoridochlorates(III) A[ClF_4] (A = K, Rb, Cs). *Eur. J. Inorg. Chem.* **2020**, *2020*, 1319–1324. [CrossRef]
42. Sansone, G.; Maschio, L.; Usvyat, D.; Schütz, M.; Karttunen, A. Toward an Accurate Estimate of the Exfoliation Energy of Black Phosphorus: A Periodic Quantum Chemical Approach. *J. Phys. Chem. Lett.* **2016**, *7*, 131–136. [CrossRef]
43. Hinuma, Y.; Pizzi, G.; Kumagai, Y.; Oba, F.; Tanaka, I. Band structure diagram paths based on crystallography. *Comput. Mater. Sci.* **2017**, *128*, 140–184. [CrossRef]
44. Scheibe, B.; Karttunen, A.J.; Weigend, F.; Kraus, F. Photochemistry with Chlorine Trifluoride: Syntheses and Characterization of Difluorooxychloronium(V) Hexafluorido(non)metallates(V), $ClOF_2MF_6$ (M=V, Nb, Ta, Ru, Os, Ir, P, Sb). *Chemistry* **2021**, *27*, 2381–2392. [CrossRef]
45. Scheibe, B.; Haiges, R.; Ivlev, S.I.; Karttunen, A.J.; Müller, U.; Christe, K.O.; Kraus, F. Difluorochloronium(III) Fluoridometallates–from Molecular Building Blocks to (Helical) Chains. *Eur. J. Inorg. Chem.* **2020**, *2020*, 4483–4496. [CrossRef]
46. Cordier, G.; Ochmann, H. Crystal structure of trisodium tecto-diantimonidoindate, Na_3InSb_2. *Z. Kristallogr.-Cryst. Mater.* **1991**, *195*, 107–108. [CrossRef]
47. Bobev, S.; Sevov, S.C. Five Ternary Zintl Phases in the Systems Alkali-Metal–Indium–Bismuth. *J. Solid State Chem.* **2002**, *163*, 436–448. [CrossRef]
48. Wolf, J.; Weber, D.; von Schnering, H.-G. Rubidium-diarsasilicat(IV) Rb_2SiAs_2, ein Derivat der SiS_2 -Struktur/Rubidium Diarsasilicate(IV) Rb_2SiAs_2, a Derivative of the SiS_2 Structure Type. *Z. Für Naturforschung B* **1986**, *41*, 731–735. [CrossRef]
49. Hurng, W.M.; Peterson, E.S.; Corbett, J.D. Synthesis and structure of the Zintl phase potassium silicon arsenide, K_2SiAs_2. *Inorg. Chem.* **1989**, *28*, 4177–4180. [CrossRef]
50. Eisenmann, B.; Somer, M. K_2SiP_2, ein Phosphidopolysilikat(IV)/K_2SiP_2, a Phosphidopolysilicate (IV). *Z. Für Naturforschung B* **1984**, *39*, 736–738. [CrossRef]
51. Eisenmann, B.; Klein, J. SiS_2-isostrukturelle Anionen [SiP_2^{2-}], [$GeAs_2^{2-}$] und [$SnAs_2^{2-}$] in Alkaliverbindungen. *J. Less Common. Met.* **1991**, *175*, 109–117. [CrossRef]
52. Asbrand, M.; Eisenmann, B. $Na_2[SnAs_2]$, die erste Zintl-Phase mit einem [$SnAs_2$]-Raumnetz aus adamantan-analogen [Sn_4As_{10}]-Einheiten/$Na_2[SnAs_2]$, the First Zintl Phase with a [$SnAs_2$] Framework Based on Adamantan Analogous [Sn_4As_{10}] Units. *Z. Für Naturforschung B* **1993**, *48*, 452–456. [CrossRef]
53. Per, M.C.; Cleland, D.M. Roadmap on post-DFT methods for nanoscience. *Nano Futures* **2020**, *4*, 32004. [CrossRef]

54. Hasnip, P.J.; Refson, K.; Probert, M.I.J.; Yates, J.R.; Clark, S.J.; Pickard, C.J. Density functional theory in the solid state. *Philos. Trans. A Math. Phys. Eng. Sci.* **2014**, *372*, 20130270. [CrossRef]
55. Ohse, L.; Somer, M.; Blase, W.; Cordier, G. Verbindungen mit SiS2-isosteren Anionen∞ 1 [AlX4/23-] und∞ 1 [InP4/23-]: Synthesen, Kristallstrukturen und Schwingungsspektren von Na3 [AlX2], K2Na [AlX2] und K3 [InP2](X = P, As)/Compounds with SiS2 Isoelectronic Anions∞ 1 [AlX4/23-] and∞ 1 [InP4/23-]: Synthesis, Crystal Structures and Vibrational Spectra of Na3 [AlX2], K2Na [AlX2] and K3 [InP2](X = P, As). *Z. Für Nat. B* **1993**, *48*, 1027–1034.

5.4 Electronic structure analysis of the $A_2TrTtPn_2$ system with A = Li-Cs; Tr = Al-In; Tt = Si-Sn; Pn = P-Sb

Sabine Zeitz, Zoe Listmann, Thomas F. Fässler

Manuscript for publication

Electronic structure analysis of the $A_2Tr/TtPn_2$ system with *A* = Li-Cs; *Tr* = Al-In; *Tt* = Si-Sn; *Pn* = P-Sb

Sabine Zeitz[a], Zoe Listmann[a], Thomas F. Fässler[a]

Abstract

With 18 known compounds the $A_2Tr/TtPn_2$ system (with *A* = Li-Cs, *Tr* = Al-In, *Tt* = Si-Sn and *Pn* = P-Sb), which crystallize in five different structure type, is a good model system to on one hand investigate crystal structure band structure relations within present for the triel and tetrel compound sub-systems. On the other hand trends identified within each sub-system can be compared to identify possible similarities and differences in the electronic structures. Thus after structure optimization band structures, density of states and crystal orbital Hamilton populations were calculated on a DFT/PBE0 level of theory. Three compounds, Li_2SiP_2, Li_2GeP_2 and Na_2SnAs_2, which all crystallize in the same structure type, showed direct band gaps and Cs_2GaSb_2 a pseudo-direct band gap. For other compounds indirect band gaps were found, which could be caused by additional alkali metal states close to the Fermi-Level and low-lying *Tt*-*Tt* anti-bonding interactions for the conduction bands at the edge of the band gap. For the triel compounds additional *Pn*-*Pn* bonds in the crystal structure also seem to influence the location of the valence band maximum with *Pn*-*Pn* anti-bonding interactions. Further on the electronegativity differences between the atoms of each compound have the most influence on the size of the band gap, with larger differences resulting in larger band gaps.

Introduction

Semiconductors are essential for the continuous development of our modern society and have a wide range of applications such as solar cells, LEDs, laser applications, etc. Efficient bandgap engineering is becoming increasingly important in the design of new and highly specialised materials as their applications become more diverse and complex.[1–5] In the search for compounds that allow a correlation between their atomic structure and the nature of their constituent elements with their properties, compound classes that have several or many representatives are particularly useful for the determination of relevant parameters. One such

system are compounds of the $A_2Tr/TtPn_2$ system (with *A* = Li-Cs, *Tr* = Al-In, *Tt* = Si-Sn and *Pn* = P-Sb), where 18 different compounds in five different structure types are experimentally known.

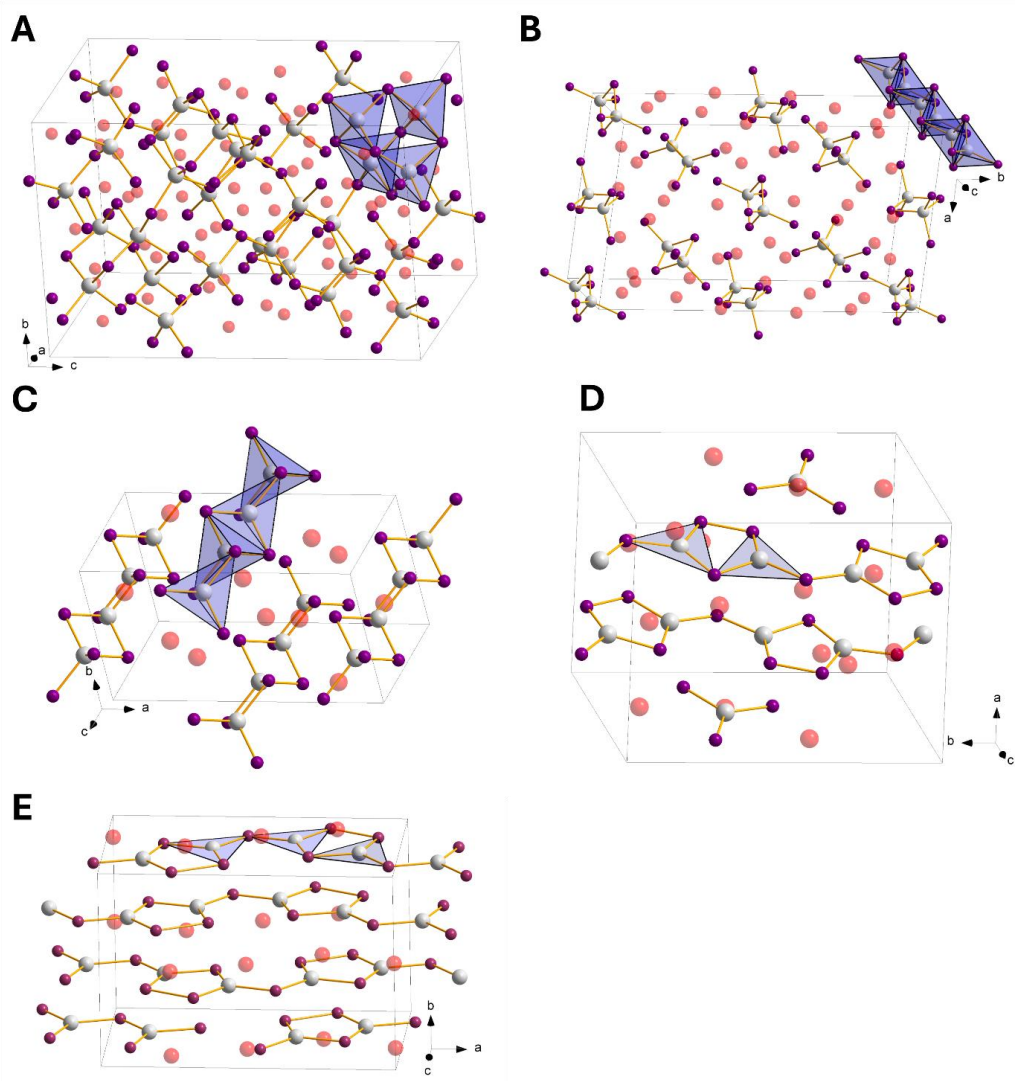

Figure 1. Structure types of the different crystal structures in the 2-1-2 system with **A** Li_2SiP_2-type, **B** Na_2SiP_2-type, **C** K_2SiP_2-type, **D** K_2GaP_2-type and **E** K_2GaSb_2-type.

Li_2SiP_2, Li_2GeP_2 and Na_2SnAs_2 crystallize in the tetragonal space group *I* $4_1/acd$ (no. 142) in the Li_2SiP_2 structure type (referred to as type **A**, Figure 1**A**). [6–8] Herin the *Pn* atoms form a distorted cubic closed packing with *Tt* occupying tetrahedral voids and *A* tetrahedral and octahedral voids. The $TtPn_4$ tetrahedra are connected via vertex sharing, with four of them building adamantane like Tt_4Pn_{10} super tetrahedra. These units are connected by their “outer vertices” and build a three-

dimensional network with an $^3_\infty[TtPn_{4/2}]^{2-}$ polyanion. Two such networks are formed independently without any bonds in between them.

Na_2SiP_2 crystallizes in the orthorhombic space group *Pccn* (no. 56) in its own structure type (type **B**, Figure 1**B**).[9] It shows the same structural motive as K_2SiP_2, Cs_2SiP_2, K_2SiAs_2, K_2GeAs_2, Rb_2SiAs_2, Rb_2SnAs_2, Cs_2SiAs_2 and Cs_2SnAs_2 which crystallize in the orthorhombic space group *Ibam* (no. 72) in the K_2SiP_2 structure type (type **C**, Figure 1**C**). [10–13] For both structure types one dimensional chains of edge-sharing $TtPn_4$ tetrahedra are formed along the c-axis. The $^1_\infty[TtPn_{4/2}]^{2-}$ polyanions formed within the unit cell run parallel to each other.

K_2GaP_2, K_2GaAs_2 and Rb_2GaAs_2 crystallize in the monoclinic space group $P\,2_1/n$ (no. 14) in the K_2GaP_2 structure type (type **D**, Figure 1**D**).[14–16] K_2GaSb_2, Rb_2GaSb_2 and Cs_2GaSb_2 crystallize with the same structural motive but in the orthorhombic space group *Pnma* (no. 62) in the K_2GaSb_2 structure type (type **E**, Figure 1**E**).[17–19] In contrast to the tetrel compounds, which build $TtPn_4$ tetrahedra, the triel compounds are coordinated triangular planarly by three *Pn* atoms. The $TrPn_3$ units are connected by corner sharing to one-dimensional chains along the b- (type **D**) and a-axis (type **E**), respectively. Within these chains, *Pn* tips of the $TrPn_3$ unit, which are not connected to neighbouring units, build *Pn-Pn* bonds, such that two neighbouring units are connected. This leads to the formation of Tr_2Pn_3 five-membered planar rings, which are connected by bridging *Pn* atoms.

Since all compounds are electron precise Zintl compounds, the formal charges can be determined by electron transfer from the alkali metal to the anionic substructure of $Tr/TtPn_2$. For the tetrel compounds structures **A**, **B** and **C**, (4b-*Tt*)^0 and (2b-*Pn*)$^-$ atoms are present, with formal charges of 0 and -1, respectively. For the triel compounds the formal charges are also +1, 0 and -1 for the alkali metal, triel and pnictogen, respectively, since (3b-*Tr*)^0 and (2b-*Pn*)$^-$ build he one-dimensional chains.

Electronic structure calculations

The computational studies of all compounds in the $A_2Tr/TtPn_2$ system (with *A* = Li-Cs, *Tr* = Al-In, *Tt* = Si-Sn and *Pn* = P-Sb) were performed using the CRYSTAL17 program package and hybrid density functional methods.[20][21] A hybrid exchange-correlation functional after Perdew, Burke, and Ernzerhof (DFT-PBE0) was used, [22] Localized, Gaussian-Type triple ζ-valence + polarization level basis sets were used for triel, tetrel and pnictogen atoms and split valence + polarization level basis sets for Li, Na, K, Rb and Cs. The basis sets were derived from the molecular Karlsruhe basis sets.[23–31] For the evaluation of Coulomb and exchange integrals (TOLINTEG), tight tolerance

factors of 8, 8, 8, 8, 16 were used for all calculations. The reciprocal space of all calculations was sampled with Monkhorst-Pack-type *k*-point grids, their respective sizes can be found in the SI. The starting geometries were taken from experimental data. Both the lattice parameters and atomic positions were fully optimized within the constraints imposed by the space group symmetry. Further on all optimized structures were confirmed to be true local minima by means of harmonic frequency calculations at Γ-point. For all compounds electronic band structures and density of states (DOS) were calculated. The Brillouin Zone paths were provided by the web service *SeeK-path* and a list can be found in the SI.[32]

Band Dos overview

For all calculations experimental data was used as starting geometry. For each compound the crystal structure was optimized, and harmonic frequencies were calculated. All compounds but one, namely K_2GaAs_2, showed no imaginary frequencies and the difference between experimental and calculated cell parameters all were below 1.5 % (See Supporting Information Table S1). For K_2GaAs_2 the crystal structure was distorted multiple times within the same space group and even without any symmetry, but one negative frequency of at least 40 cm^{-1} remained. This might be due to anharmonicity, but since including this in the frequency calculation would be to expensive, further calculations were based on the optimized structure with the lowest imaginary frequency. Band structures, density of states and crystal orbital Hamilton population were calculated. All results can be found in Table 1 in the Supporting information. The calculated band gaps can be found in Table 1and

Table *2*. Only three compounds, Li_2SiP_2, Li_2GeP_2 and Na_2SnAs_2, have a direct band gap. All other compounds, except Cs_2GaSb_2 which has a pseudo-direct band gap, have indirect band gaps.

Table 1. Overview the tetrel compounds within the 2-1-2 system. The letter in braces refers to the crystal structure. All band gaps are given in eV and direct and indirect band gaps are referred to as d and in, respectively.

A-Tt-Pn	**Li**	**Na**	**K**		**Rb**	**Cs**	
Si	Li_2SiP_2 (**A**) 3.24 / d	Na_2SiP_2 (**B**) 2.69 / in	K_2SiP_2 (**C**) 2.97 / in	K_2SiAs_2 (**C**) 2.71 / in	Rb_2SiAs_2 (**C**) 2.56 / in	Cs_2SiP_2 (**C**) 2.80 / in	Cs_2SiAs_2 (**C**) 2.71 / in
Ge	Li_2GeP_2 (**A**) 2.73 / d		K_2GeAs_2 (**C**) 2.62 / in				
Sn		Na_2SnAs_2 (**A**) 2.07 / d			Rb_2SnAs_2 (**C**) 2.45 / in	Cs_2SnAs_2 (**C**) 2.47 / in	

Table 2. Overview the triel compounds within the 2-1-2 system. The letter in braces refers to the crystal structure. All band gaps are given in eV and indirect and pseudo-direct band gaps are referred to as in and p-d, respectively.

A*-Ga-*Pn	**K**	**Rb**	**Cs**
P	K_2GaP_2 (**D**) 2.75 / in		
As	K_2GaAs_2 (**D**) 2.68 / in	Rb_2GaAs_2 (**D**) 2.48 /in	
Sb	K_2GaSb_2 (**E**) 2.25 / in	Rb_2GaSb_2 (**E**) 2.19 / in	Cs_2GaSb_2 (**E**) 2.24 / p-d

Comparing the size of the band gaps, they mostly decrease from Li to Cs as well as from P to Sb compounds for trielates as well as tetrelates. The general trend follows the electronegativity difference such that higher differences result in higher band gaps.[33] The two Na compounds, Na_2SiP_2 and Na_2SnAs_2, slightly break the trend, since both compounds have with 2.69 eV and 2.07 eV, respectively, smaller band gaps than expected. For Na_2SnAs_2 the direct band gap, which in general seem to be comparably smaller, might be the cause, while Na_2SiP_2 this might be due to the different crystal structure **B**, although it is very similar to type **C**.

Band Dos results

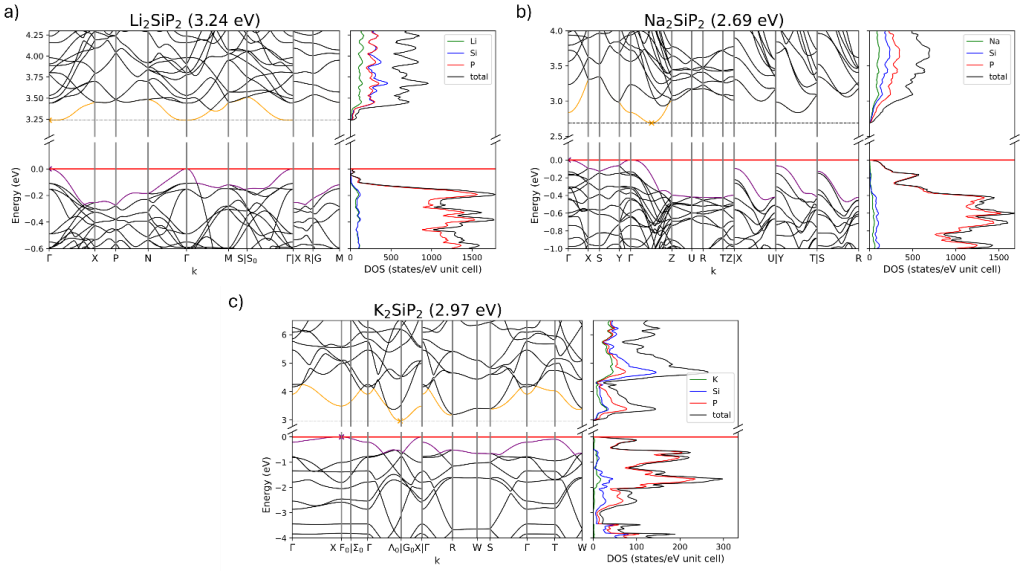

Figure 2. Band structure and density of states for a) Li_2SiP_2, b) Na_2SiP_2 and c) K_2SiP_2 with band gaps of 3.24 eV (direct), 2.69 eV (indirect) and 2.97 eV (indirect), respectively.

In Figure 2 one band structure and density of states (DOS) for the tetrel compounds are shown for each structure type exemplarily. Within each structure type the overall trends in band structure

and density of states are the same. For structure type **A**, represented by Li_2SiP_2, all compounds show direct band gaps with valence band maximum (VBM) and conduction band minimum (CBM) located at Γ and both valence and conduction band show dispersion, which is decreasing for Li_2GeP_2 and Na_2SnAs_2. The low band gap for the latter might be caused by the CBM being pulled down about 0.5 eV from the remaining conduction bands. For Li_2SiP_2 this gap is only 0.25 eV, which in comparison is only half as much. For structure type **B** only Na_2SnAs_2 is known. It shows an indirect band gap of 2.69 eV with a transition from Γ to |Γ-Z| and also shows considerable dispersion.

All remaining tetrel compound crystallize in structure type **C**, for which the band structure and DOS of K_2SiP_2 is shown. All compounds show large dispersions for valence and conduction bands, which only slightly decrease for Cs compounds. For all compounds the VBM is located at X, while the CBM has different positions (see SI Table 2). For both Sn compounds the first two conduction bands decouple from the rest and a small gap can be seen. Additionally their CBMs are located at Γ.

For all compounds the DOS looks very similar. The top valence bands primarily consist of *Pn* states, while lower bands also show *A* and *Tt* contributions. In the conductions bands for compounds of type **A** and **B** *Tt* and *Pn* contribute more states than the alkali metal. For structure type **C** *Pn* contributes the most for the first two bands, while for the higher conduction bands all atoms contribute equally.

In previous publications additional alkali metal states close to the Fermi-Leve lead to a shift of the VBM away from Γ.[34] This can be seen for this system as well, since all compounds of type **C**, for which the VBM is located at X, show a small maximum of alkali metal states close to the Fermi-Level. Since the top valence band is rather flat between Γ and T, this maximum mostly seems to arise from this segment of the band, but since the projected alkali metal DOS does not fall back in the range, where only the states around X contribute, it is still reasonable that the shift of the VBM is caused by an increase of alkali metal states.

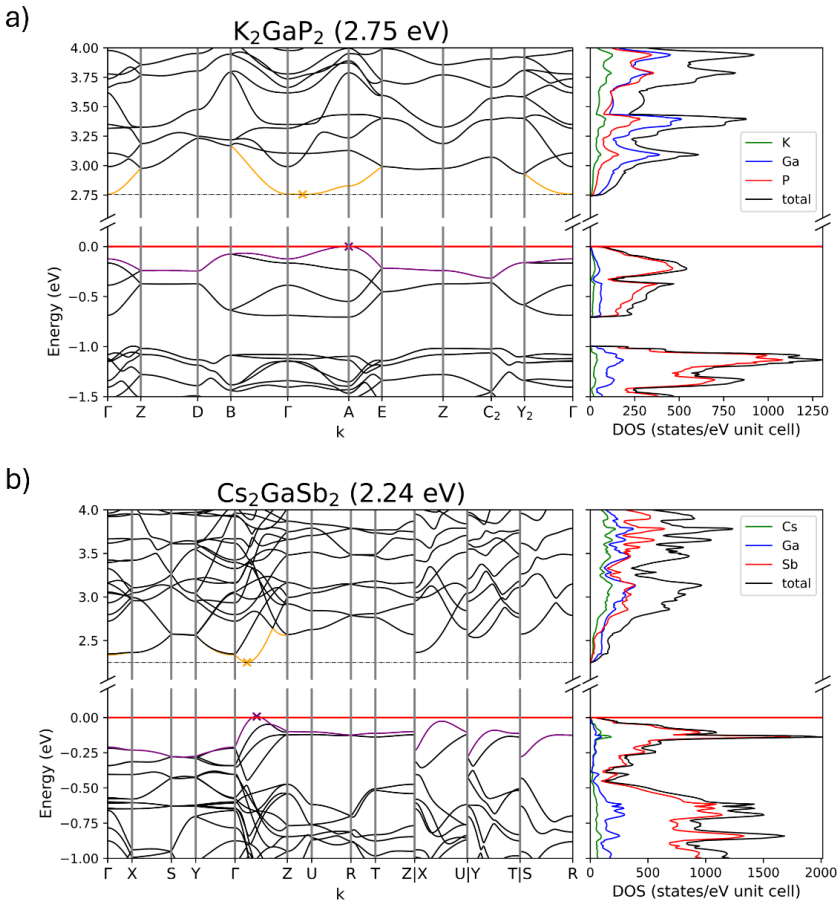

Figure 3. Band structure and density of states of a) K_2GaP_2 and b) Cs_2GaSb_2 with indirect band gaps of 2.75 eV and 2.25 eV.

In Figure 3 band structures and DOS of K_2GaP_2 and K_2GaSb_2 are shown as representatives of structure types **D** and **E**, respectively. Again, the band structures within one structure type are similar to each other. For type **D** the first four valence form their own set of bands, which is followed by a small gap of about 0.3 eV. For all compounds the VBM is located at A, while the CBM is located around Γ, since the band between Γ and A is rather flat. For Rb_2GaAs_2 this is not the case, and a sharp conduction band minimum can be seen at Γ. For the Sb compounds with structure **D** the VBM is located in the intervals |Γ-Z| or |Γ-X|. The CBM is located at Γ for K_2GaSb_2 and Rb_2GaSb_2, while for the Cs compound it is at Z, resulting in a pseudo-direct band gap, since VBM and CBM are close to each other. All compounds show a considerable dispersion.

For alle compounds the DOS is similar. The valence bands mostly consist of *Pn* states with minor contributions of the alkali metal and Ga. Since, as for the tetrel compounds, the VBM is shifted

away from Γ, additional alkali metal states can be found at the Fermi-Level. For the lower conduction bands Ga is the main contributor, but at higher energies Ga and *Pn* contribute equally with minor contribution of the alkali metal.

Mullikan analysis

To get a better insight on the bonding situation within the 2-1-2 system a Mullikan analysis was conducted. All values for the Mulliken charges as well as the overlap population between neighbouring atoms can be found in the Supporting Information. For structure types **A** to **C**, the proposed charges according to the Zintl concept are +1, 0 and -1 for the alkali metals, tetrel and pnictogen, respectively. For the alkali metals Mulliken charges between of about 0.6 to 0.8 are found, with Li having the lowest and Cs the highest. This can be explained by the decrease of electronegativity as well as better charge distribution from Li to Cs. For the tetrel atoms charges of -0.05 to about +0.2 were found and for the pnictogen of about -0.6 to -0.8. This again in good agreement with the proposed theoretical charges.

The overlap population gives an insight on the bonding situation within the crystal structure. With values of about 0.3 covalent interactions can be assumed between *Tt* and *Pn*, which are in line with the bonds assigned to the anionic substructure. The general overlap between the alkali metals and their surrounding *Tt* and *Pn* atoms is very small, thus they only interact as counterions. This again is in line with the Zintl concept, where the alkali metal is solely an electron donor in terms of bonding situation. Between two neighbouring *Tt* atoms negative overlap populations of -0.2 to -0.8 can be found, which show that two neighbouring *Tt* atoms repel each other slightly. The overlap between the Sn atoms is the smallest, which could be an explanation that on one hand the two lowest conduction bands in Rb_2SnAs_2 and Cs_2SnAs_2 are decoupled from the higher bands and on the other hand, why Na_2SnAs_2 has such a low band gap. If the interaction is weak the corresponding splitting of the bands is also lower, compared to the other compounds, and thus lower the energy of corresponding bands .

For the triel compounds, similar Mulliken charges were calculated. The alkali metals also show charges of 0.7 to 0.8, while for the pnictogen charges of -0.6 to -0.8 were calculated. Ga shows slightly negative Mulliken charges of around -0.1, which might be caused by a weak back-bonding of the *Pn*. The calculated Mulliken charges are in line with the theoretical charges imposed by the crystal structure and proposed bonding situation, with +1, 0 and -1 for alkali metal, Ga and pnictogen respectively. The overlap population shows values of about 0.35 for Ga-*Pn* interactions

and 0.23 for *Pn*-*Pn* which correspond to covalent interactions and the proposed bonds within the triangular planar units as well as the bonds to bridging *Pn* atoms. The alkali metal shows little to no interaction to its neighbouring atoms, thus only ionic interactions are present. A small repulsion can be found for neighbouring Ga atoms, which is decreasing for compounds with large *Pn* and alkali metal atoms.

COHP calculations

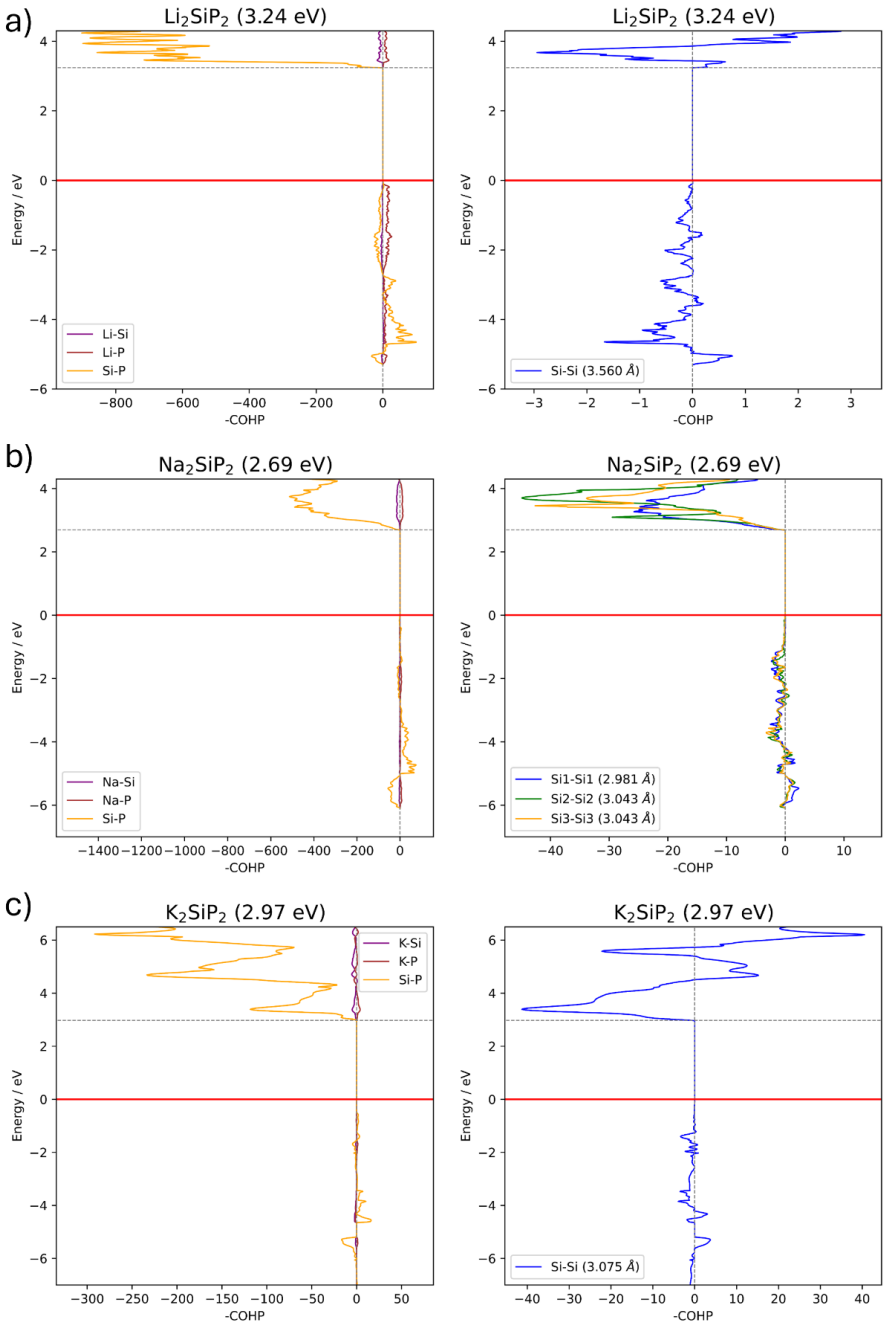

Figure 4. Crystal orbital Hamilton population of all heteroatomic (left) and neighbouring *Tt-Tt* interactions (right) for a) Li_2SiP_2, b) Na_2SiP_2 and c) K_2SiP_2, respectively.

Figure 4 shows exemplary crystal orbital Hamilton populations (COHP) for structure types **A** to **C** for all heteroatomic as well as neighbouring *Tt*-*Tt* interactions. Although many states are right below the Fermi-Level in the DOS only minor interactions are present in the COHP, which suggests that most states of the top valence band belong to non-bonding states, such as lone pairs of the *Pn* atom. For all *Tt* compounds the valence bands show mostly interactions between the tetrel and pnictogen, while interactions with the alkali metal are only small due to their dominantly ionic nature. The conduction bands show large contributions from *Tt*-*Pn* anti-bonding interactions and interactions with the alkali metal are again only minor.

Some interesting trends can be found for the *Tt*-*Tt* interaction. As discussed for the 3-1-2 system (cite TBP paper) a peak in *Tt*-*Tt* bonding states, that are right above the band gap, were able to shift the CBM away from Γ. In the *Tt* 2-1-2 system, this can be found as well. Compounds with structure type (A), that show a direct band gap, show right above the band gap a few *Tt*-*Tt* bonding states, followed by anti-bonding states. For compounds with structure **B** and **C**, most *Tt*-*Tt* COHP projections show a sharp edge above the band gap with anti-bonding states which corresponds with a shift of the CBM from Γ. Two compounds with structure **C** for which the band gap is located at Γ, Rb_2SnAs_2 and Cs_2SnAs_2, right above the band gap no edge can be found but rather the same few bonding *Tt*-*Tt* states that are present for the direct band gap compounds.

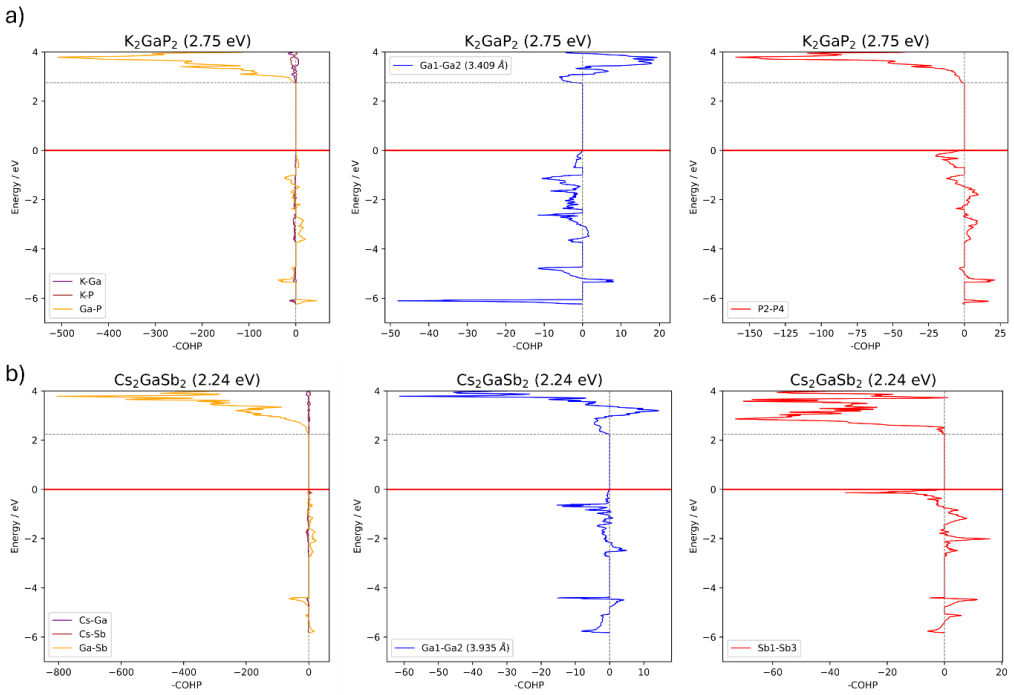

Figure 5. Crystal orbital Hamilton population of all heteroatomic (left), neighbouring *Pn*-*Pn* (middle) and Ga-Ga interactions (right) for a) K_2GaP_2, and b) Cs_2GaSb_2, respectively.

For the *Tr* compounds exemplary COHPs are shown in Figure 5. Like for the *Tt* compounds, most states below the Fermi-Level belong to non-bonding *Pn* states, since only weak interactions are found. Above the band gap, mostly Ga-*Pn* anti-bonding interactions can be found. Again all interactions with the alkali metal are only minor, since their interactions with their neighbours are of ionic nature. In this case a closer look at the Ga-Ga interaction reveals a similar trend to the tetrel compounds. Again, compounds for which the CBM is located at Γ show little or no anti-bonding interactions right above the band gap, while compounds with an indirect band gap have a sharp edge in such states.

Since within crystal structures (D) and (E) additional bridging *Pn* atoms are present, their interaction with the *Pn* atom within the corner-sharing triangular planar units Ga*Pn*$_3$ units is investigated. Their projected COHP shows some anti-bonding below the Fermi-Level, as well as above the band gap. Thus, they might play a role in the shift of the VBM away from Γ.

Conclusion

For all 18 compounds of the $A_2Tr/TtPn_2$ system (with *A* = Li-Cs, *Tr* = Al-In, *Tt* = Si-Sn and *Pn* = P-Sb), with their five different structure types, crystal structures were optimized and band structures, density of states (DOS) and crystal orbital Hamilton population (COHP) calculated. Three compounds, Li_2SiP_2, Li_2GeP_2 and Na_2SnAs_2, were found to be direct band gap semiconductors, while all other compounds, except Cs_2GaSb_2 which has a pseudo-direct band gap, have indirect band gaps. For both triel and tetrel compounds the size of the band gap is mainly determined by the electronegativity difference between the *Tr*/*Tt* and pnictogen, as well as their difference to the alkali metal.

Within this system only compounds with structure type **A** show direct band gaps for the tetrel compounds. For compounds in structure type **C** additional alkali metal states close to the Fermi-Level are present in the DOS, which might rise the top valence band at other k-points than Γ, resulting in indirect band gaps. The electronic structure was further investigated by calculation of the COHP. Here compounds with an indirect band gap show a sharp increase in anti-bonding *Tt*-*Tt* interactions right above the band gap, which might be responsible for the conduction band minimum being located at other k-points than Γ, since these states are not observed for compounds with direct band gaps.

The same effects can be seen for the triel compounds, but since these compounds incorporate additional *Pn*-*Pn* bonds, their influence on the band structure was also investigated. Here in the COHP anti-bonding *Pn*-*Pn* interactions close to the Fermi-Level are present, which might also rise the top valence band, resulting in different valence band minimums than Γ. Other than that the electronic structure of all compounds revealed mainly *Pn* non-bonding orbitals for the conduction bands, possibly from the lone electron pairs.

Further research should focus on modelling the missing compounds, to see if the trends identified can be reassured and expanded. Additionally modelling existing compounds in structure type **A**, could give some valuable insights how much influence the crystal structure has on the occurrence of direct band gaps in contrast to the composition, since in this system this is the only structure type for which they were be found.

References

[1] H. Hosono, *Journal of Non-Crystalline Solids* **2006**, *352*, 851.
[2] K. S. Kazunori Sato, H. K.-Y. Hiroshi Katayama-Yoshida, *Jpn. J. Appl. Phys.* **2000**, *39*, L555.
[3] A. Mehta, A. Mishra, S. Basu, N. P. Shetti, K. R. Reddy, T. A. Saleh, T. M. Aminabhavi, *Journal of environmental management* **2019**, *250*, 109486.
[4] T. Todorov, T. Gershon, O. Gunawan, Y. S. Lee, C. Sturdevant, L.-Y. Chang, S. Guha, *Advanced Energy Materials* **2015**, *5*.
[5] J. Wan, X. Xu, G. Zhang, Y. Li, K. Feng, Q. Peng, *Energy Environ. Sci.* **2017**, *10*, 1739.
[6] L. Toffoletti, H. Kirchhain, J. Landesfeind, W. Klein, L. van Wüllen, H. A. Gasteiger, T. F. Fässler, *Chemistry (Weinheim an der Bergstrasse, Germany)* **2016**, *22*, 17635.
[7] M. Asbrand, B. Eisenmann, *Zeitschrift für Naturforschung B* **1993**, *48*, 452.
[8] H. Eickhoff, C. Sedlmeier, W. Klein, G. Raudaschl-Sieber, H. A. Gasteiger, T. F. Fässler, *Zeitschrift anorg allge chemie* **2020**, *646*, 95.
[9] A. Haffner, A.-K. Hatz, C. Hoch, B. V. Lotsch, D. Johrendt, *Eur J Inorg Chem* **2020**, *2020*, 617.
[10] B. Eisenmann, M. Somer, *Zeitschrift für Naturforschung B* **1984**, *39*, 736.
[11] B. Eisenmann, J. Klein, *Journal of the Less Common Metals* **1991**, *175*, 109.
[12] W. M. Hurng, E. S. Peterson, J. D. Corbett, *Inorg. Chem.* **1989**, *28*, 4177.
[13] J. Wolf, D. Weber, H.-G. von Schnering, *Zeitschrift für Naturforschung B* **1986**, *41*, 731.
[14] W. Blase, G. Cordier, M. Somer, *Zeitschrift für Kristallographie - Crystalline Materials* **1991**, *195*, 115.
[15] G. Cordier, H. Ochmann, *Zeitschrift für Kristallographie - Crystalline Materials* **1991**, *195*, 111.
[16] G. Cordier, H. Ochmann, *Zeitschrift für Kristallographie* **1991**, *195*, 113.
[17] G. Cordier, H. Ochmann, H. Schäfer, *Journal of the Less Common Metals* **1986**, *119*, 291.
[18] G. Cordier, H. Ochmann, *Zeitschrift für Kristallographie - Crystalline Materials* **1991**, *195*, 125.
[19] G. Cordier, H. Ochmann, *Zeitschrift für Kristallographie - Crystalline Materials* **1991**, *195*, 310.
[20] R. Dovesi, V. R. Saunders, C. Roetti, R. Orlando, C. M. Zicovich-Wilson, F. Pascale, B. Civalleri, K. Doll, N. M. Harrison, I. J. Bush **2017**.
[21] R. Dovesi, A. Erba, R. Orlando, C. M. Zicovich-Wilson, B. Civalleri, L. Maschio, M. Rérat, S. Casassa, J. Baima, S. Salustro et al., *Wiley Interdiscip. Rev.: Comput. Mol. Sci.* **2018**, *8*.
[22] J. P. Perdew, W. Yang, K. Burke, Z. Yang, E. K. U. Gross, M. Scheffler, G. E. Scuseria, T. M. Henderson, I. Y. Zhang, A. Ruzsinszky et al., *Proc. Natl. Acad. Sci. U. S. A.* **2017**, *114*, 2801.
[23] A. J. Karttunen, T. F. Fässler, *Chemistry (Weinheim an der Bergstrasse, Germany)* **2014**, *20*, 6693.
[24] A. J. Karttunen, T. F. Fässler, M. Linnolahti, T. A. Pakkanen, *Inorg. Chem.* **2011**, *50*, 1733.
[25] T. M. F. Restle, J. V. Dums, G. Raudaschl-Sieber, T. F. Fässler, *Chemistry (Weinheim an der Bergstrasse, Germany)* **2020**, *26*, 6812.
[26] T. M. F. Restle, S. Zeitz, J. Meyer, W. Klein, G. Raudaschl-Sieber, A. J. Karttunen, T. F. Fässler, *Zeitschrift anorg allge chemie* **2021**, *647*, 1804.
[27] T. M. F. Restle, S. Zeitz, P. M. Stanley, A. J. Karttunen, J. Meyer, G. Raudaschl-Sieber, W. Klein, T. F. Fässler, *Chemistry (Weinheim an der Bergstrasse, Germany)* **2023**, e202304097.
[28] G. Sansone, L. Maschio, D. Usvyat, M. Schütz, A. Karttunen, *The journal of physical chemistry letters* **2016**, *7*, 131.
[29] B. Scheibe, A. J. Karttunen, F. Weigend, F. Kraus, *Chemistry (Weinheim an der Bergstrasse, Germany)* **2021**, *27*, 2381.

[30] L. M. Scherf, A. J. Karttunen, O. Pecher, P. C. M. M. Magusin, C. P. Grey, T. F. Fässler, *Angewandte Chemie (International ed. in English)* **2016**, *55*, 1075.
[31] R. E. Stene, B. Scheibe, A. J. Karttunen, W. Petry, F. Kraus, *Eur J Inorg Chem* **2019**, *2019*, 3672.
[32] Y. Hinuma, G. Pizzi, Y. Kumagai, F. Oba, I. Tanaka, *Comput. Mater. Sci.* **2017**, *128*, 140.
[33] A. F. Holleman, *Lehrbuch der anorganischen Chemie*, Walter de Gruyter GmbH & Co KG, **2019**.
[34] S. Zeitz, H. Antoniuk, V. Hlukhyy, T. F. Fässler, *Chemistry (Weinheim an der Bergstrasse, Germany)* **2024**, *30*, e202400002.

5.5 Electronic property calculation of *A*Sn*Pn* compounds with *A* = Na, K and *Pn* = P, As, Sb

Sabine Zeitz, Thomas F. Fässler

Manuscript for publication

Electronic property calculation of *A*Sn*Pn* compounds with *A* = Na, K and *Pn* = P, As, Sb

Sabine Zeitz[a], Thomas F. Fässler[a]

Abstract

The ASnPn (with A = Na, K; Pn = P, As, Sb) compounds represent a simple system, with its grey arsenic like layered crystal structure. For four experimentally known compounds, as well as NaSnSb and KSnP crystal structures were optimized and band structures, density of states as well as crystal orbital Hamilton populations calculated on a DFT/PBE0 level of theory. Interestingly, all Na compounds show indirect band gaps, while K compounds show direct ones. The size of the band gap is mainly determined by the electronegativity difference between Sn and the pnictogen, with decreasing band gaps from phosphides to antimonides. For NaSnAs and NaSnSb the band gap is further decreased due to the sodium's lower electronegativity. A Mullikan analysis was able to confirm the bonds assigned by the crystal structure between Sn and Pn as well as the charge distribution assigned by the Zintl-concept. The electronic structure for the valence and conduction bands consists mostly of Sn-Pn interactions, which are mostly anti-bonding around the band gap. The location of the conduction band minimum of the Na compounds between Γ and M might be caused by some Sn-Sn bonding interactions as well as Pn-Pn interactions, which are weaker or absent for the K compounds, that have the first conduction band at higher energies between Γ and M.

Introduction

Light-emitting diodes(LEDs), transistors, thermoelectrics and solar cells are only a few examples for the wide range of applications of semi-conductors. Since their requirements get more specialized and precise band gap tuning, intelligent material design as well as precise electronic structure prediction are important.[1–5] Especially for the tunability of materials it is beneficial for a compound class to show not only the same structure, but also have similar electronic properties. If one then further is able to predict, for example, the band gap size and nature just by knowing the composition and structure, the process of material design could become even more efficient. Therefore, basic research on simple compound systems is necessary to find band structure – crystal structure relationships, which help in predicting possible properties based on the structure. One such simple system is the *A*Sn*Pn* system (with *A* = Na, K and *Pn* = P, As, Sb), where all compounds crystallize in the KSnAs structure type in space group $P6_3mc$ (no, 186).[6–9] Since all compounds are electron precise Zintl compounds, the structure can be determined via the Zintl-Klemm concept. The alkali metal transfers its electron to the Sn*Pn* substructure, which then consists of $(3b\text{-}Sn)^-$ and $(3b\text{-}Pn)^0$ with (nb = n-fold bonded). Therefore, Sn and Pn form grey arsenic like two-dimensional layers of chair conformed six-membered rings, with Sn and Pn alternating. The SnPn layers are stacked with an ABAB order, where every second layer is shifted by ½ and ½ in a- and b-direction. The alkali metal atoms are located between the layers and are coordinated octahedrally by Sn_3Pn_3.

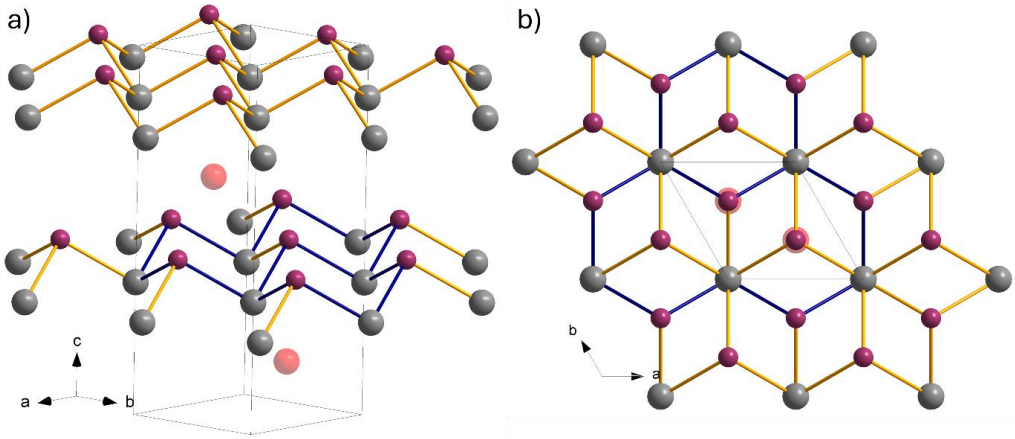

Figure 1. Crystal structure of the KSnAs structure type. Alkali metal, Sn and pnictogen are coloured in red, grey and purple, respectively. a) side view on the Sn*Pn* layers, b) view along the c-axis on the layers.

Electronic structure calculations

The computational studies of all compounds in the *A*Sn*Pn* system (with *A* = Na, K and *Pn* = P, As, Sb) were performed using the CRYSTAL17 program package and hybrid density functional methods.[10,11] A hybrid exchange-correlation functional after Perdew, Burke, and Ernzerhof (DFT-PBE0) was used, [12] Localized, Gaussian-Type triple ζ-valence + polarization level basis sets were used for Sn, P, As and Sb atoms and split valence + polarization level basis sets for Na and K.[13–16] The basis sets were derived from the molecular Karlsruhe basis sets. For the evaluation of Coulomb and exchange integrals (TOLINTEG), tight tolerance factors of 8, 8, 8, 8, 16 were used for all calculations. The reciprocal space of all calculations was sampled with 8 x 8 x 3 Monkhorst-Pack-type *k*-point grids. The starting geometries were taken from experimental data. Both the lattice parameters and atomic positions were fully optimized within the constraints imposed by the space group symmetry. Further on all optimized structures were confirmed to be true local minima by means of harmonic frequency calculations at Γ-point. For all compounds electronic band structures, density of states (DOS) and crystal orbital Hamilton population (COHP) were calculated. The Brillouin Zone path of Γ—M—K—Γ—A—L—H—A|L—M|H—K was provided by the web service *SeeK-path*.[17]

Results and Discussion:

For the electronic properties calculations experimental data was used as starting geometry, whenever possible. For LiSnSb no optimized geometry could be obtained thus the compound was excluded from further calculations. For NaSnSb and KSnP, models based on the experimental data of KSnSb and KSnAs, respectively, were used. For all compounds cell parameters and atomic positions were optimized. Subsequent frequency, band structure, density of states (DOS) and Crystal Orbital Hamilton Populations (COHP) were calculated. Results of the calculations can be found in Table 1. All calculated cell parameters only differ by a maximum of 2.3 % from the experimental ones, thus the results are reliable. Additionally, information on the band gap is given. All Na compounds show indirect, K compounds direct band gaps.

Table 1. Optimized crystal structure parameters for all calculated compounds. For each compound, the first line shows experimental (exp.), the second calculated (calc.) cell parameters and the third the percentual difference (Δ). If only one line is present and the compound is written in cursive, no experimental data was available. The transition refers to the position of the valence band maximum and conduction band minimum of the band structure.

		a / Å	c / Å	band gap / EV		transition
KSnP		3.9872	12.8070	2.20	direct	Γ -> Γ
KSnAs	**(exp.)**	4.102	12.816	1.77	direct	Γ -> Γ

(calc.)	4.104	12.898			
Δ / %	0.06	0.64			
KSnSb	4.350	13.141	1.42	direct	Γ -> Γ
	4.368	13.167			
	0.41	0.19			
NaSnP	3.880	11.667	2.42	indirect	Γ -> Γ-M
	3.886	11.507			
	0.15	-1.39			
NaSnAs	4.105	11.766	1.36	indirect	Γ -> Γ-M
	4.011	11.513			
	-2.34	-2.20			
NaSnSb	4.2924	11.6785	0.71	indirect	Γ -> Γ-M

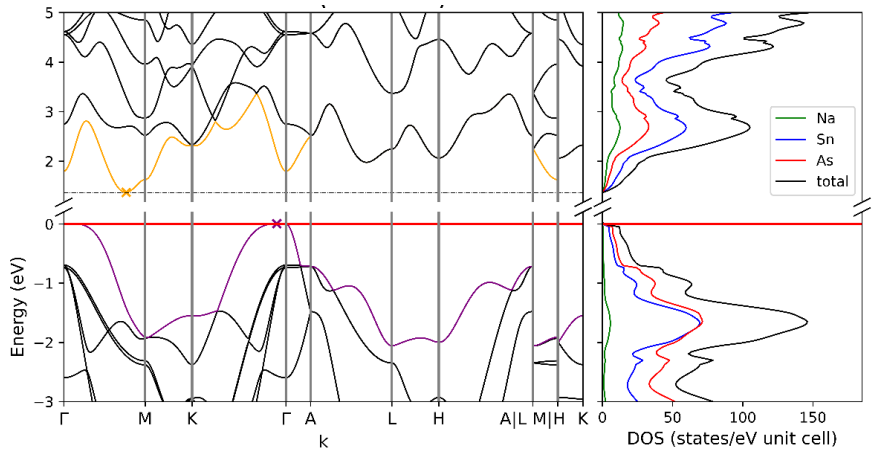

Figure 3. Band structure and DOS of NaSnAs with an indirect band gap of 1.36 eV.

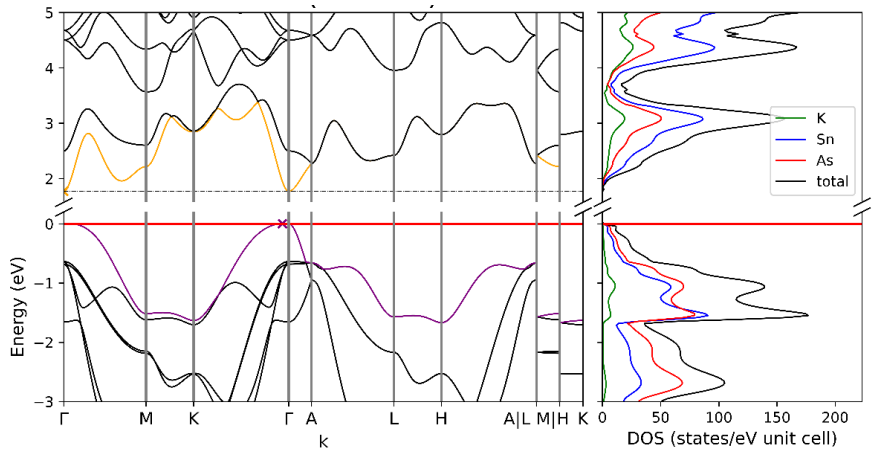

Figure 2. Band structure and DOS of KSnAs with a direct band gap of 1.77 eV.

Figure 3 and Figure 2 show two exemplary band structures for NaSnAs and KSnAs, which have an indirect and direct band gap respectively. All band structures show a large dispersion for both valence and conduction bands. While the valence band maximum (VBM) is located at Γ for all compounds, the conduction band minimum (CBM) is at Γ (K compounds) and M for all Na compounds, which results in indirect band gaps for the latter. This could be either due to an upward shift in energy of states at Γ or some interaction that lowers the energy of the states closer to M for the K compounds. The density of states DOS for all compounds has same shape: Valence bands are made up by equal contributions of Sn and Pn states with minor contribution of the alkali metal at around -1 eV. In the conduction bands all atoms contribute equally and even by zooming into the DOS at the CBM no significant difference between the Na and K compounds could be found, that would result in the observed change of the CBM.

The size of the band gap decreases from phosphides to antimonides, which can be explained by a decrease in electronegativity difference from Sn-P of 0.23 to Sn-Sb with 0.09. [18] The Na compounds surprisingly show a smaller band gap than the K compounds (except for the phosphide), NaSnAs for example has a gap of 1.36 eV while the gap for KSnAs is 1.77 eV. Normally compounds that have the same composition except for the alkali metal tend to have a decreasing band gap size for an increasing alkali metal size. [19,20] Since in this system this is not the case, it seems that the difference in electronegativity to the alkali metal herein also influences the band gap. Since it decreases from Na to K, an increase in band gap is observed. Another possibility could be the switch from an indirect band gap to a direct band gap. If one compares all direct band gaps for Γ-Γ transitions between the Na and K compounds, the sodium compounds, except for NaSnSb, would have smaller band gaps.

To get a better understanding of the electronic situation, a Mullikan analysis was conducted to get partial charges and overlap population for each compound. The values can be found in Table 2 and Table *3*.

Table 2. Partial charges obtain via Mullikan analysis for each compound.

	Na / K	Sn	P / As / Sb
NaSnP	0.801	-0.129	-0.672
NaSnAs	0.795	-0.067	-0.728
NaSnSb	0.801	-0.238	-0.563
KSnP	0.765	-0.145	-0.619
KSnAs	0.759	-0.092	-0.667
KSnSb	0.777	-0.259	-0.518

According to the Zintl concept, the alkali metal transfers its valence electron to the Sn or *Pn* atoms. They then need to form three bonds each, and keep one lone pair, in order to form a grey arsenic like anionic network of edge-sharing, six-membered rings in the chair conformation.[21] Therefore charges of +1, -1 and 0 are expected for Na/K, Sn and P/As/Sb respectively. For the alkali metal the calculated Mulliken charge is with about +0.8 close to the theoretical, thus it can be assumed that the electron transfer to the Sn*Pn* network takes place. Within the network the charge is not completely located at Sn, but rather on the pnictogen. This is due to the electronegativity difference between Sn and the pnictogen, for which the electron density is shifted to the latter. This becomes less for arsenides and antimonides compared to phosphides, due to the lower polarity of the bonds.

By having a look at the overlap population, the bonding situation can be further analysed. Values for the interactions between neighbouring atoms can be found in Table 3. With values of about

0.2 bonding interaction are present between Sn and Pn, while values of 0.1 to 0.3 suggest ionic interactions between the alkali metal and Sn / Pn. Additionally weak antibonding interactions can be found between Sn-Sn and Pn-Pn which are probably caused by the repulsion of the respective lone pairs.

Table 3. Overlap population and bond lengths for the closest interactions. Negative values are equal to repulsion of the atoms.

	r / Å	Sn-Pn	r / Å	Sn-Sn	Pn-Pn	r / Å	A-Pn	r / Å	A-Sn
NaSnP	2.599	0.205	3.886	-0.036	-0.015	2.934	0.030	3.398	0.023
NaSnAs	2.690	0.213	4.011	-0.028	-0.012	3.018	0.030	3.374	0.024
NaSnSb	2.881	0.213	4.292	-0.021	-0.010	3.266	0.028	3.342	0.024
KSnP	2.624	0.217	3.987	-0.033	-0.012	3.239	0.013	3.676	0.011
KSnAs	2.710	0.228	4.104	-0.026	-0.010	3.335	0.017	3.659	0.011
KSnSb	2.895	0.231	4.368	-0.018	-0.009	3.565	0.017	3.653	0.011

Interestingly does K seem to slightly “tighten” the Sn-Pn network, since the bond lengths are longer, but the overlap population is larger for KSn*Pn* compared to NaSn*Pn*. The alkali metal is octahedrally coordinated by three Sn and Pn each in between two SnPn layers. Since K is larger, it needs the “octahedral void” to be larger, resulting in slightly longer bonds. This could be the reason why the partial charge of the pnictogen decreases for K compounds since it keeps more of the charge to widen the octahedral void. Na on the other hand transfers most of its valence electrons to the anionic network which in return shows more interaction with the cation, represented by a slightly larger overlap population of A-Sn and A-Pn.

With this information in mind a crystal orbital Hamilton population (COHP) was calculated for each heteroatomic interaction as well as the Sn-Sn and Pn-Pn antibonding interactions for each compound. The COHPs of a) NaSnAs and b) KSnAs are exemplarily shown in Figure 4. In general, again all COHPs show the same trends: Below the Fermi-Level some anti-bonding interactions can be seen between Sn and As down to about -2 eV, followed by some bonding interactions. The conduction bands show strong anti-bonding interactions. Over the whole range the A-Sn and A-Pn interactions are negligible. Since the interactions below the Fermi-Level are rather small, compared to the conduction bands, although a lot of states are present in the DOS, there could be additional non-bonding states such as the lone pairs on Sn and Pn present.

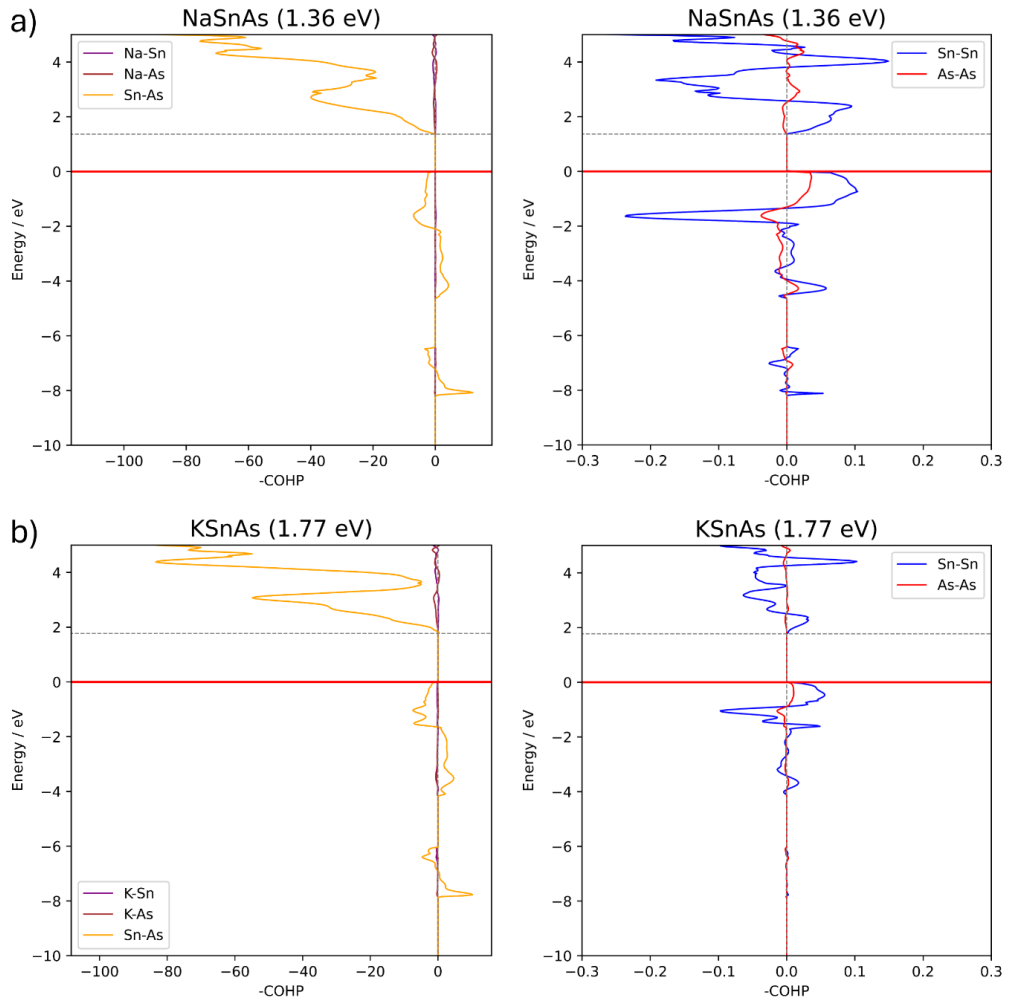

Figure 4. Crystal orbital Hamilton population for a) NaSnAs and b) KSnAs. The left plot shows all heteroatomic interactions, while the right shows homoatomic Sn-Sn (blue) and As-As (red) interactions for the respective closest atoms.

The homoatomic Sn-Sn and As-As interactions again show the same overall trend, with weak bonding interactions right below the Fermi-Level followed by anti-bonding interactions at around -2 eV. For the conduction bands again, weak bonding followed by anti-bonding interactions can be found. The main difference between the Na and K compounds is, that all interactions are stronger for the Na compounds. For compounds in the A_3TrPn_2 system (A=Li-Cs, Tr=Al-In, Pn=P, Sb) that show indirect band gaps a sharp edge at the CBM was found in the Tt-Tt COHP, which could be responsible for the shift of the CBM away from Γ. In this case there is no such sharp edge for all Na compounds, but since the interactions between two neighbouring Sn atoms in NaSnAs are twice as large in the COHP compared to KSnAs, they could still be responsible for the different

position of the CBM. Additionally, the Pn-Pn interaction at the band gap top might play a role in the position of the CBM, since for the Na compounds some Pn-Pn anti-bonding interactions can be found, which are zero for the K compounds.

Conclusion

For four experimentally known and two predicted compounds of the *A*Sn*Pn* system (with A = Na, K; Pn = P, As, Sb) crystal structures were optimized and band structures, density of states (DOS) and crystal orbital Hamilton population (COHP) calculated. For alle these compounds there is a clear separation between direct band gaps for the K compounds and indirect ones for the Na compounds. The size of the band gap decreases from phosphides to antimonides, due to the decrease in electronegativity difference. Additionally, for the As and Sb compounds the alkali metal also seems to have an influence on the band gap, since here the K compounds show larger band gaps than the Na compounds, probably due to the larger electronegativity of K or their switch to direct band gaps.

The band structures and DOS look similar for all calculated compounds, with large dispersion for valence and conduction bands and mostly Sn and Pn contribution to the total number of states around the Fermi-Level. Most of these states probably arise from non-bonding states, such as the lone pairs. For the K compounds valence band maximum and conduction band minimum are bot located at Γ, while for the Na compounds the latter is between Γ and M, which might be due to some, compared to the K compounds, stronger Sn-Sn bonding interactions and some Pn-Pn anti-bonding interactions. A Mullikan analysis provided some further insight into the charge distribution as well as the bonding situation, which was able to confirm the bonds assigned by the crystal structure between Sn and Pn.

Further research should on one hand focus on modelling the Li, Rb and Cs compounds, as well as switching Si and Ge, to see how the trends identified behave for the rest of the system, especially upon changing the alkali metal. Furter investigation should also try to synthesise the predicted NaSnSb and KSnP compounds, to check whether the models represent the real crystal structures well.

[1] H. Hosono, *Journal of Non-Crystalline Solids* **2006**, *352*, 851.
[2] K. S. Kazunori Sato, H. K.-Y. Hiroshi Katayama-Yoshida, *Jpn. J. Appl. Phys.* **2000**, *39*, L555.
[3] A. Mehta, A. Mishra, S. Basu, N. P. Shetti, K. R. Reddy, T. A. Saleh, T. M. Aminabhavi, *Journal of environmental management* **2019**, *250*, 109486.
[4] T. Todorov, T. Gershon, O. Gunawan, Y. S. Lee, C. Sturdevant, L.-Y. Chang, S. Guha, *Advanced Energy Materials* **2015**, *5*.
[5] J. Wan, X. Xu, G. Zhang, Y. Li, K. Feng, Q. Peng, *Energy Environ. Sci.* **2017**, *10*, 1739.
[6] B. Eisenmann, U. Rößler, *Zeitschrift für Kristallographie - New Crystal Structures* **1998**, *213*, 28.
[7] B. Eisenmann, J. Klein, *Zeitschrift anorg allge chemie* **1991**, *598*, 93.
[8] J. Klein, B. Eisenmann, *Materials Research Bulletin* **1988**, *23*, 587.
[9] A. M. Ochs, P. Gorai, Y. Wang, M. R. Scudder, K. Koster, C. E. Moore, V. Stevanovic, J. P. Heremans, W. Windl, E. S. Toberer et al., *Chem. Mater.* **2021**, *33*, 946.
[10] R. Dovesi, V. R. Saunders, C. Roetti, R. Orlando, C. M. Zicovich-Wilson, F. Pascale, B. Civalleri, K. Doll, N. M. Harrison, I. J. Bush **2017**.
[11] R. Dovesi, A. Erba, R. Orlando, C. M. Zicovich-Wilson, B. Civalleri, L. Maschio, M. Rérat, S. Casassa, J. Baima, S. Salustro et al., *Wiley Interdiscip. Rev.: Comput. Mol. Sci.* **2018**, *8*.
[12] J. P. Perdew, W. Yang, K. Burke, Z. Yang, E. K. U. Gross, M. Scheffler, G. E. Scuseria, T. M. Henderson, I. Y. Zhang, A. Ruzsinszky et al., *Proc. Natl. Acad. Sci. U. S. A.* **2017**, *114*, 2801.
[13] A. J. Karttunen, T. F. Fässler, *Chem.* **2014**, *20*, 6693.
[14] G. Sansone, L. Maschio, D. Usvyat, M. Schütz, A. Karttunen, *J. Phys. Chem. Lett.* **2016**, *7*, 131.
[15] B. Scheibe, A. J. Karttunen, F. Weigend, F. Kraus, *Chem.* **2021**, *27*, 2381.
[16] R. E. Stene, B. Scheibe, A. J. Karttunen, W. Petry, F. Kraus, *Eur. J. Inorg. Chem.* **2019**, *2019*, 3672.
[17] Y. Hinuma, G. Pizzi, Y. Kumagai, F. Oba, I. Tanaka, *Comput. Mater. Sci.* **2017**, *128*, 140.
[18] A. F. Holleman, *Lehrbuch der anorganischen Chemie*, Walter de Gruyter GmbH & Co KG, **2019**.
[19] T. M. F. Restle, S. Zeitz, P. M. Stanley, A. J. Karttunen, J. Meyer, G. Raudaschl-Sieber, W. Klein, T. F. Fässler, *Chem.* **2024**, *30*, e202304097.
[20] S. Zeitz, H. Antoniuk, V. Hlukhyy, T. F. Fässler, *Chemistry (Weinheim an der Bergstrasse, Germany)* **2024**, *30*, e202400002.
[21] N. C. Norman, *Chemistry of arsenic, antimony and bismuth*, Springer Science & Business Media, **1997**.

5.6 Electronic structure analysis of the ATt_3Pn_3 system with *A* = Li-Cs; *Tr* = Al-In; *Tt* = Si-Sn; *Pn* = P-Sb

Sabine Zeitz, Yulia Kuznetsova, Thomas F. Fässler

Manuscript for publication

Electronic structure analysis of the ATt_3Pn_3 system with *A* = Li-Cs; *Tr* = Al-In; *Tt* = Si-Sn; *Pn* = P-Sb

Sabine Zeitz[a], Yulia Kuznetsova[a], Thomas F. Fässler[a]

Abstract

For the ATt_3Pn_3 system (with *A* = Li-Rb, *Tt* = Si-Sn and *Pn* = P, As) a total of seven compounds in four different structure types are known, which all show a layered structure with layers of corner-sharing or interpenetrating tetrahedra. For all compounds after structure optimization band structures, density of states and crystal orbital Hamilton populations were calculated on a DFT/PBE0 level of theory. All compounds show indirect band gaps, for which the size is influenced by the crystal structure and elements present. For four compounds, KGe_3As_3, KSn_3As_3, $RbGe_3As_3$ and $RbSn_3As_3$, might show an additional pseudo-direct transition, since valence band maximum and conduction band minimum are close to each other on the k-path. At the Fermi-Level the tetrel atoms contribute the most states, followed by pnictogen states. Since they can be attributed to Tt-Pn anti-bonding states, they could be the main reason, why the valence bands show higher energies at other k-points than Γ, which result in the indirect band gaps.

Introduction

In the last decades highly specialised materials have been of growing importance for the development of our information-technology based society. Semi-conductors are among the most researched compound classes due to their various applications such as light-emitting diodes(LEDs), transistors, thermoelectrics and solar cells. [1–5] For the latter band gap tuning is especially important, to find new materials to achieve the highly discussed exit from fossil-fuel energy towards renewable energy sources. For an optimized material design process it would therefore be advantageous to predict the electronic properties just by knowing the crystal structure, to on one hand see whether newly discovered materials are interesting for specific applications and on the other hand efficiently design the structure of new materials by systematically modifying their crystal structure. Therefore crystal structure – band structure relationships need to be investigated in simple yet divers model systems.

One such system are the electron precise Zintl compounds of the ATt_3Pn_3 system (with *A* = Li-Rb, *Tt* = Si-Sn and *Pn* = P, As), for which a total of seven compounds in four different structure types are known, shown in Figure 1. Three of them show the same anionic structural motive. $LiGe_3P_3$ and $NaGe_3P_3$ crystallize in their own structure types in space groups *Pbam* (no. 55) and $Pmc2_1$ (no. 26), referred to as types **A** and **B**, respectively. [6,7] KGe_3As_3, KSn_3As_3, $RbGe_3As_3$ and $RbSn_3As_3$ crystallize in the KGe_3As_3 structure type in the orthorhombic space group *Pnma* (no. 62), referred to as type **D**.[8] For all three compounds two dimensional layers are formed as the anionic Tt-Pn structural motive with the alkali metal atoms being located in between them. The layers are built by corner-sharing of two different chains of tetrahedra. The first chain is built by corner-sharing $TtPn_4$ tetrahedra, marked in blue in Figure 1 and Figure 2a. The second chain, consists of corner-sharing Tt_2Pn_3 tetrahedra, marked in red. Both chains are connected alternatingly by corner-sharing and additional Tt-Pn (marked in green) bonds in between those chains to form a two dimensional $^2_\infty[TtPn_{4/2}Tt_2Pn_{3/2}]^{3-}$ network (see Figure 2c).

For all these compounds the alkali metal transfers its electron to the two-dimensional anionic substructure of Tt and Pn and thus has a theoretical partial charge of +1. For structures A, B and D within the two-dimensional layers all Pn atoms are $(3b\text{-}Pn)^0$, thus they have no charge (nb = n-fold bonded). For the Tt atoms, there are two different bonding situations with two $(4b\text{-}Tt)^0$ at the centre of the tetrahedra and one $(3b\text{-}Tt)^-$ at the tip of the tetrahedra marked in red. with partial charges of 0 and -1 respectively. Thus, the formal electron transfer would be from the alkali metal to the $(3b\text{-}Tt)^-$ for these electron precise Zintl compounds.

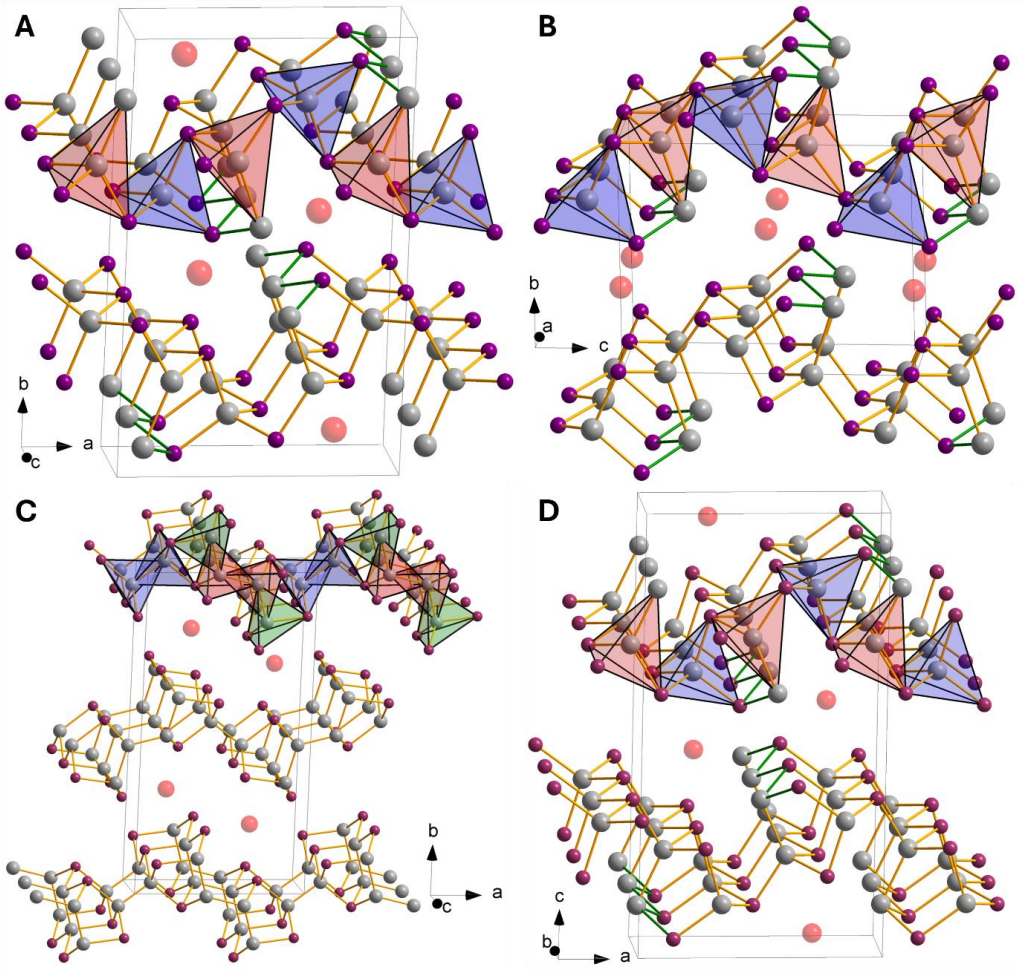

Figure 1. Crystal structures of the four different structure types of the 1-3-3 system with a) $LiGe_3P_3$ type, b) $NaGe_3P_3$ type, c) KSi_3As_3 type and d) KGe_3As_3 type.

Although the KSi_3As_3 structure type (type **C**), which crystallizes in the orthorhombic space group *Pbam* (no. 55), also forms a two-dimensional layered structure, the anionic structure is built by different building blocks.[9] Here only Tt_2Pn_3 tetrahedra are present, which also form two types of chains, which are connected by corner-sharing to two-dimensional layers. The first chain (marked in blue in Figure 1, Figure 2b and Figure 2d) consists of two interpenetrating tetrahedra and is connected to the second chain by corner-sharing. The second chain consists of two central interpenetrating Tt_2Pn_3 tetrahedra (marked in red) and two outer tetrahedra, marked in green, which are also interpenetrating with the central unit. One corner each of the inner and outer tetrahedra are the shared corners with the first chain. The alkali metal atoms are again located between these layers.

For structure type **C** the alkali metal, again, has a partial charge of +1 after transferring its valence electron. Here all Si atoms are $(4b\text{-}Si)^0$ with a neutral charge, while the As atoms are divided in two $(3b\text{-}As)^0$ and one $(2b\text{-}As)^-$ with a partial charge of -1. Therefore, the electron is transferred from K to As for this compound.

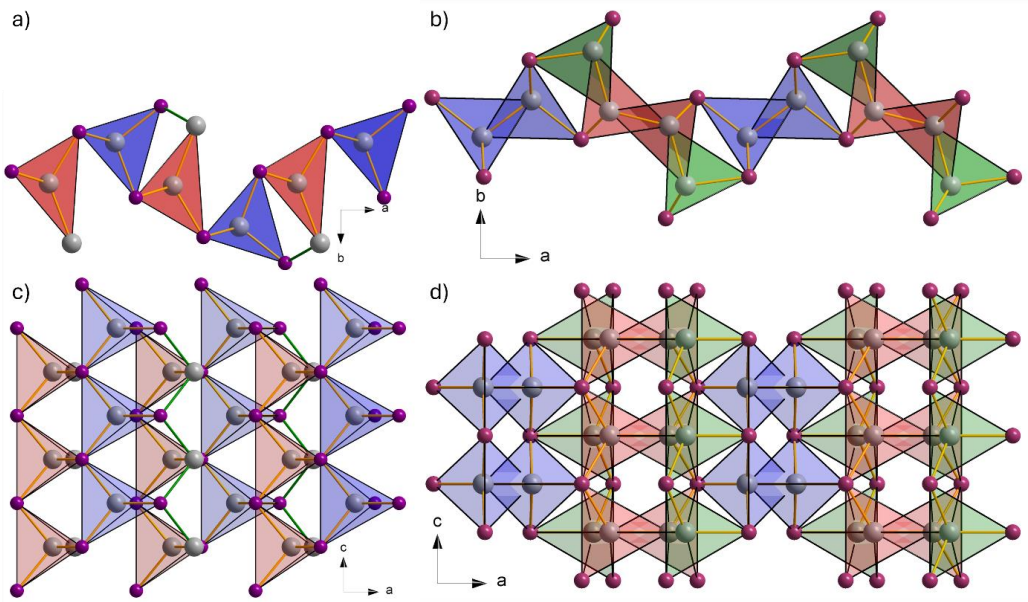

Figure 2. a) Side view of the layers of corner-sharing tetrahedra in structure types **A**, **B** and **D**. b) Side view of the layers of interpenetrating and corner-sharing tetrahedra in structure type **C**. c) Top view of the layers of corner-sharing tetrahedra in structure types **A**, **B** and **D**. c) Side view of the layers of interpenetrating and corner-sharing tetrahedra in structure type **C**.

Electronic structure calculations

The computational studies of all compounds in the ATt_3Pn_3 system (with *A* = Li-Rb, *Tt* = Si-Sn and *Pn* = P, As) were performed using the CRYSTAL17 program package and hybrid density functional methods.[10][11] A hybrid exchange-correlation functional after Perdew, Burke, and Ernzerhof (DFT-PBE0) was used, [12] Localized, Gaussian-Type triple ζ-valence + polarization level basis sets were used for Si, Ge, Sn, P and As atoms and split valence + polarization level basis sets for Li, Na, K and Rb.[13–20] The basis sets were derived from the molecular Karlsruhe basis sets. For the evaluation of Coulomb and exchange integrals (TOLINTEG), tight tolerance factors of 8, 8, 8, 8, 16 were used for all calculations. The reciprocal space of all calculations was sampled with Monkhorst-Pack-type *k*-point grids, their respective sizes can be found in the SI. The starting geometries were taken from experimental data. Both the lattice parameters and atomic positions were fully optimized within the constraints imposed by the space group symmetry. Further on all

optimized structures were confirmed to be true local minima by means of harmonic frequency calculations at Γ-point. For all compounds electronic band structures and density of states (DOS) were calculated. The Brillouin Zone paths were provided by the web service *SeeK-path* and a list can be found in the SI.[21]

Calculation results

Based on the experimentally determined crystal structure, cell parameters and atomic positions were optimized, and harmonic frequencies calculated. Since the compound KSi_3As_3 shows a slightly underoccupied K position (0.98), this was set to 1 for the calculation. For structures A to C all calculated cell parameters show only small deviations of up to 1.5 %. But for compounds with structure **D**, larger deviations of up to 6 % for the c-parameter were obtained (see SI Table S1). Since this is the axis perpendicular to layers of two-dimensional structure, these large deviations might arise from the anisotropy of the structure. Further on, since no imaginary frequencies were calculated, band structure, density of states and crystal orbital Hamilton population were calculated.

Table 1. Calculated indirect band gaps for all 1-3-3 compounds in eV. The bold letter represents the crystal structures described above.

A-Tt-Pn	**Li-P**		**Na-P**		**K-As**		**Rb-As**	
Si					2.75	**C**		
Ge	2.05	**A**	2.68	**B**	2.38	**D**	2.30	**D**
Sn					2.10	**D**	2.01	**D**

All compounds were found to be indirect band gap semiconductors (see Table 1 for values). Due to the limited number of compounds and their splitting in different structure type, a comparison between the band gap sizes cannot reveal large trends, but from a first glance the structure type seems to significantly influence the band gap. In other systems the elemental composition was the main influence on the size of band gap, even if multiple structure types were present *(3-1-2)*.[22] In this case the influence of the composition can mainly be seen for structures of type **D**, for which the band gap decreases from Ge to Sn and K to Rb. On the other hand, does the crystal structure seem to have a large influence on the size of the band gap, since $LiGe_3P_3$ has almost the lowest band gap (2.01 eV), although it is expected to have a much larger one if compared to other Li-Tt-P compounds. KSi_3As_3 on the other hand has the largest gap with 2.75 eV, but K-Tt-As compounds

are normally in the mid-range regarding band gaps. This could be a result of the different crystal structure type **C** with its slightly different charge distribution.

Band Dos Results

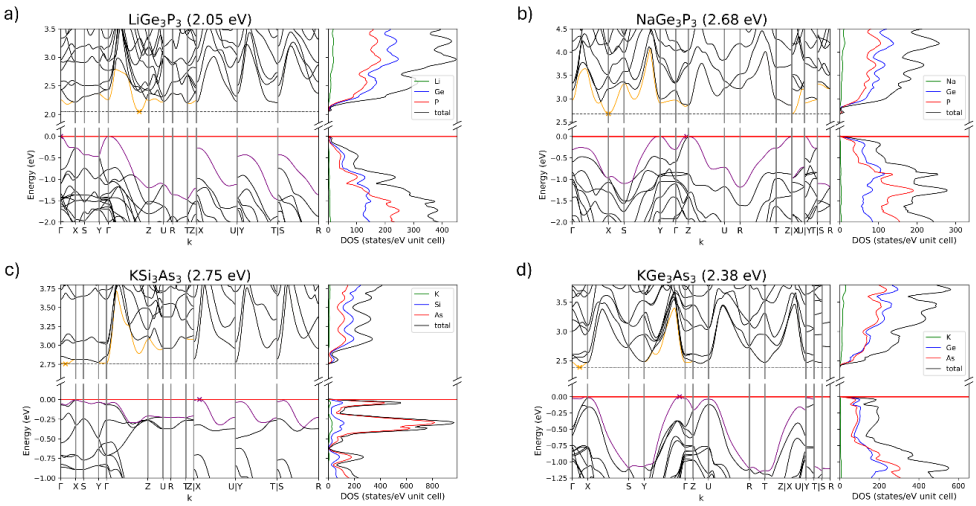

Figure 3. Band structure and density of states for a) $LiGe_3P_3$, b) $NaGe_3P_3$, c) KSi_3As_3 and d) KGe_3As_3 with indirect band gaps of 2.05 eV, 2.68 eV, 2.75 eV and 2.38 eV respectively.

Figure 3 shows band structures of $LiGe_3P_3$, $NaGe_3P_3$, KSi_3As_3 and KGe_3As_3 as representatives of structure types **A** to **D**. Since all crystal structures belong to the orthorhombic class, the k-path is the same for each compound. All compounds show a large dispersion in valence and conduction bands, which can be interpreted in such a way that the electron density is distributed over the two-dimensional layers and not only located at the atom positions. For all compounds the valance band maximum (VBM) and conduction band minimum (CBM) are other k-points than Γ, with the exception of the VBM of $LiGe_3P_3$. For all compounds with structure **D**, the VBM is located between Γ and Y (except for $RbGe_3As_3$, where it is at X), but all compounds show a second, almost identical VBM between Γ and X (Γ and Y for $RbGe_3As_3$) and the CBM between Γ and X. The VBM and CBM between Γ and X are close to each other on the k-path, thus they could be classified as

pseudo-direct band gap. From the other crystal structures this is also the case for structure **C**, where the CBM is close to X.

The density of states (DOS) is similar for structures **A**, **B** and **D**. For the valence bands Tt and Pn contribute equal amounts of states until about 1 eV. Below the contribution of Pn increases to about twice as much. For the conduction bands they again contribute equally. Over the whole energy range, the alkali metal has almost no contribution. For crystal structure **C**, the conduction band atom projected DOS shows the same contributions as the other compounds, but the for the valence bands As is main contributor. Si contributes about one fifth of the Pn states and the alkali metal also shows, although still low, some states. In previous systems, a shift of the VBM was often accompanied by an increase in alkali metal states, but for this system no such contribution can be seen, since there are no alkali metal states present at the VBM.[22] For KSi_3As_3 a small maximum can be seen for the alkali metal projected DOS below the Fermi-Level, but at the Fermi-Level there are no such states, thus the maximum arises from other k-points, for which the top valence band is close, but not at the Fermi-Level.

Mulliken

To get an insight on the electronic structure and bonding situation of these compounds a Mulliken analysis was conducted for each compound and Mulliken charges as well as overlap populations between neighbouring atoms were calculated. For the alkali metal charges of about 0.6 (Li) and 0.8 (Na, K and Rb) were obtained, which is in line with the ionic charge of +1 assigned via the Zintl concept. Li has a slightly smaller charge due to its higher electronegativity and small size.[23] For the *Pn* atoms charges of 0 up to -0.6 were obtained. Although a neutral charge is expected for structure types **A**, **B** and **D**, the *Pn* atoms have the higher electronegativity and thus pull the electrons of the polar *Tt*-*Pn* bonds towards them, resulting in the negative Mulliken charges. The charges are higher for more polar bonds. For KSi_3As_3 the 2b-As shows the most negative charge of -0.7, which is in line with its assigned negative theoretical charge. The 4b-*Tt* atoms show either a neutral or slightly positive Mulliken charge, due to the polar bonds. For the 3b-*Tt* atoms Mulliken charges of 0 to -0.2 were obtained and are always the most negatively charged *Tt* atoms within each compound, which again is in line with the assigned charge of -1 by the Zintl concept.

The overlap population shows values of about 0.3 for all Tt-Pn and Tt-Tt within the two-dimensional layer, which is line with the covalent bonds assigned by the crystal structure. Between Tt and its next but one neighbouring Tt atom, slightly repulsive interactions can be found with values of about -0.03. The same can be found for the Pn atoms and their next but one Pn

neighbours. The alkali metal atoms only show minor overlap populations with their neighbouring atoms, which is due to their primarily function as electron donors and thus ionic interactions.

COHP

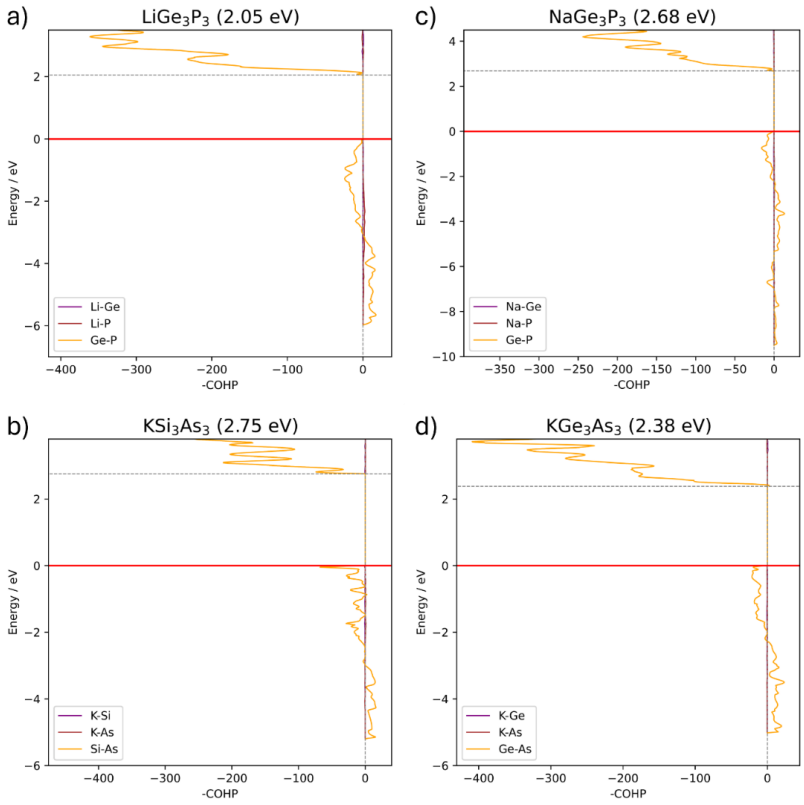

Figure 4. Crystal orbital Hamilton population of a) $LiGe_3P_3$, b) $NaGe_3P_3$, c) KSi_3As_3 and d) KGe_3As_3 for all heteroatomic interactions.

Figure 4 shows the crystal orbital Hamilton population (COHP) of $LiGe_3P_3$, $NaGe_3P_3$, KSi_3As_3 and KGe_3As_3 with crystal structures **A** to **D**, respectively. Like the DOS the COHP looks very similar for all compounds with mostly minor Tt-Pn antibonding states, from -3 eV to the Fermi-Level and for the conduction bands. While for $LiGe_3P_3$ and $NaGe_3P_3$ the Tt-Pn projected COHP falls back to 0 right below the Fermi-Level, for KSi_3As_3 and all compounds with structure type **D**, there is a local maximum of Tt-Pn states present at the Fermi-Level. This is especially prominent for KSi_3As_3, where the maximum at the Fermi-Level has about twice as much states as the average projected COHP.

For all systems that have been discussed, the projected DOS shows many and more or less exclusively Pn states, while the COHP shows only minor interactions below the Fermi-Level.[22]

Thus for these systems it was assumed, that most Pn states right below the Fermi-Level belong to non-bonding states, like the free electron pair(s). But since for compounds of the 1-3-3 system with structures **C** and **D** on one hand equal numbers of states for Tt and Pn were found and the COHP shows Tt-Pn anti-bonding interactions, they might be responsible for the VBM position.

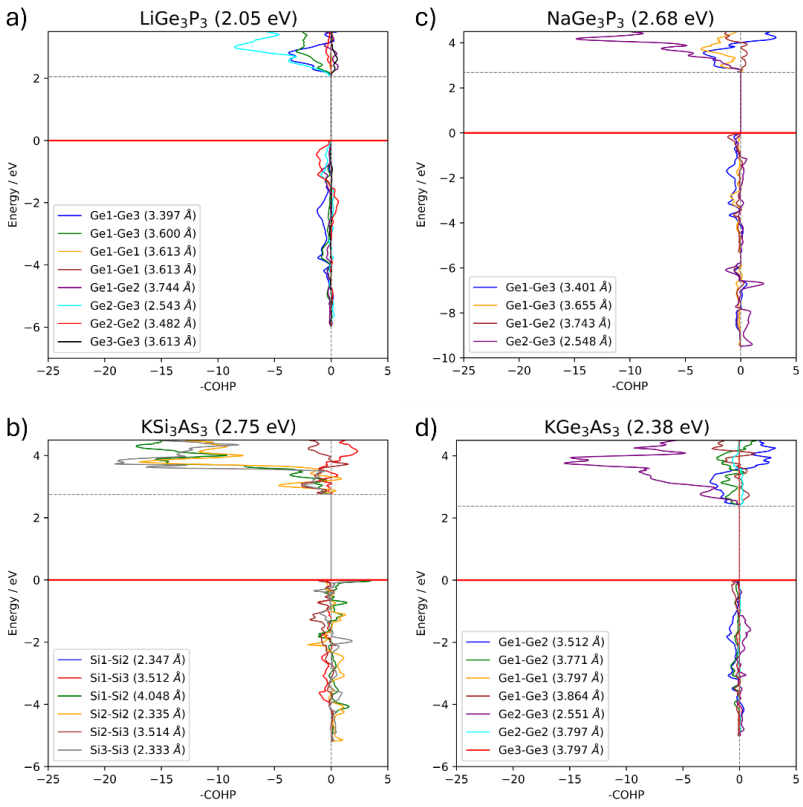

Figure 5. Crystal orbital Hamilton population of a) $LiGe_3P_3$, b) $NaGe_3P_3$, c) KSi_3As_3 and d) KGe_3As_3 for all Tt-Tt interactions of neighbouring atoms.

Figure 5 shows the COHP for all Tt-Tt interactions of neighbouring atoms, again with one example for each structure type. For all compounds several Tt-Tt interactions can be found, which are mostly of anti-bonding nature for valence and conduction bands. For structures of type **C** and **D** there are also some bonding interactions below the band gap and for higher conduction bands, especially for KSi_3As_3, where a maximum can be found right at the Fermi-Level. Although there is no direct correlation between the occurrence of pseudo-direct band gaps and the Tt-Tt COHP that stands out, but for structure types **C** and **D** there are always Tt-Tt interactions right below the

Fermi-Level, while Tt-Tt projected COHPs for $LiGe_3P_3$ and $NaGe_3P_3$ are 0 there. Thus they might also play a role in shifting the VBM away from Γ, but are probably not the main contributor.

Conclusion

For all compounds of the ATt_3Pn_3 system (with *A* = Li-Rb, *Tt* = Si-Sn and *Pn* = P, As) the crystal structure was optimized and band structure, density of states (DOS) and crystal orbital Hamilton population (COHP) calculated. The size of the band gap is mainly dependent on the electronegativity differences, but for KSi_3As_3 the different structure motive present for the two-dimensional layer, which also differs in its electronic charge distribution, a lower band gap than expected was calculated. Bonds and trends of partial charges imposed by the crystal structure could be verified by a Mullikan analysis.

All band structures show indirect band gaps, with both valence band maximum (VBM) and conduction band minimum (CBM) at other k-points than Γ. Structures with type **D** show two maxima, with identical energies, which are close to the CBM on the k-path, thus pseudo-direct energy transitions might be possible. The DOS reveals that the tetrel atoms are contributing the most states at the Fermi-Level, except for KSi_3As_3, where its As, which is rather untypical. In previous studies here mostly Pn non-bonding states could be found.[22] For these compounds anti-bonding Tt-Pn states can found at the Fermi-Level in the COHP as well as equal numbers of Tt and Pn states in the respective projected DOS. Therefore, it is possible that these high energy states rise the bands at the k-points assigned as valence band maxima, especially for structure types **C** and **D**, which show a sharp edge of states at the Fermi-Level. Additional Tt-Tt bonding and anti-bonding interactions can be found in this energy range, which might also contribute to the rise of the VBM.

Further research on in this system should focus on structure predictions for the unknown compounds as well as investigations of possible phase transitions between structure types **A**, **B** and **D**. Here the Sb compounds could also be of interest, since they might give some hints on how much the Tt-Tt interactions influence the rise of the valence bands. Since for these compounds larger Tt-Tt distances are expected for the central atoms in the tetrahedra, they should weaken the Tt-Tt interactions, which in comparison to the presented data could give some insight on their contribution at the Fermi-Level.

References

[1] H. Hosono, *Journal of Non-Crystalline Solids* **2006**, *352*, 851.
[2] K. S. Kazunori Sato, H. K.-Y. Hiroshi Katayama-Yoshida, *Jpn. J. Appl. Phys.* **2000**, *39*, L555.
[3] A. Mehta, A. Mishra, S. Basu, N. P. Shetti, K. R. Reddy, T. A. Saleh, T. M. Aminabhavi, *Journal of environmental management* **2019**, *250*, 109486.
[4] T. Todorov, T. Gershon, O. Gunawan, Y. S. Lee, C. Sturdevant, L.-Y. Chang, S. Guha, *Advanced Energy Materials* **2015**, *5*.
[5] J. Wan, X. Xu, G. Zhang, Y. Li, K. Feng, Q. Peng, *Energy Environ. Sci.* **2017**, *10*, 1739.
[6] H. Eickhoff, C. Sedlmeier, W. Klein, G. Raudaschl-Sieber, H. A. Gasteiger, T. F. Fässler, *Zeitschrift anorg allge chemie* **2020**, *646*, 95.
[7] K. Feng, W. Yin, R. He, Z. Lin, S. Jin, J. Yao, P. Fu, Y. Wu, *Dalton transactions (Cambridge, England : 2003)* **2012**, *41*, 484.
[8] M. Khatun, S. S. Stoyko, A. Mar, *Journal of Solid State Chemistry* **2016**, *238*, 229.
[9] W. M. Hurng, J. D. Corbett, S. L. Wang, R. A. Jacobson, *Inorg. Chem.* **1987**, *26*, 2392.
[10] R. Dovesi, V. R. Saunders, C. Roetti, R. Orlando, C. M. Zicovich-Wilson, F. Pascale, B. Civalleri, K. Doll, N. M. Harrison, I. J. Bush **2017**.
[11] R. Dovesi, A. Erba, R. Orlando, C. M. Zicovich-Wilson, B. Civalleri, L. Maschio, M. Rérat, S. Casassa, J. Baima, S. Salustro et al., *Wiley Interdiscip. Rev.: Comput. Mol. Sci.* **2018**, *8*.
[12] J. P. Perdew, W. Yang, K. Burke, Z. Yang, E. K. U. Gross, M. Scheffler, G. E. Scuseria, T. M. Henderson, I. Y. Zhang, A. Ruzsinszky et al., *Proc. Natl. Acad. Sci. U. S. A.* **2017**, *114*, 2801.
[13] A. J. Karttunen, T. F. Fässler, *Chemistry (Weinheim an der Bergstrasse, Germany)* **2014**, *20*, 6693.
[14] A. J. Karttunen, T. F. Fässler, M. Linnolahti, T. A. Pakkanen, *Inorg. Chem.* **2011**, *50*, 1733.
[15] T. M. F. Restle, J. V. Dums, G. Raudaschl-Sieber, T. F. Fässler, *Chemistry (Weinheim an der Bergstrasse, Germany)* **2020**, *26*, 6812.
[16] G. Sansone, L. Maschio, D. Usvyat, M. Schütz, A. Karttunen, *The journal of physical chemistry letters* **2016**, *7*, 131.
[17] B. Scheibe, S. I. Ivlev, A. J. Karttunen, F. Kraus, *Eur J Inorg Chem* **2020**, *2020*, 1319.
[18] B. Scheibe, A. J. Karttunen, F. Weigend, F. Kraus, *Chemistry (Weinheim an der Bergstrasse, Germany)* **2021**, *27*, 2381.
[19] L. M. Scherf, A. J. Karttunen, O. Pecher, P. C. M. M. Magusin, C. P. Grey, T. F. Fässler, *Angewandte Chemie (International ed. in English)* **2016**, *55*, 1075.
[20] R. E. Stene, B. Scheibe, A. J. Karttunen, W. Petry, F. Kraus, *Eur J Inorg Chem* **2019**, *2019*, 3672.
[21] Y. Hinuma, G. Pizzi, Y. Kumagai, F. Oba, I. Tanaka, *Comput. Mater. Sci.* **2017**, *128*, 140.
[22] S. Zeitz, H. Antoniuk, V. Hlukhyy, T. F. Fässler, *Chemistry (Weinheim an der Bergstrasse, Germany)* **2024**, *30*, e202400002.
[23] A. F. Holleman, *Lehrbuch der anorganischen Chemie*, Walter de Gruyter GmbH & Co KG, **2019**.

5.7 Electronic structure analysis of $A_2Tr_2Pn_3$ compounds with A = Na Cs; Tr = Al, Ga, In; Pn = As, Sb

Sabine Zeitz, Zoe Listmann, Thomas F. Fässler

Manuscript for publication

Electronic structure analysis of compounds of $A_2Tr_2Pn_3$ compounds with *A* = Na-Cs; *Tr* = Al, Ga, In; *Pn* = As, Sb

Sabine Zeitz[a], Zoe Listmann[a], Thomas F. Fässler[a]

Abstract

All eleven known electron precise Zintl compounds of the $A_2Tr_2Pn_3$ system (*A* = Na-Cs; *Tr* = Al, Ga, In; *Pn* = As, Sb) crystallize in the same crystal structure consisting of two-dimensional layers of edge- and corner-sharing $TrPn_4$ tetrahedra which are further connected by *Pn*-*Pn* bonds. For all compounds the crystal structure was optimized and band structure, density of states and crystal orbital Hamilton population were calculated on a DFT/PBE0 level of theory. Three compounds, $K_2In_2As_3$, $Rb_2In_2Sb_3$ and $Cs_2In_2Sb_3$, were found to be direct and $K_2In_2Sb_3$ pseudo-direct band gap semiconductors. The direct band gaps seem to be caused by an absence of *Tr*-*Tr* and *Pn*-*Pn* interactions right above the Fermi-Level, which otherwise would move the conduction band minimum away from Γ. For compounds with a direct band gap these states are shifted to higher energies, probably caused by stronger interactions between neighbouring *Tr* and *Pn* atoms. For most compounds additionally a flat band between Γ and B can be found, which is caused by mainly non-bonding *Tr* and *Pn* states. The size of the band gap is determined by the electronegativity of the pnictogen and alkali metal, and their difference.

Introduction

Light Emitting Diodes (LEDs), transistors, thermoelectrics and solar cells are just some examples of the wide range of semiconductor applications. As their requirements become more specialised and bandgap tuning becomes more precise, intelligent material design and accurate electronic structure prediction are important.[1–5] In particular, for material tunability, it is advantageous for a class of compounds to not only have the same structure but also similar electronic properties. Furthermore, being able to predict, for example, the bandgap size and nature just by knowing the composition and structure could make the materials design process even more efficient. In order to find band-structure-crystal-structure relationships, which help to predict possible properties based on the structure, fundamental research on simple compound systems is necessary.

One such system is the $A_2Tr_2Pn_3$ system (*A* = Na-Cs; *Tr* = Al, Ga, In; *Pn* = As, Sb) with total of eleven known compounds, which all crystallize in the $K_2Al_2Sb_3$ structure type in space group $P2_1/c$ (no. 14).[6–15] The crystal structure consists of two-dimensional layers within the ab-plane of edge- and corner sharing $TrPn_4$ tetrahedra and alkali metal atoms with are situated in between those layers (see Figure 1a). The layers are built by a recurring unit of four tetrahedra (marked in green in Figure 1b), which are connected via corner-sharing with neighbouring units in such a way, that the units are shifted by ½ along the b-axis. Within the recurring unit there are two edge-sharing double-tetrahedra which are connected by corner sharing and an additional *Pn*-*Pn* bond at the centre of the unit (bond marked in red in Figure 1b).

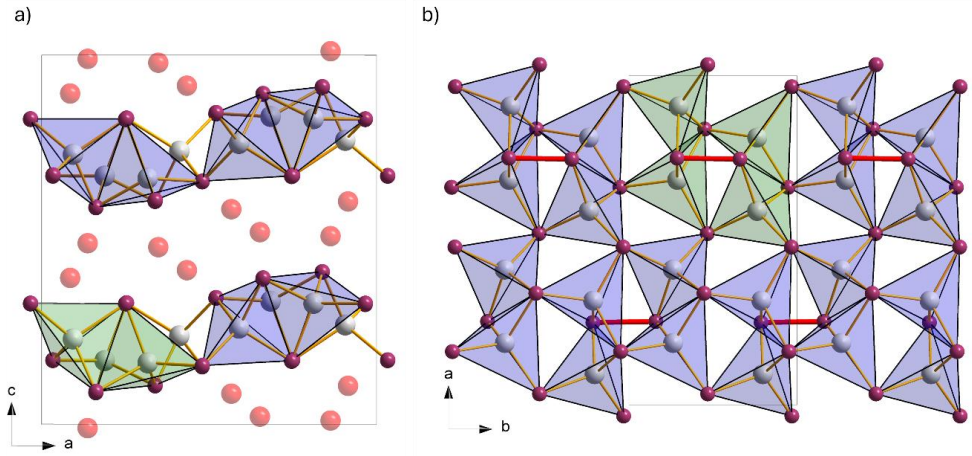

Figure 1. Crystal structure of the $K_2Al_2Sb_3$ structure type. Alkali metals, triel and pnictogen are represented in red, grey, and purple, respectively. a) Side view of the layers with marked structural motive. b) Top view on one layer with central structural motive of four edge- and corner-sharing $TrPn_4$ tetrahedra is marked in green. Additional *Pn*-*Pn* bond is marked in red.

All compounds of the 2-2-3 system can be classified as electron precise Zintl-compounds. The alkali metal transfers its electron to the anionic substructure of the triel and pnictogen and has a theoretical charge of +1. The electron is formally transferred to the triel, although the pnictogen has the higher electronegativity. The two-dimensional polyanion $^2_\infty[TrPn_{4/3}]^{2-}$ consists of (4b-*Tr*)$^-$ and (3b-*Pn*)^0 (nb = n-fold bonding). The latter is either bond to three triel or two triel and one adjacent pnictogen atom(s).

Electronic structure calculations

The computational studies of all compounds in the $A_2Tr_2Pn_3$ system (*A* = Na-Cs; *Tr* = Al, Ga, In; *Pn* = As, Sb) were performed using the CRYSTAL17 program package and hybrid density functional methods.[16][17] A hybrid exchange-correlation functional after Perdew, Burke, and Ernzerhof (DFT-

PBE0) was used, [18] Localized, Gaussian-Type triple ζ-valence + polarization level basis sets were used for Al, Ga, In, As and Sb and split valence + polarization level basis sets for Na, K, Rb and Cs. The basis sets were derived from the molecular Karlsruhe basis sets.[19–24] For the evaluation of Coulomb and exchange integrals (TOLINTEG), tight tolerance factors of 8, 8, 8, 8, 16 were used for all calculations. The reciprocal space of all calculations was sampled with 3×5×3 Monkhorst-Pack-type *k*-point grids. The starting geometries were taken from experimental data. Both lattice parameters and atomic positions were fully optimized within the constraints imposed by the space group symmetry. Further on all optimized structures were confirmed to be true local minima by means of harmonic frequency calculations at Γ-point. For all compounds and models electronic band structures, density of states (DOS) and heteroatomic crystal orbital Hamilton populations (COHP) were calculated. The Brillouin Zone path of Γ-Z-D-B-Γ-A-E-Z-C_2-Y_2-Γ was provided by the web service *SeeK-path*.[25]

Calculation Results

For all compounds within a structure optimization based on the crystallographic data available was calculated. All calculated cell parameters show a maximum deviation of 1.7 % from the experimental ones (see Table 1, Supporting information) and for each compound harmonic frequencies at Γ were calculated. Three compounds, $Na_2Ga_2As_3$, $Na_2In_2Sb_3$ and $Rb_2In_2Sb_3$, showed one imaginary frequency, therefore these structures were reoptimized after distorting the structure along that frequency *(calculations are still nor finished...)*. Since no further imaginary frequencies were found, band structures, density of states and crystal orbital Hamilton populations were calculated. All calculated band gaps can be found in Table *1*. Three compounds were found to be direct band gap semiconductors, namely $K_2In_2As_3$, $Rb_2In_2Sb_3$ and $Cs_2In_2Sb_3$, and one compound, $K_2In_2Sb_3$ showed a pseudo-direct band gap. All remaining compounds have indirect band gaps.

Table 1. Calculated band gaps for the 2-2-3 system. Direct, indirect, and pseudo-direct band gaps are denoted as (d), (in) and (pd), respectively.

A-Tr-Pn	**Na-As**	**K-As**	**Na-Sb**	**K-Sb**	**Rb-Sb**	**Cs-Sb**
Al	2.69 eV (in)		1.87 eV (in)	2.16 eV (in)		
Ga	2.65 eV (in)	2.87 eV (in)		2.13 eV (in)		
In		2.38 eV (d)	1.82 eV (in)	2.15 eV (pd)	1.96 eV (d)	2.01 eV (d)

The size of the band gaps scales with the elemental combination, depending on their electronegativity differences. The most influence on the band gap is given by the pnictogen, since

all Sb compound show gaps, which are up to 0.7 eV smaller than the corresponding arsenides. This can be explained by the larger electronegativity difference between *Tr* and As, than *Tr* and Sb.[26] The same can be seen for compounds that only differ in their alkali metal. For compounds which have different *Tr* atoms, the band gaps are very close (e.g. K-*Tr*-Sb differ by only 0.03 eV) with one exception between $K_2Ga_2As_3$ and $K_2In_2As_3$. Here the In compound shows a band gap almost 0.5 eV smaller, which might be caused by a switch to a direct band gap. This phenomenon was already found for Na_3InP_2, whose direct band gap was also significantly smaller than its corresponding indirect Ga compound, although there the crystal structure changed as well. *(cite 3-1-2 paper -> same behaviour)*

Band Dos Results

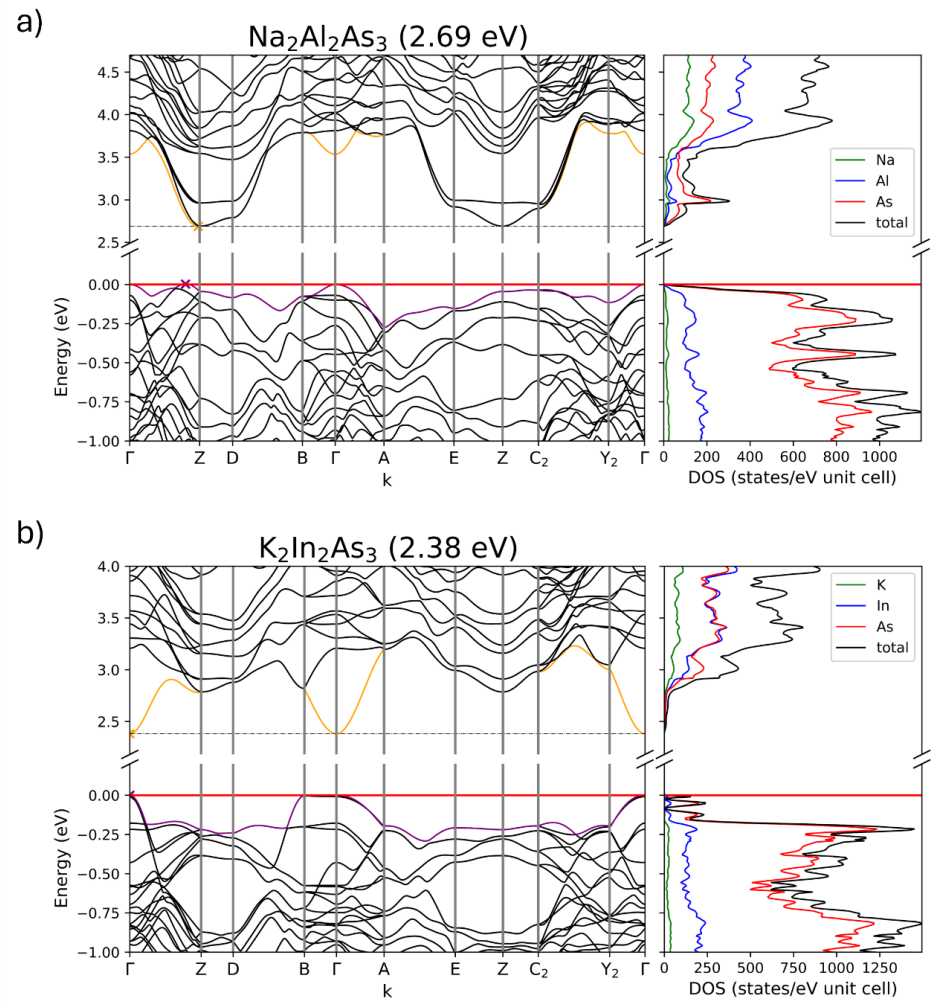

Figure 2. Band structure and density of states of a) $Na_2Al_2As_3$ and b) $K_2In_2As_3$ with a direct band gap of 2.69 eV and an indirect band gap of 2.38 eV, respectively.

Figure 2 shows two exemplarily band structures of $Na_2Al_2As_3$ and $K_2In_2As_3$ which show an indirect and a direct band gap, respectively. The general shape of the band structure is the same for all compounds. Valence and conduction bands show disperse bands, especially around the band gap, but the dispersion is slightly decreasing for compounds with heavier alkali metals. All but two compounds, $Na_2Al_2As_3$ and $Na_2In_2Sb_3$, show a very flat band between Γ and B, therefore their valence band maximum (VBM) is hard to located at one specific point, since all k-points between them have almost the same energy. The conduction band maximum (CBM) is either located at Z (indirect band gaps) or at Γ (direct band gaps). For $K_2In_2Sb_3$ the difference between direct gap at Γ and indirect Γ->Z transition is smaller than 0.02 eV, thus the band gap can be seen as pseudo-direct.

The density of states also shows similar trends for all compounds. The valence band consist mostly of *Pn* states, with, for the lower bands, some contribution of *Tr* and only few alkali metal states. In previous systems a shift of the VBM was caused by additional alkali metal states close to the Fermi-Level, but in this system, there are no such states present.[27] *(cite 3-1-2)* Instead the top two, almost completely degenerate, valence bands consist of pnictogen and triel states, in which the latter makes up a significantly larger portion compared to the lower valence bands. This can be seen as a sharp maximum in the DOS for all compounds with a flat band at the Fermi-Level between Γ and B.

Mulliken

To get a further insight into the electronic structure of the $A_2Tr_2Pn_3$ system, a Mulliken analysis was conducted for each compound. With values of about +0.8 all alkali metals the Mullikan charges are similar to the proposed charge of +1, which confirms the electron transfer to the anionic substructure. For the triel and pnictogen the Mullikan charges are somewhat reversed from what is expected by the valence electron distribution. While triel atoms have Mullikan charges of +0.1 to +0.3, pnictogens show Mullikan charges of -0.5 to -0.9. This might be caused by the polar character of the bond, since the pnictogen has the larger electronegativity and thus shifts of the electron density towards itself, which would explain the slightly negative Mullikan charge. For the *Pn* atomic positions, which forms two bonds to neighbouring *Tr* and one bond to an adjacent *Pn* atom, the Mullikan charge is about 0.1 to 0.3 larger compared to the *Pn* atoms with three *Tr*-*Pn* bonds, due to the non-polar *Pn*-*Pn* bond, which results in one less polar bond and thus slightly less attracted electron density.

For a further insight on the bonding situation the overlap population between neighbouring atoms was calculated. With values of 0.2 to 0.3 covalent bonds can be found between *Tr* and *Pn* as well as *Pn* and *Pn*. The alkali metals have little to no interactions with their neighbouring atoms, thus their interactions are of ionic nature. Further on slightly negative overlap populations can be found for adjacent *Tr* atoms with the highest values for *Tr*-*Tr* interactions of edge-sharing $TrPn_4$ tetrahedra, which are also the closest *Tr*-*Tr* neighbours. An exception are the Al compounds, for which these interactions show smaller values than the other interactions.

COHP

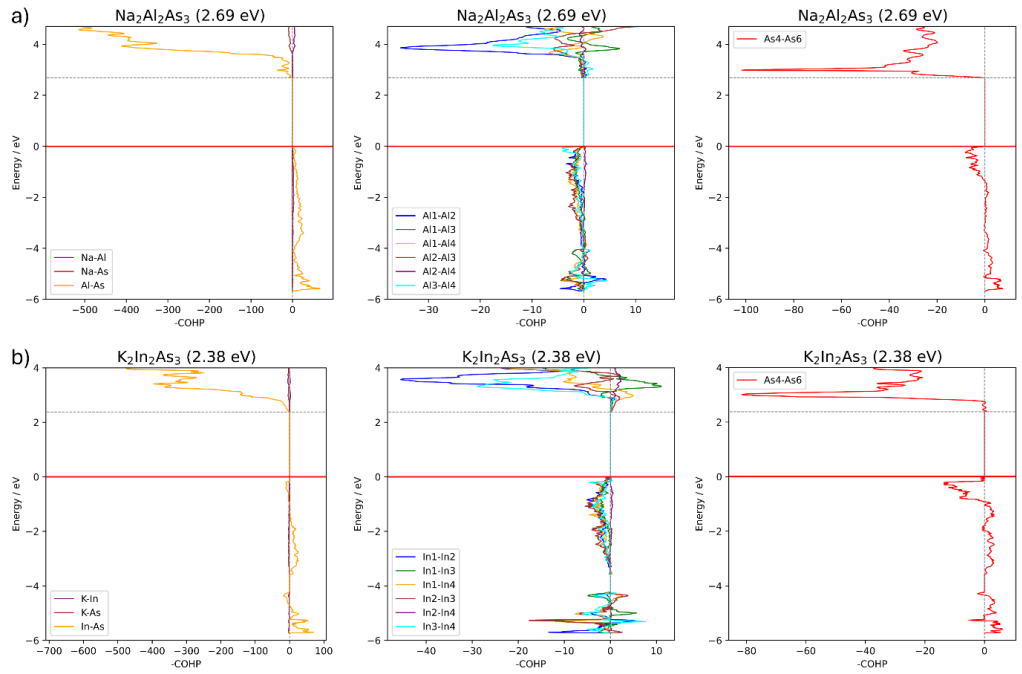

Figure 3. Crystal orbital Hamilton population of all heteroatomic interactions as well as Tr-Tr and Pn-Pn interactions of neighbouring and bonding interactions for a) $Na_2Al_2As_3$ and b) $K_2In_2As_3$.

Figure 3 shows the crystal orbital Hamilton populations (COHP) for all heteroatomic as well as between neighbouring *Tr-Tr* and *Pn-Pn* interactions again for a) $Na_2Al_2As_3$ and b) $K_2In_2As_3$ with an indirect and direct band gap, respectively. For the heteroatomic interactions, which are very similar for all compounds, mostly *Tr-Pn* interactions can be seen, but they are only minor for the valence bands, although many *Pn* states are present in the DOS. For the conduction bands large *Tr-Pn* anti-bonding interactions can be seen. The *Tr-Tr* interactions show, as it can be seen in Figure 3, no or slightly bonding interactions for the conduction bands. In other systems a sharp increase in Tr-Tr anti-bonding interactions was observed above the band gap, but here no real distinction between direct or indirect band gap compounds can be seen. *(cite 3-1-2 paper)*.

As for comparing the Tr-Tr interactions at the Fermi-Level for $Na_2Al_2As_3$ and $K_2In_2As_3$ only the latter shows the flat top valence band(s) in between Γ and B. At the same time in the *Tr-Tr* COHP a sharp edge in anti-bonding states can be found for In1-In4 and In2-In3 in $K_2In_2As_3$, while $Na_2Al_2As_3$ only has Al3-Al4 states right below the Fermi-Level. Comparing this to all other *Tr-Tr* projected COHPs, only those, that show the Γ-B flat top valence band also show the *Tr*1-*Tr*4 and *Tr*2-*Tr*3 edge. Thus,

these long-range repulsions seem to influence the energy between the k-points and could lead to a lifted top valence band between Γ and B.

Another difference between compounds with direct and indirect band gap can be seen in the *Pn-Pn* projected COHP. The general shape of the *Pn-Pn*-bond projected COHP shows anti-bonding states below and above the band gap for all compounds. But compounds with a direct band gap show a small interval right above the band gap, where only few states can be seen, while compounds with indirect band gap have a sharp increase in *Pn-Pn* states. The shape of these interactions is similar to the Tr-Tr projected COHP in the A_3TrPn_2 system, which were identified as possible source for the indirect band gaps of some compounds. Interestingly in this system the same behaviour can be seen for the Pn-Pn interactions, so they might be responsible for the direct band gaps of the In compounds.

Conclusion

For eleven experimentally known compounds within the $A_2Tr_2Pn_3$ system (*A* = Na-Cs; *Tr* = Al, Ga, In; *Pn* = As, Sb) the crystal structure was optimized as well as band structure, density of states and crystal orbital Hamilton population (COHP) calculated. Three compounds, $K_2In_2As_3$, $Rb_2In_2Sb_3$ and $Cs_2In_2Sb_3$ showed a direct band gap and $K_2In_2Sb_3$ a pseudo-direct band gap. The size of the band gap is mainly determined by the electronegativity of the pnictogen with arsenides having larger gaps than antimonides. Further on the bonding situation imposed by the crystal structure was confirmed by a Mulliken analysis.

A detailed investigation of the COHP calculations revealed, that the *Tr* and *Pn* atoms and their interactions seem to be the main factor for the occurrence of direct or indirect band gaps. The valence band maximum is located either at Γ or between Γ and B, with the latter being caused by a flat band at the Fermi-Level consisting of mostly *Tr* and *Pn* states, which are probably of non-bonding nature. The conduction band minimum (CBM) is located at Γ if the compound shows no or only minor *Tr-Tr* and *Pn-Pn* interactions right above the Fermi-Level. For indirect band gaps the CBM is accompanied by a sharp increase in anti-bonding *Pn-Pn* and *Tr-Tr* interactions right above the band gap. These occurrences might be caused by stronger interactions between neighbouring *Tr* and *Pn* atoms, which increases the splitting of states. They then end up at higher energies, resulting in direct band gaps.

Further investigations should focus on modelling the unknown compounds within the $A_2Tr_2Pn_3$ to fill in the missing links between the structures. With all compounds the trends determined can be verified further and expanded. For even further insight calculations on the phosphides would be the next step. Further on other systems with two-dimensional layered crystal structures could be

calculated to see if the results are limited to the model system or are applicable for a wider range of compounds.

References

[1] H. Hosono, *Journal of Non-Crystalline Solids* **2006**, *352*, 851.
[2] K. S. Kazunori Sato, H. K.-Y. Hiroshi Katayama-Yoshida, *Jpn. J. Appl. Phys.* **2000**, *39*, L555.
[3] T. Todorov, T. Gershon, O. Gunawan, Y. S. Lee, C. Sturdevant, L.-Y. Chang, S. Guha, *Advanced Energy Materials* **2015**, *5*.
[4] J. Wan, X. Xu, G. Zhang, Y. Li, K. Feng, Q. Peng, *Energy Environ. Sci.* **2017**, *10*, 1739.
[5] A. Mehta, A. Mishra, S. Basu, N. P. Shetti, K. R. Reddy, T. A. Saleh, T. M. Aminabhavi, *Journal of environmental management* **2019**, *250*, 109486.
[6] W. Blase, G. Cordier, L. Poth, K. G. Weil, *Zeitschrift für Kristallographie - Crystalline Materials* **1995**, *210*, 60.
[7] G. Cordier, H. Ochmann, *Zeitschrift für Kristallographie - Crystalline Materials* **1991**, *197*, 289.
[8] G. Cordier, H. Ochmann, *Zeitschrift für Kristallographie - Crystalline Materials* **1991**, *197*, 291.
[9] G. Cordier, H. Ochmann, *Zeitschrift für Kristallographie - Crystalline Materials* **1991**, *197*, 287.
[10] G. Cordier, H. Ochmann, *Zeitschrift für Kristallographie - Crystalline Materials* **1991**, *197*, 293.
[11] G. Cordier, H. Ochmann, *Zeitschrift für Kristallographie - Crystalline Materials* **1991**, *197*, 281.
[12] G. Cordier, H. Ochmann, *Zeitschrift für Kristallographie - Crystalline Materials* **1991**, *197*, 283.
[13] G. Cordier, H. Ochmann, *Zeitschrift für Kristallographie - Crystalline Materials* **1991**, *197*, 285.
[14] G. Cordier, H. Ochmann, H. Schäfer, *Revue de chimie minérale* **1984**, *21*, 282.
[15] O. Gourdon, F. Boucher, J. Gareh, M. Evain, C. O'Connor, J. Jin-Seung, *Acta Crystallogr C Cryst Struct Commun* **1996**, *52*, 2963.
[16] R. Dovesi, V. R. Saunders, C. Roetti, R. Orlando, C. M. Zicovich-Wilson, F. Pascale, B. Civalleri, K. Doll, N. M. Harrison, I. J. Bush **2017**.
[17] R. Dovesi, A. Erba, R. Orlando, C. M. Zicovich-Wilson, B. Civalleri, L. Maschio, M. Rérat, S. Casassa, J. Baima, S. Salustro et al., *Wiley Interdiscip. Rev.: Comput. Mol. Sci.* **2018**, *8*.
[18] J. P. Perdew, W. Yang, K. Burke, Z. Yang, E. K. U. Gross, M. Scheffler, G. E. Scuseria, T. M. Henderson, I. Y. Zhang, A. Ruzsinszky et al., *Proc. Natl. Acad. Sci. U. S. A.* **2017**, *114*, 2801.
[19] T. M. F. Restle, J. V. Dums, G. Raudaschl-Sieber, T. F. Fässler, *Chem.* **2020**, *26*, 6812.
[20] T. M. F. Restle, S. Zeitz, J. Meyer, W. Klein, G. Raudaschl-Sieber, A. J. Karttunen, T. F. Fässler, *Zeitschrift anorg allge chemie* **2021**, *647*, 1804.
[21] T. M. F. Restle, S. Zeitz, P. M. Stanley, A. J. Karttunen, J. Meyer, G. Raudaschl-Sieber, W. Klein, T. F. Fässler, *Chem.* **2024**, *30*, e202304097.
[22] B. Scheibe, S. I. Ivlev, A. J. Karttunen, F. Kraus, *Eur. J. Inorg. Chem.* **2020**, *2020*, 1319.
[23] B. Scheibe, A. J. Karttunen, F. Weigend, F. Kraus, *Chem.* **2021**, *27*, 2381.
[24] R. E. Stene, B. Scheibe, A. J. Karttunen, W. Petry, F. Kraus, *Eur. J. Inorg. Chem.* **2019**, *2019*, 3672.
[25] Y. Hinuma, G. Pizzi, Y. Kumagai, F. Oba, I. Tanaka, *Comput. Mater. Sci.* **2017**, *128*, 140.
[26] A. F. Holleman, *Lehrbuch der anorganischen Chemie*, Walter de Gruyter GmbH & Co KG, **2019**.
[27] S. Zeitz, H. Antoniuk, V. Hlukhyy, T. F. Fässler, *Chem.* **2024**, *30*, e202400002.

5.8 Open Sn Framework Structure Hosting Bi Guest atoms – Synthesis, Crystal and Electronic Structure of $Na_{13}Sn_{26}Bi$

S. Zeitz, M. Boyko, S. Ponou, V. Hlukhyy, T.F. Fässler

published in

Chemistry — A European Journal **2024**, e202403592

Check for updates

Chemistry–A European Journal

Research Article
doi.org/10.1002/chem.202403592

Chemistry Europe
European Chemical Societies Publishing

www.chemeurj.org

Hot Paper

Open Sn Framework Structure Hosting Bi Guest atoms– Synthesis, Crystal and Electronic Structure of $Na_{13}Sn_{26}Bi$

S. Zeitz,[a] M. Boyko,[a] S. Ponou,[a] V. Hlukhyy,[a] and T. F. Fässler*[a]

Dedicated to Professor Martin Jansen on the Occasion of His 80th Birthday

The large variety of structures of Zintl phases are generally well understood since their anionic substructures follow bonding rules according to the valence concept. But there are also exceptions, which make the semiconductors especially interesting in terms of structure-property relationships. Although several Na-Sn-Pnictides with a variety of structural motives are known, up to this point no ternary compound in the Na-Sn-Bi system has been described. In this paper we present the Zintl-phase $Na_{13}Sn_{25.73}Bi_{1.27}$ comprising a complex, open-framework structure of Sn atoms, with one mixed Sn/Bi site, hosting Na atoms. An additional Bi atom is loosely connected with only weak contacts to the framework filling a larger cavity within the network. According to band structure calculations of the two ordered variants with either full occupation of the mixed site with Sn or Bi, resulting in $Na_{13}Sn_{26}Bi$ and $Na_{13}Sn_{24}Bi_3$, respectively, both compounds are semiconductors with band gaps of 0.5 eV. A comparison of the band structures with the structurally related binary compounds Na_5Sn_{13} and Na_7Sn_{12} shows that only the perfectly charge balanced Na_7Sn_{12} is a semiconductor whereas Na_5Sn_{13} is metallic. The rather specific electronic situation in the ternary compound is traced back to the loosely bound Bi atom, which acts as a guest atom according to $Bi_x@Na_{13}Sn_{26-y}Bi_y$, with $x=1$ and $y=0.27$, capable to change its oxidation state and thus to uptake additional electrons allowing the system to be a semiconductor. Therefore, $Na_{13}Sn_{25.73}Bi_{1.27}$ can be understood as a rare example of an open framework structure of Sn atoms comprising Bi atoms in the cavities.

Introduction

Zintl phases are a versatile compound class since this subgroup of intermetallic compounds allows for a deeper understanding of structure property relationships. The structures can be understood by the formal electron transfer from the electropositive metal component to the more electronegative p-block metals. Subsequently, the anionic substructure can be determined by evaluation the valency of each element according to the (8-N) rule. Since Zintl phases are in general semiconducting, they are especially prominent materials allowing for band gap tuning which is an important property for materials with thermoelectric or optoelectronic applications. Variation by atom-to-atom substitution in binary compounds such as $A_nE^N{}_m$ with A = alkali metal and E^N element of main group N that correspond to electron-precise Zintl phases or that are rather close to an electron-precise count are of particular interest. The atoms of the polyanion adapt the 8-N rule and the addition of a small amount of a main-group elements E^{N-1} or E^{N+1} could lead to changes in the size and type of the band gap, trigger metal to insulator (semiconductor) transitions, or induce structural changes or combinations of those.[1,2]

The systematic study of binary phase diagrams such as the Na–Sn system has revealed interesting trends in the relationship between the atomic and electronic structure of Na–Sn intermetallic compounds. Merely changing the Na:Sn ratio leads to a wide variety of Sn frameworks, including discrete, isolated Sn atoms in $Na_{15}Sn_4$ and $Na_{14.8}Sn_4$; dimeric $\{Sn_2\}$ units in Na_5Sn_2 and Na_9Sn_4; two-dimensional polyanions in Na_7Sn_{12} and $NaSn_2$; three-dimensional Sn-network in Na_5Sn_{13} and $NaSn_5$, as well as isolated tetrahedral cluster $\{Sn_4\}^{4-}$ in NaSn (Na_4Sn_4) as depicted in Figure 1.[3–12]

We investigate here the influence of the electron count on the structure by aliovalent substitution of Sn in binary Zintl phases of the Na–Sn system while trying to dope them with a relatively small amount of Bi. As a starting point we used the compound Na_5Sn_{13}, which has been regarded as a Zintl phase.[11] However in order to reach the necessary number of bonds according to the 8-N rule, *Corbett* regarded a very long Sn–Sn contact of 3.6 Å as a two-electron-two center bond. Neglecting a bonding contact consequently leads to the formation of two lone pairs at the Sn atom which requires, for a charge-balanced compound, a higher negative charge at both Sn atoms. In consequence, the reported Na_5Sn_{13} would correspond to an electron-deficient Zintl phase. However, the postulation of such a long covalently bonding contact is rather vague. Substituting an appropriate number Sn atoms by Bi lead in other cases to a stabilization of electron deficient compounds. For example, corresponds the chiral clathrate $K_{6+x}Sn_{25}$

[a] S. Zeitz, M. Boyko, S. Ponou, V. Hlukhyy, T. F. Fässler
School of Natural Science, Technical University of Munich, Chair of Inorganic Chemistry with Focus on Novel Materials, Lichtenbergstraße 4, D-85747 Garching, Germany
E-mail: thomas.faessler@lrz.tum.de

Supporting information for this article is available on the WWW under https://doi.org/10.1002/chem.202403592

Chemistry–A European Journal
Research Article
doi.org/10.1002/chem.202403592
Chemistry Europe
European Chemical Societies Publishing

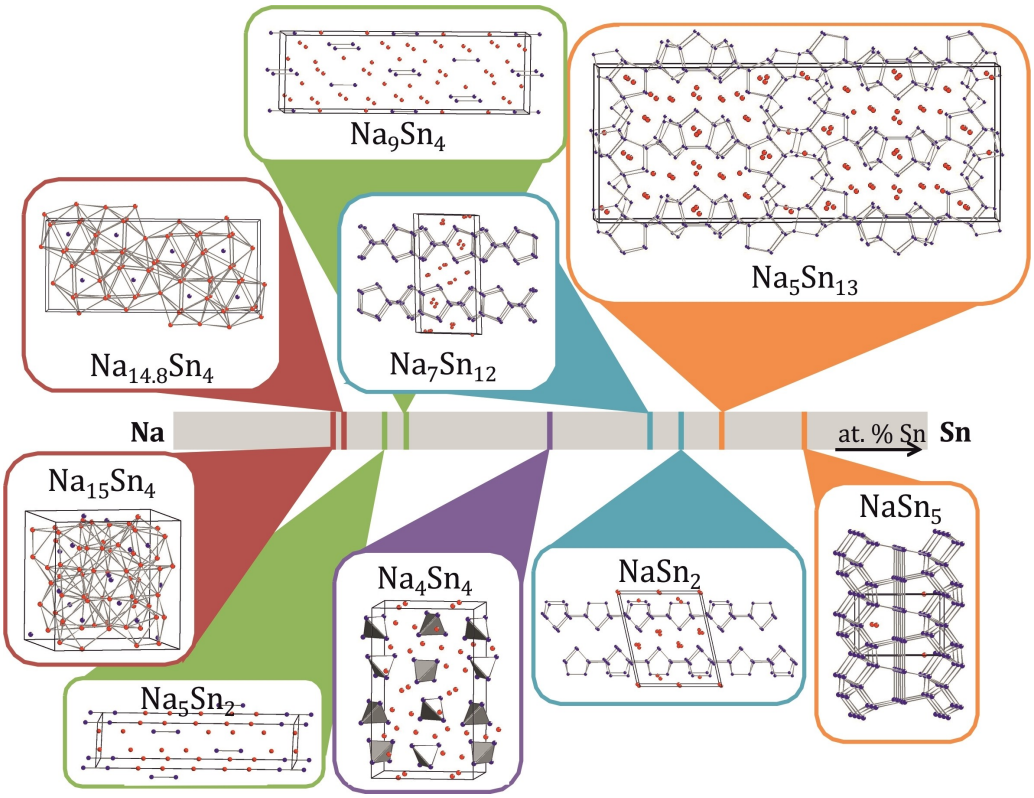

Figure 1. Fragments of the crystal structure of the binary phases in Na–Sn binary system in dependency of the Na:Sn ratio.[3] Color code according to dimensionality of the Sn anionic frameworks: isolated Sn atoms–red rectangles; dimeric $\{Sn_2\}$ units–olive green; two-dimensional polyanions–aqua blue; three-dimensional Sn-network–orange; isolated clusters–purple.

to an electron-deficient phase. Stabilization by Bi resulted in the formation of the electron-precise Zintl phase $K_6Sn_{23}Bi_2$.[13] Similarly leads the Bi versus Pb substitution in the in the Laves phase KPb_2 to a metal to semiconductor transition, by lowering the symmetry with a Peierls like distortion of the Bi/Pb network.[1]

Interestingly, no ternary Na-Sn-Bi phases are reported yet, whereas for the lighter homologues of Bi, seven compounds in the Na-Sn-*Pn* systems are reported (*Pn* = P, As and Sb), which show intriguing structure motifs reaching from one- to three-dimensional networks (Supporting Information Figure S1). The compounds similarly appear, mostly, as electron-precise Zintl phases with localized bonds, however, also compounds in which the bond description is less clear are known. In $Na_{10}Sn_2Pn_6$[14,15] (*Pn* = P, As) edge-sharing $SnPn_4$ tetrahedra form dimeric $\{Sn_2Pn_6\}^{10-}$ anions that are isolated by Na atoms. Na_2SnAs_2 and Na_5SnSb_3 possess three-dimensional structures with vertex-sharing $SnPn_4$ tetrahedra and Na_2SnAs_2[16] comprises tetrahedrally coordinated Sn atoms with $\{Sn_4As_{10}\}$ adamantane-like units. In Na_5SnSb_3[17] the main structural element can be described as $SnSb_4$ tetrahedra forming zig-zag chains. NaSnP[18] as well as $NaSn_2As_2$[19] feature both two-dimensional layers, similar to As layers in the structure of grey arsenic. However, NaSnP corresponds to an electron-precise Zintl phase according to Na^+, $(3b\text{-}Sn)^-$ and 3b-As (3b = three-fold bonded), and interestingly is $NaSn_2As_2$ with exclusively 3b-Sn and 3b-As atoms an electron-deficient Zintl phase unless very long contacts between two Sn atoms with distances of 3.3 Å are anticipated as covalent bonds.

We report here on our approach to electronically modify Na_5Sn_{13} featuring an anionic network where Sn atoms are 2-, 3- and 4-fold bonded by doping with more electron rich Bi atoms. We find the formation of a compound with a closely related framework. Surprisingly, Bi atoms do not only partially substitute Sn atoms as known for other compounds, but also act as loosely bounded host atoms within the Sn network. multicenter bonding $Na_{12.73}Sn_{25.73}Bi_{1.27}$.[11,20,21]

Chemistry–A European Journal | Research Article doi.org/10.1002/chem.202403592 | Chemistry Europe European Chemical Societies Publishing

Results and Discussion

Synthesis and Characterization

The compound $Na_{13}Sn_{25.73}Bi_{1.27}$ was synthesised through a high temperature reaction from a mixture of elements Na:Sn:Bi with the composition 5:12:1. The microcrystalline product contained some unreacted Sn as a side phase (Figure S2 Supp. Inform.) as well as some reflections, that could not be assigned to a known phase. Attempts to synthesize the title compound as phase pure material were not successful. A dark, almost black in color block-shaped single crystal was isolated from the reaction product of a sample synthesized with a longer dwelling time at 270 °C. For details see below.

Table 1. Crystallographic data and data and selected details of structure refinement for the compound $Na_{13}Sn_{25.73(2)}Bi_{1.27(2)}$.

Formula	Na13Sn25.73(2)Bi1.27(2)
Formula weight (g·mol^{-1})	3618.17
Space group	$P\bar{1}$ (No. 2)
Z	1
Unit cell parameters (Å)	$a=9.0826(4)$ $b=11.2527(5)$ $c=13.2278(6)$ $\alpha=112.114(4)^\circ$ $\beta=99.818(4)^\circ$ $\gamma=101.379(4)^\circ$
Volume (Å^3)	1182.4(1)
$D_{calcd.}$ (g·cm^{-3})	5.081
Abs. coeff. (mm^{-1})	18.128
F(000) (e)	1535
Crystal shape/color	block/black
Temperature (K)	150
Θ range (deg)	3.038–27.498
Range in hkl	$\pm11\pm14\pm17$
Reflections collected	42179 ($R_\sigma=0.0216$)
Unique reflections	5410 ($R_{int}=0.0305$)
Data/parameter	5410/189
GOF on F2	1.211
R_1, wR_2 ($I>2\,\sigma(I)$)	0.0355, 0.0844
R_1, wR_2 (all data)	0.0458, 0.0870
Largest diff. peak/hole (e Å^{-3})	2.585 and-1.944

Crystal Structure

Single crystals show triclinic symmetry and the refinement of the single crystal diffraction data result in the crystallographically determined composition $Na_{13}Sn_{25.73(2)}Bi_{1.27(2)}$. All parameters of the single crystal refinement can be found in Table 1. The atomic coordinates for twenty-one crystallographic independent atoms positions are listed in Table S1 together with anisotropic displacement parameters for all atoms given in Table S2 (Supporting Information). High residual electron density at the Sn2 position suggested the formation of a statistical mixture of Sn and Bi. The refinement showed a Sn/Bi ratio of 0.861/0.139(7) on position *E*2. No correlation between the occupancy of Na positions and a possible partial occupancy of the *E*2 site was observed revealing no significant defects on any Na position. Another disorder was found for the Bi1 position, which was refined with two split positions (Wyckoff site 2i) with an occupancy of 50% each.

$Na_{13-x}Sn_{26-x}Bi_{1+x}$ is the first and only representative of the Na-Sn-Bi ternary system. Its structure, shown in Figure 2, with all atoms shown as ellipsoids with 90% probability. All atomic positions, isotropic and anisotropic displacement parameters can be found in Table S1 and S2 in the Supporting information.

Twelve tin atoms (position Sn1, Sn3-Sn13) together with a position that possess a Sn/Bi statistical mixture (*E*2) form a complex three-dimensional network (Figure 2 and Figure 3) which is related to the binary phase Na_5Sn_{13}.[11] The network contains two major motifs that are denoted as fragments **A** and **B** shown in detail in Figure 3b and 3c, respectively. Fragment **B** is composed by four fused cages - two cages of type **I** and **II**, each, in the sequence **I–II-II–I**. The cages form parallel channels along the *a* direction (Figure 3e). Four such fragments **A** enclose the larger cavity **B** that hosts the Bi1 atom. In Figure 3d and 3e the two fragments **A** and **B** are shown along the *a* axis. Cages II and fragment **A** are encapsulating Na atoms as shown in Figure 3: Na3 and Na5 are located inside of cage **I**, whereas all the remaining Na atoms (Na1, Na2, Na4, Na5, Na6 and Na7) are located inside fragment **A**. All atoms Sn1, Sn3 to 13 as well as all Na positions are fully occupied, while the Sn2/Bi2 position is occupied by 86.1% Sn and 13.9% Bi.

Homoatomic Sn–Sn distances within the open framework of $Na_{13}Sn_{25.73}Bi_{1.27}$ are between 2.822 and 2.947 Å (Table 2), which suggests covalent interactions: Sn7, Sn8, Sn11 and Sn13 are three-, Sn1, Sn3, Sn4, Sn5, Sn6, Sn9, Sn10 and Sn12–four-fold-

Table 2. Selected interatomic distances in the compound $Na_{13}Sn_{25.73}Bi_{1.27}$. For details see Table S4 (SI).

Atom types	Distance range(Å)
Sn-Bi	3.145(8)–3.456(8)
Sn-*E*	2.965(1)–2.985(1)
Sn-Sn	2.822(1)–2.947(2)
Na-Bi	3.22(3)–3.86(1)
Na-*E*	3.243(7)–3.302(8)
Na-Sn	3.186(8)–3.925(6)
Na-Na	3.521(8)–4.080(9)

Chemistry–A European Journal
Research Article
doi.org/10.1002/chem.202403592
Chemistry Europe
European Chemical Societies Publishing

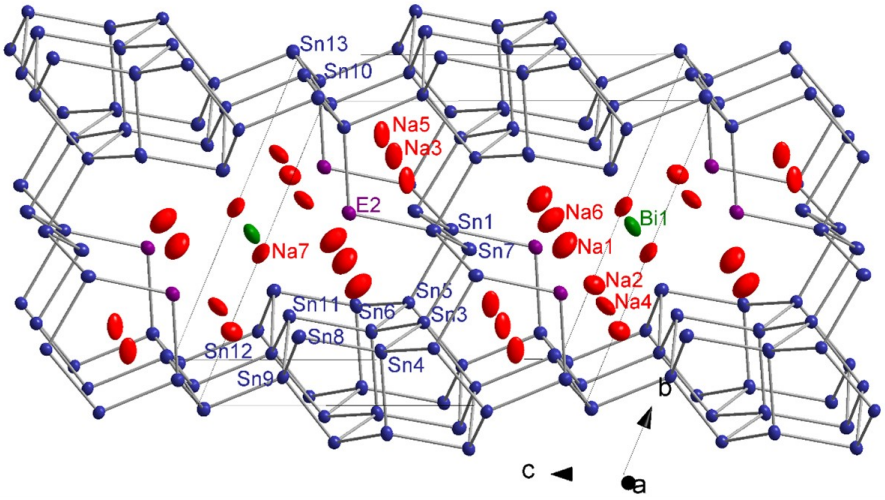

Figure 2. Extended unit cell of the compound $Na_{13}Sn_{25.73}Bi_{1.27}$. The three-dimensional framework is shown on an extended part of the unit cell. Na, Sn, Bi and the mixed Sn/Bi atoms are shown in red, blue, green, and violet color, respectively. Thermal ellipsoids are drawn with 90% probability level.

bonded to neighboring atoms. The atoms of the statistical mixture Sn/Bi (*E*2) are two-fold bonded with $d_{Sn1-E2} = 2.965$ Å and $d_{Sn10-E2} = 2.985$ Å.

The coordination of the Bi1 atom, with a site occupancy of 50%, differs since it comprises longer distances to its next neighbors: Distances to Sn11 are 3.145 Å and 3.455 Å, which are both significantly longer than the sum of the covalent radii of single-bonded Bi (1.51 Å[22]) and Sn (1.40 Å[22]). Thus $Na_{13}Sn_{25.73}Bi_{1.27}$ shows that Bi in Sn-rich Na–Sn-Bi compounds is either capable to substitute two-bonded Sn atoms, preserving the integrity of the Sn network, or may act as a loosely bound guest atom within the framework.

The structural relationship of $Na_{13}Sn_{25.73}Bi_{1.27}$ to the binary phases Na_7Sn_{12}[12] and Na_5Sn_{13}[11] is shown in Figure 4. All three compounds contain type **I** and **II** cages that are constructed by Sn-pentagons. In $Na_{13}Sn_{25.73}Bi_{1.27}$ they are condensed to tetramers **I–II-II–I** (orange ellipse in Figure 4a), forming a larger cavity as shown in Figure 3a (yellow ellipse). In Na_5Sn_{13} similar cages appear as condensed trimers **II–I-II** (red ellipse in Figure 4c), forming a three-dimensional network together with additional fragments, whereas in Na_7Sn_{12} dimers of the cages **I** and **II** are interconnected in *a*-direction forming layers (green ellipse in Figure 4b).

Electron Count

To get insight on the electron count of $Na_{13}Sn_{25.73}Bi_{1.27}$ we investigated two boundary cases in which the mixed Sn2/Bi2 position is either fully occupied by Sn or by Bi. Full occupancy with Sn (case 1) results in the composition $Na_{13}Sn_{26}Bi$ and the following electron count for the polyanionic covalent network: $[(2b\text{-}Sn^{2-})_2(3b\text{-}Sn^{-})_8(4b\text{-}Sn^{0})_{16}]$ (nb = n-fold bonded or n covalent bonds) leading to an overall charge of −12 for the three-dimensional network. Since there are 13 Na ions for charge balance, consequently the 0b-Bi1 guest atom should formally be considered as Bi^{1-} resulting in $(Na^{+})_{13}[(0b\text{-}Bi^{1-})_1(2b\text{-}Sn^{2-})_2(3b\text{-}Sn^{-})_8(4b\text{-}Sn^{0})_{16}]$. Based on this consideration, $Na_{13}Sn_{26}Bi$ is as a charge balanced Zintl phase. For the second case, with a composition of $Na_{13}Sn_{24}Bi_3$, the atom connectivity is according to $[(2b\text{–}Bi^{-})_2(3b\text{–}Sn^{-})_8(4b\text{–}Sn^{0})_{16}]$ and a total charge of −10 results. With the same number of Na counter ions, the isolated Bi1 atom is assigned with a negative charge of −3 to remain charge balance and resulting in the sum formula $(Na^{+})_{13}[(0b\text{–}Bi^{3-})_1(2b\text{–}Bi^{-})_2(3b\text{–}Sn^{-})_8(4b\text{–}Sn^{0})_{16}]$. According to the crystallographically determined composition obtained through the refinement of the SC-XRD data, $Na_{13}Sn_{25.73}Bi_{1.27}$ and the resulting ratio of $(2b\text{–}Sn1)^{2-}$ and $(2b\text{-}Bi2)^{-}$ of 86% to 14% an average sum formula of $(Na^{+})_{13}[(0b\text{–}Bi^{1-})_{0.861}(0b\text{–}Bi^{3-})_{0.139}(2b\text{–}Bi^{-})_{0.272}(2b\text{–}Sn^{2-})_{1.728}(3b\text{-}Sn^{-})_8(4b\text{-}Sn^{0})_{16}]$ results and the guest atom 0b-Bi1 takes up the required average surplus charge of 0.272 electrons remaining a charge balanced Zintl phase.

Electronic Structure

The electronic structure of $Na_{13}Sn_{25.73}Bi_{1.27}$ was calculated using two stoichiometrically precise model systems, $Na_{13}Sn_{26}Bi$ and $Na_{13}Sn_{24}Bi_3$, where the mixed Bi/Sn position was either fully occupied by Sn or Bi and the Bi1 position was fixed along the c direction in the ab-plane, lowering its Wyckoff position from 2i to 1e.

The resulting band structures and density of states calculated with a DFT-PBE0/TZVP level of theory (SVP for Na) are shown in Figure 5 and Figure 6, along lines between high symmetry points in the first Brillouin zone. Cell parameters and

Chemistry–A European Journal
Research Article
doi.org/10.1002/chem.202403592
Chemistry Europe
European Chemical Societies Publishing

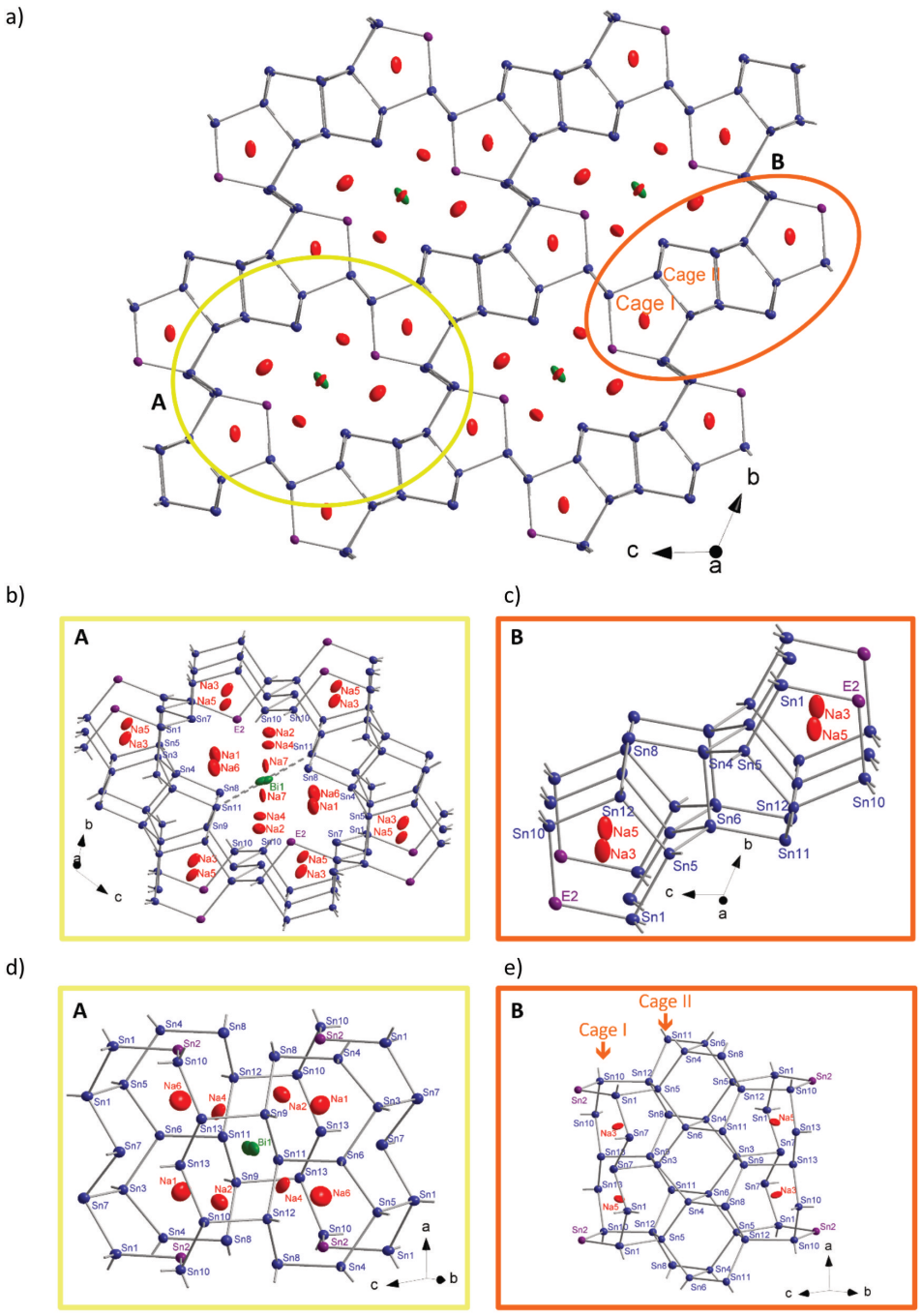

Figure 3. Structure of the polyanionic Sn network of $Na_{13}Sn_{25.73}Bi_{1.27}$, a) featuring two types of structural fragments: fragment A and B shown by the yellow and orange circle, respectively. b) enlargement of A showing cage III hosting atom B1, c) enlargement of B featuring the network of Sn pentagons that forming the cages I and II. a)–c) shown as a projection along the a direction. d) and e) show the direction perpendicular to a with emphasizing the cages. Sn, Bi and Sb/Bi atoms are shown with blue, green, and violet color. Displacement ellipsoids are shown at 90% probability.

Chemistry–A European Journal
Research Article
doi.org/10.1002/chem.202403592
Chemistry Europe
European Chemical Societies Publishing

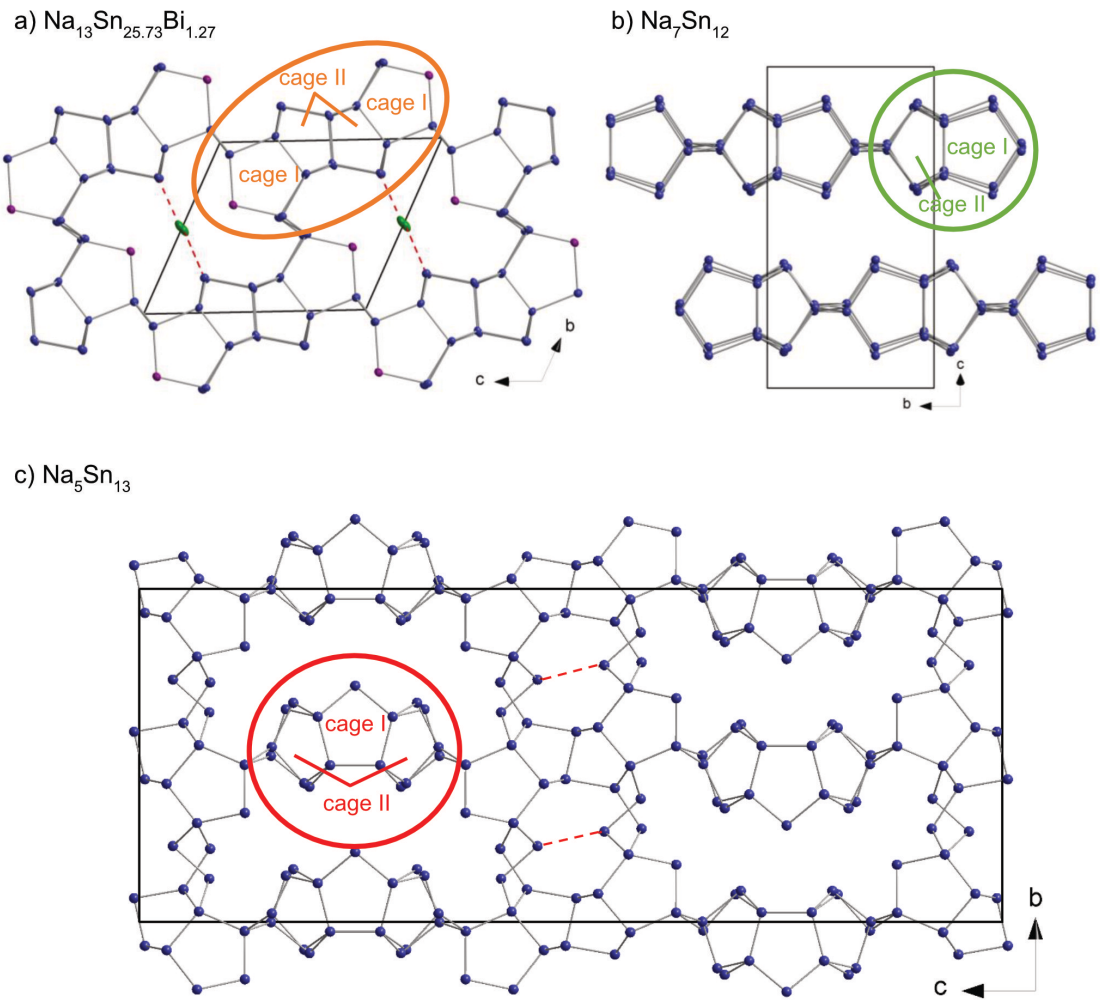

Figure 4. Structural relation of a) $Na_{13}Sn_{25.73}Bi_{1.27}$ to the binary phases b) Na_7Sn_{12} and c) Na_5Sn_{13}. In a) the elongated Sn–Bi interaction of 3.145 Å and for comparison in c) a non-bonding Sn–Sn contact of 6.011 Å is shown as dashed line.

atom coordinates of the optimized structures coincide with the by SCXRD determined ones with a maximum deviation of 1.75% (Table 7, SI). Since for both models one negative frequency of about $-25\ cm^{-2}$ was obtained, the structure was distorted and reoptimized in P1 symmetry. Here all atomic coordinates were refined without constraints. Interestingly changes the Bi1 atom, which was previously fixed on a special position, its coordinates by only a maximum of 2%.

Both model compounds, $Na_{13}Sn_{26}Bi$ and $Na_{13}Sn_{24}Bi_3$, are indirect band gap semiconductors with band gaps of 0.6 eV, with a transition from T→Γ for $Na_{13}Sn_{26}Bi$ and R→Y-Γ for $Na_{13}Sn_{24}Bi_3$. The band structures of the ordered models look in general similar but differ for the valence and conduction bands close to E_F with respect to the band dispersion and location of the valence band maximum (VBM) and conduction band minimum (CBM). For $Na_{13}Sn_{26}Bi$ the band with the CBM has a dispersion of about 0.5 eV (①) while the band with the VBM is rather flat (②). For $Na_{13}Sn_{24}Bi_3$ this is inverted, thus having a flat first conduction band (③) and a band with VBM (④) and a dispersion of 0.5 eV. Interestingly are the band gaps of both modelled compounds almost identical. The $Na_{13}Sn_{24}Bi_3$ model possesses in comparison to $Na_{13}Sn_{26}Bi$ in total 2 additional electrons. Considering a rigid band model to $Na_{13}Sn_{26}Bi$ a shift of the Fermi-Level to higher energy and filling the lowest conduction band is expected, transforming $Na_{13}Sn_{24}Bi_3$ to a metal. However, applying the Bi richer model for the calculation, the conduction band of $Na_{13}Sn_{26}Bi$ is not filled but rather in $Na_{13}Sn_{24}Bi_3$ an additional band is added below the band gap,

Chemistry–A European Journal
Research Article
doi.org/10.1002/chem.202403592
Chemistry Europe
European Chemical Societies Publishing

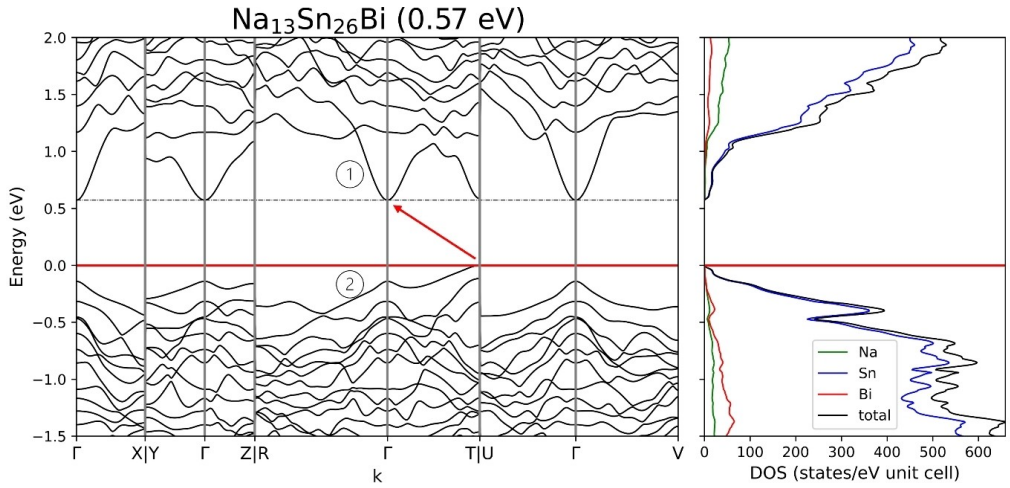

Figure 5. Band structure and density of states for $Na_{13}Sn_{26}Bi$ with a band gap of 0.6 eV with the corresponding transition marked with an arrow.

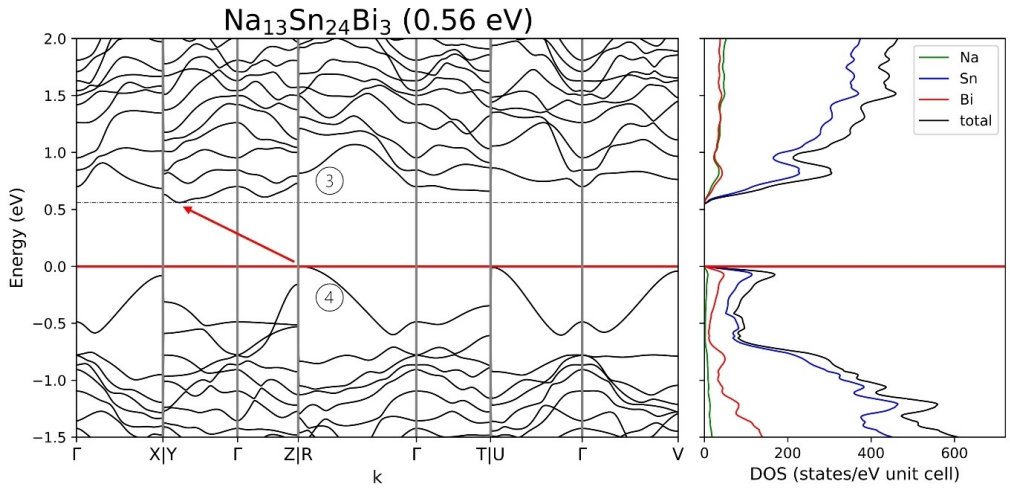

Figure 6. Band structure and density of states for $Na_{13}Sn_{24}Bi_3$ with a band gap of 0.6 eV with the corresponding transition marked with an arrow.

with a dispersion similar to the first conduction band in $Na_{13}Sn_{26}Bi$.

For both models the atom projected DOSs at the Fermi-Level gives a more detailed insight on the electronic structure. In general, for both models Sn atoms have the highest contribution within the projected DOS around the Fermi-Level followed by Bi and Na atom contributions. For the $Na_{13}Sn_{26}Bi$ the contribution of Bi states in the top valence band is only minor while in $Na_{13}Sn_{24}Bi_3$ they make up about one third of the total states and are especially present with a local maxim just below E_F. There is no Bi contribution to the conduction bands of $Na_{13}Sn_{24}Bi_3$ in contrast to a higher contribution of Bi states to the first conduction band of $Na_{13}Sn_{26}Bi$. Resolving the Bi states by their different atomic positions reveals that these states originate from the two bonded Bi2 position (see Figure 2, SI). This correlates with the chemical picture, that two-bonded Bi atoms have a formal negative charge and two non-bonding electron pairs (lone pairs) that energetically form the highest occupied orbitals.

Chemical bonding was further investigated by an analysis of the overlap population and the Mulliken charges (see Table S6–8, SI). Considering values of the overlap population larger than 0.2 as covalent bonds, the atom connectivity imposed by the electron count with 2b and 3b atoms in the framework as shown before can be confirmed. The overlap population between the isolated Bi1 and its closest Sn11 neighbour (Figure 3b) is 0.084 for $Na_{13}Sn_{26}Bi$ and 0.094 for $Na_{13}Sn_{24}Bi_3$, which accounts for a rather similar interaction for both models with the Sn11 position, but in both cases not in the range accounting for a single bond. The calculated Mulliken charges

Chemistry–A European Journal
Research Article
doi.org/10.1002/chem.202403592
Chemistry Europe
European Chemical Societies Publishing

for $Na_{13}Sn_{26}Bi$ are used to reflect the trend of the charge distribution. Notice, that Mulliken charges do neither correspond to ionic nor to formal charges but are capable to reflect trends within a structure. The Mulliken charges of the Na atoms are between +0.75 and +0.83 and no significant overlap population with neighbouring atoms are observed, thus each atom shows according to the Zintl-Klemm concept the expected charge of +1. For the isolated Bi1 the Mulliken charge is −1.04, which is also in line with the proposed charge. For the Sn atoms the Mulliken charges vary between −1.13 and +0.04. Here the charges are also in line with the specific connectivity of the atoms of the anionic substructure. Sn positions which are four-fold bonded show charges close to 0 (the formal charge according to the Lewis formula is 0.) The three-fold bonded Sn atoms show Mulliken charges of −0.45 to −0.64, which is close to the assumed formal charge of −1, and the two-fold bonded Sn2 has the largest negative charge of −1.13, which would correspond to a formal charge of −2. This value is similar to one of the Bi1, which could hint, that the formal negative charge of the isolated Bi is actually more than −1.

Most interestingly, we found that for $Na_{13}Sn_{24}Bi_3$ the overall Mulliken charge distribution is rather similar to $Na_{13}Sn_{26}Bi$. Although a charge of −3 for Bi1 is expected, almost the same Mulliken charge, as for $Na_{13}Sn_{26}Bi$ is calculated, with a value of −1.05. Considering that $Na_{13}Sn_{24}Bi_3$ possesses two more electrons than $Na_{13}Sn_{26}Bi$, the excess of charge is rather distributed over all Sn and Bi atoms of the network, than located at the Bi1 position.

Based on the study of the two borderline models $Na_{13}Sn_{26}Bi$ and $Na_{13}Sn_{24}Bi_3$ the electronic structure of the composition $Na_{13}Sn_{25.73(2)}Bi_{1.27(2)}$ as determined by a single crystal structure refinement, reflects most probably a snapshot of the phase with a certain phase width $Na_{13}Sn_{26-x}Bi_{1+x}$ with $x \in [0;2]$. Surprisingly, and in contrast to a simple rigid band filling model - i.e. considering the band structure of $Na_{13}Sn_{26}Bi$ and simply adding two electrons resulting in a metallic behaviour – both compounds are semiconductors even though $Na_{13}Sn_{24}Bi_3$ is more electron rich. The Bi1 atom, which has no strong interactions with the surrounding atoms, therefore serves as a guest atom and electron buffer.

Thus, the reported compound is an intriguing example of a Zintl phase which can retain the semiconducting property despite being non-electron precise with respect to the 8-N rule. We conducted many experiments to vary the composition, but always found the approximate composition $Na_{13}Sn_{25.73}Bi_{1.27}$. Powder diffractograms and single crystals show, within the standard deviations, always the same lattice parameters. We explain this with the compound's host-guest nature, in which the guest atom Bi can slightly change the oxidation state without changing the stiff Sn network. The band structure is remarkably flexible in shifting bands at the Fermi level retaining the band gap.

Comparison with the Electronic Structure of Na_5Sn_{13} and Na_7Sn_{12}

As a starting point for this investigation we used the compound Na_5Sn_{13}, which has been regarded as a Zintl phase if that one very long Sn–Sn contact of 3.6 Å is considered as a two-electron-two center bond.[11] Therefore, we calculated the band structure using the same computational methods for Na_5Sn_{13} and also for the related Na_7Sn_{12}, which is known as an electron precise Zintl phase.

According to the band structure shown in Figure 7, Na_7Sn_{12} is a semiconductor with an indirect band gap of 1.0 eV and Na_5Sn_{13} a metal. Na_7Sn_{12} has, similar to $Na_{13}Sn_{26}Bi$, flat bands around the band gap with a low dispersion except for the lowest conduction band which also shows a large dispersion of around 0.4 eV. Focusing on the band structure of Na_5Sn_{13}, which similar to $Na_{13}Sn_{26}Bi$ and $Na_{13}Sn_{24}Bi_3$ is not an electron precise compound at first glance, the band structure shows a large band dispersion and a high density of states at E_F as it is expected for a good metal. The partial DOS of the Sn11 atoms (Figure S4, Supp. Info), which have been reported to form an exceptionally long covalent bond,[11] contribute significantly to the total DOS at E_F and support the hypothesis that they are also largely responsible for the metallic property of Na_5Sn_{13}.

Whereas in the ternary phases, the Sn versus Bi substitution opens a band gap, Na_5Sn_{13} is a metal. Thus, introducing atoms with different size and different electronegativity values seems to be able to change the electronic property from conducting to semi-conducting.

Another difference is observed with respect to the Na contributions in the density of states. The DOS of both compounds mostly consists of Sn states. For Na_5Sn_3 there is a small maximum in Na states at the Fermi-Level, while this is absent in the Na_7Sn_{12} Na DOS. The same holds for the modelled phases for $Na_{13}Sn_{25.73}Bi_{1.27}$ where Na has only some small contribution around the Fermi level. This as well as the width of the band gap could hint, that the title compound is electronically closer related to the electron precise Zintl phase Na_7Sn_{12} than Na_5Sn_{13}.

Conclusions

$Na_{13}Sn_{25.73}Bi_{1.27}$ represents the first ternary compound in the Na-Sn-Bi system. With respect to composition and structural details it is closely related to Na_5Sn_{13}. Both phases are exceptions to the Zintl-Klemm concept since for the metallic Na_5Sn_{13} unrealistically long covalent bonds of 3.16 Å are anticipated, whereas the same characteristics (non-charge balanced and long Bi–Sn bonds) can be found in $Na_{13}Sn_{25.73}Bi_{1.27}$ which surprisingly is a semiconductor with a band gap of 0.5 eV. The electronic situation was traced back to a loosely bound Bi atom–beside a second Bi atom that is part of the covalent Sn substructure–which acts as a guest atom according to $Bi_x@Na_{13}Bi_ySn_{27-x-y}$ (x = 1, y = 0.27) and is capable to change its oxidation state and thus to uptake additional electrons allowing the system to be a semiconductor. Therefore, $Na_{13}Sn_{25.73}Bi_{1.27}$ can be understood as

Chemistry–A European Journal
Research Article
doi.org/10.1002/chem.202403592
Chemistry Europe
European Chemical Societies Publishing

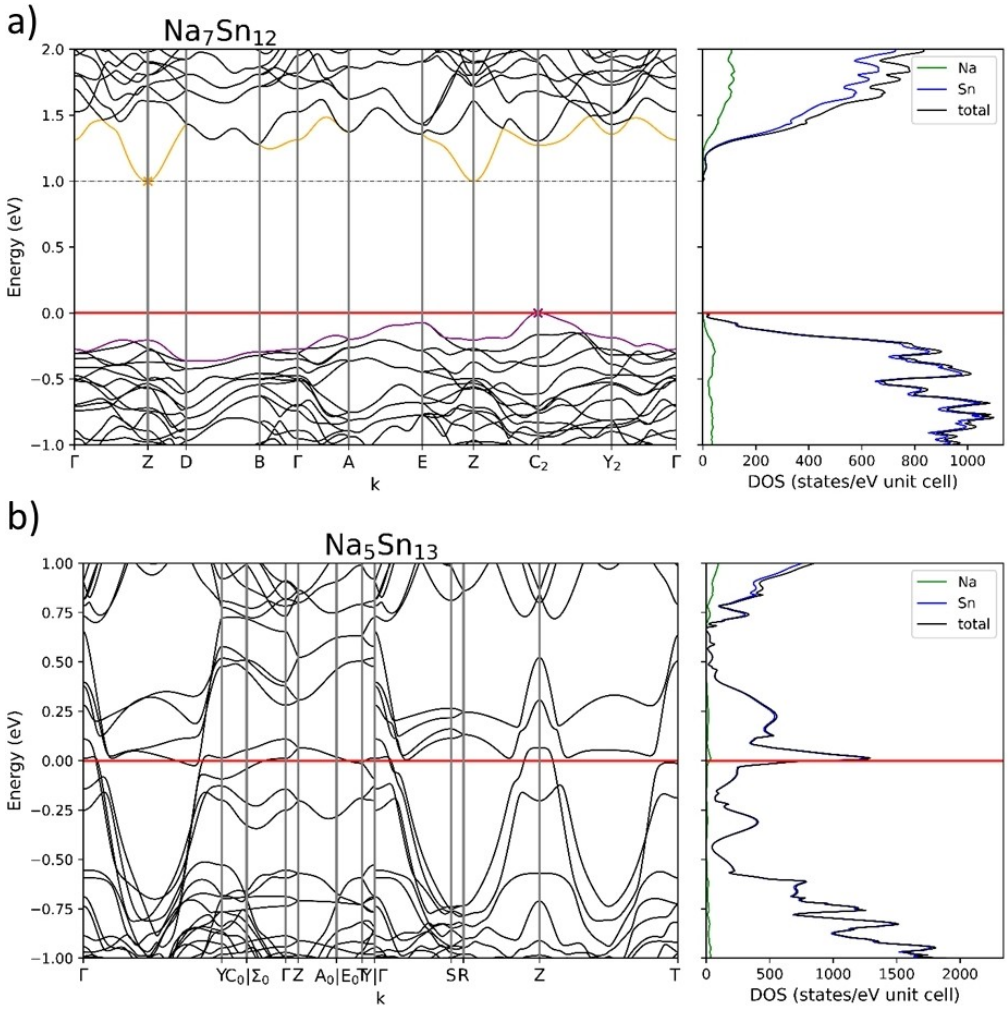

Figure 7. Band structure and density of states for a) Na_7Sn_{12} with a band gap of 1.0 eV and b) metallic Na_5Sn_{13}.

a rare example of an open framework structure of Sn atoms comprising Bi atoms in the cavities. Sn atoms that form clathrate-type framework structures based on K and Sn atoms are well known (K_8Sn_{44}[23] or $K_6Sn_{23}Bi_2$[13]). Open framework structures have also been described for examples in which Na atoms are located in cavities of a Sn–Zn framework.[24] Na_5Sn_{13} and $Na_{13}Sn_{25.73}Bi_{1.27}$ are two additional examples showing the fantastic possibilities, with respect to chemical bonding and properties, of Zintl phases that are close but not perfect electron precise semiconductors.

Experimental Section

Synthesis

A Sample of the nominal composition '$Na_5Sn_{12}Bi_1$' was obtained from a mixture of elements Na:Sn:Bi with the composition 5:12:1. The mixture was heated at the rate of 120 °C/h to 650 °C, kept there for 12 h, then cooled at the rate of 120 °C/h to 270 °C where it is annealed for at least 5 days and, subsequently cooled to room temperature by turning off the furnace. The product is air and moisture sensitive and crystallized as irregular silvery crystals. Most of the crystals appear to be twinned (multiple twinning) and not suitable for single crystal diffraction. The X-ray powder diagram of the product compares very well with the theoretical diagram calculated from the structure solution crystal data however, with some unindexed peaks indicating (an) additional yet unknown phase(s). The presence of the three elements Sn, Na and Bi was confirmed by EDX analysis, and no eventual contaminant was detected.

Chemistry–A European Journal | Research Article doi.org/10.1002/chem.202403592 | Chemistry Europe European Chemical Societies Publishing

For single crystal growth the a sample of the nominal composition '$Na_5Sn_{12}Bi_2$' was synthesized from the elements in Ta ampoule using a two-step temperature program: (1) heating up to 650 °C with the rate of 120 °C/h and holding the temperature for 12 hours and (2) slowly cooling down to 270 °C (rate 6 °C/h) and dwelling the sample for 240 hours. The sample was cooled down to room temperature by switching off the furnace.

Powder X-Ray Diffraction

For the powder X-ray diffraction (PXRD) analysis, obtained samples were finely ground in an agate mortar, sealed in a glass capillary (inner diameter 0.3 mm, wall thickness 0.01 mm, Hilgenberg GmbH) using capillary wax (Hampton Research) and measured at room temperature using a STOE Stadi P powder diffractometer with Mo–Kα (λ = 0.70932 Å) radiation, Ge (111) monochromator and a position sensitive Dectris MYTHEN DCS 1 K solid-state detector. STOE WinXPOW program package[25] was used for phase analysis, indexing, and refining cell parameters for the obtained phases.

Single Crystal X-Ray Diffraction

Crystals suitable for single crystal X-ray diffraction (SCXRD) analysis were selected under a microscope inside a glovebox and transferred into glass capillaries (inner diameter 0.1–0.3 mm, wall thickness 0.01 mm, Hilgenberg GmbH) using a glass filament dipped in perfluoropolyalkyl ether (Galden Perfluorniated Fluid LSD 230, Solvay Specialty Polymers, viscosity 1800 cSt). The capillaries were then sealed airtight using capillary wax (Hampton Research) and mounted onto a single crystal X-ray diffractometer with Mo K_α radiation (λ = 0.71073 Å). Single-crystal intensity data were collected at room temperature or in cold N_2 stream (150 K), using a Stoe Stadivari diffractometer equipped with a micro focus GeniX 3D source (high flux Mo Kα radiation) and a DECTRIS PILATUS 300 K detector. Corrections of the raw data for background, polarization, and Lorentz effects were applied. Due to a Gaussian-shaped primary X-ray beam profile, a scaling procedure within LANA was applied along with the numerical absorption correction using X-Red[26] and X-Shape[27] software. The starting atomic parameters were usually obtained by Direct Method with the SHELXS-2014.[28] The structure was refined using SHELXL-2014 (full-matrix least-squares on Fo2) with anisotropic atomic displacement parameters for all atoms. To check the composition, the occupancy parameters were refined in separate least-squares cycles. Crystallographic data and selected data and details of the structure refinement for $Na_{13}Sn_{26}Bi$ are listed in Table 1. Deposition Number CSD-2387128 contains the supplementary crystallographic data for this structure. These data are provided free of charge by the joint Cambridge Crystallographic Data Centre and Fachinformationszentrum Karlsruhe.

Presence of Bi, along with Na and Sn in the new compound were confirmed by EDX analysis (Table S3, SI). Significant deviation of the composition according to the EDX results is occurring due to oxidation of the crystal.

Electronic Structure Calculations

The computational studies of $Na_{13}Sn_{26}Bi$ and $Na_{13}Sn_{24}Bi_3$ were performed using the CRYSTAL17 program package and hybrid density functional methods.[29,30] A hybrid exchange-correlation functional after Perdew, Burke, and Ernzerhof (DFT-PBE0) was used,[31] Localized, Gaussian-Type triple ζ-valence + polarization level basis sets were used for Sn und Bi and split valence + polarization level basis sets for Na. The basis sets were derived from the molecular Karlsruhe basis sets (further basis set details are in the supporting information).[32–34] For the evaluation of the Coulomb and exchange integrals (TOLINTEG), tight tolerance factors of 8, 8, 8, 8, 16 were used for all calculations. The reciprocal space of $Na_{13}Sn_{26}Bi$ and $Na_{13}Sn_{24}Bi_3$ were sampled with 6×6×4 Monkhorst-Pack-type *k*-point grids. The starting geometries were taken from experimental data, and both the lattice parameters and atomic positions were fully optimized within the constraints imposed by the space symmetry. The optimized structures were confirmed to be true local minima by means of harmonic frequency calculations at the Γ-point (only very small imaginary frequency). Electronic band structures and density of states (DOS) were calculated. The Brillouin Zone paths of Γ-X|Y-Γ-Z|R-Γ-T|U-Γ-V were provided by the web service *SeeK-path*.[35]

Author Contributions

Synthesis, powder diffraction and solution of the first single crystal was done by S.P. Synthesis and refinement of published single crystal data was performed by M. B. and V. H. helped with single crystal solution and refinement. Electronic structure calculations, data interpretation and writing of the manuscript was done by S. Z. Project administrator, manuscript editing, and review done by T. F. F..

Acknowledgements

We thank TUM.solar in the context of the Bavarian Collaborative Research Project *Solar Technologies Go Hybrid* (SolTech) supported by the Bavarian State Ministry of Science and the Arts. Open Access funding enabled and organized by Projekt DEAL.

Conflict of Interests

The authors declare no conflict of interest.

Data Availability Statement

The data that support the findings of this study are available in the supplementary material of this article.

Keywords: Zintl phases · Electronic structure · Bismuth

[1] S. Ponou, N. Müller, T. F. Fässler, U. Häussermann, *Inorg. Chem.* **2005**, *44*, 7423.
[2] E. Zintl, A. Harder, *Z. Phys. Chem. (Berlin, Ger.)* **1932**, *16B*, 206.
[3] T. F. Fässler, *Z. anorg. allg. Chem.* **2006**, *632*, 1125.
[4] Z. Du, R. A. Dunlap, M. N. Obrovac, *J. Alloys Compd.* **2014**, *617*, 271.
[5] F. Dubois, M. Schreyer, T. F. Fässler, *Inorg. Chem.* **2005**, *44*, 477.
[6] T. F. Fässler, C. Kronseder, *Angew. Chem.* **1998**, *110*, 1641.
[7] Y. Grin, M. Baitinger, R. Kniep, H. G. von Schnering, *Z. Kristallogr. - New Cryst. Struct.* **1999**, *214*, 453.
[8] J. Mark, J. Wang, K. Wu, J. G. Lo, S. Lee, K. Kovnir, *J. Am. Chem. Soc.* **2019**, *141*, 11976.
[9] W. Müller, K. Volk, *Z. Naturforsch., B: J. Chem. Sci.* **1975**, *30*, 494.
[10] W. Müller, K. Volk, *Z. Naturforsch., B: J. Chem. Sci.* **1978**, *33*, 275.
[11] J. T. Vaughey, J. D. Corbett, *Inorg. Chem.* **1997**, *36*, 4316.

Chemistry–A European Journal | Research Article doi.org/10.1002/chem.202403592 | Chemistry Europe European Chemical Societies Publishing

[12] T. F. Fässler, S. Hoffmann, *Inorg. Chem.* **2003**, *42*, 5474.
[13] T. F. Fässler, C. Kronseder, *Z. anorg. allg. Chem.* **1998**, *624*, 561.
[14] Z. Kristallogr, *Cryst. Mater.* **1991**, *197*, 269.
[15] J. Klein, B. Eisenmann, *Z. Kristallogr. - Cryst. Mater.* **1991**, *196*, 213.
[16] M. Asbrand, B. Eisenmann, *Z. Naturforsch., B: J. Chem. Sci.* **1993**, *48*, 452.
[17] B. Eisenmann, J. Klein, *Z. Naturforsch., B: J. Chem. Sci.* **1988**, *43*, 1156.
[18] B. Eisenmann, U. Rößler, *Z. Kristallogr. - New Cryst. Struct.* **1998**, *213*, 28.
[19] M. Asbrand, B. Eisenmann, J. Klein, *Z. anorg. allg. Chem.* **1995**, *621*, 576.
[20] S. Ponou, Germanides, germanide-tungstate double salts and substitution effects in Zintl phases. Dissertation, Universitätsbibliothek der TU München, München, **2006**.
[21] M. Boyko, Polar Intermetallics at the Border Between Hume-Rothery and Zintl Phases. Investigations in the Systems Alkali Metal–Tin with Late Transition and p-Block Metals. Dissertation, Universitätsbibliothek der TU München, München, **2019**.
[22] P. Pyykkö, M. Atsumi, *Chem. - Eur. J.* **2009**, *15*, 186.
[23] J. Gallmeier, H. Schäfer, A. Weiss, *Z. Naturforsch., B: J. Chem. Sci.* **1969**, *24*, 665.
[24] S. Stegmaier, S.-J. Kim, A. Henze, T. F. Fässler, *J. Am. Chem. Soc.* **2013**, *135*, 10654.
[25] STOE & CIE GmbH, WinXPOW, Version 3.0.2.1 ed., STOE & Cie GmbH, Darmstadt, Germany, **2011**.
[26] X-RED32, STOE & Cie GmbH, Darmstadt, Germany **2016**.
[27] X-SHAPE, STOE & Cie GmbH,, Darmstadt, Germany, **2015**.
[28] G. M. Sheldrick, SHELXS-2014. *Program for the Determination of Crystal Structure*, University of Göttingen, Göttingen, Germany, **2014**.
[29] R. Dovesi, V. R. Saunders, C. Roetti, R. Orlando, C. M. Zicovich-Wilson, F. Pascale, B. Civalleri, K. Doll, N. M. Harrison, I. J. Bush, Crystal17, Turin, Italy, **2017**.
[30] R. Dovesi, A. Erba, R. Orlando, C. M. Zicovich-Wilson, B. Civalleri, L. Maschio, M. Rérat, S. Casassa, J. Baima, S. Salustro, et al., *Wiley Interdiscip. Rev.: Comput. Mol. Sci.* **2018**, *8*, e1360.
[31] J. P. Perdew, W. Yang, K. Burke, Z. Yang, E. K. U. Gross, M. Scheffler, G. E. Scuseria, T. M. Henderson, I. Y. Zhang, A. Ruzsinszky, et al., *Proc. Natl. Acad. Sci. U. S. A* **2017**, *114*, 2801.
[32] A. J. Karttunen, T. F. Fässler, *Chem. - Eur. J.* **2014**, *20*, 6693.
[33] R. E. Stene, B. Scheibe, A. J. Karttunen, W. Petry, F. Kraus, *Eur. J. Inorg. Chem.* **2019**, *2019*, 3672.
[34] B. Scheibe, R. Haiges, S. I. Ivlev, A. J. Karttunen, U. Müller, K. O. Christe, F. Kraus, *Eur. J. Inorg. Chem.* **2020**, *2020*, 4483.
[35] Y. Hinuma, G. Pizzi, Y. Kumagai, F. Oba, I. Tanaka, *Comput. Mater. Sci.* **2017**, *128*, 140.

Manuscript received: September 26, 2024
Accepted manuscript online: November 7, 2024
Version of record online: ■■, ■■

RESEARCH ARTICLE

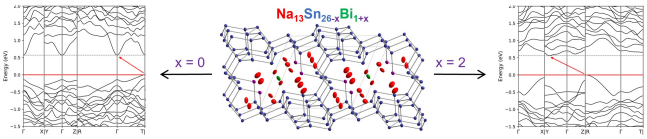

*S. Zeitz, M. Boyko, S. Ponou, V. Hlukhyy, T. F. Fässler**

$Na_{13}Sn_{26-x}Bi_{1+x}$ is the first compound in the Na-Sn-Bi ternary system. Sn atoms form a three-dimensional open framework hosting Na and also one loosely bound Bi guest atom. Interestingly, for both $x = 0$ and $x = 2$ results a semiconducting small indirect band gap Zintl compound owning the same atomic structure but different electron numbers.

Chemistry–A European Journal

Supporting Information

Open Sn Framework Structure Hosting Bi Guest atoms– Synthesis, Crystal and Electronic Structure of $Na_{13}Sn_{26}Bi$

S. Zeitz, M. Boyko, S. Ponou, V. Hlukhyy, and T. F. Fässler*

Supporting Information

Open Sn Framework Structure Hosting Bi Guest atoms – Synthesis, Crystal and Electronic Structure of $Na_{13}Sn_{26}Bi$

S. Zeitz[a], M. Boyko[a], S. Ponou[a], V. Hlukky[a], T.F. Fässler[a]

Author Affiliation:

[a] School of Natural Science, Technical University of Munich, Chair of Inorganic Chemistry with Focus on Novel Materials, Lichtenbergstraße 4, D-85747 Garching, Germany. Email: thomas.faessler@lrz.tum.de

1. Na-Sn-Pn (Pn = P, As, Sb) system: overview of known compounds

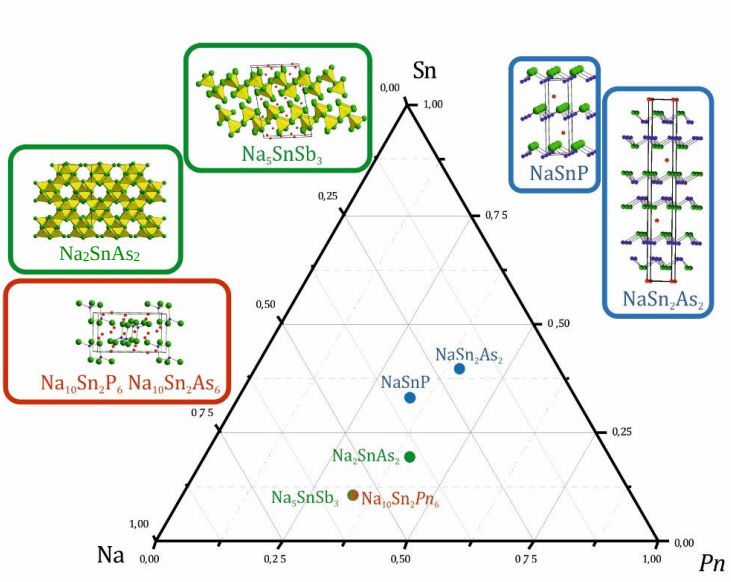

Figure S1: Crystal structures of the compounds in the Na-Sn-*Pn* (*Pn* = P, As, Sb) ternary systems. In red rectangles are phases with isolated fragments, blue – with two-dimensional nets, green – three-dimensional networks built by tetrahedrally coordinated Sn atoms. [3–8]

2. Additional information on the Crystal Structure:

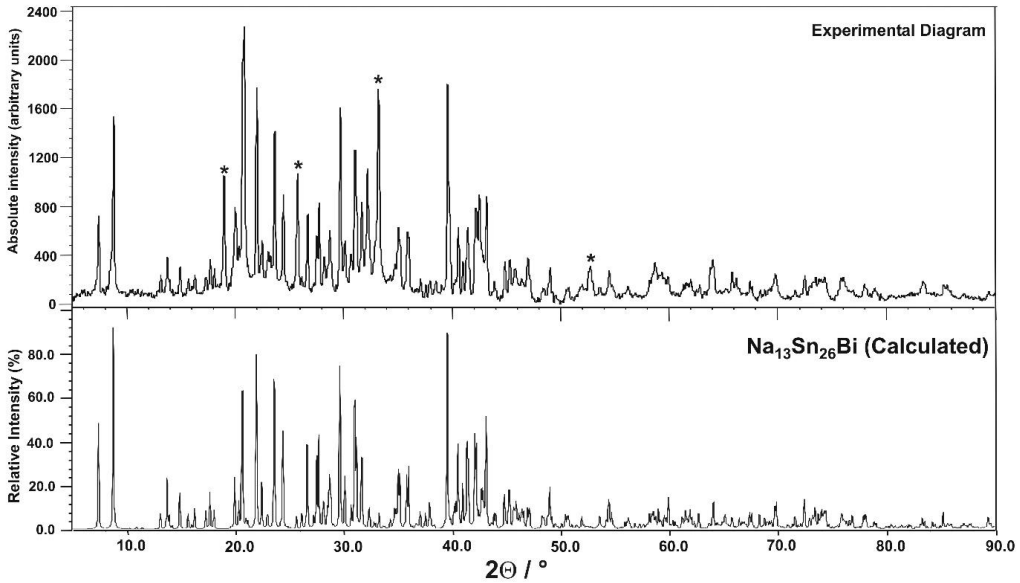

Figure S2. Experimental powder diagram of the reaction product Na:Sn:Bi = 5:12:1 (top) and theoretical powder diagram calculated for $Na_{13}Sn_{26}Bi$ (bottom). Strongest un-indexed reflections are labeled with stars (*).

Table S1: Atom coordinates and equivalent isotropic displacement parameters (Å^2) for the compound $Na_{13}Sn_{25.73(2)}Bi_{1.27(2)}$, E = statistical mixture of Sn and Bi.

Atom	Wyck.	S.O.F.	x	y	z	U_{eq}
Sn1	2i	1	0.44093(9)	0.43226(8)	0.0090(2)	0.0162(9)
Bi1	2i	0.5	0.5118(1)	0.0132(6)	0.0162(9)	0.0090(2)
E2	2i	0.864/0.136(8)	0.36986(8)	0.18593(7)	0.0095(3)	0.0095(3)
Sn3	2i	1	0.5403(1)	0.20270(9)	0.45310(7)	0.0080(2)
Sn4	2i	1	0.2026(1)	0.85338(9)	0.43784(8)	0.0091(2)
Sn5	2i	1	0.0342(1)	0.19197(9)	0.45582(7)	0.0079(2)
Sn6	2i	1	0.3007(1)	0.13760(9)	0.55179(8)	0.0086(2)
Sn7	2i	1	0.5875(1)	0.45092(9)	0.42016(8)	0.0101(2)
Sn8	2i	1	0.1261(1)	0.79320(9)	0.20159(8)	0.0097(2)
Sn9	2i	1	0.5746(1)	0.02976(9)	0.76238(7)	0.0083(2)
Sn10	2i	1	0.9075(1)	0.07131(9)	0.06880(8)	0.0087(2)
Sn11	2i	1	0.3719(1)	0.19887(9)	0.78769(8)	0.0090(2)
Sn12	2i	1	0.0706(1)	0.03159(9)	0.76016(7)	0.0082(2)
Sn13	2i	1	0.4097(1)	0.07286(9)	0.06582(8)	0.0094(2)
Na1	2i	1	0.3649(8)	0.5802(7)	0.2658(6)	0.031(2)
Na2	2i	1	0.2322(7)	0.2782(6)	0.0180(5)	0.021(1)
Na3	2i	1	0.2555(7)	0.2194(7)	0.2680(5)	0.018(1)
Na4	2i	1	0.6676(7)	0.2748(6)	0.0160(5)	0.018(1)
Na5	2i	1	0.7390(7)	0.2216(7)	0.2687(5)	0.019(1)
Na6	2i	1	0.1972(9)	0.4216(7)	0.7357(6)	0.032(2)
Na7	1c	1	0	1/2	0	0.037(3)

Table S2: Anisotropic displacement parameters (Å^2) for the compound $Na_{13}Sn_{25.73(2)}Bi_{1.27(2)}$.

Atom	U_{11}	U_{22}	U_{33}	U_{12}	U_{13}	U_{23}
Bi1	0.0171(2)	0.020(3)	0.020(3)	0.015(2)	0.008(2)	0.008(2)
Sn1	0.0077(4)	0.0081(4)	0.0109(4)	0.0037(3)	0.0025(3)	0.0021(3)
E2	0.0084(4)	0.0104(5)	0.0112(5)	0.0059(3)	0.0028(3)	0.0028(3)
Sn3	0.0076(4)	0.0084(4)	0.0080(4)	0.0035(3)	0.0021(3)	0.0023(3)
Sn4	0.0084(4)	0.0123(4)	0.0100(4)	0.0070(4)	0.0035(3)	0.0044(3)
Sn5	0.0079(4)	0.0080(4)	0.0080(4)	0.0038(3)	0.0023(3)	0.0021(3)
Sn6	0.0075(4)	0.0115(4)	0.0086(4)	0.0054(3)	0.0029(3)	0.0034(3)
Sn7	0.0093(4)	0.0091(4)	0.0120(4)	0.0051(4)	0.0024(3)	0.0021(3)
Sn8	0.0094(4)	0.0100(4)	0.0095(4)	0.0035(3)	0.0030(3)	0.0033(3)
Sn9	0.0083(4)	0.0094(4)	0.0064(4)	0.0026(3)	0.0019(3)	0.0026(3)
Sn10	0.0080(4)	0.0092(4)	0.0093(4)	0.0043(3)	0.0025(3)	0.0026(3)
Sn11	0.0092(4)	0.0096(4)	0.0091(4)	0.0048(3)	0.0028(3)	0.0029(3)
Sn12	0.0083(4)	0.0087(4)	0.0066(4)	0.0026(3)	0.0014(3)	0.0022(3)
Sn13	0.0085(4)	0.0102(4)	0.0090(4)	0.0041(3)	0.0019(3)	0.0021(3)
Na1	0.026(4)	0.032(4)	0.021(3)	0.003(3)	0.001(3)	0.004(3)
Na2	0.022(3)	0.019(3)	0.025(3)	0.011(3)	0.009(3)	0.006(3)
Na3	0.010(3)	0.036(4)	0.018(3)	0.015(3)	0.008(2)	0.014(3)
Na4	0.017(3)	0.016(3)	0.022(3)	0.013(3)	-0.001(2)	0.003(2)
Na5	0.010(3)	0.034(4)	0.017(3)	0.015(3)	0.008(2)	0.007(3)
Na6	0.033(4)	0.031(4)	0.025(4)	0.002(3)	0.010(3)	0.011(3)
Na7	0.072(8)	0.017(5)	0.007(4)	-0.001(4)	-0.005(5)	0.004(5)
Bi1	0.0171(2)	0.020(3)	0.020(3)	0.015(2)	0.008(2)	0.008(2)
Sn1	0.0077(4)	0.0081(4)	0.0109(4)	0.0037(3)	0.0025(3)	0.0021(3)
Sn2	0.0084(4)	0.0104(5)	0.0112(5)	0.0059(3)	0.0028(3)	0.0028(3)
Bi2	0.0084(4)	0.0104(5)	0.0112(5)	0.0059(3)	0.0028(3)	0.0028(3)
Sn3	0.0076(4)	0.0084(4)	0.0080(4)	0.0035(3)	0.0021(3)	0.0023(3)
Sn4	0.0084(4)	0.0123(4)	0.0100(4)	0.0070(4)	0.0035(3)	0.0044(3)
Sn5	0.0079(4)	0.0080(4)	0.0080(4)	0.0038(3)	0.0023(3)	0.0021(3)
Sn6	0.0075(4)	0.0115(4)	0.0086(4)	0.0054(3)	0.0029(3)	0.0034(3)
Sn7	0.0093(4)	0.0091(4)	0.0120(4)	0.0051(4)	0.0024(3)	0.0021(3)
Sn8	0.0094(4)	0.0100(4)	0.0095(4)	0.0035(3)	0.0030(3)	0.0033(3)
Sn9	0.0083(4)	0.0094(4)	0.0064(4)	0.0026(3)	0.0019(3)	0.0026(3)
Sn10	0.0080(4)	0.0092(4)	0.0093(4)	0.0043(3)	0.0025(3)	0.0026(3)
Sn11	0.0092(4)	0.0096(4)	0.0091(4)	0.0048(3)	0.0028(3)	0.0029(3)
Sn12	0.0083(4)	0.0087(4)	0.0066(4)	0.0026(3)	0.0014(3)	0.0022(3)
Sn13	0.0085(4)	0.0102(4)	0.0090(4)	0.0041(3)	0.0019(3)	0.0021(3)

Table S3: Results of the EDX analysis of the crystal with the refined composition $Na_{13}Sn_{25.73}Bi_{1.27}$ from the sample '$Na_5Sn_{12}Bi_2$'.

	Na (at. %)	Sn (at. %)	Bi (at. %)
EDX	39(12)	46(6)	15(6)
$Na_{13}Sn_{25.73}Bi_{1.27}$	32.5	64.3	3.2

Table S4: Interatomic distances in the $Na_{13}Sn_{25.73(2)}Bi_{1.27(2)}$.

Atom types		Distance (Å)	Atom types		Distance (Å)
Sn-Sn, Sn-Bi, Bi-Bi					
Bi1	Sn11	3.145(8)	Sn1	Sn7	2.889(1)
E2	Sn1	2.965(1)		Sn5	2.892(2)
	Sn10	2.985(1)		Sn1	2.911(1)
Sn4	Sn5	2.829(2)		E2	2.965(1)
	Sn3	2.837(2)	Sn3	Sn6	2.835(2)
	Sn6	2.843(2)		Sn4	2.837(2)
	Sn8	2.861(2)		Sn9	2.889(1)
Sn6	Sn5	2.822(1)		Sn7	2.947(2)
	Sn3	2.835(2)	Sn5	Sn6	2.822(1)
	Sn4	2.843(1)		Sn4	2.829(2)
	Sn11	2.854(2)		Sn12	2.848(1)
Sn8	Sn4	2.861(2)		Sn1	2.892(2)
	Sn12	2.878(2)	Sn7	Sn7	2.879(1)
	Sn9	2.880(1)		Sn1	2.889(1)
Sn10	Sn13	2.887(1)		Sn3	2.947(2)
	Sn12	2.900(2)	Sn9	Sn11	2.870(2)
	Sn10	2.936(1)		Sn8	2.880(1)
	E2	2.985(1)		Sn3	2.890(1)
Sn12	Sn5	2.848(1)		Sn13	2.907(2)
	Sn11	2.876(1)	Sn11	Sn6	2.854(2)
	Sn8	2.878(2)		Sn9	2.870(2)
	Sn10	2.900(2)		Sn12	2.877(1)
				Bi1	3.145(8)
			Sn13	Sn13	2.880(1)
				Sn10	2.887(1)
				Sn9	2.907(2)
Na-Sn, Na-Bi, Na-Na					
Na1	E2	3.298(7)	Na2	Bi1	3.20(1)
	Sn3	3.431(7)		E2	3.243(7)
	Sn11	3.457(8)		Sn13	3.250(8)
	Sn7	3.516(9)		Bi1	3.27(1)
	Na2	3.521(8)		Sn12	3.324(5)
	Sn6	3.614(6)		Sn11	3.377(7)
	Bi1	3.65(1)		Na1	3.521(8)
	Sn8	3.759(9)		Sn10	3.540(6)
	Sn4	3.804(8)		Na3	3.59(1)
	Bi1	3.89 (1)		Na7	3.618(7)
	Na6	3.99 (1)		Sn8	3.696(6)
	Na3	4.00(1)		Sn10	3.703(7)
Na3	Sn13	3.271(7)		Na4	3.967(9)
	Sn7	3.288(5)	Na4	Bi1	3.22(3)
	E2	3.302(8)		E2	3.246(6)
	Sn3	3.332(7)		Sn13	3.262(7)
	Sn1	3.365(7)		Sn9	3.274(5)
	Sn9	3.387(8)		Bi1	3.30(2)
	Sn10	3.389(5)		Sn11	3.384(6)
	Sn5	3.513(7)		Sn13	3.527(7)
	Sn12	3.524(7)		Na6	3.534(8)

	Na2	3.59(1)		Na5	3.59(1)
	Na1	4.00(1)		Sn8	3.623 (7)
Na5	Sn13	3.295(5)		Sn10	3.624(8)
	E2	3.298(7)		Na7	3.631(7)
	Sn3	3.315(7)		Na2	3.967(9)
	Sn7	3.319(7)	Na6	E2	3.298(9)
	Sn10	3.351(7)		Sn11	3.430(9)
	Sn9	3.439(7)		Sn5	3.463(6)
	Sn1	3.443(5)		Na4	3.534(8)
	Sn5	3.484(7)		Sn7	3.554(9)
	Sn12	3.550(8)		Sn6	3.623(8)
	Na4	3.59(1)		Bi1	3.62(1)
	Na6	3.97(1)		Sn8	3.833(9)
Na7	2× Sn8	3.186(8)		Bi1	3.86(1)
	2× E2	3.300(1)		Sn4	3.925(6)
	2× Na2	3.618(7)		Na5	3.97(1)
	2× Na4	3.631(7)		Na1	3.98(1)
	2× Na1	4.076(7)		Sn1	4.058(9)
	2× Na6	4.080(9)		Na7	4.080(9)

3. Electronic Band Structure Calculations:

Detailed description of the used basis sets and basis set listings in CRYSTAL format.

Na: taken from literature[1].

```
11 5
0 0 5 2.0 1.0
  4098.2003908     -.58535911879E-02
  616.49374031     -.43647161872E-01
  139.96644001     -.19431465884
  39.073441051     -.48685065731
  11.929847205     -.41881705137
0 0 3 2.0 1.0
  20.659966030      .85949689854E-01
  1.9838860978     -.56359144041
  .64836323942     -.51954009048
0 0 1 1.0 1.0
  0.32              1.0000000000
0 1 1 0.0 1.0
  0.16              1.0 1.0
0 2 5 6.0 1.0
  75.401862017     .154353625324E-01
  17.274818978     .997382931840E-01
  5.1842347425     .312095939659
  1.6601211973     .492956748074
  .51232528958     .324203983180
```

Sn: taken from literature[2].

```
250 13
INPUT
22   0   2   4   4   2   0
17.4204140000000  279.988682000000  0
7.63115500000000  62.3778100000000  0
16.1310240000000  66.1625230000000  0
15.6280770000000  132.174396000000  0
7.32560800000000  16.3394170000000  0
6.94251900000000  32.4889590000000  0
15.5149760000000  36.3874410000000  0
15.1881600000000  54.5078410000000  0
5.45602400000000  8.69682300000000  0
5.36310500000000  12.8402080000000  0
12.2823480000000 -12.5763330000000  0
12.2721500000000 -16.5959440000000  0
0 0 4 2.0 1.0
  1577.0715931      0.17042767713E-03
  235.26601078      0.81467057272E-03
  38.206330645     -0.39057904293E-02
  13.097031765      0.53245922343
0 0 2 2.0 1.0
  11.673161352       1.5435287275
  5.9463871497      0.76421510041
0 0 1 0.0 1.0
 1.8924497043       1.0000000000
0 0 1 0.0 1.0
 0.88429486443       1.0000000000
0 0 1 0.0 1.0
 0.23543697233       1.0000000000
0 1 1 0.0 1.0
 0.09                1.0 1.0
0 2 3 6.0 1.0
  221.55767496      0.31125177983E-03
  21.084021433      0.31108097016E-01
  8.7600138521     -0.27571560918
0 2 3 2.0 1.0
  2.5902185134      0.45912328666
  1.3409064118      0.49682867217
 0.67241607517      0.18962377821
0 2 1 0.0 1.0
  0.27895803477     1.0000000000
0 3 6 10.0 1.0
  108.33210154      0.46561853277E-03
  23.703936630      0.54063163067E-01
  22.339843906     -0.58928768877E-01
  4.0874834028      0.19588500896
  1.9737354146      0.42301799185
 0.90158257692      0.39252716176
0 3 1 0.0 1.0
 0.38237153649      1.0000000000
0 3 1 0.0 1.0
 0.191185768245     1.0000000000
0 4 1 0.0 1.0
 0.293928485        1.0000000000
```

Bi: taken from literature[9].

```
283 13
INPUT
23. 0 2 4 4 2 2
13.043090 283.264227 0
8.221682   62.471959 0
10.467777  72.001499 0
9.118901  144.002277 0
6.754791    5.007945 0
6.252592    9.991550 0
8.081474   36.396259 0
7.890595   54.597664 0
4.955556    9.984294 0
4.704559   14.981485 0
4.214546   13.713383 0
4.133400   18.194308 0
6.205709  -10.247443 0
6.227782  -12.955710 0
0 0 4 2.0 1.0
  716.41435310      0.31254307133E-03
  83.806059047      0.17624768946E-02
  21.116962853     -0.21910983437
  15.491448187      0.40411224931
0 0 2 2.0 1.0
  23.213322651     -0.68255758685E-01
  6.6412776932      0.97888046471
0 0 1 0.0 1.0
 1.7668753097       1.0000000000
0 0 1 0.0 1.0
 0.87636753866      1.0000000000
0 0 1 0.0 1.0
 0.26185055933      1.0000000000
0 1 1 0.0 1.0
 0.10               1.0 1.0
0 2 3 6.0 1.0
  15.249644669      0.74560356000
  14.846176053     -0.85578637338
  7.0636826784      0.40149159592
0 2 3 3.0 1.0
  2.5802708340      0.35542729633
  1.4990870077      0.63976991890
 0.75411119473      0.32332773839
0 2 1 0.0 1.0
  0.29617825843     1.0000000000
0 3 6 10.0 1.0
  66.404481948      0.38102878348E-03
  13.858426961      0.10746152442E-01
  7.0654519000     -0.71947646845E-01
  2.5252144035      0.26195974989
  1.3419585000      0.42594750000
 0.68340941000      0.33680325627
0 3 1 0.0 1.0
 0.32934755420      1.0000000000
0 3 1 0.0 1.0
 0.1646737771     1.0000000000
0 4 1 0.0 1.0
 0.31271            1.0000000000
```

Table S5: Comparison of the cell parameters between the experimentally determined and the optimized cell parameters of the two stoichiometric models.

	Experiment [Å]	$Na_{13}Sn_{26}Bi$ [Å]	Δ(Exp.-Calc.) [%]	$Na_{13}Sn_{24}Bi_3$ [Å]	Δ(Exp.-Calc.) [%]
a	9.0826	9.0571	-0.28	9.0449	-0.42
b	11.2527	11.2931	0.36	11.1327	-1.08
c	13.2278	13.2160	-0.09	13.4630	1.75
α	112.114	112.7620	0.57	110.5816	-1.39
β	99.818	99.7086	-0.11	100.5517	0.73
γ	101.379	101.2220	-0.16	101.7537	0.37

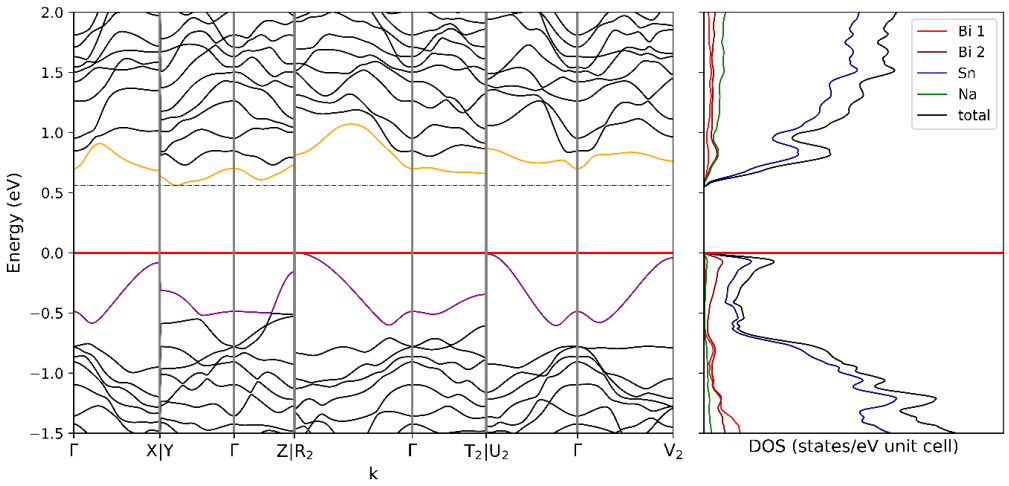

Figure S3: Band structure of $Na_{13}Sn_{24}Bi_3$ with atomic position resolved DOS for Bi.

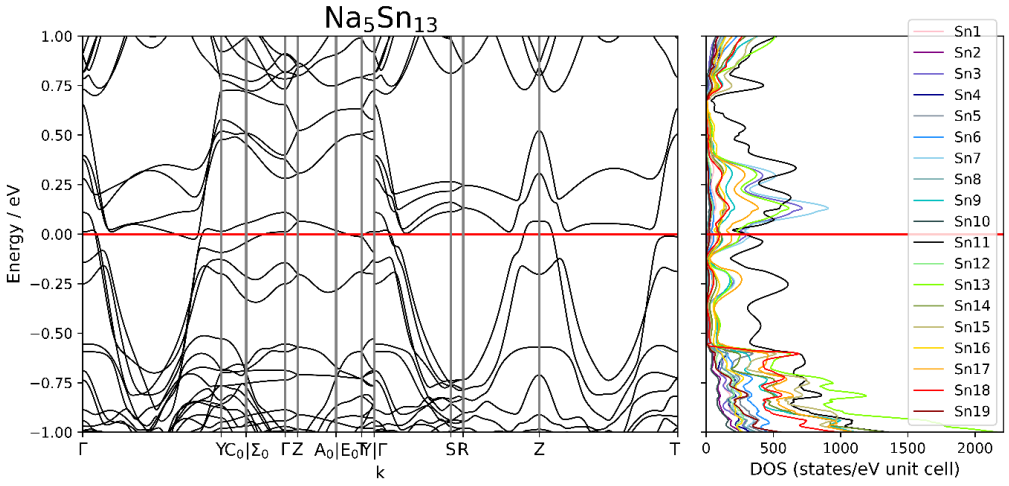

Figure S4: Band structure of Na_4Sn_{13} with atomic positions resolved DOS for Sn

Table S6: Partial charges from the Mullikan analysis. The effective charge Z_{eff} was subtracted from the number of electrons of the neutral element to get the partial charge.

$Na_{13}Sn_{26}Bi$				$Na_{13}Sn_{24}Bi_3$			
Atom	Z_{eff}:	part. ch.:	ass. ch.:	Atom	Z_{eff}:	part. ch.:	ass. ch.:
Bi1	24.038	-1.038	-1	Bi1	24.053	-1.053	-1
Sn1	22.167	-0.167	0	Sn1	22.247	-0.247	0
Sn2	23.132	-1.132	-2	Bi2	24.023	-1.023	-1
Sn3	22.348	-0.348	0	Sn3	22.310	-0.310	0
Sn4	21.96	0.04	0	Sn4	21.968	0.032	0
Sn5	22.236	-0.236	0	Sn5	22.298	-0.298	0
Sn6	22.029	-0.029	0	Sn6	22.015	-0.015	0
Sn7	22.535	-0.535	-1	Sn7	22.559	-0.559	-1
Sn8	22.538	-0.538	-1	Sn8	22.549	-0.549	-1
Sn9	22.168	-0.168	0	Sn9	22.152	-0.152	0
Sn10	22.26	-0.26	0	Sn10	22.185	-0.185	0
Sn11	22.453	-0.453	-1	Sn11	22.485	-0.485	-1
Sn12	22.148	-0.148	0	Sn12	22.15	-0.150	0
Sn13	22.64	-0.64	-1	Sn13	22.665	-0.665	-1
Na1	10.217	0.783	1	Na1	10.21	0.790	1
Na2	10.236	0.764	1	Na2	10.234	0.766	1
Na3	10.169	0.831	1	Na3	10.177	0.823	1
Na4	10.229	0.771	1	Na4	10.228	0.772	1
Na5	10.17	0.83	1	Na5	10.175	0.825	1
Na6	10.222	0.778	1	Na6	10.213	0.787	1
Na7	10.246	0.754	1	Na7	10.259	0.741	1

Table S7: Overlap population between the first six nearest neighbours calculated via Mullikan analysis for $Na_{13}Sn_{24}Bi_3$.

atom A	atom B	R(A-B) [Å]	overlap Population (AB)	atom A	atom B	R(A-B) [Å]	overlap Population (AB)
Bi1	Na2	3.118	0.047	Sn11	Sn6	2.885	0.24
	Na4	3.215	0.046		Sn12	2.889	0.234
	Sn11	3.317	0.098		Sn9	2.889	0.236
	Na1	3.904	0.019		Bi1	3.317	0.098
	Na6	3.913	0.02		Na4	3.358	0.013
	Na7	4.522	0.008		Na1	3.36	0.023
Sn1	Sn7	2.911	0.21	Sn12	Sn10	2.881	0.264
	Sn2	2.92	0.042		Sn11	2.889	0.234
	Sn5	2.934	0.217		Sn8	2.89	0.242
	Bi2	3.17	0.051		Sn10	2.912	0.255
	Na5	3.351	0.016		Na2	3.307	0.007
	Na3	3.507	0.009		Na3	3.52	0.009
Bi2	Sn10	2.952	0.206	Sn13	Sn10	2.868	0.238
	Sn1	3.17	0.051		Sn13	2.924	0.203
	Na7	3.171	0.043		Sn9	2.929	0.231
	Na2	3.174	0.048		Na4	3.218	0.028
	Na4	3.215	0.042		Na5	3.259	0.024

	Na3	3.271	0.034		Na2	3.281	0.029
Sn3	Sn4	2.834	0.27	Na1	Bi2	3.355	0.037
	Sn6	2.843	0.264		Sn11	3.36	0.023
	Sn9	2.911	0.253		S7	3.414	0.032
	Sn7	2.951	0.215		Sn3	3.542	0.01
	Na3	3.284	0.012		Sn6	3.58	0.01
	Na5	3.343	0.012		Na2	3.681	0.003
Sn4	Sn3	2.834	0.27	Na2	Bi1	3.118	0.047
	Sn6	2.84	0.286		Bi2	3.174	0.048
	Sn5	2.848	0.26		Sn13	3.281	0.029
	Sn8	2.884	0.258		Sn12	3.307	0.007
	Na6	3.84	0.006		Sn10	3.381	0.007
	Na1	3.985	0.004		Sn11	3.386	0.013
Sn5	Sn6	2.835	0.259	Na3	Bi2	3.271	0.034
	Sn4	2.848	0.26		Sn3	3.284	0.012
	Sn12	2.881	0.264		Sn13	3.333	0.023
	Sn1	2.934	0.217		Sn7	3.358	0.019
	Na5	3.334	0.012		Sn9	3.412	0.009
	Na3	3.425	0.01		Sn5	3.425	0.01
Sn6	Sn5	2.835	0.259	Na4	Bi2	3.215	0.042
	Sn4	2.84	0.286		Bi1	3.215	0.046
	Sn3	2.843	0.264		Sn13	3.218	0.028
	Sn11	2.885	0.24		Sn9	3.261	0.009
	Na1	3.58	0.01		Sn11	3.358	0.013
	Na6	3.69	0.008		Sn13	3.499	0.009
Sn7	Sn7	2.896	0.221	Na5	Sn13	3.259	0.024
	Sn1	2.911	0.21		Sn5	3.334	0.012
	Sn3	2.951	0.215		Sn3	3.343	0.012
	Na3	3.358	0.019		Sn13	3.351	0.016
	Na5	3.391	0.021		Bi2	3.37	0.028
	Na1	3.414	0.032		Sn7	3.391	0.021
Sn8	Sn4	2.884	0.258	Na6	Sn11	3.437	0.021
	Sn12	2.89	0.242		Bi2	3.443	0.031
	Sn9	2.897	0.244		Sn7	3.505	0.032
	Na7	3.233	0.04		Sn5	3.539	0.009
	Na6	3.659	0.015		Sn8	3.659	0.015
	Na1	3.729	0.013		Sn6	3.69	0.008
Sn9	Sn11	2.889	0.236	Na7	Bi2	3.171	0.043
	Sn8	2.897	0.244		Sn8	3.233	0.04
	Sn3	2.911	0.253		Na4	3.606	0.002
	Sn13	2.929	0.231		Na2	3.613	0.003
	Na4	3.261	0.009		Na1	4.187	0.001
	Na3	3.412	0.009		Na6	4.205	0.001
Sn10	Sn13	2.868	0.238				
	Sn10	2.869	0.262				
	Sn12	2.912	0.255				
	Bi2	2.952	0.206				
	Na2	3.381	0.007				
	Na3	3.495	0.008				

Table S8: Overlap population between the first six nearest neighbours calculated via Mullikan analysis for $Na_{13}Sn_{26}Bi$.

atom A	atom B	R(A-B) [Å]	overlap Population (AB)	atom A	atom B	R(A-B) [Å]	overlap Population (AB)
Bi1	Na2	3.232	0.043	Sn11	Sn6	2.862	0.246
	Sn11	3.247	0.084		Sn9	2.877	0.234
	Na4	3.268	0.043		Sn12	2.881	0.236
	Na6	3.654	0.029		Bi1	3.247	0.084
	Na1	3.705	0.027		Na2	3.353	0.014
	Na7	4.529	0.008		Na4	3.36	0.013
Sn1	Sn5	2.89	0.237	Sn12	Sn10	2.855	0.267
	Sn7	2.897	0.234		Sn8	2.878	0.246
	Sn1	2.907	0.266		Sn11	2.881	0.236
	Sn2	2.961	0.245		Sn10	2.906	0.251
	Na3	3.336	0.011		Na2	3.324	0.007
	Na5	3.419	0.01		Na3	3.502	0.009
Sn2	Sn1	2.961	0.245	Sn13	Sn13	2.887	0.21
	Sn10	2.983	0.21		Sn10	2.889	0.24
	Na2	3.229	0.046		Sn9	2.909	0.233
	Na4	3.234	0.043		Na2	3.221	0.033
	Na1	3.292	0.044		Na4	3.229	0.029
	N6	3.3	0.045		Na3	3.247	0.025
Sn3	Sn6	2.839	0.256	Na1	Sn2	3.292	0.044
	Sn4	2.843	0.261		Na2	3.43	0.005
	Sn9	2.892	0.25		Sn11	3.445	0.019
	Sn7	2.956	0.217		Sn3	3.453	0.012
	Na5	3.291	0.012		Sn7	3.527	0.026
	Na2	3.325	0.01		Sn6	3.609	0.009
Sn4	Sn5	2.828	0.273	Na2	Sn13	3.221	0.033
	Sn3	2.843	0.261		Sn2	3.229	0.046
	Sn6	2.843	0.284		Bi1	3.232	0.043
	Sn8	2.862	0.275		Sn12	3.324	0.007
	Na1	3.805	0.006		Sn11	3.353	0.014
	Na6	4.009	0.004		Na1	3.43	0.005
Sn5	Sn6	2.826	0.263	Na3	Sn13	3.247	0.025
	Sn4	2.828	0.273		Sn7	3.299	0.017
	Sn12	2.855	0.267		Sn2	3.315	0.027
	Sn1	2.89	0.237		Sn3	3.325	0.01
	Na5	3.468	0.009		S1	3.336	0.011
	Na6	3.494	0.012		Sn10	3.349	0.013
Sn6	Sn5	2.826	0.263	Na4	Sn13	3.229	0.029
	Sn3	2.839	0.256		Sn2	3.234	0.043
	Sn4	2.843	0.284		Sn9	3.252	0.007
	Sn11	2.862	0.246		Bi1	3.268	0.043
	Na1	3.609	0.009		Sn11	3.36	0.013
	Na6	3.611	0.01		Na6	3.443	0.005
Sn7	Sn7	2.891	0.195	Na5	Sn3	3.291	0.012

	Sn1	2.897	0.234		Sn13	3.292	0.02
	Sn3	2.956	0.217		Sn2	3.309	0.029
	Na3	3.299	0.017		Sn7	3.309	0.021
	Na5	3.309	0.021		Sn10	3.321	0.012
	Na1	3.527	0.026		Sn1	3.419	0.01
Sn8	Sn4	2.862	0.275	Na6	Sn2	3.3	0.045
	Sn12	2.878	0.246		Sn11	3.404	0.02
	Sn9	2.881	0.243		Na4	3.443	0.005
	Na7	3.145	0.044		Sn5	3.494	0.012
	Na4	3.622	0.013		Sn7	3.528	0.029
	Na2	3.726	0.012		Sn6	3.611	0.01
Sn9	Sn11	2.877	0.234	Sn7	Sn13	3.145	0.044
	Sn8	2.881	0.243		Sn2	3.313	0.034
	Sn3	2.892	0.25		Na2	3.64	0.002
	Sn13	2.909	0.233		Na4	3.667	0.002
	Na4	3.252	0.007		Na1	4.029	0.001
	Na3	3.374	0.01		Na6	4.055	0.001
Sn10	Sn13	2.889	0.24				
	Sn12	2.906	0.251				
	Sn10	2.928	0.257				
	Sn2	2.983	0.21				
	Na5	3.321	0.012				
	Na3	3.349	0.013				

References:

[1] R. E. Stene, B. Scheibe, A. J. Karttunen, W. Petry, F. Kraus, *Eur. J. Inorg. Chem.* **2019**, *2019*, 3672.

[2] A. J. Karttunen, T. F. Fässler, *Chemistry (Weinheim an der Bergstrasse, Germany)* **2014**, *20*, 6693.

[3] B. Eisenmann, U. Rößler, *Zeitschrift für Kristallographie - New Crystal Structures* **1998**, *213*, 28.

[4] J. Klein, B. Eisenmann, *Zeitschrift für Kristallographie - Crystalline Materials* **1991**, *196*.

[5] B. Eisenmann, J. Klein, *Zeitschrift für Naturforschung B* **1988**, *43*, 1156.

[6] M. Asbrand, B. Eisenmann, *Zeitschrift für Naturforschung B* **1993**, *48*, 452.

[7] M. Asbrand, B. Eisenmann, J. Klein, *Z. anorg. allg. Chem.* **1995**, *621*, 576.

[8] *Zeitschrift für Kristallographie - Crystalline Materials* **1991**, *197*, 269.

[9] B. Scheibe, R. Haiges, S. I. Ivlev, A. J. Karttunen, U. Müller, K. O. Christe, F. Kraus, *Eur. J. Inorg. Chem.* **2020**, *2020*, 4483.

5.9 $CaSi_{2-x}Ge_x$, solid solution and analysis of ordered structures

S. Zeitz, A. Mutschke, T.F. Fässler

Manuscript for publication

$CaSi_{2-x}Ge_x$, solid solution and analysis of ordered structures

S. Zeitz[a], A. Mutschke[a], T. F. Fässler[a]

Author Affiliation:

[a] School of Natural Science, Technical University of Munich, Chair of Inorganic Chemistry with Focus on Novel Materials, Lichtenbergstraße 4, D-85747 Garching, Germany.
Email: thomas.faessler@lrz.tum.de

Abstract

$CaSi_2$ and $CaGe_2$ are two isostructural, well understood Zintl compounds, with a simple layered structure of alternating Ca and Si/Ge layers, which therefore are perfect candidates to synthesize mixed $CaSi_{2-x}Ge_x$ compounds. In this paper we present a solid solution of $CaSi_{2-x}Ge_x$ with x = 0, 0.5, 1, 1.5 and 2 for which the structure was refined using the Rietveld method on synchrotron powder x-ray diffraction patterns. Further on where stability and electronic structure of the different known $CaSi_2$ and $CaGe_2$ polymorphs calculated on a DFT/PBE0 TZVP (SVP for Ca) level of theory, revealing that α-CaGe2 is probably a meta-stable compound stabilized by In impurities. Further on were ordered model with the composition CaSiGe calculated, one with alternating Si and Ge nets and the other with Si and Ge alternating within one layer. Their respective stability and stability towards the parent compounds and electronic structure are discussed as well. It is revealed that entropic effect are probably the stabilizing factor for the solid solution of $CaSi_{2-x}Ge_x$ since a mixture of the parent compounds is energetically slightly more stable. The electronic structure of all modelled can also be understood as a mixture of the parent compounds, especially seen in the band structures.

Introduction

$CaSi_2$ is widely used as starting material for Si nanosheets which can be used for a variety of functionalization[1–11]. As a first step $CaSi_2$ is treated with concentrated HCl at room temperature or at -30 °C depending on the required termination of the Si-nanosheets.[12,13] The electronic structures of these functionalised nanostructures have been studied in the recent years, as well as the band structure and density of states for the parent compounds,[14–17] but exploring the electronic structure further, especially regarding the mixing of $CaSi_2$ with structurally identical compounds such as $CaGe_2$, could lead to a variety of new compounds with interesting properties.

For both $CaSi_2$ and $CaGe_2$ different polymorphs of layered structures are reported which can be found in Figure 1 as an overview. For $CaSi_2$ direct synthesis from the elements leads to the $CaSi_2$-type or *hR*6-type(**A** in Figure 1), which crystallizes in space group *R*-3*mH* (gr. 166).[18,19] Si atoms build layers of hexagonal, chair conformed rings that are analogue to the monolayers of grey arsenic. As stacking

order, a pattern of AA'BB'CC', where layers with ABC are made up by the Si2 position and layers A'B'C' by Si1. Each layer is shifted so that the vertices of the six membered rings lie above the centres of the rings one layer below (in analogy to graphite however there are planar layers). This works for the substructures ABC/A'B'C' as well as the overall arrangements of layers in AA'BB'CC'. The second polymorph, called the *hR*3-type, also shows a stacking order of these Si six-membered rings of ABC, within the same symmetry, but an, in c-direction halved, unit cell (**B** in Figure 1). The *hR*3-type can be obtained by epitaxial crystal growth on *hR*6-$CaSi_2$ crystals or by sintering of *hR*6-$CaSi_2$ in an hydrogen atmosphere.[20,21] Applying pressure during the synthesis leads to the formation of two other polymorphs with either simplified stacking order of the Si layers (**C**), crystallizing in the $EuGe_2$-type or different connection of the Si atoms (**D**) in the $ThSi_2$-type. [22,23]

For $CaGe_2$ there are two known crystal structures, also named α- and β-$CaGe_2$ (also referred to as **F** and **E**, respectively, further on). β-$CaGe_2$ is isostructural to the $CaSi_2$-type and can also be synthesized directly from the elements at elevated temperatures.[24] The α-$CaGe_2$ polymorph can only be obtained by performing the synthesis in an Indium flux.[25] Compared to the β-phase it crystallizes in a different space group $P6_3mc$ (gr. 186) but has the same structural motive. It shows layered nets of six membered rings as well, but since this time the nets are not made up by separating the Ge1 and Ge2 positions, but rather having them alternating in one layer, the stacking pattern is ABC. This also results in the c-parameter being halved compared to the β-phase.

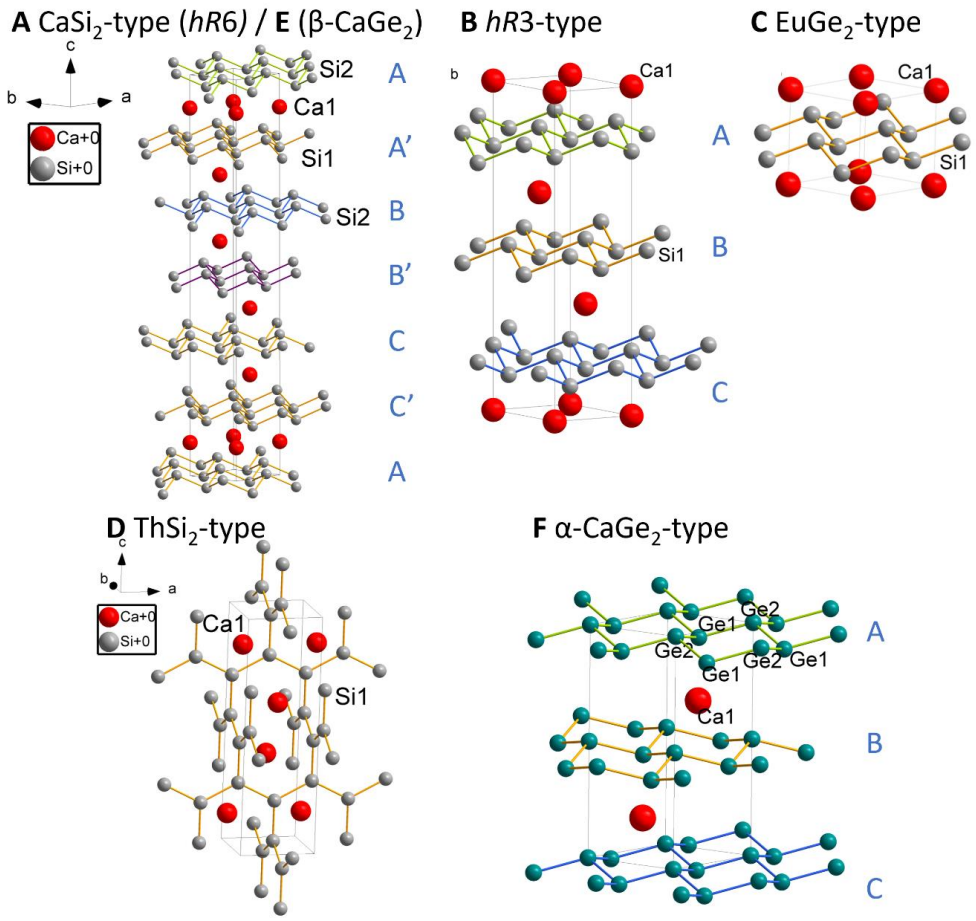

Figure 1. Overview of different structure types of $CaSi_2$ and $CaGe_2$. Ca, Si and Ge are shown in red, grey and green, respectively. Above each unit cell the structure type and reference name are written in black. The stacking order of certain structure types are marked in blue letters.

Since both $CaGe_2$ polymorphs **E** and **F** are identical in the anionic Ge substructure, only looking at the stacking order, the main difference between α- and β-$CaGe_2$ lies within the position of the Ca^{2+} cations. In the β-$CaGe_2$ (**E**) structure Ca occupies ½ of the octahedral voids between two Ge layers, so that the Ca^{2+} are positioned below the centre of the Ge2 six membered rings and above every second Si/Ge1 atom (marked as **I**). This can be seen in Figure 2 a) ($CaSi_2$/β-$CaGe_2$) and b) (α-$CaGe_2$), where the top layer within each structure is marked in green, the lower layer in yellow. For α-$CaGe_2$ the Ca^{2+} cations are located below the Ge1 positions of the top layer and on top of the centre of the lower six-membered Ge rings. This results in a tetrahedral coordination of the Ca, marked as **II**. Both structures can be transformed into each other as seen in Figure 2 c). Here the octahedral void is deformed by a movement of the Si/Ge atoms in the six-membered rings along the red and green arrows, resulting in a flipping of the rings. The largely distorted octahedral coordination **II'** is now equivalent to the tetrahedral coordination **II** in α-$CaGe_2$.

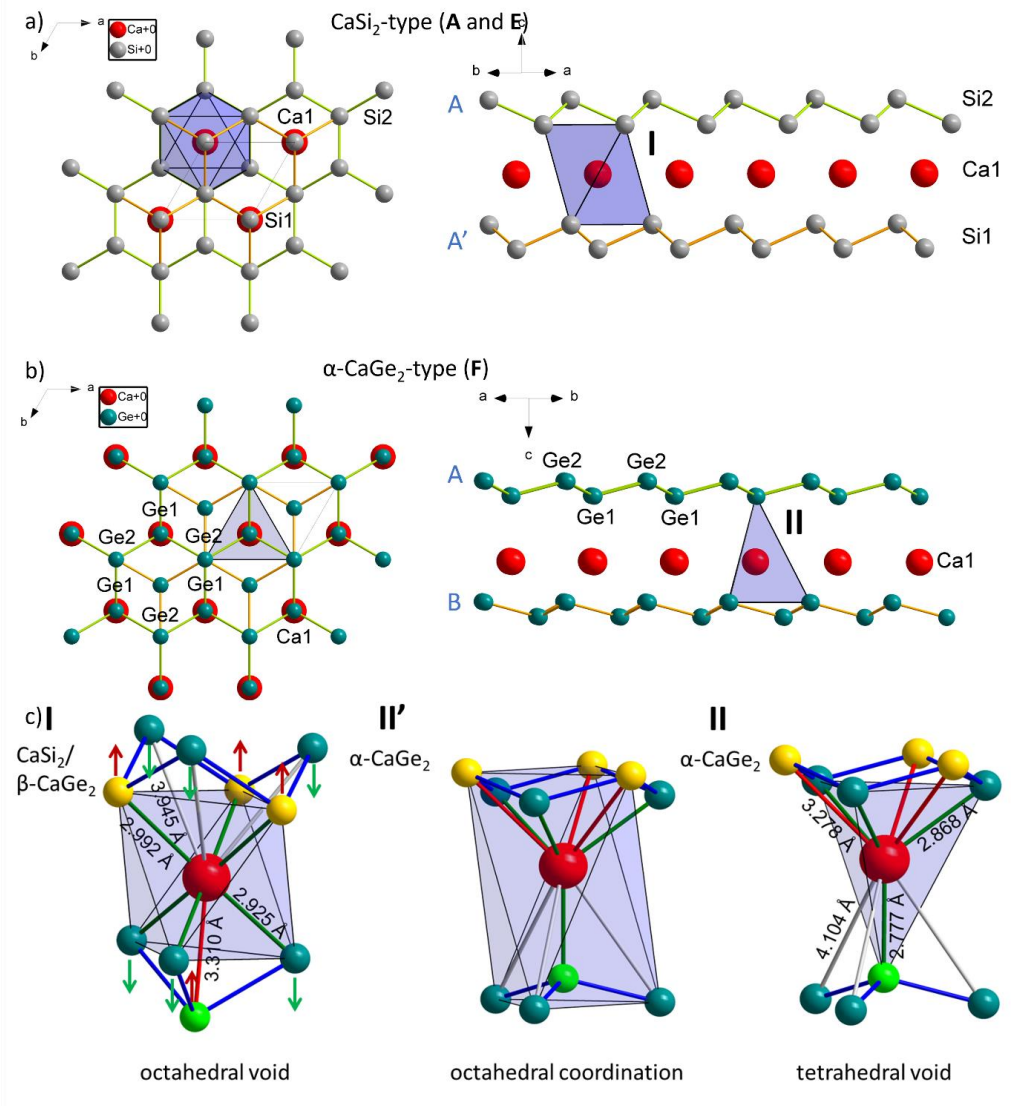

Figure 2. Comparison of the Ca coordination between a) $CaSi_2$/β-$CaGe_2$ and b) α-$CaGe_2$ with the octahedral or tetrahedral coordination marked. c) Close-up of the (distorted) octahedral coordination polyhedron in **I** $CaSi_2$/β-$CaGe_2$ and **II** α-$CaGe_2$ as well as tetrahedral coordination **II'** in α-$CaGe_2$. **I** and **II** can be transformed into each other by deformation of the six-membered rings along the green and red arrows, resulting in a flipping of the rings. The six shortest interatomic connections between Si/Ge and Ca, marked in green, define the atoms that build the coordination polyhedron. The extended first coordination incorporates additionally the next closer connected atoms marked in red. The next closer bonds are marked in grey for a better representation within the structure.

Although, if applying the Zintl-Klemm concept to make a proposal for the crystal structure, it leads to a layered structure with six membered rings as well, this concept cannot be applied to propose a possible electronic structure, since Zintl-phases normally show semiconducting behaviour, whereas both $CaSi_2$ and β-$CaGe_2$ show metallic behaviour[25,26]. This leads to the interesting question, whether an ordered but mixed compounds CaSiGe would show a similar metallic or dissimilar semi-conducting behaviour.

In this paper we present a solid-solution series of $CaSi_2$ and β-$CaGe_2$ analysed *via* laboratory and synchrotron powder XRD. Further on we performed quantum chemical calculations analysing the electronic band structure of possible ordered models as well as the parent compounds $CaSi_2$, α- and β-$CaGe_2$.

Experimental

Synthesis:

Samples of the nominal composition $CaSi_{2-x}Ge_x$ were prepared for x = 0, 0.5, 1, 1.5, and 2 in an Argon filled glove box (*MBraun*, O_2/H_2O < 2 ppm) by arc melting. Accordingly, stoichiometric amounts of Ca (Alfa Aeser, 99.5 %, chunks), Si (Wacker, 99.9 %, pulverized *via* ball milling) and/or Ge (Evochem, 99.999 %, pulverized via ball milling) were weighed. Pellets with Ca chunks embedded in the Si and/or Ge powder were pressed in a hydraulic press (*Specac*) with a pressure of 2 t. The pellet was consecutively melted in a water-cooled copper heart with an arc furnace (MAM-1, *Edmund Bühler GmbH*). The regulus was then ground in an agate mortar, pressed into a pellet again and molten twice in the arc furnace to get a phase pure product of $CaSi_{2-x}Ge_x$, since after the first arc melting step the product showed additional reflections of a $Ca_{14}Si_{19}$.[27]

Since the sample for x = 1.5 which has been synthesized for the synchrotron measurement partially decomposed to an unknown compound, a new sample with the same composition has been synthesised and PXRD data were collected in the in-house diffractometer.

Powder XRD

For powder X-ray diffraction (PXRD) measurements, the sample was ground in an agate mortar and sealed in a 0.3 mm glass capillary. PXRD measurements were performed in transmission geometry at room temperature on a Stadi P diffractometer (Stoe & Cie) equipped with a Ge(111) monochromator for Cu $K_{\alpha 1}$ radiation (λ = 1.54056 Å) and a MYTHEN DCS 1K solid-state detector (Dectris). The raw powder data was processed with the software package WinXPOW.[28]

Synchrotron measurements

Powder X-ray diffraction (PXRD) patterns for the $CaSi_{2-x}Ge_x$ samples were collected using the Canadian Brockhouse X-ray Diffraction and Scattering (BXDS) high energy wiggler beamline (WHE) at the Canadian Light Source (CLS).[29] WHE employs a Si (111) side bounce Laue monochromator and data sets were collected using a photon energy of ~30.3 keV (calibrated wavelength, λ = 0.40867 Å) and a sample-detector distance of ~496.4 mm. Two-dimensional (2D) diffraction patterns were collected on a Perkin Elmer XRD 1621 CN3 EHS detector with an active area of 409.6 mm x 409.6 mm, and a pixel size of 200 μm^2.

The 2D PXRD patterns were calibrated and integrated using the GSASII software package.[30] The sample-detector distance, detector offset and detector tilt were calibrated using an image from a

lanthanum hexaboride (LaB_6) standard reference material (NIST SRM 660a LaB_6)[31] and the calibration parameters were applied to all patterns prior to integration. After calibration, the 2D patterns were integrated to obtain standard point detector powder diffraction patterns. For the measurement, polycrystalline powders were sealed within glass capillaries (Ø 0.5 mm, 0.01 mm wall thickness).

Rietveld

Structure refinements by the Rietveld method of both laboratory and synchrotron X-ray diffraction data were conducted using the Fullprof programme package.[32] Profiles were fitted using the Thompson Cox Hastings profile function. The Cagliotti parameters (*U*, *V*, *W*), corresponding to the respective instrumental resolution as well as peak shape asymmetries and zero shifts were determined beforehand by a full refinement of externally measured LaB_6 standards. For the structure determination sample displacement, cell parameters, microstrain and size parameters, atomic positions occupations and thermal displacement parameters were freely refined. The background was corrected using interpolating background points.

Quantum chemical calculations

The computational studies of all polymorphs of $CaSi_2$, $CaGe_2$ and the ordered variants of CaSiGe (were performed using the CRYSTAL17 program package and hybrid density functional methods [33][34]. A hybrid exchange-correlation functional after Perdew, Burke, and Ernzerhof (DFT-PBE0) was used [35], Localized, Gaussian-Type triple ζ-valence + polarization level basis sets were used for Si and Ge and split valence + polarization level basis sets for Ca. The basis sets were derived from the molecular Karlsruhe basis sets[36–38]. For the evaluation of the Coulomb and exchange integrals (TOLINTEG), tight tolerance factors of 8, 8, 8, 8, 16 were used for all calculations. The reciprocal space of all monoclinic models was sampled with 5x5x2 and all orthorhombic models with 2x5x2 Monkhorst-Pack-type *k*-point grids. The starting geometries were taken from experimental data. Models for CaSiGe were derived from them by atom replacements. Both the lattice parameters and atomic positions were fully optimized within the constraints imposed by the space symmetry. Further on all optimized structures were confirmed to be true local minima by means of harmonic frequency calculations at the Γ-point. Electronic band structures and density of states (DOS) were calculated. The Brillouin Zone paths were provided by the web service *SeeK-path* [39].

Results and discussion

Crystal structure of the solid solutions $CaSi_{2-x}Ge_x$:

To see if $CaSi_2$ and $CaGe_2$ can be mixed over the whole range $CaSi_{2-x}Ge_x$ with $x \in [0;2]$ and whether the mixed compound forms ordered structures, samples with x = 0, 0.5, 1, 1.5 and 2 were prepared in an arc furnace, by melting stochiometric mixtures of the elements.

For each sample the product was analysed by PXRD measurements using a synchrotron source to determine the cell parameters and occupation of the Si/Ge mixed positions using the Rietveld method.[40] Cell parameters are listed in Table 1 and further information on the refinement is shown in the SI including the powder X-ray diffractograms. All compounds crystallize in the $CaSi_2$-type crystal structure **A**.

Table 1. Cell parameters and occupation of the Si/Ge mixed position according to Rietveld refinements. The sample with x = 1.5 (syn.) was obtained by refining the synchrotron measurement, which showed decomposition. The sample with x = 1.5 (pXRD) corresponds to the data collection using an in-house X-ray diffractometer (see Exp. Part).

x (nom. comp.)	**sample comp.**	**a**	**c**	**Si1** (x')	**Si2**(x')	**Ge1** (1-x')	**Ge2** (1-x')
0	$CaSi_2$	3.85421(6)	30.6379(5)	1	1	0	0
0.5	$CaSi_{1.42(1)}Ge_{0.58(1)}$	3.88569(8)	30.6303(6)	0.642(8)	0.781(6)	0.358(8)	0.219(6)
1	$CaSi_{0.90(1)}Ge_{1.10(1)}$	3.91984(5)	30.6184(4)	0.383(6)	0.519(5)	0.617(6)	0.481(5)
1.5 (syn)	$CaSi_{0.4(2)}Ge_{1.6(2)}$	3.9458(8)	30.591(7)	0.30(8)	0.14(8)	0.70(8)	0.86(8)
1.5 (pXRD)	$CaSi_{0.23(2)}Ge_{1.77(2)}$	3.95486(5)	30.6413(4)	0.05(1)	0.18(1)	0.95(1)	0.82(1)
2	$CaGe_2$	3.98666(5)	30.6336(4)	0	0	1	1

For $CaSi_2$ and β-$CaGe_2$ (with structure **A** and **E**, respectively) the cell parameters are in good agreement with values reported in literature of a = 3.855(5) Å and c = 30.6(1) Å for $CaSi_2$ as well as a = 3.9986(9) Å and c = 30.6(2) Å for $CaGe_2$.[41,26] In Figure 3 the cell parameters, a and c, that were obtained by a Rietveld refinement are plotted *versus* the refined composition x' and fitted with a linear regression to see if Vegard's law is appliable.[42] The plots include the R^2-values of the linear regression as well as two data points of the literature values as well as their standard deviation.

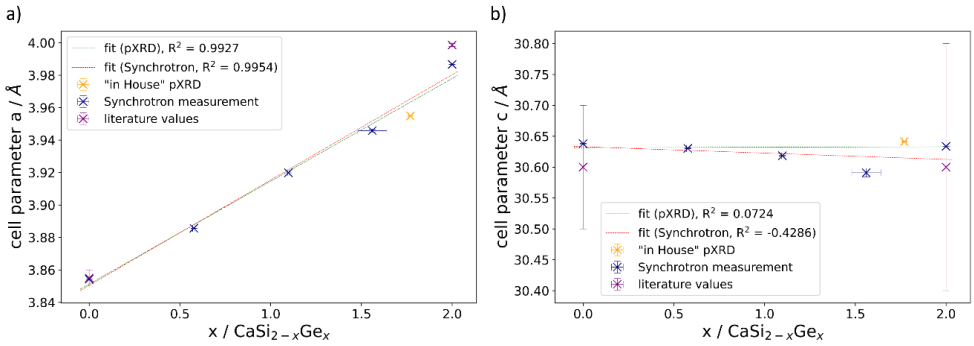

Figure 3. Cell parameter a and c plotted against the composition. Synchrotron measurements and the additional pXRD sample are marked in blue and yellow respectively. The literature values of the cell parameters and their standard deviation are marked in purple. The linear regression of the synchrotron measurements is shown in red, while the green one incorporates the pXRD sample for x = 1.5 instead.

Two linear regressions were fitted with the data. One for all synchrotron measurements and one switching the x = 1.5 decomposed sample with the refined powder pattern. The plot shows, that cell parameter a evidently follows Vegard's law. Except for the decomposed sample all points show negligible errors, represented by error bars and the coefficient of determination R^2 which is close to 1 for both fits. For the c parameter the Vegard's law seems not to apply. In general, the c parameters are within a range of 0.05 Å and seem to be smaller for mixed $CaSi_{2-x}Ge_x$ compounds compared to the parent compounds refined from synchrotron measurements. The 'in House' powder XRD refinement shows a larger c parameter than the synchrotron measurements. To further emphasis the precision with which the cell parameters were refined, the literature vales for a and c are additionally plotted with their standard deviation. While the a parameter also shows a rather small deviation, are the refined c parameters much more precise. This further leads to the conclusion, that there is no direct dependence of the c parameter on the composition. Since the two measurements with x = 1.5 also show the maximum deviation of the parameter c for these measurements, it is suggested that the deviation of c might be influenced by the synthesis.

Since the cooling rate in the arc furnace, although being not constant and depending on many variables, is fast the layers are abruptly "frozen" upon solidifying. Also do the layers of $CaSi_2$ and $CaGe_2$ have in general distances of about 5 Å towards each other and thus only interact weakly, which gives them a larger scope in movement at higher temperatures. This interplay of general variation of the cell parameter and abrupt cooling results in the not Vegard-like behaviour of cell parameter c.

Lastly from the measurement one can deduce, that in general all samples show a higher Ge content than the original stoichiometry. This seems to be a systematic error in the sample preparation, since it was observed that our Si powder has a higher adhesion on the balance disks used for weighting.

Quantum chemical calculations – $CaSi_2$ and $CaGe_2$ polymorphs:

For all $CaSi_2$ and $CaGe_2$ polymorphs crystal structures obtained from literature were optimized and subsequently harmonic frequencies were calculated at Γ. Further on, to show that the $CaSi_2$ and β-$CaGe_2$ are equivalent, models of $Casi_2$ in the β-$CaGe_2$ type and vice versa were calculated. The optimizations were performed without any externally applied pressure. The cell parameters of the published and optimized crystal structures are generally in good agreement and most differences are below 3 % (see Table S3). Some larger deviations occur for the c parameter, which might be caused by the anisotropy of the crystal structures.

For each structure type the energy and Gibbs free enthalpy are shown in Table 2, where for the calculation of the differences the lowest energy/enthalpy structure the "standard structure" obtained for arc furnace synthesis, the $CaSi_2$-type (**A**) and β-$CaGe_2$-type (**F**) were set as 0.

Table 2. Energetic comparison of different $CaSi_2$ and $CaGe_2$ polymorphs. The compound with the lowest energy (E/Z) and Gibbs free enthalpy (G/Z) respectively were set as 0. All other ΔE and ΔG values are calculated relative to them.

			E/Z (AU):	ΔE (kJ/mol)	G/Z (AU)	ΔG (kJ/mol)
$CaSi_2$	$CaSi_2$-type	**A**	-1256.2234	0	-1256.2216	0
	$EuGe_2$-type	**C**	-1256.2201	8.84	-1256.2176	10.50
	hr3-type	**B**	-1256.2251	-4.29	-1256.2222	-1.66
	ThSi2-type	**D**	-1256.2171	16.59	-1256.2161	14.44
	β-$CaGe_2$-type	**E**	-1256.2234	0.0002	-1256.2216	0.0050
$CaGe_2$	β-type	**E**	-4831.0136	0	-4831.0146	0
	α-type	**F**	-4830.9811	170.56	-4830.9811	176.04
	$CaSi_2$-type	**A**	-4831.0136	0.0020	-4831.0146	0.0023
	α'-type reduced (gr.36)	**F'**	-4831.0145	-4.47	-4831.0155	-4.67

For $CaSi_2$ the lowest energy and enthalpy structure is type **B**, followed by the standard type **A**, which is obtained in arc furnace synthesis. Structure **B** could be slightly lower in energy due to the less complex stacking order, compared to type **A**, but since the difference between the two decreases for the enthalpy and thus with higher temperatures, it still makes perfectly sense, that the main synthesis product is of structure type **A** at high temperatures. The two high pressure polymorphs **C** and **D** show higher energies, but type **D** might become more stable at higher temperatures as well.

For $CaGe_2$ the more stable polymorph is by far the experimentally available β-modification (**E**), even more for higher temperatures. This is also in line with the experimental findings, since the α-polymorph (**F**) can only be synthesised within an indium flux. This could also explain, why the frequency calculation of α-$CaGe_2$ showed a negative frequency. Therefore, the crystal structure was distorted and optimized again with a lower symmetry (space group *Cmc*2_1, no. 36), which is denoted as **F'** in Table 2. Interestingly this type now has the lowest energy of all $CaGe_2$-polymorphs, which could hint to a similar situation as the *h*R3 polymorph of $CaSi_2$ (**B**) and the lower energy could be a result of the less complex

stacking order. Further on does this crystal structure show the same octahedral coordination of Ca^{2+} as the β-type **F** and also does not much differ structurally except for the lower symmetry. This confirms that the two polymorphs **E** and **F** can be transformed into each other and are actually by distortion along the imaginary frequency. The energy comparison is also in line with the structure found for the "standard" synthesis. Since the synthesis of the α-$CaGe_2$ polymorph **F** is only possible for single crystals in an indium flux, this negative frequency could hint that the polymorph is stabilized by some indium, that is mixed into the crystal structure and that the pure α-$CaGe_2$ could maybe not be stabilized otherwise.

For each polymorph **A** to **F** band structure and density of states were calculated, which can be found in Figure 4 and with a higher resolution in the supporting Information. From all polymorphs, only α-$CaGe_2$ (**F**) shows an indirect band gap of about 1.40 eV, all others are metallic, including the distorted **F'** type which shows the same metallic behaviour as **E**. Looking closer at the crystal structure of **F'**, with focus on the coordination of Ca, this change can be explained. While reoptimizing the structure the coordination of Ca changed from the tetrahedral coordination to the same octahedral coordination as in $CaSi_2$ (**A**) and β-$CaGe_2$ (**E**). The bond lengths also change so that in the **F'** structure they are almost identical to **E**. With this it seems that only the interaction between Ca and its surrounding Si and Ge atoms determines whether the structure is conducting or semiconducting.

The shape of the band structures is very similar for all polymorphs, with a large dispersion for all bands. All polymorphs, except type **D**, show an anisotropic conducting behaviour, with the top valence band only crossing the Fermi-Level at Γ. This can be interpreted as having conducting properties only within the layers, but not trough the layers, which is again similar to graphite.[43] The **D** polymorph shows additional *k*-points, where the Fermi-Level is crossing, which might result from the three-dimensional connection of the Si atoms within the structure, which probably results in a less anisotropic conducting behaviour. For α-$CaGe_2$ the top valence band shows a much smaller dispersion, compared to the other polymorphs. For all compounds the density of states (DOS) shows mostly Si/Ge contributions over the plotted energy range of -4 to +4 eV, with especially low contribution of Ca around the Fermi-Level, where its projected DOS becomes zero. Interestingly, α-$CaGe_2$ is the only compound, where Ca shows some states at the Fermi-Level, therefore the occurrence of the band gap might be linked to this. A possible explanation could be the especially small Ca-Ge distance of 2.777 Å in α-$CaGe_2$, which might result in more interaction between the atoms lowering the valence bands below the Fermi-Level.

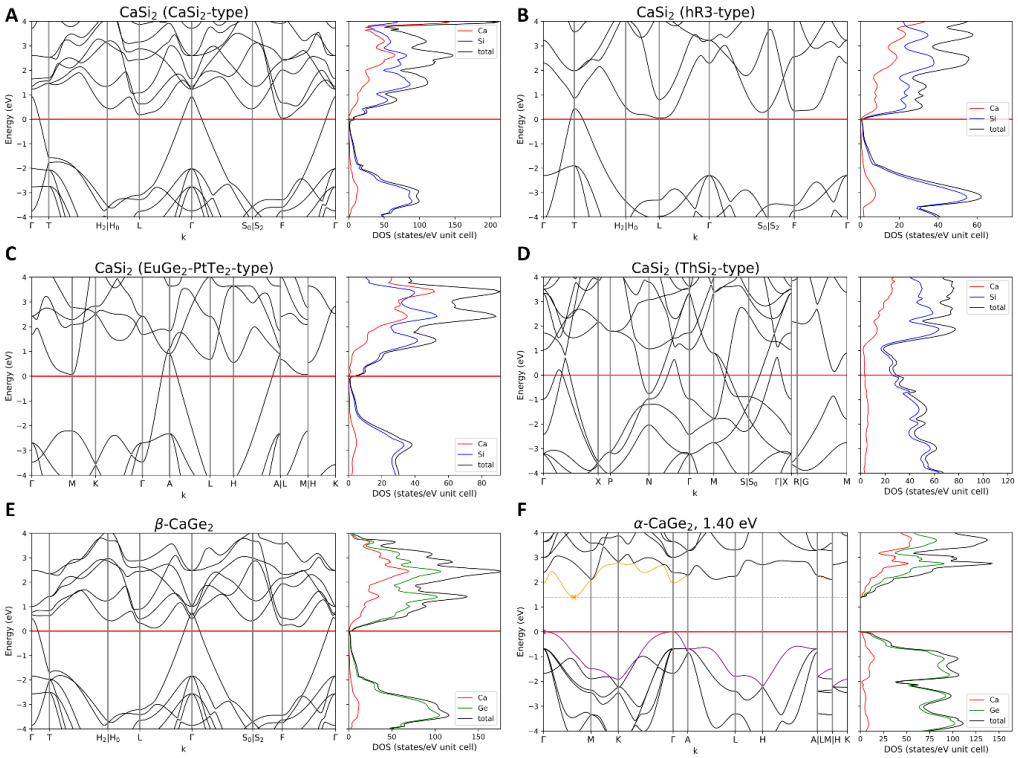

Figure 4. Band structures and density of states for all polymorphs A to F of $CaSi_2$ and $CaGe_2$. Only α-$CaGe_2$ shows an indirect band gap of 1.40 eV.

The results obtained are in line with previously published band structures for the different polymorphs of $CaSi_2$ and $CaGe_2$. [44–50,25,51] Interestingly, for the calculation of α-$CaGe_2$ (**F**) with LMTO (linear muffin tin orbitals) method a metallic behaviour was found, without any symmetry reduction, which might be due to the different approach in calculation.[25] For $Casi_2$ of type A, some Squid measurements were conducted to confirm its metallic properties.[44]

CaSiGe models based on structure types A, E and F

To compare the influence of the Si/Ge occupation of specific atom sites on the electronic band structure, ordered models resembling a mixed CaSiGe phase based on the models of the binary phases were calculated and analysed, with respect to the electronic band structures and the density of states (DOS) on a PBE0-TZVP (Ca SVP) level of theory (see SI). Since α-$CaGe_2$ has been found to be a semiconductor, ordered models based on this phase were calculated as well.

Using the experimental structures of $CaSi_2$ and α/β-$CaGe_2$, model systems of the composition CaSiGe were derived. Since $CaSi_2$ is build up by two Si positions Si1 and Si2, each of the position defining one

hexagonal layer of puckered Si atoms (see Figure 5a and Figure 1, type A). For model **1** (also referred to as layered model) Si1 is retained as Si and Si2 is substituted with Ge atoms resulting in a model with alternating Si and Ge atom and layers along the c direction (Figure 5b). A second model **2** was created by splitting each *6c-Whokoff* Si position (both Si1 and Si2) in $CaSi_2$ into two *3a* positions each, leading under retaining the lattice parameters to space group *R*3*m* (gr. 160). This allows alternating Si and Ge atoms within the same layer, with a maximum of three heteroatomic Si-Ge bonds for both atom types (Figure 5c), also referred to as alternating model. For comparison we created the same models as models **1** and **2** with β-$CaGe_2$ as the parent structure to see if the starting geometry - which for $CaSi_2$ type A and β-$CaGe_2$, type E limited to slightly different cell parameters and c coordinates for each atom position, since both structures are otherwise identical - influences the optimization process. There crystal structure models look exactly like the ones shown for $CaSi_2$ in Figure 5. Further on additional calculations were conducted for layered and alternating models **1'** and **2'**, where the atom positions of Si and Ge are swapped, which are marked with VV (*vice versa*), in case interactions of the layers with Ca affect the band structure and DOS.

For α-$CaGe_2$ the Ge1 and Ge2 positions are located within one Ge layer (Figure 6a and Figure 1, type F) therefore the alternating model **4** can be created by switching Ge1 position to Si, without reducing the symmetry (Figure 6c). To get a model, where Si and Ge-layers are alternating along the c direction, the symmetry has to be reduced to *P*3*m*1 (no. 156), such that *Wyckoff*-positions 2a and 2b are split into 1b and 1c, as well as two 1a positions. By setting one position 1a and 1b to Si, the layered model **3** is obtained. Again models **3'** and **4'** were created, with Ge and Si positions swapped, again denoted with VV.

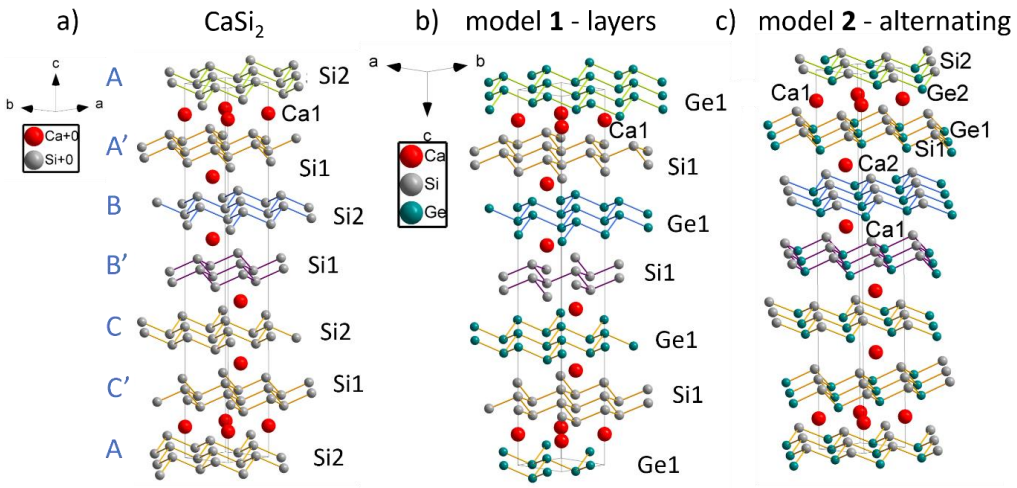

Figure 6. Created ordered models based on the $CaSi_2$ structure type shown in a). b) Layered structure model **1** with alternating Si and Ge nets along the c direction obtained without reducing the symmetry, c) symmetry reduction to group 160 (R 3 m) allowing for two-dimensional Si—Ge nets with alternating Si and Ge atoms in structure model **2**.

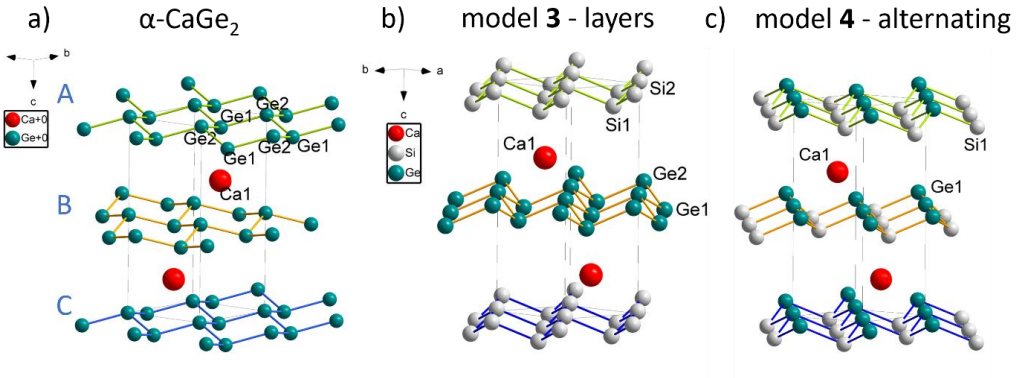

Figure 5. Created ordered models based on the α-$CaGe_2$ structure type shown in a). b) Layered structure model **3** with alternating Si and Ge nets along the c direction obtained by reducing the symmetry to group 156 (P3*m*1), c) two-dimensional Si—Ge nets with alternating Si and Ge atoms in structure model **4**, obtained without reducing the symmetry.

Energetic comparison between parent compounds and CaSiGe models:

For all ordered structural models cell parameters and atomic positions were fully optimized within the constraints of the space group. A comparison between the experimental and optimized cell parameters can be found in the SI. For the ordered models, the deviation in cell parameters from the parent compounds is also only minor and as expected: For models with $CaSi_2$ as starting geometry the a lattice parameter increases slightly, while it decreases for β-$CaGe_2$ based models. The c parameter decreases for all models, except for the $Casi_2$-type model **1** layered structure, where it slightly increases. Comparing the models from both parent compound to each other, the a parameter of all models as

well as the c- parameter for the alternating structures only deviate by a maximum of about 0.23 %. For the layered structures the c parameter differs by about 1 %, which is significantly more. The same trends can be found comparing the models with the ones where Si and Ge positions are switched (marked with **'**): a is almost identical as well as c for alternating models **2'**. For the layered structures **1'** again the value for c differs significantly. Overall, the smallest c was obtained in the $CaSi_2$ type layered model **1'** and the largest one in $CaSi_2$-type layered model **1**.

For all compounds after the optimization and frequency calculations on the same level of theory the energy as well as Gibbs' free enthalpy per number of formular unit were determined respectively for each model. All values for the ordered models can be found in Table 3.

Table 3. Energetic comparison of all modelled CaSiGe compounds. The compound with the lowest energy (E/Z) and Gibbs free enthalpy (G/Z) respectively were set as 0. All other ΔE and ΔG values are calculated relative to them. For all $CaSi_2$ and β-$CaGe_2$ a number of formular units (Z) of 4 and for all α-$CaGe_2$ a Z = 2 was used.

parent comp.		Model		E/Z (AU):	ΔE (kJ/mol)	G/Z (AU)	ΔG (kJ/mol)
$CaSi_2$	**A**	layers	**1**	-3043.6165	4.61	-3043.6161	2.86
β-$CaGe_2$	**E**		**1**	-3043.6167	4.25	-3043.6162	2.51
α-$CaGe_2$	**F**		**3**	-3043.5836	91.09	-3043.5823	91.54
$CaSi_2$	**A**	layer (VV)	**1'**	-3043.6183	0	-3043.6171	0.11
β-$CaGe_2$	**E**		**1'**	-3043.6175	2.03	-3043.6172	0
α-$CaGe_2$	**F**		**3'**	-3043.5836	91.15	-3043.5823	91.51
$CaSi_2$	**A**	alternating	**2**	-3043.6170	3.50	-3043.6165	1.75
β-$CaGe_2$	**E**		**2**	-3043.6170	3.50	-3043.6165	1.75
α-$CaGe_2$	**F**		**4**	-3043.5826	93.70	-3043.5813	94.17
$CaSi_2$	**A**	alternating (VV)	**2'**	-3043.6170	3.51	-3043.6165	1.76
β-$CaGe_2$	**E**		**2'**	-3043.6170	3.49	-3043.6165	1.76
α-$CaGe_2$	**F**		**4'**	-3043.5847	88.34	-3043.5833	89.00

For the ordered CaSiGe compounds the layered VV structure has the smallest energy for the $CaSi_2$-type and the lowest Gibbs' free enthalpy for the β-$CaGe_2$ structure type. For both, Ca coordinates the Si six-membered ring centrally and the Ge layers above a corner of the ring. Setting their energy and enthalpy as zero, all other $CaSi_2$ and β-$CaGe_2$ models only lie slightly higher in energy (< 5 kJ/mol). For all α-$CaGe_2$ models' values are about 90 kJ/mol higher in energy. This can be explained with the negative frequencies calculated for all such models as well as the parent compound, which was also the highest energy polymorph of $CaGe_2$.

Table 4. Distances and dihedral angles of the different ordered models of CaSiGe. The dihedral angle describes the angles between the centre square plane of the six-membered ring and the triangular tip.

parent comp.		Model		d_{Si-Si} (Å)	d_{Ge-Ge} (Å)	angle Si-layer (°)	angle Ge-layer (°)
CaSi2-typ	**A**	layers	**1**	2.4649	2.4913	64.117	67.323
β-CaGe2-typ	**E**		**1**	2.4675	2.4937	64.165	67.327
α-CaGe2-typ	**F**		**3**	2.4609	2.5128	60.435	67.042
CaSi2-type	**A**	layer (VV)	**1'**	2.4351	2.5189	59.838	70.167
β-CaGe2-typ	**E**		**1'**	2.4331	2.518	59.429	70.032
α-CaGe2-typ	**F**		**3'**	2.4609	2.5128	60.463	67.064
				$d_{Si1-Ge1}$ (Å)	$d_{Si2-Ge2}$ (Å)	angle Si1-layer (°)	angle Si2-layer (°)
CaSi2-typ	**A**	alternating	**2**	2.4929	2.4644	67.115	63.622
β-CaGe2-typ	**E**		**2**	2.4929	2.4641	67.086	63.562
α-CaGe2-typ	**F**		**4**	2.4847		63.268	
CaSi2-type	**A**	alternating (VV)	**2'**	2.4931	2.4643	67.101	63.579
β-CaGe2-typ	**E**		**2'**	2.4928	2.4644	67.129	63.668
α-CaGe2-typ	**F**		**4'**	2.4895		64.195	

Table 4 gives an overview of the bond lengths within and dihedral angles of the six-membered rings for each CaSiGe ordered model. For the layered models, as expected, are the Si-Si bonds slightly smaller than the Ge-Ge bonds. Since the size of the six-membered rings within each layer has to be the same when seen from the top, the larger Ge atoms compensate the slightly longer bonds by a larger dihedral angle within the six-membered ring. For the mixed CaSiGe models an average bond length between Si and Ge can be found. Here also one of the dihedral angles within the layers is slightly larger, but the difference is smaller compared to the layered models. Comparing the bond lengths with the energies and enthalpies in Table 3, the models are more stable if the Ge-Ge is larger for the layered models, probably due to less strain in the Ge six-membered rings. For the mixed models an average Si-Ge bond length and dihedral angle is present, resulting in a medium energy and enthalpy.

For the CaSiGe models the stability compared to the parent compounds can be calculated. Therefore, the energies and Gibbs free enthalpies obtained through structure optimization and frequency calculation shown in Table 2 and Table 3 can be compared using the following reaction equation:

$$^1/_2\ \mathrm{CaSi_2} + {}^1/_2\ \mathrm{CaGe_2} \rightarrow \mathrm{CaSiGe} \qquad (1)$$

With this equation the energies of the educt and product side can be compared, to see if the reaction is in favour of building mixed CaSiGe. Models **3/3'** and **4/4'** were excluded, since the formation of these structures seems unlikely at this point. The right side of equation (1) was used as reference energy/enthalpy and thus set to 0. All values for ΔE and ΔG for the difference products – educts can be found in Table 5.

Table 5. Energetic comparison between the energies of the educts and modelled mixed CaSiGe compounds. The energy of the educts (½ $CaSi_2$ + ½ $CaGe_2$) were set to 0.

				E/Z (AU):	ΔE (kJ/mol)	G/Z (AU)	ΔG (kJ/mol)
½ $CaSi_2$ + ½ $CaGe_2$	**A and E**			-3043.6185	0	-3043.6181	0
$CaSi_2$	**A**	layer	**1**	-3043.6165	5.17	-3043.6161	5.35
β-$CaGe_2$	**E**		**1**	-3043.6167	4.82	-3043.6162	5.00
$CaSi_2$	**A**	layer (VV)	**1'**	-3043.6183	0.56	-3043.6171	2.60
β-$CaGe_2$	**E**		**1'**	-3043.6175	2.59	-3043.6172	2.49
$CaSi_2$	**A**	alternating	**2**	-3043.6170	4.06	-3043.6165	4.24
β-$CaGe_2$	**E**		**2**	-3043.6170	4.07	-3043.6165	4.24
$CaSi_2$	**A**	alternating (VV)	**2'**	-3043.6170	4.07	-3043.6165	4.26
β-$CaGe_2$	**E**		**2'**	-3043.6170	4.06	-3043.6165	4.25

All values for ΔE and ΔG are positive, which means, that the reaction according to equation (1) would not start spontaneously. This comparison does take any entropic effects into account, that might play a role due to the (statistical) mixing of Si and Ge. Therefore, and since the differences are negligible, it is still reasonable, that the mixed CaSiGe compounds are formed. The influence of the temperature is also rather unfavourable by comparing the ΔE and ΔG values. For β-$CaGe_2$ with layered modelled structure **1'** ΔG is smaller, while for all other models ΔE is. This could be interpreted, that at higher temperatures, the "pure" $CaSi_2$ and $CaGe_2$ compounds are even more favoured. But since the values are still small, the reaction mixed compounds should still be formed.

For all ordered models band structure and density of states were calculated, all figures can be found in Figure 7 and Figure 8. For a higher resolution see the Supporting information. The shape of the band structure is in general very similar to the parent compounds: all $CaSi_2$ and β-$CaGe_2$ based models are metals with the Fermi-Level intersecting the top valence band at Γ-point. The overall shape of the bands is identical for all compounds, but for the layered models **1** of both parent compounds some of the bands, especially around the Γ-point, seem to be almost degenerate, since there two bands have an almost identical trend. Another trend that can be found for the layered models at Γ-point: The valence band maximum (VBM) touches the first conduction band, whereas for the alternating models a small gap of about 0.1 eV lies in between. Further on both models with the layered model **1'** show the same pulled down band at the F-point as the bare $CaSi_2$ compound.

Looking at the DOS, no significant change in shape can be seen for all alternating models **2**/**2'**. During the whole range Si and Ge have an identical contribution. In the valence bands they make up most of the states as well as in the conduction bands below 2 eV. Above the main contribution changes to Ca. For the layered structures there are differences depending on how the positions are occupied: If the Si1 position of $CaSi_2$ is still occupied by Si it is the main contributor to the valence bands, if it is occupied by Ge that has most states in the valence bands. For all layered compounds **1**/**1'** in the conduction bands around the conduction band minimum almost only Si contributes states to the DOS. This changes

above 1 eV where the element on the former Si2 position contributes most. In the higher conduction bands Ca becomes the main contributor like in the alternating models.

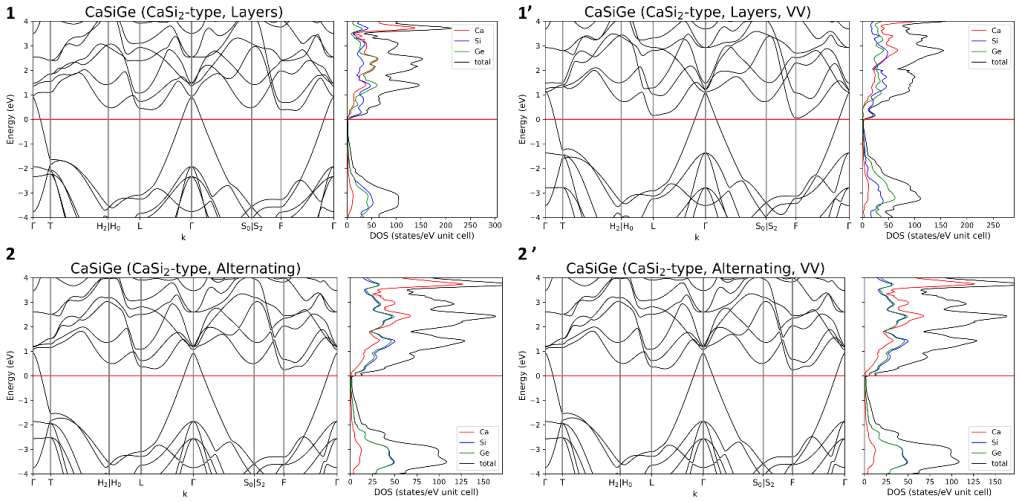

Figure 8. Band structure and density of states of all ordered models 1, 1', 2 and 2' which were calculated based on the crystal structure of $CaSi_2$.

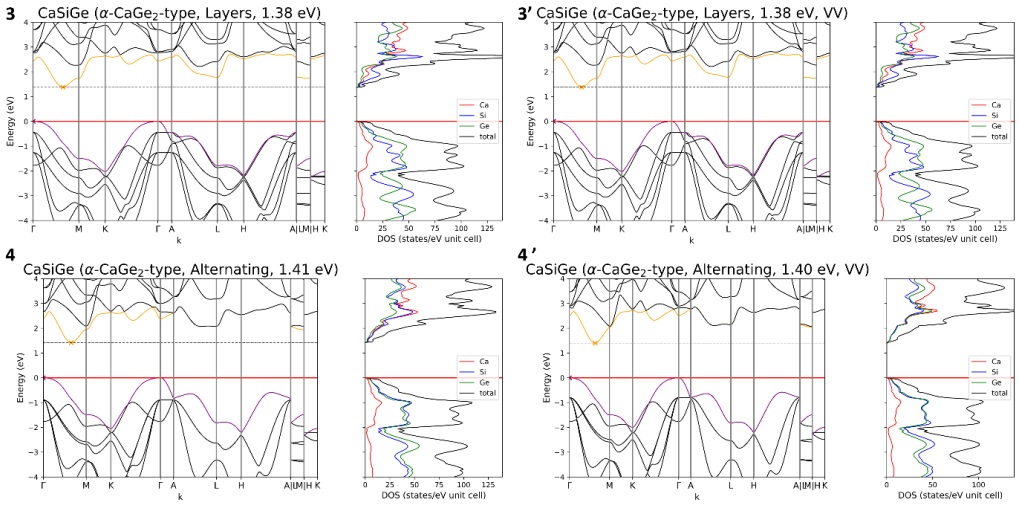

Figure 7. Band structure and density of states of all ordered models 3, 3', 4 and 4' which were calculated based on the crystal structure of α-$CaGe_2$.

For the α-$CaGe_2$ based models **3** and **4** the band structures show a band gap of around 1.4 eV. The overall shape of the band is similar to the parent compound: For all of them the transition is between the Γ-point and the minimum between Γ and M. In general, the band gap of the layered structure **3** is about 0.03 eV lower than the alternating one. Again, no difference between the models and their *vice versa* structures **3'** and **4'** can be found. The alternating structure **4'** shows more degenerated bands

between A and M which comes from the lower symmetry. The DOS shows also only slight differences: In the valence bands for all alternating structures Si and Ge contribute equally to the DOS, while Ca contributes about 1/4 of all states. In the conduction bands until about 2 eV all atoms contribute equally, up to 3 eV then Ca and Si contribute, above again Si and Ge contribute equal amounts but slightly less than Ca. For the layered models, again in the valence bands Si and Ge contribute equally, but this time minima and maxima of the DOS of Si and Ge are opposing each other. In the conduction bands Si has the most contribution up to 3 eV, followed by Ge and Si. Overall, these are the same trends as for the other layered and alternating models, which makes the DOS look similar although the band structures differ a lot.

To get a better insight in the electronic structure, further crystal orbital Hamilton population calculations and Mullikan analyses of all models were calculated. For the layered structures the following trend was found. Below the Fermi-Level mostly bonding Si-Si and Ge-Ge interactions can be found, where the atom that coordinates with its six membered ring to the Ca contributes less below the Fermi-Level. For the conduction bands, there are additional Ca-Si and Ca-Ge antibonding interaction, this time with the interaction having more contribution, where the six membered ring coordinates. For all alternating structure models, there is mostly Si-Ge antibonding interaction over the whole range and only minor contributions of Ca-Si and Ca-Ge.

For α-$CaGe_2$ based models both layered and alternating structures respectively the COHP look almost identical. For the layered structure below as well as above the Fermi Level mostly Si-Si and Ge-Ge bonding interactions and anti-bonding interactions with Ca can be found. For the alternating structures mostly Si-Ge anti-bonding interactions can be found above the Fermi-Level. Additionally depending on the model Ca-Ge anti-bonding and Ca-Si bonding interactions (vice versa for VV structure) can be found. Here the atoms closest to Ca shows the antibonding interaction.

All trends can be seen in the values for the overlap population derived from the Mullikan analysis as well: For all Si-Si, Si-Ge, and Ge-Ge bonds the overlap population shows values around 0.2 which indicates covalent bonds between them. For the interaction of Ca-Si and Ca-Ge the following values were obtained: for the closest atoms in all $CaSi_2$ (**A**) and β-$CaSi_2$ (**E**) there is an overlap of about 0.01 to 0.015. For the next closer neighbour this value doubles with values up to 0.04. All other interactions between Ca-Si and Ca-Ge have an overlap of about 0, which means that they do not interact. For models derived from α-$CaGe_2$ (**F**) these overlap populations increase significantly up to 0.05. Although the value of the overlap population, compared to the covalent interactions between Si and Ge, shows that there are only some minor interactions between Ca and its surrounding atoms this has a noticeable effect on the band structure, since these compounds show semiconducting properties. In the case of all α-$CaGe_2$ models, the interaction between Ca and adjacent Si or Ge at the tip of the tetrahedral

coordination can be seen in the Mulliken charge. For all models as well as the parent compound the partial charge at that Si/Ge position is increased while the other position(s) have a decreased charge.

This leads to the assumption that the tetrahedral coordination of Ca is favourable since a direct overlap of Ca orbitals with orbitals from Si along the c-axis leads to a better charge transfer resulting in a band gap. For all other models and parent compounds the coordination above the minimum of the layer is disadvantageous since the orbitals of the three neighbouring atoms can only partially overlap due to the orientation.

Conclusion

In this paper experimental and theoretical data was shown regarding possible solid solutions of $CaSi_2$ and β-$CaGe_2$, namely $CaSi_{2-x}Ge_x$. The synchrotron and powder XRD measurements state that mixing of Si and Ge is possible over the whole range of x. Further on we showed that these mixtures show a Vegard like trend for cell parameters a/b but not for c where the cooling rate is the main influence. As for the band structure all possible layered or alternating ordered models were optimized and their band structure calculated. Focused on the question, why only α-$CaGe_2$ based models show direct band gaps, the interaction between Ca and its closest neighbour was found to be the turning point for having a band gap.

Experimentally the α-$CaGe_2$ was only accessible via in flux synthesis, which works well with the meta-stable structure identified via comparison of Gibbs free enthalpy. Therefore, further experiments should focus on finding other ways to synthesise the α-phase, such as doping $CaGe_2$ with atoms so that the coordination above a maximum of the layer becomes less inconvenient. Mixing Ge with larger atoms such as In or Sn could enlarge the space between layers or mixing Ca with Mg or other small cations could lessen the stress Ca exerts on maximum of the layers thus preventing it from flipping for stabilization.

Acknowledgements:

Part of the research described in this paper was performed on beamline WHE at the Canadian Light Source, a national research facility of the University of Saskatchewan, which is supported by the Canada Foundation for Innovation (CFI), the Natural Sciences and Engineering Research Council (NSERC), the Canadian Institutes of Health Research (CIHR), the Government of Saskatchewan, and the University of Saskatchewan. The authors thank Joel Reid for measuring the synchrotron powder diffraction patterns of all $CaSi_{2-x}Ge_x$ samples.

References:

[1] H. Nakano, T. Ikuno, *Appl. Phys. Rev.* **2016**, *3*, 40803.

[2] T. Helbich, A. Lyuleeva, P. Marx, L. M. Scherf, T. K. Purkait, T. F. Fässler, P. Lugli, J. G. C. Veinot, B. Rieger, *Adv. Funct. Mater.* **2017**, *27*, 1606764.

[3] A. Lyuleeva, T. Helbich, B. Rieger, P. Lugli, *J. Phys. D: Appl. Phys.* **2017**, *50*, 135106.

[4] T. Helbich, A. Lyuleeva, I. M. D. Höhlein, P. Marx, L. M. Scherf, J. Kehrle, T. F. Fässler, P. Lugli, B. Rieger, *Chemistry* **2016**, *22*, 6194.

[5] T. Helbich, A. Lyuleeva, T. Ludwig, L. M. Scherf, T. F. Fässler, P. Lugli, B. Rieger, *Adv. Funct. Mater.* **2016**, *26*, 6711.

[6] M. J. Kloberg, H. Yu, E. Groß, F. Eckmann, T. M. F. Restle, T. F. Fässler, J. G. C. Veinot, B. Rieger, *Advanced materials (Deerfield Beach, Fla.)* **2021**, *33*, e2100288.

[7] A. Lyuleeva, T. Helbich, M. Bobinger, B. Rieger, M. Becherer, P. Lugli, A. Rivadeneyra, *Sensors and Actuators B: Chemical* **2019**, *283*, 451.

[8] H. Yu, T. Helbich, L. M. Scherf, J. Chen, K. Cui, T. F. Fässler, B. Rieger, J. G. Veinot, *Chem. Mater.* **2018**, *30*, 2274.

[9] S. Z. Butler, S. M. Hollen, L. Cao, Y. Cui, J. A. Gupta, H. R. Gutiérrez, T. F. Heinz, S. S. Hong, J. Huang, A. F. Ismach et al., *ACS nano* **2013**, *7*, 2898.

[10] C. Grazianetti, E. Cinquanta, L. Tao, P. de Padova, C. Quaresima, C. Ottaviani, D. Akinwande, A. Molle, *ACS nano* **2017**, *11*, 3376.

[11] B. J. Ryan, M. P. Hanrahan, Y. Wang, U. Ramesh, C. K. A. Nyamekye, R. D. Nelson, Z. Liu, C. Huang, B. Whitehead, J. Wang et al., *Chem. Mater.* **2020**, *32*, 795.

[12] S. Yamanaka, H. Matsu-ura, M. Ishikawa, *Mater. Res. Bull.* **1996**, *31*, 307.

[13] A. Weiss, G. Beil, H. Meyer, *Z. Naturforsch., B* **1980**, *35*, 25.

[14] F. Zhao, Y. Feng, Y. Wang, X. Zhang, X. Liang, Z. Li, F. Zhang, T. Wang, J. Gong, W. Feng, *Nat. Commun.* **2020**, *11*, 1443.

[15] M. J. S. Spencer, T. Morishita, M. Mikami, I. K. Snook, Y. Sugiyama, H. Nakano, *Phys. Chem. Chem. Phys.* **2011**, *13*, 15418.

[16] T. Morishita, S. P. Russo, I. K. Snook, M. J. S. Spencer, K. Nishio, M. Mikami, *Phys. Rev. B* **2010**, *82*.

[17] G. G. Guzmán-Verri, L. C. Lew Yan Voon, *J. Phys. Condens. Matter.* **2011**, *23*, 145502.

[18] F. Wöhler, *Justus Liebigs Ann. Chem.* **1863**, *127*, 257.

[19] J. Böhm, O. Hassel, *Z. Anorg. Allg. Chem.* **1927**, *160*, 152.

[20] G. Vogg, M. S. Brandt, M. Stutzmann, M. Albrecht, *Journal of Crystal Growth* **1999**, *203*, 570.

[21] R. Nedumkandathil, D. E. Benson, J. Grins, K. Spektor, U. Häussermann, *J. Solid State Chem.* **2015**, *222*, 18.

[22] P. Bordet, M. Affronte, S. Sanfilippo, M. Núñez-Regueiro, O. Laborde, G. L. Olcese, A. Palenzona, S. LeFloch, D. Levy, M. Hanfland, *Phys. Rev. B Condens. Matter.* **2000**, *62*, 11392.

[23] R. Yaokawa, A. Nagoya, H. Nakano, *J. Solid State Chem.* **2021**, *295*, 121919.

[24] H. J. Wallbaum, *Naturwissenschaften* **1944**, *32*, 76.

[25] P. H. Tobash, S. Bobev, *J. Solid State Chem.* **2007**, *180*, 1575.

[26] N. D. Cultrara, Y. Wang, M. Q. Arguilla, M. R. Scudder, S. Jiang, W. Windl, S. Bobev, J. E. Goldberger, *Chem. Mater.* **2018**, *30*, 1335.

[27] A. Currao, S. Wengert, R. Nesper, J. Curda, H. Hillebrecht, *Z. Anorg. Allg. Chem.* **1996**, *622*, 501.

[28] *WinXPOW*, STOE & Cie GmbH, Darmstadt, Germany, **2011**.

[29] A. Gomez, G. Dina, S. Kycia, *Review of Scientific Instruments* **2018**, *89*.

[30] B. H. Toby, R. B. von Dreele, *J. Appl. Crystallogr.* **2013**, *46*, 544.

[31] S. W. Freiman, N. M. Trahey, *National Institute of Standards and Technology* **2000**.

[32] J. Rodríguez-Carvajal, *Phys. B* **1993**, *192*, 55.

[33] R. Dovesi, V. R. Saunders, C. Roetti, R. Orlando, C. M. Zicovich-Wilson, F. Pascale, B. Civalleri, K. Doll, N. M. Harrison, I. J. Bush **2017**.

[34] R. Dovesi, A. Erba, R. Orlando, C. M. Zicovich-Wilson, B. Civalleri, L. Maschio, M. Rérat, S. Casassa, J. Baima, S. Salustro et al., *WIREs Comput. Mol. Sci.* **2018**, *8*.

[35] J. P. Perdew, W. Yang, K. Burke, Z. Yang, E. K. U. Gross, M. Scheffler, G. E. Scuseria, T. M. Henderson, I. Y. Zhang, A. Ruzsinszky et al., *Proc. Natl. Acad. Sci. U S A* **2017**, *114*, 2801.

[36] A. J. Karttunen, T. F. Fässler, M. Linnolahti, T. A. Pakkanen, *Inorg. Chem.* **2011**, *50*, 1733.

[37] L. M. Scherf, A. J. Karttunen, O. Pecher, P. C. M. M. Magusin, C. P. Grey, T. F. Fässler, *Angew. Chem. Int. Ed. Engl.* **2016**, *55*, 1075.

[38] K. Conley, A. J. Karttunen, *J. Phys. Chem. C* **2022**, *126*, 17266.

[39] Y. Hinuma, G. Pizzi, Y. Kumagai, F. Oba, I. Tanaka, *Comput. Mater. Sci.* **2017**, *128*, 140.

[40] L. B. McCusker, R. B. von Dreele, de Cox, D. Louër, P. Scardi, *J. Appl. Crystallogr.* **1999**, *32*, 36.

[41] J. Evers, *J. Solid State Chem.* **1979**, *28*, 369.

[42] L. Vegard, *Z. Physik* **1921**, *5*, 17.

[43] J. W. McClure, *IBM J. Res. & Dev.* **1964**, *8*, 255.

[44] M. Affronte, O. Laborde, G. L. Olcese, A. Palenzona, *Journal of Alloys and Compounds* **1998**, *274*, 68.

[45] S. Fahy, Hamann, *Phys. Rev. B Condens. Matter.* **1990**, *41*, 7587.

[46] N. G. Galkin, S. A. Dotsenko, K. N. Galkin, A. M. Maslov, D. B. Migas, V. O. Bogorodz, A. B. Filonov, V. E. Borisenko, I. Cora, B. Pécz et al., *Journal of Alloys and Compounds* **2019**, *770*, 710.

[47] Y. Guo, Y. Wang, D. Xia, J. Li, *Int. J. Mod. Phys. C* **2021**, *32*, 2150045.

[48] X. D. Li, K. Li, C. H. Wei, W. D. Han, N. G. Zhou, *Phys. B* **2018**, *538*, 54.

[49] D. D. Sarma, W. Speier, L. Kumar, C. Carbone, A. Spinsanti, O. Bisi, A. Iandelli, G. L. Olcese, A. Palenzona, *Z. Physik B - Condensed Matter* **1988**, *71*, 69.

[50] G. Satta, G. Profeta, F. Bernardini, A. Continenza, S. Massidda, *Phys. Rev. B Condens. Matter.* **2001**, *64*.

[51] Z. Yang, D. Shi, B. Wen, R. Melnik, S. Yao, T. Li, *J. Solid State Chem.* **2010**, *183*, 136.

Supporting Information: $CaSi_{2-x}Ge_x$, solid solution and analysis of ordered structures

Contents

1 Additional information on the Rietveld refinement

Table S1. Crystal structure parameters after Rietveld refinement of the synchrotron measurements and the one in house pXRD measurement.

		x	y	z	U_iso/U_eq	Occ	
$CaSi_2$	Ca1	0	0	0.08098(9)	0.0104(6)		1
	Si1	0	0	0.18269(9)	0.0126(7)		1
	Si2	0	0	0.34663(9)	0.0114(7)		1
$CaSi_{1.5}Ge_{0.5}$	Ca1	0	0	0.0807(1)	0.0108(8)		1
	Si1	0	0	0.18355(7)	0.0157(9)	0.642(8)	
	Si2	0	0	0.34764(8)	0.0119(9)	0.781(6)	
	Ge1	0	0	0.18355(7)	0.0157(9)	0.358(8)	
	Ge2	0	0	0.34764(8)	0.0119(9)	0.219(6)	
CaSiGe	Ca1	0	0	0.08054(8)	0.0134(6)		1
	Si1	0	0	0.18405(4)	0.0143(5)	0.383(6)	
	Si2	0	0	0.34858(5)	0.0166(5)	0.519(5)	
	Ge1	0	0	0.18405(4)	0.0143(5)	0.617(6)	
	Ge2	0	0	0.34858(5)	0.0166(5)	0.481(5)	
$CaSi_{0.5}Ge_{1.5}$	Ca1	0	0	0.0884(7)	0.010(8)		1
Synchrotron	Si1	0	0	0.1838(5)	0.008(6)	0.30(8)	
	Si2	0	0	0.3461(4)	0.021(6)	0.14(8)	
	Ge1	0	0	0.1838(5)	0.008(6)	0.70(8)	
	Ge2	0	0	0.3461(4)	0.021(6)	0.86(8)	
$CaSi_{0.5}Ge_{1.5}$	Ca1	0	0	0.08079(4)	0.026(1)		1
pXRD	Ge1	0	0	0.18430(2)	0.047(1)	0.95(1)	
	Ge2	0	0	0.34901(2)	0.041(1)	0.82(1)	
	Si1	0	0	0.18430(2)	0.047(1)	0.05(1)	
	Si2	0	0	0.34901(2)	0.041(1)	0.18(1)	
$CaGe_2$	Ca1	0	0	0.0810(1)	0.0134(6)		1
	Ge1	0	0	0.18460(5)	0.0097(4)		1
	Ge2	0	0	0.34988(5)	0.0128(4)		1

Table S2. Refinement parameters of Rietveld refinement.

Empiric formula	**$CaSi_2$**	**$CaSi_{1.423(7)}Ge_{0.577(7)}$**	**$CaSi_{0.902(6)}Ge_{1.098(6)}$**	**$CaSi_{0.44(8)}Ge_{1.56(8)}$**	**$CaSi_{0.23(1)}Ge_{1.77(1)}$**	**$CaGe_2$**
Formula weight	96.244 g/mol	121.933 g/mol	145.125 g/mol	212.653 g/mol	174.455 g/mol	185.245 g/mol
Temp.	293 K	293 K	293 K	293 K	293 K	293 K
Colour	black	black	black	black	black	black
crystal system	trigonal	trigonal	trigonal	trigonal	trigonal	trigonal
Space group	R-3m	R-3m	R-3m	R-3m	R-3m	R-3m
Lattice parameter (Å)						
a	3.85421(6)	3.88569(8)	3.91984(5)	3.9458(8)	3.95486(5)	3.98666(5)
c	30.6379(5)	30.6303(6)	30.6184(4)	30.591(7)	30.6413(4)	30.6336(4)
V (Å^3)	394.15(1)	400.52(1)	407.428(9)	412.5(2)	415.048(9)	421.65(1)
Z	6	6	6	6	6	6
ρ (calc)	2.433 g/cm^3	3.034 g/cm^3	3.549 g/cm^3	5.104 g/cm^3	4.201 g/cm^3	4.378 g/cm^3
Wavelength radiation	0.40867 Å	0.40867 Å	0.40867 Å	0.40867 Å	1.5406 Å	0.40867 Å
source	Synchrotron	Synchrotron	Synchrotron	Synchrotron	Cu k_α	Synchrotron
theta range (°)	2.0141 - 27.0041	2.0141 - 27.0042	2.0141 - 27.0043	2.0141 - 27.0044	3.00000 - 89.775	2.0141 - 27.0044
R_p	2.23	3.08	2.81	22.6	6.59	4.35
R_{wp}	3.67	4.91	4.14	32.2	8.96	6.24
R_{exp}	0.666	0.619	0.594	0.757	4.89	0.764
G.O.F.	5.4	7.8	6.9	42	1.8	8.1
Chi^2	30.4	62.8	48.7	1810	3.36	66.8

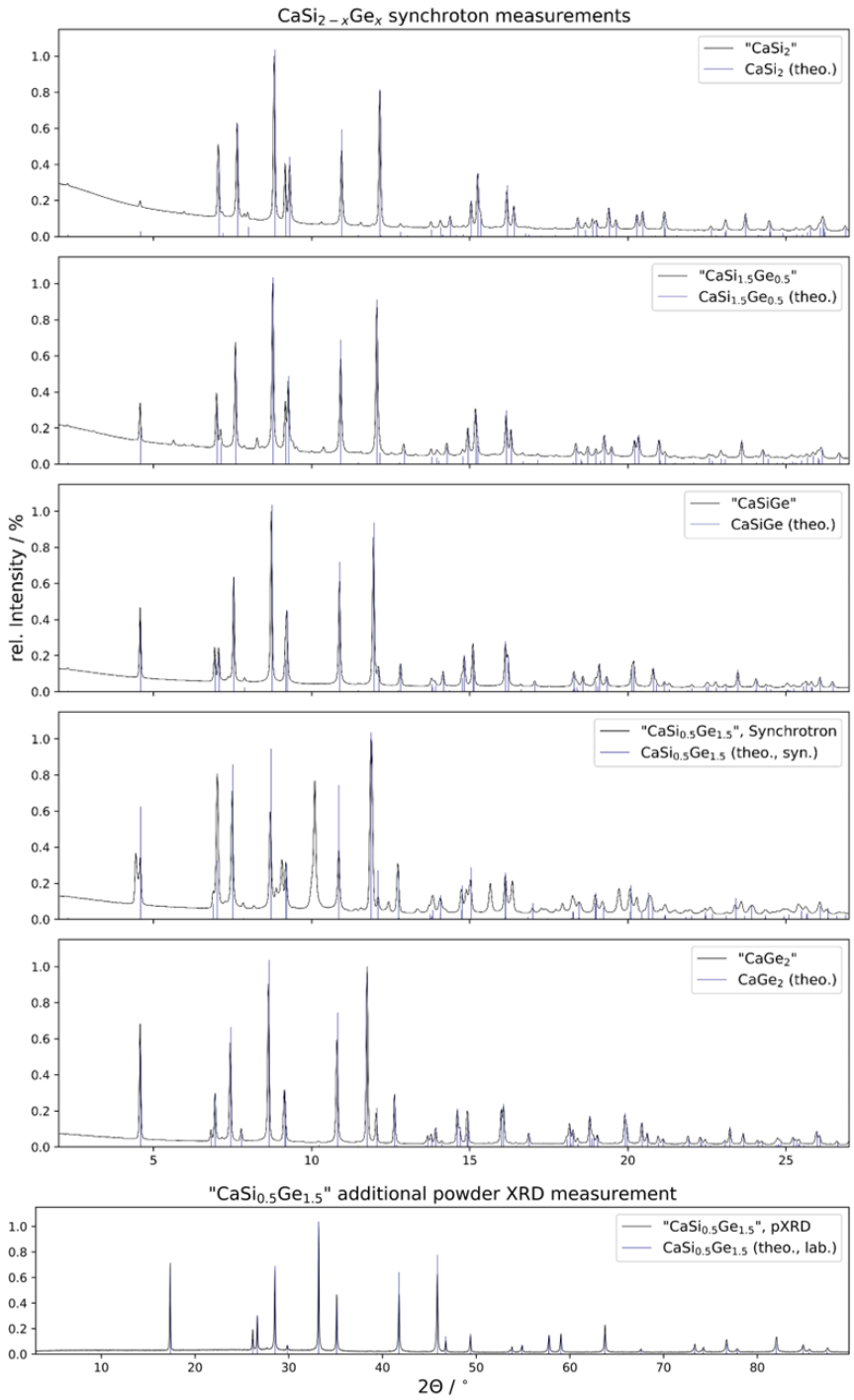

Figure S1. XRD pattern of the synchrotron and pXRD measurements.

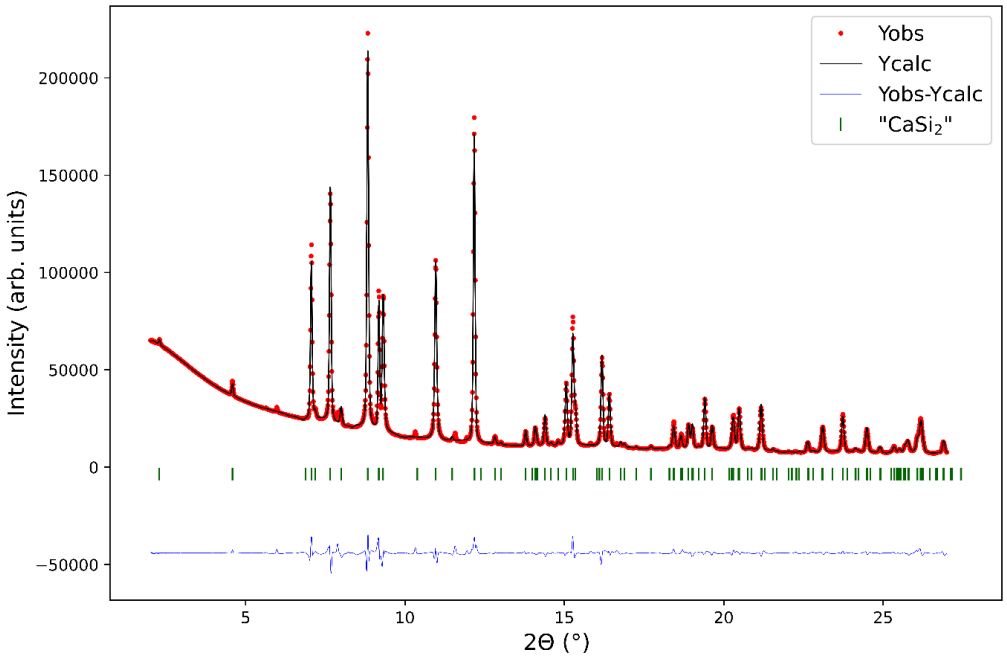

Figure S2. Rietveld refinement of the synchrotron measurement of $CaSi_2$.

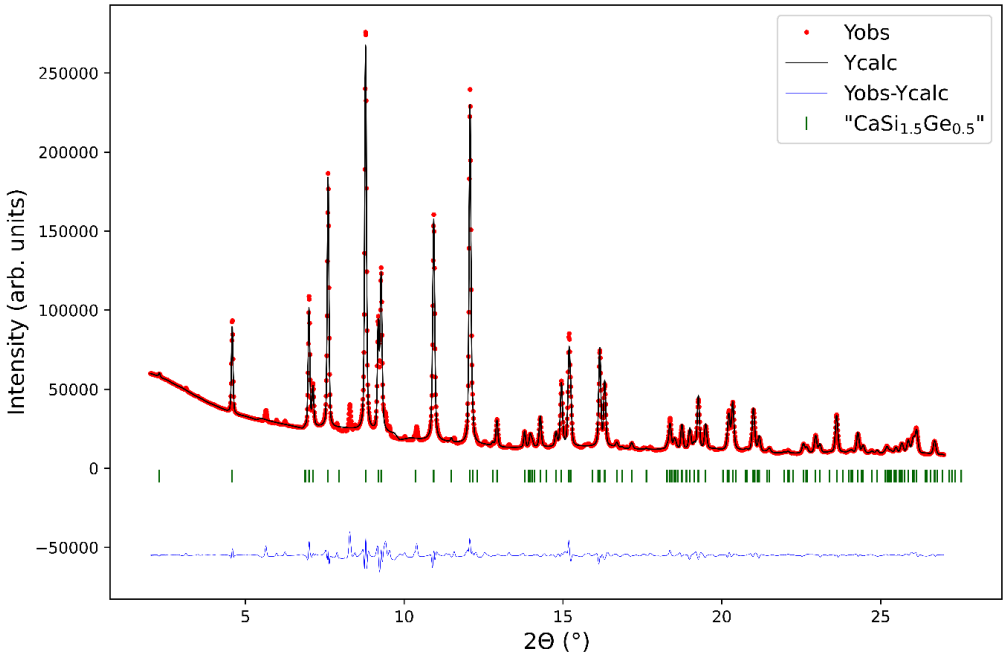

Figure S3. Rietveld refinement of the synchrotron measurement of $CaSi_{1.5}Ge_{0.5}$.

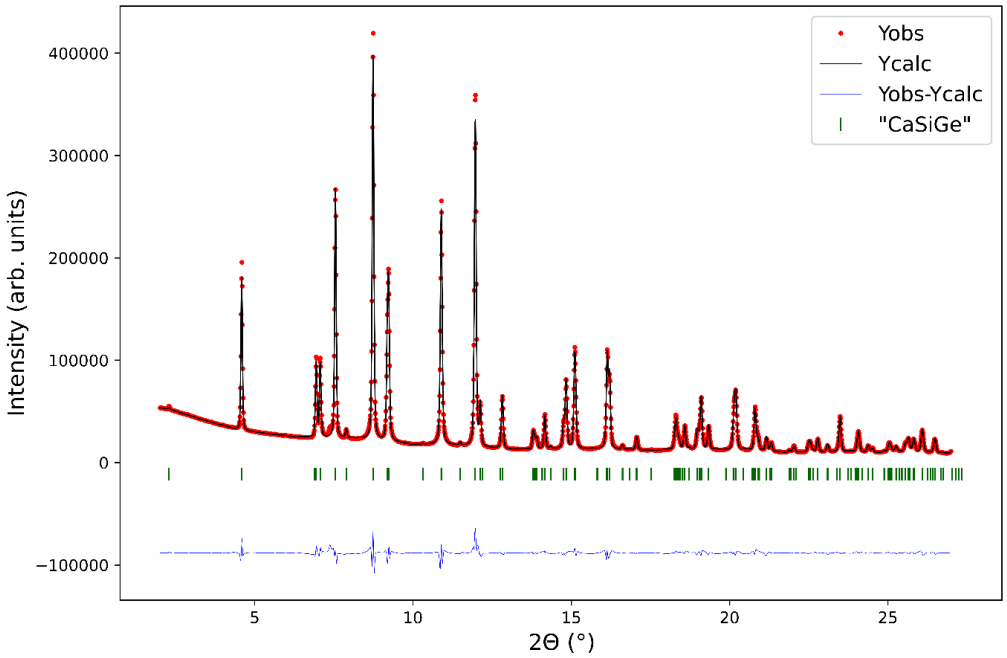

Figure S4. Rietveld refinement of the synchrotron measurement of CasiGe.

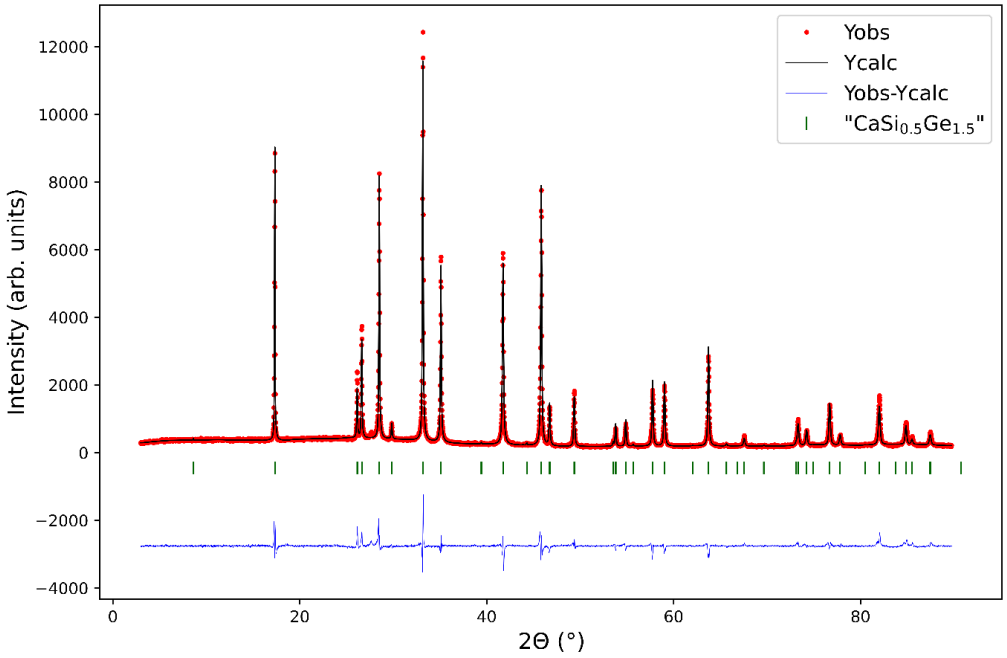

Figure S5. Rietveld refinement of the lab p-XRD measurement of $CaSi_{0.5}Ge_{1.5}$.

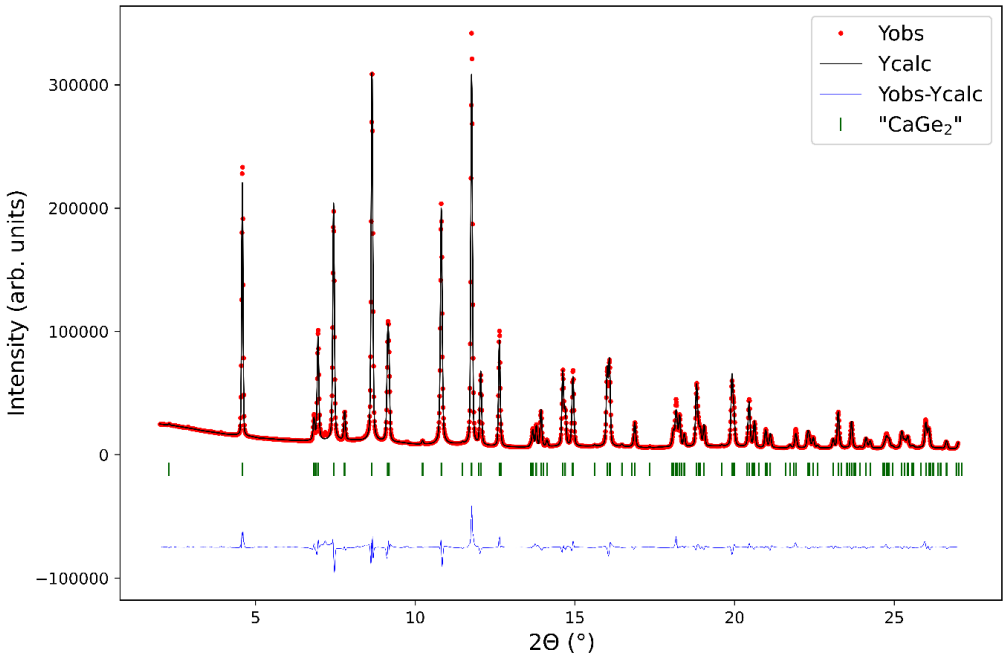

Figure S6. Rietveld refinement of the synchrotron measurement of $CaGe_2$.

2 Additional Information on the quantum chemical calculations

Basis sets used from literature: Ca[2], Si[3], Ge[4]

Table S3. Comparison of experimental and optimized cell parameters.

		a/b (Å)	c (Å)
$CaSi_2$	Exp	3.873	30.51
hR6	Calc.	3.8529	30.4070
	Δ (%)	-0.5	-0.3
hR3	Exp	3.8284	15.8966
	Calc.	3.8260	15.7320
	Δ (%)	-0.1	-1.0
$EuGe_2$-type	Exp	3.7668	4.4752
	Calc.	3.8624	4.9636
	Δ (%)	2.5	9.8
$Thsi_2$-type	Exp	4.2328	13.468
	Calc.	4.2525	13.5467
	Δ (%)	0.5	0.6
β-$GaGe_2$	Exp	3.999	30.62
	Calc.	3.9977	30.2915
	Δ (%)	-0.03	-1.08
α-$CaGe_2$	Exp	3.98542	10.2217
	Calc.	4.03669	11.32560
	Δ (%)	1.3	9.7

Table S4. Cell parameter of optimized ordered models of CaSiGe. The deviation is in relation to the pure $CaSi_2$ or $CaGe_2$ compound.

				deviation from parent compound:	
model		**a (Å)**	**c (Å)**	**Δa (%)**	**Δc (%)**
$CaSi_2$	layers	3.9202	30.5593	1.2	0.2
	alternating	3.9255	30.3735	1.3	-0.4
$CaGe_2$	layers	3.9238	30.4647	-1.9	-0.5
	alternating	3.9259	30.3675	-1.9	-0.8
Structures with Si and Ge swapped (VV)					
$CaSi_2$	layers	3.9231	30.2370	1.3	-0.9
	alternating	3.9260	30.3595	1.3	-0.5
$CaGe_2$	layers	3.9237	30.2464	-1.9	-1.2
	alternating	3.9250	30.3695	-1.9	-0.8

Table S5. Bond lengths and distances for the crystal structure of $CaGe_2$. All values for α- and β-$CaGe_2$ were taken from experimental data [1]. α'-$CaGe_2$ is the distorted and reoptimized structure of α-$CaGe_2$.

α-$CaGe_2$			**α'-$CaGe_2$ (gr. 36)**		
atom A	**atom B**	**distance (Å)**	**atom A**	**atom B**	**distance (Å)**
Ca1	Ge1	2.78(8)	Ca1	Ge2	2.995
	Ge2	2.87(5)		Ge2	2.9962
	Ge1	3.28(6)		Ge1	3.1107
	Ge2	4.10(7)		Ge1	3.1152
Ge1	Ge2	2.383(2)		Ge2	3.1563
	Ge2	2.384(2)		Ge1	3.7644
β-$CaGe_2$				Ge1	3.7647
Ca1	Ge1	2.92(7)	Ge1	Ge2	2.5388
	Ge2	2.99(8)		Ge2	2.5397
	Ge1	3.3(1)		Ge1	3.9921
	Ge2	3.9(1)		Ge1	3.994
Ge1	Ge1	2.76(7)	Ge2	Ge2	3.9921
Ge2	Ge2	2.65(7)		Ge2	3.994

Table S6. Interatomic distances and overlap population of $CaSi_2$ and polymorphs of $CaGe_2$ from the Mullikan analysis.

$CaSi_2$				**β-$CaGe_2$**			
atom A	**atom B**	**R (AB) (Å)**	**overlap population (AB)**	**atom A**	**atom B**	**R (AB) (Å)**	**overlap population (AB)**
Ca	Si2	2.996	0.011	Ca	Ge2	3.014	0.012
		3.663	0.000			3.757	0.004
	Si1	3.071	0.043		Ge1	3.085	0.036
		3.101	-0.007			3.146	0.004
	Ca	3.853	0.002		Ca	3.998	0.002
Si1	Si1	2.432	0.209		Ge1	2.556	0.201
		3.853	-0.035	Ge1		3.998	-0.026
Si2	Si2	2.401	0.223		Ge2	2.526	0.214
		3.853	-0.028			3.998	-0.018
				Ge2			
α-$CaGe_2$				**α'-$CaGe_2$ (gr. 36)**			
atom A	**atom B**	**R (AB) (Å)**	**overlap population (AB)**	**atom A**	**atom B**	**R (AB) (Å)**	**overlap population (AB)**
Ca	Ge2	2.872	0.028	Ca	Ge2	2.995	0.014
	Ge1	2.945	0.048			3.156	-0.009
		3.580	0.008		Ge1	3.111	0.035
	Ca	4.037	0.002			3.115	0.036
Ge1	Ge2	2.552	0.208			3.764	0.006
	Ge1	4.037	-0.010		Ca	3.992	0.001
Ge2	Ge2	4.037	-0.017	Ge1	Ge2	2.539	0.198
					Ge1	3.992	-0.016
						3.994	-0.023
				Ge2		3.992	-0.021
						3.994	-0.017

Table S7. Interatomic distances and overlap population of all layered and alternating models CaSiGe from the Mullikan analysis.

Layers $CaSi_2$-types				**Layers β-$CaGe_2$-type**				**Layers α-$CaGe_2$**			
atom A	**atom B**	**R (AB) (Å)**	**overlap population (AB)**	**atom A**	**atom B**	**R (AB) (Å)**	**overlap population (AB)**	**atom A**	**atom B**	**R (AB) (Å)**	**overlap population (AB)**
Ca	Ge1	3.007	0.015	Ca1	Ge1	3.001	0.013	Ca1	Ge2	2.868	0.029
		3.775	0.004			3.768	0.004		Ge1	3.598	0.007
	Si1	3.081	-0.006		Si1	3.077	-0.005		Si1	2.919	0.029
		3.090	0.040			3.088	0.040		Ca1	3.958	0.003
	Ca	3.920	0.002		Ca1	3.924	0.002	Ca2	Si2	2.874	0.028
Si1	Si1	2.465	0.200	Si1	Si1	2.468	0.200		Si1	3.504	0.006
		3.920	-0.032			3.924	-0.032		Ge1	2.937	0.050
Ge1	Ge1	2.491	0.219	Ge1	Ge1	2.494	0.217		Ca2	3.958	0.003
		3.920	-0.021			3.924	-0.021	Si1	Si2	2.461	0.219
									Si1	3.958	-0.014
								Si2	Si2	3.958	-0.022
								Ge1	Ge2	2.513	0.206
									Ge1	3.958	-0.007
								Ge2	Ge2	3.958	-0.040

10

Layers $CaSi_2$-type VV **Layers $CaGe_2$-type VV** **Layers alpha-$CaGe_2$ VV**

Ca	Si1	3.006	0.009	Ca1	Si1	3.007	0.010	Ca1	Si2	2.874	0.028
		3.656	0.000			3.653	0.000		Si1	3.504	0.006
	Ge1	3.065	0.039		Ge1	3.068	0.039		Ge1	2.937	0.050
		3.167	0.004			3.169	0.004		Ca1	3.958	0.003
	Ca	3.923	0.002		Ca1	3.924	0.002	Ca2	Ge2	2.868	0.029
Ge1	Ge1	2.519	0.201	Ge1	Ge1	2.518	0.200		Ge1	3.598	0.007
		3.923	-0.030			3.924	-0.030		Si1	2.920	0.029
Si1	Si1	2.435	0.221	Si1	Si1	2.433	0.215		Ca2	3.958	0.003
		3.923	-0.026			3.924	-0.026	Ge1	Ge2	2.513	0.206
									Ge1	3.958	-0.012
								Ge2	Ge2	3.958	-0.020
								Si1	Si2	2.461	0.219
									Si1	3.958	-0.012
								Si2	Si2	3.958	-0.047
alternating $CaSi_2$-type				**alternating α-$CaGe_2$-type**				**alternating β-$CaGe_2$-type**			
Ca1	Ge2	3.019	0.012	Ca1	Si2	2.993	0.012	Ca	Ge1	2.882	0.032
	Ge1	3.113	0.001		Si1	3.133	-0.004		Si1	2.914	0.050
	Si1	3.072	0.040		Ge1	3.087	0.040			3.557	0.004
	Si2	3.730	0.002		Ge2	3.698	0.003		Ca	3.962	0.003
	Ca1	3.926	0.002		Ca1	3.926	0.002	Si1	Ge1	2.485	0.225
Ca2	Si2	2.993	0.012	Ca2	Ge2	3.016	0.011		Si1	3.962	-0.012
	Si1	3.133	-0.004		Ge1	3.116	0.001	Ge1	Ge1	3.962	-0.023
	Ge1	3.086	0.040		Si1	3.075	0.040				
	Ge2	3.699	0.003		Si2	3.726	0.002				
	Ca2	3.926	0.002		Ca2	3.926	0.002				
Ge1	Si1	2.493	0.206	Si1	Ge1	2.493	0.207				
	Ge1	3.926	-0.033		Si1	3.926	-0.028				
Ge2	Si2	2.464	0.211	Si2	Ge2	2.464	0.211				
	Ge2	3.926	-0.022		Si2	3.926	-0.024				
Si1	Si1	3.926	-0.014	Ge1	Ge1	3.926	-0.021				
Si2	Si2	3.926	-0.033	Ge2	Ge2	3.926	-0.028				
alternating $CaSi_2$-type VV				**alternating β-$CaGe_2$-type VV**				**alternating α-$CaGe_2$-type VV**			
Ca1	Si2	2.992	0.012	Ca1	Ge2	3.016	0.011	Ca	Si1	2.857	0.022
	Si1	3.132	-0.004		Ge1	3.110	0.001		Ge1	2.947	0.037
	Ge1	3.085	0.040		Si1	3.070	0.040			3.538	0.010
	Ge2	3.697	0.003		Si2	3.727	0.002		Ca	3.958	0.003
	Ca1	3.926	0.002		Ca1	3.925	0.002	Ge1	Si1	2.489	0.198
Ca2	Ge2	3.018	0.012	Ca2	Si2	2.993	0.012		Ge1	3.958	-0.011
	Ge1	3.113	0.001		Si1	3.137	-0.004	Si1	Si1	3.958	-0.018
	Si1	3.073	0.040		Ge1	3.088	0.040				
	Si2	3.728	0.002		Ge2	3.699	0.003				
	Ca2	3.926	0.002		Ca2	3.925	0.002				
Si1	Ge1	2.493	0.206	Ge1	Si1	2.493	0.207				
	Si1	3.926	-0.028		Ge1	3.925	-0.033				
Si2	Ge2	2.464	0.211	Ge2	Si2	2.464	0.211				
	Si2	3.926	-0.023		Ge2	3.925	-0.022				
Ge1	Ge1	3.926	-0.021	Si1	Si1	3.925	-0.014				
Ge2	Ge2	3.926	-0.028	Si2	Si2	3.925	-0.033				

Table S8. Partial charge for all atoms within the parent compounds and therefrom derived models.

	Ca	part. charge	Si	part. charge	Ge	part. charge
$CaSi_2$	18.63	+ 1.37	14.65	-0.65		
			14.72	-0.72		
β-$CaGe_2$	18.61	+ 1.39			32.67	-0.67
					32.72	-0.72
α-$CaGe_2$	18.65	+ 1.35			32.37	-0.37
					32.99	-0.98
α'-$CaGe_2$ (gr. 36)	18.61	+ 1.39			32.52	-0.52
					32.87	-0.87
Layers $CaSi_2$-types	18.63	+ 1.37	14.66	-0.66	32.71	-0.71
Layers $CaSi_2$-type VV	18.61	+ 1.39	14.73	-0.73	32.65	-0.65
alternating $CaSi_2$-type	18.62	+ 1.38	14.55	-0.55	32.76	-0.76
	18.62	+ 1.38	14.59	-0.59	32.85	-0.85
alternating $CaSi_2$-type VV	18.62	+ 1.38	14.55	-0.55	32.76	-0.76
	18.62	+ 1.38	14.59	-0.59	32.85	-0.85
Layers β-$CaGe_2$-type	18.63	+ 1.37	14.66	-0.66	32.71	-0.71
Layers β-$CaGe_2$-type VV	18.61	+ 1.39	14.73	-0.73	32.65	-0.65
alternating β-$CaGe_2$-type	18.62	+ 1.38	14.55	-0.55	32.76	-0.76
	18.62	+ 1.38	14.59	-0.59	32.85	-0.85
alternating β-$CaGe_2$-type VV	18.62	+ 1.38	14.55	-0.55	32.76	-0.76
	18.63	+ 1.38	14.59	-0.59	32.85	-0.85
Layers α-$CaGe_2$	18.65	+ 1.35	14.42	-0.42	32.36	-0.36
	18.67	+ 1.33	14.93	-0.93	32.97	-0.97
Layers α-$CaGe_2$ VV	18.67	+ 1.33	14.42	-0.42	32.36	-0.36
	18.65	+ 1.35	14.93	-0.93	32.98	-0.98
alternating α-$CaGe_2$-type	18.67	+ 1.33	14.25	-0.25	33.08	-1.08
alternating alpha-$CaGe_2$-type VV	18.65	1.35	14.84	-0.84	32.51	-0.51

3 Band structures and density of states

3.1 $CaSi_2$ polymorphs

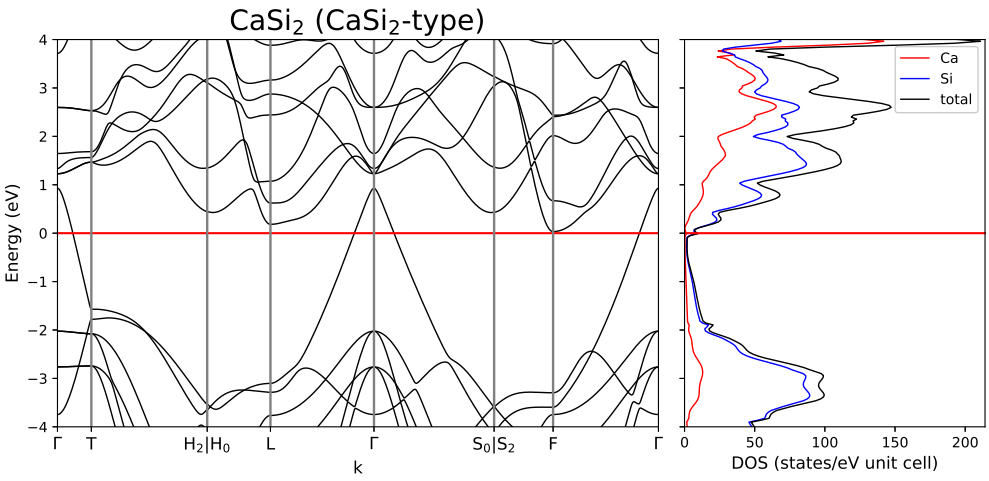

Figure S1. Band structure and density of states of $CaSi_2$ within the $CaSi_2$ structure type.

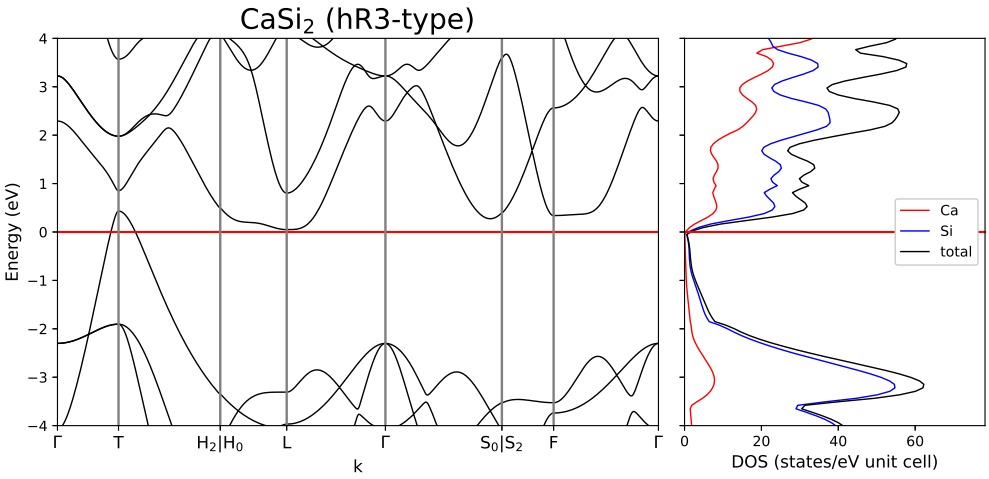

Figure S2. Band structure and density of states of $CaSi_2$ within the hR3 structure type.

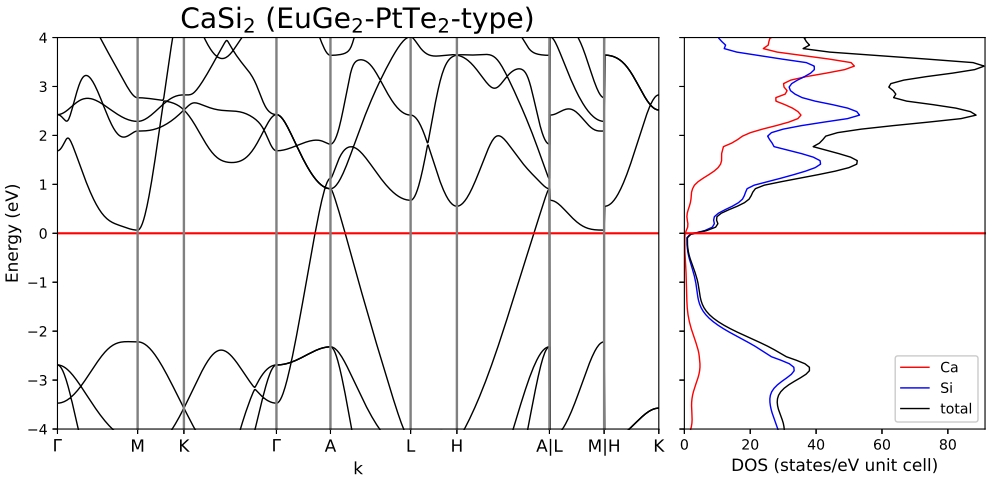

Figure S3. Band structure and density of states of $CaSi_2$ within the $EuGe_2$ structure type.

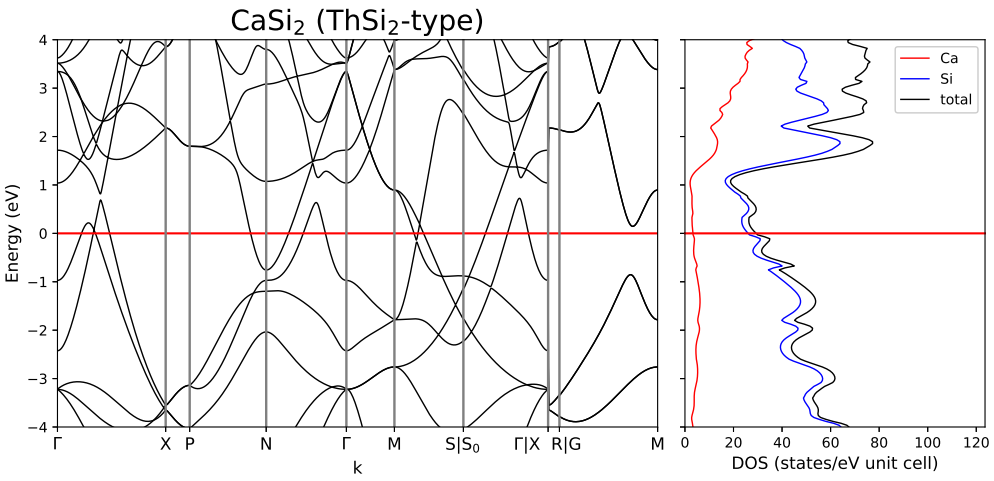

Figure S4. Band structure and density of states of $CaSi_2$ within the $ThSi_2$ structure type.

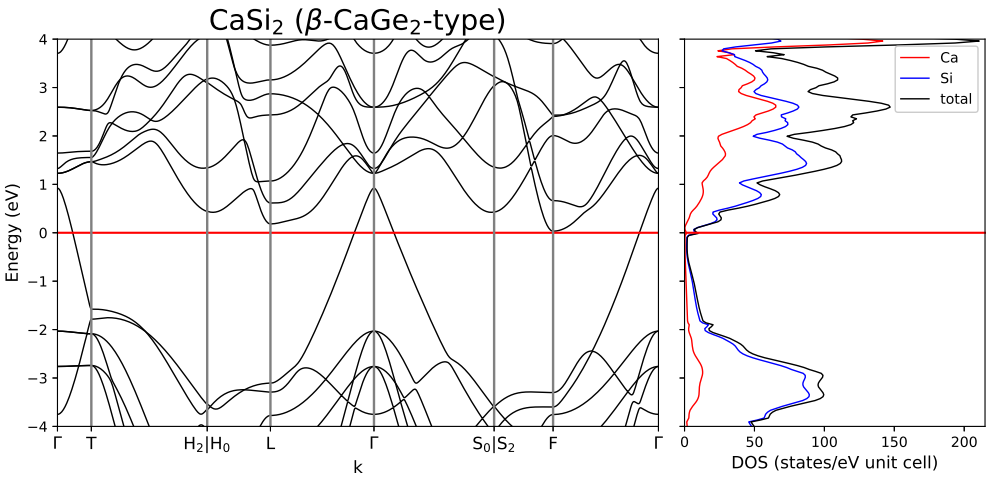

Figure S5. Band structure and density of states of $CaSi_2$ within the β-$CaGe_2$ structure type.

3.2 $CaGe_2$ polymorphs

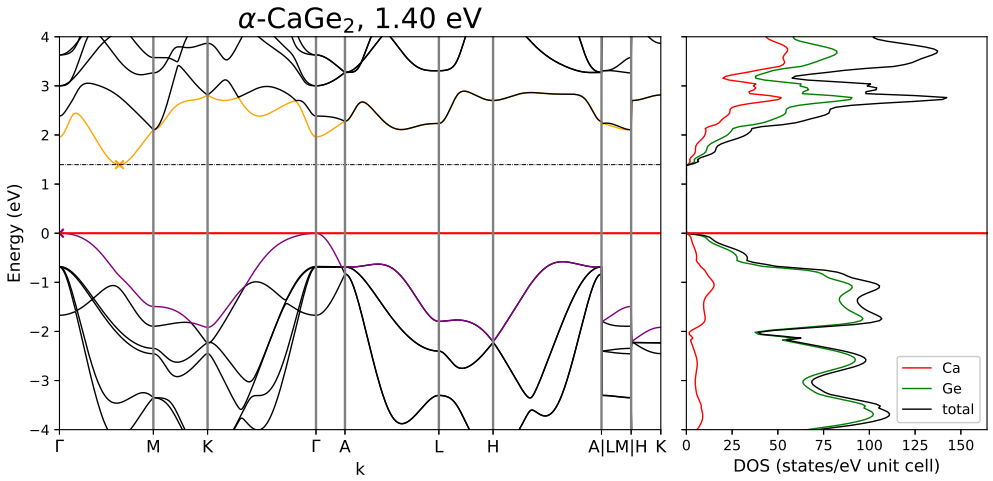

Figure S6. Band structure and density of states of α-$CaGe_2$ within the CdI_2 structure type.

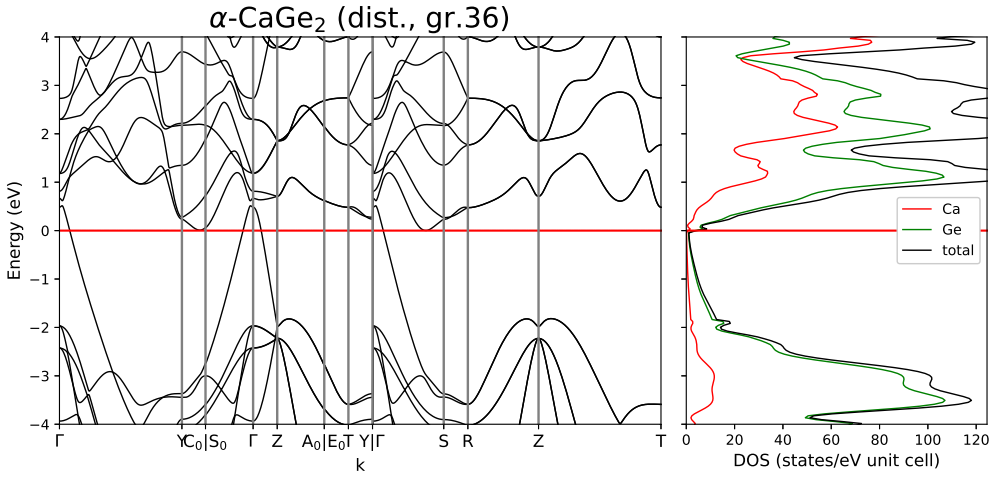

Figure S7. Band structure and density of states of α-$CaGe_2$ with reduced symmetry after distortion and re-optimization of the crystal structure in space group 36.

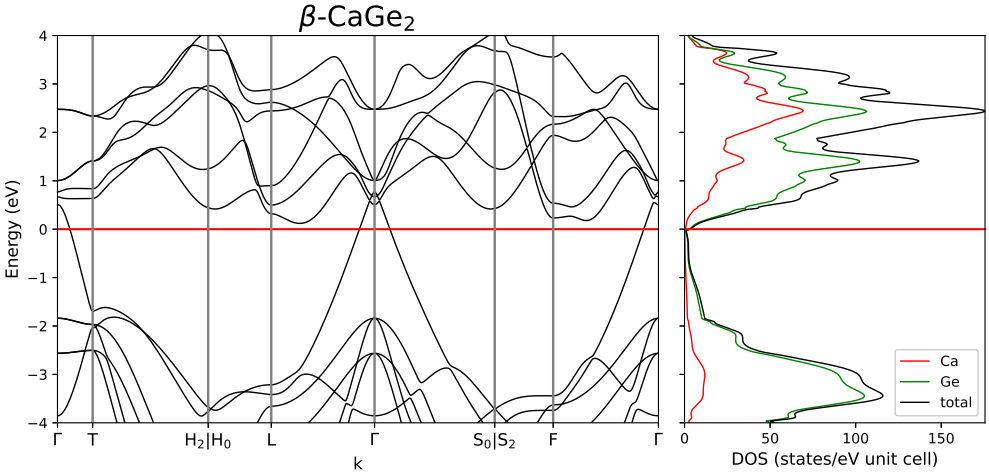

Figure S8. Band structure and density of states of β-$CaGe_2$ within the SmSI structure type.

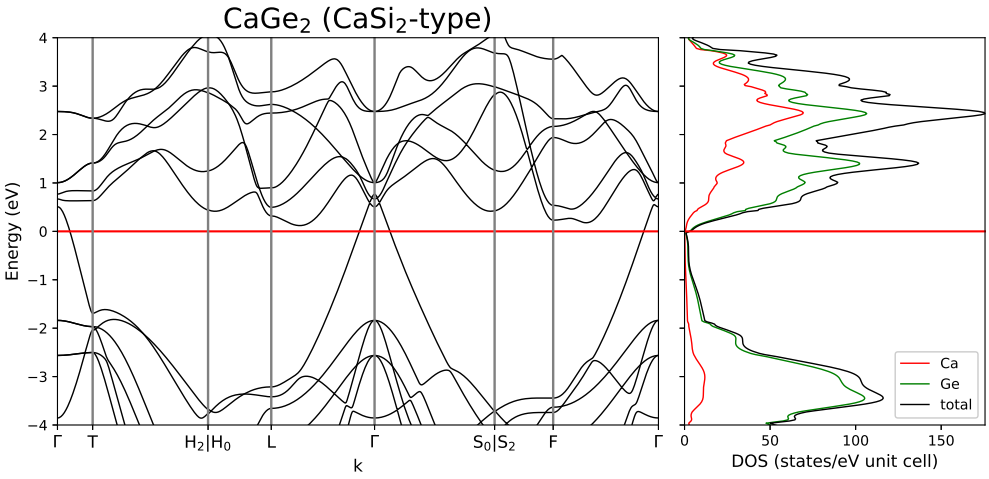

Figure S9. Band structure and density of states of $CaGe_2$ within the $CaSi_2$ structure type.

3.3 $CaSi_2$-type CaSiGe

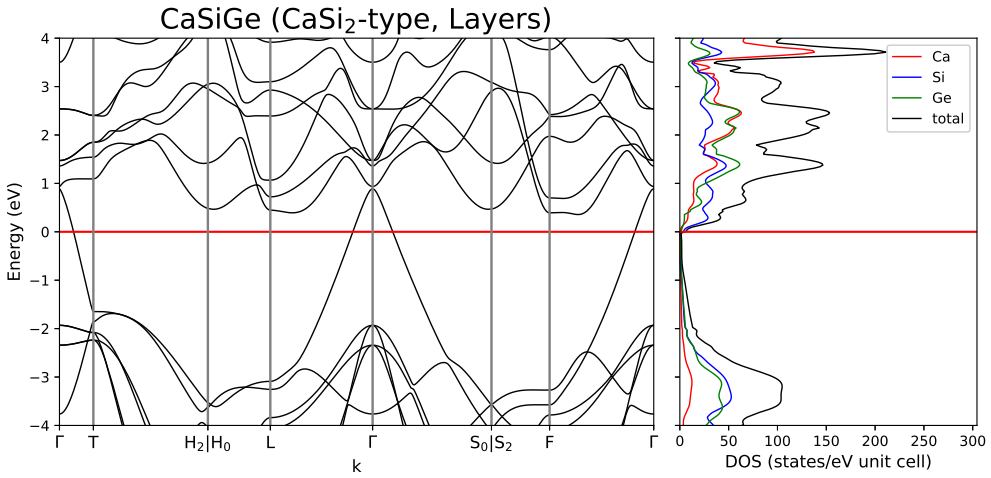

Figure S10. Band structure and density of states of layered CaSiGe within the $CaSi_2$ structure type.

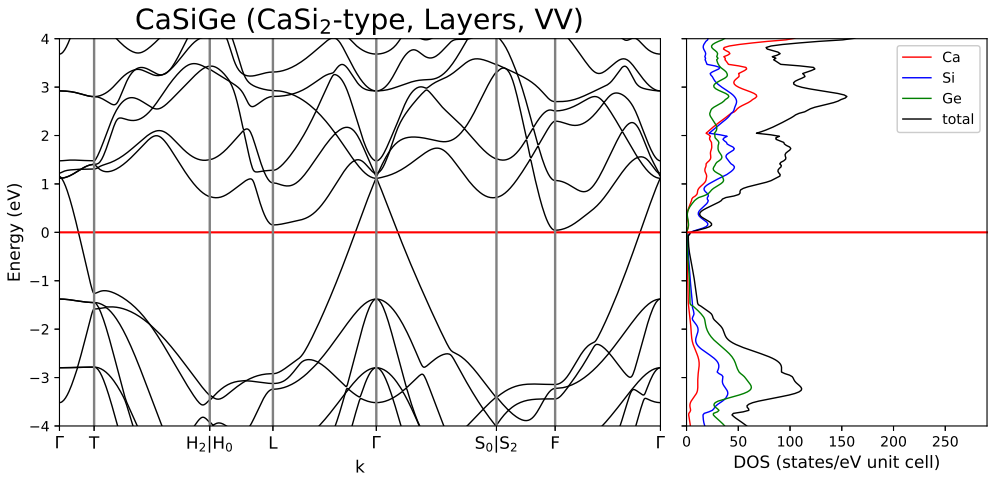

Figure S11. Band structure and density of states of layered CaSiGe within the $CaSi_2$ structure type. Compared to previous band structure, Si and Ge positions are switched.

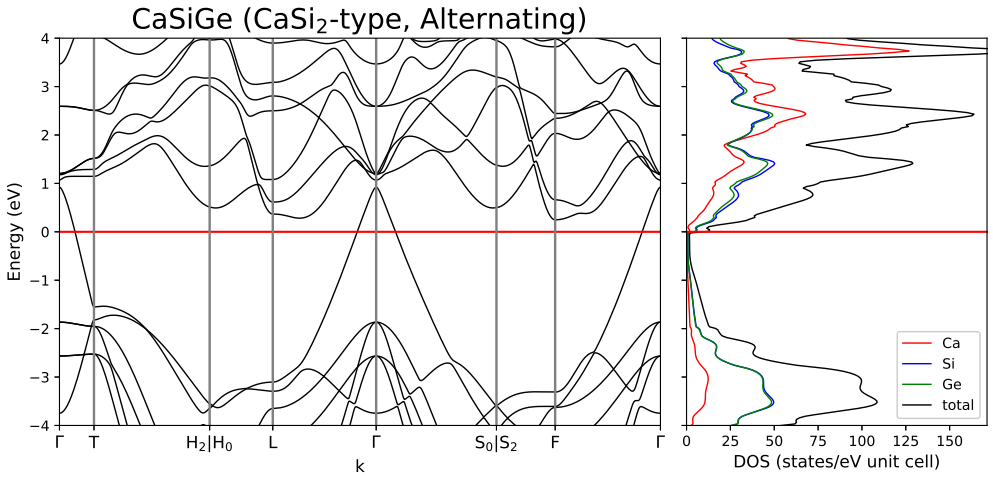

Figure S12. Band structure and density of states of alternating CaSiGe within the $CaSi_2$ structure type.

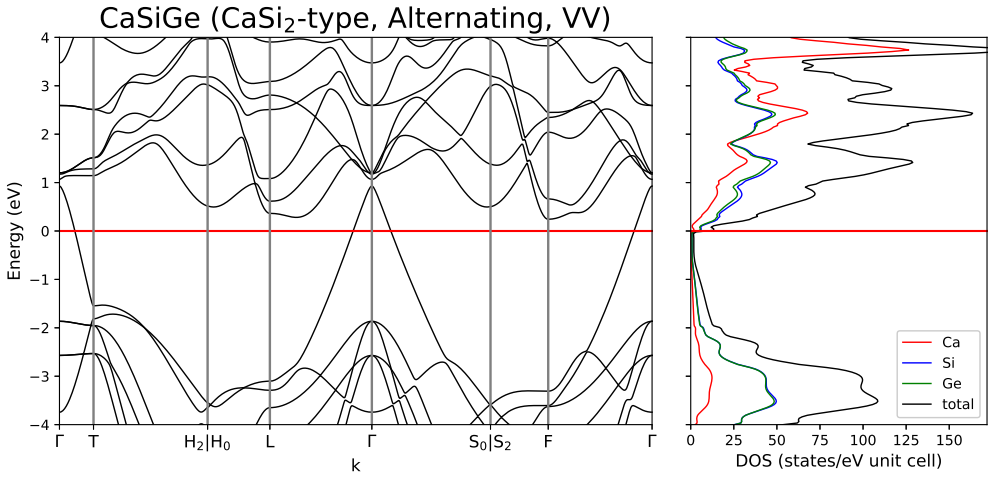

Figure S13. Band structure and density of states of alternating CaSiGe within the $CaSi_2$ structure type. Compared to previous band structure, Si and Ge positions are switched.

3.4 β-$CaGe_2$-type CaSiGe

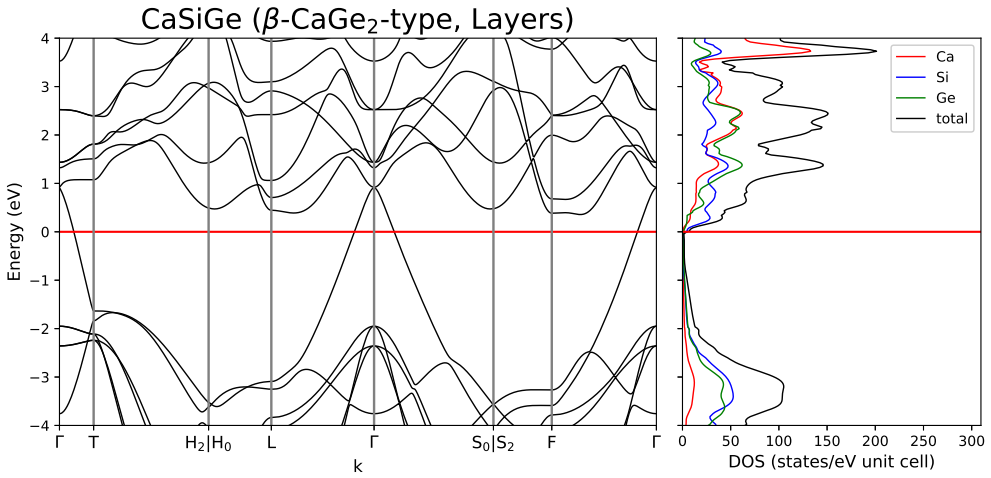

Figure S14. Band structure and density of states of layered CaSiGe within the β-$CaGe_2$ structure type.

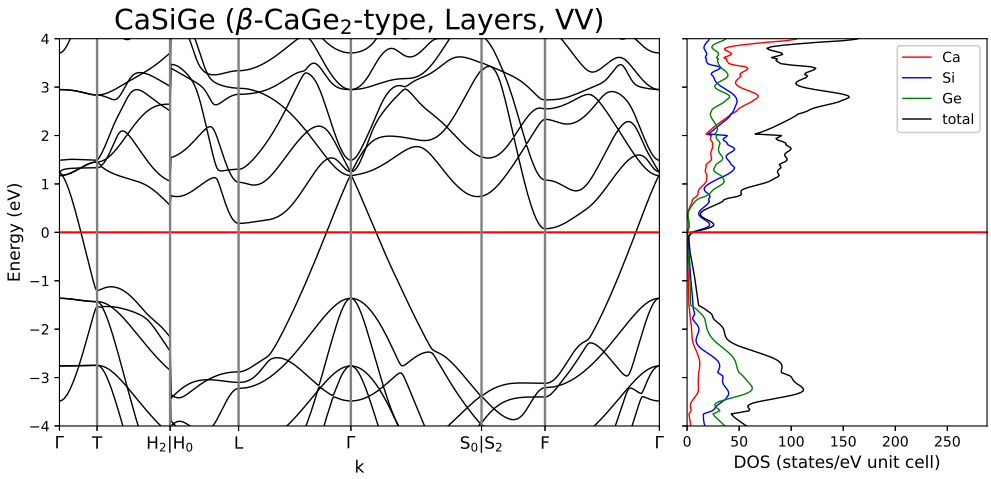

Figure S15. Band structure and density of states of layered CaSiGe within the β-$CaGe_2$ type. Compared to previous band structure, Si and Ge positions are switched.

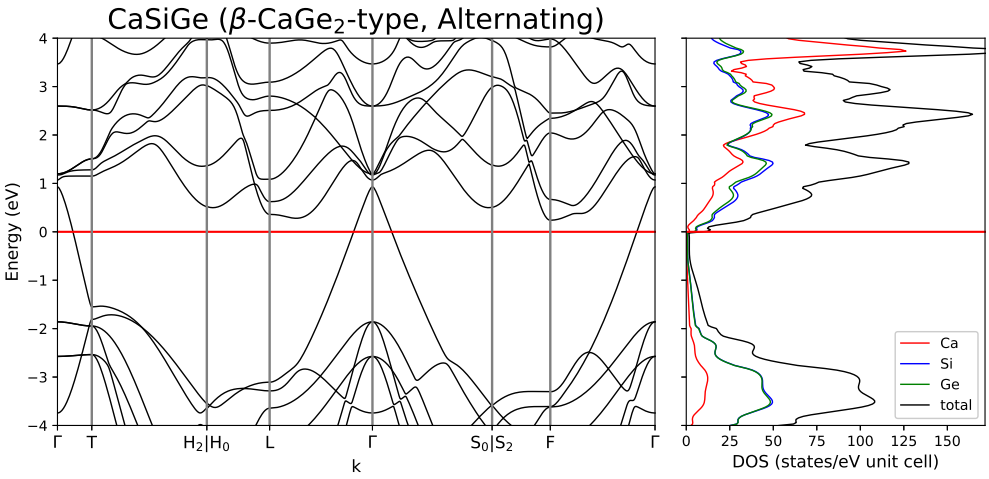

Figure S16. Band structure and density of states of alternating CaSiGe within the β-$CaGe_2$ structure type.

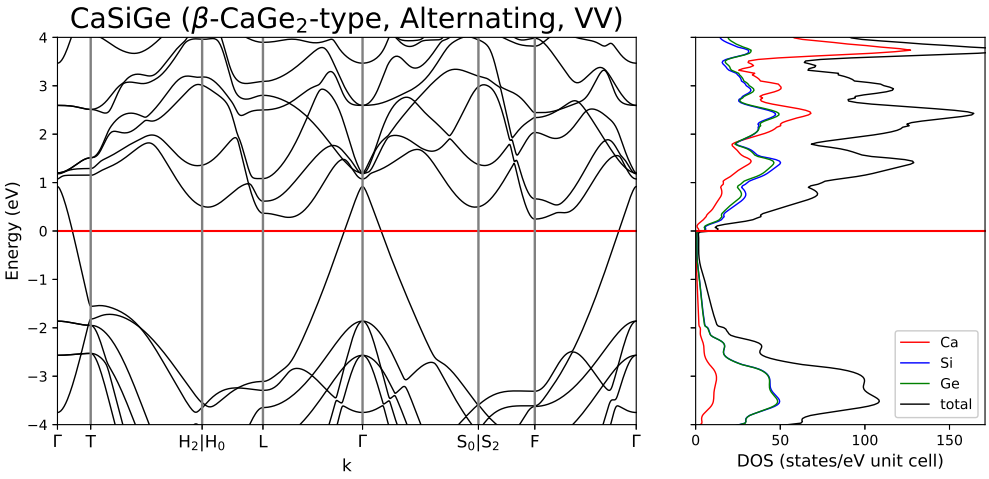

Figure S17. Band structure and density of states of alternating CaSiGe within the β-$CaGe_2$ structure type. Compared to previous band structure, Si and Ge positions are switched.

3.5 α-$CaGe_2$-type CaSiGe

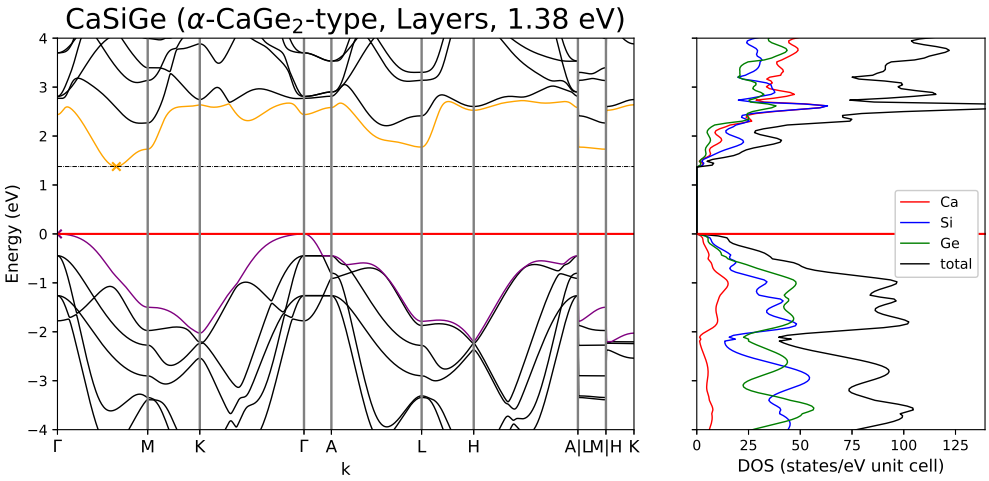

Figure S18. Band structure and density of states of layered CaSiGe within the α-$CaGe_2$ structure type.

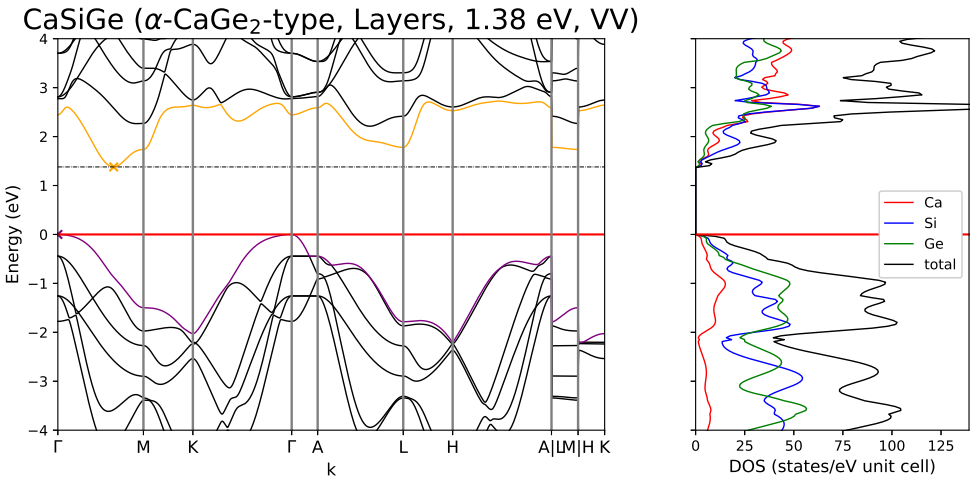

Figure S19. Band structure and density of states of layered CaSiGe within the α-$CaGe_2$ structure type. Compared to previous band structure, Si and Ge positions are switched.

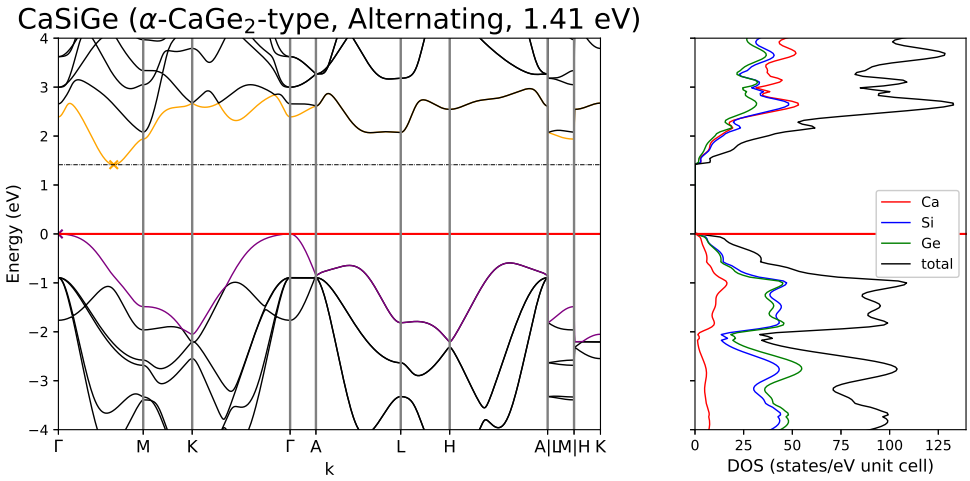

Figure S20. Band structure and density of states of alternating CaSiGe within the α-$CaGe_2$ structure type.

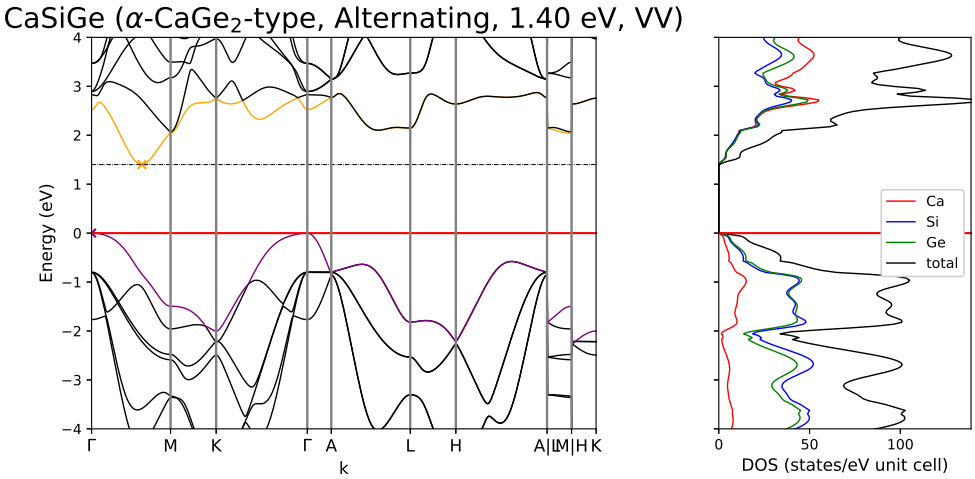

Figure S21. Band structure and density of states of alternating CaSiGe within the α-$CaGe_2$ structure type. Compared to previous band structure, Si and Ge positions are switched.

4 Band structures with position resolved density of states

4.1 $CaSi_2$ polymorphs

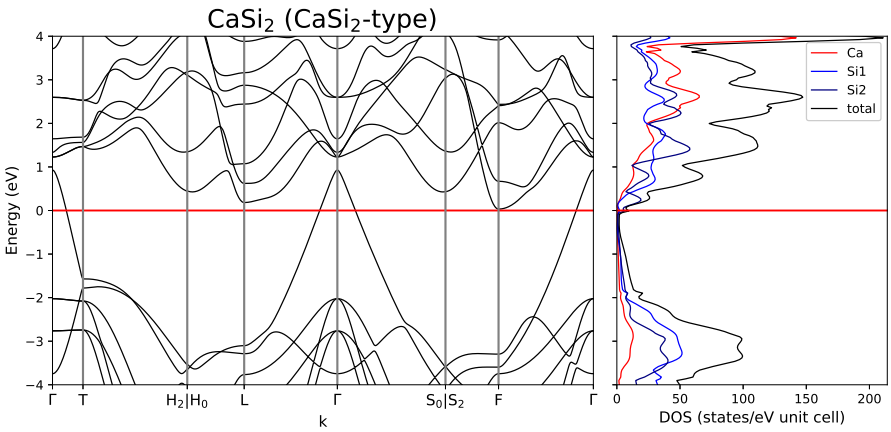

Figure S22. Band structure and density of states of $CaSi_2$ within the $CaSi_2$ structure type.

4.2 $CaGe_2$ polymorphs

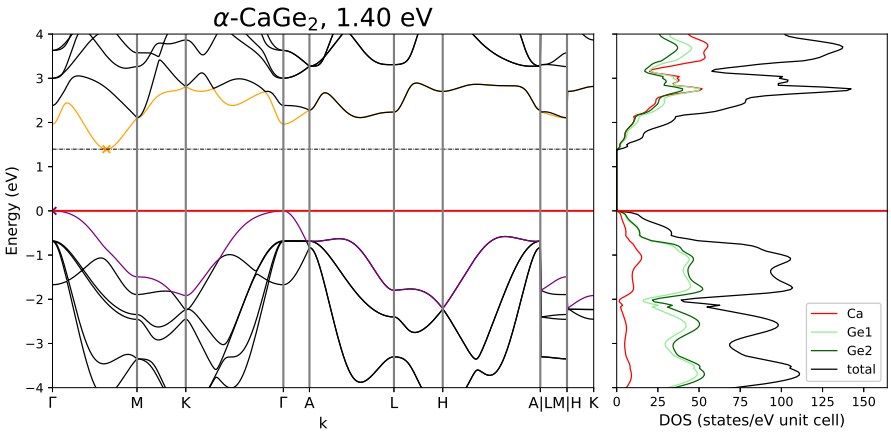

Figure S23. Band structure and density of states of α-$CaGe_2$ within the CdI_2 structure type.

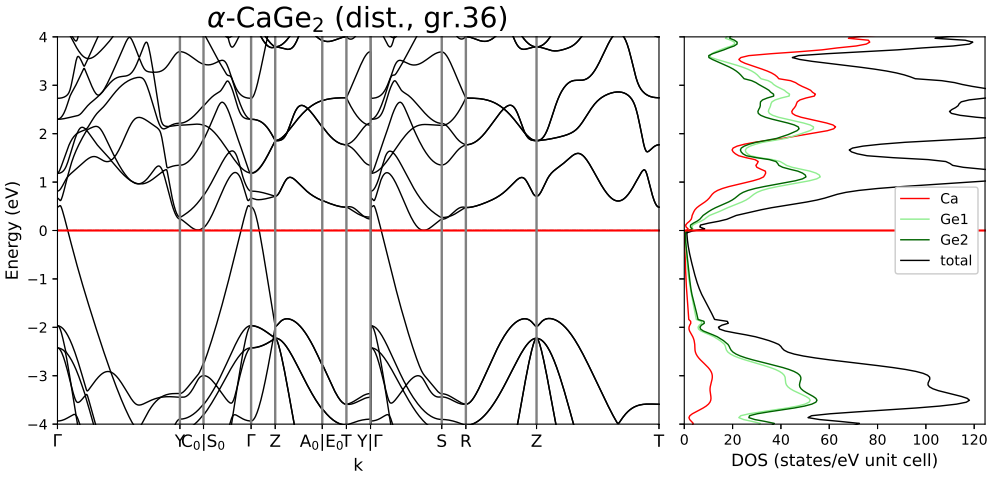

Figure S24. Band structure and density of states of α-$CaGe_2$ with reduced symmetry after distortion and re-optimization of the crystal structure in space group 36.

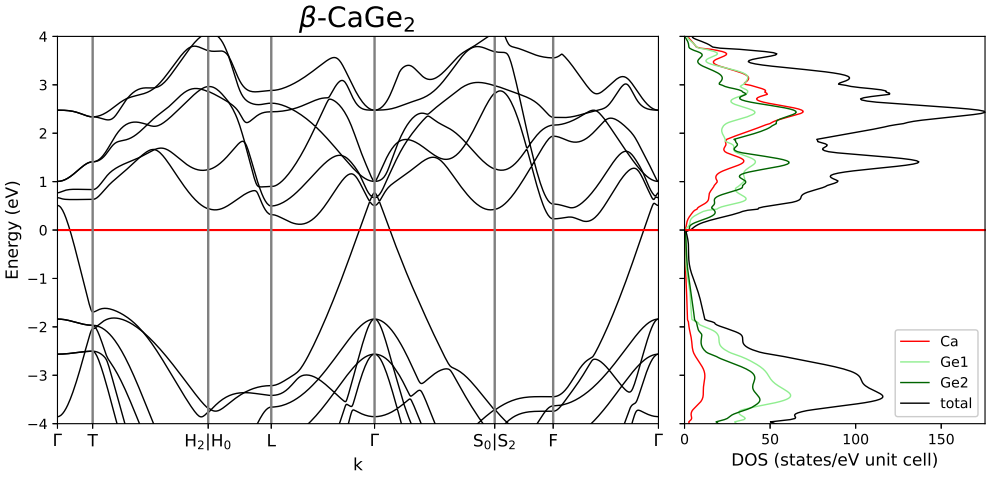

Figure S25. Band structure and density of states of β-$CaGe_2$ within the SmSI structure type.

4.3 $CaSi_2$-type CaSiGe

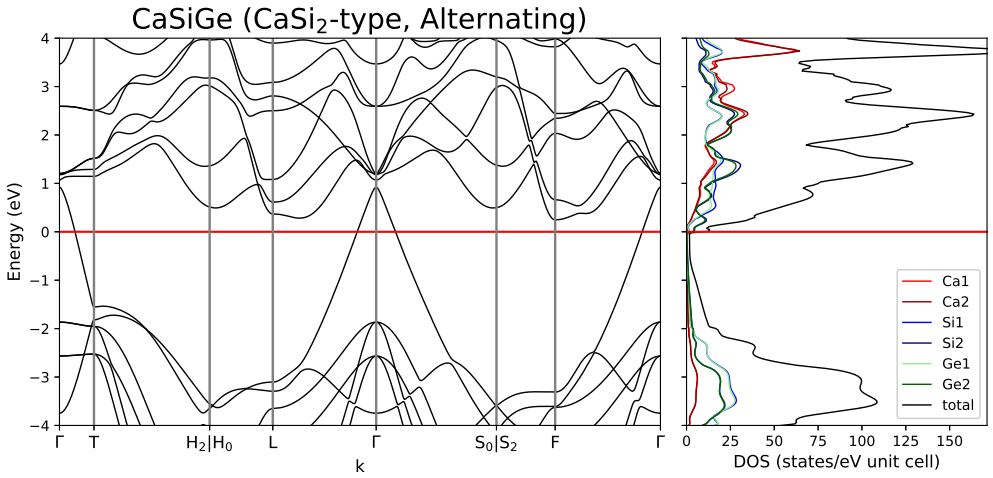

Figure S26. Band structure and density of states of alternating CaSiGe within the $CaSi_2$ structure type.

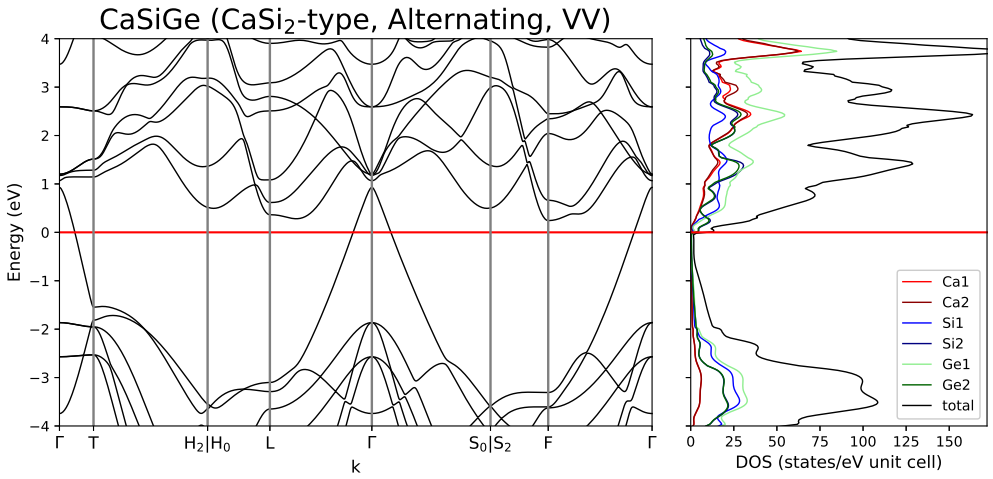

Figure S27. Band structure and density of states of alternating CaSiGe within the $CaSi_2$ structure type. Compared to previous band structure, Si and Ge positions are switched.

4.4 β-$CaGe_2$-type CaSiGe

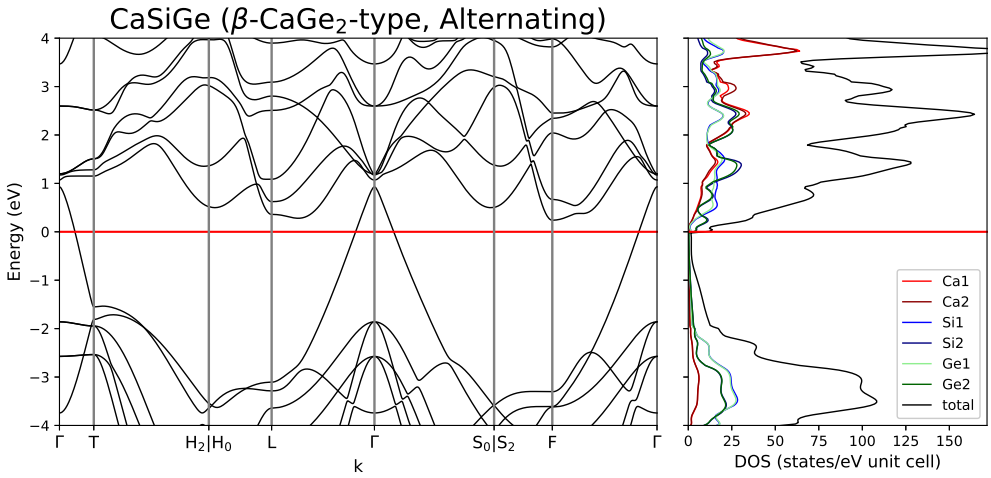

Figure S28. Band structure and density of states of alternating CaSiGe within the β-$CaGe_2$ structure type.

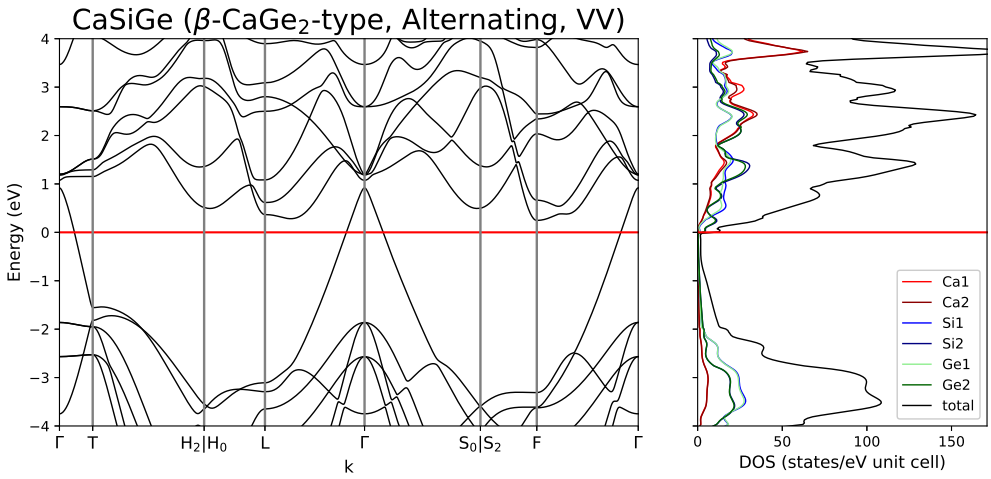

Figure S29. Band structure and density of states of alternating CaSiGe within the β-$CaGe_2$ structure type. Compared to previous band structure, Si and Ge positions are switched.

4.5 α-$CaGe_2$-type CaSiGe

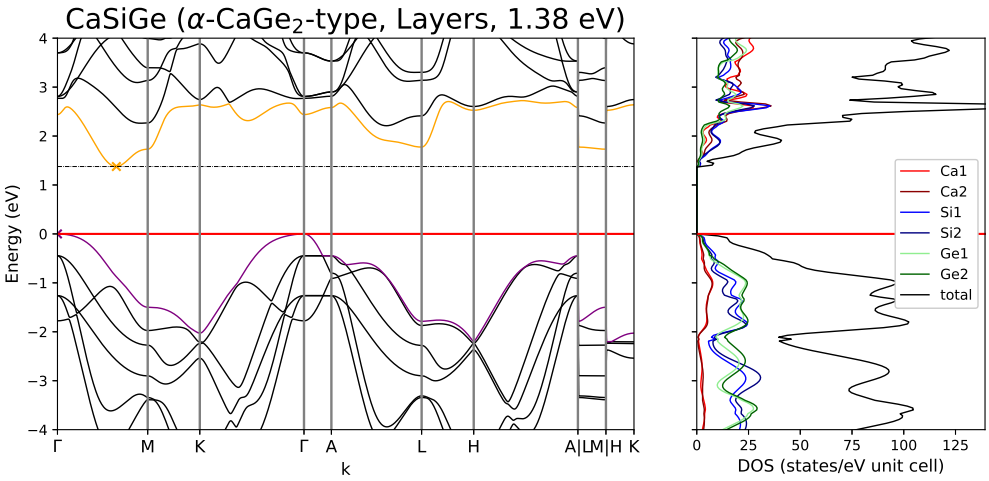

Figure S30. Band structure and density of states of layered CaSiGe within the α-$CaGe_2$ structure type.

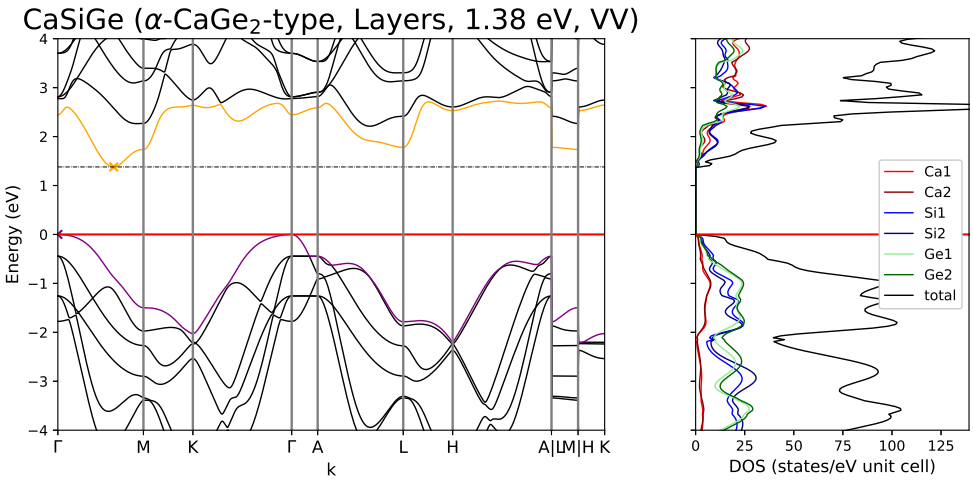

Figure S31. Band structure and density of states of layered CaSiGe within the α-$CaGe_2$ structure type. Compared to previous band structure, Si and Ge positions are switched.

5 Crystal orbital Hamilton population (COHP)

5.1 $CaSi_2$-type CaSiGe

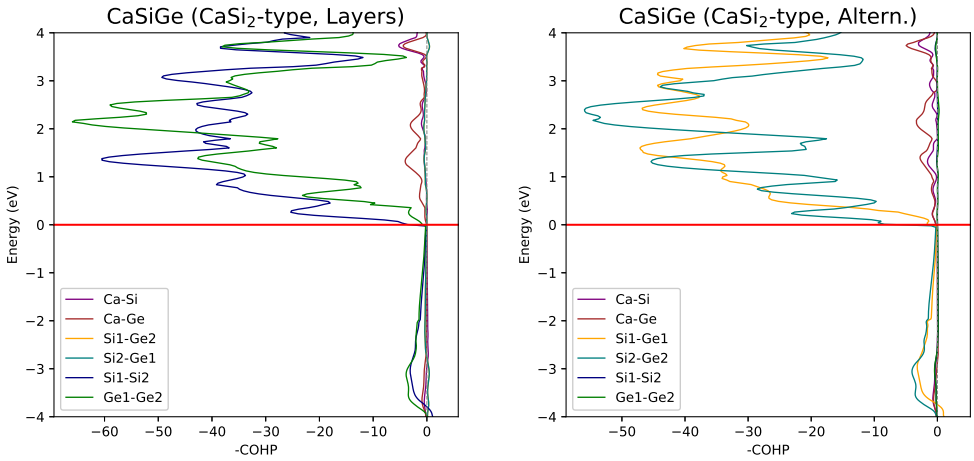

Figure S32. Left: Crystal orbital Hamilton population of layered CaSiGe within the $CaSi_2$ structure type. Right: Crystal orbital Hamilton population of alternating CaSiGe within the $CaSi_2$ structure type.

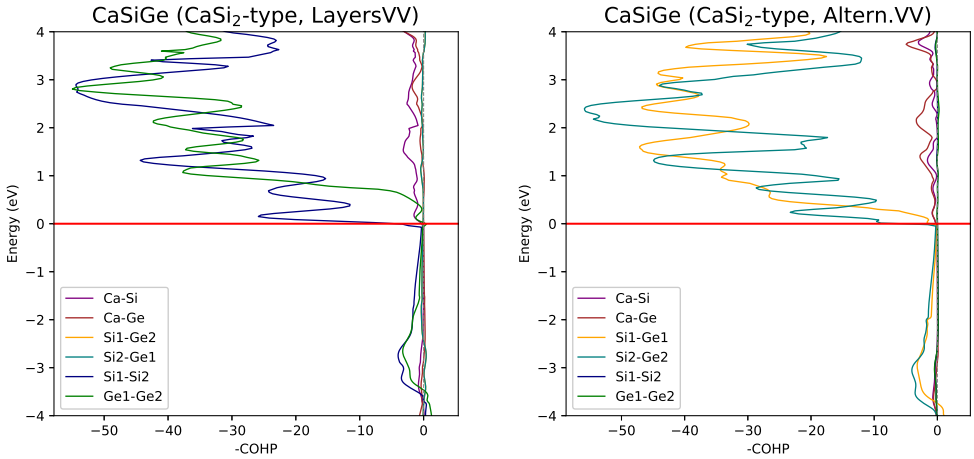

Figure S33. Left: Crystal orbital Hamilton population of layered CaSiGe within the $CaSi_2$ structure type. Right: Crystal orbital Hamilton population of alternating CaSiGe within the $CaSi_2$ structure type. In both compared to the previous figure, Si and Ge positions are switched.

5.2 β-$CaGe_2$-type CaSiGe

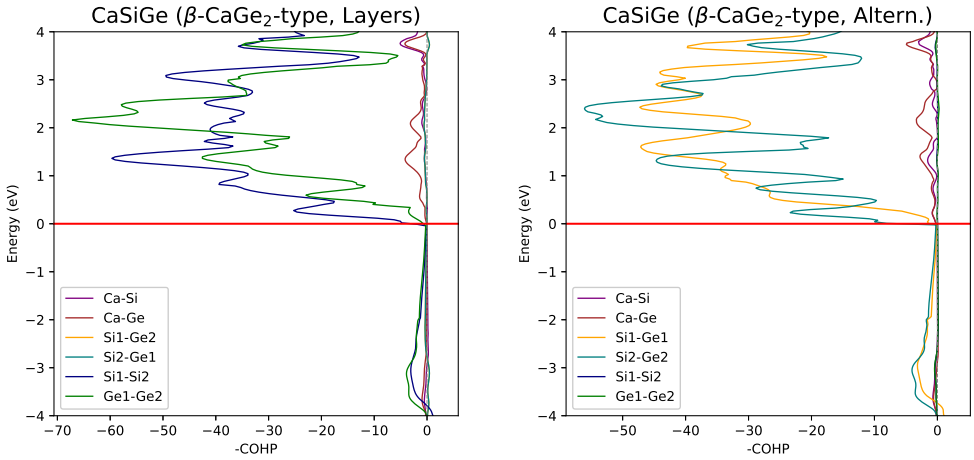

Figure S34. Left: Crystal orbital Hamilton population of layered CaSiGe within the β-$CaGe_2$ structure type. Right: Crystal orbital Hamilton population of alternating CaSiGe within the β-$CaGe_2$ structure type.

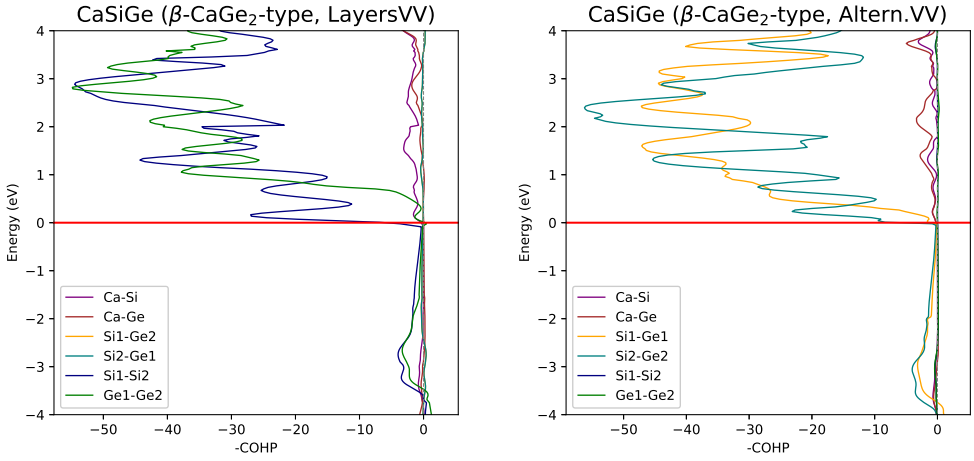

Figure S35. Left: Crystal orbital Hamilton population of layered CaSiGe within the β-$CaGe_2$ structure type. Right: Crystal orbital Hamilton population of alternating CaSiGe within the β-$CaGe_2$ structure type. In both compared to the previous figure, Si and Ge positions are switched.

5.3 α-$CaGe_2$-type CaSiGe

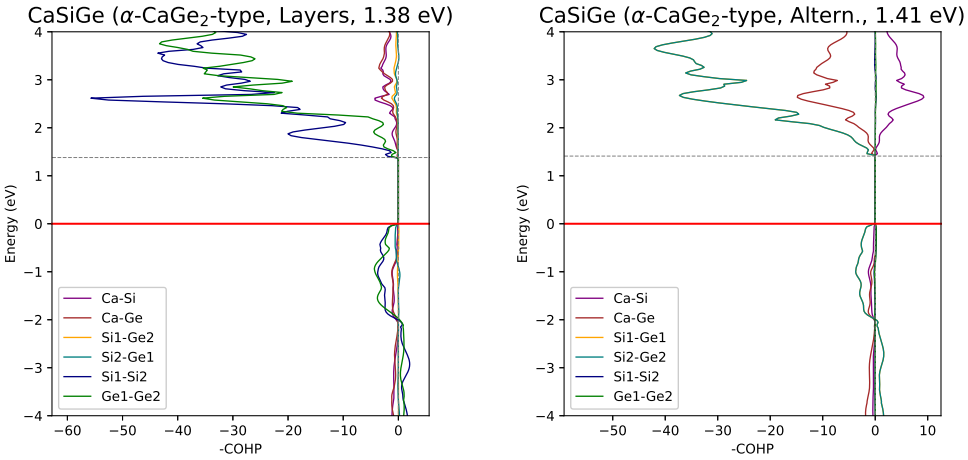

Figure S36. Left: Crystal orbital Hamilton population of layered CaSiGe within the α-$CaGe_2$ structure type. Right: Crystal orbital Hamilton population of alternating CaSiGe within the α-$CaGe_2$ structure type.

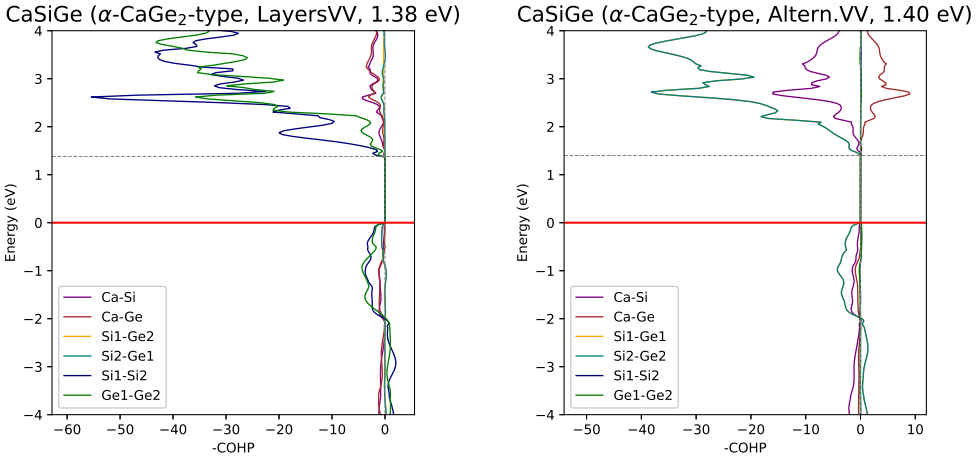

Figure S37. Left: Crystal orbital Hamilton population of layered CaSiGe within the α-$CaGe_2$ structure type. Right: Crystal orbital Hamilton population of alternating CaSiGe within the α-$CaGe_2$ structure type. In both compared to the previous figure, Si and Ge positions are switched.

References:

[1] N. D. Cultrara, Y. Wang, M. Q. Arguilla, M. R. Scudder, S. Jiang, W. Windl, S. Bobev, J. E. Goldberger, *Chem. Mater.* **2018**, *30*, 1335.
[2] K. Conley, A. J. Karttunen, *J. Phys. Chem. C* **2022**, *126*, 17266.
[3] A. J. Karttunen, T. F. Fässler, M. Linnolahti, T. A. Pakkanen, *Inorg. Chem.* **2011**, *50*, 1733.
[4] L. M. Scherf, A. J. Karttunen, O. Pecher, P. C. M. M. Magusin, C. P. Grey, T. F. Fässler, *Angew. Chem. Int. Ed. Engl.* **2016**, *55*, 1075.

Appendix

A Band Structure and Density of States Register

The following chapter contains information on all calculated compounds based on experimental data. For each compound stoichiometry an overview is given containing all details on the DFT calculations such as difference in experimental and calculated cell parameters, crystal structure properties, band gap properties and details on the DFT calculation parameters. Each crystal structure type is described briefly, band structure and density of states are shown and tables containing interatomic distances, overlap population and partial charges are given for each compound. For all cell parameters, literature data was taken from the source cited within the subsection and is presented with the significant figures given by the cited paper. Calculated cell parameters were rounded accordingly.

A.1 5-1-3

Table A.1: Overview of the crystallographic details of the 5-1-3 compounds. Cell parameters given in the first line and second line are of experimental and calculated origin, respectively. The third line shows the difference between both in percent. If only one line is given, a model was calculated. See subchapters for additional information.

compound	a / Å	b/ Å	c / Å	β / °	space group	crystal system	connectivity
Li_5SiP_3	7.2167	6.5934	11.6792	90.539	$P\ 2_1/n$ (no. 14)	monoclinic	0D (dimer)
	7.2481	6.5941	11.6805	90.545			
	0.43	0.01	0.01	0.01			
Li_5GeP_3	7.3386	6.6603	11.7988	90.533	-"-	-"-	-"-
Li_5SnP_3	7.5654	6.7739	12.1249	89.571	-"-	-"-	-"-
Na_5SiP_3	7.915	7.325	13.125	90.65	-"-	-"-	-"-
	7.855	7.204	12.977	90.27			
	-0.77	-1.68	-1.14	-0.42			
Na_5GeP_3	8.042	7.364	13.176	90.26	-"-	-"-	-"-
	7.959	7.246	13.047	90.07			
	-1.04	-1.63	-0.99	-0.21			
Na_5SnP_3	8.289	7.456	13.4	90.2	-"-	-"-	-"-
	8.198	7.340	13.2	90.4			
	-1.11	-1.58	-1.26	0.17			
K_5SnP_3	8.9431	8.0941	14.7833	90.107	-"-	-"-	-"-
	8.9296	8.1269	14.8073	90.222			
	-0.15	0.40	0.16	0.13			
Li_5SiAs_3	7.5027	6.8062	14.2735	122.30	-"-	-"-	-"-
Li_5GeP_3	7.5864	6.8692	14.4150	122.43	-"-	-"-	-"-
Na_5SiAs_3	8.177	7.529	13.466	90.5	-"-	-"-	-"-
	8.107	7.372	13.312	90.00			
	-0.86	-2.13	-1.16	-0.56			
Na_5GeAs_3	8.298	7.544	13.531	90.2	-"-	-"-	-"-
	8.207	7.418	13.368	90.18			
	-1.11	-1.69	-1.22	-0.02			
Na_5SnAs_3	8.527	7.642	13.716	90.3	-"-	-"-	-"-
	8.448	7.501	13.525	90.5			
	-0.93	-1.88	-1.41	0.18			
K_5SnAs_3	9.2190	8.2988	15.1959	90.00	-"-	-"-	-"-
	9.1719	8.2975	15.0982	90.39			
	-0.51	-0.02	-0.65	0.43			
K_5SnBi_3	10.105	8.818	16.350	90.06	-"-	-"-	-"-
	9.933	8.621	16.455	90.27			

Table A.1: Continued.

compound	a / Å	b/ Å	c / Å	β / °	space group	crystal system	connectivity
	-1.73	-2.28	0.64	0.23			
Rb_5GeP_3	13.966	5.582	15.256		*P n m a* (no. 62)	orthorhombic	0D (monomer)
	14.725	5.472	15.564				
	5.15	-2.01	1.98				
Cs_5SiP_3	14.144	5.995	15.5		-"-	-"-	-"-
	15.306	5.752	15.4				
	7.59	-4.23	-0.33				
Cs_5GeP_3	14.311	5.994	15.618		-"-	-"-	-"-
	15.419	5.733	15.693				
	7.18	-4.56	0.48				
Rb_5SiAs_3	14.169	5.671	15.479		-"-	-"-	-"-
	14.965	5.555	15.805				
	5.32	-2.09	2.06				
Cs_5SiAs_3	14.467	6.043	15.820		-"-	-"-	-"-
	14.740	5.970	15.864				
	1.85	-1.22	0.28				
Cs_5GeAs_3	14.615	6.045	15.964		-"-	-"-	-"-
	15.672	5.794	16.185				
	6.74	-4.32	1.36				
Na_5SnSb_3	12.493	9.181	18.594	98.3	P $2_1/n$ (no. 14)	monoclinic	1D (chains)
	12.274	9.079	18.198	97.5			
	-1.79	-1.13	-2.18	-0.77			

Table A.2: Calculated band gaps and transitions as well as an overview of the sampled reciprocal space defined by the Monkhorst-Pack-type *k*-point grid (SHRINK) and Brillouin Zone paths for all 5-1-3 compounds.

compound	band gap		transition	k-path	SHRINK
Li_5SiP_3	2.79	indirect	Γ -> C_2	Γ—Z—D—B—Γ—A—E—Z—C_2—Y_2—Γ	5 5 3
Li_5GeP_3	2.40	indirect	Γ -> E	-"-	-"-
Li_5SnP_3	2.54	indirect	Γ -> E-Z	-"-	-"-
Na_5SiP_3	2.99	indirect	B-Γ -> Γ-Z	-"-	-"-
Na_5GeP_3	2.71	indirect	Γ -> Γ-Z	-"-	-"-
Na_5SnP_3	2.58	direct	Γ -> Γ	-"-	-"-
K_5SnP_3	2.57	direct	Γ -> Γ	-"-	-"-
Li_5SiAs_3	2.27	indirect	Γ -> E-Z	-"-	4 4 2
Li_5GeP_3	1.92	indirect	Γ -> E-Z	-"-	-"-
Na_5SiAs_3	2.59	indirect	Γ -> Z	-"-	-"-
Na_5GeAs_3	2.25	indirect	Γ -> Γ-Z	-"-	4 4 3
Na_5SnAs_3	2.15	direct	Γ -> Γ	-"-	-"-
K_5SnAs_3	2.27	direct	Γ -> Γ	-"-	3 3 2
K_5SnBi_3	1.23	direct	Γ -> Γ	-"-	3 4 2
Rb_5GeP_3	1.98	direct	Γ -> Γ	Γ—X—S—Y—Γ—Z—U—R—T—Z|X—U|Y—T|S—R	2 5 2
Cs_5SiP_3	1.95	indirect	Γ -> T	-"-	-"-
Cs_5GeP_3	2.04	indirect	Γ -> T	-"-	-"-
Rb_5SiAs_3	1.78	direct	Γ -> Γ	-"-	2 6 2
Cs_5SiAs_3	1.88	indirect	Γ -> Y	-"-	2 5 2
Cs_5GeAs_3	1.86	pseudo-direct	Γ -> Γ	-"-	-"-
Na_5SnSb_3	1.43	direct	Γ -> Γ	Γ—Z—D—B—Γ—A—E—Z—C_2—Y_2—Γ	3 3 2

Li_5SiP_3[76]

Li_5SiP_3 crystallizes in the monoclinic space group P $2_1/n$ (no. 14) in the Na_5GeP_3 structure type.[79] It contains edge sharing double tetrahedra consisting of $[Si_2P_6]^{10-}$ units and isolated K^+ atoms which leads to a charge-balanced Zintl phase. P atoms form a distorted hexagonal packing with partially occupied tetrahedral voids. Since the unit cell harbours 3 P atoms per stoichiometric unit, with Z = 4, a total of 12 octahedral and 24 tetrahedral voids result. All octahedral voids are filled with atoms by Li, while 50 % of the tetrahedral voids are filled by Si and the remaining Li atoms.

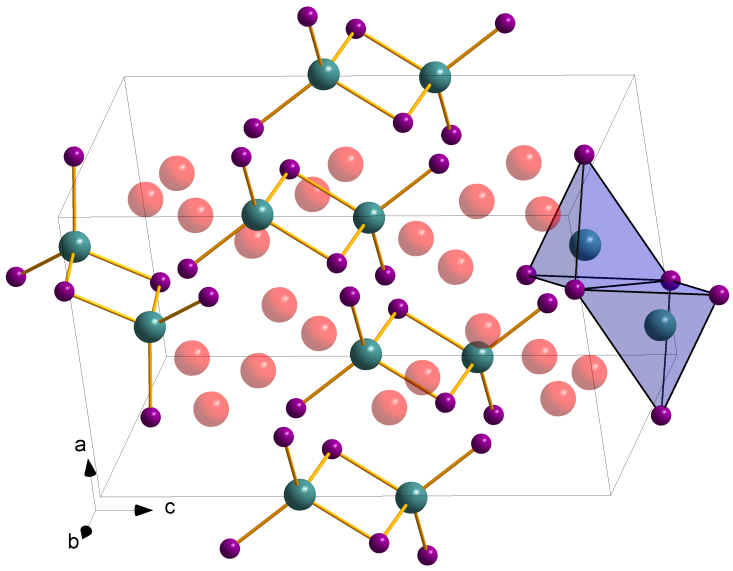

Figure A.1: Crystal structure of the Na_5GeP_3 structure type containing $[Tt_2P_6]^{10-}$ units forming edge sharing double tetrahedra.

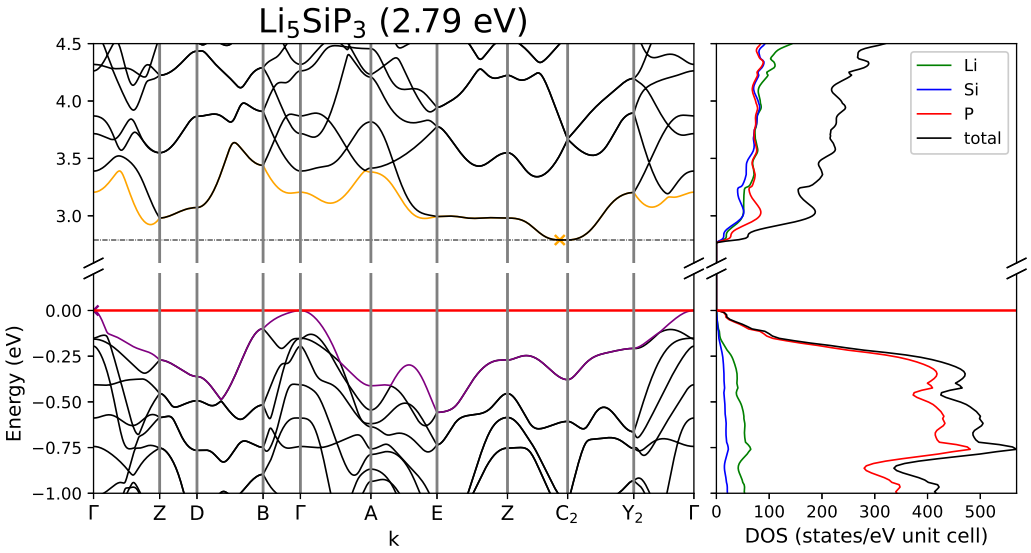

Figure A.2: Band structure and DOS of Li_5SiP_3.

Table A.3: Overlap population and interatomic distances of Li_5SiP_3.

Atom A	Atom B	r_{AB} / Å	overlap
Li1	P3	2.528	0.084
	P2	2.74	0.06
	P2	2.744	0.054
	P1	2.751	0.052
	Li4	2.788	0.008
	Li2	2.929	0.008
Li2	P2	2.495	0.092
	P1	2.497	0.074
	P3	2.532	0.085
	P3	2.546	0.075
	Li3	2.724	0.009
	Si1	2.851	0.017
Li3	P1	2.616	0.065
	P3	2.678	0.071
	P2	2.708	0.062
	P3	2.712	0.062

Atom A	Atom B	r_{AB} / Å	overlap
Li4	P2	2.523	0.087
	P1	2.544	0.076
	P3	2.557	0.087
	P2	2.592	0.082
Li5	P2	2.672	0.078
	P3	2.728	0.056
	P1	2.833	0.038
	P2	2.867	0.049
	P3	2.894	0.043
Si1	P3	2.235	0.301
	P2	2.239	0.303
	P1	2.285	0.263
	P1	2.315	0.24

Table A.4: Partial charges for each atom position in Li_5SiP_3.

Atom	Z	charge	part charge
Li1	3	2.435	0.565
Li2		2.525	0.475
Li3		2.439	0.561
Li4		2.505	0.495
Li5		2.426	0.574

Atom	Z	charge	partialcharge
Si1	14	14.029	−0.029
P1	15	15.705	−0.705
P2		15.973	−0.973
P3		15.963	−0.963

Li_5GeP_3[77]

Since Li_5GeP_3 crystallizes in an unordered cubic space group Fm-3m in which according to the CaF_2 structure type, the P atoms form a cubic closest packing (ccp) with Ge and Na atoms appearing disordered over all tetrahedral voids. Since this structure can be transformed into the Na_5GeP_3-type upon ordering, a model based on Na_5SiP_3 was calculated.

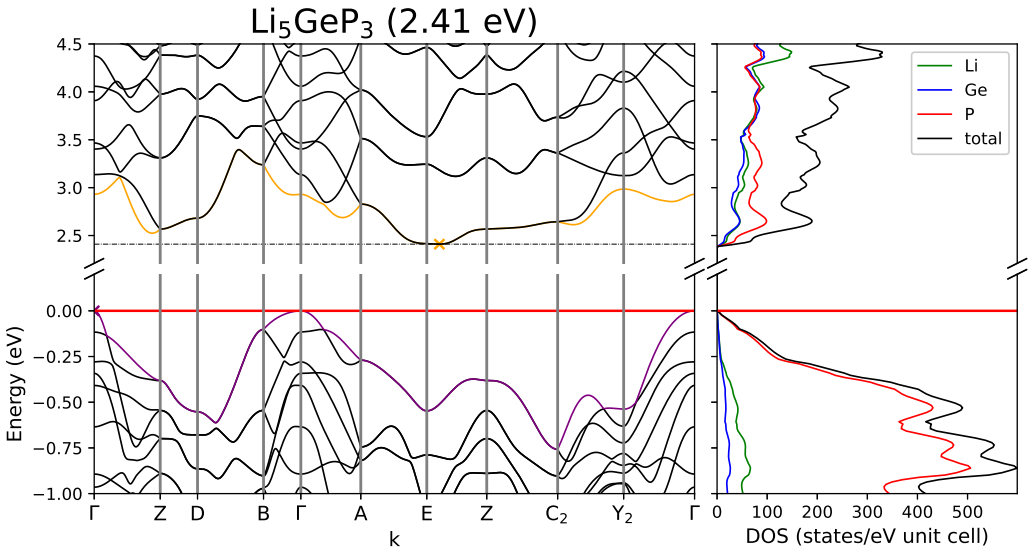

Figure A.3: Band structure and DOS of Li_5GeP_3.

Table A.5: Overlap population and interatomic distances of Li_5GeP_3.

Atom A	Atom B	r_{AB} / Å	overlap
Li1	P3	2.541	0.085
	P1	2.729	0.057
	P2	2.757	0.06
	P2	2.811	0.051
	Li4	2.843	0.008
	Li2	2.944	0.008
Li2	P2	2.492	0.094
	P1	2.515	0.075
	P3	2.534	0.088
	P3	2.58	0.071
	Li3	2.729	0.01
	Ge1	2.859	0.018
Li3	P1	2.649	0.066
	P3	2.679	0.066
	P3	2.697	0.071
	P2	2.755	0.058
	Li4	2.894	0.008
Li4	P2	2.527	0.087
	P1	2.552	0.08
	P3	2.563	0.088
	P2	2.578	0.084
Li5	P2	2.654	0.083
	P3	2.708	0.061
	P1	2.879	0.039
	P3	2.952	0.041
	P2	2.958	0.044
Ge1	P2	2.305	0.285
	P3	2.306	0.28
	P1	2.356	0.251
	P1	2.39	0.224

Table A.6: Partial charges for each atom position in Li_5GeP_3.

Atom	Z	charge	part charge
Li1	3	2.435	0.565
Li2		2.527	0.473
Li3		2.441	0.559
Li4		2.514	0.486
Li5		2.429	0.571
Ge1	32	32.208	−0.208
P1	15	15.608	−0.608
P2		15.924	−0.924
P3		15.915	−0.915

Li_5SnP_3[78]

For Li_5SnP_3 an ordered a model based on Na_5SiP_3 was calculated as well.

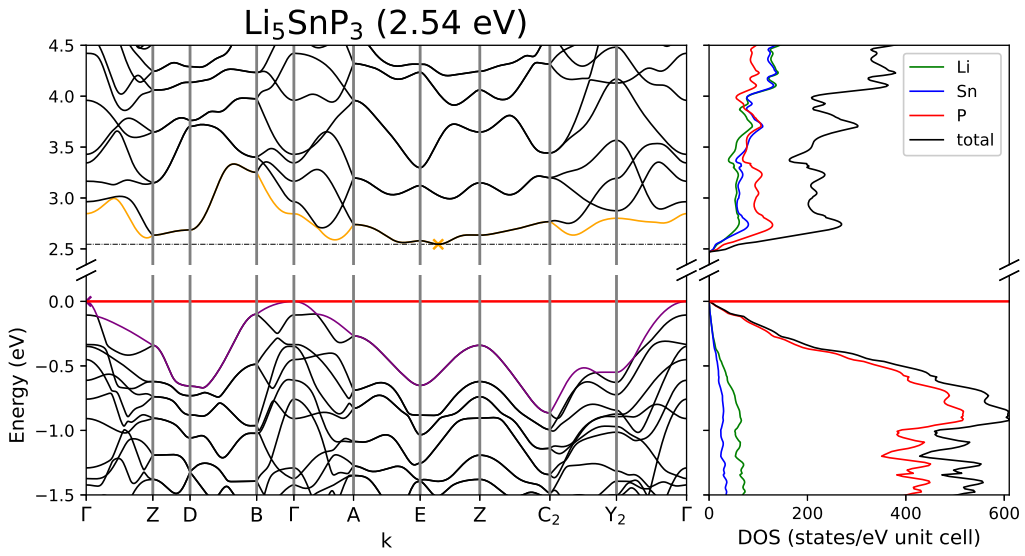

Figure A.4: Band structure and DOS of Li_5SnP_3.

Table A.7: Overlap population and interatomic distances of Li_5SnP_3.

Atom A	Atom B	r_{AB} / Å	overlap
Li1	P3	2.542	0.088
	P1	2.672	0.063
	P2	2.711	0.067
	Li2	2.908	0.008
	Li5	2.931	0.009
	Li4	3.05	0.005
Li2	P2	2.507	0.093
	P3	2.541	0.086
	P1	2.557	0.074
	P3	2.652	0.068
	Li3	2.725	0.009
	Li4	2.881	0.008
Li3	P3	2.642	0.07
	P1	2.692	0.065
	P3	2.731	0.068
	P2	2.862	0.052

Atom A	Atom B	r_{AB} / Å	overlap
Li4	P2	2.554	0.079
	P2	2.563	0.086
	P1	2.573	0.079
	P3	2.59	0.083
Li5	P2	2.604	0.09
	P3	2.657	0.067
	P2	2.93	0.049
Sn1	P2	2.467	0.276
	P3	2.468	0.271
	P1	2.527	0.24
	P1	2.581	0.219

Table A.8: Partial charges for each atom position in Li_5SnP_3.

Atom	Z	charge	part charge
Li1	3	2.429	0.571
Li2		2.51	0.49
Li3		2.429	0.571
Li4		2.491	0.509
Li5		2.424	0.576

Atom	Z	charge	partialcharge
Sn1	22	21.959	0.041
P1	15	15.747	−0.747
P2		16.007	−1.007
P3		16.006	−1.006

Na_5SiP_3[79]

For a crystal structure description see Li_5SiP_3.

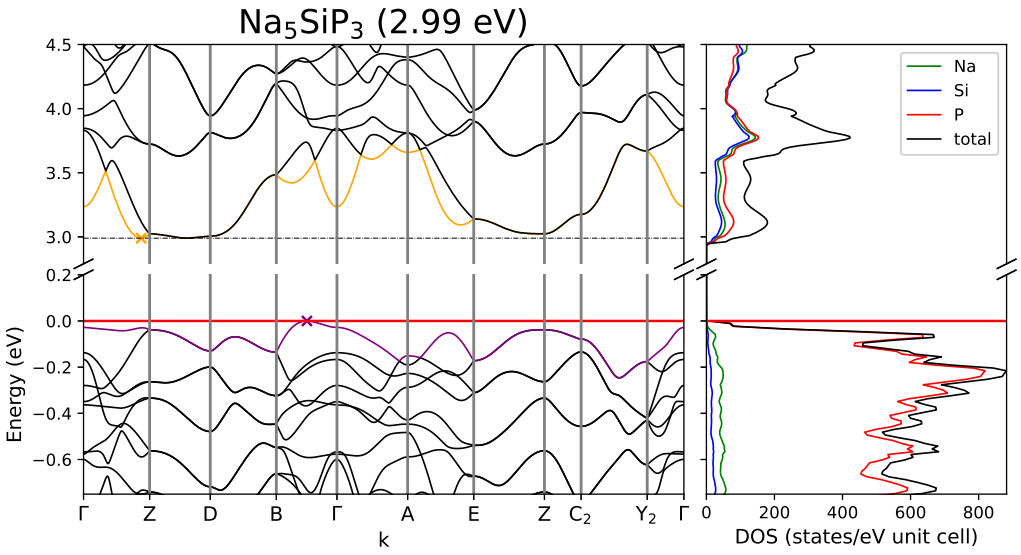

Figure A.5: Band structure and DOS of Na_5SiP_3.

Table A.9: Overlap population and interatomic distances of Na_5SiP_3.

Atom A	Atom B	r_{AB} / Å	overlap
Na1	P3	2.815	0.047
	P2	2.968	0.04
	P2	3.011	0.041
	Na5	3.049	0.006
	Si1	3.138	0.0
	Na4	3.259	0.004
Na2	P2	2.954	0.042
	P1	3.013	0.022
	P3	3.038	0.039
	P2	3.127	0.047
	Na4	3.19	0.006
	Na4	3.199	0.003
Na3	P1	2.884	0.039
	P3	2.894	0.051
	P2	2.935	0.047
	Na4	3.163	0.006
	P1	3.236	0.02
	Na5	3.242	0.005

Atom A	Atom B	r_{AB} / Å	overlap
Na4	P3	2.818	0.042
	P1	2.822	0.041
	P3	2.837	0.053
	P2	2.859	0.055
Na5	P3	2.858	0.059
	P2	2.861	0.057
	P1	2.867	0.046
	P2	2.995	0.051
Si1	P3	2.266	0.331
	P2	2.28	0.324
	P1	2.321	0.281
	P1	2.343	0.265
	Si1	3.183	−0.054

Table A.10: Partial charges for each atom position in Na_5SiP_3.

Atom	Z	charge	part charge
Na1	11	10.291	0.709
Na2		10.296	0.704
Na3		10.299	0.701
Na4		10.318	0.682
Na5		10.345	0.655

Atom	Z	charge	partialcharge
Si1	14	13.959	0.041
P1	15	15.927	−0.927
P2		16.279	−1.279
P3		16.286	−1.286

Na_5GeP_3[79]

For a crystal structure description see Li_5SiP_3.

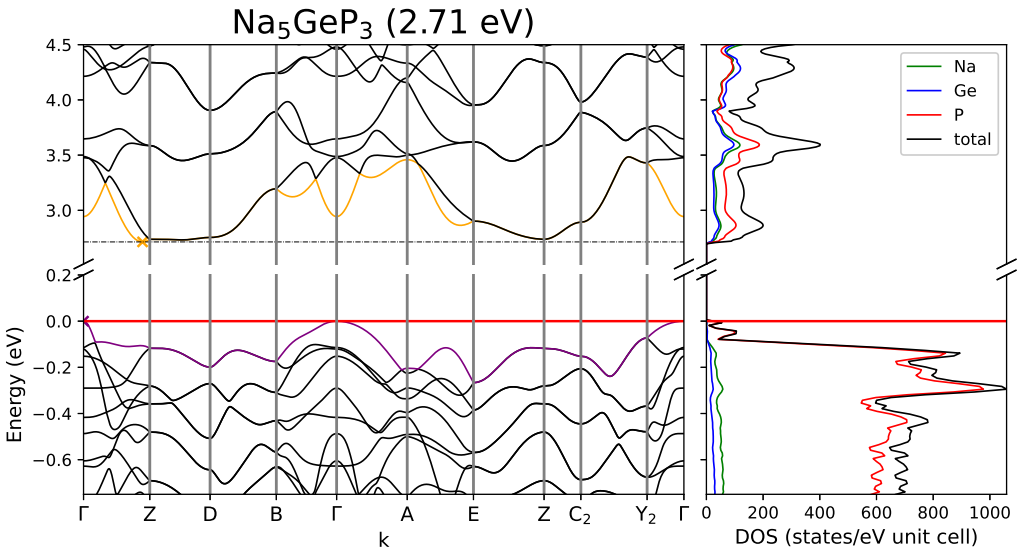

Figure A.6: Band structure and DOS of Na_5GeP_3.

Table A.11: Partial charges for each atom position in Na_5GeP_3.

Atom	Z	charge	part charge
Na1	11	10.292	0.708
Na2		10.298	0.702
Na3		10.302	0.698
Na4		10.323	0.677
Na5		10.351	0.649

Atom	Z	charge	partialcharge
Ge1	32	32.127	−0.127
P1	15	15.838	−0.838
P2		16.234	−1.234
P3		16.235	−1.235

Table A.12: Overlap population and interatomic distances of Na_5GeP_3.

Atom A	Atom B	r_{AB} / Å	overlap
Na1	P3	2.828	0.049
	P2	2.998	0.041
	P2	3.033	0.041
	Na5	3.081	0.006
	Ge1	3.181	0.001
	Na4	3.273	0.006
Na2	P2	3.007	0.041
	P1	3.048	0.025
	P3	3.092	0.039
	P2	3.127	0.048
	P3	3.221	0.032
	Na4	3.227	0.006
Na3	P1	2.904	0.041
	P3	2.921	0.052
	P2	2.966	0.046
	Na4	3.156	0.006
	P1	3.273	0.02
	Na5	3.279	0.005
Na4	P1	2.827	0.043
	P3	2.833	0.042
	P3	2.836	0.053
	P2	2.848	0.055
Na5	P2	2.857	0.056
	P3	2.858	0.061
	P1	2.869	0.049
	P2	2.979	0.052
Ge1	P3	2.336	0.308
	P2	2.348	0.304
	P1	2.391	0.263
	P1	2.417	0.245
	Ge1	3.271	−0.041

Na_5SnP_3[81]

For a crystal structure description see Li_5SiP_3.

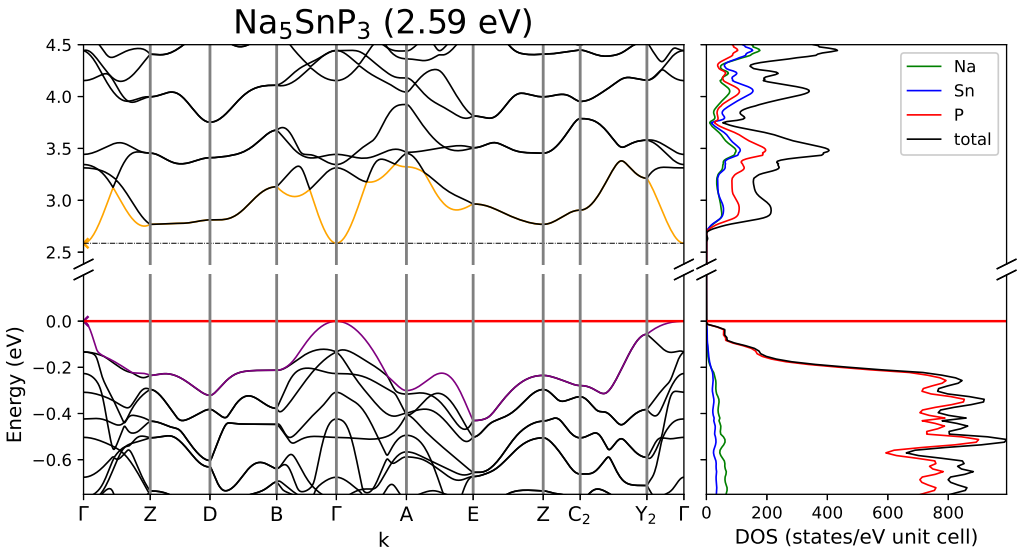

Figure A.7: Band structure and DOS of Na_5SnP_3.

Table A.13: Partial charges for each atom position in Na_5SnP_3.

Atom	Z	charge	part charge
Na1	11	10.312	0.688
Na2		10.339	0.661
Na3		10.294	0.706
Na4		10.287	0.713
Na5		10.28	0.72

Atom	Z	charge	partialcharge
Sn1	22	21.974	0.026
P1	15	16.277	−1.277
P2		16.284	−1.284
P3		15.952	−0.952

Table A.14: Overlap population and interatomic distances of Na_5SnP_3.

Atom A	Atom B	r_{AB} / Å	overlap
Na1	P1	2.827	0.053
	P3	2.838	0.041
	P2	2.839	0.054
	P1	2.877	0.04
	Na4	3.138	0.006
	Na3	3.27	0.005
Na2	P1	2.865	0.06
	P2	2.865	0.052
	P3	2.875	0.048
	P2	2.942	0.053
	Na5	3.164	0.005
	Na3	3.303	0.005
Na3	P2	3.066	0.051
	P2	3.114	0.038
	P1	3.121	0.038
	P3	3.195	0.023
	P1	3.228	0.034
Na4	P3	2.958	0.038
	P1	2.985	0.048
	P2	3.059	0.04
	P1	3.277	0.033
Na5	P1	2.858	0.047
	P2	3.08	0.04
	P2	3.106	0.036
	P3	3.184	0.032
Sn1	P1	2.499	0.3
	P2	2.503	0.3
	P3	2.562	0.247
	P3	2.596	0.227

K_5SnP_3 [69]

For a crystal structure description see Li_5SiP_3.

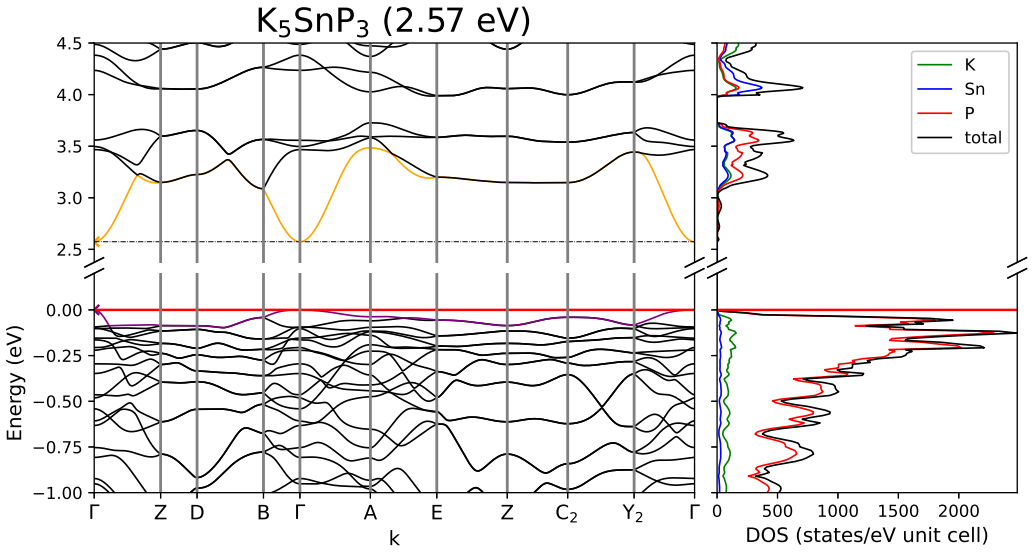

Figure A.8: Band structure and DOS of K_5SnP_3.

Table A.15: Overlap population and interatomic distances of K_5SnP_3.

Atom A	Atom B	r_{AB} / Å	overlap
K1	P2	3.186	0.02
	P1	3.216	0.017
	P2	3.249	0.025
	P3	3.279	0.031
	K3	3.583	−0.001
	K3	3.604	0.001
K2	P3	3.252	0.035
	P2	3.262	0.034
	P1	3.277	0.022
	P3	3.428	0.035
	K4	3.475	0.001
	K5	3.629	0.001
K3	P3	3.296	0.022
	P1	3.421	0.009
	P2	3.428	0.024
	Sn1	3.585	−0.008
K4	P2	3.217	0.025
	P3	3.345	0.023
	P3	3.421	0.024
	Sn1	3.518	−0.006
K5	P1	3.246	0.019
	P2	3.327	0.03
	P3	3.378	0.03
	P1	3.552	0.016
Sn1	P2	2.543	0.325
	P3	2.55	0.325
	P1	2.614	0.258
	P1	2.631	0.257

Table A.16: Partial charges for each atom position in K_5SnP_3.

Atom	Z	charge	part charge
K1	19	18.283	0.717
K2		18.314	0.686
K3		18.271	0.729
K4		18.275	0.725
K5		18.276	0.724
Sn1	22	21.903	0.097
P1	15	16.026	−1.026
P2		16.334	−1.334
P3		16.317	−1.317

Li_5SiAs_3[77]

For Li_5SiAs_3 an ordered a model based on Na_5SiP_3 was calculated as well.

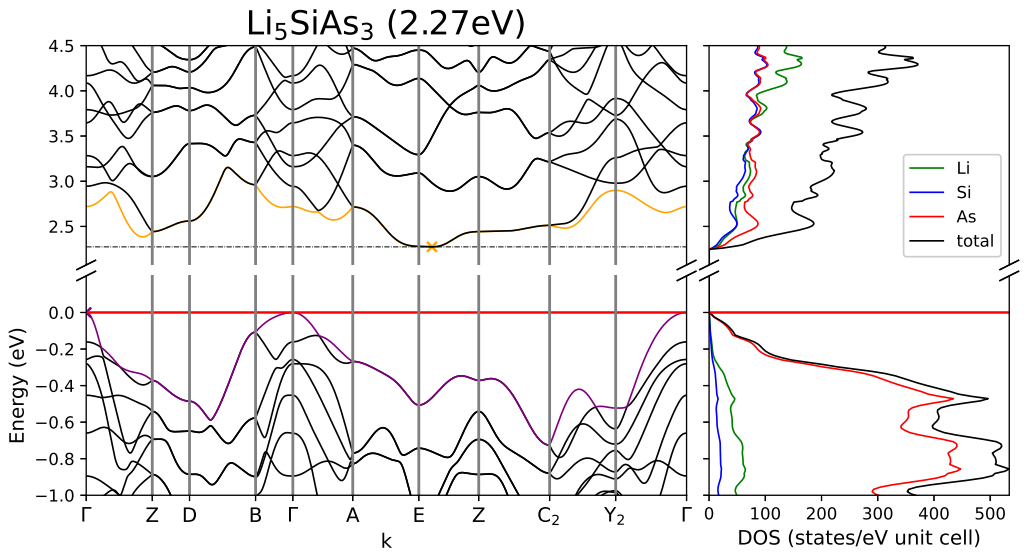

Figure A.9: Band structure and DOS of Li_5SiAs_3.

Table A.17: Partial charges for each atom position in Li_5SiAs_3.

Atom	Z	charge	part charge
Si1	14	13.737	0.263
As1	33	33.831	−0.831
As2		34.038	−1.038
As3		34.036	−1.036
Li1	3	2.438	0.562

Atom	Z	charge	partialcharge
Li2		2.432	0.568
Li3		2.442	0.558
Li4		2.525	0.475
Li5		2.522	0.478

Table A.18: Overlap population and interatomic distances of Li_5SiAs_3.

Atom A	Atom B	r_{AB} / Å	overlap
Si1	As3	2.337	0.315
	As2	2.341	0.312
	As1	2.389	0.271
	As1	2.42	0.246
	Li4	2.903	0.017
	Li1	3.08	0.006
As1	Li4	2.585	0.074
	Li5	2.616	0.08
	Li3	2.72	0.064
	Li1	2.814	0.053
As2	Li4	2.568	0.093
	Li5	2.593	0.089
	Li5	2.665	0.085
	Li2	2.746	0.081
	Li3	2.801	0.063
As3	Li4	2.605	0.087
	Li1	2.611	0.085
	Li5	2.629	0.092
	Li4	2.635	0.074
	Li3	2.754	0.073
Li1	Li5	2.901	0.008
	Li4	3.021	0.008
Li2	Li5	2.989	0.007
Li3	Li4	2.82	0.01
	Li5	2.949	0.008

Li_5GeAs_3[77]

For Li_5GeAs_3 an ordered a model based on Na_5SiP_3 was calculated as well.

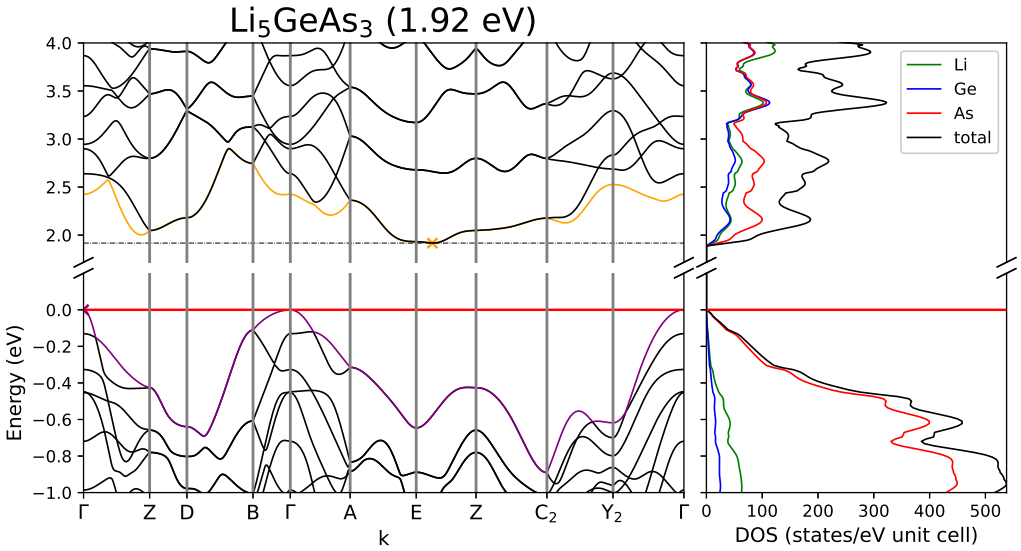

Figure A.10: Band structure and DOS Li_5GeAs_3.

Table A.19: Overlap population and interatomic distances of Li_5GeAs_3.

Atom A	Atom B	r_{AB} / Å	overlap
Ge1	As2	2.402	0.282
	As3	2.405	0.284
	As1	2.456	0.253
	As1	2.491	0.227
	Li4	2.898	0.019
	Li1	3.111	0.008
As1	Li4	2.603	0.074
	Li5	2.623	0.08
	Li3	2.755	0.064
	Li1	2.794	0.057
As2	Li4	2.564	0.094
	Li5	2.598	0.087
	Li5	2.655	0.085
	Li2	2.727	0.085
	Li1	2.827	0.063
As3	Li4	2.606	0.088
	Li1	2.623	0.086
	Li5	2.63	0.093
	Li4	2.667	0.071
	Li3	2.751	0.067
Li1	Li5	2.956	0.007
	Li4	3.032	0.008
Li2	Li5	2.987	0.007
	Li4	3.081	0.007
Li3	Li4	2.827	0.01
	Li5	2.959	0.008

Table A.20: Partial charges for each atom position in Li_5GeAs_3.

Atom	Z	charge	part charge
Ge1	32	31.925	0.075
As1	33	33.739	−0.739
As2		33.986	−0.986
As3		33.986	−0.986
Li1	3	2.44	0.56
Li2		2.435	0.565
Li3		2.442	0.558
Li4		2.525	0.475
Li5		2.522	0.478

Na_5SiAs_3[85]

For a crystal structure description see Li_5SiP_3.

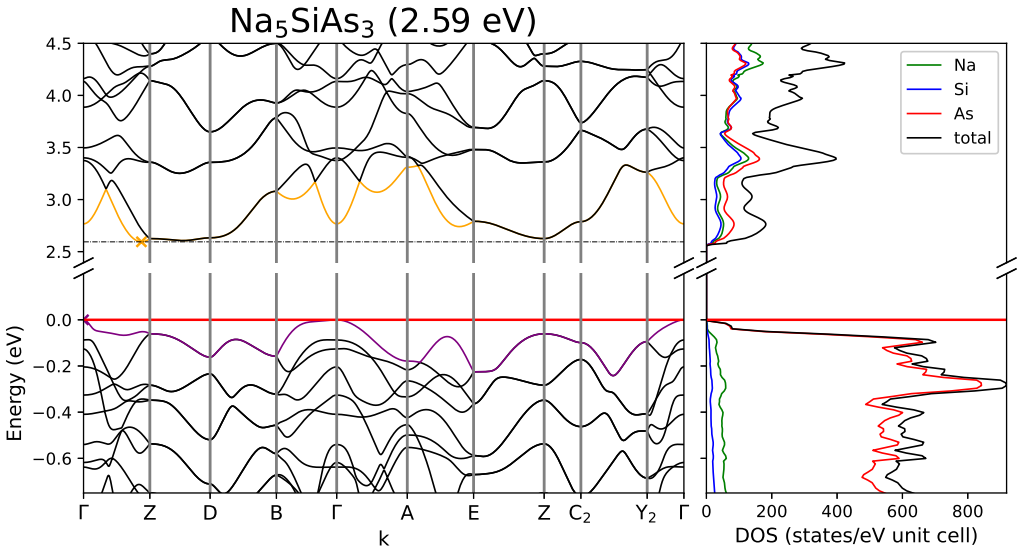

Figure A.11: Band structure and DOS of Na_5SiAs_3.

Table A.21: Overlap population and interatomic distances of Na_5SiAs_3.

Atom A	Atom B	r_{AB} / Å	overlap
Si1	As1	2.369	0.338
	As2	2.381	0.327
	As3	2.422	0.283
	As3	2.445	0.264
	Na5	3.229	0.003
	Si1	3.309	−0.046
As1	Na1	2.896	0.047
	Na5	2.9	0.053
	Na1	2.902	0.058
	Na2	2.921	0.065
	Na4	2.976	0.056
As2	Na1	2.909	0.059
	Na2	2.916	0.06
	Na4	3.023	0.05
	Na2	3.048	0.056
	Na5	3.051	0.045

Atom A	Atom B	r_{AB} / Å	overlap
As3	Na1	2.893	0.045
	Na2	2.928	0.052
	Na4	2.967	0.041
	Na3	3.087	0.025
Na1	Na4	3.222	0.006
	Na3	3.281	0.006
Na2	Na5	3.13	0.007
	Na3	3.296	0.006

Table A.22: Partial charges for each atom position in Na_5SiAs_3.

Atom	Z	charge	part charge
Si1	14	13.735	0.265
As1	33	34.286	−1.286
As2		34.286	−1.286
As3		34.005	−1.005
Na1	11	10.347	0.653

Atom	Z	charge	partialcharge
Na2		10.376	0.624
Na3		10.324	0.676
Na4		10.323	0.677
Na5		10.319	0.681

Na_5GeAs_3[80]

For a crystal structure description see Li_5SiP_3.

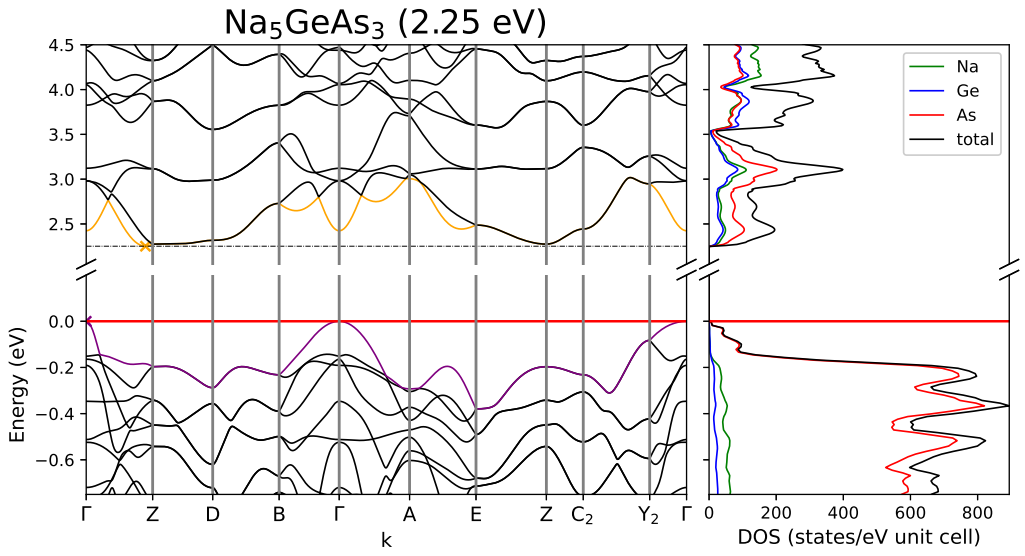

Figure A.12: Band structure and DOS of Na_5GeAs_3.

Table A.23: Partial charges for each atom position in Na_5GeAs_3.

Atom	Z	charge	part charge
Ge1	32	31.902	0.098
As1	33	34.236	−1.236
As2		34.245	−1.245
As3		33.918	−0.918
Na1	11	10.349	0.651

Atom	Z	charge	partialcharge
Na2		10.378	0.622
Na3		10.326	0.674
Na4		10.326	0.674
Na5		10.321	0.679

Table A.24: Overlap population and interatomic distances of Na_5GeAs_3.

Atom A	Atom B	r_{AB} / Å	overlap
Ge1	As1	2.434	0.314
	As2	2.446	0.302
	As3	2.489	0.265
	As3	2.512	0.246
	Na5	3.272	0.004
	Na1	3.344	0.003
As1	Na1	2.899	0.057
	Na5	2.91	0.054
	Na1	2.91	0.048
	Na2	2.923	0.067
	Na4	3.002	0.055
As2	Na1	2.9	0.059
	Na2	2.917	0.059
	Na2	3.033	0.057
	Na4	3.05	0.049
	Na5	3.08	0.045
As3	Na1	2.897	0.046
	Na2	2.931	0.053
	Na4	2.99	0.043
	Na3	3.116	0.028
Na1	Na4	3.214	0.007
	Na3	3.317	0.006
Na2	Na5	3.167	0.007
	Na3	3.332	0.006

Na_5SnAs_3[86]

For a crystal structure description see Li_5SiP_3.

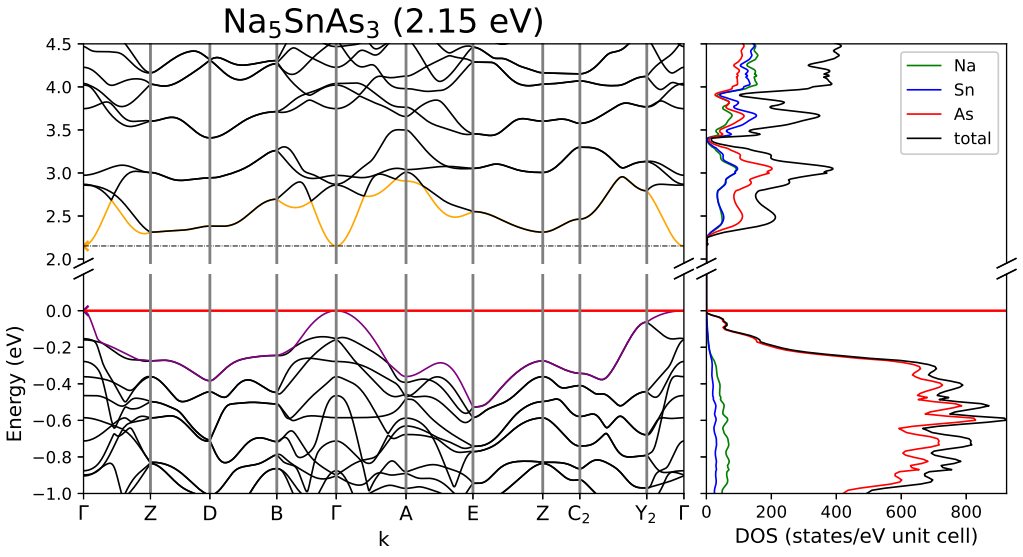

Figure A.13: Bandstructure and DOS of Na_5SnAs_3.

Table A.25: Overlap population and interatomic distances of Na_5SnAs_3.

Atom A	Atom B	r_{AB} / Å	overlap
Sn1	As1	2.593	0.298
	As2	2.596	0.293
	As3	2.652	0.248
	As3	2.688	0.23
	Na1	3.35	0.006
	Na5	3.387	0.008
As1	Na1	2.888	0.057
	Na2	2.924	0.066
	Na5	2.939	0.051
	Na1	2.954	0.045
	Na4	3.05	0.052
As2	Na1	2.897	0.058
	Na2	2.929	0.056
	Na2	2.997	0.058
	Na5	3.134	0.044
	Na4	3.135	0.043

Atom A	Atom B	r_{AB} / Å	overlap
As3	Na1	2.909	0.044
	Na2	2.938	0.052
	Na4	3.053	0.039
	Na3	3.235	0.027
Na1	Na4	3.22	0.006
Na2	Na5	3.267	0.005

Table A.26: Partial charges for each atom position in Na_5SnAs_3.

Atom	Z	charge	part charge
Sn1	22	21.831	0.169
As1	33	34.27	−1.27
As2		34.28	−1.28
As3		33.976	−0.976
Na1	11	10.338	0.662

Atom	Z	charge	partialcharge
Na2		10.368	0.632
Na3		10.32	0.68
Na4		10.311	0.689
Na5		10.306	0.694

K_5SnAs_3[87]

For a crystal structure description see Li_5SiP_3.

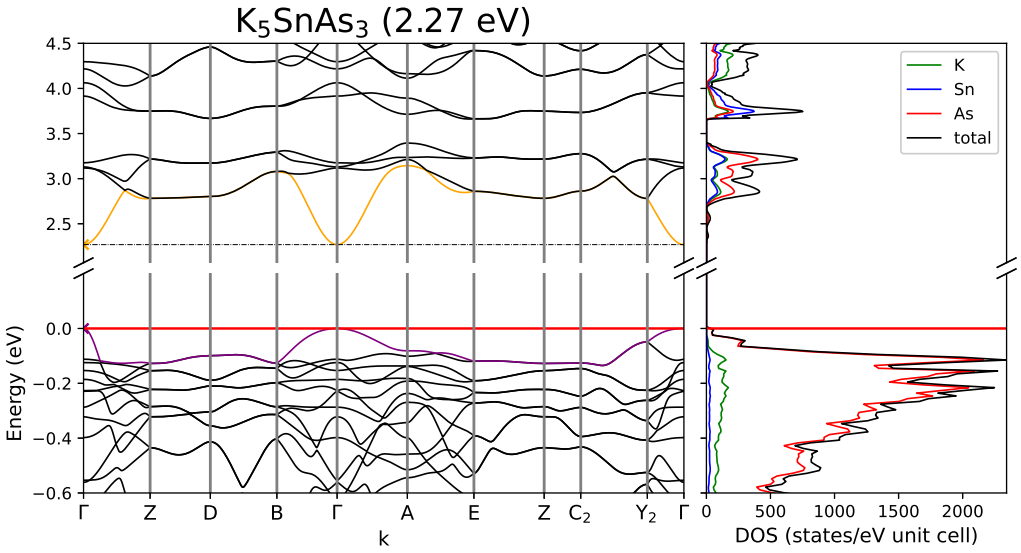

Figure A.14: Band structure and DOS of K_5SnAs_3.

Table A.27: Overlap population and interatomic distances of K_5SnAs_3.

Atom A	Atom B	r_{AB} / Å	overlap
K1	As1	3.252	0.027
	As3	3.279	0.022
	As1	3.311	0.031
	As2	3.325	0.036
	K3	3.666	0.0
	K3	3.697	0.002
K2	As2	3.308	0.04
	As1	3.327	0.041
	As3	3.34	0.029
	As2	3.479	0.04
	K5	3.553	0.002
	K4	3.717	0.003
K3	As2	3.383	0.028
	As3	3.486	0.013
	As1	3.517	0.029
	Sn1	3.676	−0.004
K4	As3	3.326	0.024
	As1	3.4	0.036
	As2	3.464	0.035
	As3	3.644	0.017
K5	As1	3.31	0.033
	As2	3.429	0.029
	As2	3.467	0.029
	Sn1	3.592	−0.002
Sn1	As1	2.637	0.325
	As2	2.642	0.323
	As3	2.703	0.252
	As3	2.72	0.252

Table A.28: Partial charges for each atom position in K_5SnAs_3.

Atom	Z	charge	part charge
K1	19	18.312	0.688
K2		18.343	0.657
K3		18.297	0.703
K4		18.299	0.701
K5		18.301	0.699

Atom	Z	charge	partialcharge
Sn1	22	21.772	0.228
As1	33	34.31	−1.31
As2		34.303	−1.303
As3		34.063	−1.063

K_5SnBi_3[148]

For a crystal structure description see Li_5SiP_3.

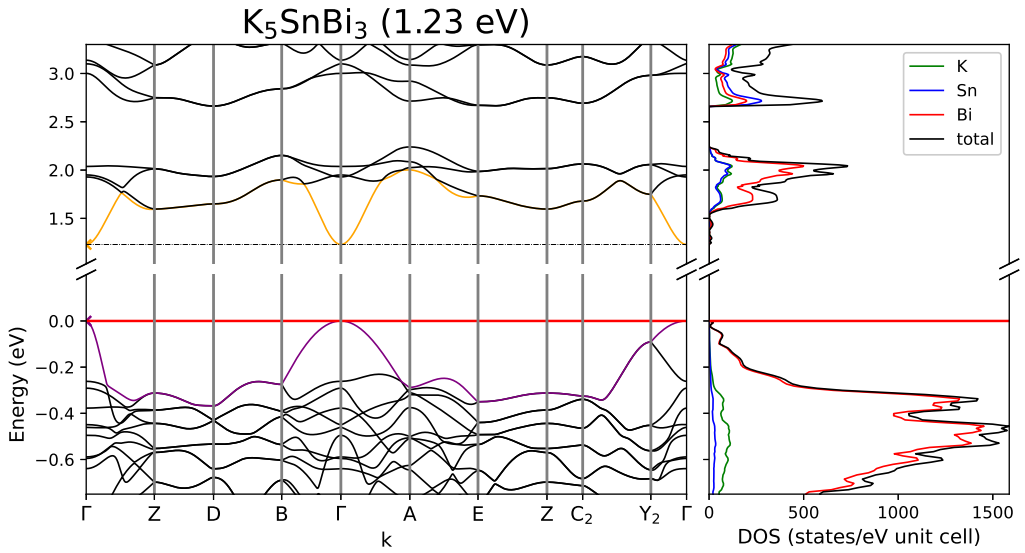

Figure A.15: Band structure and DOS of K_5SnBi_3.

Table A.29: Overlap population and interatomic distances of K_5SnBi_3.

Atom A	Atom B	r_{AB} / Å	overlap
K1	Bi2	3.51	0.031
	Bi3	3.529	0.033
	Bi1	3.57	0.024
	Bi2	3.721	0.033
	K3	3.782	0.002
	K5	3.952	0.002
K2	Bi1	3.551	0.017
	Bi3	3.608	0.027
	Bi2	3.705	0.03
	Bi1	3.763	0.015
	K4	3.979	0.002
K3	Bi3	3.558	0.025
	Bi2	3.682	0.026
	Bi2	3.71	0.025
	Sn1	3.817	0.001
	K4	3.97	0.002
K4	Bi1	3.519	0.019
	Bi3	3.523	0.028
	Bi2	3.529	0.029
	Bi3	3.542	0.025
	K5	3.888	0.001
K5	Bi2	3.641	0.023
	Bi1	3.695	0.011
	Bi3	3.779	0.025
	Sn1	3.868	−0.001
	Sn1	3.923	0.0
Sn1	Bi3	2.916	0.301
	Bi2	2.92	0.297
	Bi1	2.983	0.243
	Bi1	2.987	0.241

Table A.30: Partial charges for each atom position in K_5SnBi_3.

Atom	Z	charge	part charge
K1	19	18.301	0.699
K2		18.259	0.741
K3		18.264	0.736
K4		18.283	0.717
K5		18.255	0.745
Sn1	22	22.017	−0.017
Bi1	23	23.973	−0.973
Bi2		24.324	−1.324
Bi3		24.323	−1.323

Rb_5GeP_3[82]

Rb_5GeP_3 crystallizes in the orthorhombic space group P n m a (no. 62) in the Cs_5SiP_3 structure type. It contains triangular planar $[TtP_3]^{5-}$ units and isolated A^+ cations which are analogue to CO_3^{2-} in structure as well as bonding situation.

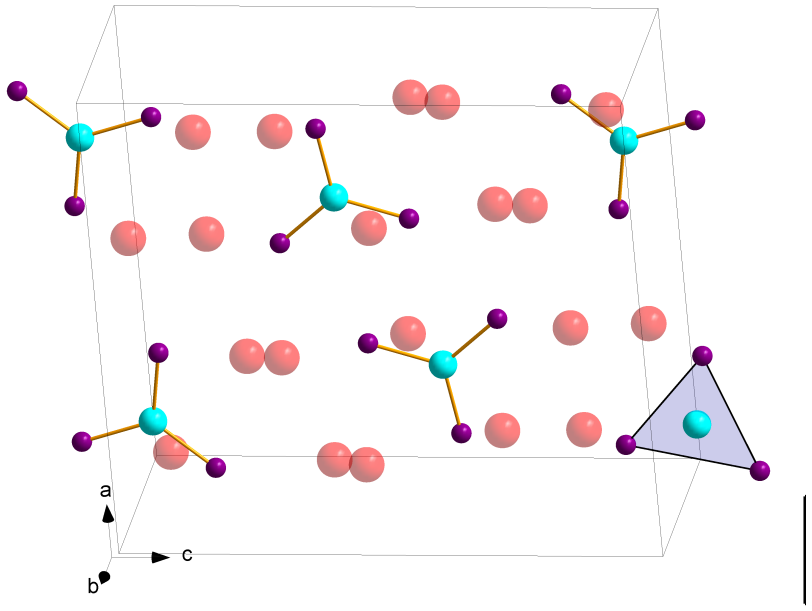

Figure A.16: Crystal structure of the Cs_5SiP_3 structure type containing CO_3^{2-} analogue $[TtP_3]^{5-}$ monomer units.

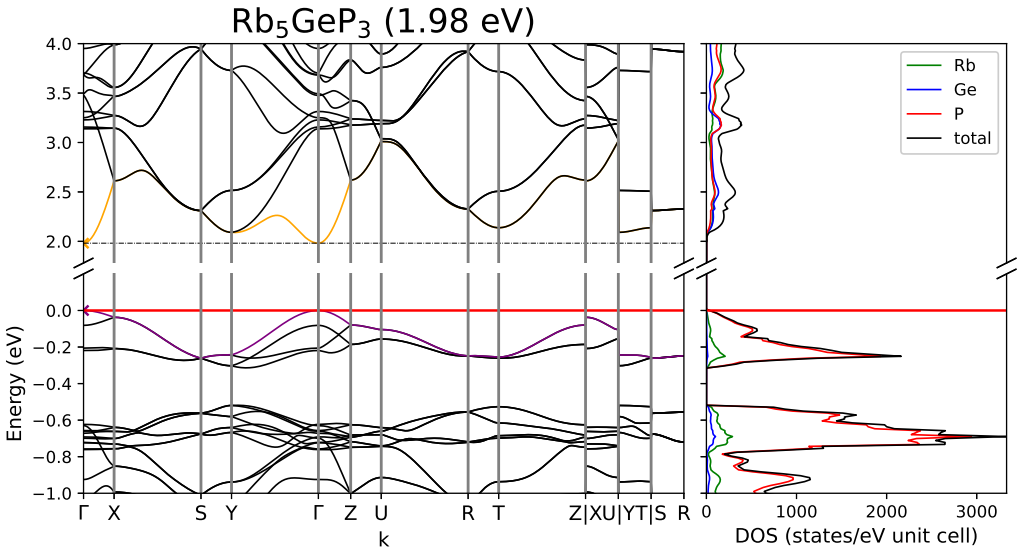

Figure A.17: Band structure and DOS of Rb_5GeP_3.

Table A.31: Overlap population and interatomic distances of Rb_5GeP_3.

Atom A	Atom B	r_{AB} / Å	overlap
Rb1	P2	3.442	0.035
	P2	3.563	0.02
	P3	3.587	0.022
	Ge1	3.619	−0.002
	Rb2	3.81	−0.002
	Rb2	3.898	−0.001
Rb2	P1	3.432	0.039
	P3	3.465	0.039
	P2	3.523	0.025
	Rb4	3.778	−0.003
Rb3	P3	3.506	0.034
	P2	3.605	0.022
	P1	3.619	0.022
	Ge1	3.678	0.0
	Rb5	3.985	0.0

Atom A	Atom B	r_{AB} / Å	overlap
Rb4	P2	3.409	0.032
	P3	3.442	0.02
	Ge1	3.576	−0.004
	P1	3.756	0.02
Rb5	P1	3.623	0.045
	P1	3.697	0.033
	P3	4.011	0.021
Ge1	P2	2.269	0.377
	P3	2.289	0.376
	P1	2.29	0.36

Table A.32: Partial charges for each atom position in Rb_5GeP_3.

Atom	Z	charge	part charge
Rb1	9	8.344	0.656
Rb2		8.345	0.655
Rb3		8.329	0.671
Rb4		8.335	0.665
Rb5		8.325	0.675

Atom	Z	charge	partialcharge
Ge1	32	32.181	−0.181
P1	15	16.04	−1.04
P2		16.059	−1.059
P3		16.042	−1.042

Cs_5SiP_3[83]

For a crystal structure description see Rb_5GeP_3.

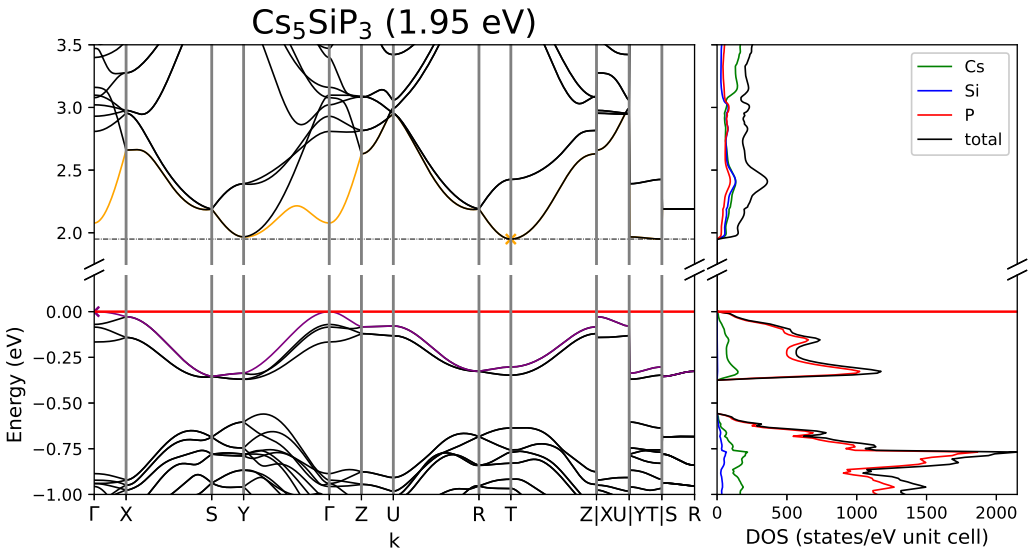

Figure A.18: Band structure and DOS of Cs_5SiP_3.

Table A.33: Partial charges for each atom position in Cs_5SiP_3.

Atom	Z	charge	part charge
Cs1	9	8.334	0.666
Cs2		8.325	0.675
Cs3		8.313	0.687
Cs4		8.326	0.674
Cs5		8.306	0.694

Atom	Z	charge	partialcharge
Si1	14	14.028	−0.028
P1	15	16.128	−1.128
P2		16.124	−1.124
P3		16.116	−1.116

Table A.34: Overlap population and interatomic distances of Cs_5SiP_3.

Atom A	Atom B	r_{AB} / Å	overlap
Cs1	P2	3.629	0.031
	P2	3.702	0.018
	P3	3.706	0.021
	Si1	3.77	−0.001
	Cs2	3.884	0.006
	Cs4	4.0	0.003
Cs2	P1	3.567	0.034
	P3	3.623	0.036
	P2	3.736	0.022
	Cs4	3.829	0.006
	Cs3	3.978	0.005
Cs3	P2	3.69	0.022
	P3	3.712	0.03
	P1	3.763	0.018
	Si1	3.835	0.0
	Cs5	3.953	0.007
Cs4	P3	3.525	0.016
	P2	3.557	0.028
	Si1	3.723	−0.004
	P1	3.865	0.017
Cs5	P1	3.678	0.043
	P1	3.77	0.032
	P3	4.324	0.015
Si1	P2	2.204	0.4
	P3	2.215	0.41
	P1	2.222	0.391
P1	P2	3.808	−0.061

Cs_5GeP_3[83]

For a crystal structure description see Rb_5GeP_3.

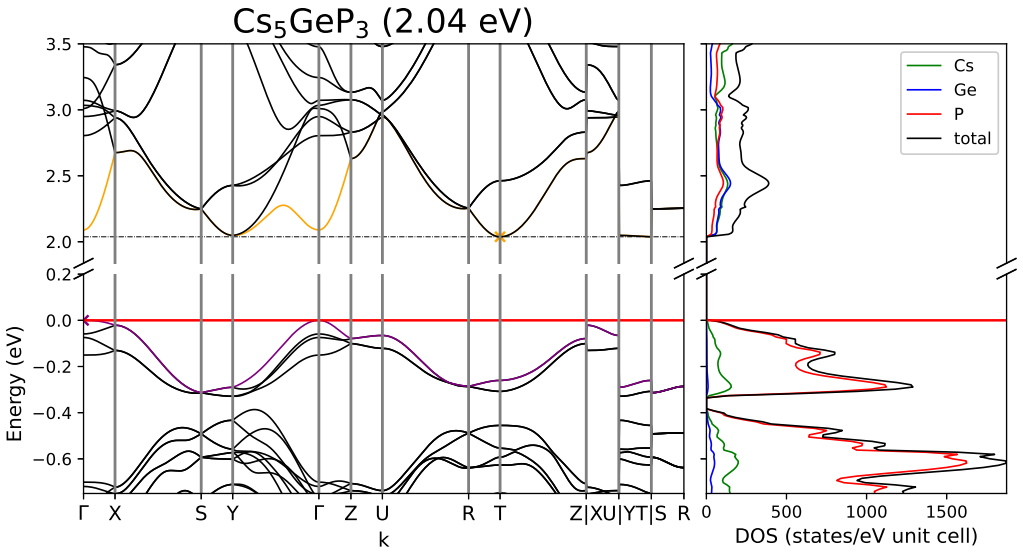

Figure A.19: Band structure and DOS of Cs_5GeP_3.

Table A.35: Overlap population and interatomic distances of Cs_5GeP_3.

Atom A	Atom B	r_{AB} / Å	overlap
Cs1	P2	3.616	0.031
	P3	3.719	0.022
	P2	3.736	0.019
	Ge1	3.799	−0.001
	Cs2	3.933	0.006
	Cs4	4.036	0.004
Cs2	P1	3.579	0.036
	P3	3.617	0.036
	P2	3.716	0.023
	Cs4	3.873	0.006
	Cs3	4.008	0.005
Cs3	P2	3.701	0.023
	P3	3.706	0.031
	P1	3.797	0.019
	Ge1	3.842	0.0
	Cs5	4.013	0.006
Cs4	P3	3.529	0.017
	P2	3.544	0.029
	Ge1	3.734	−0.004
	P1	3.917	0.017
Cs5	P1	3.698	0.044
	P1	3.747	0.034
	P3	4.333	0.015
Ge1	P2	2.274	0.374
	P3	2.288	0.38
	P1	2.292	0.364

Table A.36: Partial charges for each atom position in Cs_5GeP_3.

Atom	Z	charge	part charge
Cs1	9	8.334	0.666
Cs2		8.33	0.67
Cs3		8.315	0.685
Cs4		8.326	0.674
Cs5		8.31	0.69
Ge1	32	32.16	−0.16
P1	15	16.077	−1.077
P2		16.082	−1.082
P3		16.068	−1.068

Rb_5SiAs_3[88]

For a crystal structure description see Rb_5GeP_3.

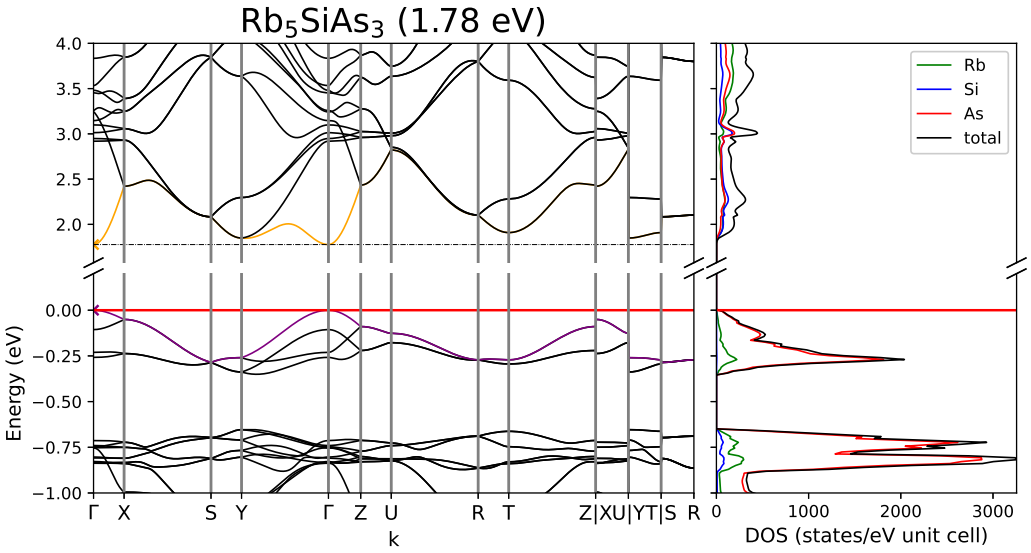

Figure A.20: Band structure and DOS of Rb_5SiAs_3.

Table A.37: Overlap population and interatomic distances of Rb_5SiAs_3.

Atom A	Atom B	r_{AB} / Å	overlap
Rb1	As2	3.522	0.04
	As2	3.611	0.023
	As3	3.632	0.026
	Si1	3.656	0.0
	Rb2	3.859	−0.001
	Rb4	3.947	−0.003
Rb2	As1	3.506	0.044
	As3	3.539	0.044
	As2	3.566	0.028
	Rb4	3.835	−0.002
	Rb3	3.949	0.0
Rb3	As3	3.588	0.038
	As2	3.658	0.025
	As1	3.659	0.025
	Si1	3.723	0.002
	Rb5	4.054	0.001

Atom A	Atom B	r_{AB} / Å	overlap
Rb4	As2	3.492	0.036
	As3	3.501	0.024
	Si1	3.618	−0.001
	As1	3.79	0.023
Rb5	As1	3.707	0.048
	As1	3.77	0.034
	As3	4.051	0.023
Si1	As2	2.298	0.393
	As3	2.322	0.399
	As1	2.323	0.383

Table A.38: Partial charges for each atom position in Rb_5SiAs_3.

Atom	Z	charge	part charge
Rb1	9	8.366	0.634
Rb2		8.363	0.637
Rb3		8.35	0.65
Rb4		8.357	0.643
Rb5		8.34	0.66

Atom	Z	charge	partialcharge
Si1	14	13.86	0.14
As1	33	34.115	−1.115
As2		34.132	−1.132
As3		34.117	−1.117

Cs_5SiAs_3[83]

For a crystal structure description see Rb_5GeP_3.

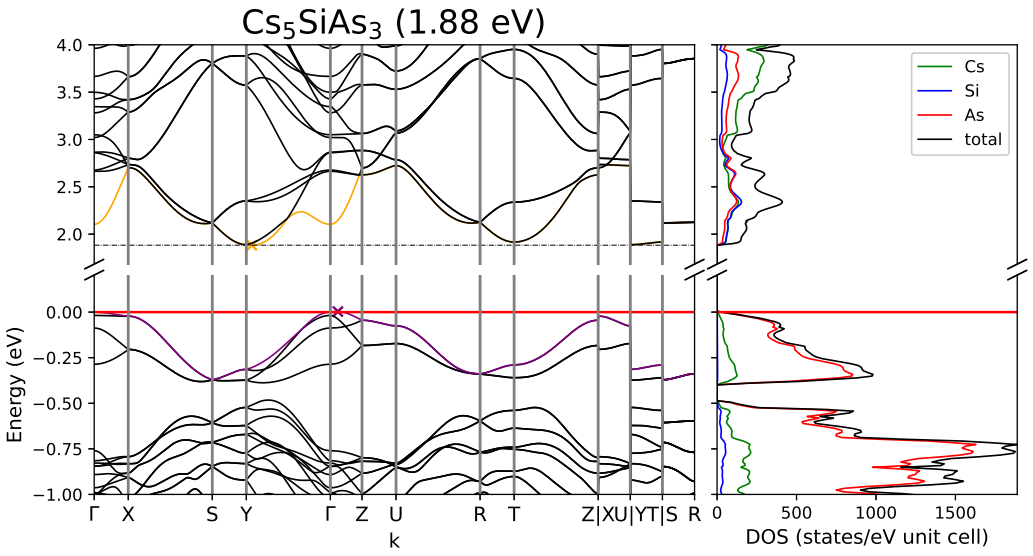

Figure A.21: Band structure and DOS of Cs_5SiAs_3.

Table A.39: Partial charges for each atom position in Cs_5SiAs_3.

Atom	Z	charge	part charge
Cs1	9	8.356	0.644
Cs2		8.355	0.645
Cs3		8.32	0.68
Cs4		8.338	0.662
Cs5		8.324	0.676

Atom	Z	charge	partialcharge
Si1	14	13.889	0.111
As1	33	34.131	−1.131
As2		34.156	−1.156
As3		34.13	−1.13

Table A.40: Overlap population and interatomic distances of Cs_5SiAs_3.

Atom A	Atom B	r_{AB} / Å	overlap
Cs1	As2	3.733	0.041
	As3	3.822	0.028
	As2	3.891	0.02
	Si1	3.896	0.003
	Cs2	3.898	0.007
	Cs4	4.016	0.004
Cs2	As1	3.609	0.035
	As3	3.71	0.041
	Cs4	3.754	0.006
	As2	3.758	0.025
	Cs3	4.095	0.006
Cs3	Cs5	3.702	0.007
	As1	3.798	0.02
	As2	3.809	0.022
	Si1	3.891	0.003
	As1	3.938	0.017
	As3	4.07	0.023
Cs4	As2	3.622	0.028
	As3	3.649	0.022
	Si1	3.772	0.001
	As1	3.929	0.02
Cs5	As1	3.831	0.034
	As1	3.857	0.029
	As3	4.141	0.021
Si1	As1	2.305	0.393
	As2	2.308	0.385
	As3	2.32	0.387

Cs_5GeAs_3[83]

For a crystal structure description see Rb_5GeP_3.

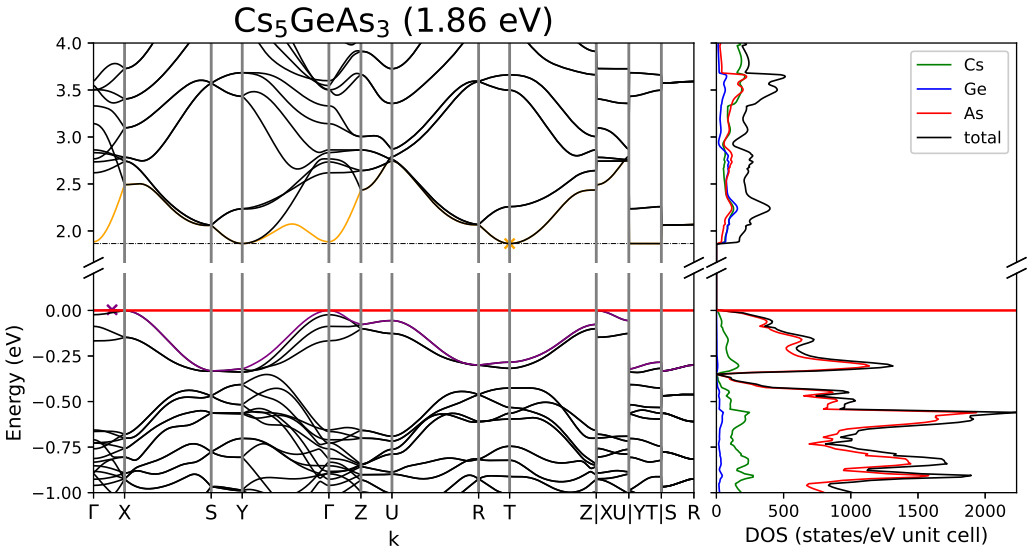

Figure A.22: Band structure and DOS of Cs_5GeAs_3.

Table A.41: Overlap population and interatomic distances of Cs_5GeAs_3.

Atom A	Atom B	r_{AB} / Å	overlap
Cs1	As2	3.683	0.037
	As2	3.77	0.023
	As3	3.787	0.025
	Ge1	3.833	0.001
	Cs2	4.004	0.006
	Cs4	4.123	0.004
Cs2	As1	3.662	0.042
	As3	3.692	0.042
	As2	3.737	0.025
	Cs4	3.945	0.006
	Cs3	4.088	0.005
Cs3	As3	3.752	0.035
	As2	3.78	0.026
	As1	3.834	0.023
	Ge1	3.886	0.002
	Cs5	4.127	0.006
Cs4	As3	3.627	0.024
	As2	3.632	0.034
	Ge1	3.77	0.0
	As1	3.955	0.02
Cs5	As1	3.807	0.047
	As1	3.86	0.035
	As3	4.27	0.019
Ge1	As2	2.367	0.361
	As3	2.388	0.37
	As1	2.389	0.357

Table A.42: Partial charges for each atom position in Cs_5GeAs_3.

Atom	Z	charge	part charge
Cs1	9	8.359	0.641
Cs2		8.35	0.65
Cs3		8.341	0.659
Cs4		8.349	0.651
Cs5		8.327	0.673
Ge1	32	32.005	−0.005
As1	33	34.087	−1.087
As2		34.1	−1.1
As3		34.081	−1.081

Na_5SnSb_3[149]

Na_5SnSb_3 crystallizes in the monoclinic space group P $2_1/n$ (no. 14) in its own structure type. Corner-sharing $SnSb_4{}^{5-}$-tetrahedra form one dimensional chains along the c-axis. Compared to the Na_5GeP_3 structure type Sb form a distorted cubic closed packing with all octahedral voids occupied by Na and 50 % of the tetrahedral voids by the remaining Na as well as Sn.

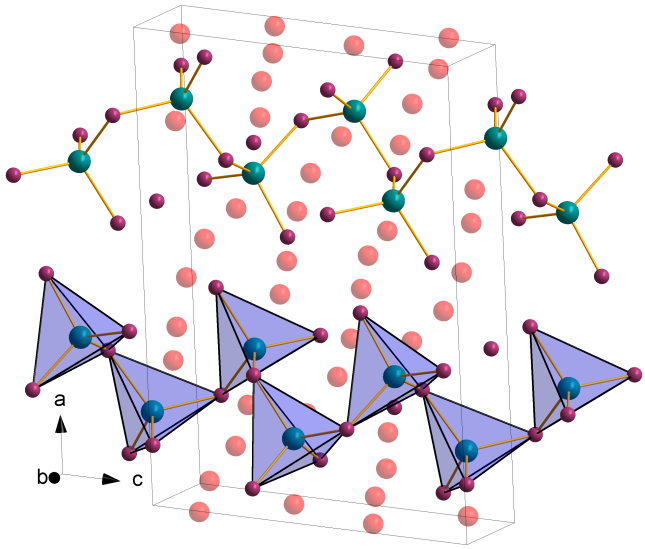

Figure A.23: Crystal structure of Na_5SnSb_3 with one dimensional corner-sharing chains of $SnSb_4$-tetrahedra along c.

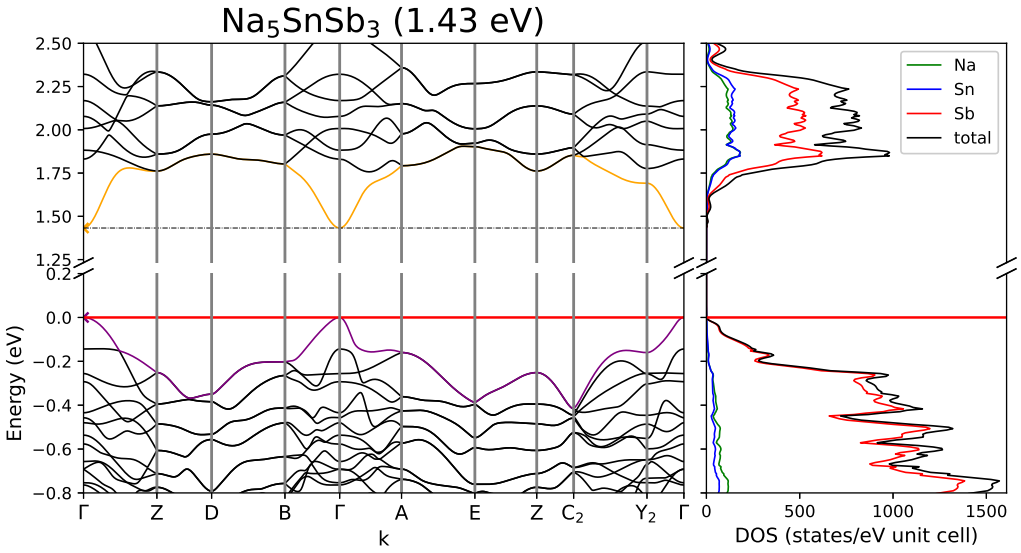

Figure A.24: Band structure and DOS of Na_5SnSb_3.

Table A.43: Overlap population and interatomic distances of Na_5SnSb_3.

Atom A	Atom B	r_{AB} / Å	overlap
Na1	Sb3	3.046	0.053
	Sb5	3.069	0.065
	Sb5	3.141	0.052
	Sb3	3.162	0.057
	Na6	3.361	0.005
	Na7	3.5	0.004
Na2	Sb2	3.008	0.056
	Sb1	3.025	0.043
	Sb6	3.035	0.055
	Sb4	3.15	0.028
	Na9	3.48	0.004
	Sn2	3.513	0.007
Na3	Sb2	3.107	0.047
	Sb1	3.265	0.032
	Sb3	3.335	0.034
	Sn2	3.345	0.009
	Sb1	3.394	0.019
	Na5	3.493	0.004
Na4	Sb3	3.073	0.061
	Sb1	3.096	0.042
	Sb5	3.138	0.052
	Sb4	3.228	0.046
	Na7	3.442	0.004
Na5	Sb6	3.015	0.057
	Sb6	3.068	0.051
	Sb2	3.139	0.061
	Sb2	3.158	0.044
	Na5	3.461	0.005
Na6	Sb4	3.126	0.038
	Sb3	3.281	0.043
	Sb3	3.312	0.043
	Sn2	3.487	0.009
	Sb5	3.553	0.028
Na7	Sb2	3.126	0.05
	Sb5	3.21	0.052
	Sb3	3.231	0.055
	Sb4	3.294	0.026
Na8	Sb5	3.218	0.05
	Sb3	3.225	0.044
	Sb5	3.237	0.049
	Sb4	3.473	0.027
	Na8	3.612	0.002
Na9	Sb6	3.256	0.056
	Sb1	3.266	0.035
	Sb6	3.328	0.045
	Sb6	3.398	0.041
Na10	Sb6	3.246	0.051
	Sb2	3.316	0.044
	Sb1	3.395	0.039
	Sb2	3.45	0.034
Sn1	Sb2	2.817	0.273
	Sb6	2.828	0.239
	Sb4	2.875	0.239
	Sb1	2.888	0.229
Sn2	Sb3	2.8	0.275
	Sb5	2.802	0.283
	Sb4	2.888	0.233
	Sb1	2.932	0.212

Table A.44: Partial charges for each atom position in Na_5SnSb_3.

Atom	Z	charge	part charge
Na1	11	10.344	0.656
Na2		10.299	0.701
Na3		10.266	0.734
Na4		10.321	0.679
Na5		10.343	0.657
Na6		10.279	0.721
Na7		10.299	0.701
Na8		10.305	0.695
Na9		10.328	0.672
Na10		10.312	0.688

Atom	Z	charge	partialcharge
Sn1	22	22.049	−0.049
Sn2		22.067	−0.067
Sb1	23	23.915	−0.915
Sb2		24.272	−1.272
Sb3		24.261	−1.261
Sb4		23.865	−0.865
Sb5		24.234	−1.234
Sb6		24.241	−1.241

A.2 6-1-3

Table A.45: Overview of the crystallographic details of the 6-1-3 compounds. Cell parameters given in the first line and second line are of experimental and calculated origin, respectively. The third line shows the difference between both in percent.

compound	a / Å	b/ Å	c / Å	β / °	space group	crystal system	connectivity
Rb_6AlSb_3	10.624	6.260	12.377	100.7	$P\ 2_1\ /\ m$ (no. 11)	monoclinic	0D (monomer)
	10.600	6.272	12.279	100.8			
	-0.23	0.20	-0.80	0.07			
Cs_6AlSb_3	10.845	6.507	12.707	100.95	-"-	-"-	-"-
	10.927	6.504	12.624	101.19			
	0.76	-0.05	-0.66	0.24			
Cs_6GaSb_3	10.858	6.490	12.729	101.1	-"-	-"-	-"-
	10.923	6.491	12.641	101.3			
	0.60	0.02	-0.69	0.19			
Cs_6InAs_3	10.469	6.356	12.208	101.3	-"-	-"-	-"-
	10.574	6.343	12.177	101.4			
	1.00	-0.21	-0.25	0.16			

Table A.46: Calculated band gaps and transitions as well as an overview of the sampled reciprocal space defined by the Monkhorst-Pack-type *k*-point grid (SHRINK) and Brillouin Zone paths for all 6-1-3 compounds.

compound	band gap		transition	k-path	SHRINK
Rb_6AlSb_3	1.36	indirect	Y_2 -> Γ	Γ—Z—D—B—Γ—A—E—Z—C_2—Y_2—Γ	3 5 3
Cs_6AlSb_3	1.72	indirect	-"-	-"-	-"-
Cs_6GaSb_3	1.68	indirect	-"-	-"-	-"-
Cs_6InAs_3	1.89	pseudo-direct	Γ -> Γ	-"-	-"-

Rb_6AlSb_3[89]

Rb_3AlSb_3 crystallizes in the Cs_3AlSb_3 structure type in space group $P\,2_1\,/\,m$ (no. 11). The structure incorporates isolated, triangular planar $AlSb_3^{6-}$ units.

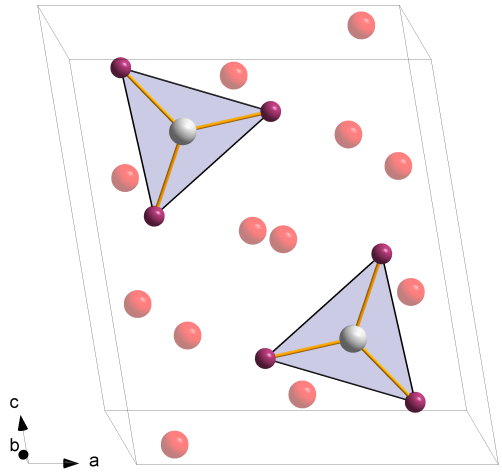

Figure A.25: Crystal structure of Rb_6AlSb_3 containing triangular planar $AlSb_3^{6-}$ units.

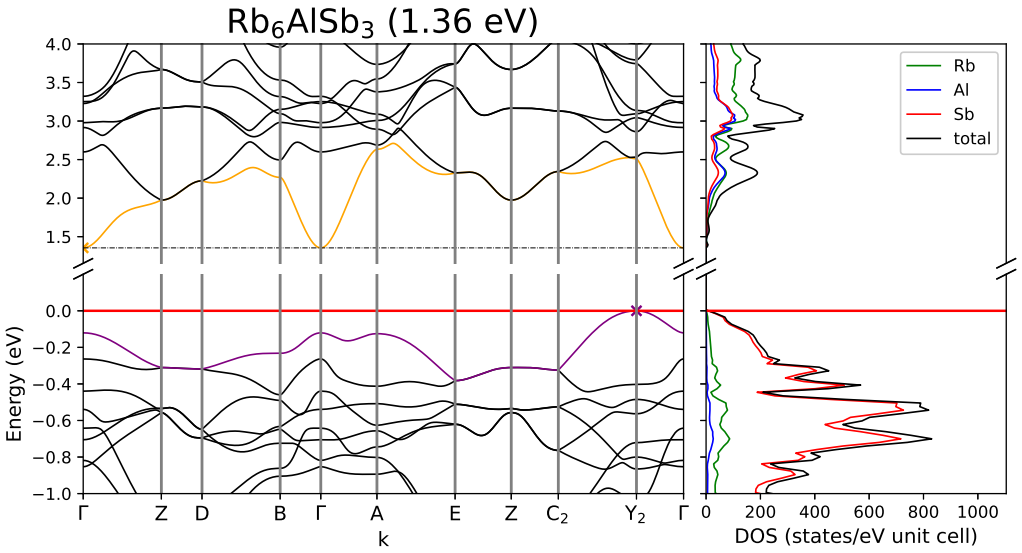

Figure A.26: Band structure and DOS of Rb_6AlSb_3.

Table A.47: Overlap population and interatomic distances of Rb_6AlSb_3.

Atom A	Atom B	r_{AB} / Å	overlap
Rb1	Sb2	3.714	0.029
	Sb3	3.751	0.039
	Rb2	3.778	−0.001
	Sb2	3.839	0.028
	Rb2	3.857	0.0
	Rb4	3.988	0.001
Rb2	Al1	3.788	0.008
	Sb2	3.818	0.035
	Sb2	3.939	0.023
	Sb3	3.981	0.028
Rb3	Sb1	3.647	0.035
	Sb3	3.661	0.04
	Sb3	3.742	0.043
	Rb5	3.883	0.001
	Rb6	3.993	0.001
	Rb3	4.18	0.002
Rb4	Rb4	3.62	−0.004
	Sb2	3.837	0.027
	Sb1	3.904	0.025
	Rb6	3.929	0.001
	Sb2	3.985	0.024
Rb5	Rb5	3.672	−0.002
	Rb6	3.808	0.001
	Sb1	3.844	0.031
	Sb1	3.949	0.027
	Al1	4.094	0.009
Rb6	Sb1	3.661	0.035
	Sb2	3.734	0.038
	Sb3	4.062	0.034
Al1	Sb1	2.613	0.387
	Sb2	2.624	0.372
	Sb3	2.677	0.34

Table A.48: Partial charges for each atom position in Rb_6AlSb_3.

Atom	Z	charge	part charge
Rb1	9	8.379	0.621
Rb2		8.368	0.632
Rb3		8.405	0.595
Rb4		8.344	0.656
Rb5		8.346	0.654
Rb6		8.374	0.626
Al1	13	12.98	0.02
Sb1	23	24.252	−1.252
Sb2		24.264	−1.264
Sb3		24.289	−1.289

Ca_6InAs_3[92]

For a crystal structure description see Rb_6AlSb_3.

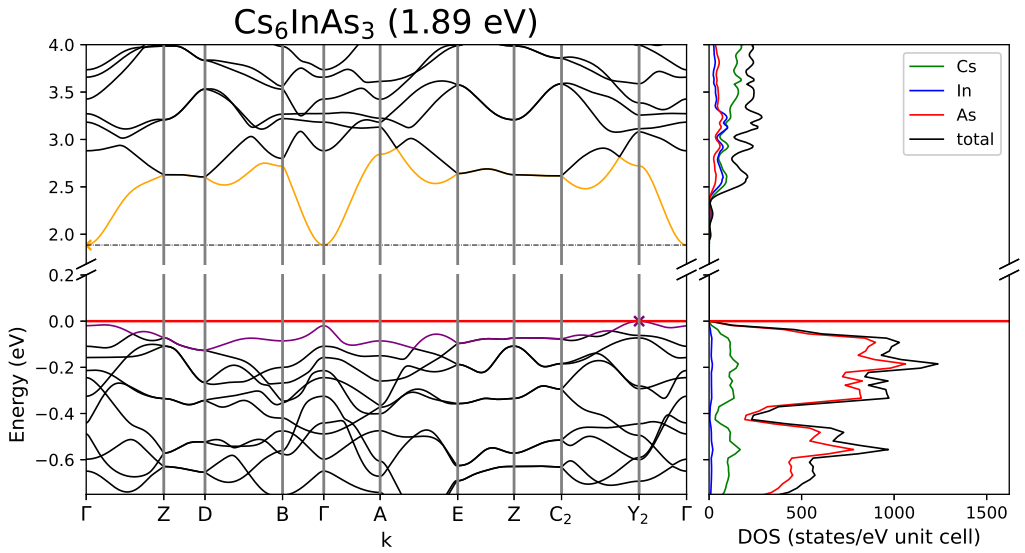

Figure A.27: Band structure and DOS of Cs_6InAs_3.

Table A.49: Partial charges for each atom position in Cs_6InAs_3.

Atom	Z	charge	part charge
Cs1	9	8.378	0.622
Cs2		8.343	0.657
Cs3		8.395	0.605
Cs4		8.332	0.668
Cs5		8.327	0.673
Cs6		8.375	0.625

Atom	Z	charge	partialcharge
In1	21	21.092	−0.092
As1	33	34.234	−1.234
As2		34.264	−1.264
As3		34.261	−1.261

Table A.50: Overlap population and interatomic distances of Cs_6InAs_3.

Atom A	Atom B	r_{AB} / Å	overlap
Cs1	As3	3.693	0.038
	As2	3.746	0.03
	As2	3.776	0.031
	Cs2	3.783	0.008
	Cs2	3.802	0.008
	Cs4	3.925	0.007
Cs2	As2	3.745	0.035
	In1	3.852	0.002
	As2	3.963	0.02
	As3	4.026	0.024
Cs3	As1	3.577	0.036
	As3	3.678	0.041
	As3	3.826	0.038
	Cs5	3.877	0.008
	Cs6	4.073	0.007
Cs4	Cs4	3.628	0.007
	As1	3.74	0.03
	As2	3.901	0.025
	Cs6	3.919	0.008
	As2	3.959	0.024
Cs5	Cs5	3.648	0.008
	Cs6	3.779	0.009
	As1	3.797	0.027
	As3	3.95	0.027
	As1	3.999	0.021
Cs6	As1	3.626	0.038
	As2	3.658	0.04
	As3	4.062	0.029
In1	As1	2.594	0.349
	As2	2.633	0.323
	As3	2.648	0.321

Cs_6AlSb_3[90]

For a crystal structure description see Rb_6AlSb_3.

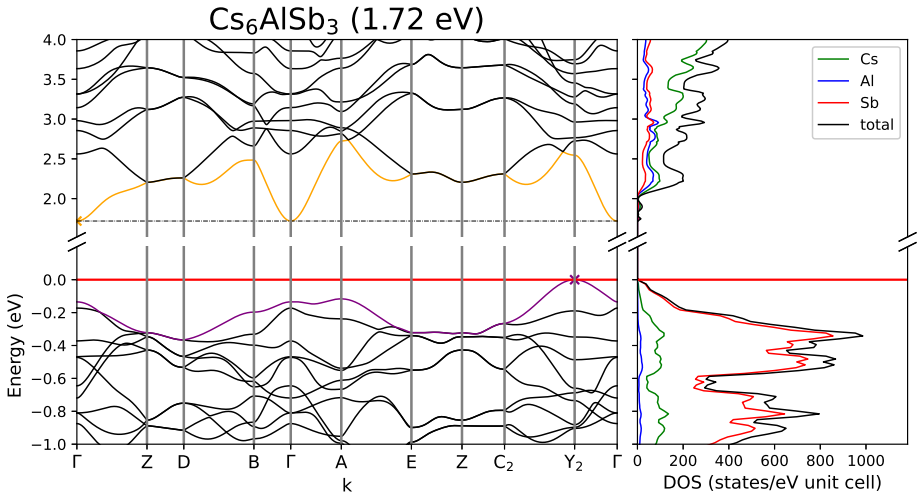

Figure A.28: Band structure and DOS of Cs_6AlSb_3.

Table A.51: Overlap population and interatomic distances of Cs_6AlSb_3.

Atom A	Atom B	r_{AB} / Å	overlap
Cs1	Cs6	3.906	0.007
	Al1	3.929	0.009
	Sb2	3.961	0.032
	Cs6	3.968	0.006
	Sb2	4.053	0.021
	Sb3	4.111	0.025
Cs2	Sb1	3.779	0.036
	Sb3	3.824	0.038
	Sb3	3.983	0.039
	Cs3	3.986	0.007
	Cs4	4.149	0.006
Cs3	Cs3	3.796	0.007
	Cs4	3.934	0.007
	Sb1	3.973	0.027
	Sb1	4.108	0.023
	Sb3	4.145	0.025
Cs4	Sb1	3.78	0.035
	Sb2	3.874	0.037
	Cs5	3.991	0.007
	Sb3	4.213	0.03
Cs5	Cs5	3.767	0.007
	Sb1	3.97	0.028
	Sb2	4.003	0.025
	Sb2	4.096	0.023
	Cs6	4.099	0.006
Cs6	Sb2	3.882	0.029
	Sb3	3.898	0.037
	Sb2	3.908	0.03
Al1	Sb1	2.629	0.386
	Sb2	2.643	0.368
	Sb3	2.683	0.347

Table A.52: Partial charges for each atom position in Cs_6AlSb_3.

Atom	Z	charge	part charge
Cs1	9	8.351	0.649
Cs2		8.388	0.612
Cs3		8.338	0.662
Cs4		8.36	0.64
Cs5		8.338	0.662
Cs6		8.367	0.633

Atom	Z	charge	partialcharge
Al1	13	12.976	0.024
Sb1	23	24.277	−1.277
Sb2		24.293	−1.293
Sb3		24.312	−1.312

Cs_6GaSb_3[91]

For a crystal structure description see Rb_6AlSb_3.

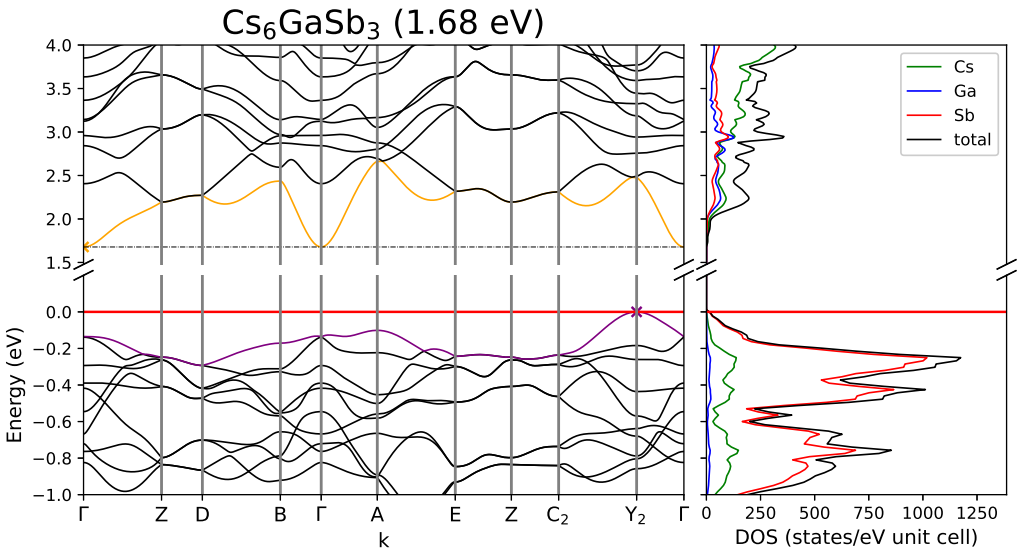

Figure A.29: Band structure and DOS of Cs_6GaSb_3.

Table A.53: Overlap population and interatomic distances of Cs_6GaSb_3.

Atom A	Atom B	r_{AB} / Å	overlap
Cs1	Sb2	3.875	0.029
	Sb3	3.888	0.037
	Sb2	3.905	0.03
	Cs2	3.907	0.007
	Cs2	3.97	0.007
	Cs4	4.094	0.006
Cs2	Ga1	3.904	0.003
	Sb2	3.97	0.032
	Sb2	4.046	0.02
	Sb3	4.107	0.025
Cs3	Sb1	3.774	0.036
	Sb3	3.815	0.039
	Sb3	3.982	0.039
	Cs5	3.99	0.007
	Cs6	4.146	0.007
Cs4	Cs4	3.767	0.007
	Sb1	3.979	0.029
	Cs6	3.987	0.007
	Sb2	4.01	0.026
	Sb2	4.087	0.022

Atom A	Atom B	r_{AB} / Å	overlap
Cs5	Cs5	3.797	0.007
	Cs6	3.929	0.007
	Sb1	3.984	0.027
	Sb1	4.092	0.022
	Sb3	4.147	0.026
Cs6	Sb1	3.779	0.036
	Sb2	3.867	0.036
	Sb3	4.223	0.029
Ga1	Sb1	2.631	0.368
	Sb2	2.647	0.345
	Sb3	2.685	0.326

Table A.54: Partial charges for each atom position in Cs_6GaSb_3.

Atom	Z	charge	part charge
Cs1	9	8.371	0.629
Cs2		8.336	0.664
Cs3		8.392	0.608
Cs4		8.33	0.67
Cs5		8.326	0.674
Cs6		8.363	0.637

Atom	Z	charge	partialcharge
Ga1	31	31.155	−0.155
Sb1	23	24.225	−1.225
Sb2		24.242	−1.242
Sb3		24.26	−1.26

A.3 3-1-2

Table A.55: Overview of the crystallographic details of the 3-1-2 compounds. Cell parameters given in the first line and second line are of experimental and calculated origin, respectively. The third line shows the difference between both in percent.

compound	a / Å	b/ Å	c / Å	α / °	β / °	γ / °	space group	crystal system	connectivity
K_3BP_2	9.362	8.894	9.013		110.99		*C 2/c* (no. 15)	monoclinic	0D (BP_2^{3-})
	9.403	8.833	8.913		110.78				
	0.44	-0.69	-1.12		-0.19				
Rb_3BP_2	9.533	9.229	9.418		110.53		-"-	-"-	-"-
	9.684	9.271	9.350		109.97				
	1.56	0.45	-0.73		-0.51				
Cs_3BP_2	9.834	9.674	9.859		109.77		-"-	-"-	-"-
	9.890	9.697	9.829		110.08				
	0.56	0.24	-0.30		0.28				
K_3BAs_3	9.609	9.109	9.194		111.68		-"-	-"-	-"-
	9.646	9.002	9.120		111.33				
	0.38	-1.19	-0.81		-0.32				
Rb_3BAs_2	9.772	9.443	9.649		111.08		-"-	-"-	-"-
	9.906	9.447	9.574		110.62				
	1.35	0.05	-0.79		-0.42				
Cs_3BAs_2	10.06	9.87	10.17		110.62		-"-	-"-	-"-
	10.15	9.83	10.01		110.41				
	0.86	-0.35	-1.60		-0.19				
Na_3BP_2	6.995	9.279	9.159		111.03		*P* $2_1/c$ (no. 14)	monoclinic	-"-
	6.928	9.313	9.150		111.02				
	-0.96	0.36	-0.10		-0.01				
Li_3AlP_2	11.5138	11.7634	5.8202				*C m c e* (no. 64)	orthorhombic	2D
	11.5388	11.7560	5.8267						
	0.22	-0.06	0.11						
Li_3GaP_2	11.5839	11.7809	5.8129				-"-	-"-	-"-
	11.5910	11.7834	5.8289						
	0.06	0.02	0.27						
Li_3AlAs_2	11.894	12.150	6.005				-"-	-"-	-"-
	11.932	12.139	6.011						
	0.32	-0.09	0.11						
Li_3GaAs_2	11.9626	12.1629	5.9984				-"-	-"-	-"-
	11.9959	12.1610	6.0145						
	0.28	-0.02	0.27						
Li_3InP_2	12.0065		23.9165				*I* $4_1/a$ *c d* (no. 142)	tetragonal	3D
	12.0407		23.9862						
	0.28		0.29						
Li_3InAs_2	12.388		24.6587				-"-	-"-	-"-
	12.409		24.7284						
	0.17		0.28						
Na_3AlP_2	13.176	6.764	6.065				*I b a m* (no. 72)	orthorhombic	2D
	13.261	6.468	6.008						
	0.64	-4.57	-0.94						
Na_3GaP_2	13.081	6.728	6.211				-"-	-"-	-"-
	13.304	6.339	6.123						
	1.68	-6.13	-1.44						
K_3InP_2	14.489	7.658	6.816				-"-	-"-	-"-
	14.523	7.499	6.781						
	0.23	-2.12	-0.52						
Na_3AlAs_2	13.604	6.895	6.227				-"-	-"-	-"-
	13.741	6.458	6.187						
	1.00	-6.77	-0.64						
K_3InAs_2	7.821	14.759	6.936				-"-	-"-	-"-
	7.613	14.817	6.964						
	-2.73	0.39	0.40						
Na_3InP_2	9.401	7.371	15.358		92.4		*P* $2_1/c$ (no. 14)	monoclinic	3D
	9.342	7.277	15.236		92.6				
	-0.63	-1.30	-0.80		0.22				

Table A.55: Continued.

compound	a / Å	b/ Å	c / Å	α / °	β / °	γ / °	space group	crystal system	connectivity
Na_3InAs_2	9.677	7.547	15.731		92.6		-"-	-"-	-"-
	9.624	7.439	15.611		92.9				
	-0.55	-1.45	-0.77		0.29				
Na_3InSb_2	10.285	7.963	16.652		92.6		-"-	-"-	-"-
	10.248	7.849	16.527		92.9				
	-0.36	-1.45	-0.76		0.28				
Na_3InBi_2	18.841	9.235	12.661		98.67		$P\ 2_1/c$ (no. 14)	monoclinic	3D
	18.561	9.166	12.506		98.34				
	-1.51	-0.75	-1.24		-0.34				
K_3AlP_2	8.871	11.879	15.280	72.47	73.35	71.62	$P\ \overline{1}$ (no. 2)	triclinic	1D + 0D (dimer)
	8.822	11.767	15.140	72.94	73.45	72.40			
	-0.55	-0.95	-0.92	0.65	0.14	1.07			
Rb_3InP_2	9.397	12.500	15.927	97.16	107.00	106.72	-"-	-"-	-"-
	9.462	12.556	15.935	96.87	107.40	106.18			
	0.69	0.45	0.05	-0.30	0.38	-0.51			
K_3AlAs_2	9.062	12.164	15.570	72.40	73.05	71.63	-"-	-"-	-"-
	8.969	12.070	15.508	72.69	73.27	72.16			
	-1.03	-0.78	-0.40	0.40	0.30	0.74			
Cs_3InP_2	9.662	12.884	15.840	81.1	81.6	70.7	$P\ \overline{1}$ (no. 2)	triclinic	1D + 0D (dimer)
	9.750	12.922	15.843	80.6	81.6	71.2			
	0.90	0.29	0.02	-0.57	0.01	0.81			
Rb_3GaP_2	14.634	24.893	9.163				*P b c a* (no. 61)	orthorhombic	0D (dimers)
	14.930	24.905	9.115						
	1.99	0.05	-0.53						
Cs_3AlP_2	11.233	8.641	18.986		100.056		$P\ 2_1/c$ (no. 14)	monoclinic	0D (dimers)
	11.253	8.684	19.181		100.912				
	0.17	0.50	1.02		0.85				
Cs_3GaP_2	11.173	8.661	18.939		99.64		-"-	-"-	-"-
	11.241	8.672	19.173		100.77				
	0.60	0.12	1.22		1.13				
Cs_3AlAs_2	11.458	8.831	19.453		99.68		-"-	-"-	-"-
	11.427	8.844	19.578		100.31				
	-0.27	0.14	0.64		0.63				
Cs_3GaAs_2	11.371	8.857	19.460		99.225		-"-	-"-	-"-
	11.413	8.836	19.571		100.180				
	0.37	-0.25	0.57		0.95				

Table A.56: Calculated band gaps and transitions as well as an overview of the sampled reciprocal space defined by the Monkhorst-Pack-type *k*-point grid (SHRINK) and Brillouin Zone paths for all 3-1-2 compounds.

compound	band gap		transition	k-path	SHRINK
K_3BP_2	3.69	indirect	Y -> Γ-Y	Γ—A—I_2|I—M_2—Γ—Y|L_2—Γ—V_2	4 4 4
Rb_3BP_2	3.23	indirect	Y -> Γ	-"-	-"-
Cs_3BP_2	3.37	indirect	Y -> Γ-Y	-"-	3 3 3
K_3BAs_3	3.39	indirect	Y -> L_2	-"-	4 4 4
Rb_3BAs_2	3.06	indirect	Y -> Γ	-"-	-"-
Cs_3BAs_2	3.26	indirect	Γ-Y -> Γ	-"-	3 3 3
Na_3BP_2	3.30	indirect	Y2 -> Γ	Γ—Z—D—B—Γ—A—E—Z—C_2—Y_2—Γ	5 4 4
Li_3AlP_2	3.06	direct	Γ -> Γ	Γ-Y-T-Z-R-S-Γ|Σ_0-Γ-Z-A_0	4 4 6
Li_3GaP_2	2.83	direct	Γ -> Γ	-"-	-"-
Li_3AlAs_2	2.85	direct	Γ -> Γ	Γ—Y|S_0—Γ—Z—A_0|T—Y|Γ—S—R—Z—T	3 3 6
Li_3GaAs_2	2.43	direct	Γ -> Γ	-"-	4 4 5
Li_3InP_2	2.69	direct	Γ -> Γ	Γ-X-P-N-Γ-M-S|S_0-Γ|G-M	3 3 3
Li_3InAs_2	2.26	direct	Γ -> Γ	Γ—X—P—N—Γ—M—S|S_0—Γ|X—R|G—M	2 2 2
Na_3AlP_2	3.34	indirect	X-Γ -> G_0-X	Σ_0-Γ-Λ_0|G_0-X-Γ-R-W-S-Γ-T-W	4 4 4
Na_3GaP_2	2.88	indirect	Γ -> G_0-X	G_0-X-Γ-R-W-S-Γ-T-W	-"-
K_3InP_2	2.89	direct	Γ -> Γ	Γ—X—F_0|S_0—Γ—L_0|G_0—X|Γ—R—W—S—Γ—T—W	10 10 10
Na_3AlAs_2	2.98	indirect	Γ -> G0-X	-"-	4 4 4
K_3InAs_2	2.69	direct	Γ -> Γ	-"-	-"-
Na_3InP_2	2.09	direct	Γ -> Γ	Γ—Z—D—B—Γ—A—E—Z—C_2—Y_2—Γ	4 5 2
Na_3InAs_2	1.69	direct	Γ -> Γ	-"-	-"-

Table A.56: Continued.

compound	band gap		transition	k-path	SHRINK
Na_3InSb_2	1.51	pseudo-direct	Γ -> Γ	-"-	3 4 2
Na_3InBi_2	0.44	direct	Γ -> Γ	Γ—Z—D—B—Γ—A—E—Z—C_2—Y_2—Γ	2 4 3
K_3AlP_2	2.42	direct	Γ -> Γ	Γ—X|Y—Γ—Z|R—Γ—T|U—Γ—V	8 6 4
Rb_3InP_2	1.73	direct	Γ -> Γ	-"-	-"-
K_3AlAs_2	2.27	direct	Γ -> Γ	-"-	4 3 2
Cs_3InP_2	1.99	direct	Γ -> Γ	Γ—X|Y—Γ—Z|R—Γ—T|U—Γ—V	8 6 4
Rb_3GaP_2	2.41	direct	Γ -> Γ	Γ—X—S—Y—Γ—Z—U—R—T—Z|X—U|Y—T|S—R	6 4 8
Cs_3AlP_2	2.54	pseudo-direct	Γ -> Γ	Γ—Z—D—B—Γ—A—E—Z—C_2—Y_2—Γ	6 8 4
Cs_3GaP_2	2.54	pseudo-direct	Γ -> Γ	-"-	-"-
Cs_3AlAs_2	2.26	pseudo-direct	Γ -> Γ	-"-	3 4 2
Cs_3GaAs_2	2.35	pseudo-direct	Γ -> Γ	-"-	-"-

K_3BP_2[150]

K_3BP_2 crystallizes in the monoclinic space group *C 2/c* (no.15) in its own structure type. The unit cell contains isolated, almost ideally, linear BP_2^{3-} units (∠ P-B-P: 177.55 °). All units are aligned parallel to each other along the [101] crystallographic plane.

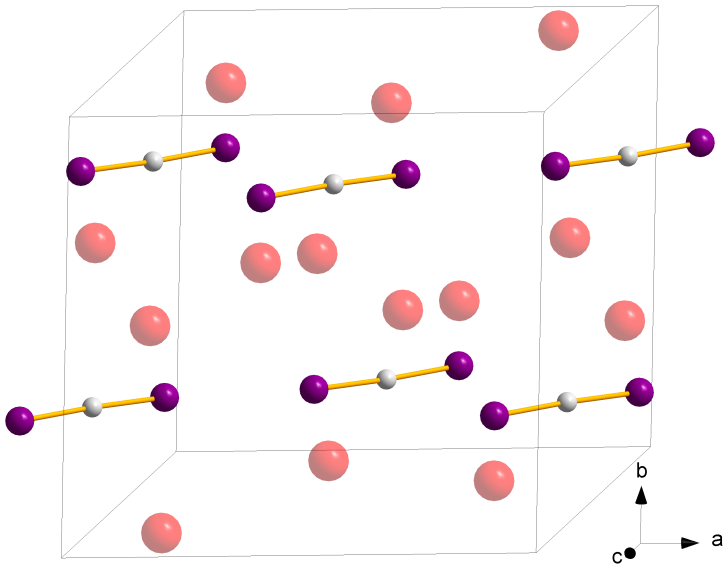

Figure A.30: Crystal structure of K_3BP_2 containing linear BP_2^{3-} units.

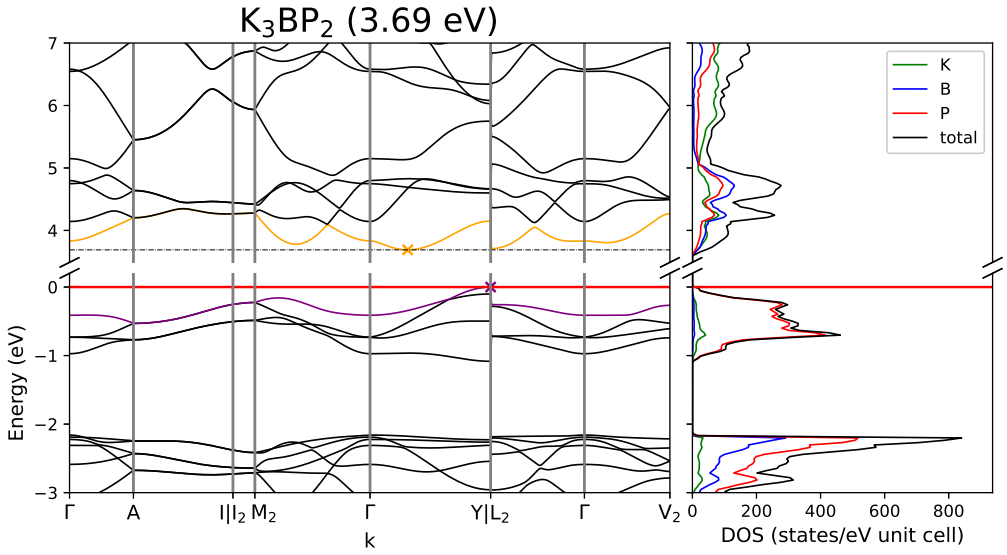

Figure A.31: Band structure and DOS of K_3BP_2.

Table A.57: Overlap population and interatomic distances of K_3BP_2.

Atom A	Atom B	r_{AB} / Å	overlap
K1	B1	3.056	0.008
	B1	3.309	0.008
	P1	3.309	0.017
	P1	3.421	0.021
	P1	3.455	0.018
	K2	3.461	−0.001

Atom A	Atom B	r_{AB} / Å	overlap
K2	B1	3.259	0.009
	P1	3.364	0.021
	P1	3.455	0.019
	P1	3.743	0.011
P1	B1	1.771	0.564

Table A.58: Partial charges for each atom position in K_3BP_2.

Atom	Z	charge	part charge
K1	19	18.246	0.754
K2		18.237	0.763
P1	15	16.004	−1.004

Atom	Z	charge	partialcharge
B1	5	5.262	−0.262

Rb_3BP_2[151]

For a crystal structure description see K_3BP_2.

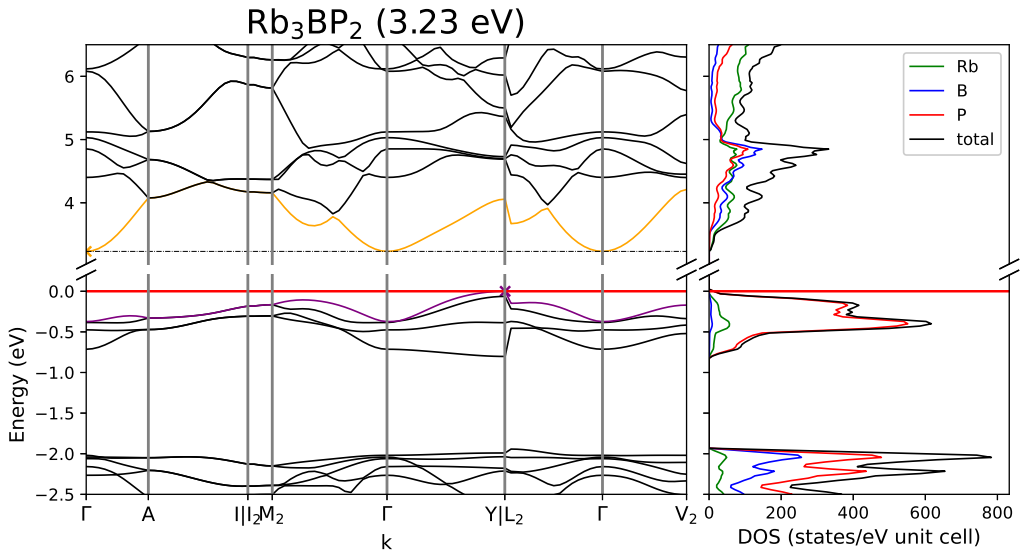

Figure A.32: Band structure and DOS of Rb_3BP_2.

Table A.59: Overlap population and interatomic distances of Rb_3BP_2.

Atom A	Atom B	r_{AB} / Å	overlap
Rb1	B1	3.461	0.012
	P1	3.536	0.024
	P1	3.625	0.022
	Rb2	3.632	−0.006
	P1	3.917	0.012
	Rb2	4.273	0.0
Rb2	B1	3.227	0.012
	B1	3.451	0.011
	P1	3.459	0.02
	P1	3.617	0.024
	P1	3.64	0.02
P1	B1	1.775	0.556
	P1	3.549	−0.062

Table A.60: Partial charges for each atom position in Rb_3BP_2.

Atom	Z	charge	part charge
Rb1	9	8.29	0.71
Rb2		8.303	0.697
P1	15	15.938	−0.938
B1	5	5.229	−0.229

Cs_3BP_2[152]

For a crystal structure description see K_3BP_2.

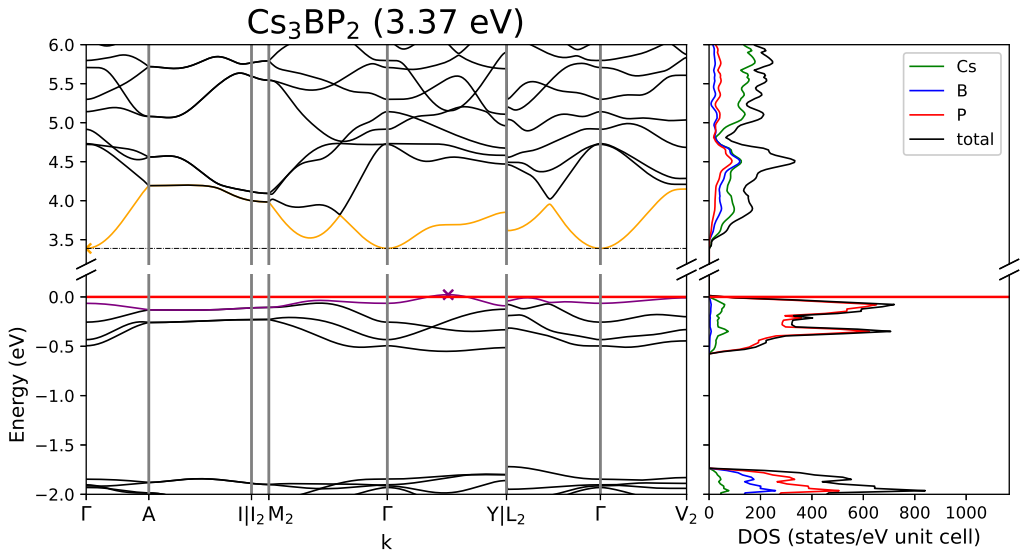

Figure A.33: Band structure and DOS of Cs_3BP_2.

Table A.61: Overlap population and interatomic distances of Cs_3BP_2.

Atom A	Atom B	r_{AB} / Å	overlap
Cs1	B1	3.372	0.01
	B1	3.558	0.01
	P1	3.589	0.02
	P1	3.756	0.018
	Cs2	3.795	0.005
	P1	3.817	0.02
Cs2	B1	3.61	0.011
	P1	3.712	0.022
	P1	3.773	0.022
	P1	4.046	0.013

Atom A	Atom B	r_{AB} / Å	overlap
P1	B1	1.774	0.564
	P1	3.548	−0.064

Table A.62: Partial charges for each atom position in Cs_3BP_2.

Atom	Z	charge	part charge
Cs1	9	8.295	0.705
Cs2		8.274	0.726
P1	15	15.961	−0.961

Atom	Z	charge	partialcharge
B1	5	5.216	−0.216

K_3BAs_2[153]

For a crystal structure description see K_3BP_2.

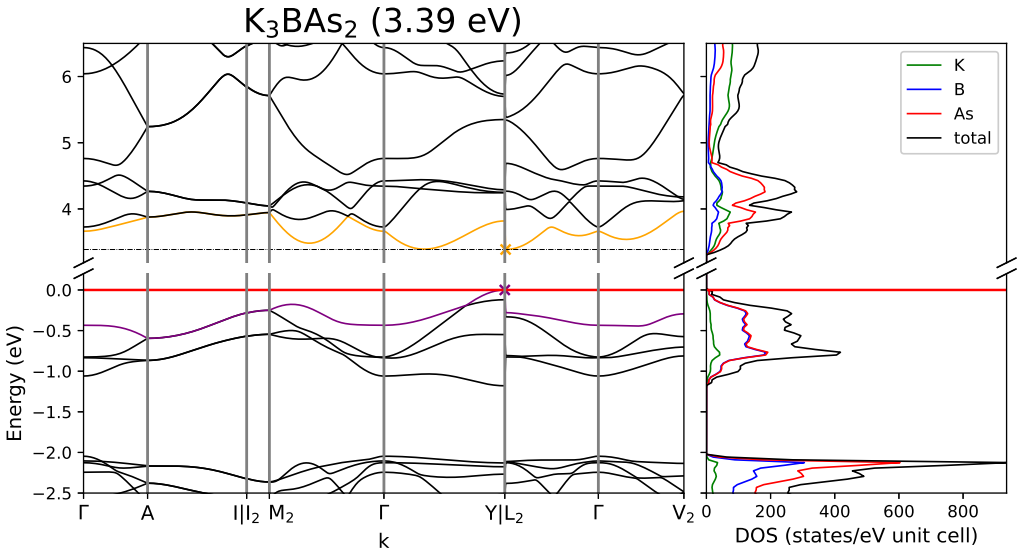

Figure A.34: Band structure and DOS of K_3BAs_2.

Table A.63: Overlap population and interatomic distances of K_3BAs_2.

Atom A	Atom B	r_{AB} / Å	overlap
K1	B1	3.091	0.011
	B1	3.37	0.01
	As1	3.378	0.02
	As1	3.502	0.025
	As1	3.513	0.022
	K2	3.533	−0.001

Atom A	Atom B	r_{AB} / Å	overlap
K2	B1	3.259	0.011
	As1	3.425	0.024
	As1	3.513	0.021
	As1	3.792	0.013
As1	B1	1.867	0.533

Table A.64: Partial charges for each atom position in K_3BAs_2.

Atom	Z	charge	part charge
K1	19	18.267	0.733
K2		18.258	0.742
As1	33	34.064	−1.064

Atom	Z	charge	partialcharge
B1	5	5.078	−0.078

Rb_3BAs_2[151]

For a crystal structure description see K_3BP_2.

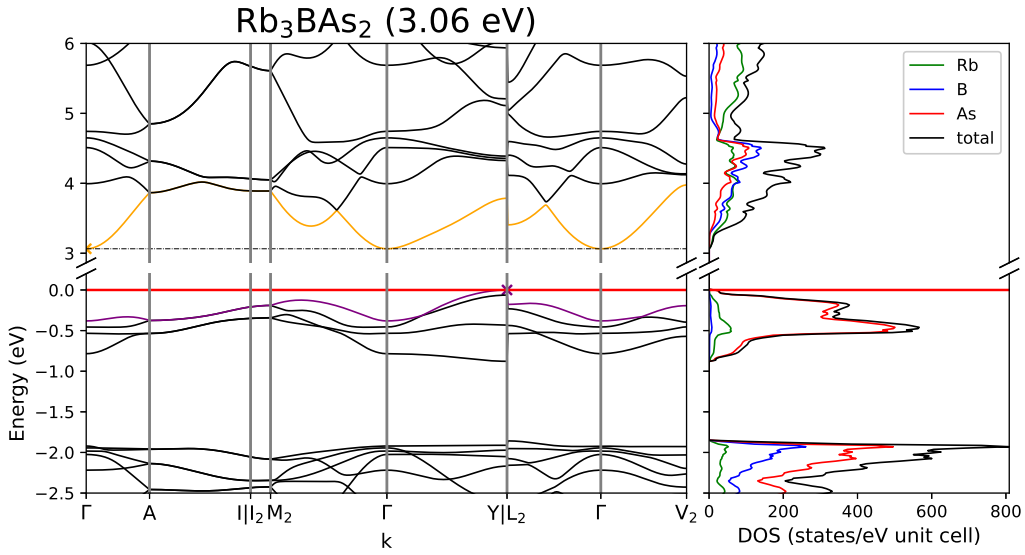

Figure A.35: Band structure and DOS of Rb_3BAs_2.

Table A.65: Overlap population and interatomic distances of Rb_3BAs_2.

Atom A	Atom B	r_{AB} / Å	overlap
Rb1	B1	3.262	0.014
	B1	3.504	0.012
	As1	3.526	0.024
	Rb2	3.693	−0.005
	As1	3.699	0.027
	As1	3.71	0.023

Atom A	Atom B	r_{AB} / Å	overlap
Rb2	B1	3.465	0.013
	As1	3.593	0.027
	As1	3.681	0.024
	As1	3.967	0.014
As1	B1	1.871	0.527

Table A.66: Partial charges for each atom position in Rb_3BAs_2.

Atom	Z	charge	part charge
Rb1	9	8.322	0.678
Rb2		8.31	0.69
As1	33	34.0	−1.0

Atom	Z	charge	partialcharge
B1	5	5.045	−0.045

Cs_3BAs_2[154]

For a crystal structure description see K_3BP_2.

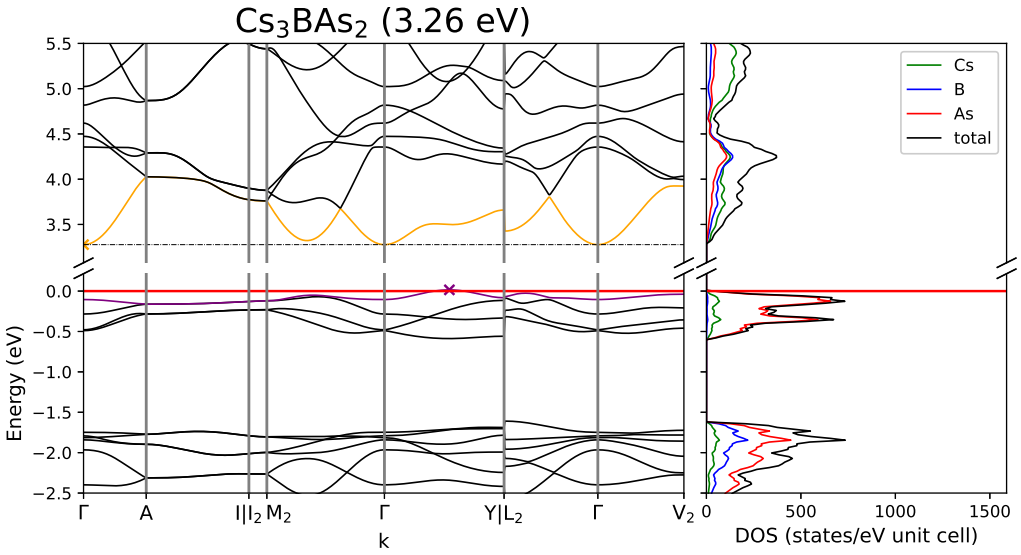

Figure A.36: Band structure and DOS of Cs_3BAs_2.

Table A.67: Partial charges for each atom position in Cs_3BAs_2.

Atom	Z	charge	part charge
Cs1	9	8.315	0.685
Cs2		8.297	0.703
As1	33	34.023	−1.023

Atom	Z	charge	partialcharge
B1	5	5.026	−0.026

Table A.68: Overlap population and interatomic distances of Cs_3BAs_2.

Atom A	Atom B	r_{AB} / Å	overlap
Cs1	B1	3.408	0.012
	B1	3.614	0.011
	As1	3.66	0.024
	As1	3.837	0.021
	Cs2	3.839	0.005
	As1	3.87	0.023
Cs2	B1	3.622	0.012
	As1	3.763	0.026
	As1	3.832	0.024
	As1	4.1	0.015

Atom A	Atom B	r_{AB} / Å	overlap
As1	B1	1.871	0.535
	As1	3.741	−0.073

Na_3BP_2[155]

Na_3BP_2 crystallizes in space group $P\ 2_1/c$ (no. 14) and shows the same isolated linear BP_2^{3-} units as K_3BP_2 (∠ P-B-P: 177.55 °). The arrangement of the linear units differs since two neighbouring units are tilted against each other along c.

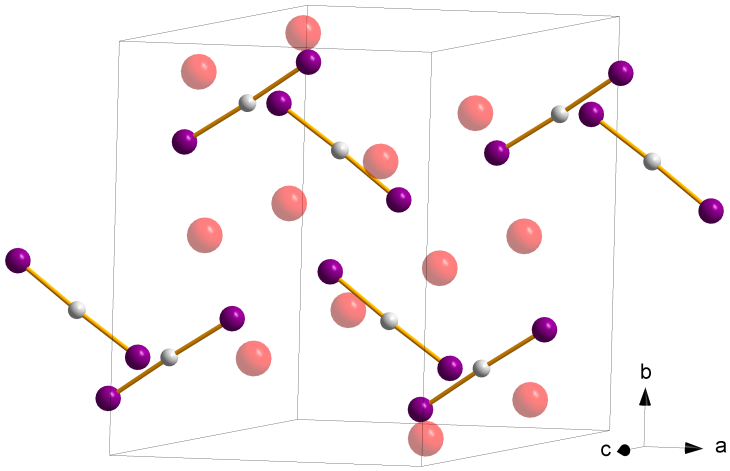

Figure A.37: Crystal structure of Na_3BP_2 containing linear BP_2^{3-} units.

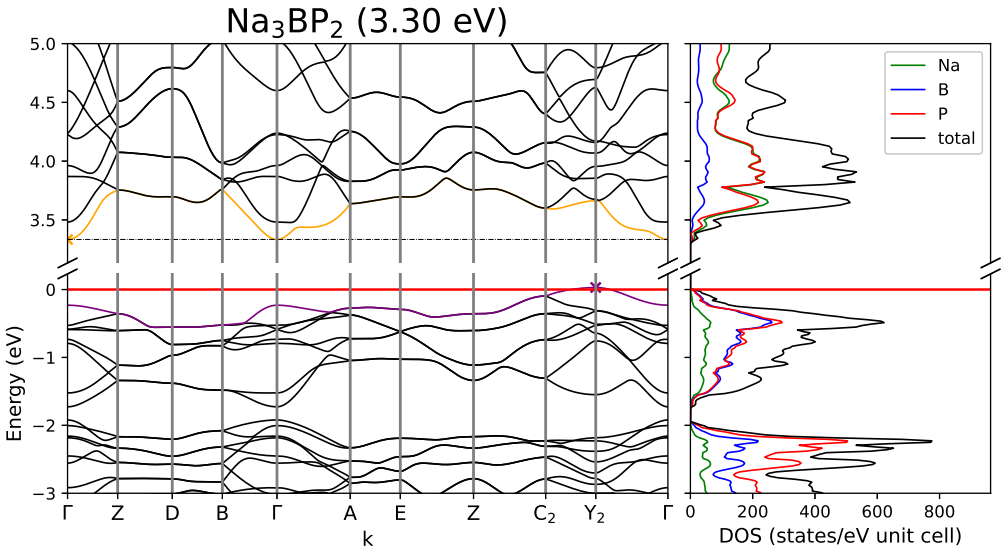

Figure A.38: Band structure and DOS of Na_3BP_2.

Table A.69: Overlap population and interatomic distances of Na_3BP_2.

Atom A	Atom B	r_{AB} / Å	overlap
Na1	P2	2.811	0.087
	P2	2.816	0.09
	P1	2.878	0.07
	P1	2.88	0.077
	Na3	3.421	0.009
	B1	3.46	0.01
Na2	B1	2.828	0.029
	P1	2.976	0.067
	P2	3.006	0.062
	P2	3.044	0.056
	B1	3.115	0.018
	P1	3.125	0.052

Atom A	Atom B	r_{AB} / Å	overlap
Na3	P1	2.934	0.077
	P2	2.968	0.063
	B1	2.999	0.021
	P2	3.0	0.061
	P1	3.166	0.059
	B1	3.419	0.009
P1	B1	1.778	0.538
P2	B1	1.775	0.541

Table A.70: Partial charges for each atom position in Na_3BP_2.

Atom	Z	charge	part charge
Na1	11	10.523	0.477
Na2		10.465	0.535
Na3		10.468	0.532
P1	15	15.661	−0.661

Atom	Z	charge	partialcharge
P2		15.656	−0.656
B1	5	5.226	−0.226

Li_3AlP_2[27]

Li_3AlP_2 crystallizes in space group *C m c e* (no. 64) where P forms a distorted cubic closed packing (ccp). Whitin the ccp tetrahedral voids are filled in two alternating layers: One solely by Li, while the other has only half of the voids occupied by Li, while the other half is filled by Al. This results in layers as the structural motive for the TrP_4 tetrahedra, where always two adjacent voids are filled with the same element in such a manner, that double-tetrahedra units of $[Tr_2P_6]^{6-}$ are build. These dimeric units are further connected by their vertices to neighbouring units forming two-dimensional layers.

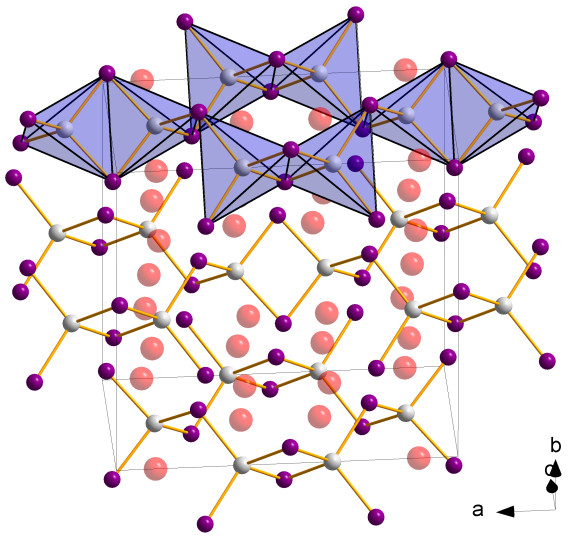

Figure A.39: Crystal structure of Li_3AlP_2 forming layers of corner-sharing edge-sharing dimers.

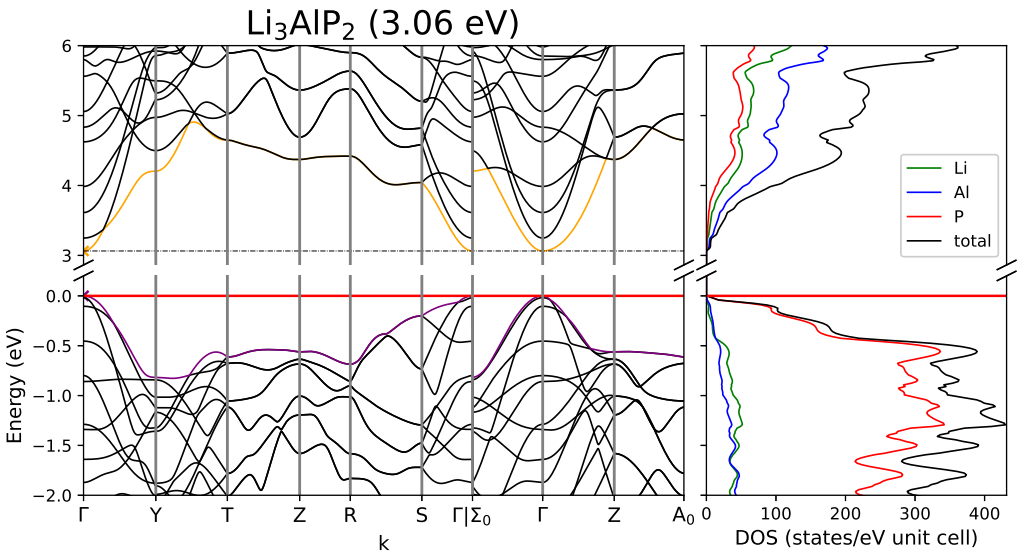

Figure A.40: Band structure and DOS of Li_3AlP_2.

Table A.71: Overlap population and interatomic distances of Li_3AlP_2.

Atom A	Atom B	r_{AB} / Å	overlap
Li1	P2	2.533	0.059
	P1	2.556	0.067
	Li1	2.651	0.01
	Li2	2.841	0.007
	Al1	2.918	0.013
	Al1	2.92	0.013
Li2	P1	2.564	0.071
	P1	2.572	0.067
	P2	2.587	0.062
	P2	2.608	0.076
	Li2	2.858	0.007

Atom A	Atom B	r_{AB} / Å	overlap
Al1	P1	2.398	0.283
	P2	2.414	0.289
	Al1	3.052	−0.023
P1	P1	3.7	−0.056
	P2	3.938	−0.03
P2	P2	3.991	−0.034

Table A.72: Partial charges for each atom position in Li_3AlP_2.

Atom	Z	charge	part charge
Li1	3	2.423	0.577
Li2		2.426	0.574
Al1	13	12.655	0.345

Atom	Z	charge	partialcharge
P1	15	16.052	−1.052
P2		16.018	−1.018

Li_3GaP_2[27]

For a crystal structure description see Li_3AlP_2.

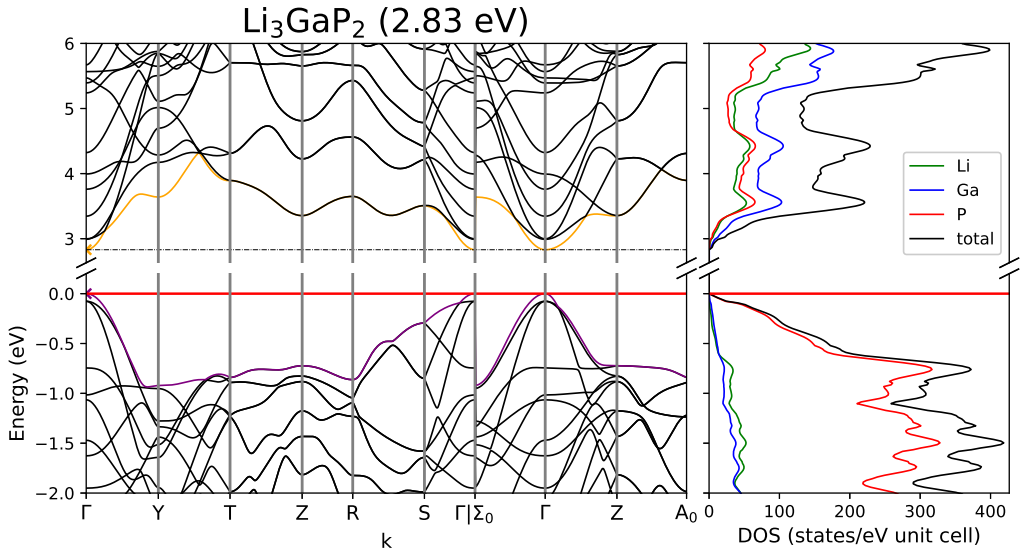

Figure A.41: Band structure and DOS of Li_3GaP_2.

Table A.73: Partial charges for each atom position in Li_3GaP_2.

Atom	Z	charge	part charge
Li1	3	2.442	0.558
Li2		2.427	0.573
Ga1	31	30.895	0.105

Atom	Z	charge	partialcharge
P1	15	15.913	−0.913
P2		15.881	−0.881

Table A.74: Overlap population and interatomic distances of Li_3GaP_2.

Atom A	Atom B	r_{AB} / Å	overlap
Li1	P1	2.564	0.07
	P1	2.569	0.073
	P2	2.592	0.061
	P2	2.599	0.081
	Li1	2.841	0.008
	Li2	2.851	0.007
Li2	P2	2.549	0.058
	P1	2.557	0.07
	Li2	2.679	0.01
	Ga1	2.908	0.012
	Ga1	2.922	0.013

Atom A	Atom B	r_{AB} / Å	overlap
Ga1	P1	2.419	0.248
	P2	2.427	0.255
	Ga1	3.095	−0.055
P1	P1	3.718	−0.04
	P2	3.956	−0.027

Li_3AlAs_2[98]

For a crystal structure description see Li_3AlP_2.

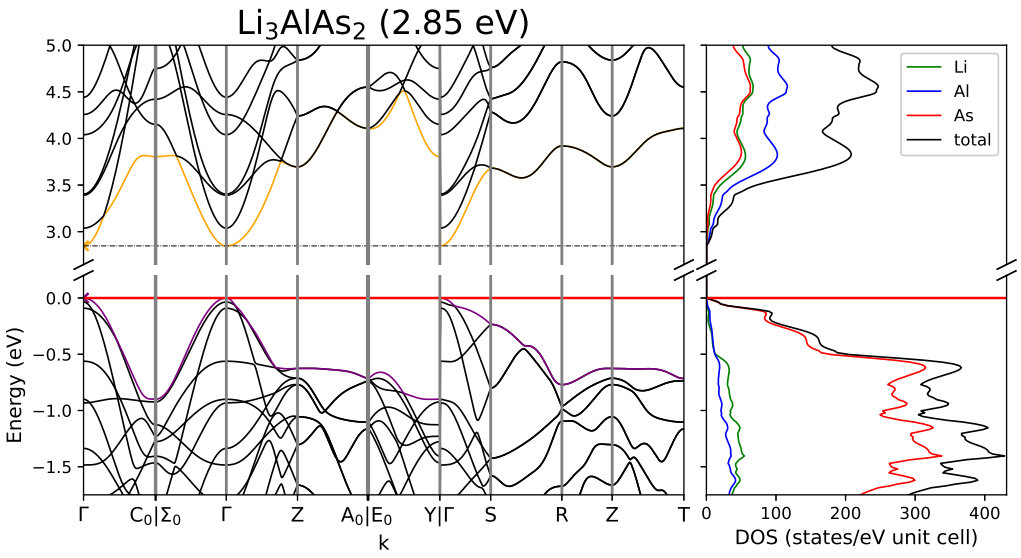

Figure A.42: Band structure and DOS of Li_3AlAs_2.

Table A.75: Overlap population and interatomic distances of Li_3AlAs_2.

Atom A	Atom B	r_{AB} / Å	overlap
As1	Al1	2.491	0.277
	Li1	2.64	0.07
	Li2	2.643	0.072
	Li2	2.644	0.072
	As1	3.857	−0.043
	As2	4.079	−0.026
As2	Al1	2.507	0.282
	Li1	2.62	0.061
	Li2	2.664	0.061
	Li2	2.676	0.083
Al1	Li1	3.007	0.013
	Li1	3.012	0.013
	Li2	3.138	0.01
	Al1	3.153	−0.014
Li1	Li1	2.765	0.01
	Li2	2.939	0.006
Li2	Li2	2.949	0.007

Table A.76: Partial charges for each atom position in Li_3AlAs_2.

Atom	Z	charge	part charge
As1	33	34.126	−1.126
As2		34.086	−1.086
Al1	13	12.492	0.508
Li1	3	2.428	0.572
Li2		2.434	0.566

Li_3GaAs_2[98]

For a crystal structure description see Li_3AlP_2.

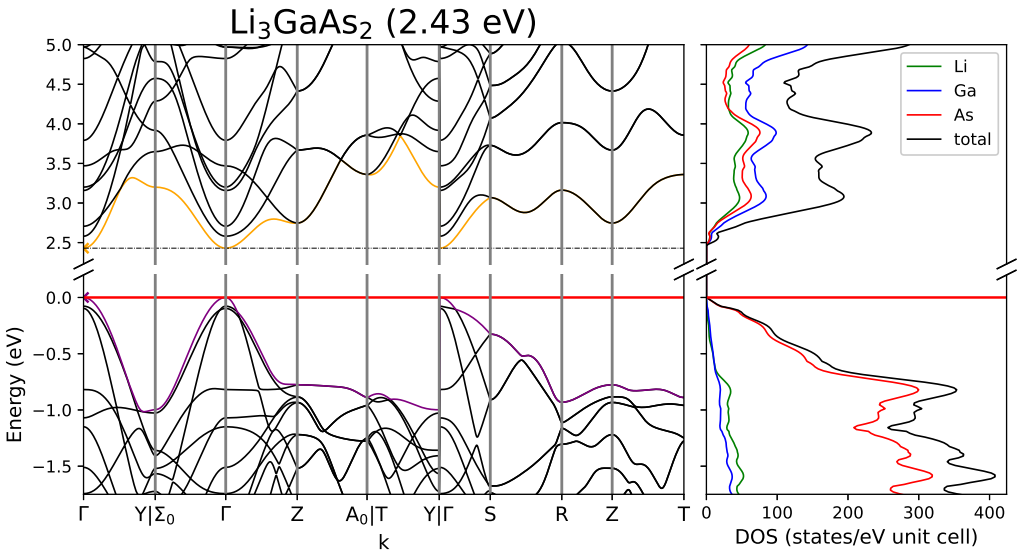

Figure A.43: Band structure and DOS of Li_3GaAs_2.

Table A.77: Overlap population and interatomic distances of Li_3GaAs_2.

Atom A	Atom B	r_{AB} / Å	overlap
Li1	As2	2.637	0.06
	As1	2.644	0.071
	Li1	2.796	0.01
	Li2	2.943	0.007
	Ga1	2.994	0.012
	Ga1	3.014	0.012
Li2	As1	2.637	0.074
	As1	2.654	0.071
	As2	2.668	0.086
	As2	2.675	0.059
	Li2	2.927	0.008

Atom A	Atom B	r_{AB} / Å	overlap
Ga1	As1	2.508	0.236
	As2	2.517	0.245
	Ga1	3.211	−0.033
As1	As1	3.853	−0.032
	As2	4.095	−0.025

Table A.78: Partial charges for each atom position in Li_3GaAs_2.

Atom	Z	charge	part charge
Li1	3	2.425	0.575
Li2		2.44	0.56
Ga1	31	30.712	0.288

Atom	Z	charge	partialcharge
As1	33	34.012	−1.012
As2		33.97	−0.97

Li_3InP_2[28]

Li_3InP_2 forms a three dimensional structure in space group *I* $4_1/a$ *c d* (no. 142). Herein P forms a tetragonally distorted ccp, in which all tetrahedral voids are occupied. In occupies the 32g Wyckoff position which results in four neighbouring tetrahedral voids being connected via vertex sharing. They form $[In_4P_{10}]^{12-}$ "super tetrahedra". These units are again connected via their "outer vertices" to neighbouring super-tetrahedra, resulting in two independent three dimensional networks of tetrahedra.

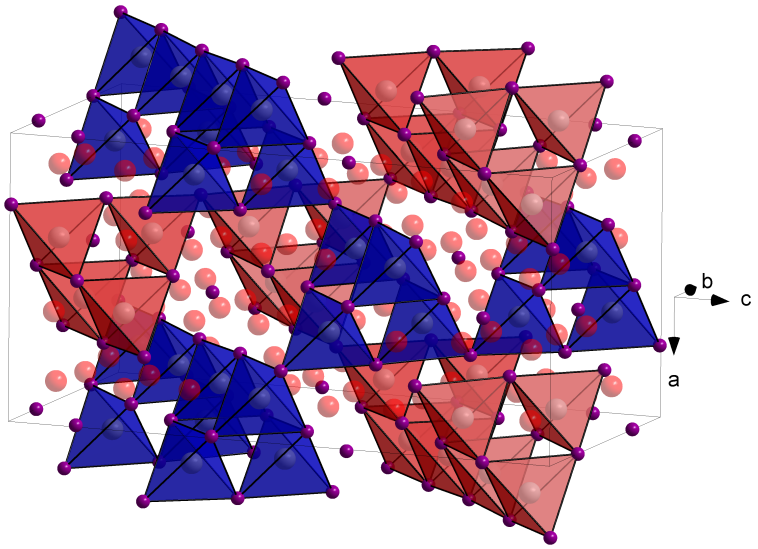

Figure A.44: Crystal structure of Li_3InP_2 forming two independent networks of T_4 super tetrahedra.

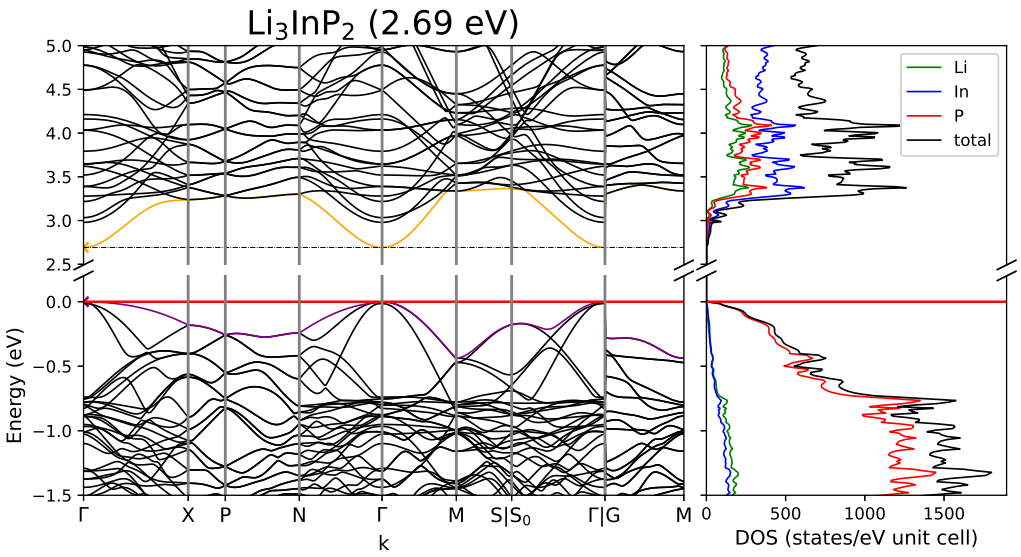

Figure A.45: Band structure and DOS of Li_3InP_2.

Table A.79: Overlap population and interatomic distances of Li_3InP_2.

Atom A	Atom B	r_{AB} / Å	overlap
Li1	P3	2.532	0.085
	P1	2.577	0.083
	P3	2.634	0.057
	P2	2.674	0.056
	Li3	2.903	0.007
	Li3	2.927	0.006
Li2	P3	2.551	0.086
	P1	2.591	0.063
	P2	2.605	0.062
	P3	2.682	0.055
	Li3	2.857	0.007
	Li2	2.885	0.006

Atom A	Atom B	r_{AB} / Å	overlap
Li3	P2	2.535	0.086
	P3	2.635	0.058
	P3	2.658	0.056
	P1	2.682	0.054
In1	P1	2.574	0.225
	P3	2.577	0.223
	P2	2.594	0.231
	P3	2.595	0.232
P1	P2	4.16	−0.02
	P3	4.242	−0.004
P2	P3	4.197	−0.014

Table A.80: Partial charges for each atom position in Li_3InP_2.

Atom	Z	charge	part charge
Li1	3	2.426	0.574
Li2		2.418	0.582
Li3		2.418	0.582
In1	21	20.742	0.258

Atom	Z	charge	partialcharge
P1	15	16.004	−1.004
P2		15.988	−0.988
P3		16.0	−1.0

Li_3InAs_2[98]

For a crystal structure description see Li_3InP_2.

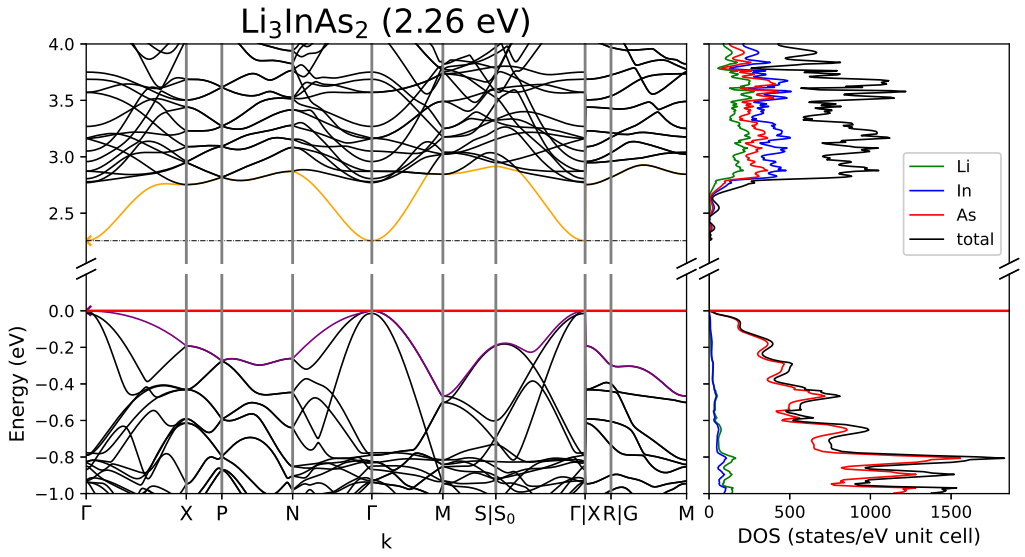

Figure A.46: Band structure and DOS of Li_3InAs_2.

Table A.81: Partial charges for each atom position in Li_3InAs_2.

Atom	Z	charge	part charge
Li1	7	2.42	4.58
Li2		2.423	4.577
Li3		2.43	4.57
In1	21	20.633	0.367

Atom	Z	charge	partialcharge
As1	33	34.055	−1.055
As2		34.038	−1.038
As3		34.048	−1.048

Table A.82: Overlap population and interatomic distances of Li_3InAs_2.

Atom A	Atom B	r_{AB} / Å	overlap
Li1	As3	2.632	0.089
	As2	2.667	0.068
	As1	2.677	0.061
	As3	2.76	0.054
	Li2	2.943	0.007
	Li1	2.997	0.006
Li2	As2	2.634	0.085
	As3	2.717	0.06
	As3	2.733	0.059
	As1	2.76	0.057
	Li3	2.991	0.006
Li3	As3	2.61	0.088
	As1	2.65	0.086
	As3	2.709	0.057
	As2	2.726	0.057
In1	As1	2.66	0.218
	As3	2.664	0.216
	As3	2.684	0.226
	As2	2.687	0.228
As1	As2	4.298	−0.019
	As3	4.353	−0.004
As2	As3	4.325	−0.012

Na_3AlP_2[29]

Na_3AlP_2 crystallize in space group *I b a m* (no. 72). P forms an orthorhombically distorted ccp in which a quarter of all tetrahedral voids is occupied by the triel atom and three quarters by Na. Voids are filled in a way, that adjacent Al filled voids form one dimensional chains of edge sharing tetrahedra along the c-axis which are analogue to the chains in the SiS_2 structure type.[110]

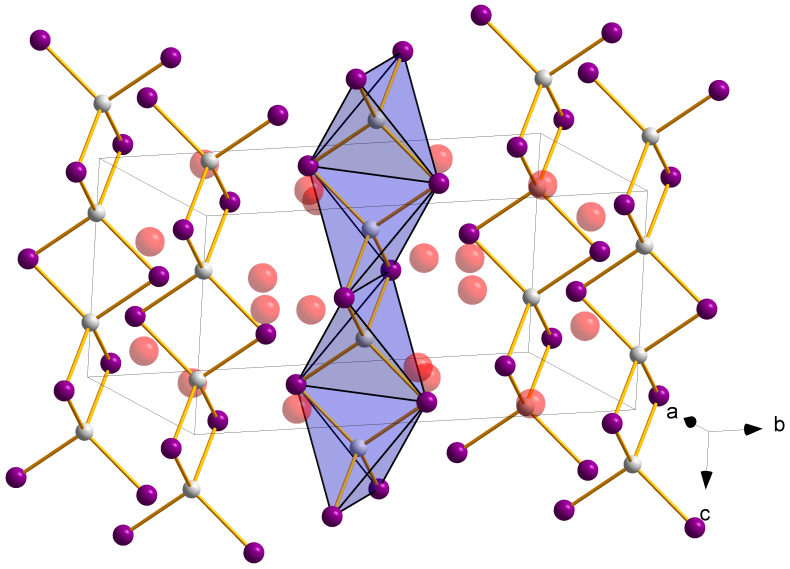

Figure A.47: Crystal structure of Na_3AlP_2 forming chains of edge-sharing tetrahedra along c.

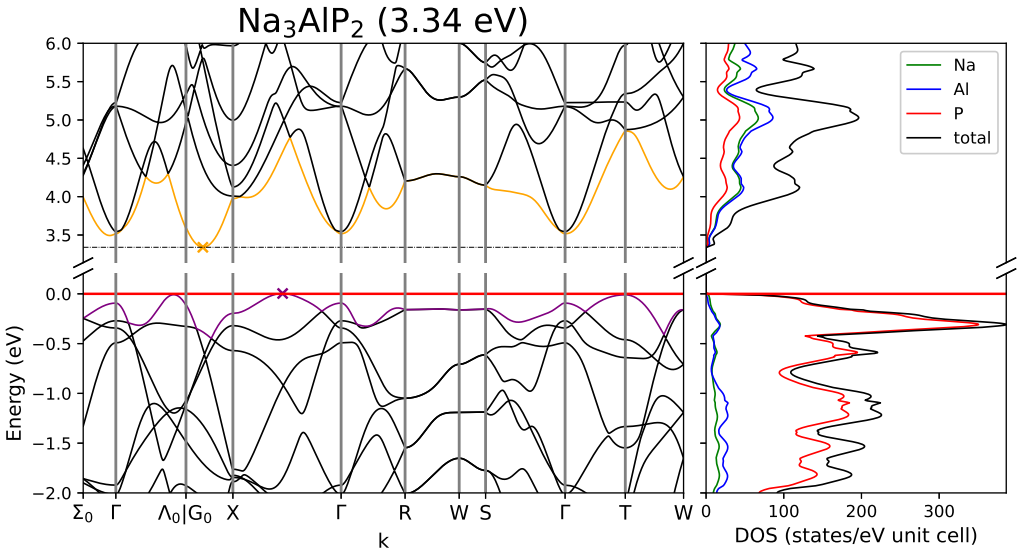

Figure A.48: Band structure and DOS of Na_3AlP_2.

Table A.83: Overlap population and interatomic distances of Na_3AlP_2.

Atom A	Atom B	r_{AB} / Å	overlap
Na1	P1	2.83	0.059
	P1	2.877	0.027
	P1	3.196	0.025
	Al1	3.198	0.003
	Na2	3.448	0.003
	Na1	3.481	0.003
Na2	P1	2.812	0.04
	Na2	3.004	0.006
	Al1	3.234	0.005
	Al1	4.414	−0.001

Atom A	Atom B	r_{AB} / Å	overlap
Al1	P1	2.423	0.291
	Al1	3.004	0.008
P1	P1	3.801	−0.072

Table A.84: Partial charges for each atom position in Na_3AlP_2.

Atom	Z	charge	part charge
Na1	11	10.244	0.756
Na2		10.282	0.718
Al1	13	12.859	0.141

Atom	Z	charge	partialcharge
P1	15	16.185	−1.185

Na_3GaP_2[74]

For a crystal structure description see Na_3AlP_2.

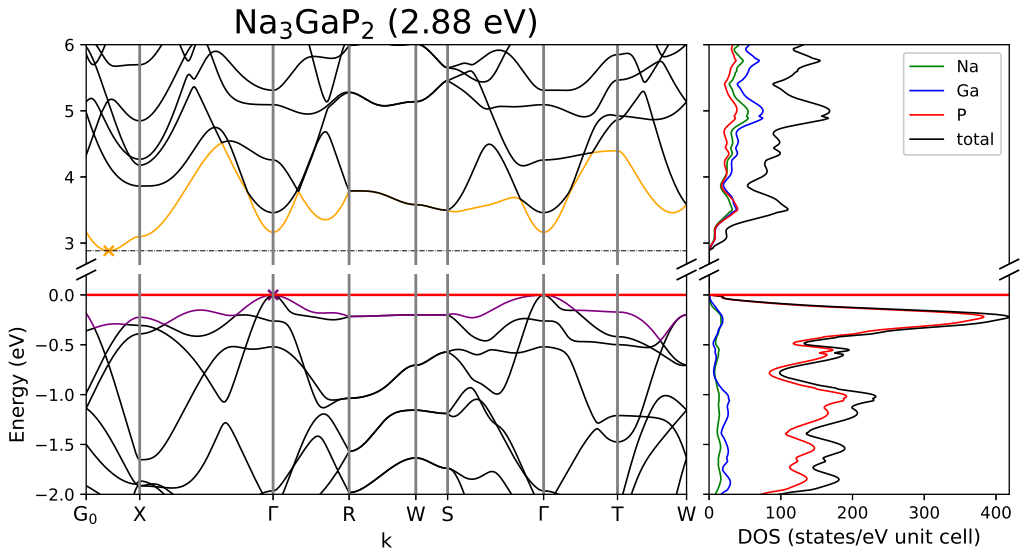

Figure A.49: Band structure and DOS of Na_3GaP_2.

Table A.85: Overlap population and interatomic distances of Na_3GaP_2.

Atom A	Atom B	r_{AB} / Å	overlap
Na1	P1	2.804	0.04
	Na1	3.061	0.006
	Ga1	3.17	0.002
	Na2	3.392	0.003
	Ga1	4.407	−0.001
	Na2	4.683	0.0
Na2	P1	2.834	0.061
	P1	2.88	0.028
	Ga1	3.21	0.001
	P1	3.237	0.021
	Na2	3.545	0.003

Atom A	Atom B	r_{AB} / Å	overlap
Ga1	P1	2.446	0.267
	Ga1	3.061	−0.038

Table A.86: Partial charges for each atom position in Na_3GaP_2.

Atom	Z	charge	part charge
Na1	11	10.276	0.724
Na2		10.237	0.763
Ga1	31	31.13	−0.13

Atom	Z	charge	partialcharge
P1	15	16.06	−1.06

K_3InP_2[29]

For a crystal structure description see Na_3AlP_2.

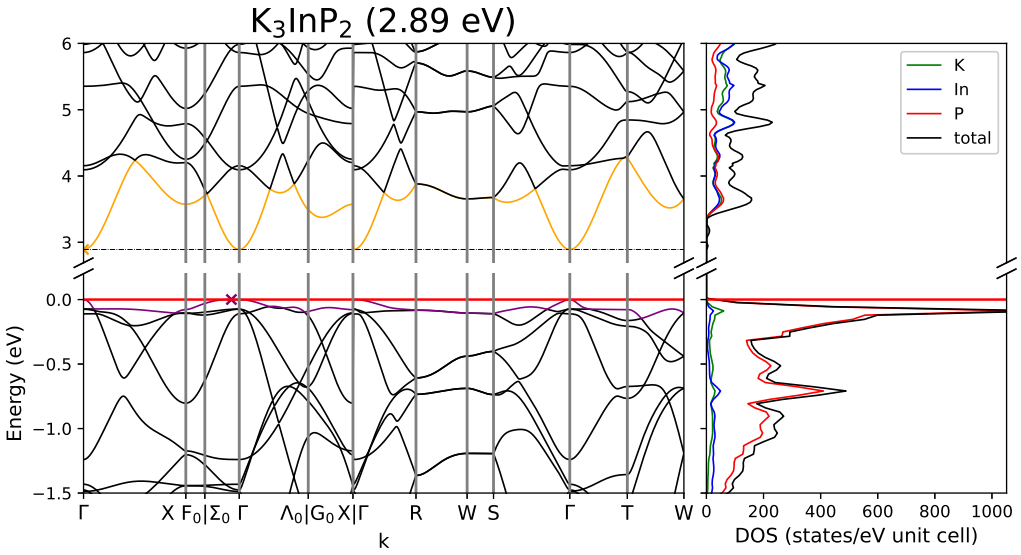

Figure A.50: Band structure and DOS of K_3InP_2.

Table A.87: Partial charges for each atom position in K_3InP_2.

Atom	Z	charge	part charge
K1	19	18.226	0.774
K2		18.26	0.74
In1	21	20.914	0.086

Atom	Z	charge	partialcharge
P1	15	16.187	−1.187

Table A.88: Overlap population and interatomic distances of K_3InP_2.

Atom A	Atom B	r_{AB} / Å	overlap
K1	P1	3.251	0.003
	P1	3.263	0.038
	In1	3.517	−0.01
	P1	3.605	0.014
	K2	3.825	0.001
	K1	3.963	0.002
K2	P1	3.202	0.016
	K2	3.39	−0.002
	In1	3.749	−0.009
	In1	5.055	0.0

Atom A	Atom B	r_{AB} / Å	overlap
In1	P1	2.646	0.261
	In1	3.39	−0.048
P1	P1	4.063	−0.052

Na_3AlAs_2[99]

For a crystal structure description see Na_3AlP_2.

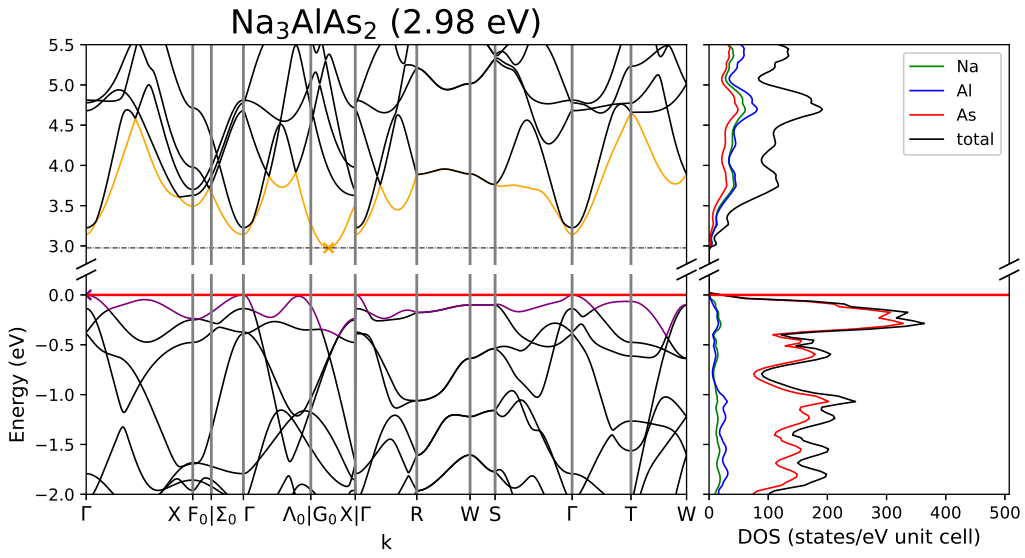

Figure A.51: Band structure and DOS of Na_3AlAs_2.

Table A.89: Overlap population and interatomic distances of Na_3AlAs_2.

Atom A	Atom B	r_{AB} / Å	overlap
Na1	As1	2.912	0.062
	As1	2.991	0.032
	As1	3.261	0.026
	Al1	3.298	0.006
	Na2	3.416	0.004
	Na1	3.622	0.002
Na2	As1	2.87	0.045
	Na2	3.094	0.006
	Al1	3.229	0.008
	Al1	4.472	−0.001

Atom A	Atom B	r_{AB} / Å	overlap
Al1	As1	2.52	0.283
	Al1	3.094	0.012

Table A.90: Partial charges for each atom position in Na_3AlAs_2.

Atom	Z	charge	part charge
Na1	11	10.27	0.73
Na2		10.319	0.681
Al1	13	12.743	0.257

Atom	Z	charge	partialcharge
As1	33	34.199	−1.199

K_3InAs_2[104]

For a crystal structure description see Na_3AlP_2.

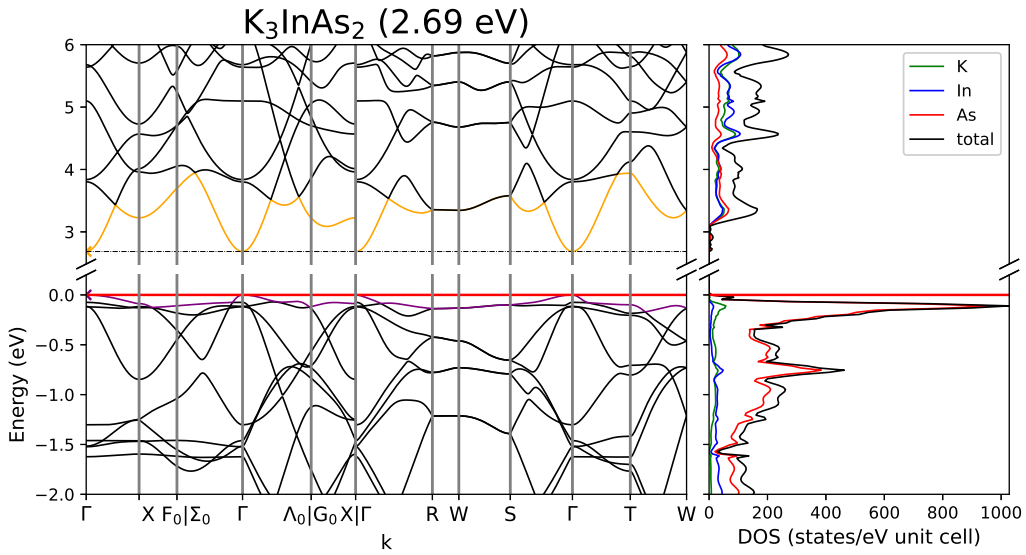

Figure A.52: Band structure and DOS of K_3InAs_2.

Table A.91: Overlap population and interatomic distances of K_3InAs_2.

Atom A	Atom B	r_{AB} / Å	overlap
K1	As1	3.333	0.01
	As1	3.339	0.043
	In1	3.572	−0.006
	As1	3.678	0.015
	K2	3.853	0.001
	K1	4.097	0.002
K2	As1	3.256	0.021
	K2	3.482	0.0
	In1	3.807	−0.007
	In1	5.159	0.0

Atom A	Atom B	r_{AB} / Å	overlap
In1	As1	2.728	0.254
	In1	3.482	−0.035

Table A.92: Partial charges for each atom position in K_3InAs_2.

Atom	Z	charge	part charge
K1	19	18.243	0.757
K2		18.286	0.714
In1	21	20.831	0.169

Atom	Z	charge	partialcharge
As1	33	34.198	−1.198

Na_3InP_2[30]

Na_3InP_2 crystallizes in space group $P\ 2_1/c$ (no. 14) and the InP_4 tetrahedra form a three-dimensional network via edge and vertex sharing. P forms a ccp, where half of the tetrahedral voids are filled by In and Na and all octahedral voids by Na.

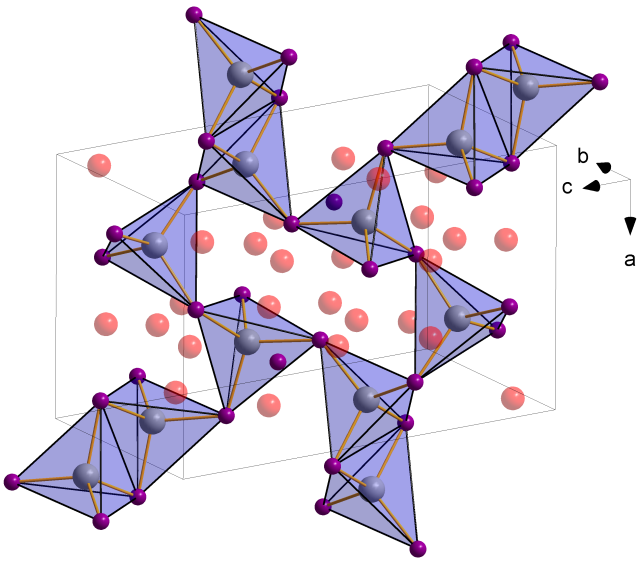

Figure A.53: Crystal structure of Na_3InP_2 forming a three dimensional network of edge and corner-sharing tetrahedra.

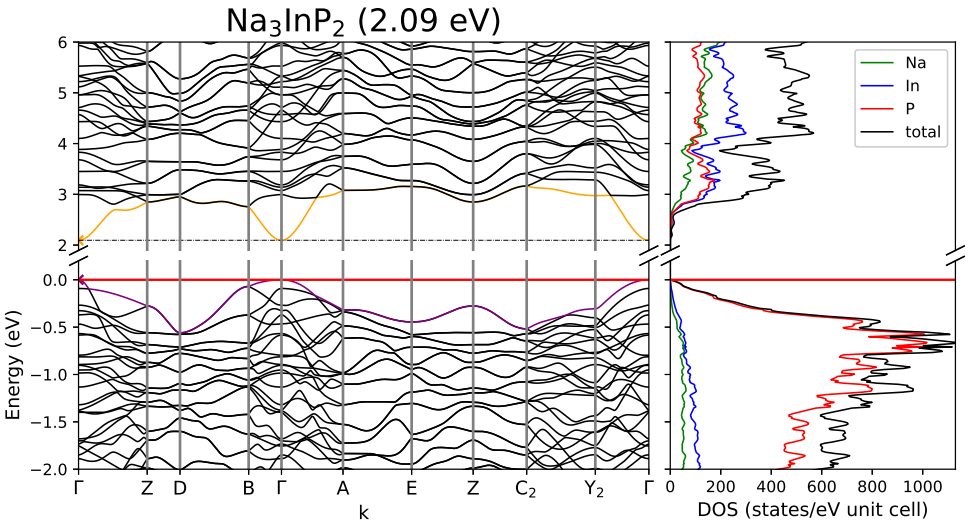

Figure A.54: Band structure and DOS of Na_3InP_2.

Table A.93: Partial charges for each atom position in Na_3InP_2.

Atom	Z	charge	part charge
Na1	11	10.266	0.734
Na2		10.232	0.768
Na3		10.242	0.758
Na4		10.305	0.695
Na5		10.227	0.773
Na6		10.231	0.769
In1	21	21.159	−0.159

Atom	Z	charge	partialcharge
In2		21.047	−0.047
P1	15	16.062	−1.062
P2		16.067	−1.067
P3		16.048	−1.048
P4		16.116	−1.116

Table A.94: Overlap population and interatomic distances of Na_3InP_2.

Atom A	Atom B	r_{AB} / Å	overlap
Na1	P4	2.779	0.042
	P3	2.831	0.043
	P2	2.86	0.052
	P2	2.867	0.023
	Na3	3.222	0.006
	Na5	3.237	0.004
Na2	P1	2.884	0.048
	P3	2.993	0.021
	P1	3.077	0.033
	P3	3.176	0.027
	In1	3.181	0.003
	Na4	3.219	0.006
Na3	P4	3.028	0.028
	P3	3.032	0.052
	P1	3.086	0.017
	P2	3.103	0.031
	In2	3.26	0.003
Na4	P3	2.785	0.041
	P4	2.817	0.052
	P1	2.85	0.057
	P1	2.86	0.04
	Na6	3.091	0.005
Na5	P4	2.933	0.037
	P4	3.007	0.033
	P2	3.067	0.034
	P1	3.182	0.013
Na6	P2	2.843	0.027
	P3	3.081	0.033
	P4	3.199	0.036
	P3	3.204	0.016
	P1	3.242	0.026
In1	P2	2.6	0.256
	P3	2.604	0.274
	P1	2.649	0.249
	P3	2.675	0.235
In2	P4	2.585	0.249
	P2	2.624	0.246
	P1	2.625	0.261
	P4	2.641	0.228

Na_3InAs_2[100]

For a crystal structure description see Na_3InP_2.

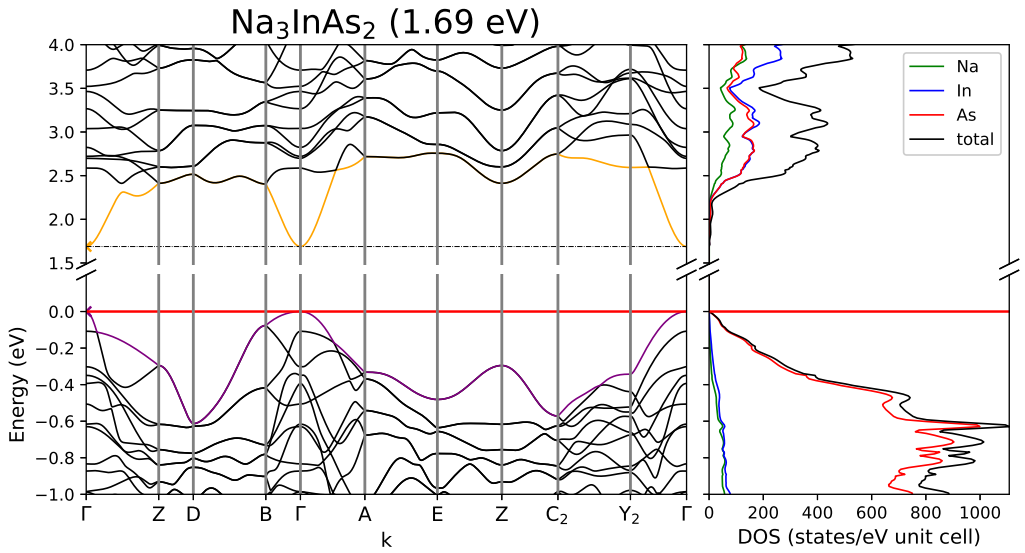

Figure A.55: Band structure and DOS of Na_3InAs_2.

Table A.95: Partial charges for each atom position in Na_3InAs_2.

Atom	Z	charge	part charge
Na1	11	10.293	0.707
Na2		10.26	0.74
Na3		10.269	0.731
Na4		10.332	0.668
Na5		10.251	0.749
Na6		10.257	0.743
In1	21	21.07	−0.07

Atom	Z	charge	partialcharge
In2		20.95	0.05
As1	33	34.078	−1.078
As2		34.067	−1.067
As3		34.049	−1.049
As4		34.125	−1.125

Table A.96: Overlap population and interatomic distances of Na_3InAs_2.

Atom A	Atom B	r_{AB} / Å	overlap
Na1	As4	2.851	0.047
	As3	2.899	0.047
	As2	2.927	0.055
	As2	2.943	0.028
	Na3	3.316	0.006
	In2	3.323	0.003
Na2	As1	2.969	0.051
	As3	3.073	0.026
	As1	3.127	0.035
	As3	3.226	0.03
	In1	3.267	0.006
	Na4	3.302	0.006
Na3	As4	3.094	0.033
	As3	3.104	0.053
	As1	3.158	0.021
	As2	3.159	0.033
	In2	3.339	0.006
Na4	As3	2.856	0.045
	As4	2.881	0.056
	As1	2.908	0.06
	As1	2.927	0.045
	Na6	3.19	0.006
Na5	As4	3.01	0.04
	As4	3.078	0.036
	As2	3.141	0.034
	As1	3.267	0.016
Na6	As2	2.929	0.032
	As3	3.138	0.035
	As4	3.279	0.035
	As3	3.281	0.018
	As1	3.291	0.029
In1	As2	2.682	0.253
	As3	2.689	0.268
	As1	2.733	0.248
	As3	2.763	0.242
In2	As4	2.671	0.245
	As1	2.707	0.253
	As2	2.707	0.248
	As4	2.724	0.227

Na_3InSb_2[101]

For a crystal structure description see Na_3InP_2.

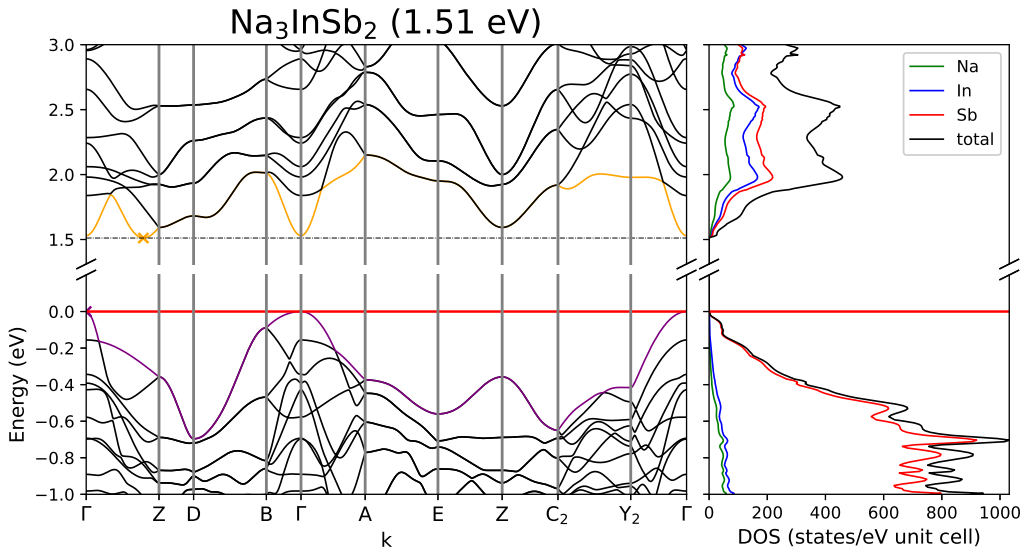

Figure A.56: Band structure and DOS of Na_3InSb_2.

Table A.97: Partial charges for each atom position in Na_3InSb_2.

Atom	Z	charge	part charge
Na1	11	10.292	0.708
Na2		10.257	0.743
Na3		10.262	0.738
Na4		10.324	0.676
Na5		10.251	0.749
Na6		10.258	0.742
In1	21	21.226	−0.226

Atom	Z	charge	partialcharge
In2		21.066	−0.066
Sb1	23	24.016	−1.016
Sb2		23.984	−0.984
Sb3		23.986	−0.986
Sb4		24.078	−1.078

Table A.98: Overlap population and interatomic distances of Na_3InSb_2.

Atom A	Atom B	r_{AB} / Å	overlap
Na1	Sb4	3.019	0.048
	Sb3	3.065	0.047
	Sb2	3.096	0.055
	Sb2	3.135	0.03
	In2	3.478	0.008
	Na5	3.506	0.004
Na2	Sb1	3.161	0.051
	Sb3	3.256	0.028
	Sb1	3.279	0.036
	Sb3	3.364	0.033
	In1	3.442	0.007
	Na4	3.491	0.004
Na3	Sb4	3.273	0.035
	Sb3	3.278	0.05
	Sb2	3.32	0.032
	Sb1	3.332	0.023
	In2	3.505	0.007
	Na4	3.545	0.003
Na4	Sb3	3.026	0.048
	Sb4	3.049	0.056
	Sb1	3.062	0.059
	Sb1	3.103	0.047
	Na6	3.39	0.004
Na5	Sb4	3.172	0.043
	Sb4	3.257	0.036
	Sb2	3.363	0.031
	Sb1	3.449	0.016
	Sb2	3.49	0.028
Na6	Sb2	3.119	0.034
	Sb3	3.297	0.036
	Sb1	3.418	0.033
	Sb4	3.471	0.033
	Sb3	3.495	0.019
In1	Sb2	2.864	0.252
	Sb3	2.874	0.259
	Sb1	2.916	0.251
	Sb3	2.955	0.243
In2	Sb4	2.855	0.243
	Sb2	2.887	0.246
	Sb1	2.896	0.248
	Sb4	2.91	0.228

Na_3InBi_2[102]

Na_3InBi_2 crystallizes in space group $P\ 2_1/c$ (no. 14) and the InP_4 tetrahedra form a three-dimensional network via edge and vertex sharing.

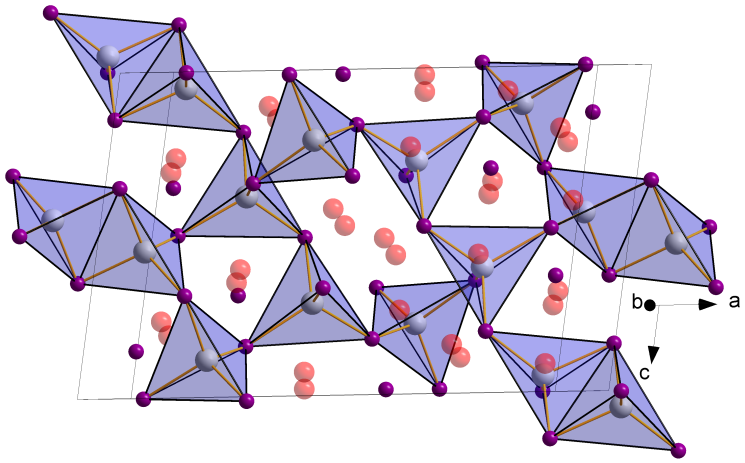

Figure A.57: Crystal structure of Na_3InBi_2 forming a three dimensional network of edge and corner-sharing tetrahedra.

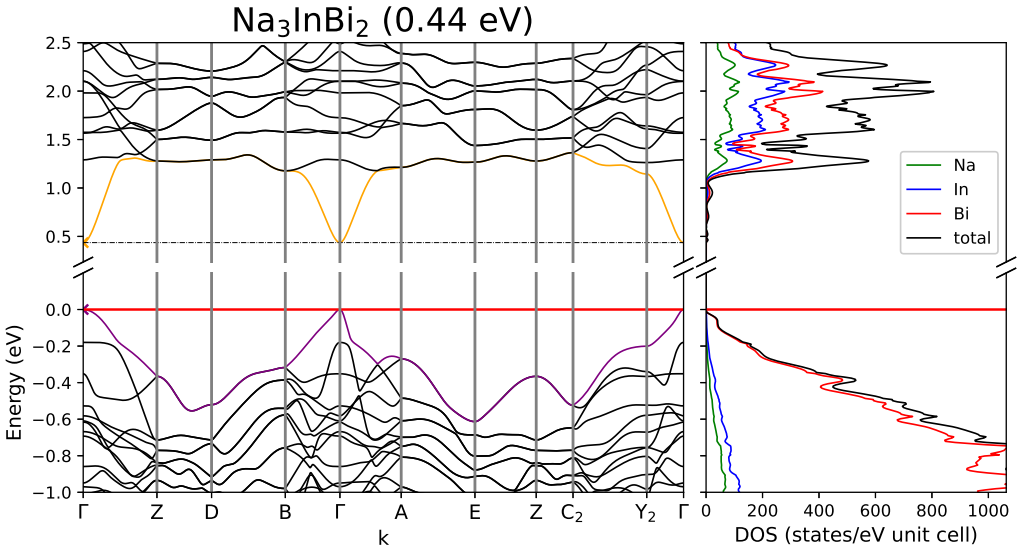

Figure A.58: Band structure and DOS of Na_3InBi_2.

Table A.99: Overlap population and interatomic distances of Na_3InBi_2.

Atom A	Atom B	r_{AB} / Å	overlap
Bi1	In1	2.976	0.25
	In3	3.02	0.236
	Na3	3.076	0.037
	Na2	3.076	0.042
	Na5	3.292	0.043
	Na7	3.327	0.029
Bi2	In2	2.972	0.234
	In1	2.979	0.229
	Na2	3.14	0.046
	Na1	3.205	0.025
	Na4	3.205	0.028
	Na8	3.358	0.03
Bi3	In2	2.96	0.23
	In2	2.994	0.206
	Na1	3.097	0.05
	Na1	3.132	0.041
	Na7	3.242	0.039
	Na5	3.309	0.031
Bi4	In3	2.976	0.245
	In3	3.053	0.226
	Na3	3.101	0.047
	Na3	3.2	0.041
	Na8	3.261	0.041
	Na8	3.316	0.026
Bi5	In2	2.94	0.25
	In1	3.014	0.223
	Na1	3.082	0.04
	Na2	3.119	0.042
	Na6	3.283	0.037
	Na7	3.382	0.03
Bi6	In1	2.951	0.243
	In3	2.956	0.244
	Na3	3.151	0.047
	Na9	3.168	0.033
	Na2	3.181	0.026
	Na8	3.335	0.029
In1	Na7	3.429	0.008
	Na4	3.524	0.008
In2	Na1	3.523	0.01
	Na7	3.537	0.007
In3	Na4	3.497	0.009
	Na2	3.538	0.008
Na1	Na6	3.526	0.002
Na3	Na9	3.546	0.003

Table A.100: Partial charges for each atom position in Na_3InBi_2.

Atom	Z	charge	part charge
Bi1	23	23.988	−0.988
Bi2		24.003	−1.003
Bi3		24.096	−1.096
Bi4		24.017	−1.017
Bi5		24.016	−1.016
Bi6		23.948	−0.948
In1	21	21.313	−0.313
In2		21.172	−0.172
In3		21.315	−0.315
Na1	11	10.255	0.745
Na2		10.255	0.745
Na3		10.269	0.731
Na4		10.192	0.808
Na5		10.24	0.76
Na6		10.252	0.748
Na7		10.222	0.778
Na8		10.232	0.768
Na9		10.214	0.786

K_3AlP_2[103]

K_3AlP_2 crystallizes in group $P\,\bar{1}$ (no. 2) incorporating two different structural motives. On one hand edge-sharing AlP_4 tetrahedra are forming one dimensional chains along b, on the other isolated, dimeric slightly bent triangular planar $[Al_2P_4]^{6-}$ units, with a dihedral angle of 3.6 °.

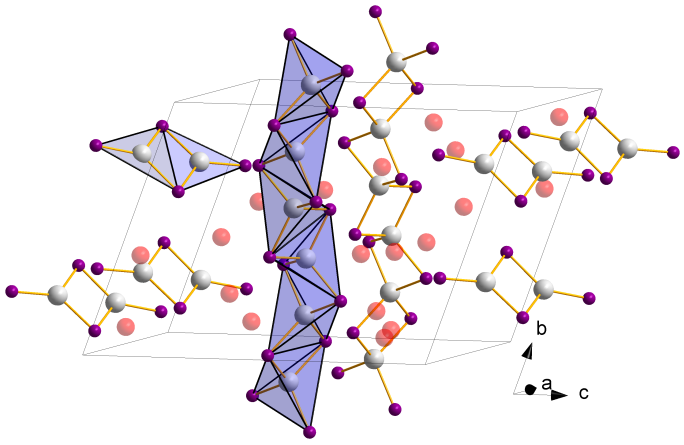

Figure A.59: Crystal structure of K_3AlP_2 with one dimensional chains of edge-sharing AlP_4 tetrahedra and isolated, dimeric triangular planar $[Al_2P_4]^{6-}$ units.

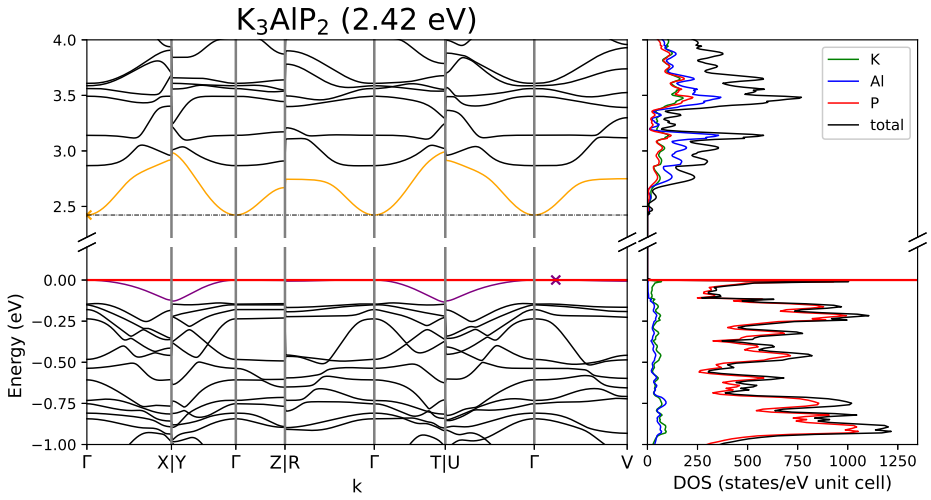

Figure A.60: Band structure and DOS of K_3AlP_2.

Table A.101: Overlap population and interatomic distances of K_3AlP_2.

Atom A	Atom B	r_{AB} / Å	overlap
K1	K4	3.112	−0.006
	P8	3.17	−0.001
	Al2	3.269	−0.015
	P1	3.309	0.009
	Al2	3.325	−0.013
	K7	3.34	−0.003
K2	P3	3.302	0.011
	Al1	3.338	−0.011
	P4	3.398	0.009
	Al1	3.418	−0.008
	P6	3.494	0.02
	P1	3.499	0.018
K3	P3	3.164	0.013
	P2	3.217	0.023
	P5	3.362	0.025
	P4	3.365	0.025
	K4	3.478	−0.001
	Al2	3.614	−0.009
K4	P3	3.076	0.014
	P4	3.092	0.026
	P2	3.272	0.019
	P5	3.338	0.024
K5	P1	3.217	0.018
	P6	3.235	0.026
	P7	3.364	0.022
	P4	3.397	0.032
	K10	3.478	0.0
K6	P1	3.227	0.016
	P2	3.246	0.024
	P4	3.469	0.027
	P2	3.571	0.036
	Al2	3.721	−0.006
K7	P6	3.155	0.025
	P2	3.265	0.027
	P8	3.356	0.02
	P1	3.391	0.022
	K10	3.616	0.0
K8	P6	3.281	0.02
	P3	3.33	0.041
	Al3	3.397	−0.001
	Al4	3.529	−0.002
	P8	3.561	0.013
K9	P1	3.199	0.038
	P5	3.427	0.022
	P7	3.465	0.014
	Al3	3.498	−0.002
	P8	3.524	0.016
	Al4	3.591	0.002
K10	K10	3.278	−0.001
	P1	3.424	0.016
	P3	3.445	0.013
	P4	3.495	0.029
K11	P5	3.231	0.026
	K11	3.253	−0.002
	K12	3.298	−0.002
	P8	3.334	0.019
	P6	3.4	0.029
	P8	3.563	0.011
K12	P7	3.219	0.024
	P5	3.302	0.026
	P6	3.406	0.027
	P7	3.626	0.012
	Al3	3.677	−0.001
Al1	P4	2.43	0.324
	P1	2.432	0.308
	P3	2.441	0.303
	P4	2.454	0.302
	Al2	3.061	−0.013
	Al1	3.227	−0.014
Al2	P1	2.434	0.308
	P2	2.443	0.33
	P3	2.453	0.309
	P2	2.512	0.285
Al3	P5	2.251	0.505
	P7	2.359	0.333
	P8	2.383	0.308
	Al4	2.935	−0.032
Al4	P6	2.232	0.503
	P8	2.324	0.333
	P7	2.374	0.307

Table A.102: Partial charges for each atom position in K_3AlP_2.

Atom	Z	charge	part charge
K1	19	18.218	0.782
K2		18.229	0.771
K3		18.256	0.744
K4		18.282	0.718
K5		18.259	0.741
K6		18.286	0.714
K7		18.267	0.733
K8		18.25	0.75
K9		18.255	0.745
K10		18.256	0.744
K11		18.256	0.744
K12		18.251	0.749
Al1	13	12.755	0.245
Al2		12.807	0.193
Al3		12.975	0.025
Al4		12.941	0.059
P1	15	16.211	−1.211
P2		16.219	−1.219
P3		16.212	−1.212
P4		16.193	−1.193
P5		16.256	−1.256
P6		16.263	−1.263
P7		16.054	−1.054
P8		16.05	−1.05

Rb_3InP_2[31]

For a crystal structure description see K_3AlP_2.

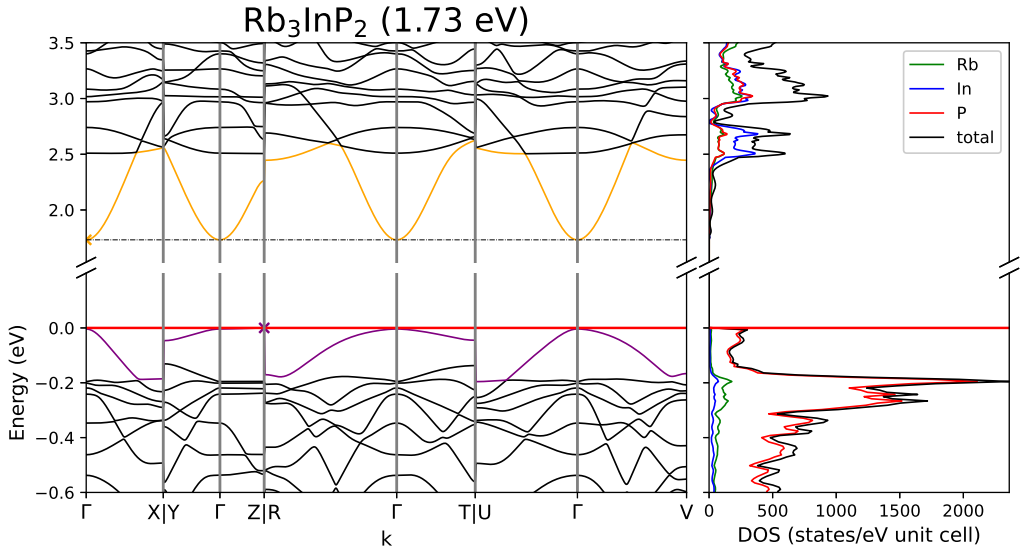

Figure A.61: Band structure and DOS of Rb_3InP_2.

Table A.103: Overlap population and interatomic distances of Rb_3InP_2.

Atom A	Atom B	r_{AB} / Å	overlap
In1	P2	2.634	0.259
	P3	2.647	0.269
	P1	2.649	0.255
	P3	2.71	0.244
	In2	3.33	−0.042
	Rb1	3.465	−0.021
In2	P2	2.631	0.257
	P4	2.633	0.264
	P4	2.646	0.254
	P1	2.648	0.253
	In2	3.535	−0.042
In3	P5	2.434	0.415
	P6	2.56	0.296
	P7	2.596	0.272
	In4	3.305	−0.096
	Rb4	3.66	−0.006
	Rb1	3.729	−0.016
In4	P8	2.414	0.391
	P7	2.525	0.295
	P6	2.584	0.271
	Rb4	3.801	−0.008
	Rb7	3.884	−0.003
Rb1	P7	3.341	0.003
	Rb2	3.357	−0.013
	P2	3.518	0.012
	Rb8	3.545	−0.007
Rb2	P4	3.253	0.028
	P1	3.287	0.021
	P3	3.477	0.026
	P5	3.512	0.028
	Rb5	3.755	−0.003
Rb3	P1	3.562	0.014
	P4	3.603	0.013
	Rb9	3.751	−0.002
	P8	3.76	0.019
Rb4	P8	3.448	0.027
	P1	3.506	0.045
	P7	3.858	0.013
Rb5	P1	3.396	0.022
	P3	3.413	0.03
	P5	3.555	0.026
	P4	3.586	0.029
Rb6	P3	3.45	0.031
	P2	3.459	0.024
	P4	3.725	0.029
	P3	3.816	0.033
Rb7	P2	3.373	0.044
	P5	3.66	0.024
	P6	3.677	0.016
	P7	3.746	0.018
Rb8	P8	3.354	0.034
	P3	3.486	0.033
	P7	3.55	0.025
	P2	3.612	0.027
	Rb10	3.816	−0.002
Rb9	P8	3.372	0.027
	P2	3.374	0.025
	P6	3.551	0.029
	P4	3.624	0.034
	Rb10	3.749	−0.003
Rb10	Rb10	3.533	−0.005
	P2	3.644	0.018
	P1	3.66	0.018
	P4	3.692	0.031
	P1	3.798	0.024
Rb11	P5	3.381	0.032
	Rb11	3.483	−0.008
	P7	3.507	0.028
	Rb12	3.545	−0.006
	P8	3.565	0.03
	P7	3.696	0.012
Rb12	P6	3.383	0.033
	P5	3.523	0.029
	P8	3.561	0.034
	P6	3.811	0.011

Table A.104: Partial charges for each atom position in Rb_3InP_2.

Atom	Z	charge	part charge
In1	21	20.945	0.055
In2		20.891	0.109
In3		21.155	−0.155
In4		21.13	−0.13
Rb1	9	8.26	0.74
Rb2		8.346	0.654
Rb3		8.269	0.731
Rb4		8.294	0.706
Rb5		8.312	0.688
Rb6		8.339	0.661
Rb7		8.3	0.7
Rb8		8.33	0.67
Rb9		8.317	0.683
Rb10		8.295	0.705
Rb11		8.304	0.696
Rb12		8.306	0.694
P1	15	16.055	−1.055
P2		16.052	−1.052
P3		16.072	−1.072
P4		16.057	−1.057
P5		16.072	−1.072
P6		15.918	−0.918
P7		15.918	−0.918
P8		16.064	−1.064

K_3AlAs_2[105]

For a crystal structure description see K_3AlP_2.

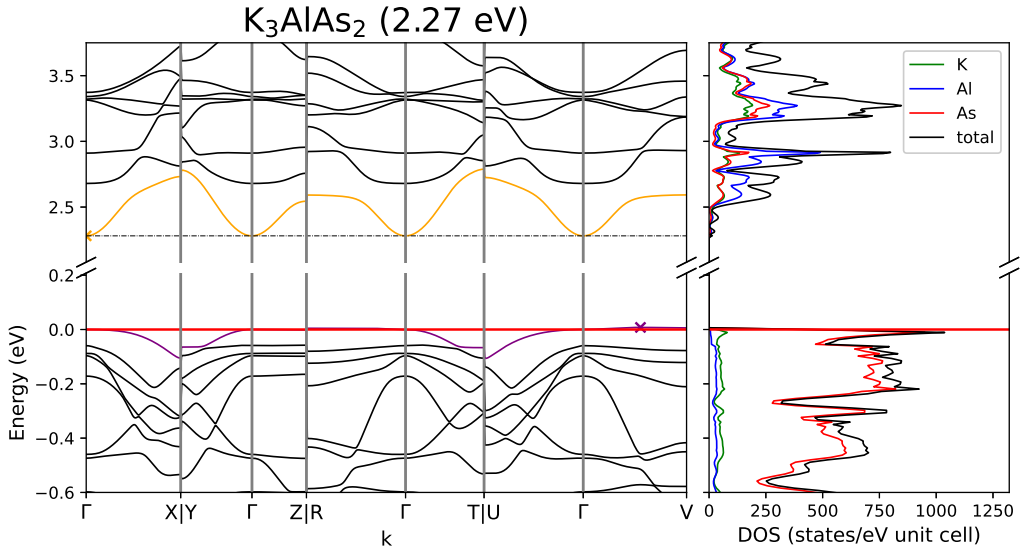

Figure A.62: Band structure and DOS of K_3AlAs_2.

Table A.105: Overlap population and interatomic distances of K_3AlAs_2.

Atom A	Atom B	r_{AB} / Å	overlap
K1	K4	3.174	−0.005
	As8	3.222	0.002
	Al2	3.321	−0.01
	As1	3.364	0.012
	Al2	3.373	−0.008
	As2	3.451	0.009
K2	As3	3.379	0.015
	Al1	3.399	−0.006
	Al1	3.472	−0.004
	As4	3.496	0.013
	As1	3.545	0.021
	As6	3.549	0.025
K3	As3	3.244	0.022
	As2	3.274	0.026
	As4	3.424	0.029
	As5	3.452	0.029
	K4	3.541	0.0
	Al2	3.686	−0.005
K4	As3	3.146	0.019
	As4	3.155	0.033
	As2	3.326	0.024
	As5	3.398	0.029
K5	As6	3.288	0.029
	As1	3.29	0.023
	As7	3.446	0.027
	As4	3.449	0.037
	K10	3.546	0.001
K6	As2	3.289	0.028
	As1	3.339	0.023
	As4	3.519	0.03
	As2	3.632	0.037
K7	As6	3.235	0.032
	As2	3.334	0.033
	As8	3.393	0.022
	As1	3.528	0.025
	K10	3.751	0.001
K8	As6	3.372	0.026
	As3	3.404	0.045
	Al3	3.459	0.002
	As8	3.578	0.017
	Al4	3.581	0.002
K9	As1	3.25	0.042
	As5	3.453	0.027
	As7	3.557	0.018
	Al3	3.562	0.002
	Al4	3.611	0.005
	As8	3.689	0.018
K10	K10	3.375	0.0
	As1	3.473	0.02
	As3	3.492	0.018
	As4	3.518	0.033
	Al1	3.696	−0.002
K11	As5	3.313	0.032
	K11	3.337	0.0
	K12	3.352	−0.001
	As8	3.399	0.026
	As6	3.449	0.036
	As8	3.739	0.011
K12	As7	3.304	0.032
	As5	3.393	0.031
	As6	3.505	0.031
	As7	3.631	0.014
	Al3	3.731	0.0
Al1	As1	2.517	0.3
	As4	2.524	0.309
	As3	2.533	0.294
	As4	2.539	0.296
	Al2	3.11	−0.004
	Al1	3.318	−0.016
Al2	As1	2.523	0.3
	As2	2.532	0.317
	As3	2.552	0.3
	As2	2.606	0.278
Al3	As5	2.347	0.482
	As7	2.457	0.323
	As8	2.481	0.3
	Al4	3.025	−0.023
Al4	As6	2.321	0.484
	As8	2.412	0.327
	As7	2.469	0.296

Table A.106: Partial charges for each atom position in K_3AlAs_2.

Atom	Z	charge	part charge
K1	19	18.245	0.755
K2		18.257	0.743
K3		18.281	0.719
K4		18.3	0.7
K5		18.277	0.723
K6		18.31	0.69
K7		18.288	0.712
K8		18.275	0.725
K9		18.278	0.722
K10		18.279	0.721
K11		18.283	0.717
K12		18.274	0.726
Al1	13	12.638	0.362
Al2		12.705	0.295
Al3		12.868	0.132
Al4		12.82	0.18
As1	33	34.232	−1.232
As2		34.233	−1.233
As3		34.23	−1.23
As4		34.219	−1.219
As5		34.253	−1.253
As6		34.261	−1.261
As7		34.1	−1.1
As8		34.095	−1.095

Cs_3InP_2[156]

Cs_3InP_2 crystallizes in group $P\ \bar{1}$ (no. 2) incorporating two different structural motives. On one hand edge-sharing InP_4 tetrahedra are forming one dimensional chains along b, on the other isolated, dimeric triangular planar $[In_2P_4]^{6-}$ units. Compared to the structure of K_3AlP_2 the unit cell is shifted by ½ along the c-axis and the triangular planar units are not bent.

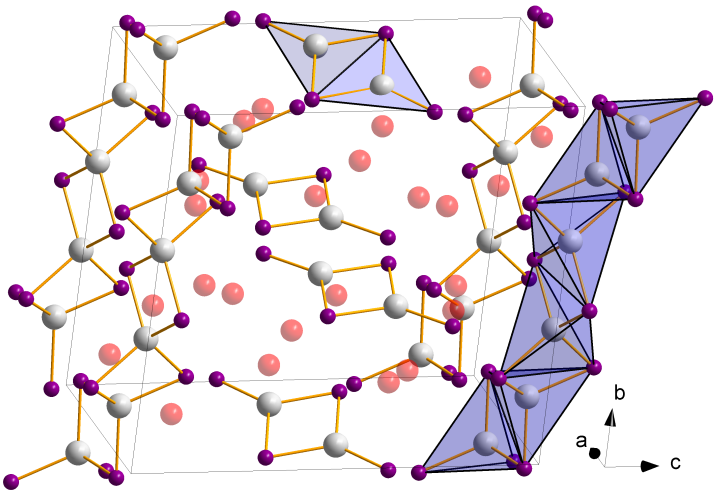

Figure A.63: Crystal structure of Cs_3InP_4 with one dimensional chains of edge-sharing InP_4 tetrahedra and isolated, dimeric triangular planar $[In_2P_4]^{6-}$ units.

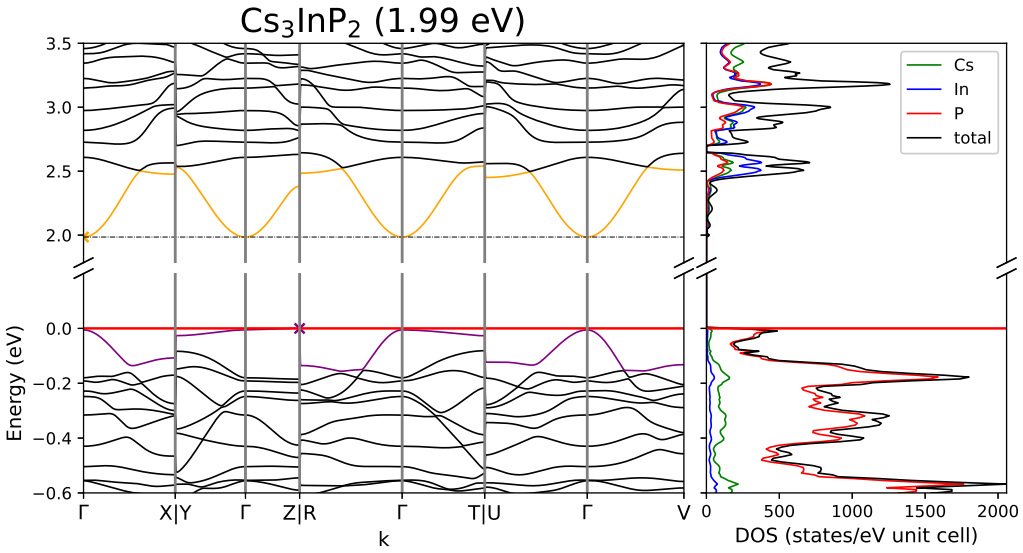

Figure A.64: Band structure and DOS of Cs_3InP_2.

Table A.107: Overlap population and interatomic distances of Cs_3InP_2.

Atom A	Atom B	r_{AB} / Å	overlap
Cs1	P5	3.482	0.009
	P6	3.492	0.004
	In1	3.577	−0.019
	Cs7	3.634	0.006
	P4	3.702	0.008
	In1	3.769	−0.009
Cs2	P3	3.535	0.012
	P1	3.623	0.009
	In2	3.655	−0.014
	P2	3.771	0.01
	In2	3.774	−0.009
	Cs6	3.877	0.006
Cs3	P3	3.438	0.014
	P4	3.516	0.027
	P1	3.548	0.028
	Cs7	3.822	0.006
	In1	3.927	−0.011
	P8	3.93	0.02
Cs4	P3	3.565	0.04
	P7	3.577	0.025
	P2	3.788	0.017
	In3	3.836	−0.009
	In4	3.858	0.005
	P6	3.969	0.015
Cs5	P5	3.486	0.017
	P4	3.513	0.03
	P1	3.817	0.027
	P4	4.049	0.027
	In1	4.059	−0.008
Cs6	P5	3.419	0.022
	P7	3.504	0.024
	P1	3.63	0.031
	P2	3.68	0.026
	Cs12	3.847	0.006
Cs7	P3	3.367	0.02
	P1	3.501	0.027
	P4	3.628	0.029
	P8	3.811	0.028
Cs8	P7	3.507	0.027
	P7	3.736	0.032
	P6	3.785	0.022
	In3	3.901	−0.009
	P2	3.927	0.011
Cs9	P5	3.614	0.038
	In4	3.754	−0.007
	P8	3.774	0.025
	P2	3.872	0.014
	P6	3.887	0.019
	In3	3.967	0.002
Cs10	P2	3.512	0.028
	Cs10	3.653	0.007
	P6	3.72	0.019
	P8	3.759	0.035
	In4	3.805	−0.006
	P8	3.889	0.022
Cs11	P7	3.593	0.035
	P6	3.755	0.029
	P8	3.856	0.03
	P4	3.899	0.029
Cs12	P5	3.622	0.013
	P3	3.627	0.013
	Cs12	3.864	0.007
	In2	3.902	−0.006
	In1	3.93	−0.005
In1	P4	2.633	0.275
	P3	2.644	0.254
	P5	2.66	0.261
	P4	2.716	0.244
	In2	3.367	−0.06
	In1	3.541	−0.058
In2	P5	2.632	0.26
	P1	2.644	0.267
	P3	2.656	0.25
	P1	2.661	0.255
	In2	3.485	−0.045
In3	P7	2.431	0.387
	P2	2.548	0.292
	P2	2.587	0.279
	In3	3.284	−0.102
In4	P8	2.444	0.416
	P6	2.545	0.298
	P6	2.616	0.247
	In4	3.352	−0.1

Table A.108: Partial charges for each atom position in Cs_3InP_2.

Atom	Z	charge	part charge
Cs1	9	8.239	0.761
Cs2		8.246	0.754
Cs3		8.301	0.699
Cs4		8.288	0.712
Cs5		8.327	0.673
Cs6		8.307	0.693
Cs7		8.334	0.666
Cs8		8.281	0.719
Cs9		8.268	0.732
Cs10		8.292	0.708
Cs11		8.311	0.689
Cs12		8.263	0.737
In1	21	20.944	0.056

Atom	Z	charge	partialcharge
In2		20.909	0.091
In3		21.13	−0.13
In4		21.15	−0.15
P1	15	16.081	−1.081
P2		15.947	−0.947
P3		16.091	−1.091
P4		16.079	−1.079
P5		16.077	−1.077
P6		15.95	−0.95
P7		16.089	−1.089
P8		16.096	−1.096

Rb_3GaP_2[157]

Rb_3GaP_2 crystallizes in space group *P b c a* (no.61) and incorporates edge-sharing triangular planar $[Ga_2P_4]^{6-}$ units. Their geometry is slightly bent with a dihedral angle of 14.6 °.

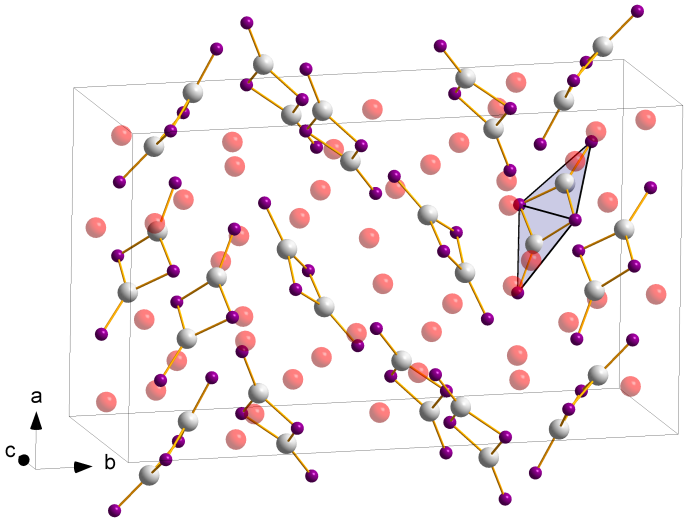

Figure A.65: Crystal structure of Rb_3GaP_2 with edge-sharing triangular planar $[Ga_2P_4]^{6-}$ units.

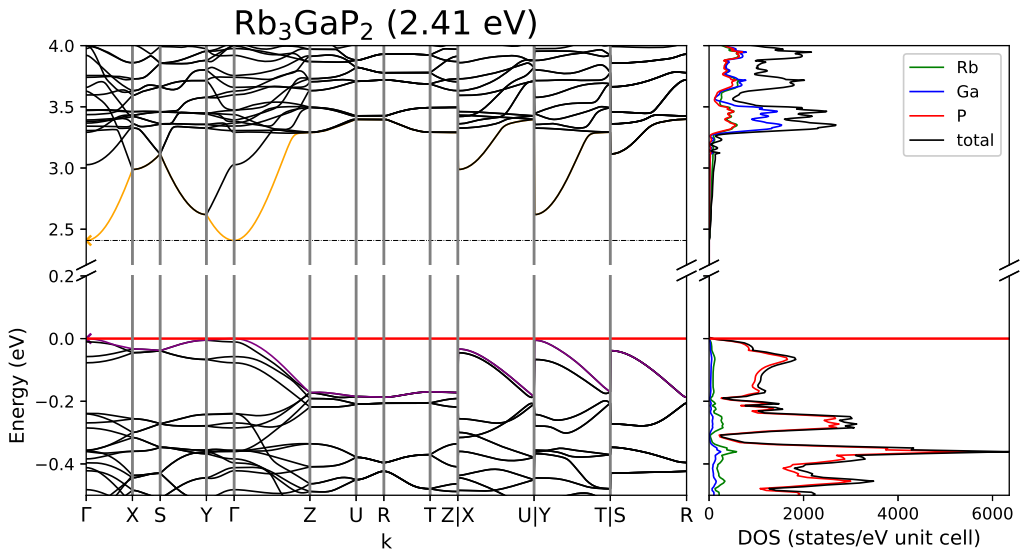

Figure A.66: Band structure and DOS of Rb_3GaP_2.

Table A.109: Partial charges for each atom position in Rb_3GaP_2.

Atom	Z	charge	part charge
Rb1	9	8.3	0.7
Rb2		8.31	0.69
Rb3		8.288	0.712
Rb4		8.268	0.732
Rb5		8.312	0.688
Rb6		8.306	0.694
Ga1	31	31.246	−0.246

Atom	Z	charge	partialcharge
Ga2		31.192	−0.192
P1	15	15.848	−0.848
P2		16.086	−1.086
P3		15.798	−0.798
P4		16.047	−1.047

Table A.110: Overlap population and interatomic distances of Rb_3GaP_2.

Atom A	Atom B	r_{AB} / Å	overlap
Rb1	P2	3.412	0.018
	P4	3.476	0.03
	P1	3.521	0.013
	Ga1	3.559	−0.015
	P2	3.568	0.029
	Rb5	3.663	−0.004
Rb2	P4	3.363	0.032
	P4	3.389	0.029
	P3	3.496	0.018
	P2	3.63	0.024
	Ga1	3.771	−0.011
	Rb6	3.895	−0.001
Rb3	P1	3.491	0.016
	P3	3.52	0.016
	Ga1	3.536	−0.012
	Ga1	3.589	−0.011
	P2	3.594	0.028
	P2	3.642	0.022
Rb4	P4	3.368	0.032
	P3	3.372	0.017
	Ga2	3.634	−0.01
	P4	3.641	0.022
	Ga1	3.664	−0.003
	Ga2	3.77	−0.001
Rb5	P2	3.468	0.033
	P3	3.571	0.014
	P2	3.603	0.037
	Ga2	3.662	−0.007
	P1	3.677	0.028
Rb6	P4	3.58	0.031
	P1	3.59	0.018
	P3	3.652	0.028
	P2	3.734	0.032
	Ga2	3.842	−0.006
Ga1	P2	2.27	0.423
	P3	2.347	0.325
	P1	2.4	0.308
	Ga2	2.991	−0.087
Ga2	P4	2.243	0.46
	P3	2.384	0.318
	P1	2.392	0.299

Cs_3AlP_2[106]

Cs_3AlP_2 crystallizes in space group $P\ 2_1/c$ (no. 14). The structural motive is the same as in Rb_3GaP_2, but the edge-sharing triangular planar $[Al_2P_4]^{6-}$ units do not show a dihedral angle.

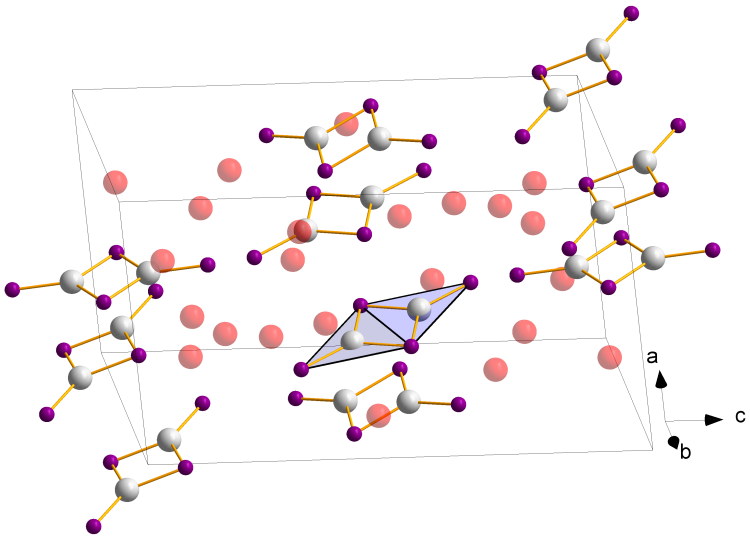

Figure A.67: Crystal structure of Cs_3AlP_2 with edge-sharing triangular planar $[Al_2P_4]^{6-}$ units.

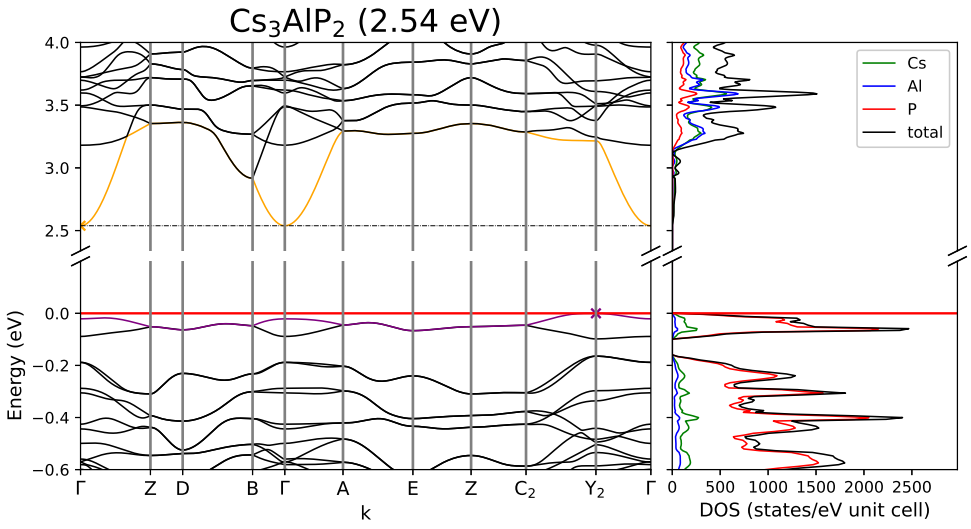

Figure A.68: Band structure and DOS of Cs_3AlP_2.

Table A.111: Overlap population and interatomic distances of Cs_3AlP_2.

Atom A	Atom B	r_{AB} / Å	overlap
Cs1	P4	3.511	0.016
	P1	3.555	0.034
	P1	3.647	0.029
	P2	3.659	0.032
	Al2	3.833	−0.003
	Cs5	4.103	0.004
Cs2	P2	3.49	0.022
	P3	3.491	0.012
	P1	3.662	0.033
	P2	3.734	0.024
	Al1	3.801	−0.006
	Cs4	3.801	0.006
Cs3	Al2	3.572	0.007
	P3	3.646	0.016
	P2	3.692	0.03
	P4	3.8	0.012
	Al1	3.804	−0.002
	Cs4	3.904	0.006
Cs4	P2	3.63	0.024
	Al2	3.729	0.004
	P1	3.774	0.022
	P3	3.797	0.014
	Al1	3.886	−0.001

Atom A	Atom B	r_{AB} / Å	overlap
Cs5	P4	3.54	0.021
	P1	3.564	0.029
	P2	3.669	0.028
	Al1	3.744	0.003
	P3	3.905	0.014
Cs6	P4	3.599	0.017
	P1	3.784	0.028
	Al2	3.831	0.001
	Al1	3.839	0.009
	Cs6	3.848	0.005
	P1	3.883	0.02
Al1	P2	2.272	0.471
	P3	2.36	0.34
	P3	2.373	0.327
	Al1	2.922	−0.04
Al2	P1	2.246	0.497
	P4	2.345	0.328
	P4	2.351	0.316
	Al2	2.913	−0.037
P3	P3	3.723	−0.08
P4	P4	3.683	−0.09

Table A.112: Partial charges for each atom position in Cs_3AlP_2.

Atom	Z	charge	part charge
Cs1	9	8.318	0.682
Cs2		8.3	0.7
Cs3		8.271	0.729
Cs4		8.292	0.708
Cs5		8.294	0.706
Cs6		8.269	0.731
Al1	13	12.909	0.091

Atom	Z	charge	partialcharge
Al2		12.926	0.074
P1	15	16.213	−1.213
P2		16.233	−1.233
P3		15.989	−0.989
P4		15.985	−0.985

Cs_3GaP_2[107]

For a crystal structure description see Cs_3AlP_2.

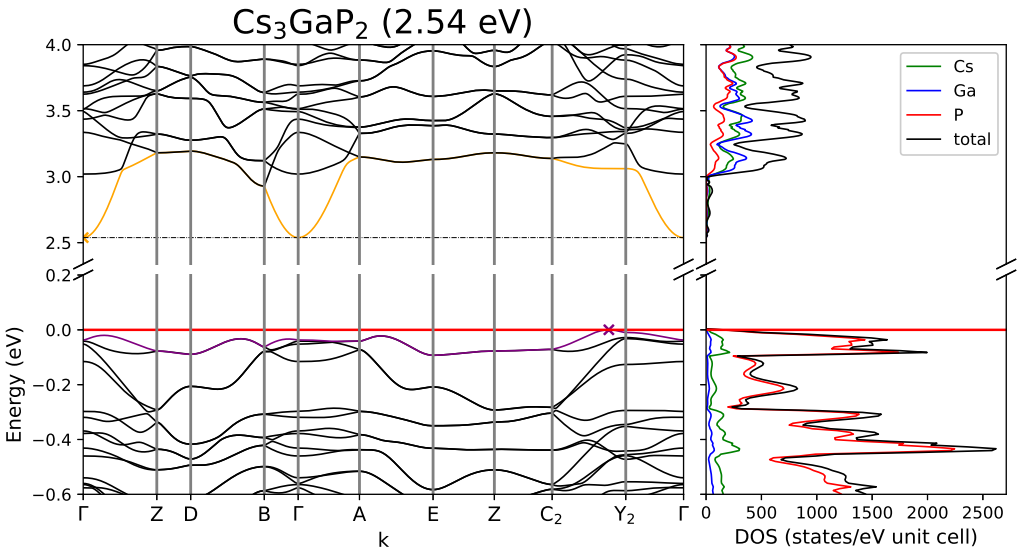

Figure A.69: Band structure and DOS of Cs_3GaP_2.

Table A.113: Overlap population and interatomic distances of Cs_3GaP_2.

Atom A	Atom B	r_{AB} / Å	overlap
Cs1	P4	3.625	0.023
	Ga1	3.71	−0.003
	P1	3.764	0.02
	P3	3.769	0.014
	Cs6	3.814	0.006
	Ga2	3.859	−0.008
Cs2	P1	3.527	0.029
	P2	3.556	0.024
	P4	3.637	0.027
	Ga2	3.711	−0.003
	P3	3.893	0.015
	Cs6	3.959	0.007
Cs3	P2	3.579	0.019
	P1	3.803	0.026
	Ga1	3.809	−0.005
	Ga2	3.826	0.004
	Cs3	3.851	0.005
	P1	3.889	0.018
Cs4	Ga1	3.569	0.0
	P3	3.642	0.016
	P4	3.716	0.029
	P2	3.768	0.013
	Ga2	3.782	−0.009
Cs5	P2	3.493	0.018
	P1	3.547	0.034
	P4	3.644	0.033
	P1	3.648	0.028
	Ga1	3.787	−0.011
Cs6	P3	3.473	0.012
	P4	3.491	0.021
	P1	3.65	0.034
	P4	3.727	0.025
	Ga2	3.754	−0.014
Ga1	P1	2.251	0.463
	P2	2.363	0.313
	P2	2.366	0.301
	Ga1	3.006	−0.08
Ga2	P4	2.277	0.423
	P3	2.375	0.328
	P3	2.39	0.315
	Ga2	3.01	−0.082
P2	P2	3.651	−0.08
P3	P3	3.694	−0.071

Table A.114: Partial charges for each atom position in Cs_3GaP_2.

Atom	Z	charge	part charge
Cs1	9	8.281	0.719
Cs2		8.291	0.709
Cs3		8.25	0.75
Cs4		8.256	0.744
Cs5		8.315	0.685
Cs6		8.298	0.702
Ga1	31	31.203	−0.203
Ga2		31.197	−0.197
P1	15	16.109	−1.109
P2		15.837	−0.837
P3		15.836	−0.836
P4		16.126	−1.126

Cs_3AlAs_2[108]

For a crystal structure description see Cs_3AlP_2.

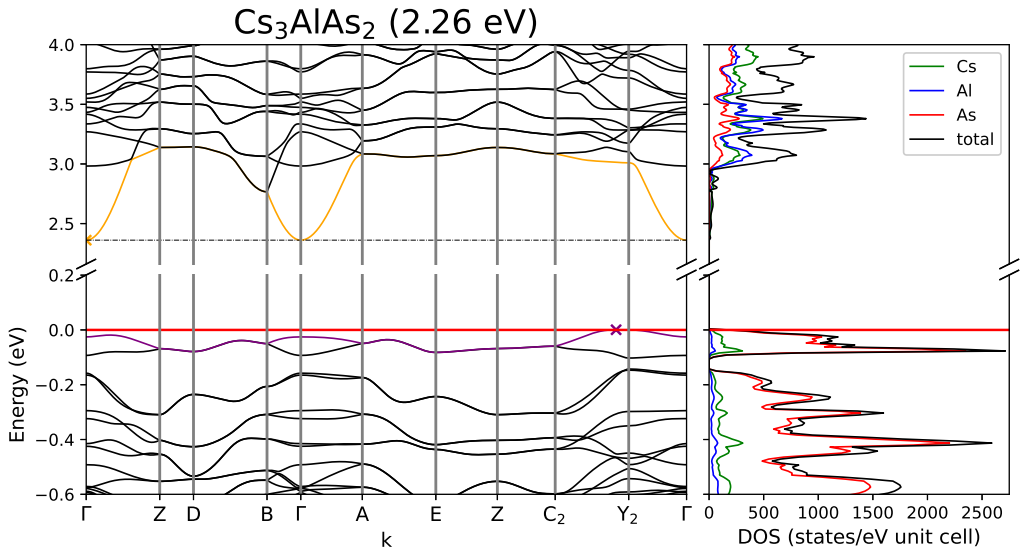

Figure A.70: Band structure and DOS of Cs_3AlAs_2.

Table A.115: Partial charges for each atom position in Cs_3AlAs_2.

Atom	Z	charge	part charge
Cs1	9	8.339	0.661
Cs2		8.323	0.677
Cs3		8.294	0.706
Cs4		8.318	0.682
Cs5		8.316	0.684
Cs6		8.29	0.71
Al1	13	12.782	0.218

Atom	Z	charge	partialcharge
Al2		12.789	0.211
As1	33	34.223	−1.223
As2		34.237	−1.237
As3		34.045	−1.045
As4		34.042	−1.042

Table A.116: Overlap population and interatomic distances of Cs_3AlAs_2.

Atom A	Atom B	r_{AB} / Å	overlap
Cs1	As3	3.58	0.02
	As1	3.598	0.04
	As2	3.71	0.037
	As1	3.717	0.035
	Al2	3.904	0.0
	Cs2	4.212	0.005
Cs2	As4	3.563	0.015
	As2	3.571	0.03
	As1	3.722	0.038
	As2	3.769	0.029
	Cs4	3.869	0.007
	Al1	3.888	−0.002
Cs3	Al2	3.613	0.012
	As4	3.75	0.018
	As2	3.777	0.035
	As3	3.854	0.016
	Al1	3.885	0.002
	Cs4	4.003	0.006
Cs4	As2	3.721	0.029
	Al2	3.782	0.007
	As4	3.839	0.016
	As1	3.842	0.026
	Al1	3.964	0.002
Cs5	As1	3.606	0.034
	As3	3.614	0.025
	As2	3.701	0.03
	Al1	3.761	0.006
	As4	3.965	0.017
Cs6	As3	3.669	0.02
	Al1	3.875	0.011
	As1	3.883	0.031
	Al2	3.89	0.004
	Cs6	3.91	0.005
	As1	3.94	0.023
Al1	As2	2.362	0.451
	As4	2.453	0.332
	As4	2.468	0.319
	Al1	3.006	−0.027
Al2	As1	2.334	0.475
	As3	2.437	0.322
	As3	2.442	0.312
	Al2	2.991	−0.029
As4	As4	3.897	−0.064

Cs_3GaAs_2[109]

For a crystal structure description see Cs_3AlP_2.

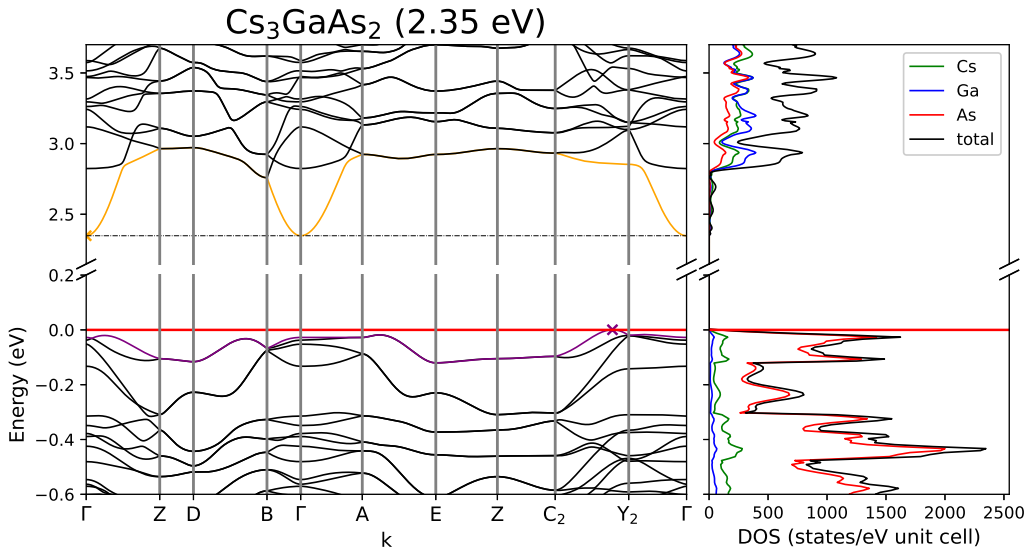

Figure A.71: Band structure and DOS of Cs_3GaAs_2.

Table A.117: Partial charges for each atom position in Cs_3GaAs_2.

Atom	Z	charge	part charge
Cs1	9	8.306	0.694
Cs2		8.311	0.689
Cs3		8.271	0.729
Cs4		8.278	0.722
Cs5		8.334	0.666
Cs6		8.32	0.68
Ga1	31	31.06	−0.06

Atom	Z	charge	partialcharge
Ga2		31.056	−0.056
As1	33	34.129	−1.129
As2		33.899	−0.899
As3		33.898	−0.898
As4		34.137	−1.137

Table A.118: Overlap population and interatomic distances of Cs_3GaAs_2.

Atom A	Atom B	r_{AB} / Å	overlap
Cs1	As4	3.717	0.028
	Ga1	3.758	0.001
	As3	3.819	0.016
	As1	3.836	0.024
	Cs6	3.893	0.007
	Ga2	3.934	−0.003
Cs2	As1	3.57	0.033
	As2	3.638	0.028
	As4	3.666	0.029
	Ga2	3.73	−0.001
	As3	3.944	0.017
	As4	4.009	0.018
Cs3	As2	3.65	0.02
	Ga2	3.86	0.007
	Ga1	3.866	−0.001
	As1	3.903	0.029
	Cs3	3.915	0.006
	As1	3.935	0.022
Cs4	Ga1	3.607	0.004
	As3	3.744	0.018
	As4	3.81	0.034
	As2	3.833	0.017
	Ga2	3.865	−0.003
Cs5	As2	3.557	0.02
	As1	3.589	0.039
	As4	3.699	0.037
	As1	3.721	0.032
	Ga1	3.852	−0.005
Cs6	As3	3.544	0.014
	As4	3.572	0.028
	As1	3.72	0.04
	As4	3.767	0.03
	Ga2	3.832	−0.007
Ga1	As1	2.335	0.43
	As2	2.452	0.295
	As2	2.455	0.305
	Ga1	3.098	−0.067
Ga2	As4	2.364	0.397
	As3	2.465	0.322
	As3	2.484	0.305
	Ga2	3.108	−0.065
As2	As2	3.805	−0.07
As3	As3	3.851	−0.063

A.4 2-1-2

Table A.119: Overview of the crystallographic details of the 2-1-2 compounds. Cell parameters given in the first line and second line are of experimental and calculated origin, respectively. The third line shows the difference between both in percent.

compound	a / Å	b/ Å	c / Å	β / °	space group	crystal system	connectivity
Li_2SiP_2	12.121	18.613			*I* 4_1/ *acd* (no. 142)	tetragonal	3D
	12.168	18.758					
	0.39	0.77					
Li_2GeP_2	12.3223	19.0123			-"-	-"- -	"-
	12.3453	19.1480					
	0.19	0.71					
Na_2SnAs_2	14.166	21.191			-"-	-"-	-"-
	14.100	21.191					
	-0.47	0.00					
Na_2SiP_2	12.7929	22.3109	6.0522		*P c c n* (no. 56)	orthorhombic	1D
	12.6409	22.1882	6.0852				
	-1.20	-0.55	0.54				
K_2SiP_2	12.926	6.867	6.107		*I b a m* (n. 72)	orthorhombic	1D
	12.950	6.840	6.151				
	0.19	-0.40	0.71				
Cs_2SiP_2	14.127	7.462	6.196		-"-	-"-	-"-
	14.201	7.502	6.251				
	0.52	0.53	0.88				
K_2SiAs_2	13.132	6.999	6.340		-"-	-"-	-"-
	13.299	6.952	6.397				
	1.25	-0.68	0.90				
K_2GeAs_2	13.292	7.028	6.548		-"-	-"-	-"-
	13.363	6.964	6.572				
	0.53	-0.92	0.36				
Rb_2SiAs_2	13.77	7.266	6.389		-"-	-"-	-"-
	13.88	7.275	6.461				
	0.80	0.13	1.11				
Rb_2SnAs_2	13.974	7.454	6.942		-"-	-"-	-"-
	14.135	7.424	6.981				
	1.14	-0.41	0.56				
Cs_2SiAs_2	14.425	7.571	6.420		-"-	-"-	-"-
	14.525	7.573	6.493				
	0.69	0.03	1.13				
Cs_2SnAs_2	14.657	7.733	6.953		-"-	-"-	-"-

Table A.119: Continued.

compound	a / Å	b/ Å	c / Å	β / °	space group	crystal system	connectivity
	14.741	7.696	7.011				
	0.57	-0.48	0.83				
K_2GaP_2	10.215	14.016	8.636	109.4	*P* 2_1 / *n* (no. 14)	monoclinic	1D
	10.204	14.036	8.663	109.5			
	-0.11	0.14	0.31	0.08			
K_2GaAs_2	10.476	14.393	8.884	110.2	-"-	-"-	-"-
	10.462	14.457	8.912	110.2			
	-0.13	0.45	0.32	0.04			
Rb_2GaAs_2	10.867	14.751	8.992	108.4	-"-	-"-	-"-
	10.936	14.828	9.087	108.3			
	0.63	0.52	1.05	-0.08			
K_2GaSb_2	15.062	10.373	9.145		*P n m a* (no. 62)	orthorhombic	1D
	15.124	10.355	9.122				
	0.41	-0.18	-0.25				
Rb_2GaSb_2	15.408	10.776	9.302		-"-	-"-	-"-
	15.490	10.879	9.352				
	0.53	0.94	0.53				
Cs_2GaSb_2	18.060	11.167	8.358		-"-	-"-	-"-
	18.097	11.237	8.434				
	0.20	0.63	0.90				

Table A.120: Calculated band gaps and transitions as well as an overview of the sampled reciprocal space defined by the Monkhorst-Pack-type *k*-point grid (SHRINK) and Brillouin Zone paths for all 2-1-2 compounds.

compound	band gap		transition	k-path	SHRINK
Li_2SiP_2	3.24	direct	Γ -> Γ	Γ—X—P—N—Γ—M—S|S_0—Γ|X—R|G—M	8 8 8
Li_2GeP_2	2.73	direct	-"-	-"-	-"-
Na_2SnAs_2	2.07	direct	-"-	-"-	-"-
Na_2SiP_2	2.69	indirect	Γ -> Γ-Z	Γ—X—S—Y—Γ—Z—U—R—T—Z|X—U|Y—T|S—R	3 2 5
K_2SiP_2	2.97	indirect	X -> Λ_0	Γ—X—F_0|Σ_0—Γ—Λ_0|G_0—X|Γ—R—W—S—Γ—T—W	8 8 8
Cs_2SiP_2	2.80	indirect	X -> Γ-Λ_0	-"-	-"-
K_2SiAs_2	2.71	indirect	X -> Λ_0	-"-	-"-
K_2GeAs_2	2.62	indirect	X -> G_0-X	-"-	-"-
Rb_2SiAs_2	2.56	indirect	X -> Λ_0	-"-	-"-
Rb_2SnAs_2	2.45	indirect	X -> Γ	-"-	-"-
Cs_2SiAs_2	2.71	indirect	X -> Γ-Λ_0	-"-	-"-
Cs_2SnAs_2	2.47	indirect	X -> Γ	-"-	-"-
K_2GaP_2	2.75	indirect	A -> Γ-A	Γ—Z—D—B—Γ—A—E—Z—C_2—Y_2—Γ	8 8 8
K_2GaAs_2	2.68	indirect	-"-	-"-	-"-
Rb_2GaAs_2	2.48	indirect	A -> Γ	-"-	-"-
K_2GaSb_2	2.25	indirect	Γ-X -> Γ	Γ—X—S—Y—Γ—Z—U—R—T—Z|X—U|Y—T|S—R	8 8 8
Rb_2GaSb_2	2.19	indirect	Γ-Z -> Γ	-"-	-"-
Cs_2GaSb_2	2.24	pseudo-direct	Γ-Z -> Γ-Z	-"-	2 3 4

Li_2SiP_2[111]

Li_2SiP_2 crystallizes in the tetragonal space group *I* $4_1/$ *acd* (no. 142) in the Na_2SiAs_2-structure type. P atoms form a distorted cubic closed packing in which Si occupies tetrahedral voids. SiP_4-tetrahedra are formed and are arranged in T4-super-tetrahedra by corner sharing. The T4-super-tetrahedra are further connected by corner-sharing to two independent three-dimensional networks. The Li atoms occupy the octahedral voids as well as some remaining tetrahedral voids.

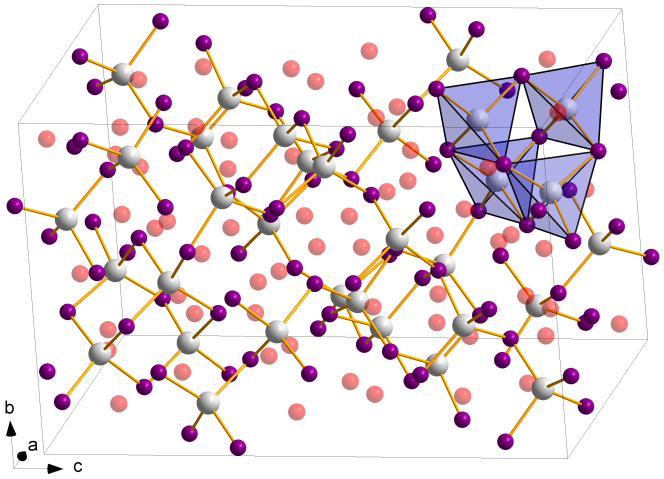

Figure A.72: Crystal structure of Li_2SiP_2 incorporating two independent three dimensional networks of corner-sharing T4 super-tetrahedra.

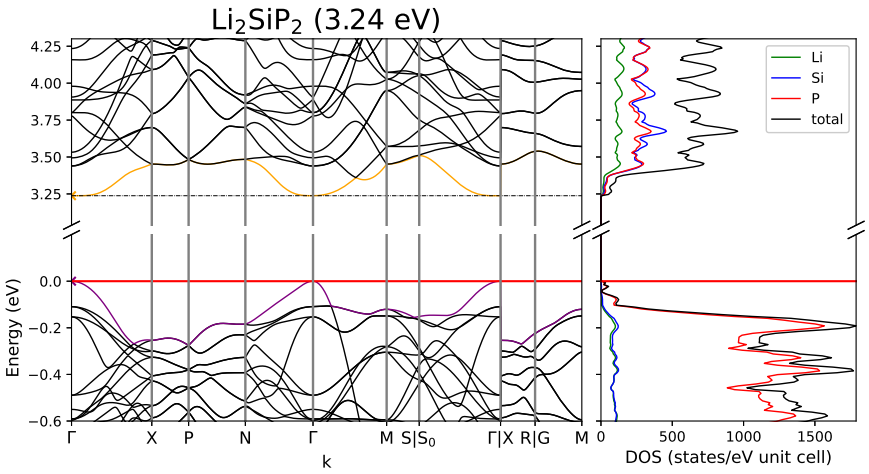

Figure A.73: Band structure and DOS of Li_2SiP_2.

Table A.121: Overlap population and interatomic distances of Li_2SiP_2.

Atom A	Atom B	r_{AB} / Å	overlap
Li1	P3	2.461	0.08
	P1	2.563	0.073
	Li3	3.084	0.004
	Li2	3.089	0.004
	Li1	3.235	0.003
	Li3	3.925	0.001
Li2	P2	2.652	0.062
	P3	2.775	0.052
	Li3	2.911	0.007
	Si1	3.158	0.004
	P1	3.298	0.013
Li3	P2	2.56	0.073
	P3	2.581	0.062
	P3	2.611	0.061
	P1	2.612	0.054
	Si1	2.959	0.012
Si1	P3	2.246	0.31
	P3	2.265	0.294
	P2	2.266	0.291
	P1	2.282	0.289
P1	P3	3.732	−0.051
	P2	3.793	−0.024
P2	P3	3.525	−0.03
	P3	3.583	−0.046

Table A.122: Partial charges for each atom position in Li_2SiP_2.

Atom	Z	charge	part charge
Li1	3	2.428	0.572
Li2		2.383	0.617
Li3		2.41	0.59
Si1	14	13.852	0.148
P1	15	15.692	−0.692
P2		15.652	−0.652
P3		15.661	−0.661

Li_2GeP_2[120]

For a crystal structure description see Li_2SiP_2.

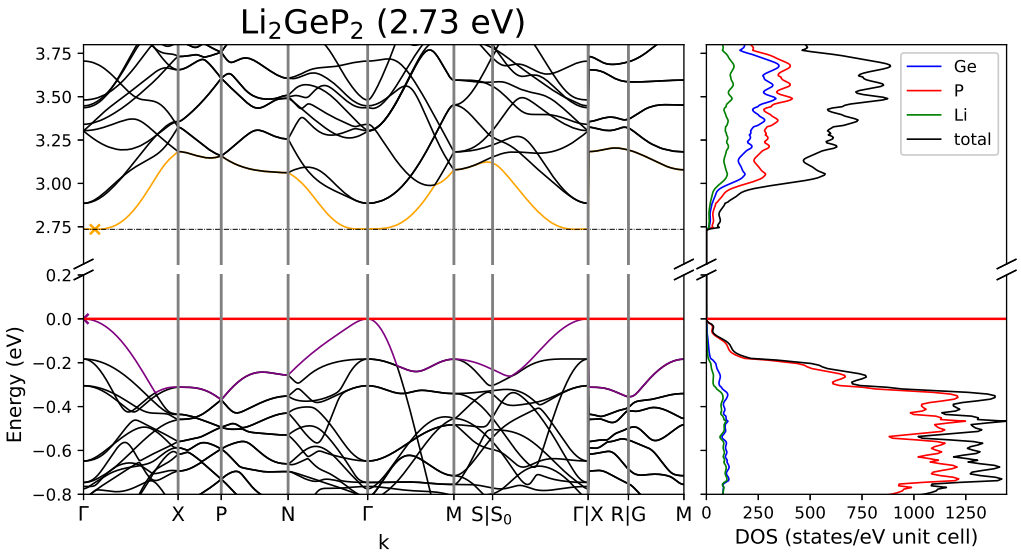

Figure A.74: Band structure and DOS of Li_2GeP_2.

Table A.123: Overlap population and interatomic distances of Li_2GeP_2.

Atom A	Atom B	r_{AB} / Å	overlap
Ge1	P3	2.32	0.277
	P1	2.333	0.279
	P3	2.335	0.273
	P2	2.35	0.267
	Li3	2.985	0.013
	Li3	3.096	0.007
P1	Li3	2.562	0.078
	Li1	2.69	0.064
	P3	3.633	−0.021
	P3	3.67	−0.037
	P2	3.92	−0.018
P2	Li2	2.566	0.075
	Li3	2.648	0.054
	Li1	3.389	0.01
	P3	3.857	−0.037

Atom A	Atom B	r_{AB} / Å	overlap
P3	Li2	2.48	0.083
	Li3	2.61	0.06
	Li3	2.63	0.061
	Li1	2.745	0.058
Li1	Li3	2.951	0.008
	Li2	3.189	0.003
Li2	Li3	3.177	0.004
	Li2	3.247	0.003
	Li3	3.954	0.001

Table A.124: Partial charges for each atom position in Li_2GeP_2.

Atom	Z	charge	part charge
Ge1	32	32.05	−0.05
P1	15	15.525	−0.525
P2		15.59	−0.59
P3		15.567	−0.567

Atom	Z	charge	partialcharge
Li1	3	2.396	0.604
Li2		2.438	0.562
Li3		2.409	0.591

Na_2SnAs_2[112]

For a crystal structure description see Li_2SiP_2.

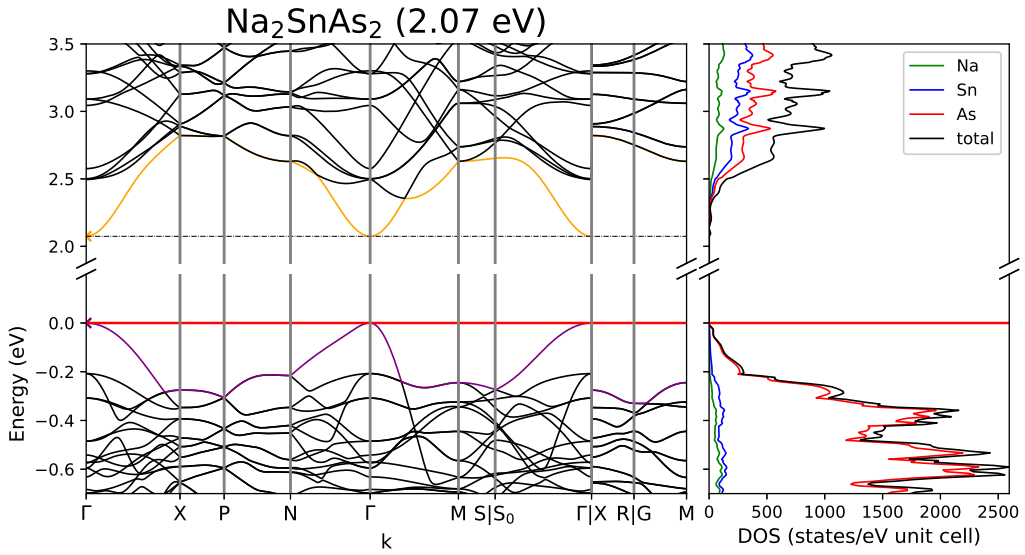

Figure A.75: Band structure and DOS of Na_2SnAs_2.

Table A.125: Partial charges for each atom position in Na_2SnAs_2.

Atom	Z	charge	part charge
Na1	11	10.249	0.751
Na2		10.265	0.735
Na3		10.268	0.732
Sn1	22	21.654	0.346

Atom	Z	charge	partialcharge
As1	33	33.908	−0.908
As2		33.894	−0.894
As3		33.95	−0.95

Table A.126: Overlap population and interatomic distances of Na_2SnAs_2.

Atom A	Atom B	r_{AB} / Å	overlap
Na1	As2	2.942	0.046
	As1	2.992	0.036
	As3	3.024	0.033
	As1	3.025	0.031
	Na3	3.393	0.004
	Na2	3.416	0.003
Na2	As1	2.797	0.047
	As3	2.937	0.045
	Na3	3.578	0.002
	Na2	3.977	0.0
Na3	As2	3.049	0.042
	As1	3.209	0.032
	As3	3.676	0.011
	Sn1	3.699	0.004

Atom A	Atom B	r_{AB} / Å	overlap
Sn1	As1	2.599	0.278
	As1	2.615	0.28
	As2	2.625	0.28
	As3	2.646	0.256
As2	As3	4.414	−0.014
As3	As3	4.322	−0.001

Na_2SiP_2[113]

Na_2SiP_2 crystallizes in the orthorhombic space group *P c c n* (no. 56). Edge-sharing, one dimensional chains of SiP_4 tetrahedra are formed as the main structural motive. All chains within the unit cell are parallel to each other and propagate along the c-axis.

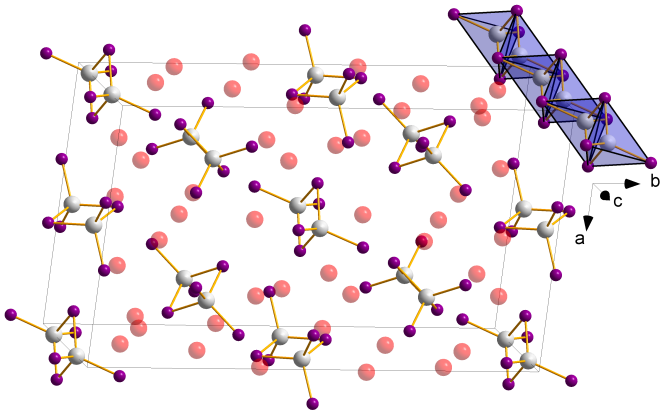

Figure A.76: Crystal structure of Na_2SiP_2 incorporating one dimensional chains of edge-sharing SiP_4 tetrahedra along c.

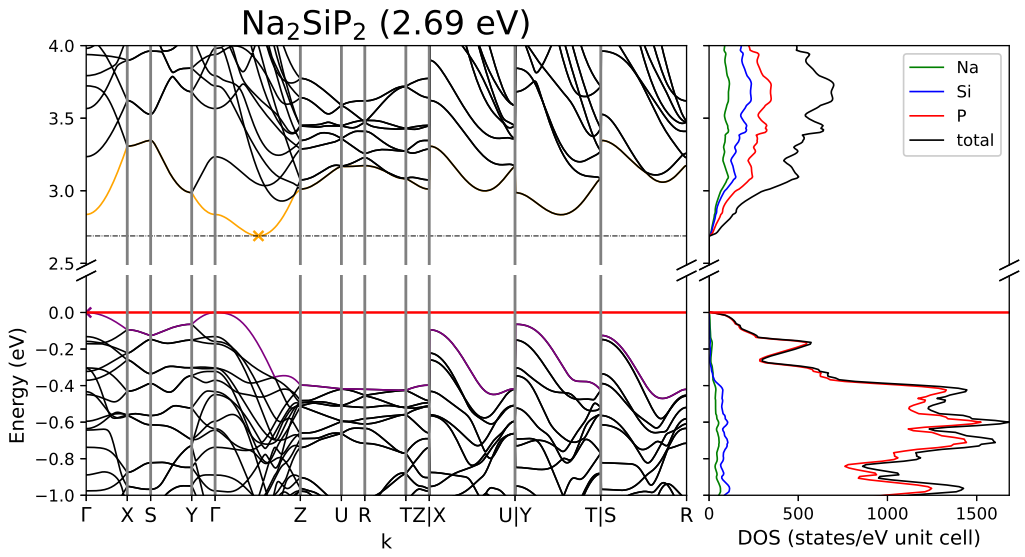

Figure A.77: Band structure and DOS of Na_2SiP_2.

Table A.127: Partial charges for each atom position in Na_2SiP_2.

Atom	Z	charge	part charge
P1	15	15.793	−0.793
P2		15.777	−0.777
P3		15.858	−0.858
P4		15.848	−0.848
Si1	14	13.994	0.006
Si2		13.851	0.149

Atom	Z	charge	partialcharge
Si3		13.815	0.185
Na1	11	10.23	0.77
Na2		10.229	0.771
Na3		10.234	0.766
Na4		10.205	0.795

Table A.128: Overlap population and interatomic distances of Na_2SiP_2.

Atom A	Atom B	r_{AB} / Å	overlap
P1	Si1	2.272	0.303
	Si1	2.287	0.297
	Na3	2.889	0.036
	Na1	3.043	0.037
	Na2	3.061	0.027
	Na4	3.17	0.01
P2	Si1	2.285	0.278
	Si1	2.289	0.263
	Na3	2.893	0.044
	Na4	2.906	0.026
	Na2	2.931	0.033
	Na2	3.064	0.026
P3	Si3	2.264	0.316
	Si3	2.266	0.312
	Na4	2.764	0.044
	Na1	2.883	0.035
	Na2	2.913	0.031
	Na1	3.134	0.024
P4	Si2	2.261	0.316
	Si2	2.262	0.298
	Na4	2.769	0.036
	Na3	2.957	0.029
	Na1	2.982	0.029
	Na1	3.092	0.031
Si1	Si1	2.981	−0.08
	Na4	3.008	−0.005
Si2	Si2	3.043	−0.067
	Na1	3.393	0.002
	Na3	3.548	0.002
	Na1	4.162	0.001
Si3	Si3	3.043	−0.084
	Na1	3.325	0.001
	Na2	3.627	0.001
	Na1	3.834	0.0
Na2	Na2	3.044	0.005
Na3	Na3	3.335	0.003

K_2SiP_2[114]

K_2SiP_2 crystallizes in the orthorhombic space group *I b a m* (no. 72). Like in Na_2SiP_2 edge-sharing chains of SiP_4 tetrahedra are formed along c.

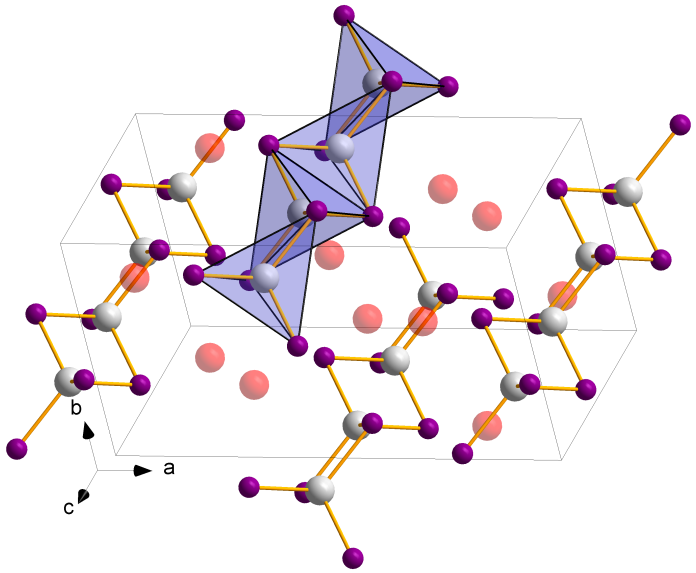

Figure A.78: Crystal structure of K_2SiP_2 incorporating one dimensional chains of edge-sharing SiP_4 tetrahedra along c.

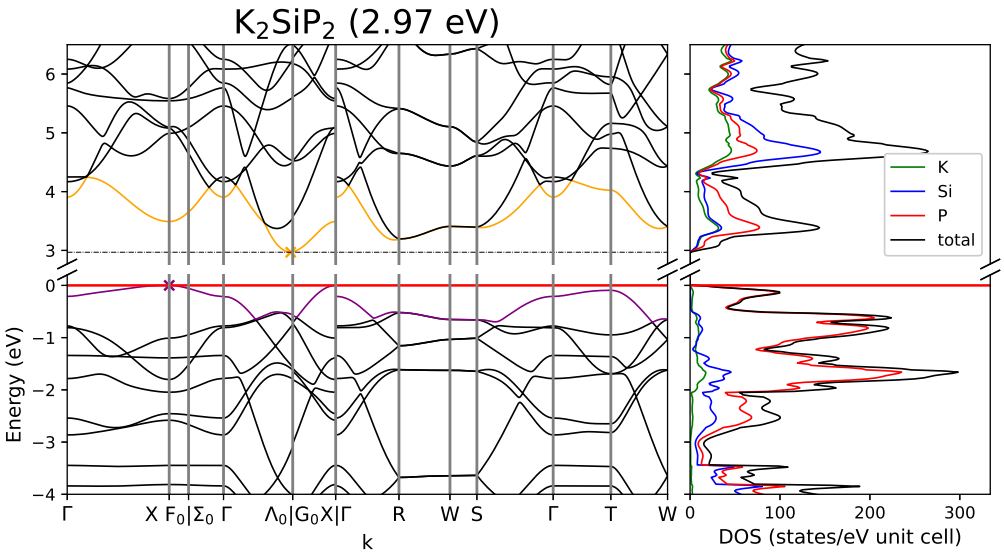

Figure A.79: Band structure and DOS of K_2SiP_2.

Table A.129: Overlap population and interatomic distances of K_2SiP_2.

Atom A	Atom B	r_{AB} / Å	overlap
K1	P1	3.323	0.023
	P1	3.367	0.009
	P1	3.378	0.008
	Si1	3.379	−0.012
	P1	3.436	0.025
	P1	3.521	0.011

Atom A	Atom B	r_{AB} / Å	overlap
Si1	P1	2.283	0.306
	Si1	3.075	−0.062
	P1	4.912	0.001
P1	P1	3.375	−0.132

Table A.130: Partial charges for each atom position in K_2SiP_2.

Atom	Z	charge	part charge
K1	19	18.206	0.794
Si1	14	14.034	−0.034

Atom	Z	charge	partialcharge
P1	15	15.777	−0.777

Cs_2SiP_2[115]

For a crystal structure description see K_2SiP_2.

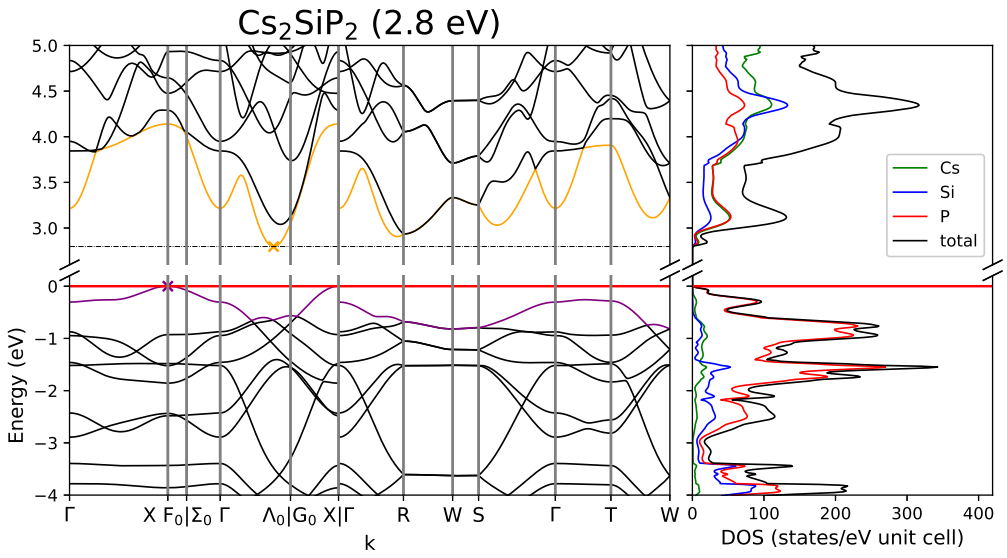

Figure A.80: Band structure and DOS of Cs_2SiP_2.

Table A.131: Overlap population and interatomic distances of Cs_2SiP_2.

Atom A	Atom B	r_{AB} / Å	overlap
Cs1	P1	3.516	0.01
	Si1	3.614	−0.012
	P1	3.614	0.012
	P1	3.721	0.012
	P1	3.762	0.027
	P1	3.964	0.022

Atom A	Atom B	r_{AB} / Å	overlap
Si1	P1	2.297	0.307
	Si1	3.126	−0.074
	P1	4.982	0.001
P1	P1	3.367	−0.131

Table A.132: Partial charges for each atom position in Cs_2SiP_2.

Atom	Z	charge	part charge
Cs1	9	8.243	0.757
Si1	14	14.029	−0.029

Atom	Z	charge	partialcharge
P1	15	15.743	−0.743

K_2SiAs_2[116]

For a crystal structure description see K_2SiP_2.

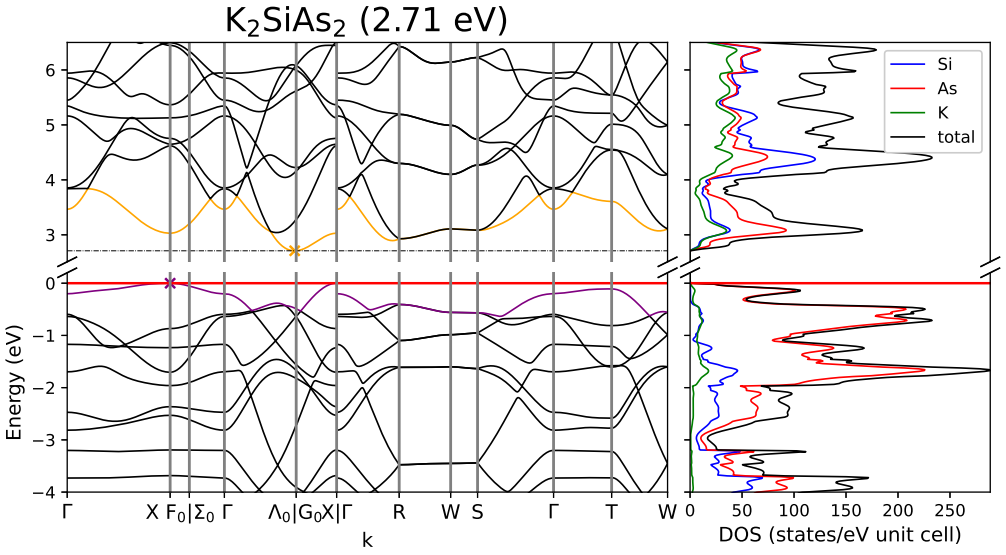

Figure A.81: Band structure and DOS of K_2SiAs_2.

Table A.133: Overlap population and interatomic distances of K_2SiAs_2.

Atom A	Atom B	r_{AB} / Å	overlap
Si1	As1	2.386	0.309
	Si1	3.199	−0.057
	K1	3.431	−0.008
	As1	5.114	0.001
	K1	5.124	0.0
	K1	5.228	0.0

Atom A	Atom B	r_{AB} / Å	overlap
As1	K1	3.395	0.028
	K1	3.465	0.009
	K1	3.47	0.011
	K1	3.488	0.029
	As1	3.54	−0.106

Table A.134: Partial charges for each atom position in K_2SiAs_2.

Atom	Z	charge	part charge
Si1	14	13.785	0.215
As1	33	33.884	−0.884

Atom	Z	charge	partialcharge
K1	19	18.223	0.777

K_2GeAs_2[115]

For a crystal structure description see K_2SiP_2.

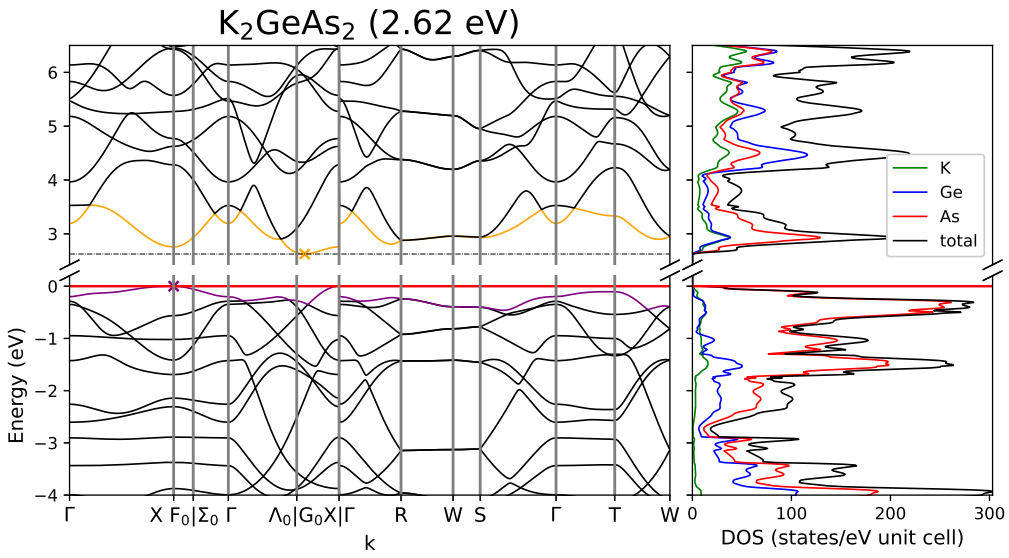

Figure A.82: Band structure and DOS of K_2GeAs_2.

Table A.135: Overlap population and interatomic distances of K_2GeAs_2.

Atom A	Atom B	r_{AB} / Å	overlap
K1	As1	3.387	0.029
	Ge1	3.454	−0.007
	As1	3.464	0.031
	As1	3.5	0.013
	As1	3.531	0.01
	As1	3.581	0.014

Atom A	Atom B	r_{AB} / Å	overlap
Ge1	As1	2.45	0.291
	Ge1	3.286	−0.04
	As1	5.254	0.001

Table A.136: Partial charges for each atom position in K_2GeAs_2.

Atom	Z	charge	part charge
K1	19	18.227	0.773
Ge1	32	31.981	0.019

Atom	Z	charge	partialcharge
As1	33	33.783	−0.783

Rb_2SiAs_2[158]

For a crystal structure description see K_2SiP_2.

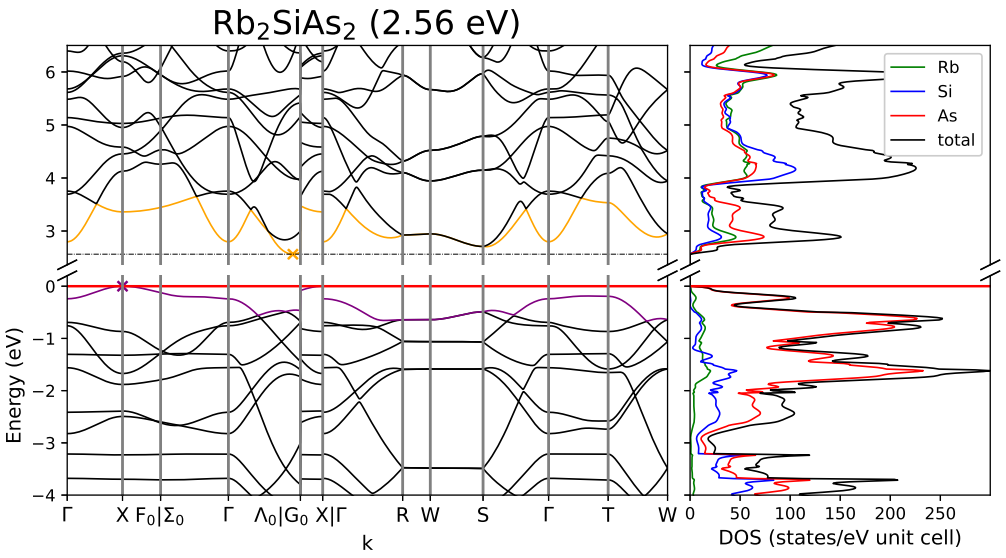

Figure A.83: Band structure and DOS of Rb_2SiAs_2.

Table A.137: Overlap population and interatomic distances of Rb_2SiAs_2.

Atom A	Atom B	r_{AB} / Å	overlap
Rb1	As1	3.55	0.009
	Si1	3.57	−0.007
	As1	3.588	0.033
	As1	3.597	0.013
	As1	3.684	0.015
	As1	3.719	0.03

Atom A	Atom B	r_{AB} / Å	overlap
As1	Si1	2.394	0.312
	As1	3.534	−0.103
Si1	Si1	3.23	−0.061

Table A.138: Partial charges for each atom position in Rb_2SiAs_2.

Atom	Z	charge	part charge
Rb1	9	8.28	0.72
As1	33	33.841	−0.841

Atom	Z	charge	partialcharge
Si1	14	13.757	0.243

Rb_2SnAs_2[115]

For a crystal structure description see K_2SiP_2.

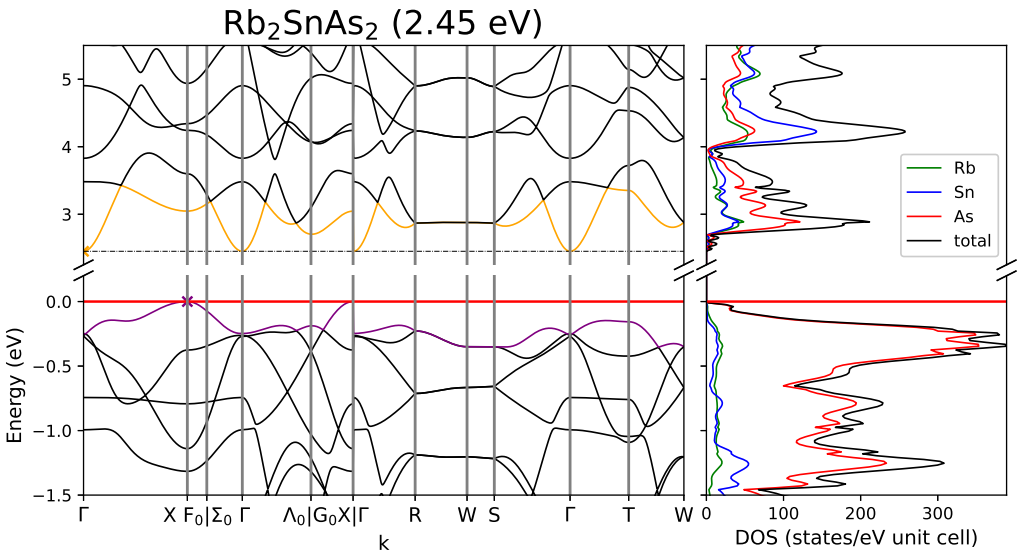

Figure A.84: Band structure and DOS of Rb_2SnAs_2.

Table A.139: Overlap population and interatomic distances of Rb_2SnAs_2.

Atom A	Atom B	r_{AB} / Å	overlap
Rb1	As1	3.549	0.033
	As1	3.62	0.032
	Sn1	3.71	−0.007
	As1	3.724	0.014
	As1	3.747	0.01
	As1	3.907	0.013

Atom A	Atom B	r_{AB} / Å	overlap
Sn1	As1	2.627	0.283
	Sn1	3.491	−0.033
	As1	5.592	0.0

Table A.140: Partial charges for each atom position in Rb_2SnAs_2.

Atom	Z	charge	part charge
Rb1	9	8.273	0.727
Sn1	22	21.83	0.17

Atom	Z	charge	partialcharge
As1	33	33.812	−0.812

Cs_2SiAs_2[115]

For a crystal structure description see K_2SiP_2.

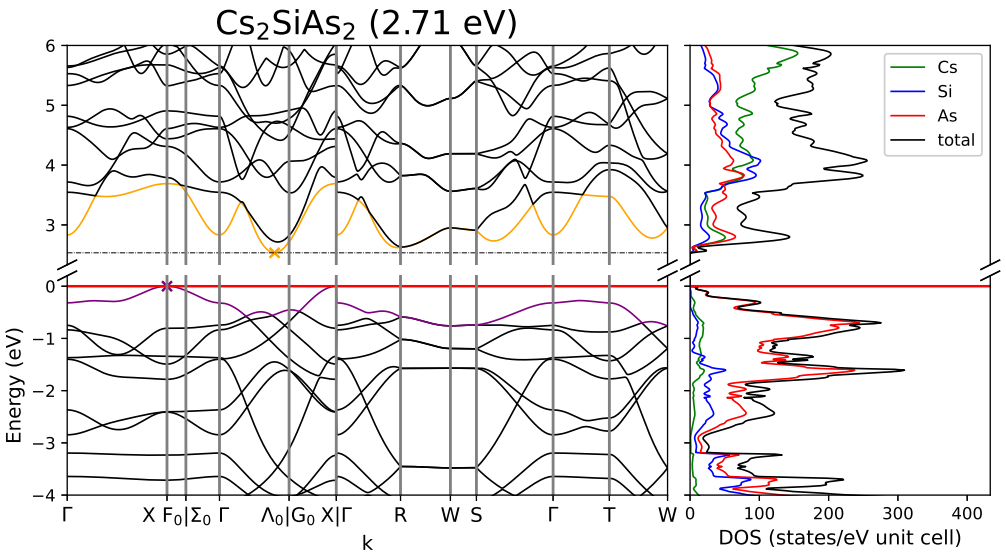

Figure A.85: Band structure and DOS of Cs_2SiAs_2.

Table A.141: Overlap population and interatomic distances of Cs_2SiAs_2.

Atom A	Atom B	r_{AB} / Å	overlap
Cs1	As1	3.605	0.011
	Si1	3.669	−0.006
	As1	3.7	0.014
	As1	3.772	0.015
	As1	3.823	0.031
	As1	3.96	0.026

Atom A	Atom B	r_{AB} / Å	overlap
Si1	As1	2.401	0.31
	Si1	3.247	−0.063
	As1	5.181	0.001
As1	As1	3.539	−0.102

Table A.142: Partial charges for each atom position in Cs_2SiAs_2.

Atom	Z	charge	part charge
Cs1	9	8.264	0.736
Si1	14	13.778	0.222

Atom	Z	charge	partialcharge
As1	33	33.847	−0.847

Cs_2SnAs_2[115]

For a crystal structure description see K_2SiP_2.

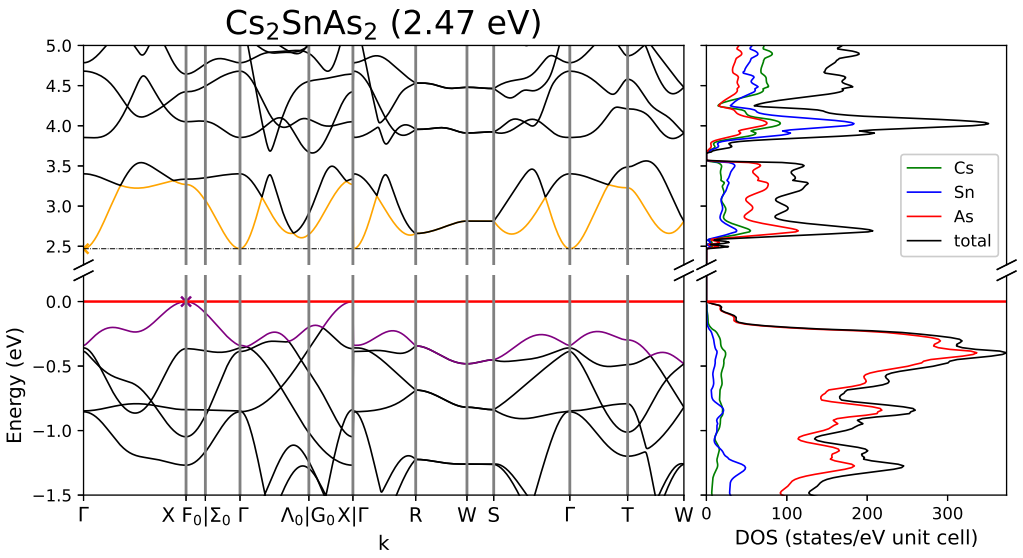

Figure A.86: Band structure and DOS of Cs_2SnAs_2.

Table A.143: Overlap population and interatomic distances of Cs_2SnAs_2.

Atom A	Atom B	r_{AB} / Å	overlap
Cs1	As1	3.757	0.033
	As1	3.796	0.013
	Sn1	3.807	−0.006
	As1	3.831	0.014
	As1	3.839	0.029
	As1	3.987	0.015

Atom A	Atom B	r_{AB} / Å	overlap
Sn1	As1	2.634	0.283
	Sn1	3.506	−0.037
	As1	5.614	0.0
As1	As1	3.933	−0.052

Table A.144: Partial charges for each atom position in Cs_2SnAs_2.

Atom	Z	charge	part charge
Cs1	9	8.255	0.745
Sn1	22	21.85	0.15

Atom	Z	charge	partialcharge
As1	33	33.82	−0.82

K_2GaP_2[123]

K_2GaP_2 crystallizes in the monoclinic space group $P\ 2_1\ /\ n$ (no. 14). In contrast to the tetrel compounds with the same stoichiometry, chains of Ga_2P_3 five membered rings bridged by the remaining P atoms are build. The chains prolongate along the b axis and incorporate a triangular planar coordination by P for the Ga atoms, which are connected via corner-sharing. The K atoms lie in between the chains.

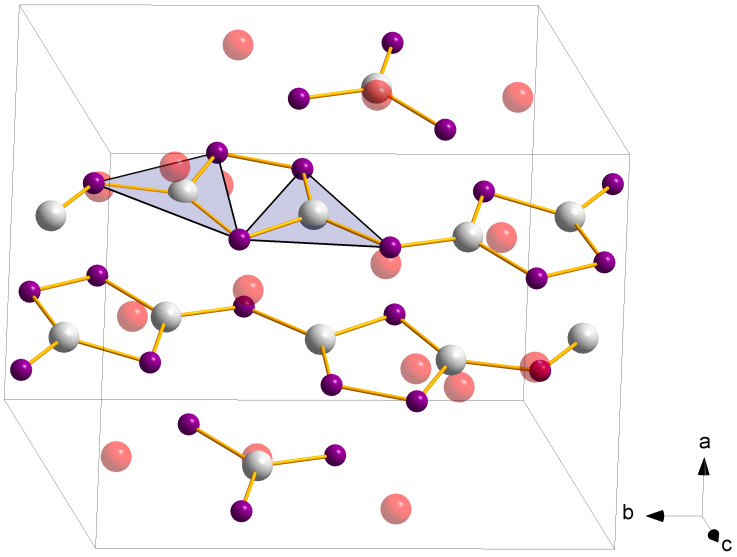

Figure A.87: Crystal structure of K_2GaP_2 incorporating chains of corner-sharing triangular planar GaP_3-units within chains of Ga_2P_3 five membered rings connected by P atoms.

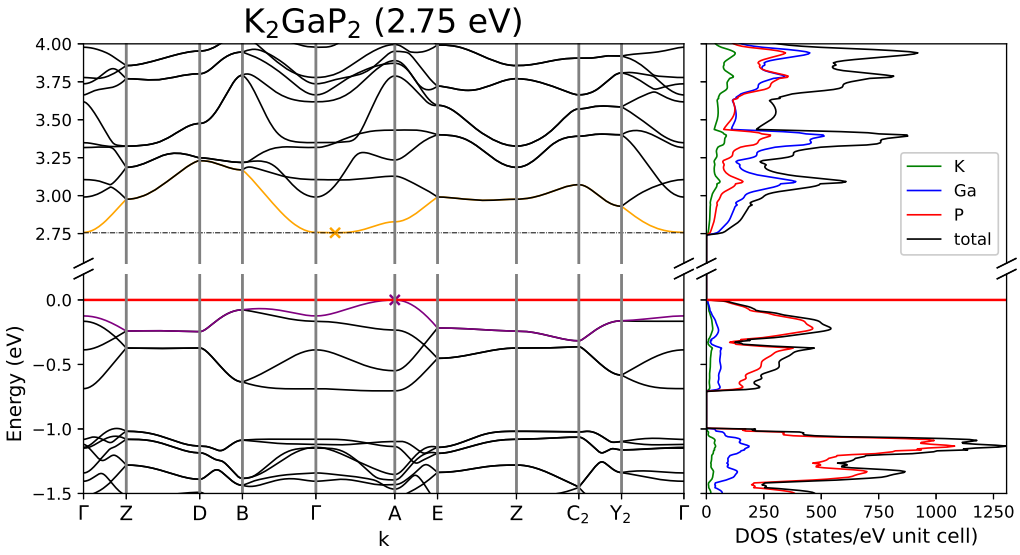

Figure A.88: Band structure and DOS of K_2GaP_2.

Table A.145: Overlap population and interatomic distances of K_2GaP_2.

Atom A	Atom B	r_{AB} / Å	overlap
K1	P1	3.201	0.005
	Ga2	3.371	−0.013
	P4	3.371	0.016
	P4	3.41	0.005
	Ga1	3.431	−0.016
	Ga1	3.56	−0.005
K2	P3	3.287	0.012
	P4	3.33	0.018
	P2	3.364	0.008
	P4	3.412	0.008
	P2	3.428	0.015
	K4	3.635	0.0
K3	P2	3.325	0.014
	P3	3.426	0.013
	P1	3.443	0.009
	Ga1	3.481	−0.011
	P1	3.586	0.011
	Ga2	3.595	−0.006
K4	P1	3.207	0.009
	P2	3.272	0.014
	P3	3.272	0.018
	P3	3.34	0.017
	K4	3.556	−0.001
Ga1	P2	2.285	0.388
	P1	2.303	0.37
	P3	2.33	0.345
	Ga2	3.409	−0.09
Ga2	P4	2.292	0.379
	P1	2.32	0.353
	P3	2.321	0.35
	P2	3.576	−0.059
P2	P4	2.245	0.19

Table A.146: Partial charges for each atom position in K_2GaP_2.

Atom	Z	charge	part charge
K1	19	18.168	0.832
K2		18.192	0.808
K3		18.175	0.825
K4		18.206	0.794
Ga1	31	31.235	−0.235
Ga2		31.198	−0.198
P1	15	15.747	−0.747
P2		15.678	−0.678
P3		15.733	−0.733
P4		15.668	−0.668

K_2GaAs_2[124]

For a crystal structure description see K_2GaP_2.

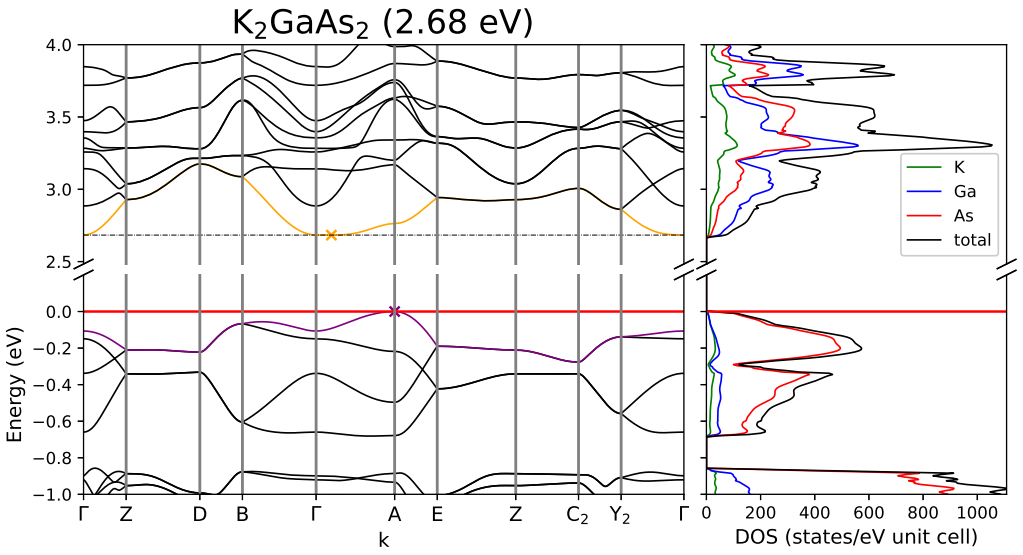

Figure A.89: Band structure and DOS of K_2GaAs_2.

Table A.147: Partial charges for each atom position in K_2GaAs_2.

Atom	Z	charge	part charge
K1	19	18.187	0.813
K2		18.209	0.791
K3		18.196	0.804
K4		18.224	0.776
Ga1	31	31.136	−0.136
Ga2		31.091	−0.091

Atom	Z	charge	partialcharge
As1	33	33.794	−0.794
As2		33.694	−0.694
As3		33.806	−0.806
As4		33.664	−0.664

Table A.148: Overlap population and interatomic distances of K_2GaAs_2.

Atom A	Atom B	r_{AB} / Å	overlap
K1	As1	3.279	0.008
	Ga2	3.438	−0.009
	As4	3.441	0.009
	As4	3.455	0.017
	Ga1	3.485	−0.012
	Ga1	3.607	−0.003
K2	As3	3.349	0.014
	As4	3.384	0.022
	As2	3.417	0.012
	As4	3.462	0.011
	As2	3.487	0.017
	K4	3.744	0.001
K3	As2	3.423	0.019
	As3	3.479	0.016
	As1	3.518	0.013
	Ga1	3.552	−0.007
	As1	3.626	0.013
	Ga2	3.651	−0.002
K4	As1	3.257	0.013
	As3	3.344	0.023
	As2	3.383	0.021
	As3	3.428	0.02
	K4	3.675	0.001
	Ga1	3.711	−0.002
Ga1	As2	2.378	0.332
	As1	2.385	0.339
	As3	2.422	0.322
	Ga2	3.533	−0.077
Ga2	As4	2.374	0.325
	As1	2.407	0.33
	As3	2.415	0.325
As2	As4	2.46	0.233

Rb_2GaAs_2[126]

For a crystal structure description see K_2GaP_2.

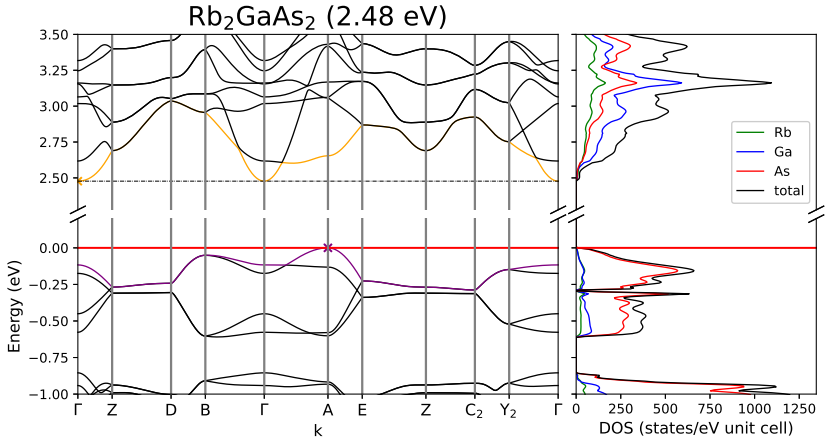

Figure A.90: Band structure and DOS of Rb_2GaAs_2.

Table A.149: Overlap population and interatomic distances of Rb_2GaAs_2.

Atom A	Atom B	r_{AB} / Å	overlap
Rb1	As1	3.445	0.015
	Ga2	3.558	−0.007
	Ga1	3.627	−0.011
	As4	3.631	0.022
	As4	3.679	0.011
	As1	3.763	0.012
Rb2	As4	3.55	0.026
	As3	3.552	0.021
	As2	3.572	0.015
	As2	3.579	0.021
	As4	3.647	0.014
	Rb4	3.849	−0.003
Rb3	As2	3.557	0.021
	Ga1	3.675	−0.008
	As3	3.7	0.019
	As1	3.727	0.013
	As3	3.756	0.008
	As1	3.801	0.017

Atom A	Atom B	r_{AB} / Å	overlap
Rb4	As1	3.456	0.016
	As2	3.479	0.021
	As3	3.511	0.026
	As3	3.559	0.024
	Rb4	3.794	−0.003
Ga1	As2	2.374	0.355
	As1	2.398	0.344
	As3	2.437	0.321
	Ga2	3.561	−0.068
Ga2	As4	2.384	0.354
	As3	2.419	0.335
	As1	2.419	0.337
	As2	3.781	−0.037
As2	As4	2.455	0.226

Table A.150: Partial charges for each atom position in Rb_2GaAs_2.

Atom	Z	charge	part charge
Rb1	9	8.25	0.75
Rb2		8.272	0.728
Rb3		8.254	0.746
Rb4		8.284	0.716
Ga1	31	31.072	−0.072
Ga2		31.029	−0.029

Atom	Z	charge	partialcharge
As1	33	33.765	−0.765
As2		33.651	−0.651
As3		33.764	−0.764
As4		33.66	−0.66

K_2GaSb_2[125]

K_2GaSb_2 crystallizes in the orthorhombic space group *P n m a* (no. 62) and shows the same structural motive as K_2GaP_2 with its chains of Ga_2Sb_3 five membered rings connected via bridging Sb atoms. They also show corner sharing triangular planar $GaSb_3$ units within these chains.

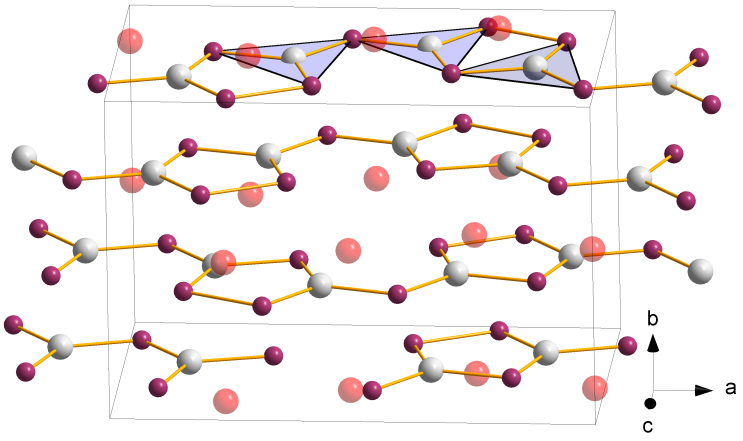

Figure A.91: Crystal structure of K_2GaSb_2 incorporating chains of corner-sharing triangular planar GaP_3-units within chains of Ga_2P_3 five membered rings connected by P atoms.

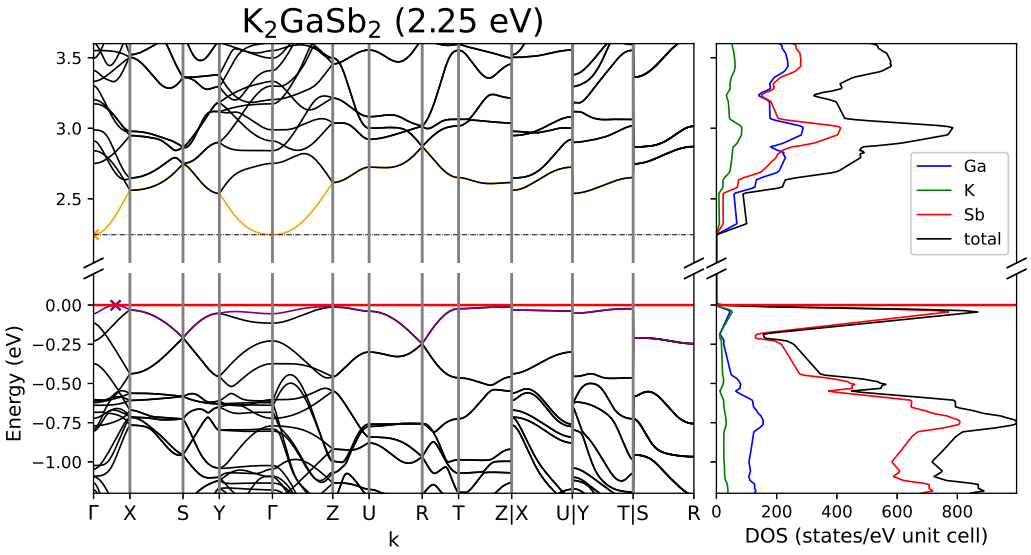

Figure A.92: Band structure and DOS of K_2GaSb_2.

Table A.151: Overlap population and interatomic distances of K_2GaSb_2.

Atom A	Atom B	r_{AB} / Å	overlap
Ga1	Sb4	2.571	0.307
	Sb2	2.574	0.328
	Sb1	2.582	0.315
	K1	3.574	−0.003
	K2	3.754	0.001
	Ga2	3.828	−0.037
Ga2	Sb3	2.588	0.328
	Sb1	2.621	0.308
	Sb2	2.64	0.321
	K1	3.605	−0.002
	K1	3.768	−0.004
	K2	3.815	0.004

Atom A	Atom B	r_{AB} / Å	overlap
K1	Sb1	3.48	0.011
	Sb4	3.519	0.015
	Sb4	3.595	0.005
	Sb2	3.607	0.009
K2	Sb1	3.66	0.017
	Sb3	3.805	0.022
	Sb4	3.845	0.016
	Sb1	3.873	0.007
Sb1	Sb4	4.274	−0.022
Sb3	Sb4	2.849	0.248

Table A.152: Partial charges for each atom position in K_2GaSb_2.

Atom	Z	charge	part charge
Ga1	31	31.113	−0.113
Ga2		31.207	−0.207
K1	19	18.203	0.797
K2		18.214	0.786
Sb1	23	23.759	−0.759
Sb2		23.698	−0.698
Sb3		23.639	−0.639
Sb4		23.75	−0.75

Rb_2GaSb_2[127]

For a crystal structure description see K_2GaSb_2.

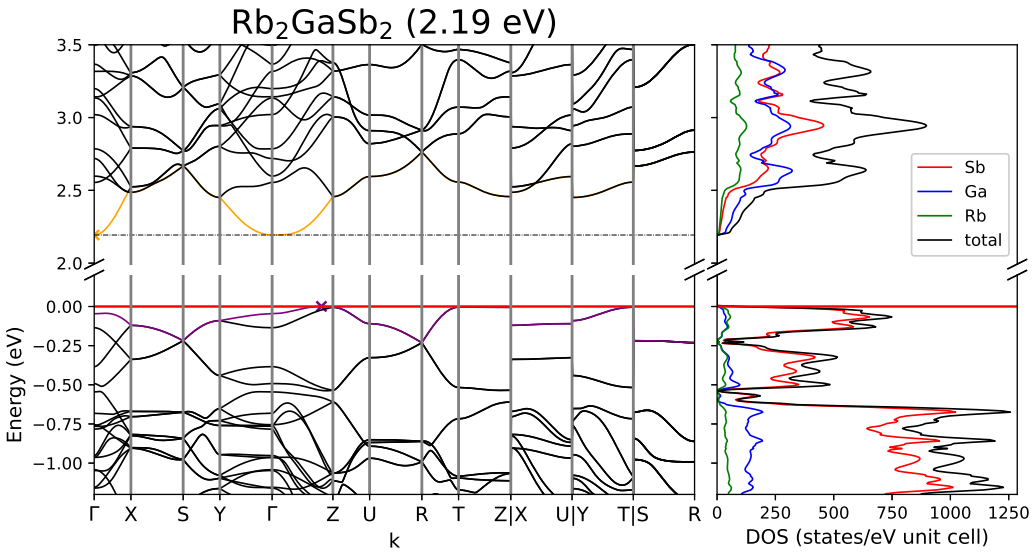

Figure A.93: Band structure and DOS of Rb_2GaSb_2.

Table A.153: Partial charges for each atom position in Rb_2GaSb_2.

Atom	Z	charge	part charge
Sb1	23	23.707	−0.707
Sb2		23.688	−0.688
Sb3		23.629	−0.629
Sb4		23.674	−0.674
Ga1	31	31.106	−0.106
Ga2		31.144	−0.144
Rb1	9	8.261	0.739
Rb2		8.264	0.736

Table A.154: Overlap population and interatomic distances of Rb_2GaSb_2.

Atom A	Atom B	r_{AB} / Å	overlap
Sb1	Ga1	2.592	0.329
	Ga2	2.633	0.315
	Rb1	3.629	0.015
	Rb2	3.847	0.02
	Rb2	3.988	0.011
	Sb4	4.251	−0.025
Sb2	Ga1	2.578	0.336
	Ga2	2.652	0.323
	Rb1	3.732	0.011
	Rb1	4.064	0.009
	Rb2	4.161	0.013
Sb3	Ga2	2.589	0.34
	Sb4	2.844	0.251
	Rb1	3.839	0.009
	Rb2	3.979	0.023
	Rb2	4.134	0.016
	Ga1	4.25	−0.023

Atom A	Atom B	r_{AB} / Å	overlap
Sb4	Ga1	2.575	0.329
	Rb1	3.685	0.018
	Rb1	3.767	0.008
	Rb2	3.914	0.02
	Ga2	4.146	−0.028
Ga1	Rb1	3.74	−0.003
	Ga2	3.854	−0.041
	Rb2	3.914	0.001
Ga2	Rb1	3.764	−0.002
	Rb1	3.936	−0.004

Cs_2GaSb_2[128]

For a crystal structure description see K_2GaSb_2.

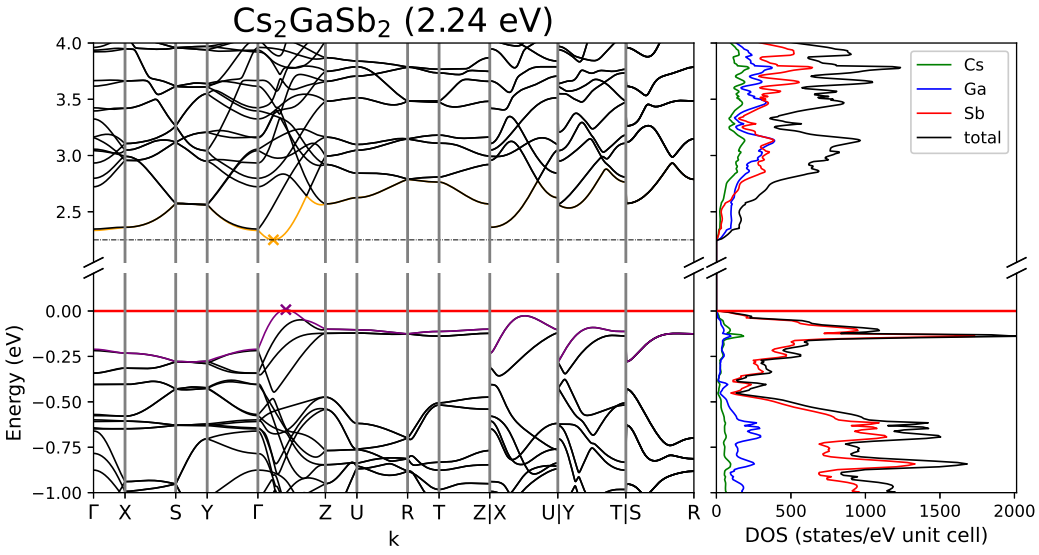

Figure A.94: Band structure and DOS of Cs_2GaSb_2.

Table A.155: Overlap population and interatomic distances of Cs_2GaSb_2.

Atom A	Atom B	r_{AB} / Å	overlap
Cs1	Sb2	3.838	0.017
	Sb4	3.892	0.007
	Sb1	3.936	0.015
	Sb3	3.956	0.014
	Ga1	3.997	0.004
	Sb4	4.0	0.019
Cs2	Sb2	3.82	0.017
	Sb4	3.966	0.02
	Sb3	3.99	0.012
	Sb1	4.013	0.012
	Ga1	4.05	0.004
	Ga2	4.087	0.005
Ga1	Sb2	2.57	0.328
	Sb3	2.585	0.347
	Sb4	2.618	0.327
	Ga2	3.935	−0.033
Ga2	Sb2	2.572	0.33
	Sb1	2.585	0.348
	Sb4	2.619	0.329
Sb1	Sb3	2.899	0.231
Sb2	Sb4	4.226	−0.026
	Sb4	4.232	−0.025

Table A.156: Partial charges for each atom position in Cs_2GaSb_2.

Atom	Z	charge	part charge
Cs1	9	8.241	0.759
Cs2		8.249	0.751
Ga1	31	31.113	−0.113
Ga2		31.086	−0.086
Sb1	23	23.698	−0.698
Sb2		23.738	−0.738
Sb3		23.68	−0.68
Sb4		23.705	−0.705

A.5 1-1-1

Table A.157: Overview of the crystallographic details of the 1-1-1 compounds. Cell parameters given in the first line and second line are of experimental and calculated origin, respectively. The third line shows the difference between both in percent.

compound	a / Å	c / Å	space group	crystal system	connectivity
KSnAs	4.102	12.816	$P6_3mc$ (no .186)	hexagonal	grey As like layers
	4.104	12.898			
	0.06	0.64			
KSnSb	4.350	13.141	-"-	-"-	-"-
	4.368	13.167			
	0.41	0.19			
NaSnP	3.880	11.667	-"-	-"-	-"-
	3.886	11.507			
	0.15	-1.39			
NaSnAs	4.105	11.766	-"-	-"-	-"-
	4.011	11.513			
	-2.34	-2.20			
NaSnSb	xxx	xxx	-"-	-"-	-"-
	4.2924	11.6785			
	xxx	xxx			

Table A.158: Calculated band gaps and transitions as well as an overview of the sampled reciprocal space defined by the Monkhorst-Pack-type *k*-point grid (SHRINK) and Brillouin Zone paths for all 1-1-1 compounds.

compound	band gap		transition	k-path	SHRINK
KSnAs	1.77	direct	Γ -> Γ	Γ—M—K—Γ—A—L—H—A|L—M|H—K	8 8 3
KSnSb	1.42	direct	-"-		-"-
NaSnP	1.76	indirect	Γ -> Γ-M		-"-
NaSnAs	1.36	indirect	-"-		-"-
NaSnSb	0.71	indirect	-"-		-"-

NaSnP[118]

NaSnP crystallizes in the hexagonal space group $P6_3mc$ (no. 186). Sn an P form layers of chair-conformed six membered rings which are analogue to grey arsenic. The Na atoms lie in between these layers and are coordinated (distorted) octahedrally by 3 Sn and P each.

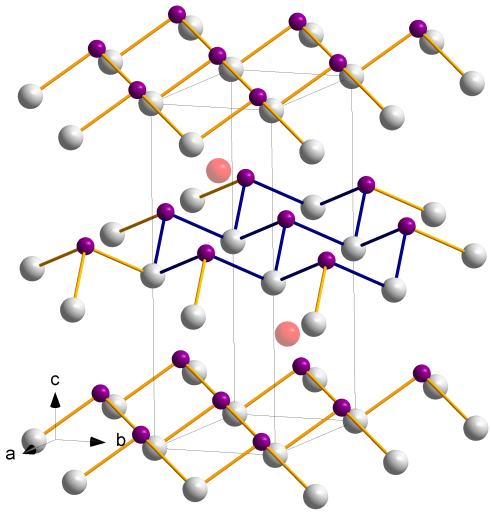

Figure A.95: Crystal structure of NaSnP incorporating grey arsenic like layers of Sn-P six membered rings.

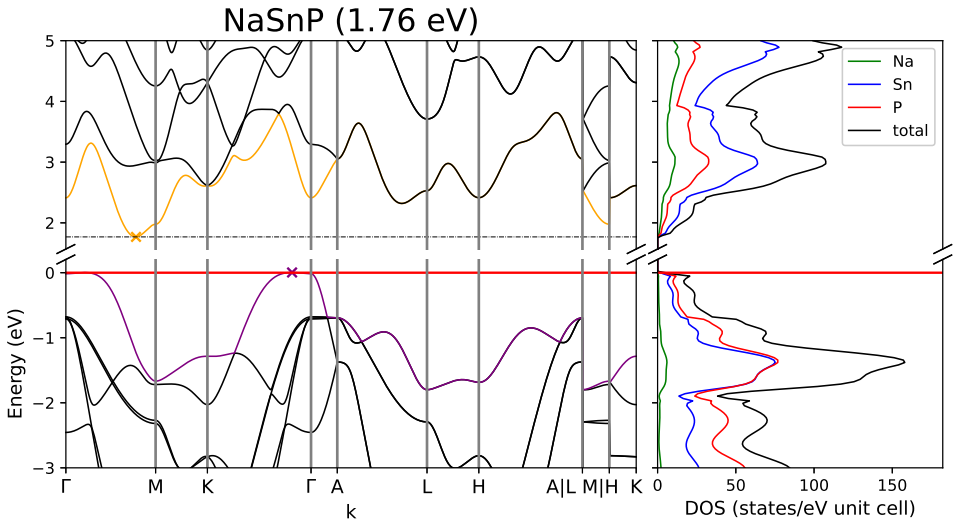

Figure A.96: Band structure and DOS of NaSnP.

Table A.159: Overlap population and interatomic distances of NaSnP.

Atom A	Atom B	r_{AB} / Å	overlap
Na1	P1	2.934	0.03
	Sn1	3.398	0.023
	P1	3.864	−0.003
	Na1	3.886	0.001
	Sn1	3.91	−0.001
	P1	4.869	0.0

Atom A	Atom B	r_{AB} / Å	overlap
Sn1	P1	2.599	0.205
	Sn1	3.886	−0.036
	P1	4.675	−0.003
	P1	4.976	0.0
P1	P1	3.886	−0.015

Table A.160: Partial charges for each atom position in NaSnP.

Atom	Z	charge	part charge
Na1	11	10.199	0.801
Sn1	22	22.129	−0.129

Atom	Z	charge	partialcharge
P1	15	15.672	−0.672

NaSnAs[119]

For a crystal structure description see NaSnP.

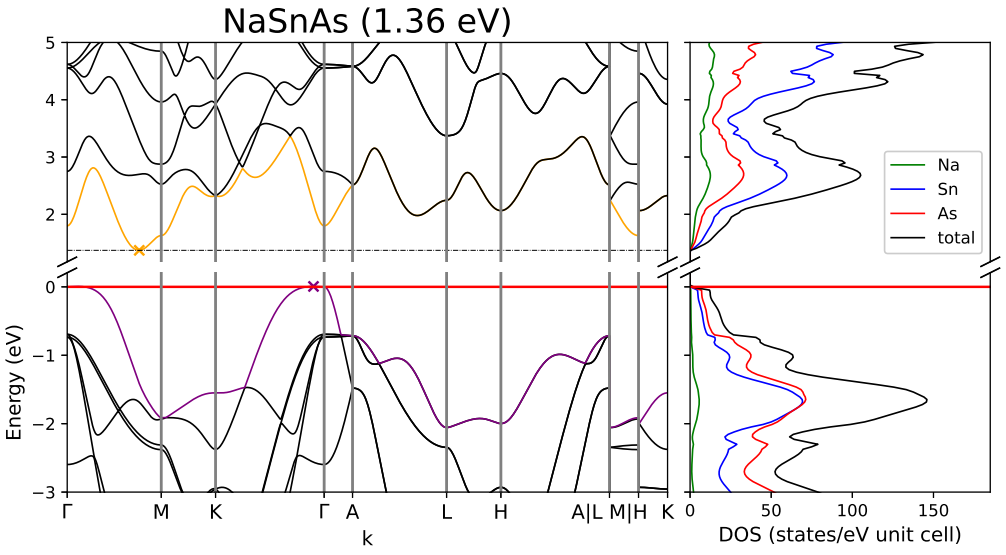

Figure A.97: Band structure and DOS of NaSnAs.

Table A.161: Overlap population and interatomic distances of NaSnAs.

Atom A	Atom B	r_{AB} / Å	overlap
Na1	As1	3.018	0.03
	Sn1	3.374	0.024
	As1	3.821	0.0
	Na1	4.011	0.001
	Sn1	4.034	0.0
	As1	5.02	0.0

Atom A	Atom B	r_{AB} / Å	overlap
Sn1	As1	2.69	0.213
	Sn1	4.011	−0.028
	As1	4.83	−0.002
	As1	4.962	0.0
As1	As1	4.011	−0.012

Table A.162: Partial charges for each atom position in NaSnAs.

Atom	Z	charge	part charge
Na1	11	10.205	0.795
Sn1	22	22.067	−0.067

Atom	Z	charge	partialcharge
As1	33	33.728	−0.728

NaSnSb - modelled based on NaSnAs

For a crystal structure description see NaSnP.

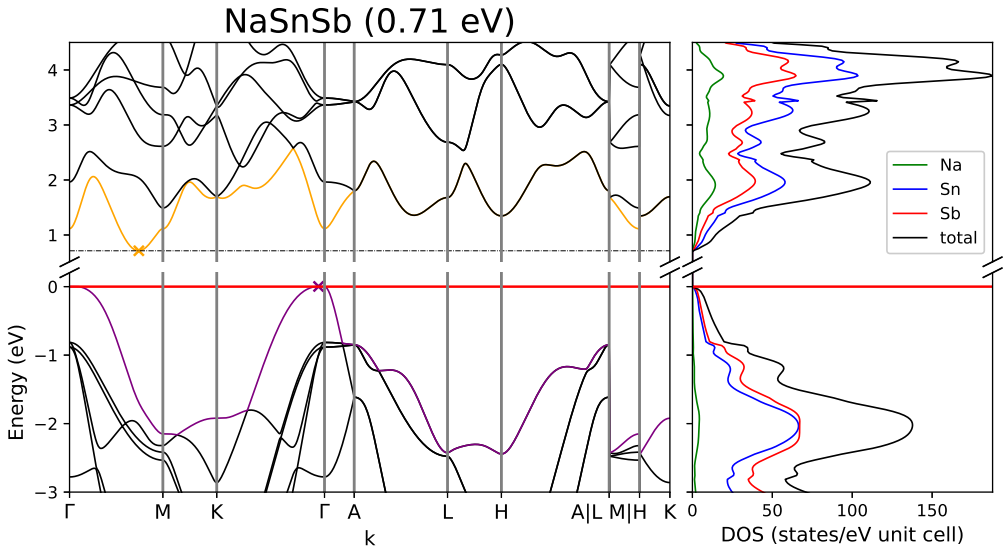

Figure A.98: Band structure and DOS of NaSnSb.

Table A.163: Overlap population and interatomic distances of NaSnSb.

Atom A	Atom B	r_{AB} / Å	overlap
Na1	Sb1	3.266	0.028
	Sn1	3.342	0.024
	Sb1	3.712	0.003
	Na1	4.292	0.0
	Sn1	4.368	0.0
	Sb1	5.394	0.0

Atom A	Atom B	r_{AB} / Å	overlap
Sn1	Sb1	2.881	0.213
	Sn1	4.292	−0.021
	Sb1	5.024	0.003
	Sb1	5.17	−0.002
Sb1	Sb1	4.292	−0.01

Table A.164: Partial charges for each atom position in NaSnSb.

Atom	Z	charge	part charge
Na1	11	10.199	0.801
Sn1	22	22.238	−0.238

Atom	Z	charge	partialcharge
Sb1	23	23.563	−0.563

KSnAs[32]

For a crystal structure description see NaSnP.

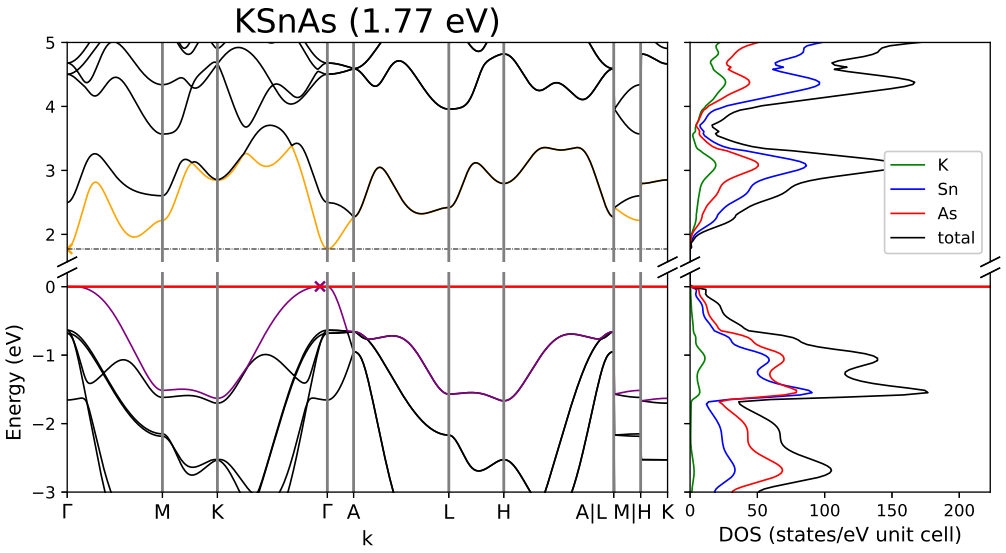

Figure A.99: Band structure and DOS of KSnAs.

Table A.165: Overlap population and interatomic distances of KSnAs.

Atom A	Atom B	r_{AB} / Å	overlap
K1	As1	3.335	0.017
	Sn1	3.659	0.011
	As1	4.103	0.0
	K1	4.104	0.001
	Sn1	4.361	−0.001
	As1	5.288	0.0

Atom A	Atom B	r_{AB} / Å	overlap
Sn1	As1	2.71	0.228
	Sn1	4.104	−0.026
	As1	4.918	−0.001
As1	As1	4.104	−0.01

Table A.166: Partial charges for each atom position in KSnAs.

Atom	Z	charge	part charge
K1	19	18.241	0.759
Sn1	22	22.092	−0.092

Atom	Z	charge	partialcharge
As1	33	33.667	−0.667

KSnSb[117]

For a crystal structure description see NaSnP.

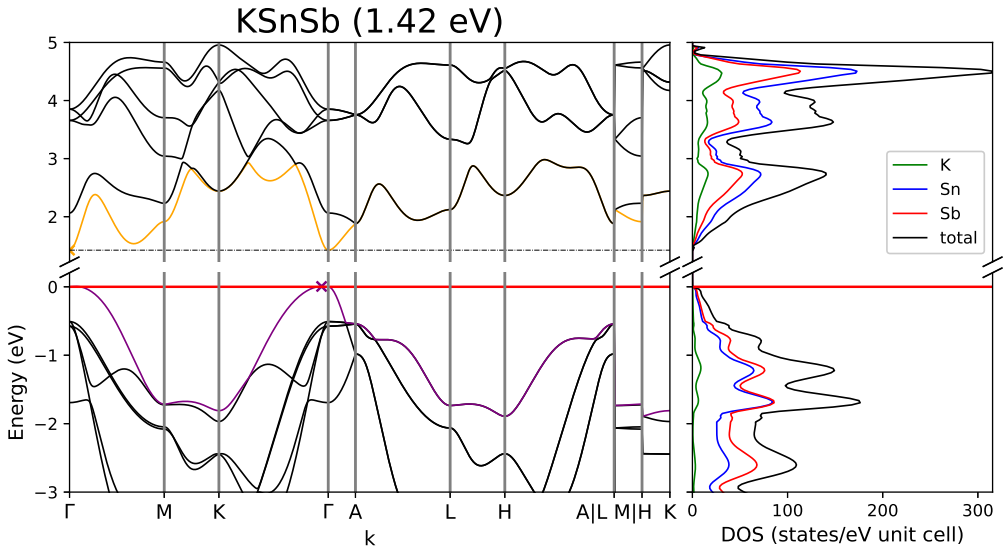

Figure A.100: Band structure and DOS of KSnSb.

Table A.167: Overlap population and interatomic distances of KSnSb.

Atom A	Atom B	r_{AB} / Å	overlap
K1	Sb1	3.565	0.017
	Sn1	3.653	0.011
	Sb1	4.064	−0.001
	K1	4.368	0.001
	Sn1	4.678	0.0
	Sb1	5.638	0.0

Atom A	Atom B	r_{AB} / Å	overlap
Sn1	Sb1	2.895	0.231
	Sn1	4.368	−0.018
	Sb1	5.24	−0.001
Sb1	Sb1	4.368	−0.009

Table A.168: Partial charges for each atom position in KSnSb.

Atom	Z	charge	part charge
K1	19	18.223	0.777
Sn1	22	22.259	−0.259

Atom	Z	charge	partialcharge
Sb1	23	23.518	−0.518

A.6 1-3-3

Table A.169: Overview of the crystallographic details of the 1-3-3 compounds. Cell parameters given in the first line and second line are of experimental and calculated origin, respectively. The third line shows the difference between both in percent.

compound	a / Å	b/ Å	c / Å	space group	crystal system	connectivity
$LiGe_3P_3$	9.8398	15.7865	3.6049	*Pbam* (no. 55)	orthorhombic	1D
	9.9335	16.0326	3.6129			
	0.94	1.53	0.22			
$NaGe_3P_3$	3.6276	8.407	10.332	$Pmc2_1$ (no. 26)	orthorhombic	1D
	3.627	8.413	10.408			
	-0.03	0.07	0.73			
KSi_3As_3	10.010	19.139	3.664	*Pbam* (no. 55)	orthorhombic	
	10.085	19.414	3.680			
	0.74	1.42	0.42			
KGe_3As_3	9.993	3.7664	18.607	*Pnma* (no. 62)	orthorhombic	1D
	10.126	3.7967	19.768			
	1.31	0.80	5.87			
KSn_3As_3	10.199	4.0840	19.240	-"-	-"-	-"-
	10.507	4.0694	20.315			
	2.94	-0.36	5.29			
$RbGe_3As_3$	10.166	3.7595	19.028	-"-	-"-	-"-
	10.241	3.8130	20.269			
	0.73	1.40	6.12			
$RbSn_3As_3$	10.321	4.0917	19.570	-"-	-"-	-"-
	10.619	4.0903	20.575			
	2.80	-0.03	4.88			

Table A.170: Calculated band gaps and transitions as well as an overview of the sampled reciprocal space defined by the Monkhorst-Pack-type *k*-point grid (SHRINK) and Brillouin Zone paths for all 1-3-3 compounds.

compound	band gap		transition	k-path	SHRINK
$LiGe_3P_3$	2.05	indirect	Γ -> Γ-Z	Γ—X—S—Y—Γ—Z—U—R—T—Z|X—U|Y—T|S—R	3 2 10
$NaGe_3P_3$	2.68	indirect	Z -> X	-"-	10 4 3
KSi_3As_3	2.75	indirect	X -> Γ-X	-"-	3 2 10
KGe_3As_3	2.38	indirect	Y-Γ -> Γ-X	-"-	6 16 4
KSn_3As_3	2.10	indirect	Y-Γ -> Γ-X	-"-	-"-
$RbGe_3As_3$	2.30	indirect	Γ-X -> Γ-X	-"-	3 8 2
$RbSn_3As_3$	2.01	indirect	Y-Γ -> Γ-X	-"-	-"-

$LiGe_3P_3$[120]

$LiGe_3P_3$ crystallizes in the orthorhombic space group *P b a m* (no. 55). The main structural motive consists of chains of edge-sharing Ge_4P_5-clusters. Within these clusters, chains of corner-sharing GeP_4- tetrahedra can be found which are further connected via vertex sharing with mixed Ge_2P_3-tetrahedra. These chains of clusters are further connected to layers. The Li atoms are located in between those layers and are octahedrally coordinated by P and Ge.

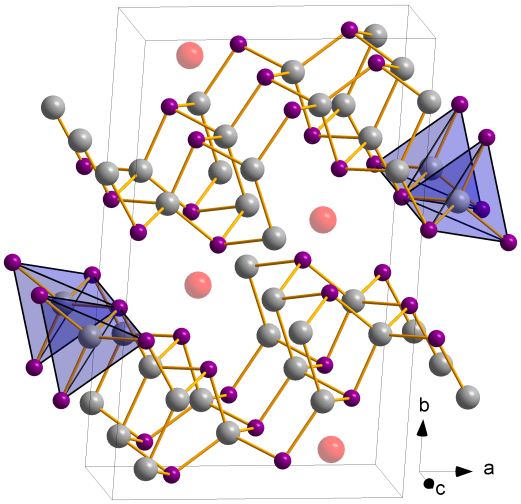

Figure A.101: Crystal structure of $LiGe_3P_3$ incorporating chains of corner-sharing GeP_4-tetrahedra within layers of Ge_4P_5-clusters.

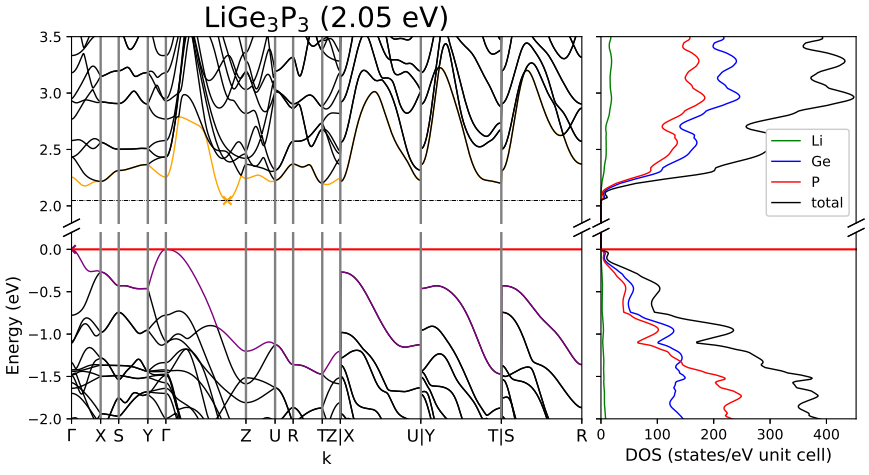

Figure A.102: Band structure and DOS of $LiGe_3P_3$.

Table A.171: Overlap population and interatomic distances of $LiGe_3P_3$.

Atom A	Atom B	r_{AB} / Å	overlap
Li1	P3	2.693	0.054
	Ge2	2.737	0.07
	P2	2.744	0.049
	P1	2.989	0.025
	Ge2	3.135	0.006
	Ge3	3.193	0.003
Ge1	P3	2.321	0.283
	P2	2.332	0.281
	P1	2.339	0.268
	Ge3	3.397	−0.047
	Ge3	3.6	−0.032
	Ge1	3.613	−0.033
Ge2	P3	2.413	0.219
	Ge3	2.543	0.248
	Ge2	3.482	−0.019
	Ge2	3.613	−0.025
Ge3	P2	2.363	0.238
	P1	2.377	0.241
P1	P2	3.578	−0.023
	P1	3.613	−0.02
P2	P2	3.613	−0.018
	P3	3.856	−0.014
P3	P3	3.613	−0.025

Table A.172: Partial charges for each atom position in $LiGe_3P_3$.

Atom	Z	charge	part charge
Li1	3	2.364	0.636
Ge1	32	32.078	−0.078
Ge2		32.173	−0.173
Ge3		32.137	−0.137
P1	15	15.067	−0.067
P2		14.999	0.001
P3		15.182	−0.182

$NaGe_3P_3$[121]

$NaGe_3P_3$ crystallizes in the orthorhombic space group $P\ m\ c\ 2_1$ (no. 26). Similar to $LiGe_3P_3$ the main structural motive consists of edge-sharing Ge_4P_5-clusters which are further connected to layers. Chains of corner-sharing GeP_4-tetrahedra which are connected via vertices to chains of Ge_2P_3-tetrahedra are present as well. Again the Na atoms lie in between the layers and are octahedrally coordinated by P and Ge.

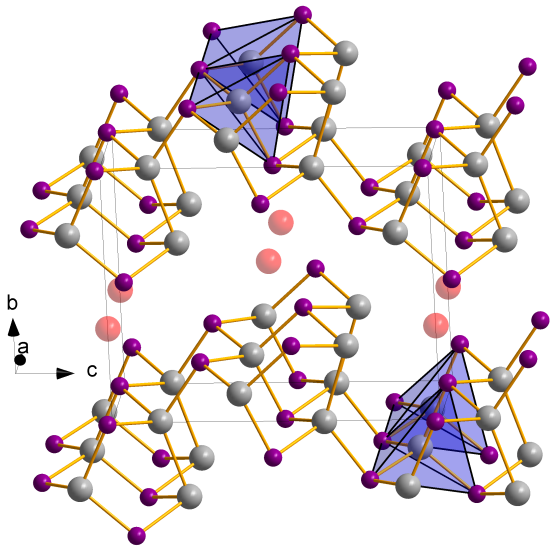

Figure A.103: Crystal structure of $NaGe_3P_3$ incorporating chains of corner-sharing GeP_4-tetrahedra within layers of Ge_4P_5-clusters.

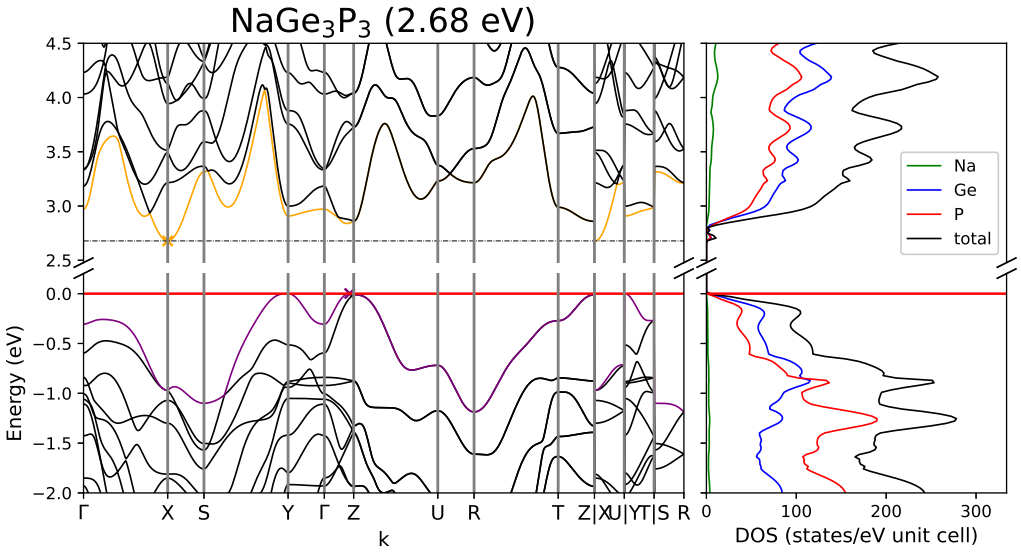

Figure A.104: Band structure and DOS of $NaGe_3P_3$.

Table A.173: Overlap population and interatomic distances of $NaGe_3P_3$.

Atom A	Atom B	r_{AB} / Å	overlap
Na1	P3	2.964	0.032
	Ge2	3.011	0.039
	P2	3.122	0.021
	P1	3.13	0.022
	Ge3	3.488	−0.002
	Na1	3.627	0.001
Ge1	P3	2.321	0.271
	P2	2.331	0.28
	P1	2.334	0.285
	Ge3	3.401	−0.053
	Ge1	3.627	−0.033
	Ge3	3.655	−0.032
Ge2	P3	2.404	0.235
	Ge3	2.548	0.257
	Ge2	3.627	−0.024
Ge3	P1	2.36	0.254
	P2	2.379	0.246
	Ge3	3.627	−0.029
P1	P2	3.577	−0.021
	P1	3.627	−0.017
	P3	3.804	−0.014
P2	P2	3.627	−0.017
	P3	3.741	−0.042
P3	P3	3.627	−0.022

Table A.174: Partial charges for each atom position in $NaGe_3P_3$.

Atom	Z	charge	part charge
Na1	11	10.206	0.794
Ge1	32	32.06	−0.06
Ge2		32.179	−0.179
Ge3		32.107	−0.107
P1	15	15.028	−0.028
P2		15.141	−0.141
P3		15.279	−0.279

KSi_3As_3[122]

KSi_3As_3 crystallizes in the orthorhombic space group *P b a m* (no. 55). Chains of edge-sharing Ge_5As_4-clusters build the main structural motive. Within these chains corner-sharing Ge_2P_3-tetrahedra are present. The cluster chains are further connected to layers by the Ge-Ge bonds, leading to an intersection of the Ge_2P_3-tetrahedra of neighbouring chains. K atoms are located in between the cluster-layers.
To calculate the structure of KSi_3As_3 the occupancy of K was changed from 0.98 % to 1.

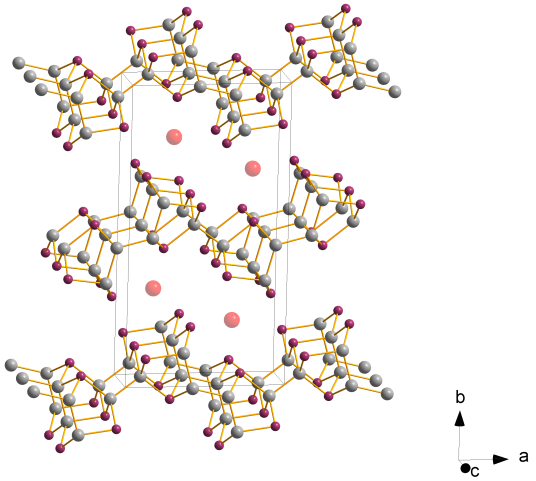

Figure A.105: Crystal structure of KSi_3As_3 incorporating intersecting chains of Ge_2P_3-tetrahedra.

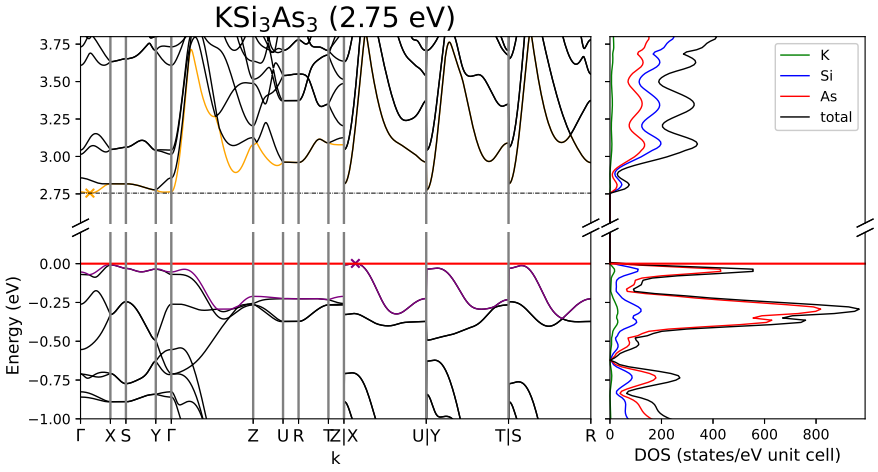

Figure A.106: Band structure and DOS of KSi_3As_3.

Table A.175: Overlap population and interatomic distances of KSi_3As_3.

Atom A	Atom B	r_{AB} / Å	overlap
As1	Si1	2.343	0.333
	K1	3.471	0.018
	K1	3.493	0.016
	As1	3.68	−0.032
	As3	3.968	−0.022
	Si2	3.971	−0.021
As2	Si2	2.387	0.288
	Si3	2.41	0.265
	K1	3.542	0.008
	As2	3.68	−0.029
	Si3	3.789	−0.035
	Si2	3.839	−0.022
As3	Si3	2.383	0.299
	Si1	2.428	0.264
	Si2	3.582	−0.056
	As3	3.68	−0.022
	K1	3.844	0.003
	Si3	3.877	−0.022

Atom A	Atom B	r_{AB} / Å	overlap
K1	Si1	3.608	−0.007
	K1	3.68	0.0
Si1	Si2	2.347	0.341
	Si3	3.512	−0.035
	Si1	3.68	−0.017
Si2	Si2	2.335	0.352
	Si3	3.514	−0.042
	Si2	3.68	−0.024
Si3	Si3	2.333	0.344
	Si3	3.68	−0.026

Table A.176: Partial charges for each atom position in KSi_3As_3.

Atom	Z	charge	part charge
As1	33	33.681	−0.681
As2		33.418	−0.418
As3		33.307	−0.307
K1	19	18.194	0.806

Atom	Z	charge	partialcharge
Si1	14	13.794	0.206
Si2		13.834	0.166
Si3		13.773	0.227

KGe_3As_3[37]

KGe_3As_3 crystallizes in the orthorhombic space group *P n m a* (no. 62). The structure incorporates again layers of Ge_4As_5-clusters similar to $LiGe_3P_3$. Again chains of corner-sharing $GeAs_4$ and Ge_2P_3-tetrahedra are connected via vertices to layers.

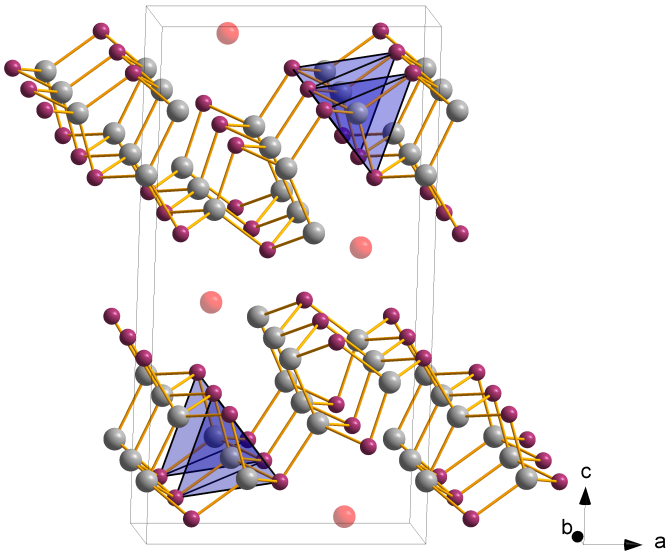

Figure A.107: Crystal structure of KGe_3As_3 incorporating chains of corner-sharing $GeAs_4$-tetrahedra within layers of Ge_4As_5-clusters.

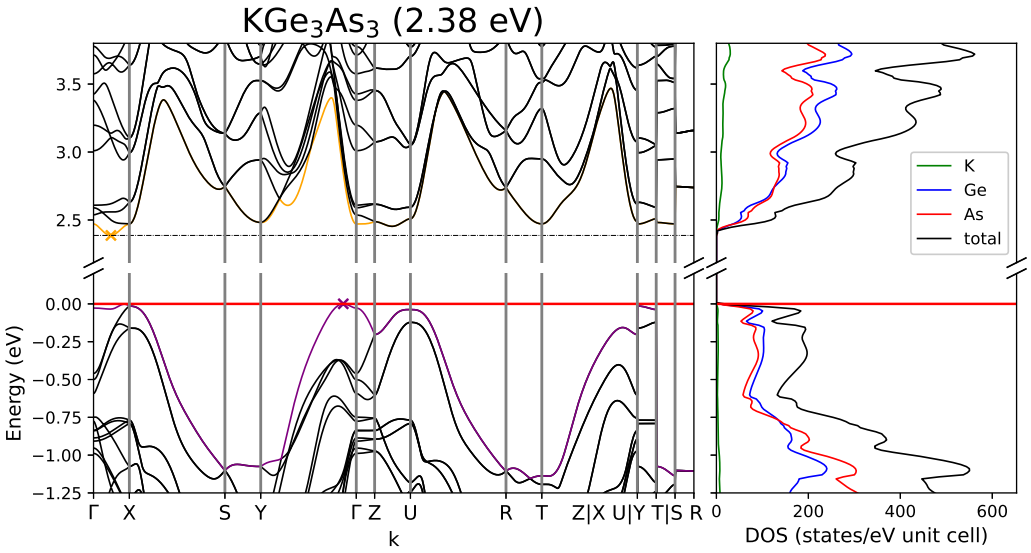

Figure A.108: Band structure and DOS of KGe_3As_3.

Table A.177: Overlap population and interatomic distances of KGe_3As_3.

Atom A	Atom B	r_{AB} / Å	overlap
K1	As3	3.353	0.003
	As2	3.403	0.015
	Ge3	3.569	0.011
	As1	3.645	0.012
	K1	3.797	0.0
	Ge3	4.1	−0.001
Ge1	As3	2.411	0.297
	As2	2.418	0.292
	As1	2.451	0.283
	Ge2	3.512	−0.032
	Ge2	3.771	−0.026
	Ge1	3.797	−0.021
Ge2	As3	2.476	0.262
	As1	2.479	0.26
	Ge3	2.551	0.276
	As2	3.793	−0.022
Ge3	As2	2.519	0.239
	As3	3.761	0.001
	Ge3	3.797	−0.021
As1	As3	3.709	−0.017
	As1	3.797	−0.019
	As3	3.996	−0.024
As2	As2	3.797	−0.013
	As3	3.884	−0.039
As3	As3	3.797	−0.014

Table A.178: Partial charges for each atom position in KGe_3As_3.

Atom	Z	charge	part charge
K1	19	18.194	0.806
Ge1	32	31.769	0.231
Ge2		31.886	0.114
Ge3		32.19	−0.19
As1	33	33.34	−0.34
As2		33.404	−0.404
As3		33.217	−0.217

KSn_3As_3[37]

For a crystal structure description see KGe_3As_3.

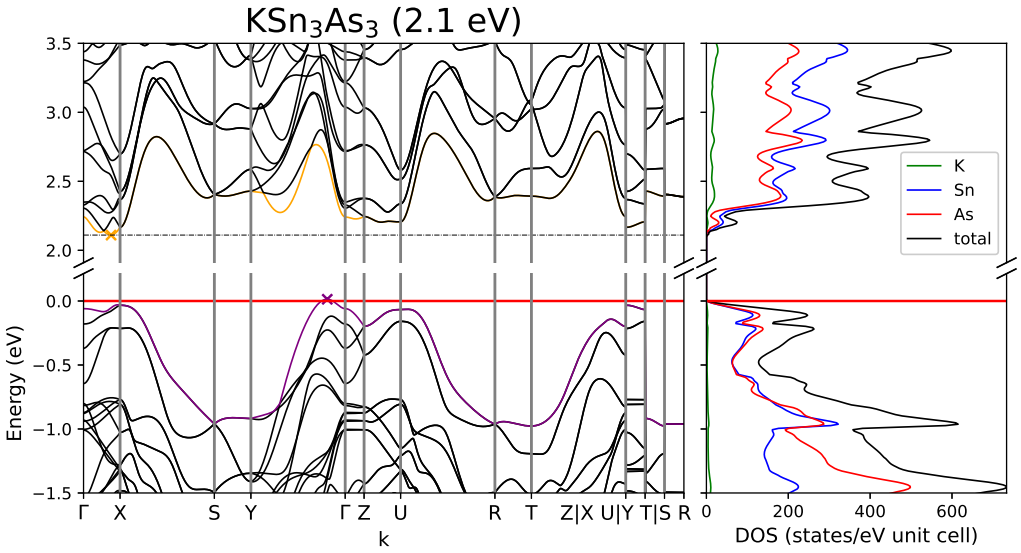

Figure A.109: Band structure and DOS of KSn_3As_3.

Table A.179: Overlap population and interatomic distances of KSn_3As_3.

Atom A	Atom B	r_{AB} / Å	overlap
K1	As2	3.403	0.015
	As3	3.488	0.004
	As1	3.539	0.012
	Sn3	3.79	0.006
	K1	4.069	0.0
	Sn3	4.24	−0.001
Sn1	As2	2.587	0.292
	As3	2.609	0.276
	As1	2.641	0.274
	Sn2	3.744	−0.031
	Sn2	3.991	−0.032
	Sn1	4.069	−0.019
Sn2	As1	2.656	0.246
	As3	2.67	0.256
	Sn3	2.914	0.23
	Sn2	4.069	−0.022

Atom A	Atom B	r_{AB} / Å	overlap
Sn3	As2	2.718	0.218
	As3	3.754	0.001
	Sn3	4.069	−0.022
As1	As3	4.015	−0.008
	As1	4.069	−0.012
	As3	4.291	−0.017
As2	As2	4.069	−0.009
	As3	4.29	−0.022
As3	As3	4.069	−0.008

Table A.180: Partial charges for each atom position in KSn_3As_3.

Atom	Z	charge	part charge
K1	19	18.18	0.82
Sn1	22	21.539	0.461
Sn2		21.758	0.242
Sn3		22.021	−0.021

Atom	Z	charge	partialcharge
As1	33	33.533	−0.533
As2		33.598	−0.598
As3		33.371	−0.371

$RbGe_3As_3$[37]

For a crystal structure description see KGe_3As_3.

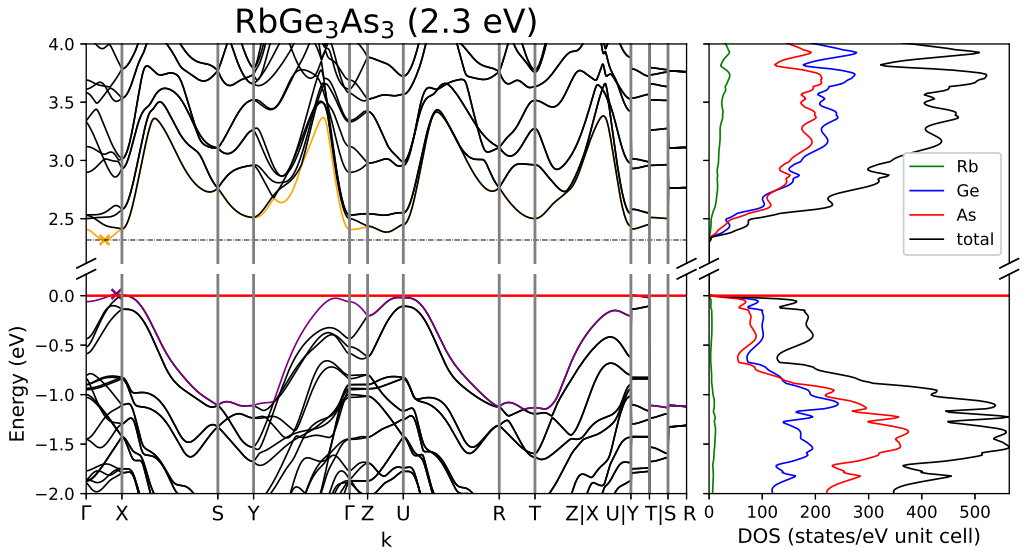

Figure A.110: Band structure and DOS of $RbGe_3As_3$.

Table A.181: Partial charges for each atom position in $RbGe_3As_3$.

Atom	Z	charge	part charge
Rb1	9	8.244	0.756
Ge1	32	31.789	0.211
Ge2		31.894	0.106
Ge3		32.16	−0.16

Atom	Z	charge	partialcharge
As1	33	33.335	−0.335
As2		33.382	−0.382
As3		33.197	−0.197

Table A.182: Overlap population and interatomic distances of $RbGe_3As_3$.

Atom A	Atom B	r_{AB} / Å	overlap
Rb1	As3	3.485	0.004
	As2	3.546	0.017
	Ge3	3.713	0.011
	As1	3.782	0.013
	Rb1	3.813	−0.003
	As2	4.211	−0.001
Ge1	As3	2.413	0.293
	As2	2.418	0.292
	As1	2.456	0.282
	Ge2	3.507	−0.033
	Ge2	3.784	−0.026
	Ge1	3.813	−0.02
Ge2	As1	2.481	0.263
	As3	2.481	0.261
	Ge3	2.551	0.273
	As2	3.792	−0.021
Ge3	As2	2.52	0.24
	As3	3.781	0.002
	Ge3	3.813	−0.022
As1	As3	3.736	−0.016
	As1	3.813	−0.019
	As3	4.019	−0.022
As2	As2	3.813	−0.013
	As3	3.891	−0.039
As3	As3	3.813	−0.014

$RbSn_3As_3$[37]

For a crystal structure description see KGe_3As_3.

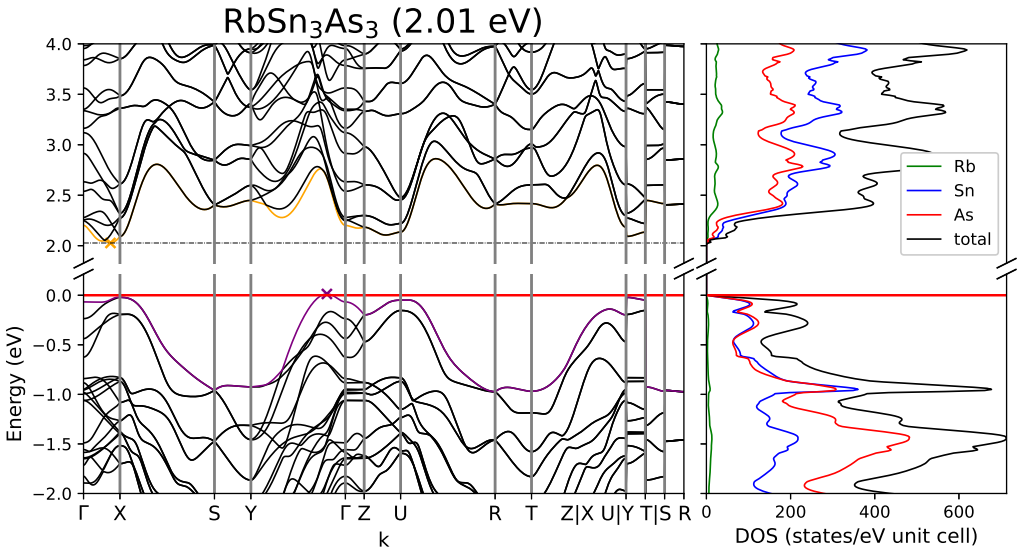

Figure A.111: Band structure and DOS of $RbSn_3As_3$.

Table A.183: Overlap population and interatomic distances of $RbSn_3As_3$.

Atom A	Atom B	r_{AB} / Å	overlap
Rb1	As2	3.532	0.017
	As3	3.604	0.005
	As1	3.686	0.013
	Sn3	3.917	0.004
	Rb1	4.09	−0.001
	As1	4.441	0.004
Sn1	As2	2.586	0.29
	As3	2.611	0.277
	As1	2.647	0.272
	Sn2	3.74	−0.031
	Sn2	3.998	−0.03
	Sn1	4.09	−0.02
Sn2	As1	2.662	0.248
	As3	2.677	0.256
	Sn3	2.919	0.225
	Sn2	4.09	−0.021
Sn3	As2	2.718	0.222
	As3	3.755	0.001
	Sn3	4.09	−0.023
As1	As3	4.053	−0.008
	As1	4.09	−0.012
	As2	4.319	−0.012
As2	As2	4.09	−0.008
	As3	4.297	−0.021
As3	As3	4.09	−0.008

Table A.184: Partial charges for each atom position in $RbSn_3As_3$.

Atom	Z	charge	part charge
Rb1	9	8.231	0.769
Sn1	22	21.57	0.43
Sn2		21.758	0.242
Sn3		21.988	0.012
As1	33	33.528	−0.528
As2		33.567	−0.567
As3		33.357	−0.357

A.7 2-3-3

Table A.185: Overview of the crystallographic details of the 2-3-3 compounds. Cell parameters given in the first line and second line are of experimental and calculated origin, respectively. The third line shows the difference between both in percent.

compound	a / Å	b/ Å	c / Å	β / °	space group	crystal system	connectivity
$Na_2Ga_3Sb_3$	26.890	4.283	7.236		*P n m a* (no. 62)	orthorhombic	–
	26.746	4.293	7.249				
	-0.54	0.24	0.18				
$Na_2Ge_3P_3$	17.639	3.6176	11.3540	92.74	*C* 2/ *m* (no. 12)	monoclinic	1D
	17.4878	3.6330	11.3259	93.06			
	-0.86	0.42	-0.25	0.35			
$K_2Ge_3As_3$	14.1466		16.300	3.7489	*P n n m* (no. 58)	orthorhombic	–
	14.1400		16.534	3.7931			
	-0.05	1.41	1.17				

Table A.186: Calculated band gaps and transitions as well as an overview of the sampled reciprocal space defined by the Monkhorst-Pack-type *k*-point grid (SHRINK) and Brillouin Zone paths for all 2-3-3 compounds.

compound	band gap		transition	k-path	SHRINK
$Na_2Ga_3Sb_3$	1.46	pseudo-direct	Γ -> Γ	Γ-X-S-Y-Γ-Z-U-R-T-Z|X-U|Y-T|S-R	2 8 4
$K_2Ge_3As_3$	2.70	pseudo-direct	Γ -> Γ	Γ-X-S-Y-Γ-Z-U-R-T-Z|X-U|Y-T|S-R	2 2 8
$Na_2Ge_3P_3$	2.50	indirect	Y_2 -> D_2-A	Γ—C|C_2—Y_2—G—M_2—D|D_2—A—Γ|L_2—Γ—V_2	4 4 3

$Na_2Ga_3Sb_3$[159]

$Na_2Ga_3Sb_3$ crystallizes in the orthorhombic space group *P n m a* (no. 62). The general structural motive of this compound consists of GaSb alternating six-membered rings, of which 3 are connected along c. Within such a three layer unit the outer layers and the inner layer are analogue to grey arsenic and black phosphorous, respectively. The outer layers are connected to the inner layer via Ga1-Ga3 and Sb2-Ga2, forming channels in which Na1 is incorporated. Na2 is located in between units of layers.

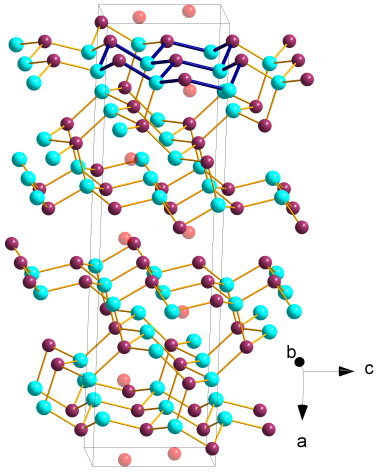

Figure A.112: Crystal structure of $Na_2Ga_3Sb_3$ incorporating three in c-direction connected layers of GaSb-mixed-six-membered rings.

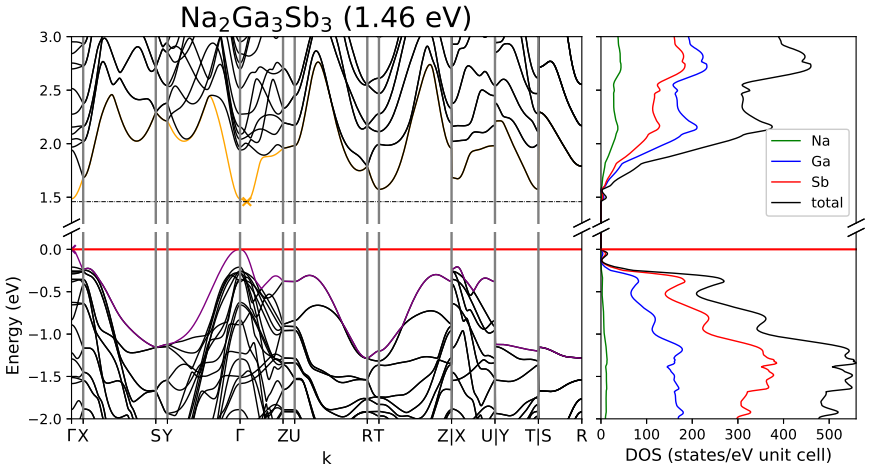

Figure A.113: Band structure and DOS of $Na_2Ga_3Sb_3$.

Table A.187: Overlap population and interatomic distances of $Na_2Ga_3Sb_3$.

Atom A	Atom B	r_{AB} / Å	overlap
Sb1	Ga2	2.624	0.283
	Ga3	2.667	0.28
	Na2	3.228	0.022
	Na2	3.253	0.027
	Na1	3.855	0.004
	Sb2	4.219	−0.017
Sb2	Ga2	2.688	0.287
	Ga3	2.721	0.295
	Na2	3.335	0.031
	Na2	3.386	0.033
	Na1	3.425	0.012
Sb3	Ga1	2.711	0.265
	Ga2	2.725	0.246
	Ga1	2.798	0.248
	Na1	3.405	0.012
	Na1	3.45	0.01
	Na1	4.069	0.001
Ga1	Ga3	2.54	0.141
	Na1	3.224	0.014
	Na1	3.233	0.003
	Ga2	3.927	−0.033
Ga2	Na1	3.05	0.012
	Ga3	3.848	−0.03
	Na2	3.923	0.003
Ga3	Na1	3.128	0.006
	Na2	4.026	0.0
Na2	Na2	3.792	0.002

Table A.188: Partial charges for each atom position in $Na_2Ga_3Sb_3$.

Atom	Z	charge	part charge
Sb1	23	23.479	−0.479
Sb2		23.45	−0.45
Sb3		23.141	−0.141
Ga1	31	31.312	−0.312
Ga2		31.045	−0.045
Ga3		31.198	−0.198
Na1	11	10.135	0.865
Na2		10.24	0.76

$Na_2Ge_3P_3$[160]

$Na_2Ge_3P_3$ crystallizes in the monoclinic space group *C* 2/ *m* (no.12). The main strcutural motive are chains of side-sharing Ge_4P_5-clusters along the b-axis. Two adjacent chains are linked via a Ge-Ge bond. These cluster chains can be further described by a connection of GeP_4- and Ge_3P_2-tetrahedra: at the Ge-Ge bond connecting two adjacent chains two along that bond intersecting Ge_3P_2-tetrahedra are formed. Two such intersected tetrahedra are

further connected via a shared vertex that at the same time belongs to a GeP_4-tetrahedron, which is located at the outer side of the chains. these GeP_4-tetrahdra are connected to each other via shared corners and together with the Ge_3P_2-tetrahedra form empty, six-membered ring shaped channels. Na is located in layers between the dimeric chains. Adjacent dimeric chains are parallel to each other along a.

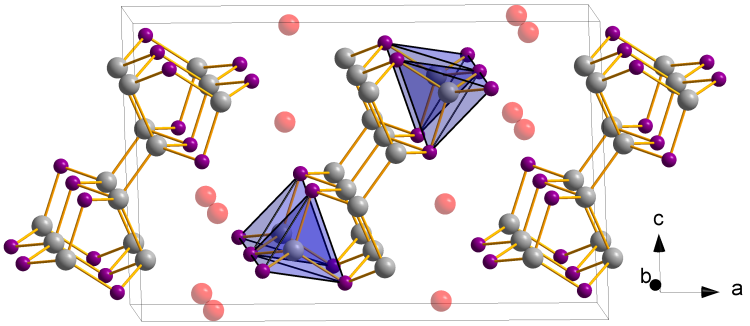

Figure A.114: Crystal structure of $Na_2Ge_3P_3$ with dimeric chains of side-sharing Ge_4P_5-clusters incorporating one dimensional chains of corner-sharing GeP_4-tetrahedra.

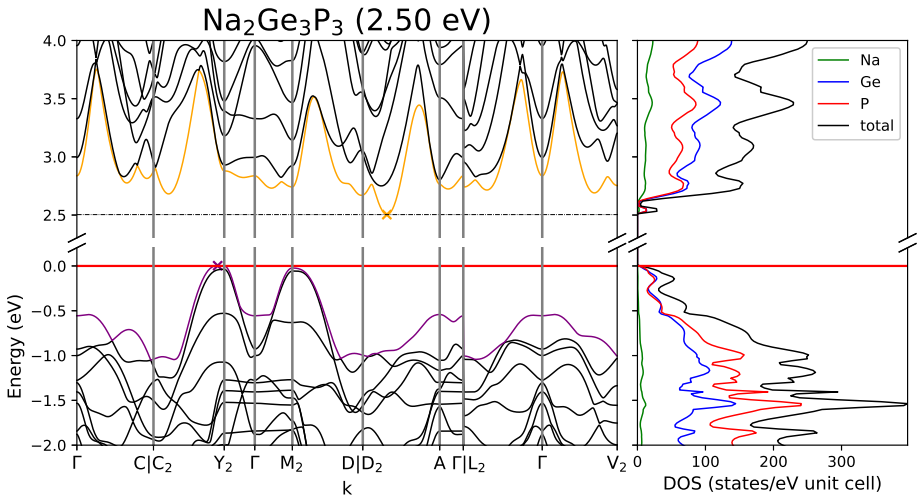

Figure A.115: Band structure and DOS of $Na_2Ge_3P_3$.

Table A.189: Partial charges for each atom position in $Na_2Ge_3P_3$.

Atom	Z	charge	part charge
Na1	11	10.21	0.79
Na2		10.218	0.782
Ge1	32	32.091	−0.091
Ge2		32.305	−0.305
Ge3		32.032	−0.032

Atom	Z	charge	partialcharge
P1	15	15.285	−0.285
P2		15.647	−0.647
P3		15.213	−0.213

Table A.190: Overlap population and interatomic distances of $Na_2Ge_3P_3$.

Atom A	Atom B	r_{AB} / Å	overlap
Na1	P2	3.004	0.034
	P1	3.043	0.028
	Ge2	3.149	0.032
	Ge1	3.188	−0.003
	Ge3	3.476	0.001
	Na1	3.633	0.002
Na2	P3	2.981	0.029
	P2	3.005	0.033
	P2	3.198	0.028
	Ge2	3.241	0.024
	Ge1	3.61	−0.001
	Na2	3.633	0.002
Ge1	P3	2.323	0.268
	P2	2.323	0.283
	P1	2.364	0.249
	Ge3	3.43	−0.057
Ge2	P3	2.382	0.253
	Ge3	2.542	0.283
	Ge2	3.633	−0.028
Ge3	P1	2.367	0.251
	Ge3	2.454	0.297
	Ge3	3.633	−0.033
P1	P1	3.633	−0.02
	P3	3.743	−0.042
P2	P2	3.633	−0.036
P3	P3	3.633	−0.024
	P3	3.742	0.001

$K_2Ge_3As_3$[161]

$K_2Ge_3As_3$ crystallizes in the orthorhombic space group *P n n m* (no. 58). It incorporates the same dimeric chains as Na_3GeP_4, but the atom arrangement within the Ge_4As_5-clusters is different. This time intersecting Ge_2As_3-tetrahedra are formed along the Ge-Ge bond connecting two adjacent chains. These tetrahedra are further connected by corner-sharing with themself as well as to Ge_2As_3-tetrahedra at the outer side of the chains. With this, in contrast to $Na_2Ge_3P_3$, no pure Ge-centred pnictide tetrahedra are present. Further on every second chain is twisted by 90 °.

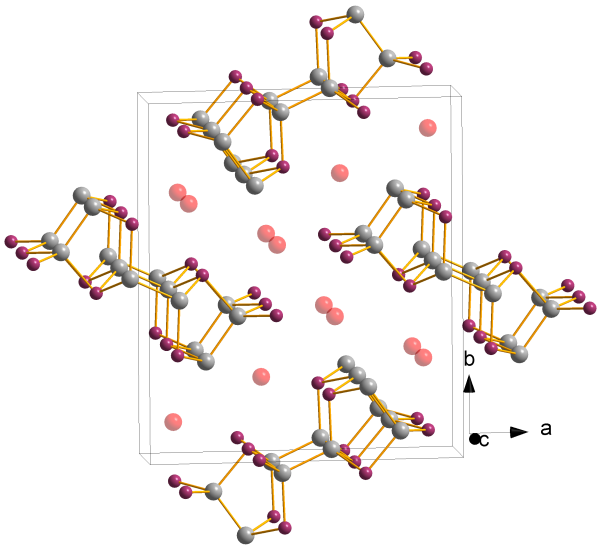

Figure A.116: Crystal structure of $K_2Ge_3As_3$

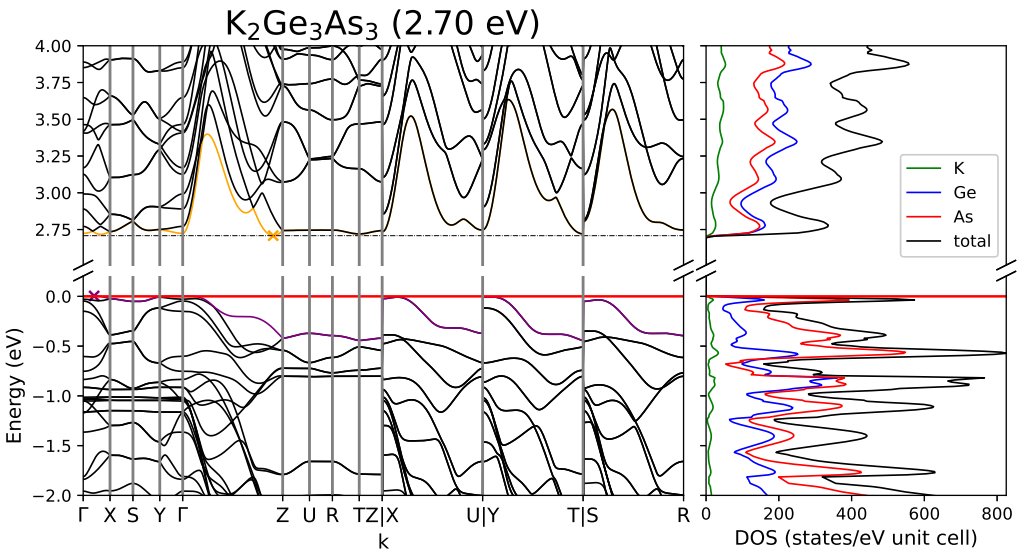

Figure A.117: Band structure and DOS of $K_2Ge_3As_3$.

Table A.191: Partial charges for each atom position in $K_2Ge_3As_3$.

Atom	Z	charge	part charge
K1	19	18.209	0.791
K2		18.217	0.783
Ge1	32	31.843	0.157
Ge2		31.874	0.126
Ge3		32.379	−0.379

Atom	Z	charge	partialcharge
As1	33	33.391	−0.391
As2		33.357	−0.357
As3		33.73	−0.73

Table A.192: Overlap population and interatomic distances of $K_2Ge_3As_3$.

Atom A	Atom B	r_{AB} / Å	overlap
K1	As3	3.481	0.015
	As3	3.531	0.018
	As2	3.587	0.008
	As1	3.683	0.003
	Ge2	3.719	−0.004
	Ge3	3.727	0.01
K2	As3	3.338	0.023
	As2	3.362	0.016
	As1	3.414	0.017
	Ge3	3.556	0.007
	K2	3.793	0.0
	Ge2	3.814	−0.003
Ge1	As2	2.441	0.278
	As1	2.465	0.263
	Ge1	2.466	0.298
	Ge2	3.616	−0.032
	Ge1	3.793	−0.028
	Ge3	3.916	−0.026

Atom A	Atom B	r_{AB} / Å	overlap
Ge2	As3	2.43	0.307
	As2	2.486	0.253
	Ge3	2.514	0.309
	As1	3.769	−0.021
Ge3	As1	2.493	0.249
	Ge3	3.793	−0.02
As1	As1	3.793	−0.017
As2	As2	3.793	−0.015
	As3	3.942	−0.022
As3	As3	3.793	−0.022

A.8 3-2-3

Table A.193: Overview of the crystallographic details of the 3-2-3 compounds. Cell parameters given in the first line and second line are of experimental and calculated origin, respectively. The third line shows the difference between both in percent.

compound	a / Å	b/ Å	c / Å	β / °	space group	crystal system	connectivity
$Na_3In_2P_3$	13.795	7.6632	6.9266		*C m c* 2_1 (no. 36)	orthorhombic	3D
	13.635	7.6730	6.9457				
	-1.17	0.13	0.28				
$K_3Al_2As_3$	10.494	5.991	7.534	110.5	*P* 2_1 / *m* (no. 11)	monoclinic	1D
	10.459	6.007	7.538	110.0			
	-0.33	0.27	0.05	-0.44			
$K_3In_2As_3$	19.764	6.784	14.871		*C m c a* (no. 64)	orthorhombic	2D
	19.896	6.778	14.775				
	0.67	-0.09	-0.65				
$Na_3Ge_2P_3$	7.2894	14.7725	7.0528	106.331	*P* 2_1 / *c* (no. 14)	monoclinic	3D
	7.2137	14.6654	7.0381	107.258			
	-1.05	-0.73	-0.21	0.86			

Table A.194: Calculated band gaps and transitions as well as an overview of the sampled reciprocal space defined by the Monkhorst-Pack-type *k*-point grid (SHRINK) and Brillouin Zone paths for all 3-2-3 compounds.

compound	band gap		transition	k-path	SHRINK
$Na_3In_2P_3$	1.99	direct	Γ -> Γ	Γ-S-Y-Z-Γ-Y-T-Z	5 5 5
$K_3Al_2As_3$	3.00	direct	Γ -> Γ	Γ—Z—D—B—Γ—A—E—Z—C_2—Y_2—Γ	8 8 8
$K_3In_2As_3$	2.37	indirect	Y -> Γ	Γ-Y-F_0|Γ-Z-B_0|T-Y|Γ-S-R-Z-T	8 8 8
$Na_3Ge_2P_3$	2.95	indirect	Γ -> E-Z	Γ—Z—D—B—Γ—A—E—Z—C_2—Y_2—Γ	5 3 5

$K_3Al_2As_3$[162]

$K_3Al_2As_3$ crystallizes in the monoclinic space group $P\ 2_1\ /\ m$ (no.11). The AlP_4 tetrahedra form one dimensional double-chains of edge sharing tetrahedra along the b axis. The chains can be further described as dimers of edge-sharing tetrahedra which form chains along b by further edge-sharing.

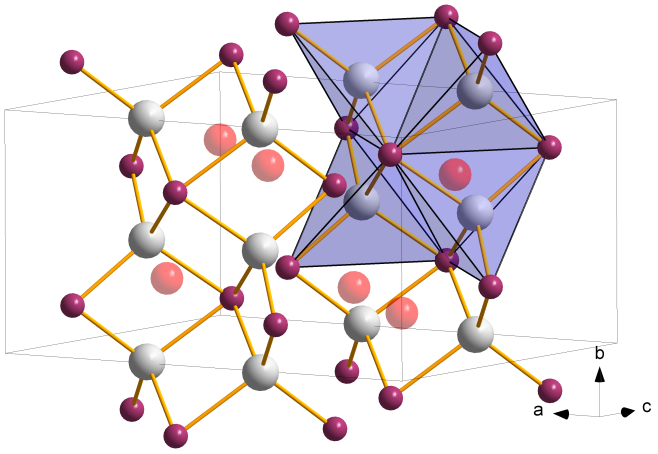

Figure A.118: Crystal structure of $K_3Al_2As_3$ showing one dimensional double chains along b.

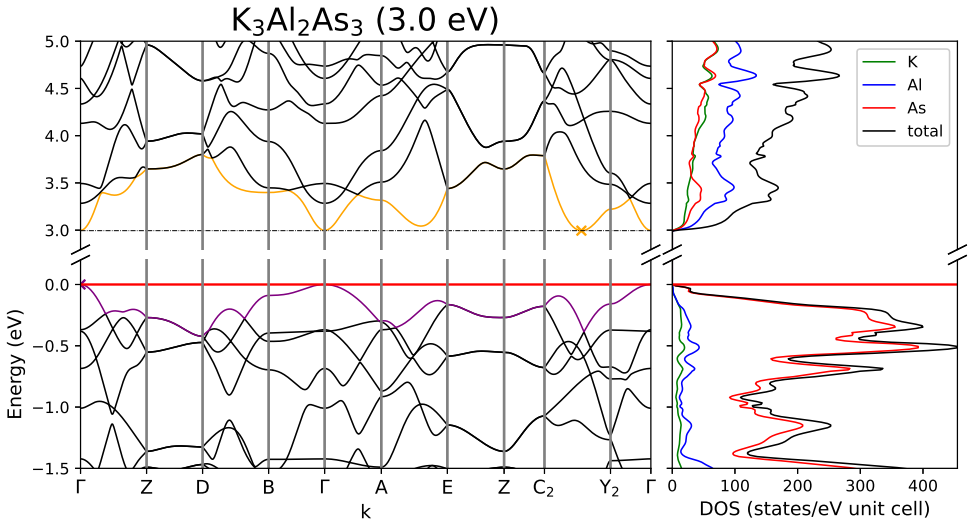

Figure A.119: Band structure and DOS of $K_3Al_2As_3$.

Table A.195: Overlap population and interatomic distances of $K_3Al_2As_3$.

Atom A	Atom B	r_{AB} / Å	overlap
K1	As2	3.322	0.018
	As3	3.324	0.01
	As1	3.361	0.009
	As1	3.5	0.005
	K1	3.682	−0.001
	Al1	3.824	−0.004
K2	As3	3.267	0.02
	As1	3.292	0.0
	As2	3.345	0.028
	As2	3.411	0.02
	Al1	3.624	−0.005
	K3	3.97	0.001
K3	As3	3.373	0.024
	As2	3.471	0.012
	As3	3.544	0.017
	K3	3.65	0.001
	Al1	3.767	−0.001

Atom A	Atom B	r_{AB} / Å	overlap
Al1	As3	2.442	0.346
	As2	2.466	0.331
	As1	2.57	0.204
	As1	2.588	0.205
	Al1	3.003	0.031
	Al1	3.004	0.025
As1	As3	4.018	−0.049

Table A.196: Partial charges for each atom position in $K_3Al_2As_3$.

Atom	Z	charge	part charge
K1	19	18.211	0.789
K2		18.237	0.763
K3		18.238	0.762
Al1	13	12.598	0.402

Atom	Z	charge	partialcharge
As1	33	33.897	−0.897
As2		34.126	−1.126
As3		34.096	−1.096

$Na_3Ge_2P_3$[70]

$Na_3Ge_2P_3$ crystallizes in the monoclinic space group $P\ 2_1\ /\ c$ (no. 14). It shows a three dimensional network of mixed Ge_2P_3 tetrahedra. Within this network corner- and edge-sharing dimers of intersecting mixed tetrahedra can be found.

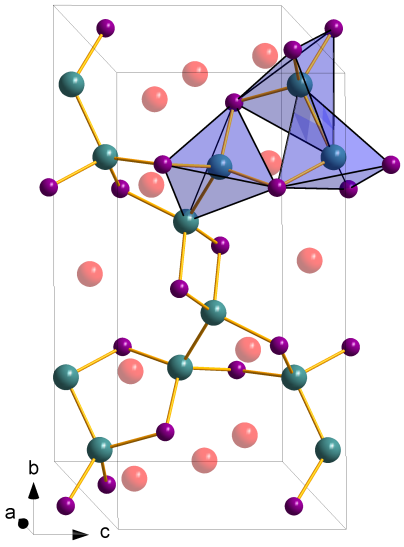

Figure A.120: Crystal structure of $Na_3Ge_2P_3$ incorporating a three dimensional network of mixed edge- and corner-sharing Ge_2P_3 tetrahedra.

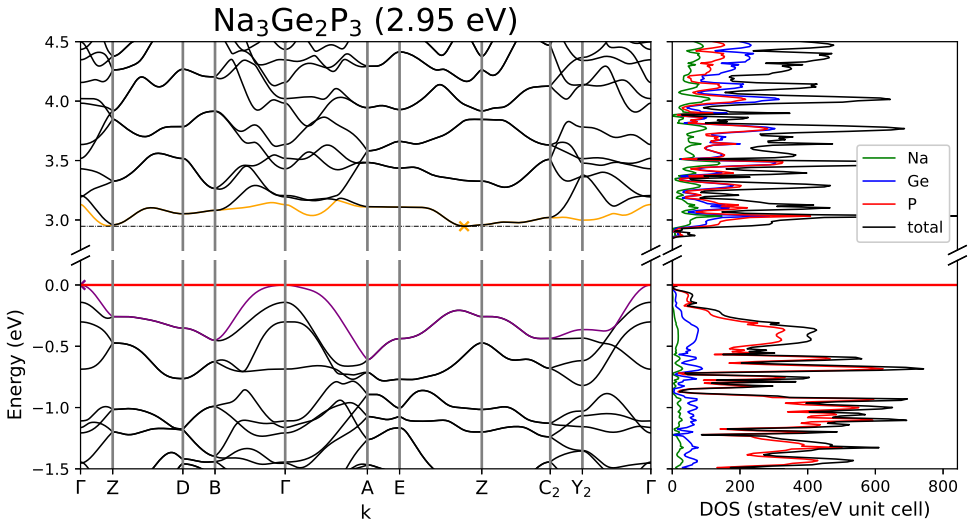

Figure A.121: Band structure and DOS of $Na_3Ge_2P_3$.

Table A.197: Overlap population and interatomic distances of $Na_3Ge_2P_3$.

Atom A	Atom B	r_{AB} / Å	overlap
Na1	P1	2.891	0.034
	P3	2.959	0.035
	P2	2.989	0.027
	P1	3.01	0.039
	P2	3.165	0.031
	Na2	3.295	0.003
Na2	P2	2.782	0.036
	P3	2.822	0.053
	P1	2.827	0.036
	P3	3.079	0.034
	P2	3.209	0.025
	Ge1	3.26	−0.004
Na3	P1	2.953	0.029
	P2	2.956	0.044
	P3	3.036	0.037
	P1	3.18	0.036
	Na3	3.209	0.005
	Ge1	3.28	0.001

Atom A	Atom B	r_{AB} / Å	overlap
Ge1	P2	2.318	0.26
	P2	2.322	0.288
	P1	2.341	0.28
	Ge2	2.482	0.303
Ge2	P1	2.328	0.262
	P3	2.352	0.285
	P3	2.361	0.273
	Ge2	3.01	−0.063

Table A.198: Partial charges for each atom position in $Na_3Ge_2P_3$.

Atom	Z	charge	part charge
Na1	11	10.224	0.776
Na2		10.267	0.733
Na3		10.246	0.754
Ge1	32	32.072	−0.072
Ge2		31.963	0.037

Atom	Z	charge	partialcharge
P1	15	15.771	−0.771
P2		15.697	−0.697
P3		15.76	−0.76

$Na_3In_2P_3$[72]

$Na_3In_2P_3$ crystallizes in the orthorhombic space group $C\ m\ c\ 2_1$ (no. 36). The P atoms form a distorted hcp, where In occupies one third of the tetrahedral voids. The compound further shows a three dimensional network of corner-sharing InP_4 tetrahedra. The tetrahedra therein form six membered rings within the ab-plane, which are connected via corner sharing to rings within the lower lying layer.

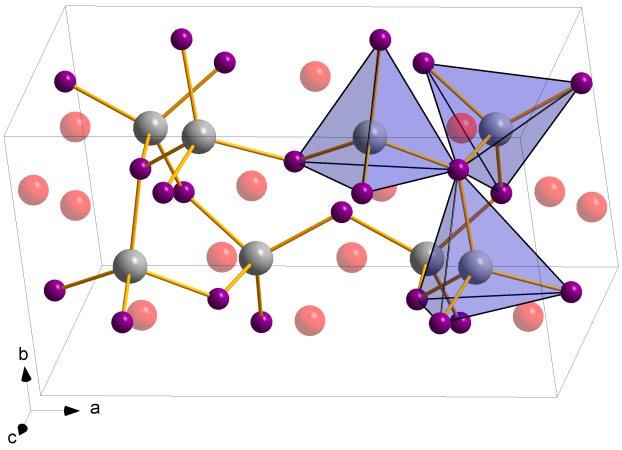

Figure A.122: Crystal structure of $Na_3In_2P_3$ forming a three dimensional network of corner-sharing InP_4 tetrahedra.

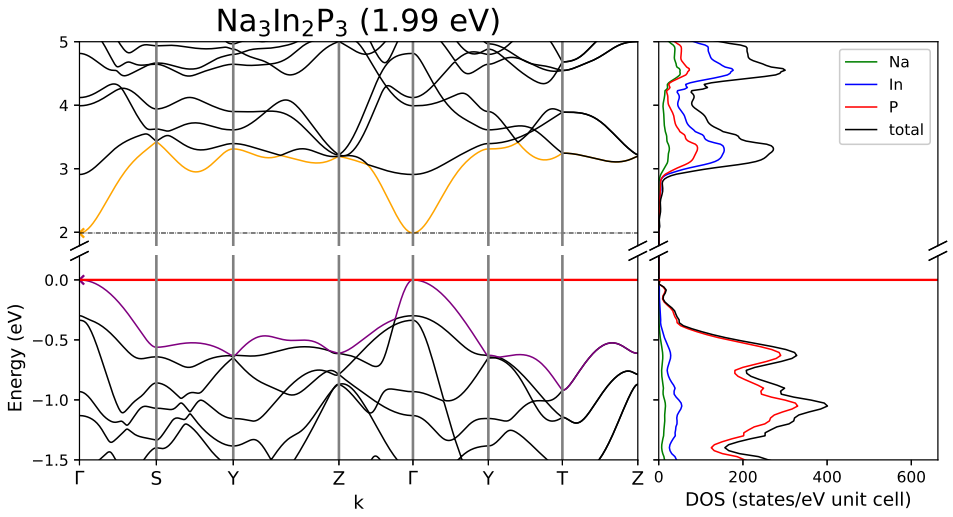

Figure A.123: Band structure and DOS of $Na_3In_2P_3$.

Table A.199: Overlap population and interatomic distances of $Na_3In_2P_3$.

Atom A	Atom B	r_{AB} / Å	overlap
Na1	P2	2.807	0.04
	P1	2.932	0.049
	Na2	3.271	0.006
	In1	3.277	0.006
	P1	3.578	0.005
	Na2	3.869	0.001
Na2	P1	2.83	0.044
	P2	3.012	0.025
	P2	3.03	0.016
	P1	3.055	0.036
	In1	3.13	0.001

Atom A	Atom B	r_{AB} / Å	overlap
In1	P2	2.568	0.257
	P1	2.57	0.275
	P2	2.604	0.256
	P2	2.612	0.252
P1	P2	4.182	−0.019

Table A.200: Partial charges for each atom position in $Na_3In_2P_3$.

Atom	Z	charge	part charge
Na1	11	10.235	0.765
Na2		10.217	0.783
In1	21	20.972	0.028

Atom	Z	charge	partialcharge
P1	15	15.996	−0.996
P2		15.696	−0.696

$K_3In_2As_3$[163]

$K_3In_2As_3$ crystallizes in the orthorhombic space group *C m c a* (no. 64). Within the structure $InAs_4$ tetrahedra form two dimensional layers. Within the layers hexagonal channels are formed which align along c. The channels are build by two edge-sharing tetrahedra at the sides which are connected to two further tetrahedra by corner-sharing. With this individual six membered rings are formed which are connected to layers by edge-sharing of the tetrahedra at the tip of the six membered rings.

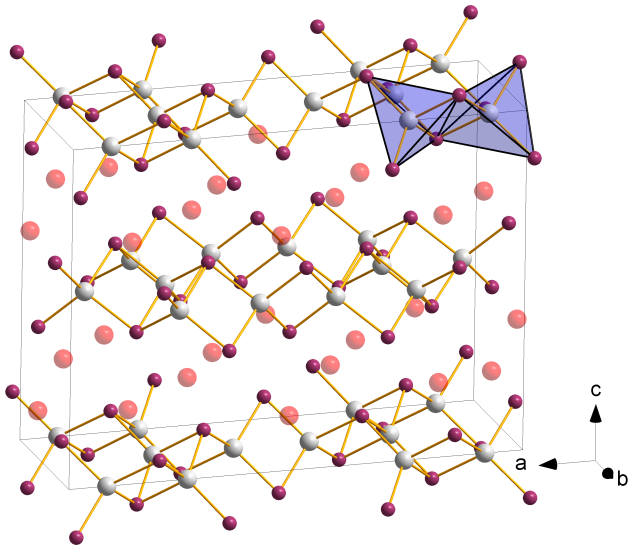

Figure A.124: Crystal structure of $K_3In_2As_3$ incorporating layers of edge-sharing $InAs_2$ tetrahedra forming channels along c.

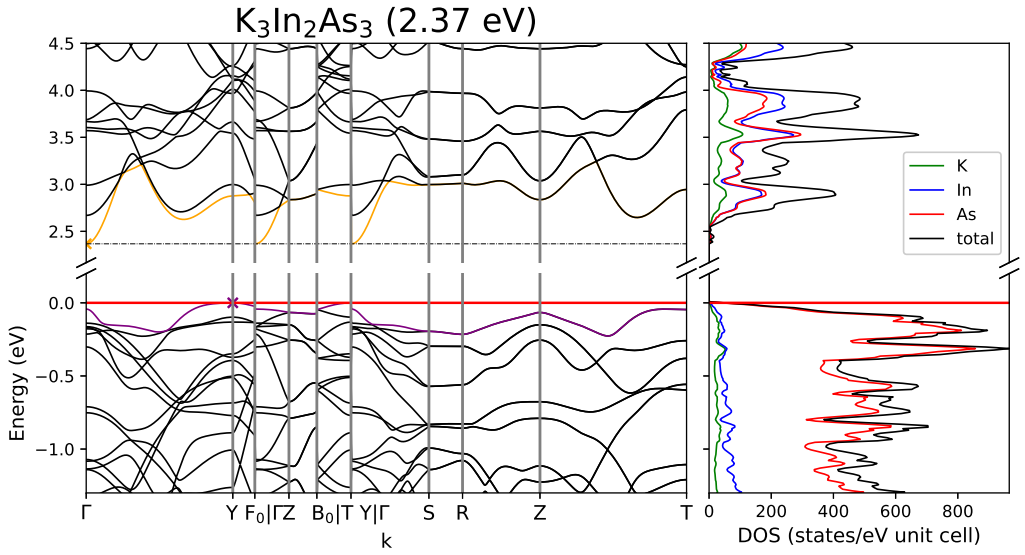

Figure A.125: Band structure and DOS of $K_3In_2As_3$.

Table A.201: Overlap population and interatomic distances of $K_3In_2As_3$.

Atom A	Atom B	r_{AB} / Å	overlap
K1	As1	3.343	0.035
	As1	3.457	0.008
	In1	3.548	−0.009
	As1	3.59	0.029
	As2	3.642	0.009
	As1	4.029	0.006
K2	As1	3.34	0.014
	As2	3.38	0.033
	In2	3.434	−0.011
	In1	3.524	−0.01
	As2	3.54	0.008
	As2	3.588	0.007

Atom A	Atom B	r_{AB} / Å	overlap
In1	As1	2.634	0.293
	As2	2.77	0.205
	In1	3.297	−0.127
	In2	3.547	−0.064
In2	As2	2.671	0.247
	As2	2.693	0.241
	In2	3.418	−0.066

Table A.202: Partial charges for each atom position in $K_3In_2As_3$.

Atom	Z	charge	part charge
K1	19	18.221	0.779
K2		18.2	0.8
In1	21	20.9	0.1
In2		20.826	0.174

Atom	Z	charge	partialcharge
As1	33	34.008	−1.008
As2		33.823	−0.823

A.9 2-2-3

Table A.203: Overview of the crystallographic details of the 2-2-3 compounds. Cell parameters given in the first line and second line are of experimental and calculated origin, respectively. The third line shows the difference between both in percent.

compound	a / Å	b/ Å	c / Å	β / °	space group	crystal system	connectivity
$Na_2Ge_2P_3$	17.639	3.6176	11.354	92.74	$C2/m$ (no. 12)	monoclinic	1D
	17.482	3.6335	11.329	93.11			
	-0.90	0.44	-0.22	0.40			
$Na_2Al_2As_3$	13.114	6.710	14.448	90.0	$P2_1/c$ (no. 14)	monoclinic	2D
	13.090	6.717	14.337	89.9			
	-0.18	0.10	-0.77	-0.08			
$Na_2Ga_2As_3$	13.1175	6.705	14.459	90.2	-"-	-"-	-"-
	13.1339	6.707	14.327	89.9			
	0.12	0.03	-0.92	-0.38			
$K_2Ga_2As_3$	13.782	6.739	15.644	90.4	-"-	-"-	-"-
	13.824	6.770	15.701	90.4			
	0.30	0.45	0.36	-0.03			
$K_2In_2As_3$	14.344	7.112	15.85	90.3	-"-	-"-	-"-
	14.432	7.160	15.94	90.3			
	0.61	0.67	0.59	-0.01			
$Na_2Al_2Sb_3$	14.100	7.220	15.440	90.3	-"-	-"-	-"-
	14.066	7.200	15.264	90.4			
	-0.24	-0.28	-1.15	0.14			
$K_2Al_2Sb_3$	14.720	7.230	16.640	90.6	-"-	-"-	-"-
	14.800	7.249	16.617	90.6			
	0.54	0.26	-0.14	-0.05			
$K_2Ga_2Sb_3$	14.743	7.185	16.584	90.5	-"-	-"-	-"-
	14.804	7.244	16.549	90.5			
	0.41	0.81	-0.21	-0.02			
$Na_2In_2Sb_3$	14.595	7.532	15.635	90.0	-"-	-"-	-"-
	14.626	7.578	15.489	90.1			
	0.21	0.61	-0.94	0.10			
$K_2In_2Sb_3$	15.254	7.534	16.798	90.5	-"-	-"-	-"-
	15.366	7.617	16.794	90.4			
	0.73	1.10	-0.03	-0.07			
$Rb_2In_2Sb_3$	15.555	7.5692	17.362	90.60	-"-	-"-	-"-
	15.655	7.666	17.454	90.52			
	0.64	1.26	0.53	-0.08			
$Cs_2In_2Sb_3$	15.820	7.568	17.998	90.7	-"-	-"-	-"-
	15.925	7.698	18.083	90.6			
	0.66	1.68	0.47	-0.06			

Table A.204: Calculated band gaps and transitions as well as an overview of the sampled reciprocal space defined by the Monkhorst-Pack-type *k*-point grid (SHRINK) and Brillouin Zone paths for all 2-2-3 compounds.

compound	band gap		transition	k-path	SHRINK
$Na_2Ge_2P_3$	2.51	indirect	Y_2 -> D_2-A	Γ—C|C_2—Y_2—Γ—M_2—D|D_2—A—Γ|L_2—Γ—V_2	4 4 3
$Na_2Al_2As_3$	2.69	indirect	Γ-Z -> Z	Γ—Z—D—B—Γ—A—E—Z—C_2—Y_2—Γ	3 5 3
$Na_2Ga_2As_3$	2.65	indirect	Γ-> Z	-"-	-"-
$K_2Ga_2As_3$	2.87	indirect	Γ/B -> Z	-"-	-"-
$K_2In_2As_3$	2.38	direct	Γ -> Γ	-"-	-"-
$Na_2Al_2Sb_3$	1.87	indirect	Γ-> Z	-"-	-"-
$K_2Al_2Sb_3$	2.16	indirect	Γ/B -> Z	-"-	-"-
$K_2Ga_2Sb_3$	2.13	indirect	Γ/B -> Z	-"-	-"-
$Na_2In_2Sb_3$	1.82	indirect	Γ-> Z	-"-	-"-
$K_2In_2Sb_3$	2.15	pseudo-direct	Γ -> Γ	-"-	-"-
$Rb_2In_2Sb_3$	1.96	direct	Γ -> Γ	-"-	-"-
$Cs_2In_2Sb_3$	2.01	direct	Γ -> Γ	-"-	-"-

$Na_2Al_2As_3$[129]

$Na_2Al_2As_3$ crystallizes in the monoclinic space group $P\ 2_1\ /\ c$ (no. 14). Edge and corner-sharing $AlAs_4$ tetrahedra form layers within the ab plane. The Na atoms lie in between these layers.

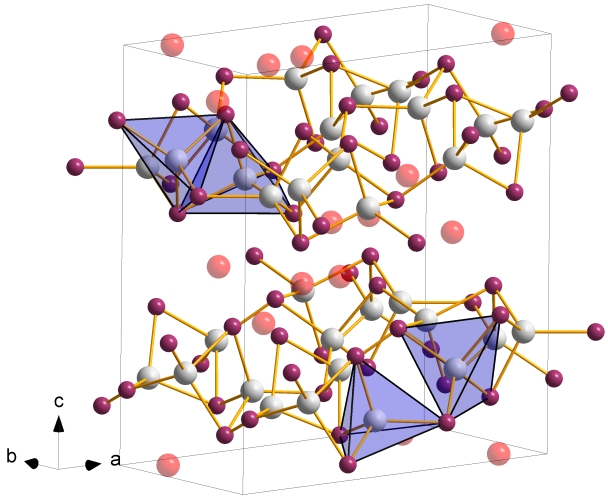

Figure A.126: Crystal structure of $Na_2Al_2As_3$ with layers of corner- and edge-sharing $AlAs_4$ tetrahedra.

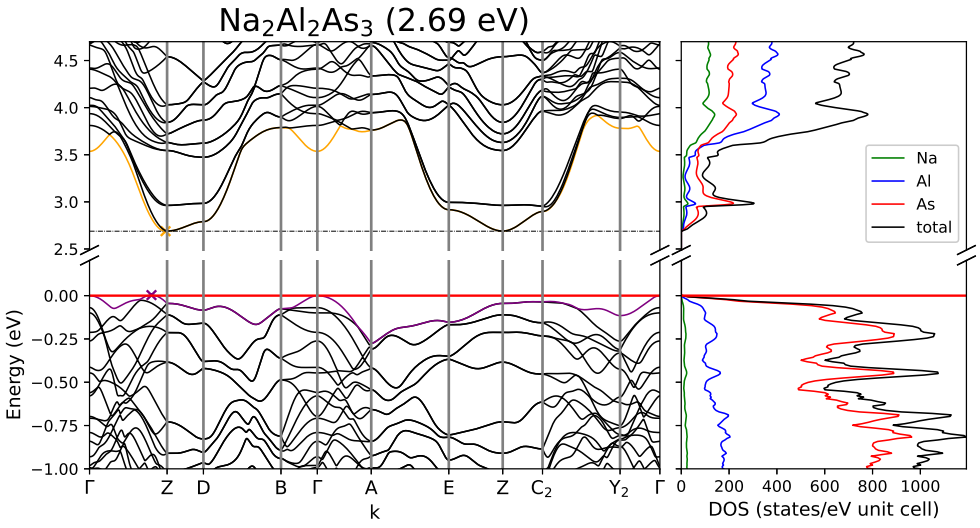

Figure A.127: Band structure and DOS of $Na_2Al_2As_3$.

Table A.205: Overlap population and interatomic distances of $Na_2Al_2As_3$.

Atom A	Atom B	r_{AB} / Å	overlap
Na1	As6	2.973	0.018
	As2	3.0	0.026
	As1	3.006	0.032
	As4	3.11	0.02
	As1	3.209	0.037
	As3	3.213	0.016
Na2	As3	2.983	0.029
	As4	2.996	0.031
	As5	3.003	0.038
	As2	3.029	0.021
	As5	3.165	0.022
	Al1	3.375	0.007
Na3	As2	3.003	0.046
	As4	3.049	0.037
	Al2	3.115	0.008
	As1	3.244	0.012
	As2	3.249	0.023
	As6	3.289	0.017
Na4	As6	2.834	0.031
	As3	3.004	0.038
	As3	3.11	0.042
	Al4	3.175	0.007
	As5	3.192	0.025
	Na4	3.245	0.006
Al1	As3	2.447	0.314
	As6	2.467	0.274
	As5	2.472	0.318
	As2	2.585	0.261
	Al2	3.062	−0.013
Al2	As1	2.463	0.322
	As1	2.471	0.313
	As6	2.481	0.284
	As2	2.493	0.275
Al3	As2	2.453	0.304
	As1	2.47	0.322
	As4	2.519	0.28
	As3	2.536	0.276
	Al4	3.098	−0.018
Al4	As5	2.483	0.315
	As5	2.488	0.295
	As3	2.525	0.268
	As4	2.53	0.284
As4	As6	2.488	0.203

Table A.206: Partial charges for each atom position in $Na_2Al_2As_3$.

Atom	Z	charge	part charge
Na1	11	10.213	0.787
Na2		10.222	0.778
Na3		10.223	0.777
Na4		10.237	0.763
Al1	13	12.468	0.532
Al2		12.603	0.397
Al3		12.511	0.489
Al4		12.545	0.455
As1	33	33.824	−0.824
As2		33.97	−0.97
As3		33.959	−0.959
As4		33.689	−0.689
As5		33.853	−0.853
As6		33.683	−0.683

$Na_2Ga_2As_3$[131]

For a crystal structure description see $Na_2Al_2As_3$.

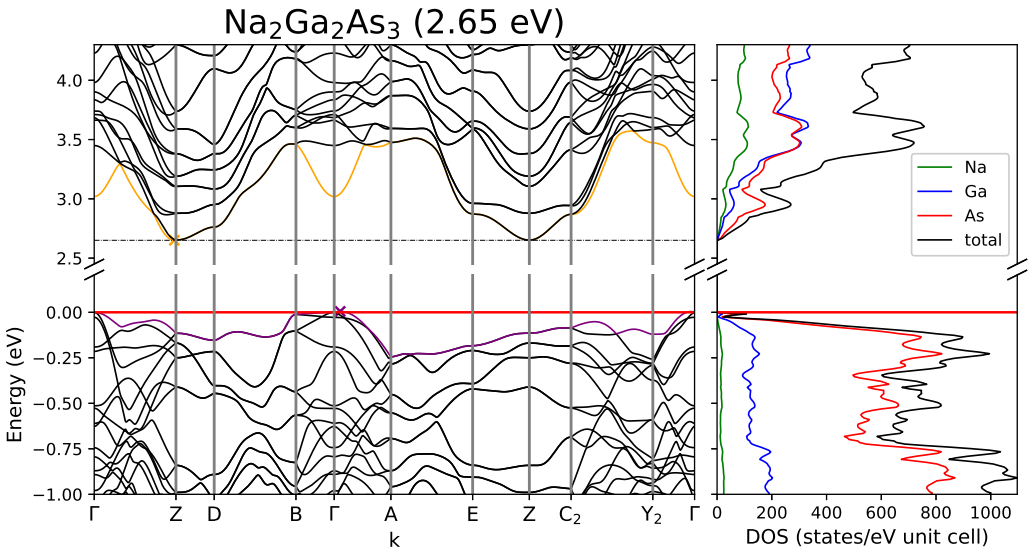

Figure A.128: Band structure and DOS of $Na_2Ga_2As_3$.

Table A.207: Partial charges for each atom position in $Na_2Ga_2As_3$.

Atom	Z	charge	part charge
Na1	11	10.208	0.792
Na2		10.213	0.787
Na3		10.212	0.788
Na4		10.231	0.769
Ga1	31	30.723	0.277
Ga2		30.899	0.101
Ga3		30.77	0.23
Ga4		30.827	0.173

Atom	Z	charge	partialcharge
As1	33	33.579	−0.579
As2		33.792	−0.792
As3		33.761	−0.761
As4		33.561	−0.561
As5		33.635	−0.635
As6		33.59	−0.59

Table A.208: Overlap population and interatomic distances of $Na_2Ga_2As_3$.

Atom A	Atom B	r_{AB} / Å	overlap
Na1	As6	2.991	0.019
	As1	2.998	0.029
	As2	3.021	0.025
	As4	3.094	0.022
	As1	3.152	0.04
	As3	3.203	0.014
Na2	As5	2.983	0.04
	As4	3.008	0.031
	As3	3.013	0.028
	As2	3.032	0.019
	As5	3.183	0.019
	Ga1	3.328	0.007
Na3	As2	3.005	0.048
	As4	3.061	0.038
	Ga2	3.084	0.005
	As2	3.239	0.022
	Ga2	3.245	0.006
	As1	3.274	0.01
Na4	As6	2.854	0.032
	As3	2.983	0.038
	As3	3.124	0.043
	Ga4	3.136	0.003
	As5	3.223	0.025
	As4	3.257	0.009

Atom A	Atom B	r_{AB} / Å	overlap
Ga1	As3	2.442	0.285
	As6	2.472	0.235
	As5	2.478	0.294
	As2	2.589	0.254
	Ga2	3.129	−0.052
Ga2	As1	2.465	0.293
	As1	2.467	0.282
	As6	2.496	0.256
	As2	2.5	0.257
Ga3	As2	2.454	0.284
	As1	2.474	0.299
	As4	2.516	0.254
	As3	2.538	0.261
	Ga4	3.156	−0.054
Ga4	As5	2.48	0.292
	As5	2.486	0.259
	As3	2.533	0.245
	As4	2.536	0.272
As4	As6	2.474	0.229

$K_2Ga_2As_3$[133]

For a crystal structure description see $Na_2Al_2As_3$.

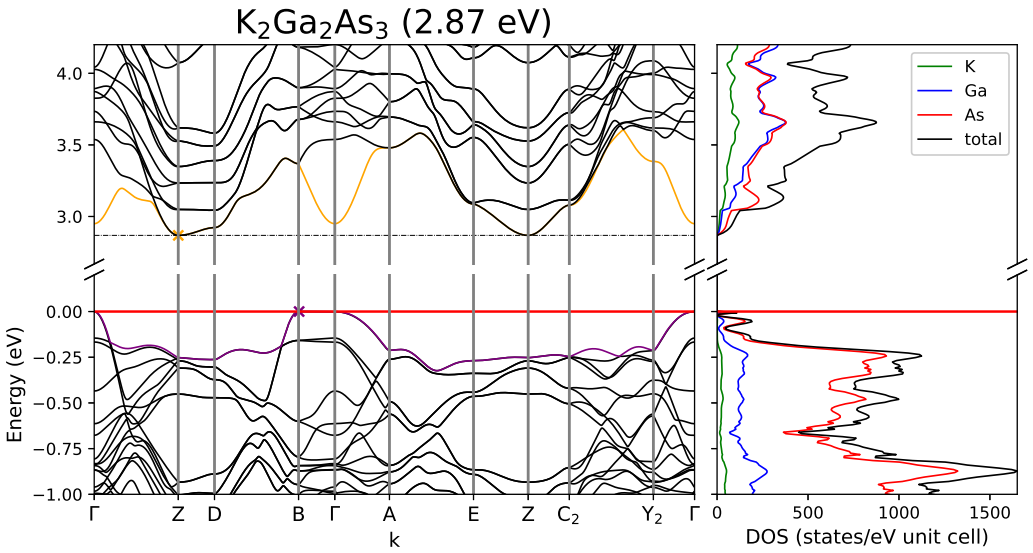

Figure A.129: Band structure and DOS of $K_2Ga_2As_3$.

Table A.209: Partial charges for each atom position in $K_2Ga_2As_3$.

Atom	Z	charge	part charge
K1	19	18.22	0.78
K2		18.235	0.765
K3		18.204	0.796
K4		18.196	0.804
Ga1	31	30.721	0.279
Ga2		30.879	0.121
Ga3		30.743	0.257
Ga4		30.872	0.128

Atom	Z	charge	partialcharge
As1	33	33.592	−0.592
As2		33.79	−0.79
As3		33.752	−0.752
As4		33.568	−0.568
As5		33.628	−0.628
As6		33.6	−0.6

Table A.210: Overlap population and interatomic distances of $K_2Ga_2As_3$.

Atom A	Atom B	r_{AB} / Å	overlap
K1	As2	3.3	0.009
	As3	3.3	0.004
	As6	3.314	0.006
	As1	3.322	0.013
	As4	3.382	0.011
	Ga3	3.508	−0.01
K2	As2	3.255	0.004
	As3	3.392	0.015
	As4	3.395	0.019
	As5	3.407	0.025
	As5	3.487	0.014
	Ga1	3.62	−0.008
K3	Ga2	3.287	−0.016
	As4	3.377	0.017
	Ga2	3.389	−0.01
	As2	3.392	0.01
	As6	3.414	0.006
	As1	3.45	−0.004
K4	As6	3.154	0.004
	As3	3.207	0.006
	As4	3.266	−0.005
	Ga4	3.307	−0.015
	Ga4	3.4	−0.011
	K4	3.562	0.001

Atom A	Atom B	r_{AB} / Å	overlap
Ga1	As3	2.459	0.298
	As6	2.477	0.258
	As5	2.505	0.295
	As2	2.615	0.272
	Ga2	3.221	−0.055
	As4	3.591	−0.049
Ga2	As2	2.5	0.278
	As1	2.502	0.299
	As1	2.508	0.295
	As6	2.518	0.263
Ga3	As2	2.466	0.293
	As1	2.501	0.304
	As4	2.515	0.27
	As3	2.531	0.271
	Ga4	3.248	−0.054
Ga4	As3	2.525	0.28
	As5	2.528	0.276
	As5	2.532	0.295
	As4	2.572	0.282
As4	As6	2.473	0.233

$K_2In_2As_3$[135]

For a crystal structure description see $Na_2Al_2As_3$.

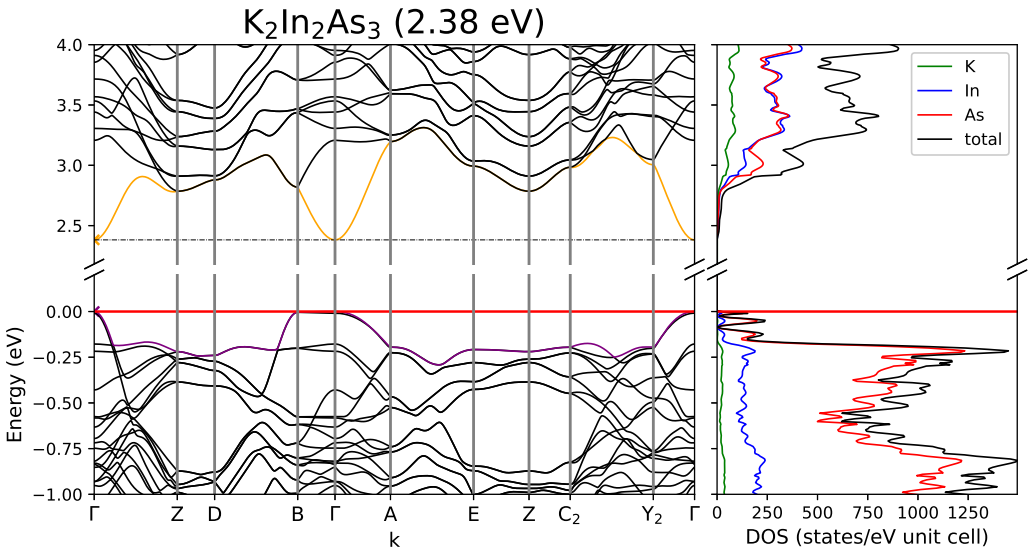

Figure A.130: Band structure and DOS of $K_2In_2As_3$.

Table A.211: Partial charges for each atom position in $K_2In_2As_3$.

Atom	Z	charge	part charge
K1	19	18.2	0.8
K2		18.213	0.787
K3		18.198	0.802
K4		18.196	0.804
In1	21	20.611	0.389
In2		20.764	0.236
In3		20.65	0.35
In4		20.712	0.288

Atom	Z	charge	partialcharge
As1	33	33.695	−0.695
As2		33.833	−0.833
As3		33.86	−0.86
As4		33.639	−0.639
As5		33.757	−0.757
As6		33.671	−0.671

Table A.212: Overlap population and interatomic distances of $K_2In_2As_3$.

Atom A	Atom B	r_{AB} / Å	overlap
K1	As2	3.285	0.009
	As6	3.321	0.005
	As1	3.355	0.011
	As4	3.384	0.01
	As3	3.438	0.005
	As1	3.581	0.023
K2	As2	3.333	0.006
	As3	3.353	0.014
	As5	3.377	0.02
	As4	3.433	0.018
	As5	3.556	0.012
	In1	3.732	−0.007
K3	In2	3.409	−0.014
	As2	3.451	0.029
	As4	3.472	0.02
	In2	3.529	−0.008
	As2	3.58	0.012
	As6	3.593	0.009
K4	As6	3.179	0.007
	As3	3.328	0.012
	As4	3.385	−0.001
	In4	3.47	−0.01
	In4	3.613	−0.007
	K4	3.626	0.001

Atom A	Atom B	r_{AB} / Å	overlap
In1	As3	2.626	0.277
	As6	2.657	0.224
	As5	2.671	0.265
	As2	2.797	0.242
	In2	3.421	−0.075
In2	As1	2.643	0.268
	As2	2.662	0.247
	As1	2.669	0.27
	As6	2.686	0.228
In3	As2	2.635	0.282
	As1	2.659	0.272
	As4	2.704	0.223
	As3	2.729	0.249
	In4	3.445	−0.058
In4	As5	2.683	0.267
	As5	2.69	0.249
	As3	2.704	0.251
	As4	2.752	0.248
As4	As6	2.477	0.229

$Na_2Al_2Sb_3$[130]

For a crystal structure description see $Na_2Al_2As_3$.

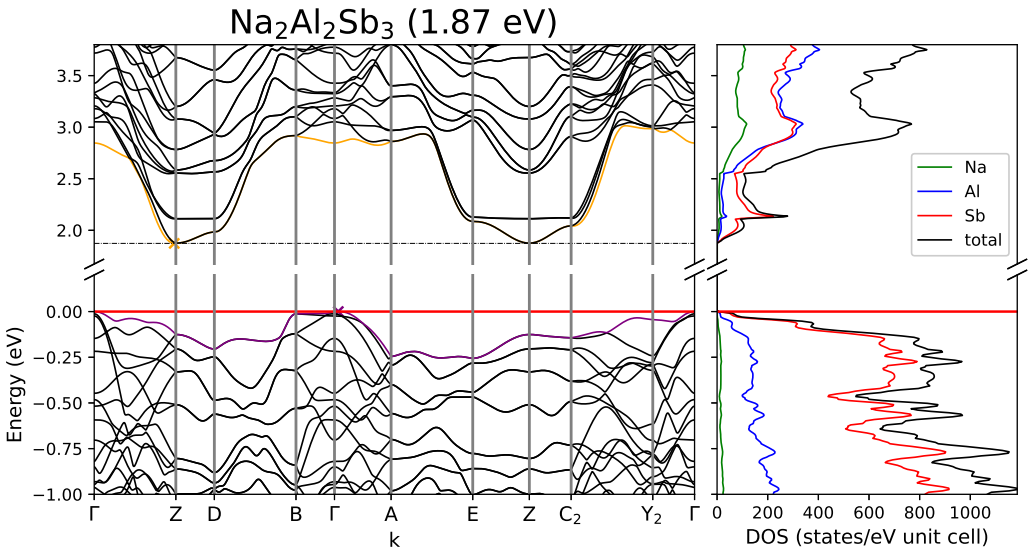

Figure A.131: Band structure and DOS of $Na_2Al_2Sb_3$.

Table A.213: Partial charges for each atom position in $Na_2Al_2Sb_3$.

Atom	Z	charge	part charge
Al1	13	12.669	0.331
Al2		12.826	0.174
Al3		12.692	0.308
Al4		12.822	0.178
Na1	11	10.221	0.779
Na2		10.221	0.779
Na3		10.216	0.784
Na4		10.228	0.772

Atom	Z	charge	partialcharge
Sb1	23	23.652	−0.652
Sb2		23.832	−0.832
Sb3		23.798	−0.798
Sb4		23.578	−0.578
Sb5		23.655	−0.655
Sb6		23.589	−0.589

Table A.214: Overlap population and interatomic distances of $Na_2Al_2Sb_3$.

Atom A	Atom B	r_{AB} / Å	overlap
Al1	Sb3	2.662	0.308
	Sb6	2.676	0.272
	Sb5	2.697	0.309
	Sb2	2.78	0.251
	Al2	3.253	−0.001
	Na2	3.444	0.009
Al2	Sb1	2.677	0.304
	Sb1	2.683	0.311
	Sb6	2.694	0.27
	Sb2	2.699	0.265
	Na3	3.228	0.011
Al3	Sb2	2.655	0.295
	Sb1	2.69	0.31
	Sb4	2.713	0.278
	Sb3	2.748	0.263
	Al4	3.284	0.001
	Na1	3.47	0.007
Al4	Sb5	2.679	0.296
	Sb5	2.699	0.309
	Sb3	2.729	0.261
	Sb4	2.743	0.268
	Na4	3.256	0.01
Na1	Sb1	3.182	0.031
	Sb2	3.264	0.025
	Sb6	3.265	0.019
	Sb1	3.28	0.042
	Sb4	3.304	0.022
	Sb3	3.336	0.019
Na2	Sb5	3.169	0.041
	Sb2	3.234	0.022
	Sb4	3.256	0.03
	Sb3	3.308	0.025
	Sb5	3.309	0.023
Na3	Sb2	3.212	0.043
	Sb4	3.262	0.034
	Sb2	3.39	0.022
	Sb1	3.393	0.013
Na4	Sb6	3.084	0.03
	Sb3	3.13	0.039
	Sb4	3.317	0.016
	Sb3	3.374	0.04
Sb4	Sb6	2.879	0.215

$K_2Al_2Sb_3$[130]

For a crystal structure description see $Na_2Al_2As_3$.

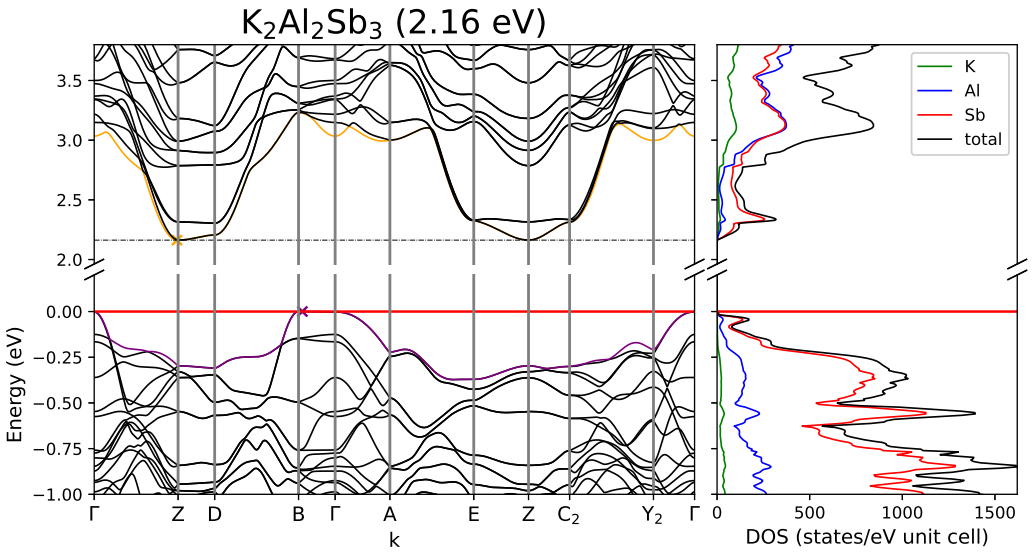

Figure A.132: Band structure and DOS of $K_2Al_2Sb_3$.

Table A.215: Partial charges for each atom position in $K_2Al_2Sb_3$.

Atom	Z	charge	part charge
Al1	13	12.657	0.343
Al2		12.803	0.197
Al3		12.684	0.316
Al4		12.818	0.182
K1	19	18.218	0.782
K2		18.23	0.77
K3		18.208	0.792
K4		18.199	0.801

Atom	Z	charge	partialcharge
Sb1	23	23.662	−0.662
Sb2		23.837	−0.837
Sb3		23.795	−0.795
Sb4		23.58	−0.58
Sb5		23.692	−0.692
Sb6		23.618	−0.618

Table A.216: Overlap population and interatomic distances of $K_2Al_2Sb_3$.

Atom A	Atom B	r_{AB} / Å	overlap
Al1	Sb3	2.67	0.313
	Sb6	2.675	0.285
	Sb5	2.719	0.31
	Sb2	2.792	0.268
	Al2	3.387	−0.013
	K2	3.761	−0.001
Al2	Sb2	2.704	0.283
	Sb6	2.709	0.28
	Sb1	2.709	0.304
	Sb1	2.716	0.313
	K3	3.454	−0.005
Al3	Sb2	2.665	0.304
	Sb4	2.713	0.289
	Sb1	2.714	0.315
	Sb3	2.74	0.278
	Al4	3.411	−0.013
	K1	3.693	−0.002
Al4	Sb5	2.717	0.292
	Sb3	2.72	0.288
	Sb5	2.754	0.307
	Sb4	2.762	0.286
	K4	3.463	−0.005
K1	Sb3	3.472	0.005
	Sb1	3.51	0.014
	Sb2	3.531	0.01
	Sb6	3.541	0.006
	Sb4	3.587	0.011
K2	Sb2	3.448	0.006
	Sb5	3.583	0.026
	Sb4	3.588	0.017
	Sb3	3.622	0.014
	Sb5	3.644	0.015
K3	Sb4	3.556	0.017
	Sb2	3.561	0.011
	Sb6	3.606	0.009
	Sb1	3.65	0.0
K4	Sb6	3.372	0.005
	Sb3	3.394	0.009
	Sb4	3.478	−0.001
	Sb5	3.865	0.002
Sb4	Sb6	2.869	0.232

$K_2Ga_2Sb_3$[134]

For a crystal structure description see $Na_2Al_2As_3$.

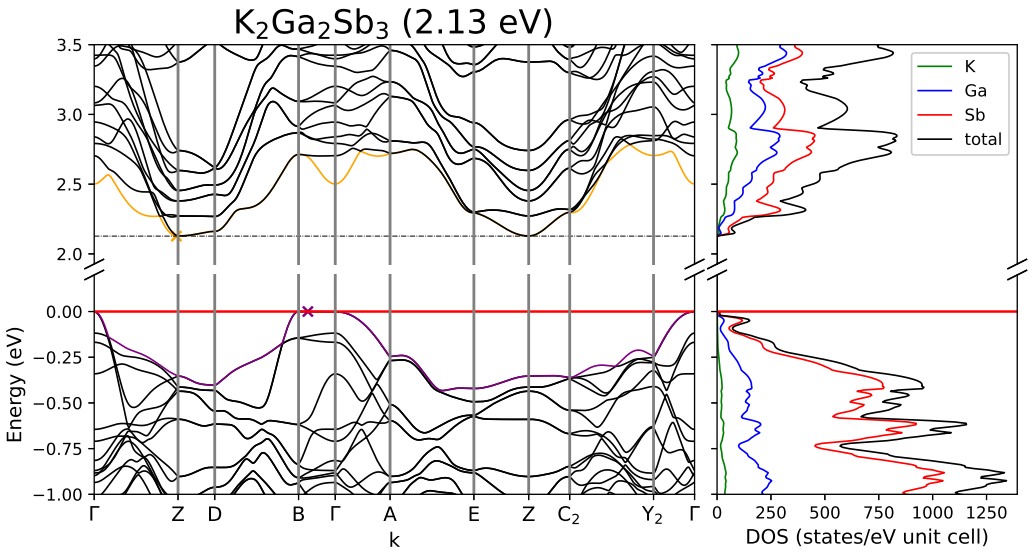

Figure A.133: Band structure and DOS of $K_2Ga_2Sb_3$.

Table A.217: Partial charges for each atom position in $K_2Ga_2Sb_3$.

Atom	Z	charge	part charge
K1	19	18.221	0.779
K2		18.229	0.771
K3		18.204	0.796
K4		18.195	0.805
Ga1	31	30.864	0.136
Ga2		31.028	−0.028
Ga3		30.858	0.142
Ga4		31.043	−0.043

Atom	Z	charge	partialcharge
Sb1	23	23.466	−0.466
Sb2		23.707	−0.707
Sb3		23.647	−0.647
Sb4		23.493	−0.493
Sb5		23.504	−0.504
Sb6		23.541	−0.541

Table A.218: Overlap population and interatomic distances of $K_2Ga_2Sb_3$.

Atom A	Atom B	r_{AB} / Å	overlap
K1	Sb3	3.467	0.005
	Sb1	3.493	0.013
	Sb2	3.548	0.011
	Sb6	3.56	0.007
	Sb4	3.579	0.012
	Ga3	3.643	−0.006
K2	Sb2	3.447	0.005
	Sb5	3.558	0.025
	Sb4	3.594	0.017
	Sb3	3.636	0.014
	Sb5	3.639	0.014
	Ga1	3.719	−0.005
K3	Ga2	3.428	−0.01
	Ga2	3.534	−0.005
	Sb2	3.555	0.011
	Sb4	3.571	0.018
	Sb6	3.604	0.008
	Sb1	3.642	−0.001
K4	Sb3	3.386	0.01
	Sb6	3.388	0.007
	Ga4	3.443	−0.009
	Sb4	3.478	−0.001
	Ga4	3.492	−0.007
	Sb5	3.85	0.0

Atom A	Atom B	r_{AB} / Å	overlap
Ga1	Sb3	2.658	0.298
	Sb6	2.668	0.248
	Sb5	2.705	0.289
	Sb2	2.791	0.262
	Ga2	3.446	−0.033
Ga2	Sb2	2.69	0.258
	Sb1	2.698	0.286
	Sb6	2.704	0.252
	Sb1	2.707	0.294
Ga3	Sb2	2.656	0.284
	Sb4	2.693	0.264
	Sb1	2.703	0.293
	Sb3	2.732	0.26
	Ga4	3.47	−0.032
Ga4	Sb5	2.707	0.272
	Sb3	2.712	0.263
	Sb5	2.743	0.291
	Sb4	2.754	0.273
Sb4	Sb6	2.856	0.245

$Na_2In_2Sb_3$[132]

For a crystal structure description see $Na_2Al_2As_3$.

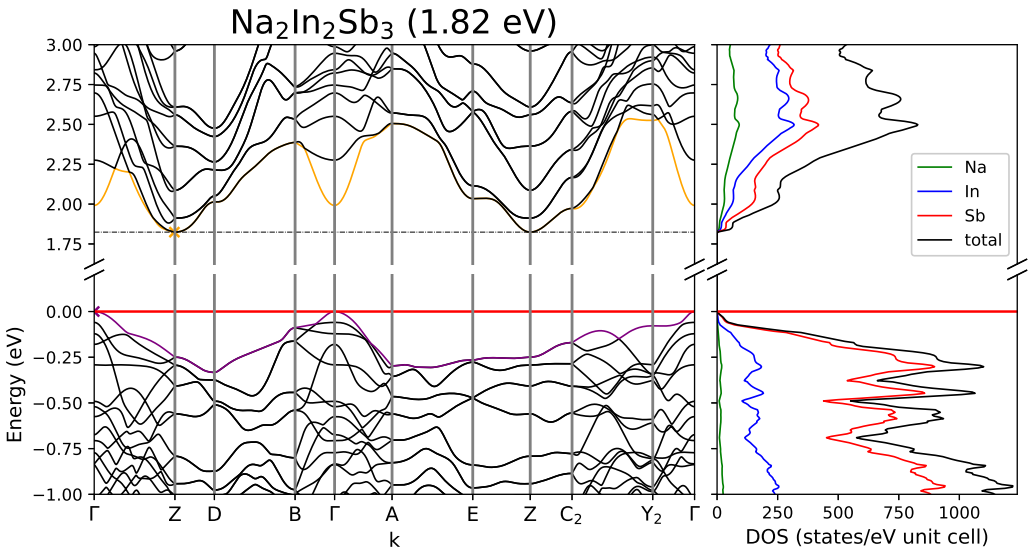

Figure A.134: Band structure and DOS of $Na_2In_2Sb_3$.

Table A.219: Partial charges for each atom position in $Na_2In_2Sb_3$.

Atom	Z	charge	part charge
Na1	11	10.206	0.794
Na2		10.211	0.789
Na3		10.202	0.798
Na4		10.227	0.773
In1	21	20.776	0.224
In2		20.962	0.038
In3		20.825	0.175
In4		20.895	0.105

Atom	Z	charge	partialcharge
Sb1	23	23.548	−0.548
Sb2		23.758	−0.758
Sb3		23.77	−0.77
Sb4		23.514	−0.514
Sb5		23.571	−0.571
Sb6		23.535	−0.535

Table A.220: Overlap population and interatomic distances of $Na_2In_2Sb_3$.

Atom A	Atom B	r_{AB} / Å	overlap
Na1	Sb2	3.246	0.026
	Sb1	3.246	0.025
	Sb6	3.28	0.021
	Sb1	3.3	0.035
	Sb4	3.323	0.022
	Sb3	3.431	0.016
Na2	Sb5	3.18	0.037
	Sb3	3.247	0.027
	Sb4	3.254	0.031
	Sb2	3.272	0.022
	Sb5	3.424	0.016
	In1	3.49	0.012
Na3	Sb2	3.184	0.046
	In2	3.287	0.012
	Sb4	3.296	0.035
	In2	3.514	0.011
	Sb1	3.556	0.012
	Sb2	3.595	0.016
Na4	Sb6	3.099	0.035
	Sb3	3.202	0.04
	Sb3	3.25	0.044
	In4	3.378	0.008
	Sb5	3.461	0.022
	Na4	3.579	0.003

Atom A	Atom B	r_{AB} / Å	overlap
In1	Sb3	2.809	0.277
	Sb6	2.846	0.227
	Sb5	2.857	0.265
	Sb2	2.958	0.218
	In2	3.532	−0.048
In2	Sb1	2.818	0.272
	Sb1	2.831	0.275
	Sb6	2.855	0.228
	Sb2	2.873	0.227
In3	Sb2	2.816	0.266
	Sb1	2.844	0.266
	Sb4	2.875	0.214
	Sb3	2.933	0.231
	In4	3.579	−0.045
In4	Sb5	2.832	0.268
	Sb5	2.832	0.238
	Sb4	2.897	0.246
	Sb3	2.911	0.203
Sb4	Sb6	2.861	0.235

$K_2In_2Sb_3$[136]

For a crystal structure description see $Na_2Al_2As_3$.

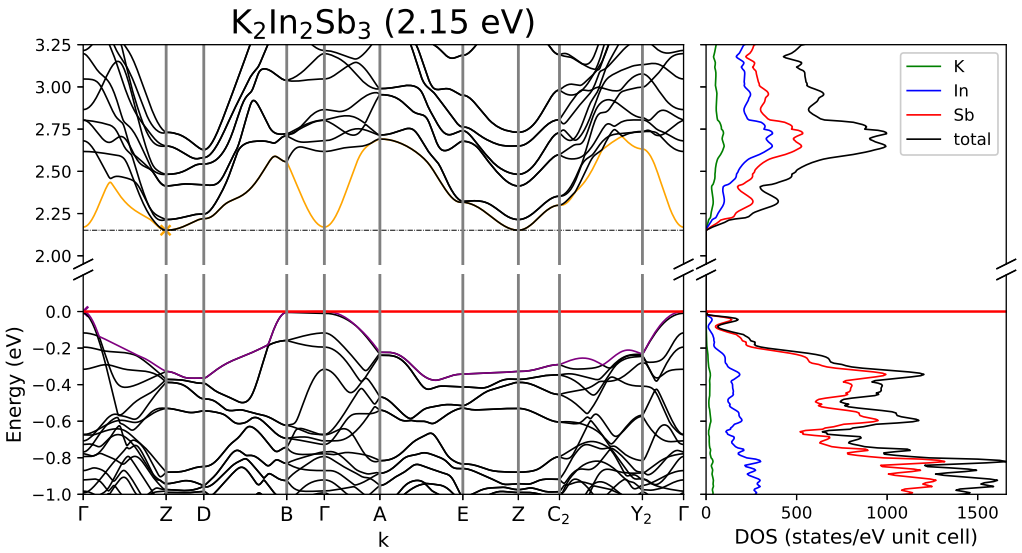

Figure A.135: Band structure and DOS of $K_2In_2Sb_3$.

Table A.221: Partial charges for each atom position in $K_2In_2Sb_3$.

Atom	Z	charge	part charge
K1	19	18.202	0.798
K2		18.208	0.792
K3		18.192	0.808
K4		18.191	0.809
In1	21	20.777	0.223
In2		20.942	0.058
In3		20.809	0.191
In4		20.944	0.056

Atom	Z	charge	partialcharge
Sb1	23	23.557	−0.557
Sb2		23.765	−0.765
Sb3		23.718	−0.718
Sb4		23.526	−0.526
Sb5		23.592	−0.592
Sb6		23.576	−0.576

Table A.222: Overlap population and interatomic distances of $K_2In_2Sb_3$.

Atom A	Atom B	r_{AB} / Å	overlap
K1	Sb2	3.519	0.011
	Sb1	3.524	0.012
	Sb3	3.569	0.006
	Sb6	3.574	0.007
	Sb4	3.58	0.011
	Sb1	3.693	0.025
K2	Sb2	3.502	0.007
	Sb5	3.541	0.022
	Sb3	3.609	0.014
	Sb4	3.634	0.017
	Sb5	3.711	0.012
	In1	3.812	−0.003
K3	In2	3.532	−0.008
	Sb4	3.638	0.02
	Sb2	3.658	0.028
	In2	3.658	−0.004
	Sb2	3.727	0.012
	Sb1	3.766	0.001
K4	Sb6	3.41	0.009
	Sb3	3.478	0.014
	In4	3.573	−0.008
	Sb4	3.576	0.002
	In4	3.65	−0.005
	Sb3	3.94	0.024
In1	Sb3	2.819	0.293
	Sb6	2.848	0.227
	Sb5	2.869	0.272
	Sb2	2.976	0.246
	In2	3.61	−0.046
In2	Sb1	2.85	0.285
	Sb1	2.855	0.287
	Sb2	2.859	0.25
	Sb6	2.868	0.234
In3	Sb2	2.816	0.288
	Sb1	2.86	0.278
	Sb4	2.881	0.229
	Sb3	2.92	0.251
	In4	3.632	−0.039
In4	Sb5	2.868	0.267
	Sb5	2.886	0.274
	Sb3	2.887	0.248
	Sb4	2.929	0.253
Sb4	Sb6	2.862	0.249

$Rb_2In_2Sb_3$[137]

For a crystal structure description see $Na_2Al_2As_3$.

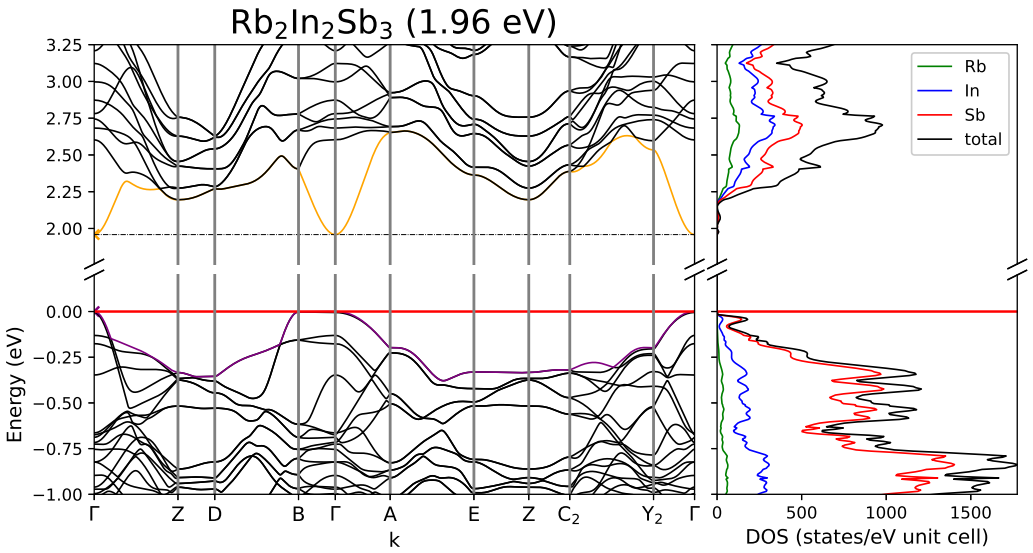

Figure A.136: Band structure and DOS of $Rb_2In_2Sb_3$.

Table A.223: Partial charges for each atom position in $Rb_2In_2Sb_3$.

Atom	Z	charge	part charge
Rb1	9	8.269	0.731
Rb2		8.278	0.722
Rb3		8.248	0.752
Rb4		8.244	0.756
In1	21	20.782	0.218
In2		20.924	0.076
In3		20.81	0.19
In4		20.921	0.079

Atom	Z	charge	partialcharge
Sb1	23	23.54	−0.54
Sb2		23.714	−0.714
Sb3		23.67	−0.67
Sb4		23.486	−0.486
Sb5		23.577	−0.577
Sb6		23.538	−0.538

Table A.224: Overlap population and interatomic distances of $Rb_2In_2Sb_3$.

Atom A	Atom B	r_{AB} / Å	overlap
Rb1	Sb2	3.658	0.015
	Sb3	3.671	0.009
	Sb1	3.676	0.015
	Sb6	3.712	0.009
	Sb4	3.734	0.013
	In3	3.886	−0.007
Rb2	Sb2	3.629	0.01
	Sb5	3.73	0.025
	Sb3	3.745	0.018
	Sb4	3.774	0.021
	Sb5	3.856	0.016
	In1	3.983	−0.005
Rb3	In2	3.652	−0.01
	In2	3.765	−0.006
	Sb4	3.773	0.021
	Sb2	3.809	0.014
	Sb6	3.839	0.01
	Sb2	3.868	0.03
Rb4	Sb6	3.538	0.011
	Sb3	3.586	0.012
	Sb4	3.673	0.002
	In4	3.694	−0.008
	In4	3.762	−0.007
	Rb4	4.021	0.0

Atom A	Atom B	r_{AB} / Å	overlap
In1	Sb3	2.823	0.292
	Sb6	2.848	0.239
	Sb5	2.874	0.272
	Sb2	2.983	0.248
	In2	3.662	−0.046
In2	Sb2	2.863	0.257
	Sb1	2.867	0.283
	Sb1	2.869	0.284
	Sb6	2.878	0.242
In3	Sb2	2.823	0.291
	Sb1	2.869	0.279
	Sb4	2.882	0.241
	Sb3	2.912	0.255
	In4	3.685	−0.043
In4	Sb5	2.885	0.267
	Sb3	2.888	0.26
	Sb5	2.908	0.273
	Sb4	2.936	0.257
Sb4	Sb6	2.858	0.249

$Cs_2In_2Sb_3$[138]

For a crystal structure description see $Na_2Al_2As_3$.

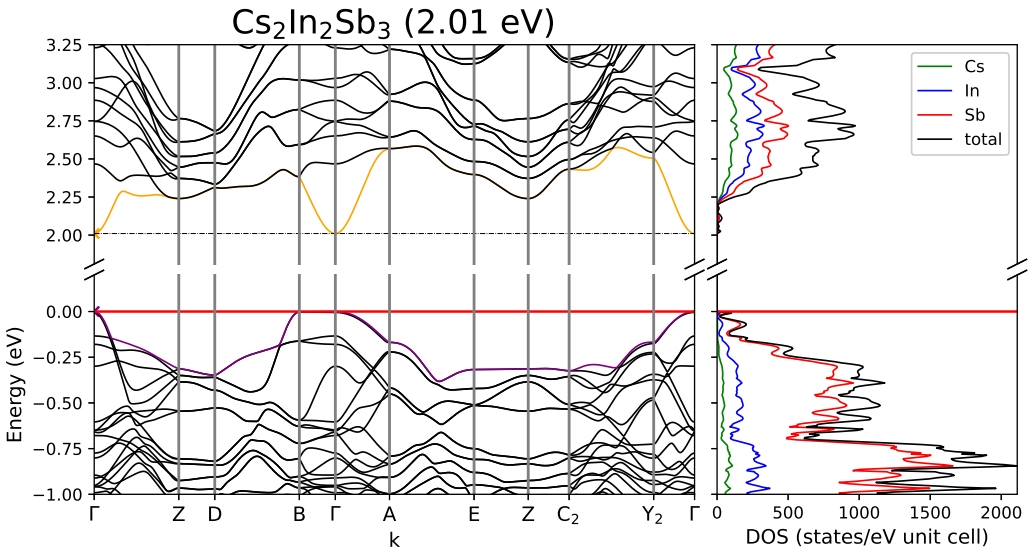

Figure A.137: Band structure and DOS of $Cs_2In_2Sb_3$.

Table A.225: Partial charges for each atom position in $Cs_2In_2Sb_3$.

Atom	Z	charge	part charge
Cs1	9	8.249	0.751
Cs2		8.261	0.739
Cs3		8.22	0.78
Cs4		8.214	0.786
In1	21	20.794	0.206
In2		20.953	0.047
In3		20.813	0.187
In4		20.952	0.048

Atom	Z	charge	partialcharge
Sb1	23	23.53	−0.53
Sb2		23.723	−0.723
Sb3		23.678	−0.678
Sb4		23.495	−0.495
Sb5		23.573	−0.573
Sb6		23.544	−0.544

Table A.226: Overlap population and interatomic distances of $Cs_2In_2Sb_3$.

Atom A	Atom B	r_{AB} / Å	overlap
Cs1	Sb3	3.739	0.011
	Sb2	3.777	0.019
	Sb1	3.812	0.016
	Sb6	3.844	0.013
	Sb4	3.883	0.015
	In3	4.001	−0.001
Cs2	Sb2	3.73	0.012
	Sb3	3.89	0.023
	Sb4	3.922	0.022
	Sb5	3.94	0.025
	Sb5	3.974	0.019
	In1	4.118	0.0
Cs3	In2	3.735	−0.007
	In2	3.844	−0.004
	Sb2	3.874	0.014
	Sb4	3.88	0.019
	Sb6	3.911	0.011
	Sb1	3.957	−0.002
Cs4	Sb6	3.658	0.011
	Sb3	3.677	0.009
	Sb4	3.746	0.001
	In4	3.772	−0.006
	In4	3.803	−0.004
	Sb5	4.141	0.016
In1	Sb3	2.832	0.289
	Sb6	2.854	0.248
	Sb5	2.883	0.271
	Sb2	2.982	0.25
	In2	3.688	−0.049
In2	Sb2	2.864	0.254
	Sb6	2.882	0.228
	Sb1	2.884	0.28
	Sb1	2.884	0.282
In3	Sb2	2.836	0.288
	Sb1	2.875	0.277
	Sb4	2.886	0.245
	Sb3	2.902	0.257
	In4	3.724	−0.045
In4	Sb3	2.884	0.265
	Sb5	2.901	0.268
	Sb5	2.933	0.272
	Sb4	2.944	0.258
Sb4	Sb6	2.851	0.246

$Na_2Ge_2P_3$[164]

$Na_2Ge_2P_3$ crystallizes in the monoclinic space group $C\ 2/\ m$ (no. 12). The compound incorporates one dimensional chains of edge-sharing Ge_5P_2 clusters, which dimerize by Ge-Ge bonds and are further connected by bridging P atoms. Within these chains of Clusters chains of corner-sharing GeP_4 tetrahedra can be found.

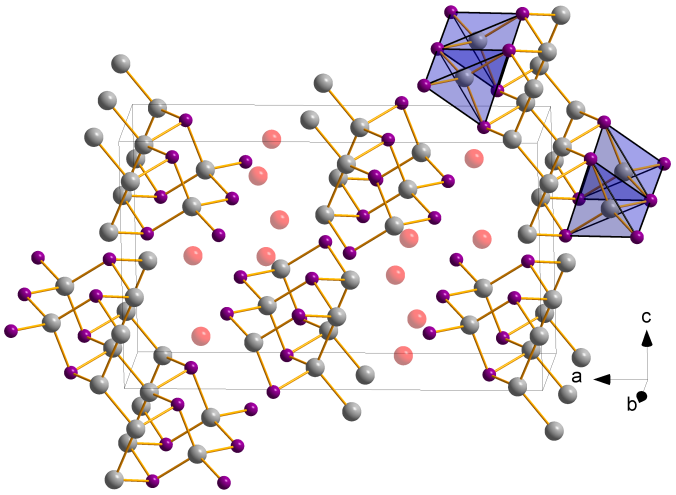

Figure A.138: Crystal structure of $Na_2Ge_2P_3$ with one dimensional chains of corner sharing GeP_4 tetrahedra within dimerized chains of edge-sharing Ge_5P_2 clusters.

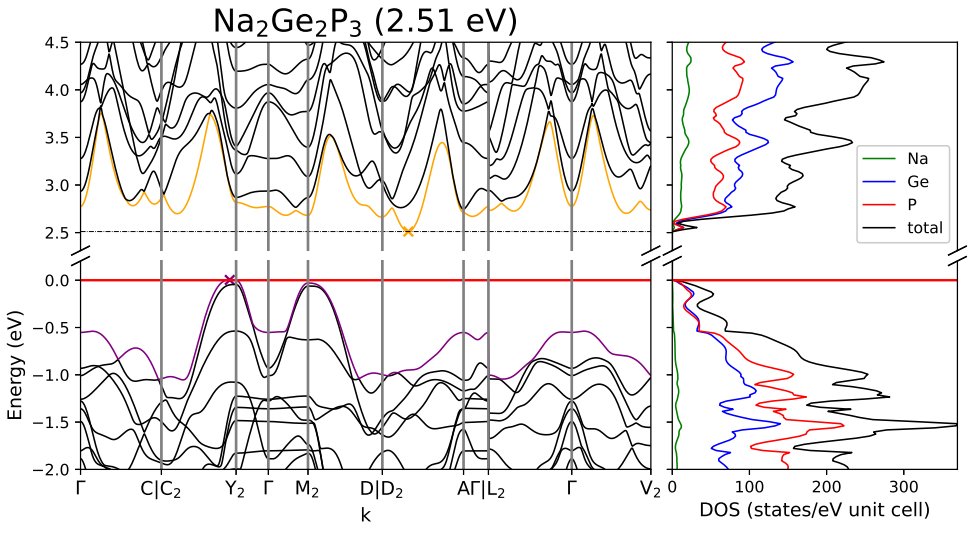

Figure A.139: Band structure and DOS of $Na_2Ge_2P_3$.

Table A.227: Overlap population and interatomic distances of $Na_2Ge_2P_3$.

Atom A	Atom B	r_{AB} / Å	overlap
Na1	P2	3.004	0.034
	P1	3.042	0.028
	Ge3	3.148	0.032
	Ge1	3.187	−0.003
	Ge2	3.476	0.001
	Na1	3.634	0.002
Na2	P3	2.978	0.029
	P2	3.002	0.033
	P2	3.196	0.028
	Ge3	3.249	0.023
	Ge1	3.606	−0.001
	Na2	3.634	0.002
Ge1	P2	2.324	0.282
	P3	2.324	0.268
	P1	2.364	0.249
	Ge2	3.43	−0.057
Ge2	P1	2.367	0.251
	Ge2	2.455	0.297
	Ge3	2.544	0.283
	Ge2	3.634	−0.033
Ge3	P3	2.383	0.253
	Ge3	3.634	−0.028
P1	P1	3.634	−0.02
	P3	3.743	−0.042
P2	P2	3.634	−0.036
P3	P3	3.634	−0.024

Table A.228: Partial charges for each atom position in $Na_2Ge_2P_3$.

Atom	Z	charge	part charge
Na1	11	10.21	0.79
Na2		10.218	0.782
Ge1	32	32.092	−0.092
Ge2		32.032	−0.032
Ge3		32.303	−0.303
P1	15	15.286	−0.286
P2		15.646	−0.646
P3		15.213	−0.213

A.10 7-1-4, 8-1-4, 9-1-4

All compounds with stoichiometries of 7-1-4, 8-1-4 and 9-1-4 show a structural similarity to the CaF_2 structure type. Within a cubic closed packing of P the Tr, Tt or Tm atom occupies tetrahedral voids forming isolated MPn_4 tetrahedra as the main structural motive. Different structures within this compound class differ mainly in the relative arrangement of these tetrahedra within their unit cell as well as the voids (tetrahedral and/or octahedral) which are occupied. Since the focus within this work is on the anionic substructure and their influence on the electronic properties, for this supplementary chapter only one exemplary crystal structure of K_8SnSb_4 is shown. For a detailed crystal structure description please refer to the respective sources.

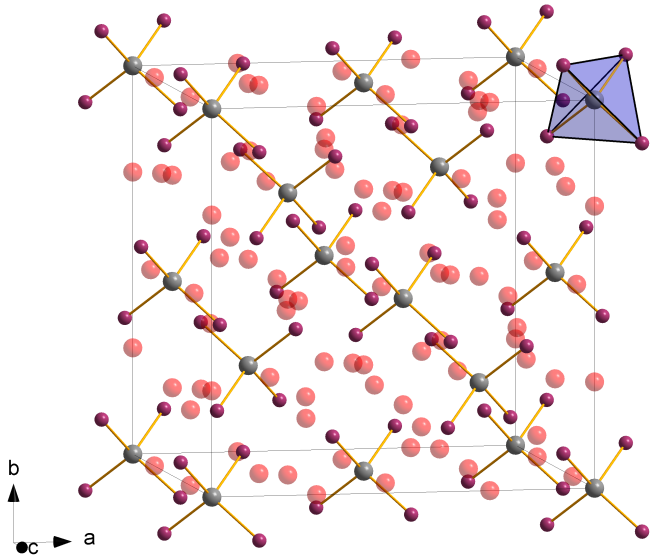

Figure A.140: Crystal structure of K_8snSb_4 incorporating isolated $SnSb_4$ tetrahedra.

The basic crystallographic information for each compound can be extracted from the compound overview tables.

Table A.229: Overview of the crystallographic details of the 7-1-4, 8-1-4 and 9-1-4 compounds. Cell parameters given in the first line and second line are of experimental and calculated origin, respectively. The third line shows the difference between both in percent.

compound	a / Å	b/ Å	space group	crystal system	connectivity
α-Li_8SiP_4	11.6784		*P a* $\overline{3}$ (no. 205)	cubic	0D
	11.6694				
	-0.08				
α-Li_8GeP_4	11.80203		-"-		-"-
	11.75828				
	-0.37				
α-Li_8SnP_4	11.93268		-"-	cubic	-"-
	11.94060				
	0.07				
β-Li_8SiP_4	11.6640		*P* $\overline{4}$ 3 *n* (no. 218)	cubic	-"-
β-Li_8GeP_4	11.7831		-"-	cubic	-"-
	11.7503				
	-0.28				
β-Li_8SnP_4	11.94217		-"-	cubic	-"-
	11.95798				
	0.13				
γ-Li_8TiP_4	8.37202	5.90134	*P* 4_2 *m c* (no. 105)	tetragonal	-"-
	8.34956	5.87528			
	-0.27	-0.44			
Na_8GeP_4	13.4230		*F d* $\overline{3}$ *m* (no. 227)	cubic	-"-
	13.3588				
	-0.48				
Na_8SnP_4	13.6178		*F d* $\overline{3}$ *m* (no. 227)	cubic	-"-
	13.4573				
	-1.19				
K_8SnSb_4	16.279		*F d* $\overline{3}$ *m* (no. 227)	cubic	-"-
	16.178				
	-0.62				

Table A.229: Continued.

compound	a / Å	b/ Å	space group	crystal system	connectivity
Na_8SnSb_4	14.816 14.588 -1.56		-"-	-"-	-"-
Li_7TaP_4	11.80859 11.79492 -0.12		*P a* $\overline{3}$ (no. 205)	cubic	-"-
α-Li_9AlP_4	11.70737 11.82985 1.04		*P* 2_1 3 (no. 198)	cubic	-"-
β-Li_9AlP_4	11.852 11.838 1.11		*P* $\overline{4}$ 3 *n* (no. 218)	cubic	-"-
Na_9InSb_4	14.7037 14.5147 -1.30		*F d* $\overline{3}$ *m* (no. 227)	cubic	-"-

Table A.230: Calculated band gaps and transitions as well as an overview of the sampled reciprocal space defined by the Monkhorst-Pack-type *k*-point grid (SHRINK) and Brillouin Zone paths for all 7-1-4, 8-1-4 and 9-1-4 compounds.

compound	band gap		transition	k-path	SHRINK
α-Li_8SiP_4	2.88	direct	Γ -> Γ	Γ—X—M—Γ—R—X|R—M—X_1	3 3 3
α-Li_8GeP_4	2.79	direct	-"-	-"-	-"-
α-Li_8SnP_4	2.74	direct	-"-	-"-	-"-
β-Li_8SiP_4	3.31	direct	-"-	Γ—X—M—Γ—R—X|R—M	3 3 3
β-Li_8GeP_4	2.82	direct	-"-	-"-	-"-
β-Li_8SnP_4	2.87	direct	-"-	-"-	-"-
γ-Li_8TiP_4	2.49	direct	-"-	Γ—X—M—Γ—Z—R—A—Z|X—R|M—A	4 4 6
Na_8GeP_4	1.78	indirect	M-Γ -> Γ	Γ—X—U|K—Γ—L—W—X	6 6 6
Na_8SnP_4	3.04	pseudo-direct	Γ -> Γ	Γ-X-U|K-Γ-L-W-X	4 4 4
K_8SnSb_4	2.47	pseudo-direct	-"-	Γ—X—U|K—Γ—L—W—X	3 3 3
Na_8SnSb_4	2.02	pseudo-direct	-"-	-"-	-"-
Li_7TaP_4	3.52	direct	-"-	Γ—X—M—Γ—R—X|R—M—X_1	3 3 3
α-Li_9AlP_4	3.27	direct	Γ -> Γ	Γ—X—M—Γ—R—X|R—M—X_1	3 3 3
β-Li_9AlP_4	3.00	direct	-"-	Γ—X—M—Γ—R—X|R—M	3 3 3
Na_9InSb_4	1.25	direct	-"-	Γ—X—U|K—Γ—L—W—X	6 6 6

α-Li_8SiP_4[111]

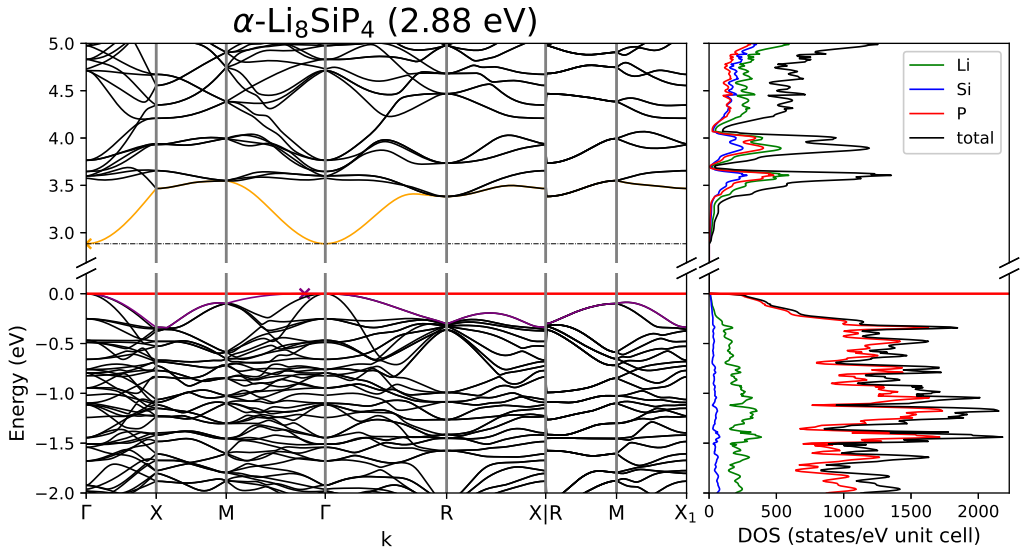

Figure A.141: Band structure and DOS of α-Li_8SiP_4.

Table A.231: Overlap population and interatomic distances of α-Li_8SiP_4.

Atom A	Atom B	r_{AB} / Å	overlap
Li1	P1	2.468	0.069
	P2	2.597	0.079
	Li5	2.719	0.01
	Li3	2.845	0.007
	Li2	3.141	0.004
	Li2	3.792	0.001
Li2	P1	2.421	0.08
	P2	2.59	0.073
	P2	2.595	0.085
	Li5	2.618	0.013
	Li3	2.7	0.008
	P2	2.704	0.057
Li3	P1	2.493	0.081
	P2	2.528	0.077
	P2	2.558	0.075
	Li4	2.607	0.012
	P2	2.697	0.072

Atom A	Atom B	r_{AB} / Å	overlap
Li4	Si1	2.691	0.01
	P2	2.847	0.046
Li5	P2	3.012	0.049
	Si1	4.812	0.0
Si1	P1	2.229	0.318
	P2	2.327	0.278
P1	P2	3.762	−0.046
	P2	4.175	−0.004

Table A.232: Partial charges for each atom position in α-Li_8SiP_4.

Atom	Z	charge	part charge
Li1	3	2.47	0.53
Li2		2.478	0.522
Li3		2.478	0.522
Li4		2.494	0.506
Li5		2.52	0.48

Atom	Z	charge	partialcharge
Si1	14	13.885	0.115
P1	15	16.099	−1.099
P2		16.057	−1.057

β-Li_8SiP_4 (model)

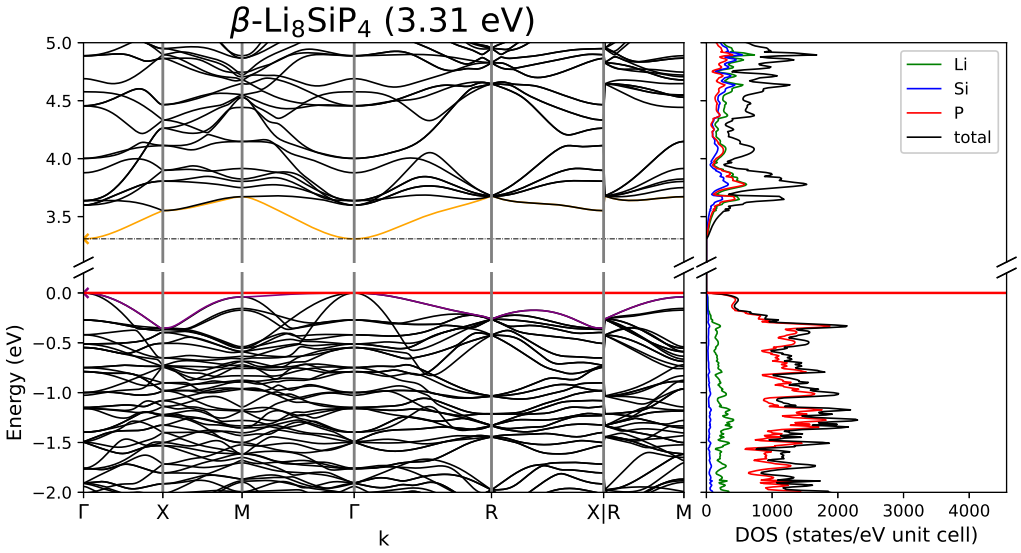

Figure A.142: Band structure and DOS of β-Li_8SiP_4.

Table A.233: Partial charges for each atom position in β-Li_8SiP_4.

Atom	Z	charge	part charge
Si1	14	14.237	−0.237
Si2		13.837	0.163
P1	15	15.979	−0.979
P2		16.078	−1.078
Li1	3	2.439	0.561
Li2		2.458	0.542

Atom	Z	charge	partialcharge
Li3		2.478	0.522
Li4		2.498	0.502
Li5		2.478	0.522
Li6		2.519	0.481

Table A.234: Overlap population and interatomic distances of β-Li_8SiP_4.

Atom A	Atom B	r_{AB} / Å	overlap
Si1	P1	2.253	0.255
	Li6	2.667	0.013
	Li4	3.15	0.002
	Li5	4.182	−0.002
	Li3	4.815	−0.002
	P2	4.919	−0.001
Si2	P2	2.33	0.299
	Li1	2.916	0.012
	Li5	2.948	0.01
	Li4	3.962	0.0
	Li2	4.124	−0.001
	Li3	4.131	0.0
P1	Li3	2.562	0.07
	Li4	2.608	0.065
	Li5	2.67	0.07
	Li6	2.861	0.042
	P1	3.679	−0.066
P2	Li5	2.403	0.094
	Li4	2.486	0.09
	Li5	2.497	0.078
	Li1	2.545	0.069
	Li3	2.605	0.08

Atom A	Atom B	r_{AB} / Å	overlap
Li1	Li4	2.682	0.008
	Li2	2.916	0.007
	Li5	4.025	0.0
	Li5	4.068	0.0
Li2	Li5	2.805	0.008
	Li4	3.962	0.0
	Li3	4.131	0.0
Li3	Li6	2.619	0.012
	Li5	2.772	0.008
	Li5	3.078	0.005
	Li4	3.949	0.0
Li4	Li6	2.708	0.011
	Li5	2.889	0.008
	Li5	3.039	0.005
Li5	Li6	2.542	0.014

α-Li_8GeP_4[165]

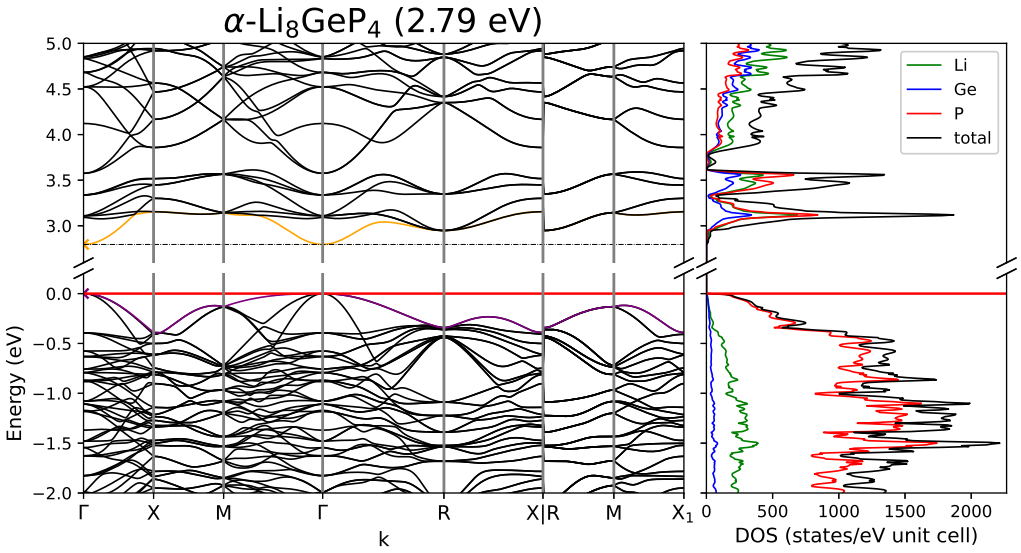

Figure A.143: Band structure and DOS of α-Li_8GeP_4.

Table A.235: Overlap population and interatomic distances of α-Li_8GeP_4.

Atom A	Atom B	r_{AB} / Å	overlap
Li1	P1	2.47	0.069
	P2	2.598	0.081
	Li5	2.707	0.01
	Li3	2.87	0.007
	Li2	3.158	0.004
	Li2	3.855	0.001
Li2	P1	2.44	0.079
	P2	2.583	0.089
	P2	2.613	0.071
	Li5	2.643	0.013
	P2	2.707	0.057
	Li3	2.741	0.008
Li3	P1	2.493	0.084
	P2	2.561	0.075
	P2	2.581	0.074
	Li4	2.629	0.012
	P2	2.679	0.075
Li4	Ge1	2.71	0.013
	P2	2.885	0.044
Li5	P2	3.009	0.049
	Ge1	4.849	−0.001
Ge1	P1	2.296	0.287
	P2	2.399	0.258
P1	P2	3.883	−0.034
	P2	4.175	−0.003

Table A.236: Partial charges for each atom position in α-Li_8GeP_4.

Atom	Z	charge	part charge
Li1	3	2.477	0.523
Li2		2.48	0.52
Li3		2.479	0.521
Li4		2.486	0.514
Li5		2.52	0.48

Atom	Z	charge	partialcharge
Ge1	32	32.084	−0.084
P1	15	16.032	−1.032
P2		16.009	−1.009

β-Li_8GeP_4[165]

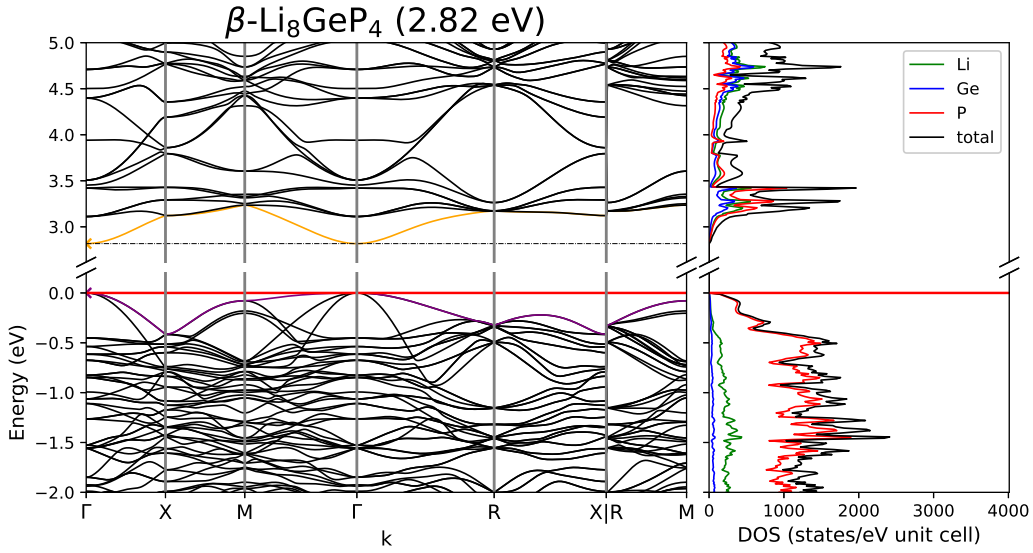

Figure A.144: Band structure and DOS of β-Li_8GeP_4.

Table A.237: Partial charges for each atom position in β-Li_8GeP_4.

Atom	Z	charge	part charge
Ge1	32	32.427	−0.427
Ge2		32.036	−0.036
P1	15	15.925	−0.925
P2		16.026	−1.026
Li1	3	2.431	0.569
Li2		2.459	0.541

Atom	Z	charge	partialcharge
Li3		2.486	0.514
Li4		2.505	0.495
Li5		2.478	0.522
Li6		2.516	0.484

Table A.238: Overlap population and interatomic distances of β-Li_8GeP_4.

Atom A	Atom B	r_{AB} / Å	overlap
Ge1	P1	2.321	0.241
	Li6	2.709	0.015
	Li4	3.168	0.004
	Li5	4.209	−0.002
	Li3	4.873	−0.002
	P2	4.924	−0.001
Ge2	P2	2.402	0.274
	Li1	2.938	0.013
	Li5	2.955	0.011
	Li4	3.995	0.0
	Li2	4.154	−0.001
	Li3	4.16	−0.001
P1	Li3	2.552	0.072
	Li4	2.633	0.065
	Li5	2.652	0.074
	Li6	2.921	0.038
	P1	3.79	−0.051
P2	Li5	2.422	0.092
	Li4	2.486	0.092
	Li5	2.523	0.075
	Li1	2.578	0.067
	Li3	2.596	0.081

Atom A	Atom B	r_{AB} / Å	overlap
Li1	Li4	2.707	0.008
	Li2	2.938	0.007
	Li5	4.079	0.0
	Li5	4.101	0.0
Li2	Li5	2.846	0.007
	Li4	3.995	0.0
	Li3	4.16	0.0
Li3	Li6	2.594	0.012
	Li5	2.778	0.008
	Li5	3.111	0.005
	Li4	3.994	0.0
Li4	Li6	2.732	0.01
	Li5	2.926	0.008
	Li5	3.04	0.006
Li5	Li6	2.566	0.014

α-Li_8SnP_4[166]

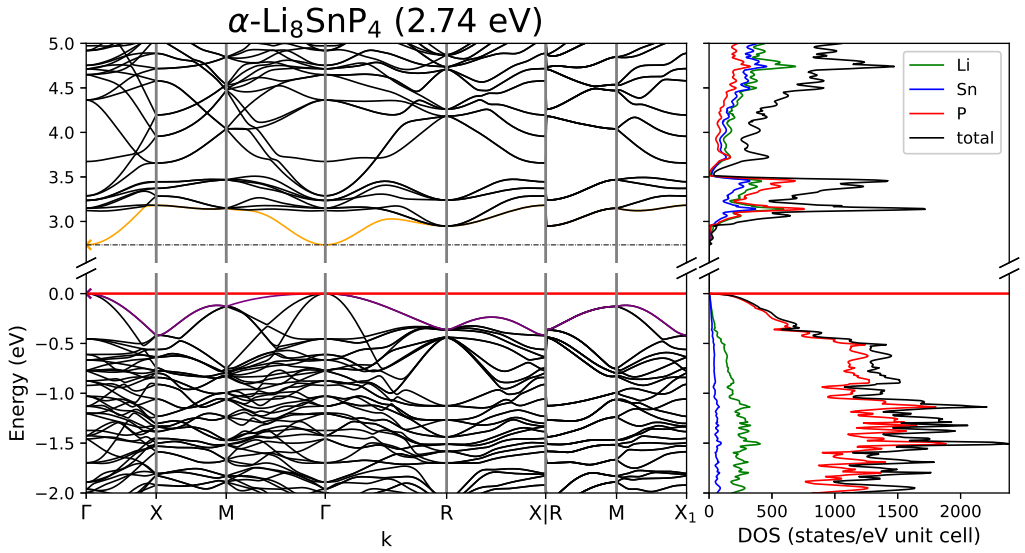

Figure A.145: Band structure and DOS of α-Li_8SnP_4.

Table A.239: Overlap population and interatomic distances of α-Li_8SnP_4.

Atom A	Atom B	r_{AB} / Å	overlap
Li1	P1	2.459	0.069
	P2	2.612	0.078
	Li5	2.686	0.011
	Li3	2.927	0.006
	Li2	3.197	0.004
	Li2	3.963	0.0
Li2	P1	2.509	0.077
	P2	2.565	0.09
	P2	2.663	0.063
	Li5	2.699	0.012
	P2	2.728	0.062
	Li3	2.786	0.007
Li3	P1	2.493	0.084
	P2	2.631	0.07
	P2	2.637	0.071
	P2	2.669	0.076
	Li4	2.679	0.012
Li4	Sn1	2.776	0.016
	P2	2.973	0.043
Li5	P2	3.016	0.048
	Sn1	4.933	0.0
Sn1	P1	2.444	0.249
	P2	2.549	0.239
P1	P2	4.147	−0.025
	P2	4.17	−0.004

Table A.240: Partial charges for each atom position in α-Li_8SnP_4.

Atom	Z	charge	part charge
Li1	3	2.462	0.538
Li2		2.471	0.529
Li3		2.467	0.533
Li4		2.491	0.509
Li5		2.506	0.494

Atom	Z	charge	partialcharge
Sn1	22	21.87	0.13
P1	15	16.121	−1.121
P2		16.078	−1.078

β-Li_8SnP_4[166]

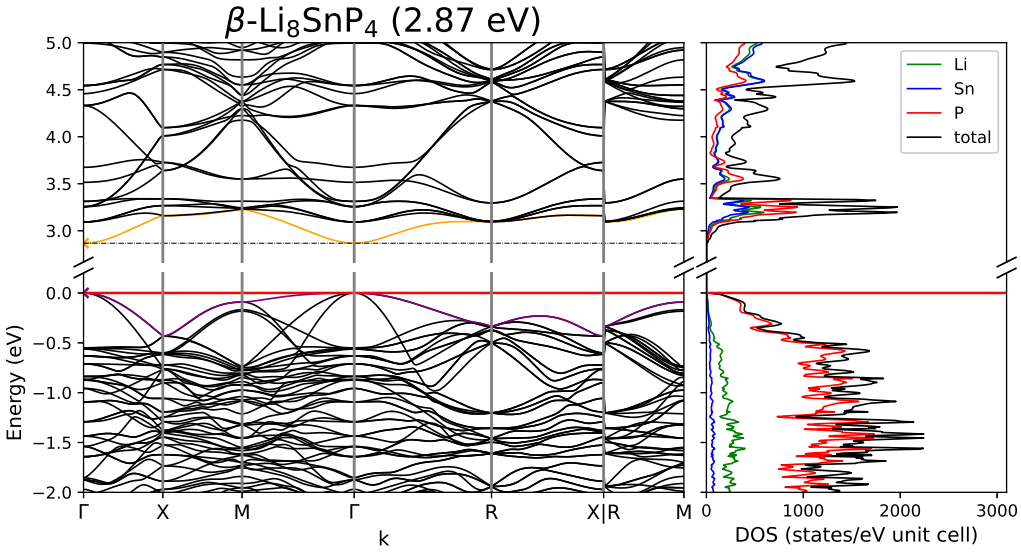

Figure A.146: Band structure and DOS of β-Li_8SnP_4.

Table A.241: Partial charges for each atom position in β-Li_8SnP_4.

Atom	Z	charge	part charge
Sn1	22	22.225	−0.225
Sn2		21.82	0.18
P1	15	16.002	−1.002
P2		16.101	−1.101
Li1	3	2.428	0.572
Li2		2.447	0.553

Atom	Z	charge	partialcharge
Li3		2.478	0.522
Li4		2.491	0.509
Li5		2.466	0.534
Li6		2.507	0.493

Table A.242: Overlap population and interatomic distances of β-Li_8SnP_4.

Atom A	Atom B	r_{AB} / Å	overlap
Sn1	P1	2.471	0.232
	Li6	2.869	0.016
	Li4	3.2	0.006
	Li5	4.276	−0.002
	P2	4.946	−0.002
	Li3	4.981	−0.002
Sn2	P2	2.55	0.252
	Li1	2.989	0.017
	Li5	3.008	0.013
	Li4	4.082	0.001
	Li2	4.228	0.0
	Li3	4.232	0.0
P1	Li3	2.51	0.079
	Li5	2.623	0.078
	Li4	2.686	0.063
	Li6	3.1	0.03
	P1	4.034	−0.034
P2	Li5	2.483	0.088
	Li4	2.497	0.091
	Li3	2.602	0.078
	Li5	2.618	0.068
	Li5	2.634	0.06

Atom A	Atom B	r_{AB} / Å	overlap
Li1	Li4	2.779	0.008
	Li2	2.989	0.006
	Li5	4.159	0.0
	Li5	4.183	0.0
Li2	Li5	2.909	0.007
	Li4	4.082	0.0
	Li3	4.232	0.0
Li3	Li6	2.507	0.012
	Li5	2.791	0.007
	Li5	3.199	0.004
	Li4	4.08	0.0
Li4	Li6	2.805	0.01
	Li5	2.977	0.007
	Li5	3.082	0.005
Li5	Li6	2.607	0.013

γ-Li_8TiP_4[167]

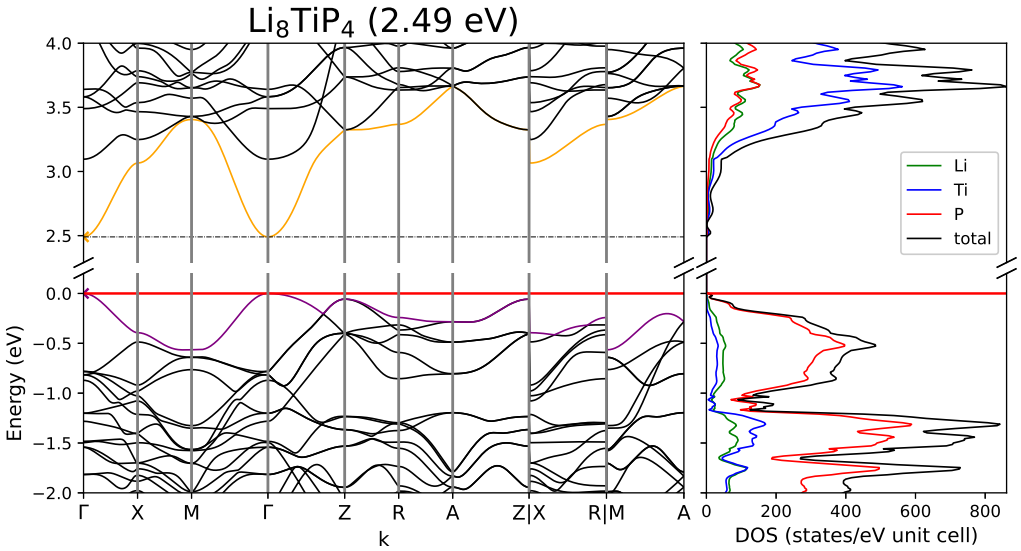

Figure A.147: Band structure and DOS of γ-Li_8TiP_4.

Table A.243: Overlap population and interatomic distances of γ-Li_8TiP_4.

Atom A	Atom B	r_{AB} / Å	overlap
Ti1	P2	2.369	0.24
	P1	2.383	0.245
	Li1	2.896	0.024
	Li1	2.979	0.017
	Li2	3.094	0.015
	Li3	3.095	0.018
P1	Li3	2.585	0.082
	Li1	2.592	0.081
	Li2	2.623	0.074
	Li2	2.644	0.072
	Li3	2.723	0.063
P2	Li2	2.479	0.085
	Li2	2.523	0.08
	Li1	2.529	0.084
	Li4	2.608	0.076
	Li4	2.743	0.066

Atom A	Atom B	r_{AB} / Å	overlap
Li1	Li2	2.817	0.009
	Li3	3.233	0.005
Li2	Li3	2.695	0.01
	Li3	2.812	0.01
Li3	Li3	2.773	0.007
Li4	Li4	2.938	0.007

Table A.244: Partial charges for each atom position in γ-Li_8TiP_4.

Atom	Z	charge	part charge
Ti1	22	21.185	0.815
P1	15	16.179	−1.179
P2		16.231	−1.231
Li1	3	2.551	0.449

Atom	Z	charge	partialcharge
Li2		2.506	0.494
Li3		2.488	0.512
Li4		2.443	0.557

Na_8GeP_4[71]

Since a high electronic conductivity was measured for this compound, the band structure and DOS were calculated with a Na TZVP basis set. Thus the band gap is significantly lower than other other Na-Ge-P compounds. A more thorough discussion can be found in the Results and Discussion chapter.

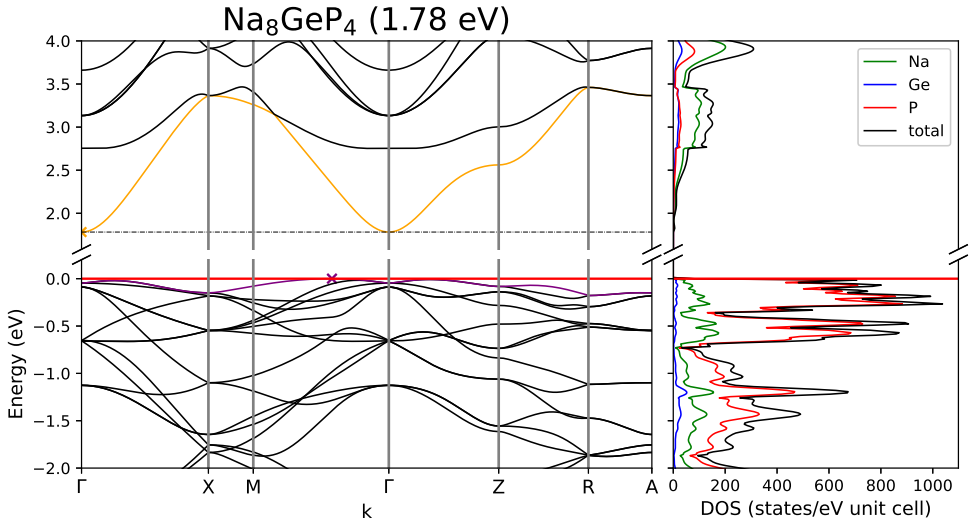

Figure A.148: Band structure and DOS of Na_8GeP_4.

Table A.245: Partial charges for each atom position in Na_8GeP_4.

Atom	Z	charge	part charge
Na1	11	10.444	0.556
Na2		10.563	0.437
Ge1	32	32.34	−0.34

Atom	Z	charge	partialcharge
P1	15	15.848	−0.848

Table A.246: Overlap population and interatomic distances of Na_8GeP_4.

Atom A	Atom B	r_{AB} / Å	overlap
Na1	Ge1	2.892	−0.009
	P1	3.083	0.041
	Na2	3.09	0.012
	Na1	4.723	−0.001
	P1	5.296	0.001
	Na2	5.45	−0.001
Na2	P1	2.959	0.098
	P1	3.004	0.066
	Na2	3.371	0.012
	Ge1	3.662	−0.006
	Na2	4.267	0.005

Atom A	Atom B	r_{AB} / Å	overlap
Ge1	P1	2.403	0.299
	P1	5.474	0.0
	Ge1	5.785	−0.001
P1	P1	3.925	−0.03
	P1	4.757	−0.004

Na_8SnP_4[168]

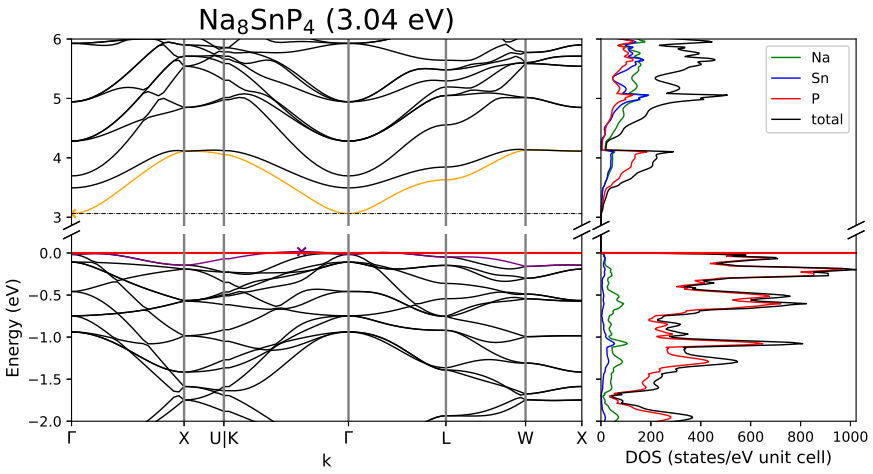

Figure A.149: Band structure and DOS of Na_8SnP_4.

Table A.247: Partial charges for each atom position in Na_8SnP_4.

Atom	Z	charge	part charge
Na1	11	10.29	0.71
Na2		10.332	0.668
P1	15	16.314	−1.314

Atom	Z	charge	partialcharge
Sn1	22	22.172	−0.172

Table A.248: Overlap population and interatomic distances of Na_8SnP_4.

Atom A	Atom B	r_{AB} / Å	overlap
Na1	Sn1	2.914	−0.001
	Na2	3.106	0.007
	P1	3.169	0.028
	Na1	4.758	0.0
	P1	5.465	0.0
	Na2	5.492	0.0
Na2	P1	2.915	0.06
	P1	3.034	0.045
	Na2	3.394	0.004
	Sn1	3.679	−0.002
	Na2	4.313	0.0

Atom A	Atom B	r_{AB} / Å	overlap
P1	Sn1	2.551	0.28
	P1	4.166	−0.033
	P1	4.776	−0.005
Sn1	Sn1	5.827	0.0

Na_8SnSb_4[169]

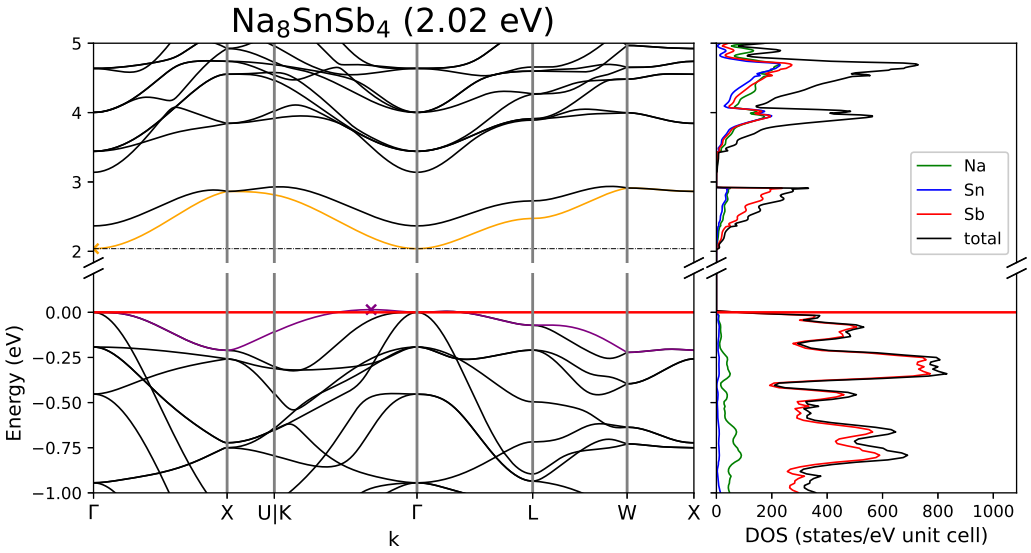

Figure A.150: Band structure and DOS of Na_8SnSb_4.

Table A.249: Overlap population and interatomic distances of Na_8SnSb_4.

Atom A	Atom B	r_{AB} / Å	overlap
Na1	Sn1	3.158	0.01
	Na2	3.308	0.006
	Sb1	3.475	0.03
	Na1	5.158	0.0
	Na2	5.978	0.0
	Sb1	6.003	0.0
Na2	Sb1	3.159	0.06
	Sb1	3.236	0.049
	Na2	3.664	0.003
	Sn1	3.895	0.001
	Na2	4.806	0.0

Atom A	Atom B	r_{AB} / Å	overlap
Sb1	Sn1	2.845	0.272
	Sb1	4.645	−0.031
	Sb1	5.17	−0.005
Sn1	Sn1	6.317	0.0

Table A.250: Partial charges for each atom position in Na_8SnSb_4.

Atom	Z	charge	part charge
Na1	11	10.331	0.669
Na2		10.336	0.664
Sb1	23	24.299	−1.299

Atom	Z	charge	partialcharge
Sn1	22	22.129	−0.129

K_8SnSb_4[149]

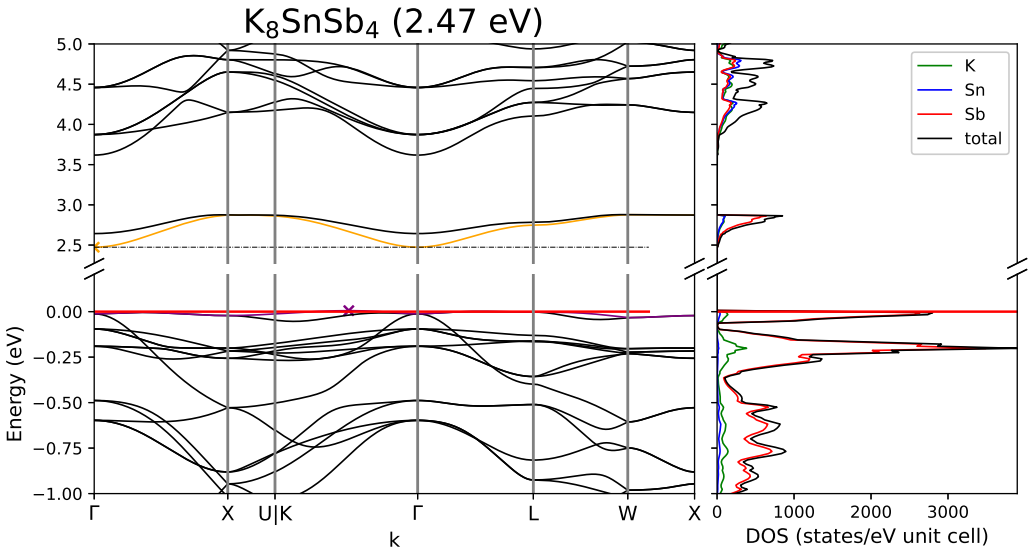

Figure A.151: Band structure and DOS of K_8SnSb_4.

Table A.251: Overlap population and interatomic distances of K_8SnSb_4.

Atom A	Atom B	r_{AB} / Å	overlap
K1	Sn1	3.503	−0.008
	K2	3.705	0.002
	Sb1	3.737	0.019
	K1	5.72	0.0
	Sb1	6.419	0.0
	K2	6.614	0.0
K2	Sb1	3.595	0.035
	Sb1	3.602	0.043
	K2	4.072	0.003
	Sn1	4.377	−0.001
	K2	5.249	0.0
Sn1	Sb1	2.916	0.292
	Sb1	6.63	0.0
	Sn1	7.005	0.0
Sb1	Sb1	4.762	−0.024
	Sb1	5.76	−0.002

Table A.252: Partial charges for each atom position in K_8SnSb_4.

Atom	Z	charge	part charge
K1	19	18.287	0.713
K2		18.327	0.673
Sn1	22	22.012	−0.012
Sb1	23	24.363	−1.363

Li_7TaP_4[170]

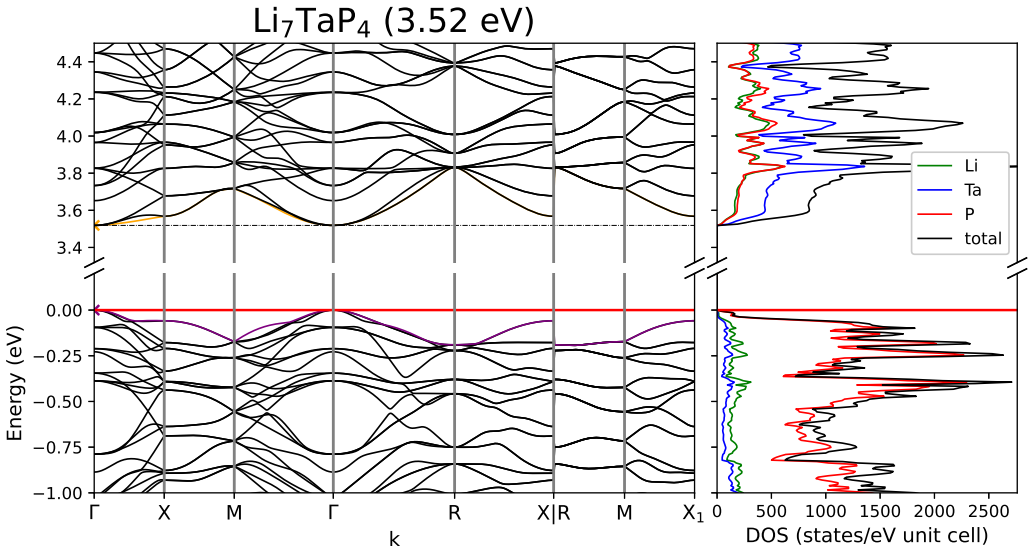

Figure A.152: Band structure and DOS of Li_7TaP_4.

Table A.253: Partial charges for each atom position in Li_7TaP_4.

Atom	Z	charge	part charge
Li1	3	2.413	0.587
Li2		2.467	0.533
Li3		2.468	0.532
Ta1	13	12.204	0.796

Atom	Z	charge	partialcharge
P1	15	16.134	−1.134
P2		16.149	−1.149

Table A.254: Overlap population and interatomic distances of Li_7TaP_4.

Atom A	Atom B	r_{AB} / Å	overlap
Li1	P1	2.548	0.067
	P2	2.581	0.067
	Li3	2.977	0.005
	Li2	3.01	0.005
	Li2	4.033	0.0
	Li3	4.068	0.0
Li2	P2	2.582	0.067
	P1	2.587	0.077
	P2	2.588	0.077
	P2	2.592	0.07
	Li3	2.82	0.007
	Li2	2.874	0.007
Li3	P2	2.54	0.08
	P2	2.59	0.076
	P1	2.592	0.069
	P2	2.614	0.068
	Li3	2.897	0.007
Ta1	P1	2.385	0.28
	P2	2.398	0.283
P1	P2	3.903	−0.026
	P2	4.205	−0.003

α-Li_9AlP_4[171]

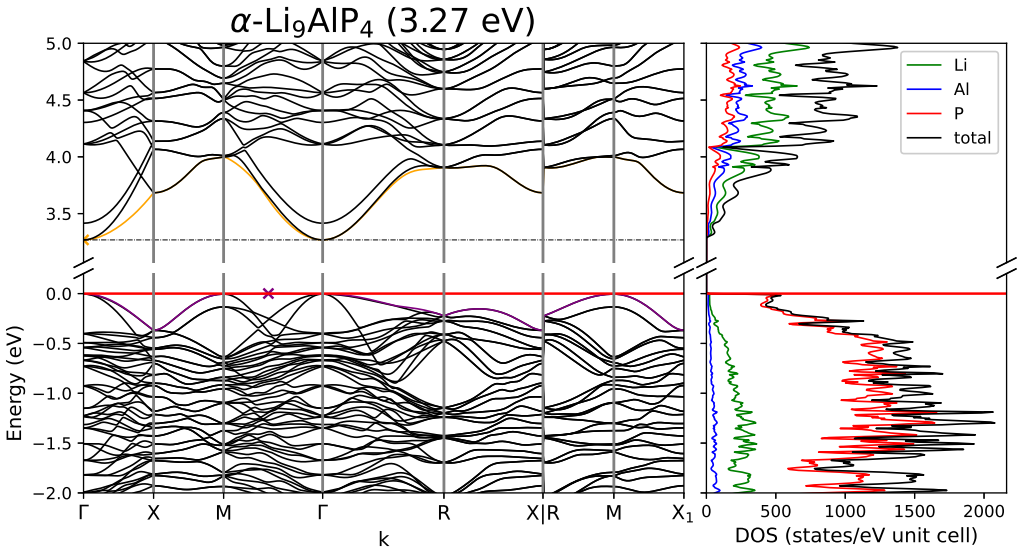

Figure A.153: Band structure and DOS of α-Li_9AlP_4.

Table A.255: Overlap population and interatomic distances of α-Li_9AlP_4.

Atom A	Atom B	r_{AB} / Å	overlap
Li1	P3	2.664	0.079
	P1	2.724	0.063
	Li3	2.788	0.008
	Li8	2.819	0.008
	Li6	3.957	0.001
	Li2	4.085	0.0
Li2	P3	2.517	0.091
	P1	2.564	0.072
	P2	2.632	0.075
	P2	2.668	0.067
	Li5	2.699	0.01
	Li8	2.733	0.008
Li3	P3	2.459	0.085
	P1	2.53	0.086
	P3	2.533	0.07
	Li5	2.583	0.013
	Li4	2.649	0.01
	P2	2.781	0.061
Li4	Al2	2.627	0.018
	Al1	2.656	0.017
	Li6	2.662	0.01
	P3	2.797	0.047
	P2	2.931	0.034
Li5	Li6	2.555	0.012
	Li7	2.58	0.011
	Li8	2.621	0.013
	Li6	2.722	0.009
Li6	P2	2.471	0.085
	P4	2.526	0.087
	P3	2.537	0.087
Li7	P2	2.454	0.098
	P4	2.853	0.041
	Li8	3.881	0.001
Li8	P3	2.486	0.086
	P3	2.623	0.074
	P4	2.709	0.06
	P2	2.738	0.072
Al1	P1	2.351	0.307
	P2	2.401	0.291
Al2	P4	2.404	0.315
	P3	2.468	0.276
P1	P2	3.878	−0.047

Table A.256: Partial charges for each atom position in α-Li_9AlP_4.

Atom	Z	charge	part charge
Li1	3	2.462	0.538
Li2		2.495	0.505
Li3		2.488	0.512
Li4		2.456	0.544
Li5		2.486	0.514
Li6		2.507	0.493
Li7		2.535	0.465
Li8		2.475	0.525
Al1	13	13.13	−0.13
Al2		12.833	0.167
P1	15	16.13	−1.13
P2		16.114	−1.114
P3		16.203	−1.203
P4		16.147	−1.147

β-Li_9AlP_4[171]

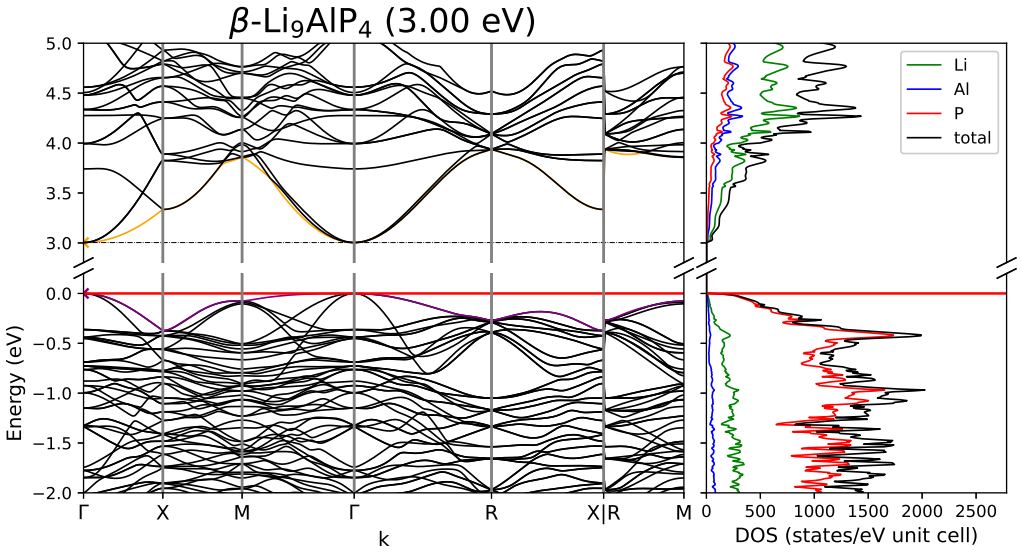

Figure A.154: Band structure and DOS of β-Li_9AlP_4.

Table A.257: Partial charges for each atom position in β-Li_9AlP_4.

Atom	Z	charge	part charge
Al1	13	12.95	0.05
Al2		12.772	0.228
P1	15	16.159	−1.159
P2		16.158	−1.158
Li1	3	2.512	0.488

Atom	Z	charge	partialcharge
Li2		2.496	0.504
Li3		2.484	0.516
Li4		2.502	0.498
Li5		2.485	0.515

Table A.258: Overlap population and interatomic distances of β-Li_9AlP_4.

Atom A	Atom B	r_{AB} / Å	overlap
Al1	P2	2.405	0.299
	Li5	2.953	0.012
	Li3	2.96	0.015
	Li4	3.227	0.007
	Li1	4.123	0.0
	Li2	4.185	−0.001
Al2	P1	2.435	0.296
	Li1	3.049	0.012
	Li4	3.885	0.002
	Li5	4.743	−0.001
	P2	5.105	0.0
	Li3	5.919	0.0
P1	Li4	2.579	0.08
	Li1	2.579	0.072
	Li5	2.622	0.075
	P1	3.977	−0.033
	P2	4.186	−0.013
P2	Li4	2.482	0.09
	Li2	2.541	0.079
	Li4	2.55	0.087
	Li3	2.561	0.072
	Li5	2.589	0.079

Atom A	Atom B	r_{AB} / Å	overlap
Li1	Li4	2.759	0.01
	Li5	2.777	0.011
	Li4	2.794	0.009
	Li3	2.871	0.009
Li2	Li5	2.894	0.007
	Li3	2.96	0.006
	Li4	3.197	0.004
Li3	Li5	3.283	0.004
	Li4	4.19	0.0
Li4	Li5	2.473	0.01
	Li5	2.629	0.012
	Li5	2.722	0.009

Na_9InSb_4[172]

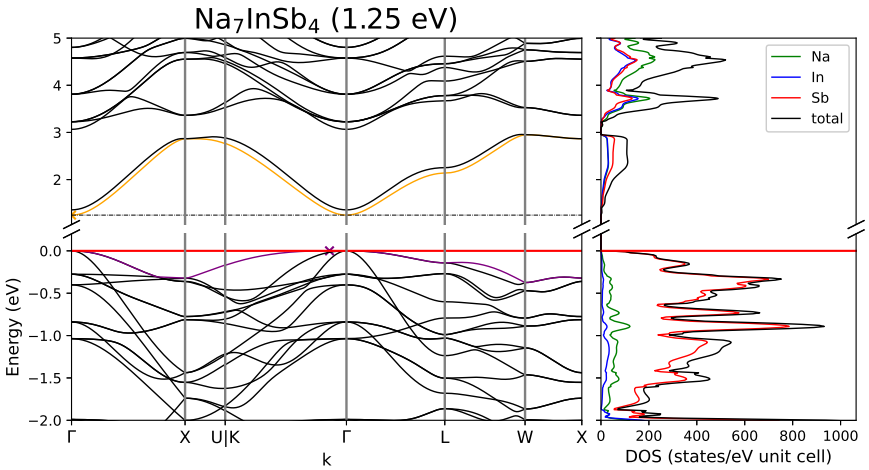

Figure A.155: Band structure and DOS of Na_9InSb_4.

Table A.259: Partial charges for each atom position in Na_9InSb_4.

Atom	Z	charge	part charge
Na1	11	10.351	0.649
Na2		10.318	0.682
Na3		10.342	0.658

Atom	Z	charge	partialcharge
In1	21	21.28	−0.28
Sb1	23	24.409	−1.409

Table A.260: Overlap population and interatomic distances of Na_9InSb_4.

Atom A	Atom B	r_{AB} / Å	overlap
Na1	Sb1	3.142	0.064
	Sb1	3.176	0.047
	Na2	3.232	0.007
	Na3	3.477	0.004
	Na1	3.635	0.003
	In1	3.78	0.004
Na2	In1	3.142	0.012
	Sb1	3.51	0.028
	Na2	5.132	0.0
	Na3	6.017	0.0

Atom A	Atom B	r_{AB} / Å	overlap
Na3	Sb1	3.355	0.053
	Sb1	6.058	0.0
	Na3	6.285	0.0
In1	Sb1	2.93	0.26
	Sb1	5.984	−0.002
Sb1	Sb1	4.785	−0.026

A.11 1-1-4

Table A.261: Overview of the crystallographic details of the 1-1-4 compounds. Cell parameters given in the first line and second line are of experimental and calculated origin, respectively. The third line shows the difference between both in percent.

compound	a / Å	b/ Å	c / Å	space group	crystal system	connectivity
$CsAlSb_4$	10.74871	4.230633	18.56545	*P n m a* (no. 62)	orthorhombic	1D
	10.90421	4.250700	18.74063			
	1.43	0.47	0.93			
$CsGaSb_4$	10.7421	4.218855	18.44829	-"-	-"-	-"-
	10.8266	4.275806	18.64269			
	0.78	1.33	1.04			
$KAlSb_4$	10.366	4.220	17.865	-"-	-"-	-"-
	10.472	4.217	18.067			
	1.02	-0.08	1.12			
$KGaSb_4$	10.348	4.203	17.823	-"-	-"-	-"-
	10.467	4.211	17.985			
	1.14	0.19	0.90			
$RbAlSb_4$	10.53141	4.21886	18.21602	-"-	-"-	-"-
	10.69783	4.23242	18.43121			
	1.56	0.32	1.17			
$RbGaSb_4$	10.52169	4.211279	18.09999	-"-	-"-	-"-
	10.67843	4.226141	18.36771			
	1.47	0.35	1.46			

Table A.262: Calculated band gaps and transitions as well as an overview of the sampled reciprocal space defined by the Monkhorst-Pack-type *k*-point grid (SHRINK) and Brillouin Zone paths for all 1-1-4 compounds.

compound	band gap		transition	k-path	SHRINK
$CsAlSb_4$	1.42	direct	Γ -> Γ	Γ—X—S—Y—Γ—Z—U—R—T—Z|X—U|Y—T|S—R	3 8 2
$CsGaSb_4$	1.34	direct	-"-	-"-	-"-
$KAlSb_4$	1.24	direct	-"-	-"-	-"-
$KGaSb_4$	1.27	direct	-"-	-"-	-"-
$RbAlSb_4$	1.34	direct	-"-	-"-	-"-
$RbGaSb_4$	1.38	direct	-"-	-"-	-"-

$KAlSb_4$[35]

$KAlSb_4$ crystallizes in the orthorhombic space group *P n m a* (no. 62). The structure consists of a three dimensional network Al and Sb forming channels which incorporate the K atoms. Within this complex network, linear chains of corner sharing $AlSb_4$ tetrahedra along b are present. These chains are connected by bridging Sb atoms.

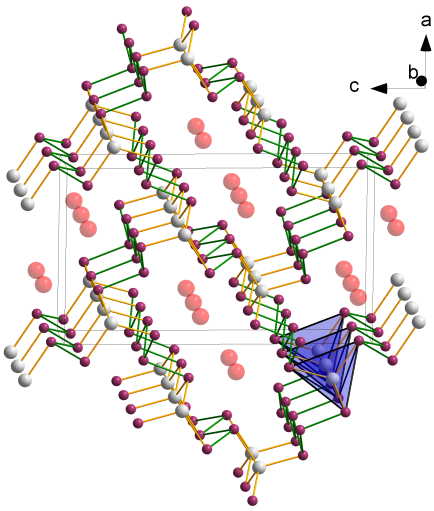

Figure A.156: Crystal structure of $KaAlSb_4$ incorporating chains of corner-sharing $AlSb_4$ tetrahedra.

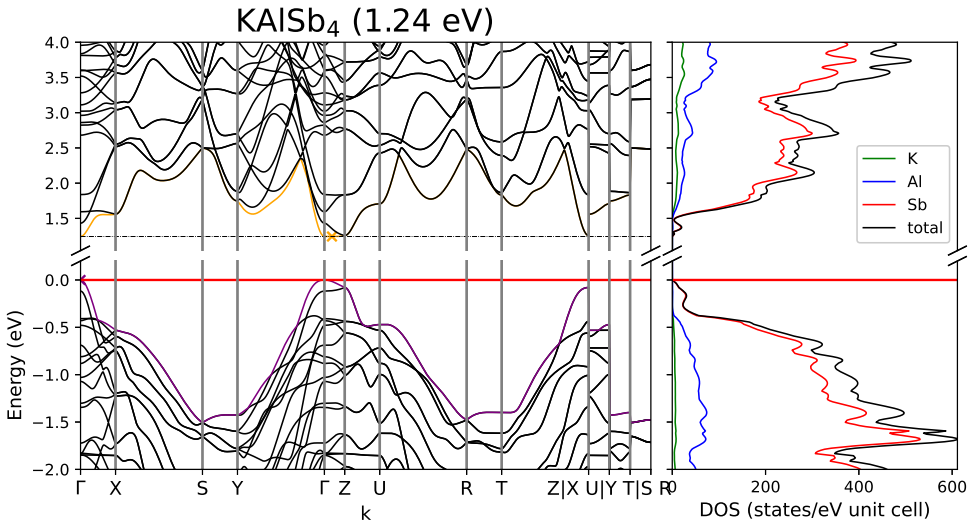

Figure A.157: Band structure and DOS of $KAlSb_4$.

Table A.263: Overlap population and interatomic distances of $KAlSb_4$.

Atom A	Atom B	r_{AB} / Å	overlap
K1	Sb2	3.635	0.013
	Sb3	3.689	0.013
	Sb1	3.694	0.013
	Sb1	3.696	0.017
	Al1	3.877	−0.003
	Sb4	4.181	0.0
Al1	Sb1	2.68	0.295
	Sb2	2.684	0.3
	Sb3	2.704	0.299
	Sb4	3.952	−0.012
	Sb4	4.017	−0.012
Sb1	Sb4	2.837	0.24
	Sb3	4.108	0.002
	Sb1	4.217	−0.027
Sb2	Sb4	2.863	0.224
	Sb4	3.98	0.007
	Sb2	4.217	−0.009
Sb3	Sb3	2.857	0.23
	Sb3	4.217	−0.006

Table A.264: Partial charges for each atom position in $KAlSb_4$.

Atom	Z	charge	part charge
K1	19	18.21	0.79
Al1	13	12.757	0.243
Sb1	23	23.502	−0.502
Sb2		23.316	−0.316
Sb3		23.26	−0.26
Sb4		22.955	0.045

$KGaSb_4$[173]

For a crystal structure description see $KAlSb_4$.

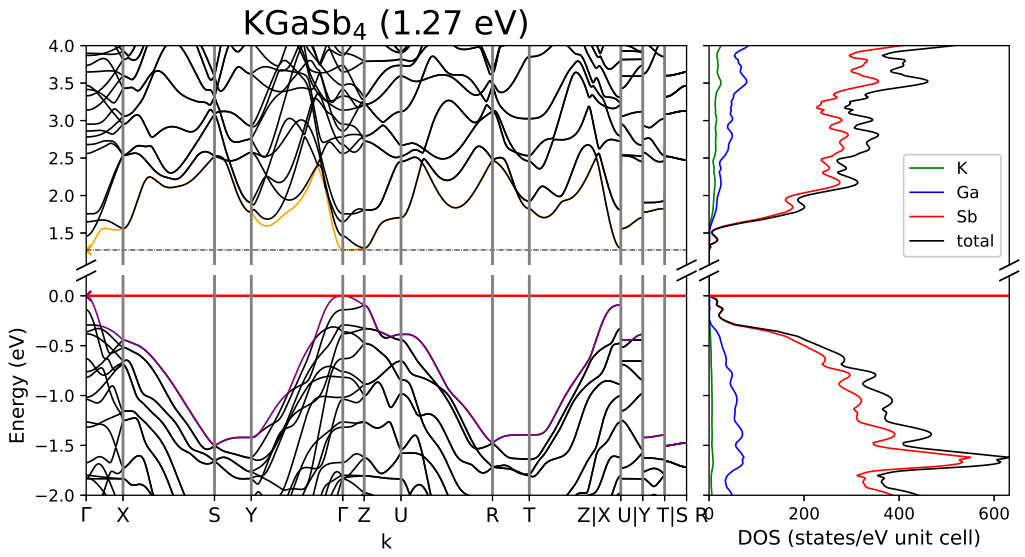

Figure A.158: Band structure and DOS of $KGaSb_4$.

Table A.265: Overlap population and interatomic distances of $KGaSb_4$.

Atom A	Atom B	r_{AB} / Å	overlap
K1	Sb2	3.641	0.013
	Sb3	3.68	0.013
	Sb1	3.696	0.013
	Sb1	3.707	0.016
	Ga1	3.833	−0.006
	Sb4	4.196	0.0
Ga1	Sb2	2.669	0.27
	Sb1	2.669	0.258
	Sb3	2.682	0.278
	Sb4	3.946	−0.016
	Sb4	4.022	−0.018

Atom A	Atom B	r_{AB} / Å	overlap
Sb1	Sb4	2.83	0.242
	Sb3	4.155	0.004
	Sb1	4.211	−0.021
Sb2	Sb4	2.86	0.227
	Sb4	3.971	0.007
	Sb2	4.211	−0.008
Sb3	Sb3	2.855	0.231
	Sb4	4.206	0.008

Table A.266: Partial charges for each atom position in $KGaSb_4$.

Atom	Z	charge	part charge
K1	19	18.208	0.792
Ga1	31	30.921	0.079
Sb1	23	23.409	−0.409
Sb2		23.27	−0.27

Atom	Z	charge	partialcharge
Sb3		23.221	−0.221
Sb4		22.971	0.029

$RbAlSb_4$[174]

For a crystal structure description see $KAlSb_4$.

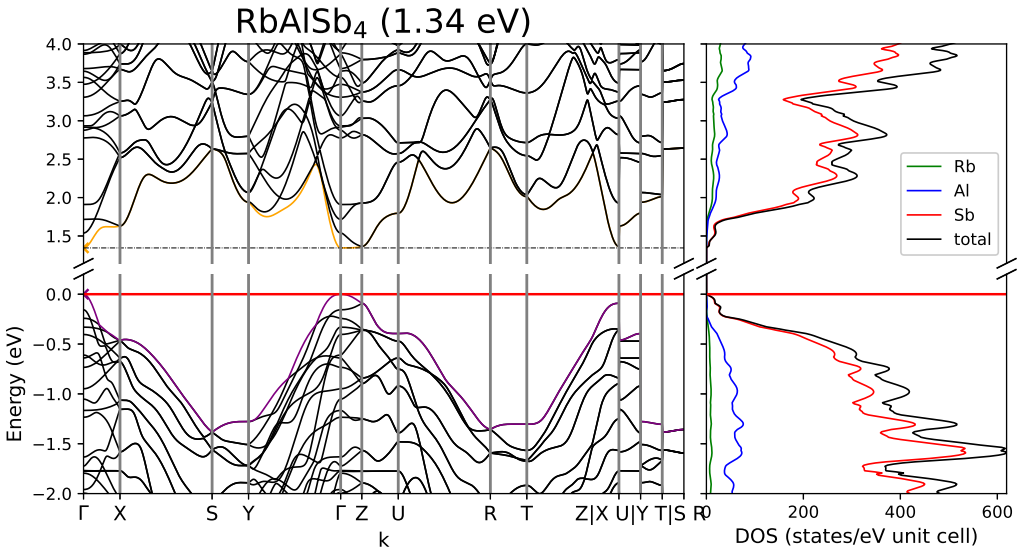

Figure A.159: Band structure and DOS of $RbAlSb_4$.

Table A.267: Partial charges for each atom position in $RbAlSb_4$.

Atom	Z	charge	part charge
Rb1	9	8.266	0.734
Al1	13	12.756	0.244
Sb1	23	23.468	−0.468
Sb2		23.29	−0.29

Atom	Z	charge	partialcharge
Sb3		23.248	−0.248
Sb4		22.972	0.028

Table A.268: Overlap population and interatomic distances of $RbAlSb_4$.

Atom A	Atom B	r_{AB} / Å	overlap
Rb1	Sb2	3.759	0.013
	Sb3	3.793	0.014
	Sb1	3.84	0.014
	Sb1	3.854	0.019
	Al1	4.038	−0.004
	Rb1	4.232	0.0
Al1	Sb1	2.682	0.296
	Sb2	2.686	0.299
	Sb3	2.706	0.298
	Sb4	4.001	−0.012
	Sb4	4.073	−0.011

Atom A	Atom B	r_{AB} / Å	overlap
Sb1	Sb4	2.839	0.242
	Sb3	4.174	0.002
	Sb1	4.232	−0.026
Sb2	Sb4	2.864	0.227
	Sb4	4.074	0.007
	Sb2	4.232	−0.008
Sb3	Sb3	2.857	0.232
	Sb3	4.232	−0.006
Sb4	Sb4	4.232	−0.007

$RbGaSb_4$[174]

For a crystal structure description see $KAlSb_4$.

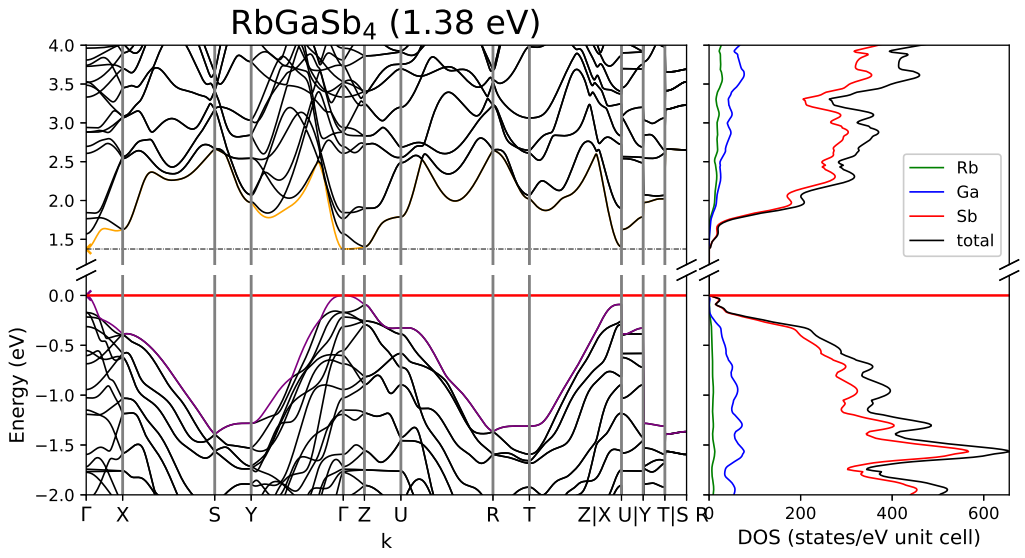

Figure A.160: Band structure and DOS of $RbGaSb_4$.

Table A.269: Overlap population and interatomic distances of $RbGaSb_4$.

Atom A	Atom B	r_{AB} / Å	overlap
Rb1	Sb2	3.769	0.013
	Sb3	3.788	0.014
	Sb1	3.841	0.014
	Sb1	3.856	0.019
	Ga1	4.004	−0.007
	Sb4	4.216	0.006
Ga1	Sb2	2.669	0.27
	Sb1	2.671	0.263
	Sb3	2.683	0.275
	Sb4	3.997	−0.016
	Sb4	4.071	−0.018
Sb1	Sb4	2.833	0.245
	Sb3	4.206	0.004
	Sb1	4.226	−0.019
Sb2	Sb4	2.861	0.23
	Sb4	4.061	0.007
	Sb2	4.226	−0.008
Sb3	Sb3	2.855	0.234
	Sb3	4.226	−0.006

Table A.270: Partial charges for each atom position in $RbGaSb_4$.

Atom	Z	charge	part charge
Rb1	9	8.267	0.733
Ga1	31	30.93	0.07
Sb1	23	23.369	−0.369
Sb2		23.238	−0.238
Sb3		23.204	−0.204
Sb4		22.99	0.01

$CsAlSb_4$[174]

For a crystal structure description see $KAlSb_4$.

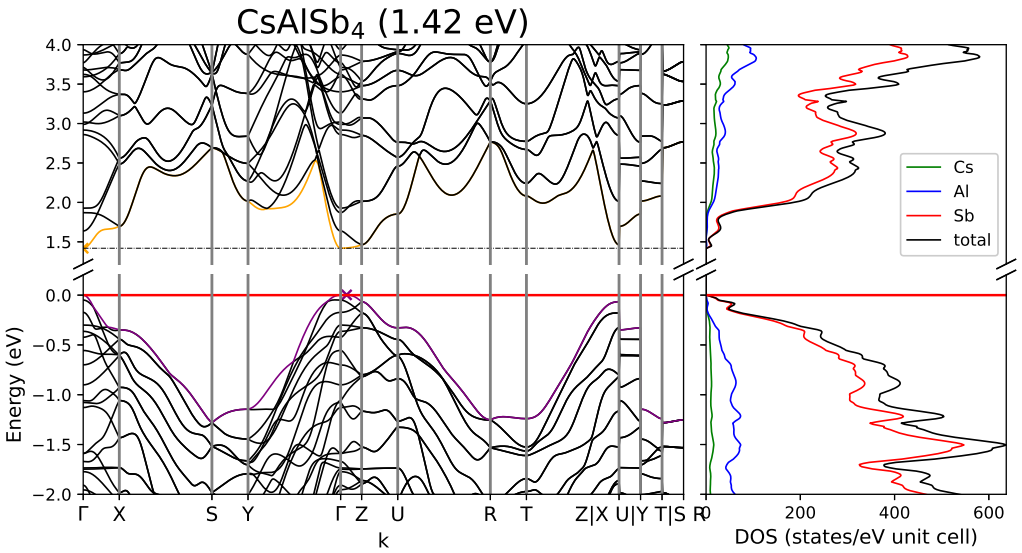

Figure A.161: Band structure and DOS of $CsAlSb_4$.

Table A.271: Overlap population and interatomic distances of $CsAlSb_4$.

Atom A	Atom B	r_{AB} / Å	overlap
Cs1	Sb2	3.875	0.014
	Sb3	3.881	0.015
	Sb1	3.968	0.014
	Sb1	4.009	0.022
	Al1	4.164	0.0
	Sb4	4.248	0.01
Al1	Sb1	2.686	0.296
	Sb2	2.688	0.299
	Sb3	2.708	0.298
	Sb4	4.045	−0.011
	Sb4	4.127	−0.011

Atom A	Atom B	r_{AB} / Å	overlap
Sb1	Sb4	2.841	0.245
	Sb1	4.251	−0.025
	Sb3	4.253	0.003
Sb2	Sb4	2.866	0.231
	Sb4	4.165	0.006
	Sb2	4.251	−0.008
Sb3	Sb3	2.858	0.233
	Sb3	4.251	−0.007

Table A.272: Partial charges for each atom position in $CsAlSb_4$.

Atom	Z	charge	part charge
Cs1	9	8.246	0.754
Al1	13	12.757	0.243
Sb1	23	23.467	−0.467
Sb2		23.29	−0.29
Sb3		23.256	−0.256
Sb4		22.984	0.016

$CsGaSb_4$[174]

For a crystal structure description see $KAlSb_4$.

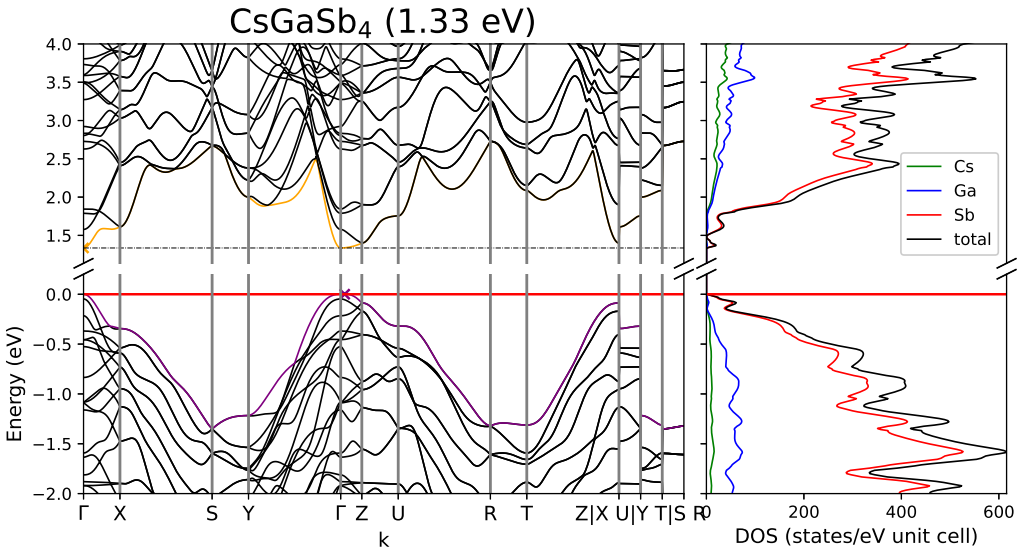

Figure A.162: Band structure and DOS of $CsGaSb_4$.

Table A.273: Partial charges for each atom position in $CsGaSb_4$.

Atom	Z	charge	part charge
Cs1	9	8.245	0.755
Ga1	31	30.933	0.067
Sb1	23	23.367	−0.367
Sb2		23.238	−0.238
Sb3		23.212	−0.212
Sb4		23.005	−0.005

Table A.274: Overlap population and interatomic distances of $CsGaSb_4$.

Atom A	Atom B	r_{AB} / Å	overlap
Cs1	Sb3	3.866	0.015
	Sb2	3.89	0.015
	Sb1	3.965	0.015
	Sb1	3.996	0.022
	Ga1	4.107	−0.002
	Sb4	4.203	0.01
Ga1	Sb2	2.667	0.271
	Sb1	2.679	0.266
	Sb3	2.685	0.275
	Sb4	4.04	−0.016
	Sb4	4.114	−0.017
Sb1	Sb4	2.833	0.249
	Sb2	4.248	−0.012
	Sb3	4.271	0.004
Sb2	Sb4	2.869	0.232
	Sb4	4.145	0.008
	Sb3	4.269	−0.02
Sb3	Sb3	2.862	0.234

A.12 1-1-2

Table A.275: Overview of the crystallographic details of the 1-1-2 compounds. Cell parameters given in the first line and second line are of experimental and calculated origin, respectively. The third line shows the difference between both in percent.

compound	a / Å	b/ Å	c / Å	space group	crystal system	connectivity
$KGaSb_2$	7.65	18.048	29.64	C m c a (no. 64)	orthorhombic	1D
	7.71	18.129	29.70			
	0.79	0.44	0.23			
$CsGaSb_2$	8.4192		15.890	P 42/n m c (no. 137)	tetragonal	1D
	8.4910		16.067			
	0.85		1.10			
$RbGaSb_2$	8.3348		15.483	-"-	-"-	-"-
	8.4093		15.677			
	0.89		1.24			

Table A.276: Calculated band gaps and transitions as well as an overview of the sampled reciprocal space defined by the Monkhorst-Pack-type *k*-point grid (SHRINK) and Brillouin Zone paths for all 1-1-2 compounds.

compound	band gap		transition	k-path	SHRINK
$KGaSb_2$	2.20	indirect	Y-C_0 -> Γ-Y	Γ—Y—C_0|S_0—Γ—Z—A_0|E_0—T—Y|Γ—S—R—Z—T	3 3 1
$CsGaSb_2$	2.05	pseudo-direct	M -> M	Γ—X—M—Γ—Z—R—A—Z|X—R|M—A	4 4 2
$RbGaSb_2$	1.88	direct	-"-	-"-	-"-

$KGaSb_2$[175]

$KGaSb_2$ crystallizes in the orthorhombic space group *Cmca* (np. 64). The compound incorporates one dimensional chains of alternating corner and edge-sharing $GaSb_4$ tetrahedra along the a axis. Two chains dimerize further by corner-sharing.

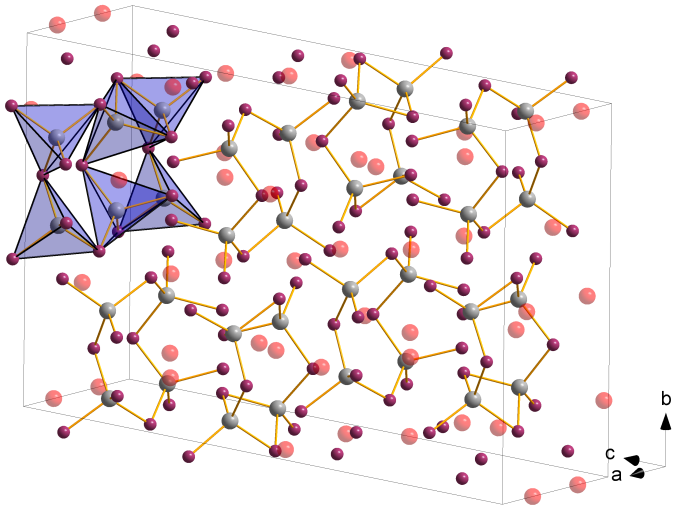

Figure A.163: Crystal structure of $KGaSb_2$ with dimerized one dimensional chains of corner- and edge-sharing chains of $GaSb_4$ tetrahedra.

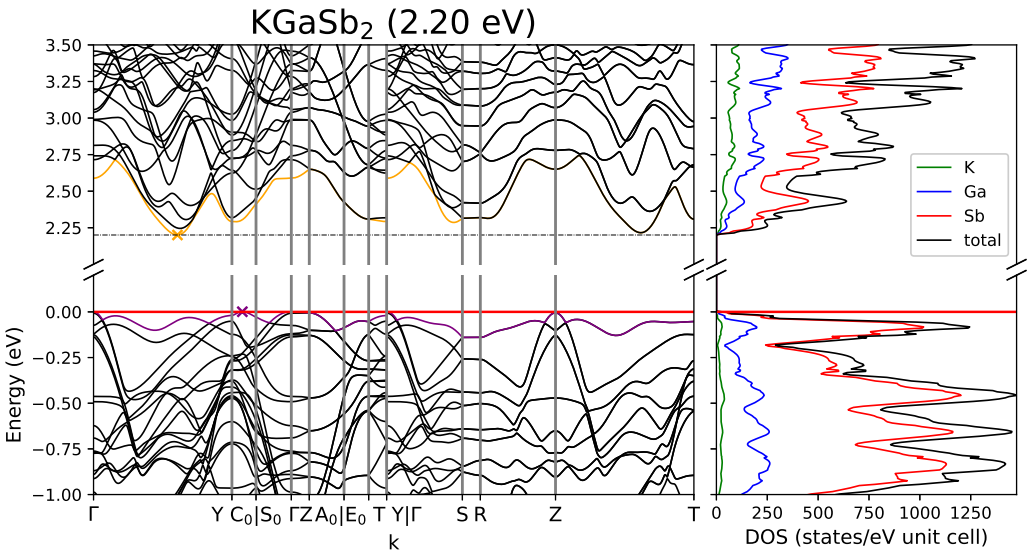

Figure A.164: Band structure and DOS of $KGaSb_2$.

Table A.277: Overlap population and interatomic distances of $KGaSb_2$.

Atom A	Atom B	r_{AB} / Å	overlap
K1	K1	3.363	−0.001
	Sb3	3.445	0.014
	Sb7	3.596	0.017
	Sb4	3.803	0.017
	Ga2	3.95	−0.004
	K3	4.24	0.001
K2	Sb6	3.559	0.014
	Ga2	3.581	−0.005
	Sb2	3.647	0.013
	Ga1	3.649	−0.005
	Sb1	3.657	−0.001
	Sb7	3.799	0.002
K3	Sb3	3.555	0.02
	Sb7	3.571	0.008
	Sb7	3.662	0.023
	Sb4	4.01	0.006
	Ga1	4.016	−0.002
K4	Sb5	3.569	0.016
	Sb1	3.59	0.016
	K4	3.855	0.001
	Sb2	3.966	0.011
	Sb6	4.092	0.009
	Ga2	4.352	−0.001

Atom A	Atom B	r_{AB} / Å	overlap
Ga1	Sb1	2.692	0.287
	Sb7	2.71	0.264
	Sb4	2.715	0.268
	Sb2	2.717	0.263
	Ga1	3.403	−0.046
Ga2	Sb3	2.681	0.259
	Sb5	2.684	0.29
	Sb7	2.697	0.266
	Sb6	2.712	0.271
	Ga2	3.478	−0.045
Sb1	Sb3	2.778	0.226
Sb2	Sb6	2.831	0.255
	Sb4	4.067	−0.047
Sb3	Sb6	3.991	−0.045
Sb4	Sb5	2.826	0.219
Sb7	Sb7	2.839	0.263

Table A.278: Partial charges for each atom position in $KGaSb_2$.

Atom	Z	charge	part charge
K1	19	18.227	0.773
K2		18.141	0.859
K3		18.21	0.79
K4		18.214	0.786
Ga1	31	30.996	0.004
Ga2		30.984	0.016
Sb1	23	23.295	−0.295

Atom	Z	charge	partialcharge
Sb2		23.432	−0.432
Sb3		23.506	−0.506
Sb4		23.43	−0.43
Sb5		23.277	−0.277
Sb6		23.424	−0.424
Sb7		23.441	−0.441

$RbGaSb_2$[176]

$RbGaSb_2$ crystallizes in the tetragonal space group $P4_2/nmc$ (no. 137). The structure is build by, through corner-sharing dimerized, chains of $GaSb_4$ tetrahedra.

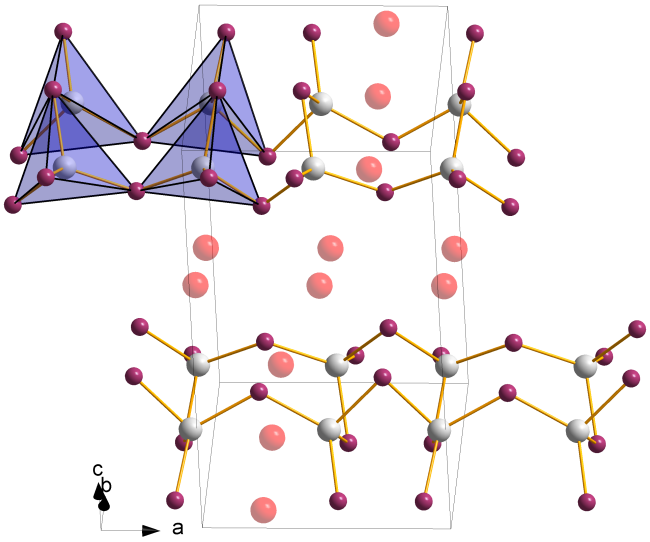

Figure A.165: Crystal structure of $RbGaSb_2$ with dimerized corner-sharing chains of $GaSb_4$ tetrahedra.

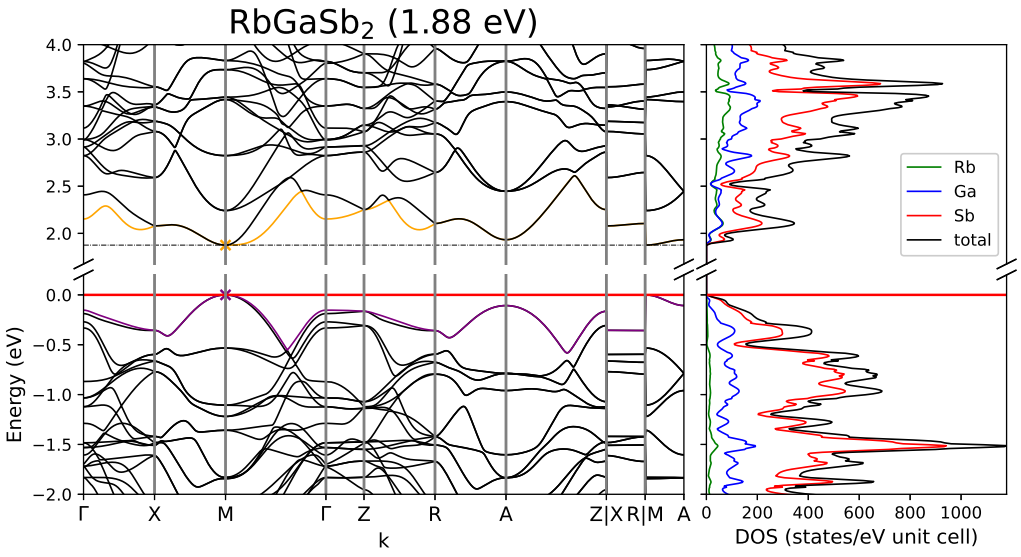

Figure A.166: Band structure and DOS of $RbGaSb_2$.

Table A.279: Overlap population and interatomic distances of $RbGaSb_2$.

Atom A	Atom B	r_{AB} / Å	overlap
Rb1	Sb2	3.733	0.014
	Sb2	3.781	0.01
	Ga1	3.957	−0.004
	Sb1	3.978	0.013
	Rb1	4.195	0.0
	Rb1	4.214	0.0
Ga1	Sb2	2.666	0.26
	Sb1	2.691	0.279
	Ga1	3.717	−0.033
	Sb2	4.197	−0.013
	Sb1	4.233	−0.016

Atom A	Atom B	r_{AB} / Å	overlap
Sb1	Sb1	2.872	0.248
	Sb2	4.249	−0.017
Sb2	Sb2	2.826	0.232
	Sb2	4.22	−0.029

Table A.280: Partial charges for each atom position in $RbGaSb_2$.

Atom	Z	charge	part charge
Rb1	9	8.246	0.754
Ga1	31	30.984	0.016
Sb1	23	23.327	−0.327

Atom	Z	charge	partialcharge
Sb2		23.443	−0.443

$CsGaSb_2$[176]

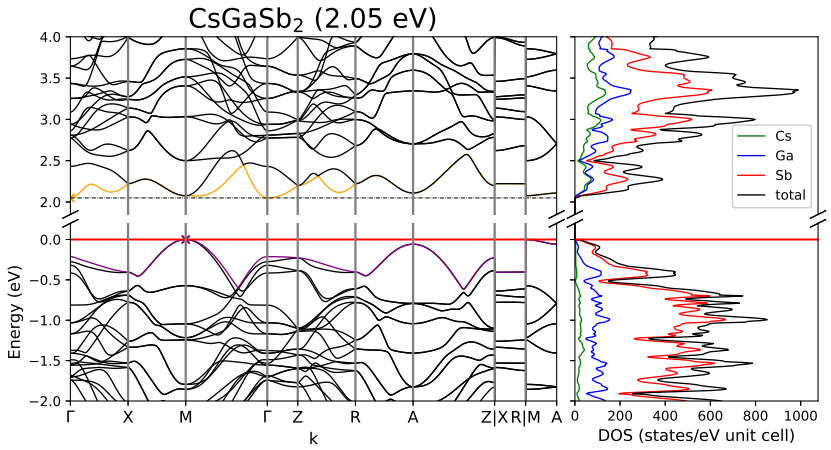

Figure A.167: Band structure and DOS of $CsGaSb_2$.

Table A.281: Overlap population and interatomic distances of $CsGaSb_2$.

Atom A	Atom B	r_{AB} / Å	overlap
Cs1	Sb2	3.813	0.012
	Sb2	3.883	0.012
	Ga1	4.039	−0.001
	Sb1	4.066	0.015
	Cs1	4.241	0.003
	Cs1	4.25	0.004
Ga1	Sb2	2.67	0.263
	Sb1	2.709	0.279
	Ga1	3.749	−0.035
	Sb2	4.207	−0.012
	Sb1	4.253	−0.016

Atom A	Atom B	r_{AB} / Å	overlap
Sb1	Sb1	2.867	0.25
	Sb2	4.289	−0.016
Sb2	Sb2	2.82	0.234
	Sb2	4.193	−0.03

Table A.282: Partial charges for each atom position in $CsGaSb_2$.

Atom	Z	charge	part charge
Cs1	9	8.221	0.779
Ga1	31	30.993	0.007
Sb1	23	23.334	−0.334

Atom	Z	charge	partialcharge
Sb2		23.452	−0.452

A.13 Rest

Table A.283: Overview of the crystallographic details of the remaining compounds. Cell parameters given in the first line and second line are of experimental and calculated origin, respectively. The third line shows the difference between both in percent.

compound	a / Å	b/ Å	c / Å	α / °	β / °	γ / °	space group	crystal system	connectivity
K_2SnBi	6.804	13.39	6.499				P b c m(no. 57)	orthorhombic	–
	6.765	13.41	6.555						
	-0.58	0.15	0.86						
$Li_3Si_3P_7$	6.3356	7.2198	10.6176		102.941		P 21/m (no. 11)	monoclinic	2D
	6.3691	7.2630	10.7094		103.127				
	0.53	0.59	0.86		0.18				
$Na_{10}AlTaP_4$	8.0790	7.3489	13.2054		90.773		P 21/n(no. 14)	monoclinic	0D (dimers)
	8.0790	7.3489	15.3875		120.895		P 1 c 1 (no. 7)	monoclinic	
	8.0112	7.2237	15.3152		120.965				
	-0.85	-1.73	-0.47		0.06				
KSi_2P_3	10.1327	10.1382	21.118		96.881		C 1 2/c 1(no. 15)	monoclinic	2D
	10.1767	10.1763	21.300		96.852				
	0.43	0.37	0.85		-0.03				
$NaGe_6As_6$	22.063	3.8032	7.202		92.744		C 1 2/m 1(no. 12)	monoclinic	2D
	21.544	4.0749	7.070		90.786				
	-2.41	6.67	-1.87		-2.16				
Rb_4SnSb_6	14.920		14.426				P -3 (no. 147)	trigonal	–
	15.151		14.403						
	1.52		-0.16						
$Cs_5In_3As_4$	17.037	12.253	18.105		117.24		P 1 21/c 1(no. 14)	monoclinic	0D, 1D, (2D)
	17.095	12.379	18.320		117.27				
	0.34	1.02	1.17		0.03				
$K_6Sn_3As_5$	14.800	10.728	10.934				P m m n (no. 59)	orthorhombic	1D
	14.821	10.740	10.963						
	0.14	0.12	0.26						
$Na_7Al_2Sb_5$	8.190	13.590	7.720		118.0		P 1 21/m 1(no. 11)	monoclinic	1D
	8.087	13.442	7.633		118.2				
	-1.27	-1.10	-1.14		0.18				
$K_{10}In_5Sb_9$	16.744	12.558	17.691		116.9		P 1 21/n 1(no. 14)	monoclinic	0D, 1D, (2D)
	16.818	12.326	17.654		114.9				
	0.44	-1.88	-0.21		-1.78				
$Cs_{14}In_8Bi_{12}$	10.1851	10.2318	27.617	94.457	91.462	90.214	P-1 (no. 2)	triclinic	1D
	10.273	10.3368	27.789	94.476	90.848	90.306			
	0.85	1.02	0.62	0.02	-0.68	0.10			
$Na_{19}Si_{13}P_{25}$	13.3550	15.3909	15.4609	118.054	111.705	93.054	P-1 (no. 2)	triclinic	3D
	13.2995	15.3919	15.4079	118.266	111.589	93.087			
	-0.42	0.01	-0.34	0.18	-0.10	0.04			
$Na_{23}Si_{19}P_{33}$	28.499	16.3175	13.8732		102.351		C 1 2/c 1 (no. 15)	monoclinic	3D
	28.458	16.2973	13.8973		102.630				
	-0.14	-0.12	0.17		0.27				

Table A.284: Calculated band gaps and transitions as well as an overview of the sampled reciprocal space defined by the Monkhorst-Pack-type *k*-point grid (SHRINK) and Brillouin Zone paths for all remaining compounds.

compound	band gap		transition	k-path	SHRINK
K_2SnBi	0.92	indirect	S -> Y	Γ—X—S—Y—Γ—Z—U—R—T—Z|X—U|Y—T|S—R	5 3 5
$Li_3Si_3P_7$	2.27	pseudo-direct	Y_2 -> Y_2	Γ—Z—D—B—Γ—A—E—Z—C_2—Y_2—Γ	5 5 3
$Na_{10}AlTaP_4$	2.94	pseudo-direct	Z -> Z	Γ—Z—D—B—Γ—A—E—Z—C_2—Y_2—Γ	4 5 2
KSi_2P_3	2.38	indirect	Γ-V_2 -> Γ	Γ—A—I_2|M_2—Γ—Y|L_2—Γ—V_2	5 5 2
$NaGe_6As_6$	–	metallic	–	Γ—C|C_2—Y_2—Γ—M_2—D|D_2—A—Γ|L_2—Γ—V_2	3 3 5
Rb_4SnSb_6	2.38	indirect	K -> Γ	Γ—M—K—Γ—A—L—H—A|L—M|H—K—H_2	3 3 3
$Cs_5In_3As_4$	2.17	indirect	Γ -> Γ-Z	Γ—Z—D—B—Γ—A—E—Z—C_2—Y_2—Γ	2 3 2
$K_6Sn_3As_5$	1.93	direct	Γ -> Γ	Γ—X—S—Y—Γ—Z—U—R—T—Z|X—U|Y—T|S—R	2 3 3
$Na_7Al_2Sb_5$	1.40	indirect	A -> Γ	Γ—Z—D—B—Γ—A—E—Z—C_2—Y_2—Γ	4 3 4
$K_{10}In_5Sb_9$	1.67	indirect	Γ -> Γ-Z	Γ—Z—D—B—Γ—A—E—Z—C_2—Y_2—Γ	2 3 2
$Cs_{14}In_8Bi_{12}$	1.26	pseudo-direct	Γ -> Γ	Γ—X|Y—Γ—Z|R_2—Γ—T_2|U_2—Γ—V_2	3 3 2
$Na_{19}Si_{13}P_{25}$	3.17	direct	V -> V	Γ—X|Y—Γ—Z|R—Γ—T|U—Γ—V	3 2 2
$Na_{23}Si_{19}P_{33}$	2.88	direct	Γ -> Γ	Γ—C|C_2—Y_2—Γ—M_2—D|D_2—A—Γ|L_2—Γ—V_2	2 2 3

$NaSn_2As_2$[177]

$NaSn_2As_2$ crystallizes in the trigonal space group $R\ \bar{3}\ m\ H$ (no .166). It has a layered structure where grey arsenic like SnAs-layers are build. Within the six-membered ring As and Sn are alternating. The Na atoms form layers between the SnAs-layers.

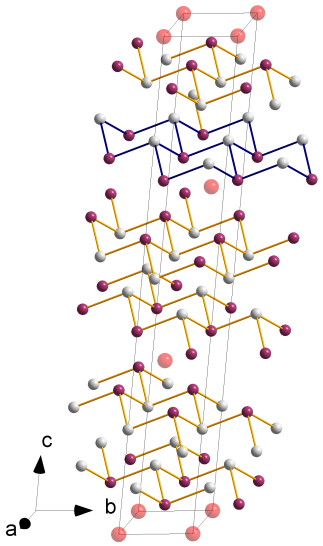

Figure A.168: Crystal structure of $NaSn_2As_2$ with grey-arsenic like SnAs-layers.

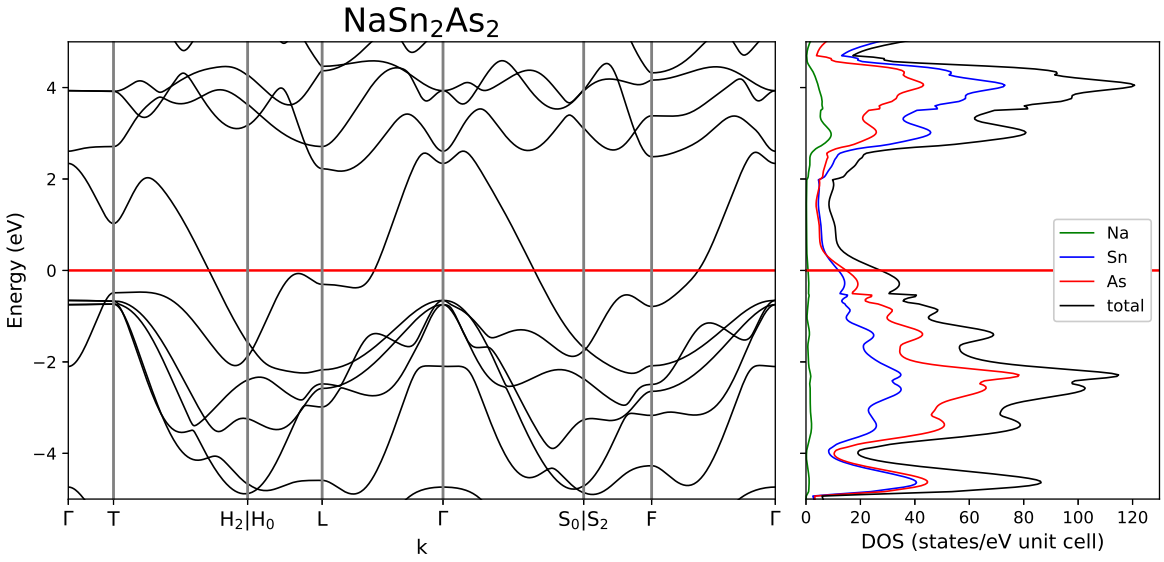

Figure A.169: Band structure and DOS of $NaSn_2As_2$.

Table A.285: Overlap population and interatomic distances of $NaSn_2As_2$.

Atom A	Atom B	r_{AB} / Å	overlap
Na1	As1	3.076	0.028
	Na1	4.007	0.0
	Sn1	4.087	0.0
	As1	5.051	0.0
	Sn1	5.723	0.0
	Sn1	5.833	0.0
Sn1	As1	2.674	0.223
	Sn1	3.379	0.076
	Sn1	4.007	−0.035
	As1	4.454	−0.017
	As1	4.817	0.0

Atom A	Atom B	r_{AB} / Å	overlap
As1	As1	4.007	−0.005
	As1	4.668	0.001

Table A.286: Partial charges for each atom position in $NaSn_2As_2$.

Atom	Z	charge	part charge
Na1	11	10.216	0.784
Sn1	22	21.696	0.304

Atom	Z	charge	partialcharge
As1	33	33.696	−0.696

$Li_3Si_3P_7$[76]

$Li_3Si_3P_7$ crystallizes in the monoclinic space group $P2_1/m$ (no. 11). Corner-sharing SiP_4 tetrahedra form layers within the ab plane. All tetrahedral tips are oriented along c with two the tips of two neighbouring layers facing each other and forming P-P in between them. With this the structure can be further described as having dimers of layers.

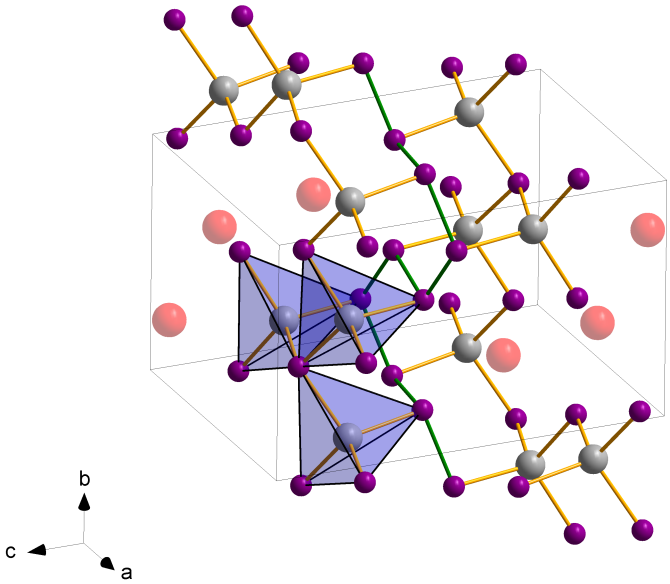

Figure A.170: Crystal structure of $Li_3Si_3P_7$ with by P-P bonds connected dimer layers of corner-sharing tetrahedra.

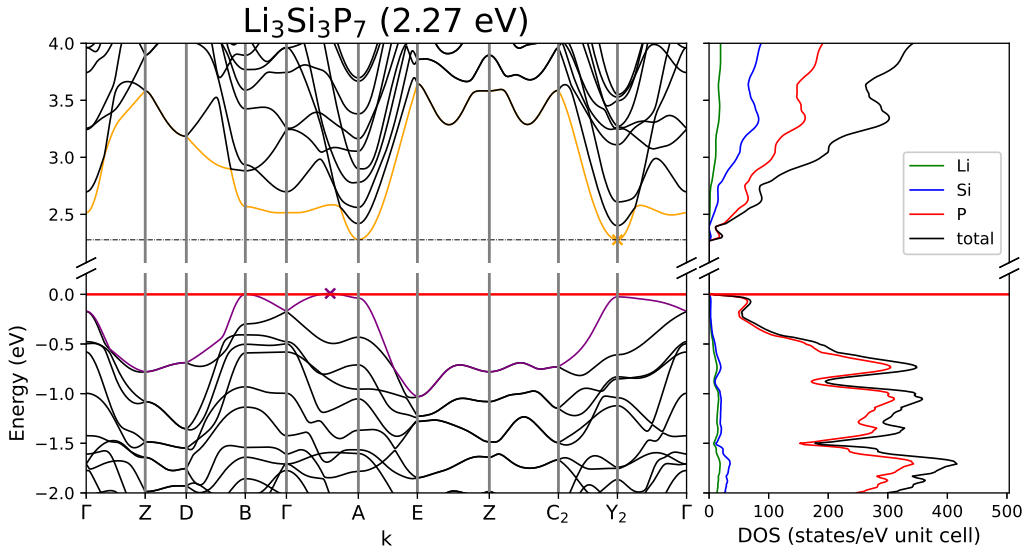

Figure A.171: Band structure and DOS of $Li_3Si_3P_7$.

Table A.287: Overlap population and interatomic distances of $Li_3Si_3P_7$.

Atom A	Atom B	r_{AB} / Å	overlap
Li1	P5	2.454	0.083
	P1	2.505	0.072
	P2	2.572	0.068
	Li2	2.961	0.005
	Li3	3.123	0.003
	Li3	3.472	0.002
Li2	P1	2.629	0.054
	P4	2.701	0.039
	P5	2.74	0.047
	P3	2.754	0.035
	Si2	3.7	0.001
Li3	P5	2.527	0.081
	P1	2.617	0.066
	Si1	2.998	0.005
	P2	3.172	0.013
	P1	3.389	0.012
Si1	P1	2.225	0.315
	P3	2.278	0.285
	P2	2.308	0.262
	P4	3.466	−0.037
	Si2	3.571	−0.04
Si2	P1	2.223	0.346
	P5	2.236	0.338
	P4	2.289	0.263
	P2	2.312	0.274
	P3	3.368	−0.033
P2	P5	3.633	−0.024
P3	P4	2.217	0.196
	P4	3.606	−0.01
	P4	3.607	−0.019
P4	P4	2.229	0.163
	P4	3.384	−0.029

Table A.288: Partial charges for each atom position in $Li_3Si_3P_7$.

Atom	Z	charge	part charge
Li1	3	2.397	0.603
Li2		2.349	0.651
Li3		2.364	0.636
Si1	14	13.869	0.131
Si2		13.834	0.166
P1	15	15.565	−0.565
P2		15.323	−0.323
P3		15.114	−0.114
P4		15.117	−0.117
P5		15.552	−0.552

$Na_{10}AlTaP_4$[74]

$Na_{10}AlTaP_4$ crystallizes in the monoclinic space group $P2_1/n$ (no. 14). Similar to the dimer structures for the $A_{10}Tt_2P_6$ compounds, the main structural motive are edge-sharing mixed $AlTaP_6$ tetrahedra dimers with a Al:Ta ratio of 50:50. To calculate the structure a model in space group $P\,c$ (no. 7) was created where within each double tetrahedron one Al and one Ta was placed.

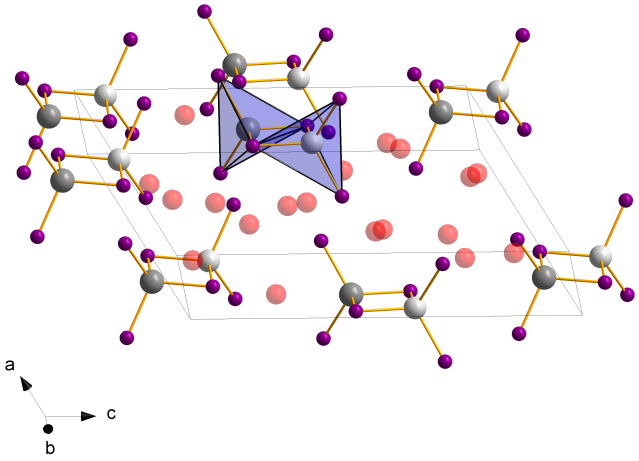

Figure A.172: Crystal structure of $Na_{10}AlTaP_4$ incorporating dimers of edge-sharing, mixed $AlTaP_6$ tetrahedra.

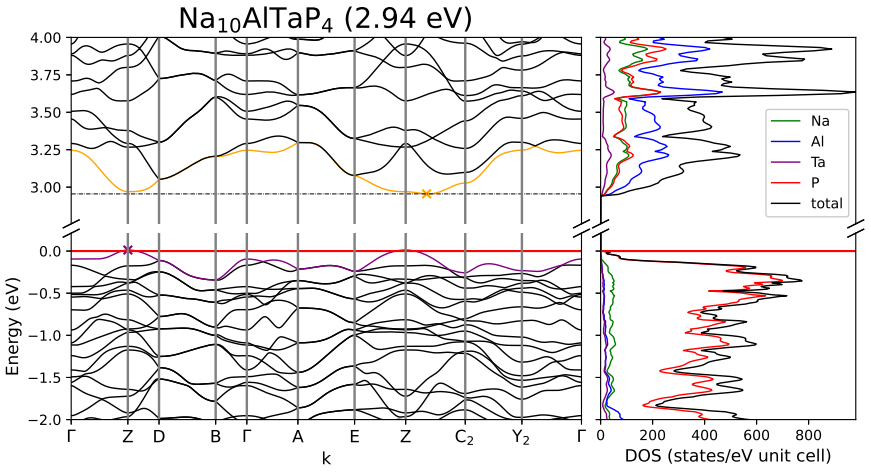

Figure A.173: Band structure and DOS of $Na_{10}TaAlP_6$.

Table A.289: Overlap population and interatomic distances of $Na_{10}TaAlP_6$.

Atom A	Atom B	r_{AB} / Å	overlap
Na1	P1	2.825	0.049
	P3	2.978	0.038
	Na8	3.101	0.005
	P4	3.168	0.037
	P6	3.225	0.026
	Al1	3.26	0.0
Na2	P2	2.862	0.045
	P3	3.006	0.044
	P4	3.044	0.04
	Al1	3.119	0.007
	Na7	3.136	0.005
	P5	3.272	0.026
Na3	P5	2.882	0.028
	P3	2.963	0.047
	P2	2.995	0.044
	P6	3.197	0.028
	Na8	3.22	0.005
	Na6	3.22	0.005
Na4	P1	2.872	0.055
	P6	2.896	0.044
	P4	3.033	0.044
	P5	3.093	0.019
	Na5	3.197	0.005
	Na7	3.247	0.004
Na5	P1	2.81	0.058
	P3	2.826	0.059
	P5	2.832	0.043
	P2	2.853	0.041
	Na9	3.104	0.007
Na6	P1	2.811	0.049
	P6	2.815	0.03
	P2	2.853	0.04
	P4	2.89	0.045
	Na9	3.2	0.003
Na7	P1	2.821	0.064
	P3	2.843	0.063
	P5	2.875	0.036
	P4	2.996	0.039
	Na10	3.128	0.006
Na8	P6	2.845	0.035
	P4	2.864	0.049
	P2	2.871	0.045
	P3	2.963	0.062
Na9	P3	3.023	0.057
	P1	3.024	0.039
	P4	3.044	0.04
	P5	3.196	0.02
Na10	P3	2.91	0.044
	P4	3.132	0.038
	P2	3.136	0.037
	P1	3.177	0.04
	P6	3.237	0.02
Al1	P1	2.378	0.361
	P3	2.384	0.354
	P5	2.484	0.228
	P6	2.53	0.211
	Ta1	3.156	0.028
Ta1	P2	2.397	0.302
	P6	2.406	0.274
	P4	2.409	0.299
	P5	2.42	0.271

Table A.290: Partial charges for each atom position in $Na_{10}TaAlP_6$.

Atom	Z	charge	part charge
Na1	11	10.309	0.691
Na2		10.293	0.707
Na3		10.305	0.695
Na4		10.308	0.692
Na5		10.344	0.656
Na6		10.285	0.715
Na7		10.333	0.667
Na8		10.315	0.685
Na9		10.315	0.685
Na10		10.307	0.693

Atom	Z	charge	partialcharge
Al1	13	12.918	0.082
Ta1		12.235	0.765
P1	15	16.405	−1.405
P2		16.354	−1.354
P3		16.397	−1.397
P4		16.368	−1.368
P5		16.108	−1.108
P6		16.102	−1.102

$Na_7Al_2Sb_5$[178]

$Na_7Al_2Sb_5$ crystallizes in the monoclinic space group $P2_1/m$ (no. 11). Within thw structure alternating corner- and edge-sharing $AlSb_4$ form one dimensional chains along b. Neighbouring chains are further connected to layers by Sb-Sb bonds between the free corners of the tetrahedra.

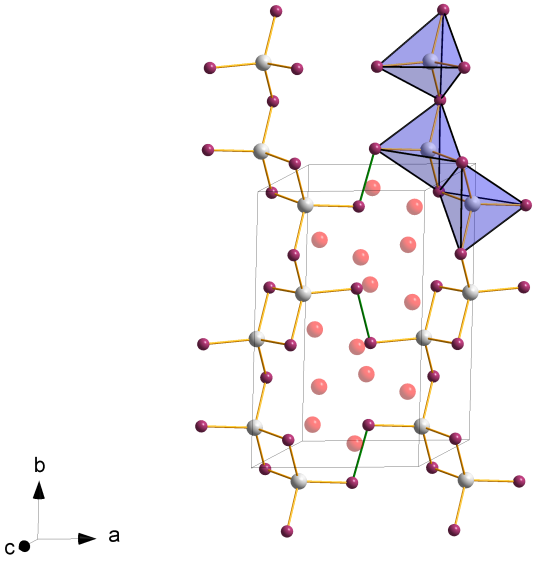

Figure A.174: Crystal structure of $Na_7Al_2Sb_5$ forming chains of corner- and edge-sharing tetrahedra.

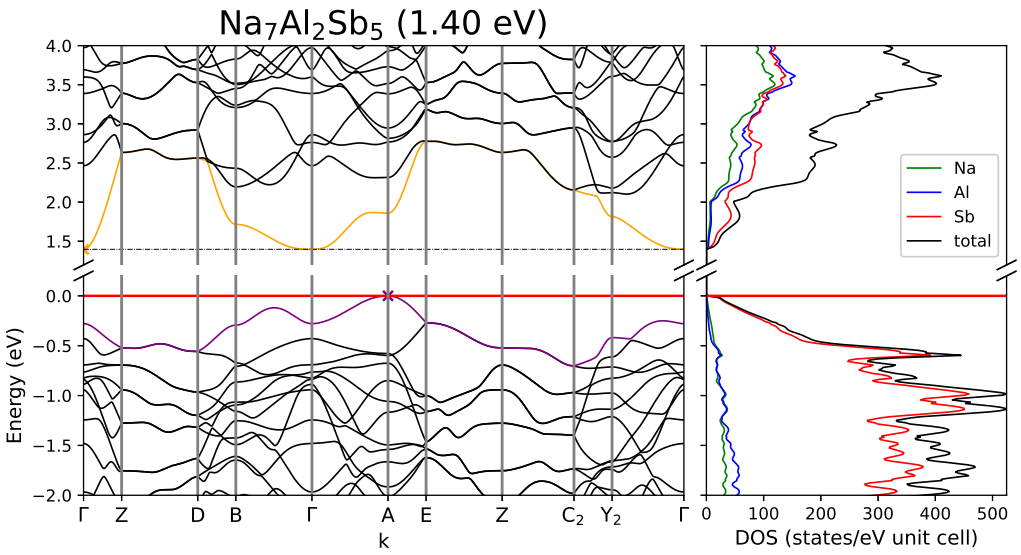

Figure A.175: Band structure and DOS of $Na_7Al_2Sb_5$.

Table A.291: Overlap population and interatomic distances of $Na_7Al_2Sb_5$.

Atom A	Atom B	r_{AB} / Å	overlap
Na1	Sb2	3.051	0.052
	Sb1	3.189	0.048
	Sb1	3.202	0.038
	Sb3	3.255	0.038
	Na1	3.298	0.004
	Sb2	3.408	0.016
Na2	Sb2	3.052	0.052
	Sb1	3.104	0.043
	Sb3	3.227	0.04
	Sb1	3.282	0.054
	Na2	3.314	0.007
	Al1	3.388	0.006
Na3	Sb1	3.174	0.041
	Sb3	3.239	0.034
	Sb2	3.286	0.038
	Na5	3.686	0.003
Na4	Sb2	3.205	0.037
	Sb3	3.271	0.051
	Sb1	3.285	0.03
	Al1	3.44	0.006
Na5	Sb2	3.203	0.037
	Sb3	3.207	0.041
	Sb1	3.267	0.042
Al1	Sb2	2.711	0.306
	Sb1	2.725	0.278
	Sb3	2.741	0.28
	Sb1	2.76	0.261
	Al1	3.345	0.017
Sb2	Sb2	2.896	0.173

Table A.292: Partial charges for each atom position in $Na_7Al_2Sb_5$.

Atom	Z	charge	part charge
Na1	11	10.309	0.691
Na2		10.317	0.683
Na3		10.296	0.704
Na4		10.282	0.718
Na5		10.307	0.693

Atom	Z	charge	partialcharge
Al1	13	12.862	0.138
Sb1	23	24.141	−1.141
Sb2		23.877	−0.877
Sb3		24.103	−1.103

$Na_{19}Si_{13}P_{25}$[34]

$Na_{19}Si_{13}P_{25}$ crystallizes in the triclinic space group $P\bar{1}$ (no. 2). The anionic structural motive consists of T3-super-tetrahedra build by corner-sharing SiP_4 tetrahedra. These super-tetrahedra are further connected via their corners to units made up by 3 corner- and edge-sharing SiP_4 tetrahedra, which build link the T3 super-tetrahedra to a three dimensional network. Two of these networks are build independently.

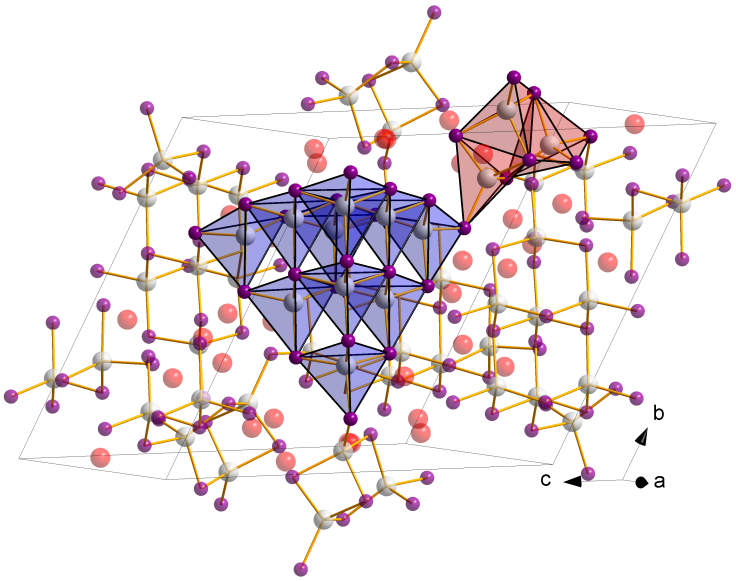

Figure A.176: Crystal structure of $Na_{19}Si_{13}P_{25}$ incorporating T3 super-tetrahedra linked via 3 corner- and edge sharing SiP_4 tetrahedra.

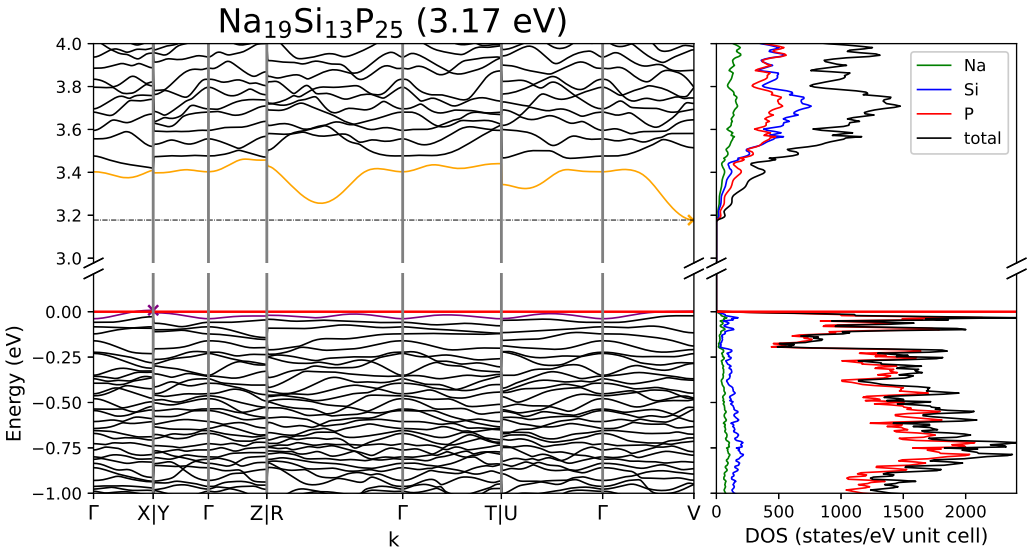

Figure A.177: Band structure and DOS of $Na_{19}Si_{13}P_{25}$.

Table A.293: Partial charges for each atom position in $Na_{19}Si_{13}P_{25}$.

Atom	Z	charge	part charge
Na1	11	10.245	0.755
Na2		10.245	0.755
Na3		10.248	0.752
Na4		10.212	0.788
Na5		10.223	0.777
Na6		10.246	0.754
Na7		10.255	0.745
Na8		10.227	0.773
Na9		10.251	0.749
Na10		10.224	0.776
Na11		10.241	0.759
Na12		10.237	0.763
Na13		10.246	0.754
Na14		10.258	0.742
Na15		10.239	0.761
Na16		10.219	0.781
Na17		10.27	0.73
Na18		10.241	0.759
Na19		10.255	0.745
Na20		10.219	0.781
Si1	14	13.876	0.124
Si2		13.895	0.105
Si3		13.827	0.173
Si4		13.819	0.181
Si5		13.845	0.155
Si6		13.829	0.171
Si7		13.84	0.16
Si8		13.757	0.243
Si9		13.875	0.125
Si10		13.873	0.127

Atom	Z	charge	partialcharge
Si11		13.929	0.071
Si12		13.932	0.068
Si13		13.857	0.143
P1	15	15.436	−0.436
P2		15.438	−0.438
P3		15.782	−0.782
P4		15.703	−0.703
P5		15.766	−0.766
P6		15.687	−0.687
P7		15.361	−0.361
P8		15.743	−0.743
P9		15.695	−0.695
P10		15.73	−0.73
P11		15.413	−0.413
P12		15.697	−0.697
P13		15.424	−0.424
P14		15.779	−0.779
P15		15.774	−0.774
P16		15.251	−0.251
P17		15.81	−0.81
P18		15.721	−0.721
P19		15.767	−0.767
P20		15.794	−0.794
P21		15.611	−0.611
P22		15.676	−0.676
P23		15.682	−0.682
P24		15.772	−0.772
P25		15.768	−0.768

Table A.294: Overlap population and interatomic distances of $Na_{19}Si_{13}P_{25}$.

AtomA	AtomB	r_{AB}/Å	overlap
Na1	P6	2.946	0.045
	P4	2.949	0.044
	P8	3.059	0.036
	Si2	3.126	−0.003
	P7	3.158	0.022
	Si1	3.349	−0.003
Na2	P3	2.878	0.032
	P6	2.897	0.04
	P2	2.994	0.022
	P10	3.066	0.033
	P2	3.257	0.018
	P14	3.308	0.025
Na3	P3	2.918	0.03
	P12	2.944	0.036
	P1	2.953	0.025
	P1	3.094	0.021
	P9	3.118	0.033
	Na5	3.171	0.005
Na4	P6	2.824	0.039
	P11	2.88	0.022
	P5	3.036	0.036
	P15	3.051	0.035
	P5	3.396	0.017
	Si12	3.407	−0.004
Na5	P11	2.791	0.018
	P3	2.813	0.034
	P4	2.873	0.037
	P5	2.939	0.032
	P23	2.955	0.031
Na6	P15	2.817	0.027
	P9	2.868	0.036
	P4	2.977	0.041
	P8	3.006	0.033
	P5	3.046	0.029
	Na8	3.28	0.004
Na7	P7	2.883	0.034
	P25	3.019	0.036
	P8	3.058	0.036
	Na11	3.106	0.005
	P17	3.157	0.031
	Si13	3.175	−0.004
Na8	P21	2.911	0.035
	P24	2.935	0.028
	P9	2.958	0.033
	P8	3.016	0.029
	P1	3.052	0.023
	Na12	3.172	0.004
Na9	P3	2.72	0.045
	P19	2.798	0.055
	P14	3.016	0.033
	P24	3.19	0.028
	Si8	3.525	−0.002
Na10	P15	2.837	0.038
	P8	2.982	0.028
	P22	3.009	0.031
	P18	3.025	0.04
	Si11	3.144	0.001
Na11	P16	2.907	0.035
	P20	2.914	0.039
	P25	3.036	0.032
	P20	3.068	0.041
	P17	3.221	0.032
Na12	P21	2.841	0.05
	P23	2.95	0.039
	P12	2.995	0.043
	P19	3.18	0.023
	Si10	3.423	−0.001
Na13	P19	2.849	0.042
	P13	2.894	0.025
	P12	2.921	0.035
	P17	2.968	0.035
	P14	3.042	0.035
	Si7	3.349	0.0
Na14	P24	2.77	0.04
	P23	2.793	0.044
	P17	2.929	0.04
	P20	2.963	0.043
	P16	3.222	0.003
Na15	P18	2.806	0.043
	P10	2.867	0.044
	P22	2.915	0.036
	P17	3.156	0.031
	Na16	3.366	0.003
	Na17	3.663	0.002
Na16	P9	2.841	0.039
	P19	2.988	0.037
	P18	3.13	0.027
	P22	3.245	0.028
	P13	3.562	0.011
Na17	P2	2.822	0.026
	P10	2.916	0.046
	P24	2.971	0.038
	P14	3.088	0.038
	P25	3.096	0.033
	Si3	3.396	0.0
Na18	P10	2.905	0.028
	P5	2.938	0.036
	P25	2.965	0.044
	P22	3.032	0.036
	Si12	3.237	−0.002
	P16	3.476	0.015
Na19	P13	2.892	0.029
	P18	3.196	0.033
	P14	3.343	0.025
	Si9	3.604	0.0
	Si6	3.731	0.0
Na20	P15	2.767	0.027
	P21	3.131	0.027
	Si10	3.302	0.001
	Si12	3.5	0.002
	P22	3.588	0.013
Si1	P4	2.225	0.334
	P8	2.23	0.315
	P7	2.272	0.251
	P1	2.275	0.262
	Si7	3.497	−0.026
Si2	P6	2.222	0.339
	P25	2.248	0.322
	P2	2.265	0.253
	P7	2.285	0.253
Si3	P3	2.206	0.34
	P24	2.236	0.333
	P1	2.261	0.277
	P2	2.274	0.264
	Si13	3.502	−0.04
Si4	P5	2.247	0.335
	P3	2.25	0.305
	P9	2.254	0.322
	P10	2.262	0.323
	Si6	3.51	−0.032
Si5	P12	2.224	0.354
	P9	2.227	0.349
	P13	2.275	0.259
	P1	2.283	0.262
	Si7	3.523	−0.042
Si6	P10	2.2	0.344
	P14	2.217	0.36
	P13	2.273	0.276
	P2	2.274	0.256
	Si8	3.509	−0.034
Si7	P23	2.255	0.322
	P12	2.272	0.325
	P4	2.285	0.314
	P17	2.297	0.291
Si8	P19	2.263	0.311
	P18	2.267	0.326
	P14	2.286	0.309
	P6	2.287	0.316
Si9	P18	2.223	0.328
	P17	2.258	0.331
	P7	2.276	0.25
	P13	2.293	0.255
Si10	P19	2.213	0.345
	P15	2.257	0.321
	P21	2.258	0.332
	P11	2.31	0.212
	Si12	2.963	−0.121
	Si11	3.288	−0.05
Si11	P21	2.235	0.301
	P22	2.261	0.287
	P20	2.275	0.3
	P16	2.304	0.257
	P11	3.224	−0.082
Si12	P5	2.231	0.309
	P22	2.255	0.319
	P11	2.273	0.267
	P15	2.279	0.273
Si13	P20	2.255	0.306
	P8	2.274	0.311
	P24	2.281	0.313
	P25	2.286	0.3
P7	P8	3.64	−0.033
P11	P16	2.183	0.203
	P15	3.136	−0.136
P14	P19	3.282	−0.062
P16	P23	2.223	0.191

$Na_{23}Si_{19}P_{33}$[34]

$Na_{23}Si_{19}P_{33}$ crystallizes in the monoclinic space group $C2/c$ (no. 15). Corner sharing SiP_4 tetrahedra form a three dimensional network of corner-sharing T3 super-tetrahedra. Two independent networks are formed penetrating each other.

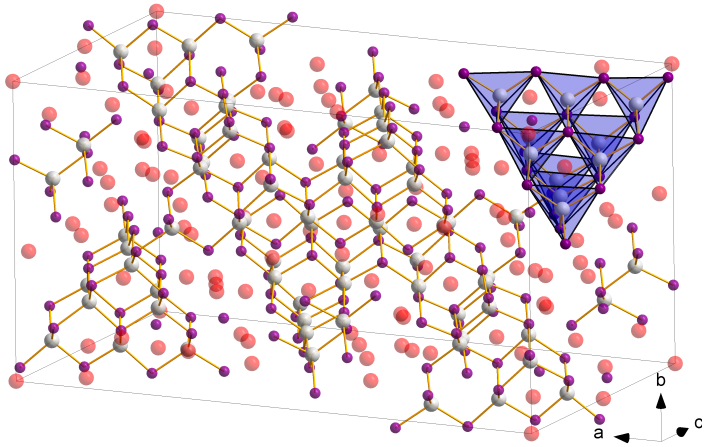

Figure A.178: Crystal structure of $Na_{23}Si_{19}P_{33}$ showing two independent three dimensional networks of corner-sharing T3 super-tetrahedra.

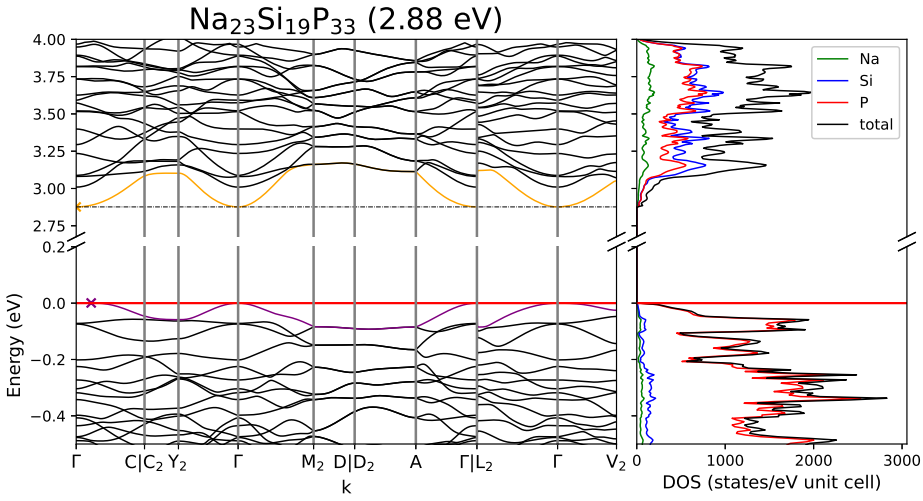

Figure A.179: Band structure and DOS of $Na_{23}Si_{19}P_{33}$.

Table A.295: Overlap population and interatomic distances of $Na_{23}Si_{19}P_{33}$.

Atom A	Atom B	r_{AB} / Å	overlap
Na1	P16	2.849	0.037
	P3	2.85	0.026
	P15	2.871	0.038
	P15	2.888	0.045
	Na2	2.938	0.005
	Na1	3.218	0.006
Na2	P7	2.774	0.044
	P5	2.854	0.033
	P15	2.866	0.031
	P3	2.937	0.022
	P17	2.938	0.036
Na3	P16	2.782	0.043
	P8	2.864	0.048
	P2	2.883	0.035
	P1	3.21	0.023
	Na11	3.374	0.003
	P14	3.413	0.021
Na4	P13	2.777	0.027
	P2	2.93	0.028
	P6	3.045	0.02
	P8	3.07	0.035
	P1	3.076	0.023
	P4	3.136	0.018
Na5	P10	2.846	0.035
	P6	2.878	0.024
	P12	3.015	0.035
	P5	3.123	0.03
	P10	3.151	0.032
	Na7	3.475	0.003
Na6	P8	2.989	0.027
	P7	3.005	0.026
	P13	3.025	0.026
	P12	3.191	0.023
	Na7	3.223	0.003
	P11	3.233	0.021
Na7	P12	2.71	0.042
	P11	2.784	0.047
	P5	2.935	0.038
	P10	3.264	0.026
	P7	3.306	0.021
Na8	P13	2.742	0.043
	P10	2.786	0.049
	P14	2.949	0.039
	P11	3.003	0.038
	Na12	3.293	0.005
Na9	P12	2.85	0.033
	P15	2.961	0.027
	P9	2.976	0.023
	P11	2.989	0.029
	P14	3.086	0.033
	P7	3.322	0.018
Na10	P16	2.818	0.04
	P7	2.936	0.052
	P17	2.961	0.036
	P14	3.199	0.024
Na11	P14	3.052	0.025
	P2	3.091	0.023
	P16	3.208	0.02
	Si9	3.414	0.002
	P4	3.929	0.004
Na12	P9	2.89	0.026
	P13	3.009	0.032
	P11	3.194	0.03
	Si8	3.547	0.0
Na13	P4	2.827	0.031
	P2	2.924	0.037
	P1	3.366	0.016
	Si3	3.499	−0.001
Si1	P16	2.209	0.339
	P3	2.266	0.266
	P4	2.272	0.289
	P1	2.294	0.276
	Si9	3.513	−0.037
Si2	P5	2.237	0.382
	P3	2.275	0.275
	P6	2.278	0.252
	P1	2.333	0.262
Si3	P2	2.229	0.332
	P8	2.236	0.324
	P6	2.266	0.262
	P4	2.27	0.245
Si4	P7	2.239	0.31
	P9	2.245	0.285
	P15	2.249	0.356
	P3	2.313	0.247
Si5	P10	2.247	0.323
	P12	2.264	0.335
	P7	2.306	0.304
	P5	2.337	0.292
Si6	P10	2.206	0.323
	P11	2.212	0.325
	P9	2.272	0.269
	P6	2.279	0.269
Si7	P12	2.253	0.345
	P11	2.256	0.323
	P13	2.263	0.321
	P8	2.271	0.336
Si8	P13	2.232	0.361
	P14	2.253	0.324
	P9	2.267	0.25
	P4	2.284	0.266
	Si9	3.481	−0.036
Si9	P16	2.256	0.308
	P14	2.275	0.334
	P15	2.284	0.295
	P17	2.293	0.315
Si10	P2	2.219	0.355
	P1	2.296	0.265
P3	P5	3.66	−0.043
P5	P12	3.591	−0.03
P9	P13	3.612	−0.042

Table A.296: Partial charges for each atom position in $Na_{23}Si_{19}P_{33}$.

Atom	Z	charge	part charge
Na1	11	10.264	0.736
Na2		10.251	0.749
Na3		10.238	0.762
Na4		10.201	0.799
Na5		10.239	0.761
Na6		10.198	0.802
Na7		10.251	0.749
Na8		10.27	0.73
Na9		10.229	0.771
Na10		10.267	0.733
Na11		10.19	0.81
Na12		10.251	0.749
Na13		10.232	0.768
Si1	14	13.863	0.137
Si2		13.827	0.173
Si3		13.857	0.143
Si4		13.841	0.159
Si5		13.889	0.111
Si6		13.858	0.142
Si7		13.841	0.159
Si8		13.853	0.147
Si9		13.867	0.133
Si10		13.845	0.155
P1	15	15.386	−0.386
P2		15.682	−0.682
P3		15.391	−0.391
P4		15.361	−0.361
P5		15.692	−0.692
P6		15.372	−0.372
P7		15.711	−0.711
P8		15.693	−0.693
P9		15.352	−0.352
P10		15.711	−0.711
P11		15.731	−0.731
P12		15.743	−0.743
P13		15.737	−0.737
P14		15.713	−0.713
P15		15.771	−0.771
P16		15.67	−0.67
P17		15.843	−0.843

$NaGe_6As_6$[179]

$NaGe_6As_6$ crystallizes in the monoclinic space group $C2/m$ (no. 12). The anionic structure consists of layers of corner-sharing As_6 octahedra centred by Ge-Ge dumbbells. The Na atoms are located in between these layers.

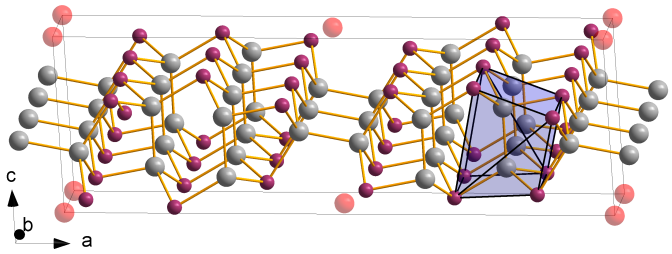

Figure A.180: Crystal structure of $NaGe_6As_6$ with layers of corner-sharing (Ge−Ge)As_6 octahedra, centred by Ge-Ge dumbbells.

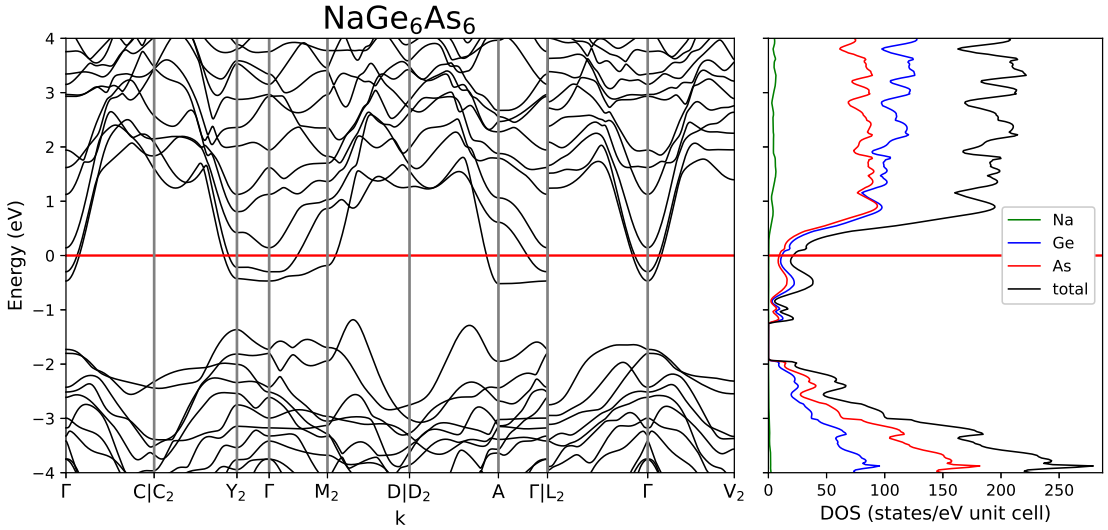

Figure A.181: Band structure and DOS of $NaGe_6As_6$.

Table A.297: Overlap population and interatomic distances of $NaGe_6As_6$.

Atom A	Atom B	r_{AB} / Å	overlap
Na1	As1	3.12	0.032
	As3	3.138	0.025
	Ge1	3.448	0.002
	Ge1	4.011	0.0
	Na1	4.075	0.001
	Ge3	4.937	0.0
Ge1	Ge1	2.446	0.296
	As1	2.45	0.281
	As3	2.492	0.201
	Ge3	3.57	−0.03
	Ge2	3.613	−0.042
Ge2	As2	2.443	0.281
	Ge3	2.463	0.249
	As1	2.475	0.194
	As3	3.63	−0.013
	Ge3	3.654	−0.024
Ge3	As3	2.434	0.248
	As2	2.503	0.216
	As1	3.94	−0.016
As1	As2	3.658	0.006
	As2	3.995	−0.016
As2	As2	3.24	0.016
	As3	3.971	−0.01

Table A.298: Partial charges for each atom position in $NaGe_6As_6$.

Atom	Z	charge	part charge
Na1	11	10.209	0.791
Ge1	32	31.953	0.047
Ge2		31.852	0.148
Ge3		31.894	0.106
As1	33	33.25	−0.25
As2		33.117	−0.117
As3		33.33	−0.33

$K_{10}In_5Sb_9$[180]

$K_{10}In_5Sb_9$ crystallizes in the monoclinic space group $P2_1/n$ (no. 14). It consists of two different structural motives: In2 and In4 form one dimensional chains of edge-sharing $InSb_4$ tetrahedra along b, with additional bridging Sb atoms. In3 forms edge-sharing dimers of $InSb_4$ tetrahedra which connect linear chains of edge-sharing $(In-In)Sb_6$ octahedra, forming layers.

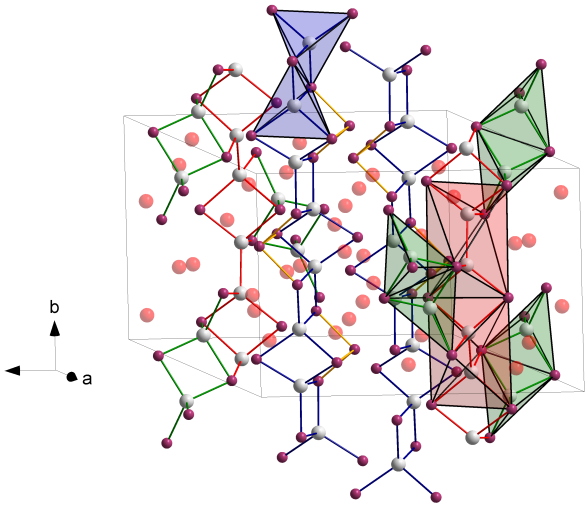

Figure A.182: Crystal structure of $K_{10}In_5Sb_9$ incorporating one dimensional chains of edge-sharing $InSb_4$ and layers of edge-sharing $(In-In)Sb_6$ chains connected by dimeric units of edge-sharing$InSb_4$.

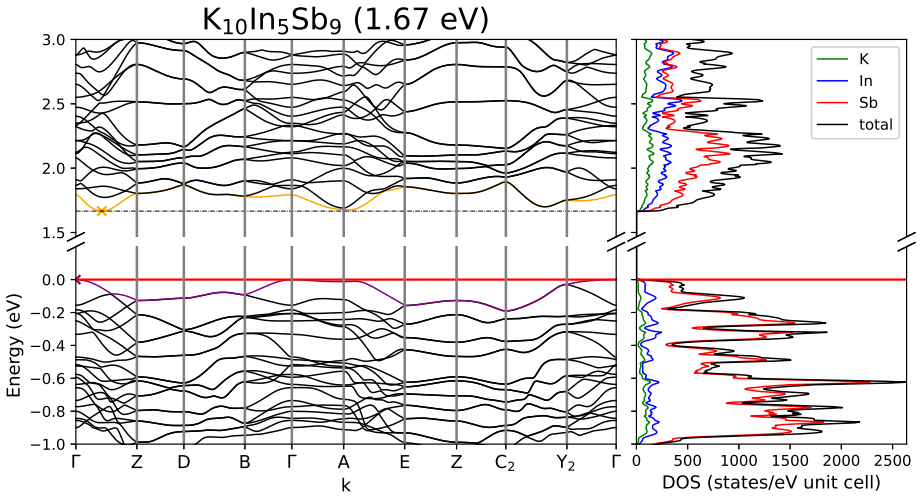

Figure A.183: Band structure and DOS of $K_{10}In_5Sb_9$.

Table A.299: Overlap population and interatomic distances of $K_{10}In_5Sb_9$.

Atom A	Atom B	r_{AB} / Å	overlap
K1	Sb7	3.497	0.013
	Sb6	3.57	0.029
	Sb1	3.621	0.017
	Sb7	3.63	0.011
	Sb5	3.685	0.012
	Sb2	3.693	0.013
K2	Sb9	3.479	0.02
	In2	3.631	−0.007
	Sb4	3.693	0.019
	Sb7	3.711	0.013
	Sb2	3.711	−0.001
	Sb3	3.726	0.015
K3	Sb9	3.37	0.012
	Sb2	3.497	0.016
	Sb8	3.542	0.021
	Sb5	3.564	0.015
	Sb6	3.769	0.022
	In3	3.881	−0.007
K4	Sb1	3.461	0.026
	In3	3.52	−0.009
	In5	3.551	−0.01
	Sb9	3.609	0.0
	Sb6	3.68	0.02
	Sb4	3.817	0.007
K5	In4	3.542	−0.009
	Sb8	3.557	0.033
	K10	3.572	0.001
	In2	3.696	−0.008
	Sb3	3.702	0.013
	Sb5	3.709	−0.001
K6	Sb9	3.531	0.018
	Sb3	3.636	0.02
	Sb7	3.67	0.021
	Sb5	3.788	0.018
	In5	3.795	−0.004
	Sb4	3.829	0.019
K7	Sb6	3.702	0.019
	Sb3	3.794	0.02
	In5	3.806	−0.005
	Sb9	3.815	0.017
	Sb8	3.826	0.021
	Sb4	3.874	0.011
K8	Sb3	3.559	0.028
	Sb7	3.628	0.015
	Sb2	3.629	0.007
	Sb1	3.685	0.021
	Sb1	3.714	0.023
	K8	3.777	0.001
K9	Sb3	3.552	0.022
	In1	3.555	−0.007
	Sb1	3.692	0.027
	Sb8	3.759	0.019
K10	Sb8	3.498	0.019
	Sb6	3.662	0.025
	Sb4	3.722	0.014
	In1	3.761	−0.006
	Sb7	3.806	0.024
In1	In5	2.919	0.285
	Sb6	2.942	0.257
	Sb8	2.967	0.235
	Sb4	2.968	0.214
	In3	3.413	−0.028
In2	Sb1	2.857	0.225
	Sb3	2.884	0.222
	Sb2	2.896	0.212
	Sb5	2.937	0.238
	In4	3.088	−0.176
In3	Sb8	2.865	0.266
	Sb9	2.882	0.261
	Sb9	2.941	0.221
	Sb4	2.946	0.219
In4	Sb3	2.873	0.286
	Sb1	2.876	0.254
	Sb5	2.903	0.214
	Sb2	2.958	0.245
In5	Sb6	2.886	0.275
	Sb9	3.012	0.209
	Sb4	3.013	0.199
Sb2	Sb7	2.86	0.214
	Sb5	3.57	−0.012
Sb5	Sb7	2.861	0.215

Table A.300: Partial charges for each atom position in $K_{10}In_5Sb_9$.

Atom	Z	charge	part charge
K1	19	18.253	0.747
K2		18.211	0.789
K3		18.268	0.732
K4		18.206	0.794
K5		18.23	0.77
K6		18.242	0.758
K7		18.219	0.781
K8		18.255	0.745
K9		18.24	0.76
K10		18.243	0.757
In1	21	21.061	−0.061
In2		21.064	−0.064
In3		21.009	−0.009
In4		21.088	−0.088
In5		21.14	−0.14
Sb1	23	24.007	−1.007
Sb2		23.511	−0.511
Sb3		23.939	−0.939
Sb4		23.81	−0.81
Sb5		23.48	−0.48
Sb6		23.987	−0.987
Sb7		23.71	−0.71
Sb8		24.036	−1.036
Sb9		23.79	−0.79

KSi_2P_3[33]

KSi_2P_3 crystallizes in the monoclinic space group $C2/c$ (no. 15). The structure consists of layers build by corner-sharing SiP_4 tetrahedra within the ab plane. Three layers are further connected via corner sharing. The K atoms lie in between.

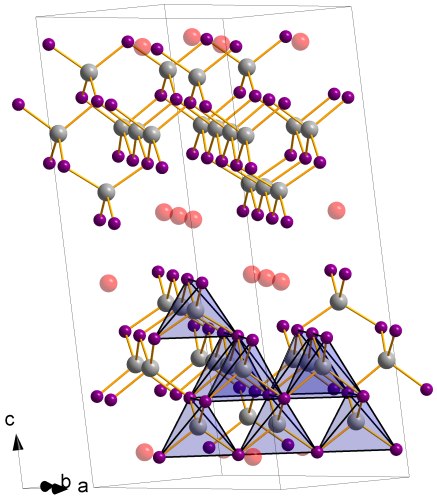

Figure A.184: Crystal structure of KSi_2P_3 consisting of layers of corner-sharing tetrahedra build made up by three corner-sharing layers of SiP_4 tetrahedra.

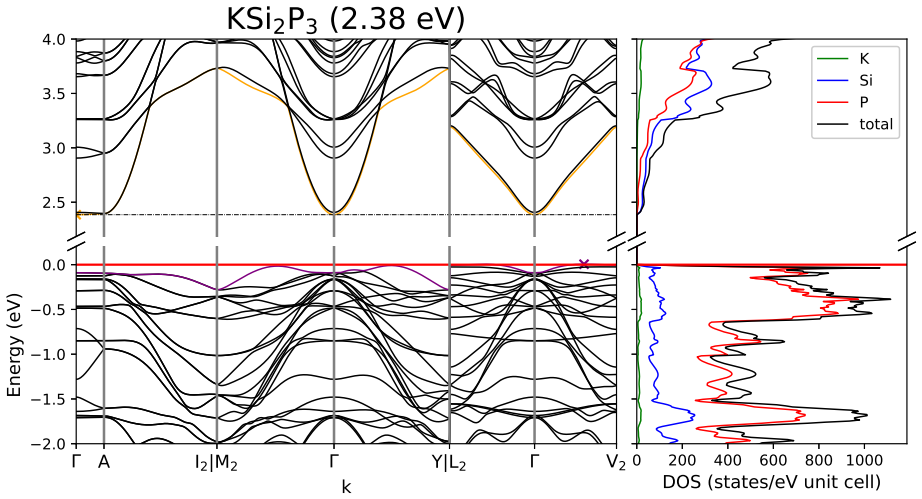

Figure A.185: Band structure and DOS of KSi_2P_3.

Table A.301: Overlap population and interatomic distances of KSi_2P_3.

Atom A	Atom B	r_{AB} / Å	overlap
K1	P4	3.306	0.01
	P5	3.314	0.01
	P2	3.492	0.004
	P3	3.492	0.004
	P1	3.503	0.004
	P6	3.504	0.004
K2	P4	3.312	0.01
	P5	3.315	0.01
	P2	3.491	0.004
	P3	3.491	0.004
	P6	3.503	0.004
	P1	3.503	0.004
Si1	P2	2.27	0.295
	P1	2.278	0.294
	Si4	3.572	−0.04
	Si4	3.624	−0.042
	Si3	3.629	−0.024
	Si2	3.637	−0.025
Si2	P4	2.234	0.376
	P5	2.234	0.376
	P6	2.267	0.247
	P1	2.268	0.247
	Si3	3.598	−0.028
	Si3	3.598	−0.028
Si3	P4	2.234	0.374
	P5	2.234	0.373
	P2	2.264	0.241
	P3	2.264	0.241
Si4	P2	2.27	0.295
	P3	2.27	0.295
	P1	2.278	0.294
	P6	2.278	0.294
	Si5	3.572	−0.04
Si5	P3	2.27	0.295
	P6	2.278	0.294
P1	P6	3.378	−0.046
P2	P3	3.368	−0.044
P4	P5	3.592	−0.028

Table A.302: Partial charges for each atom position in KSi_2P_3.

Atom	Z	charge	part charge
K1	19	18.176	0.824
K2		18.177	0.823
Si1	14	13.844	0.156
Si2		13.886	0.114
Si3		13.89	0.11
Si4		13.844	0.156
Si5		13.844	0.156
P1	15	15.253	−0.253
P2		15.246	−0.246
P3		15.245	−0.245
P4		15.593	−0.593
P5		15.592	−0.592
P6		15.253	−0.253

K_2SnBi[181]

K_2SnBi crystallizes in the orthorhombic space group *Pbcm* (no. 57) and consists of Sn-Bi zig-zag-chains along c.

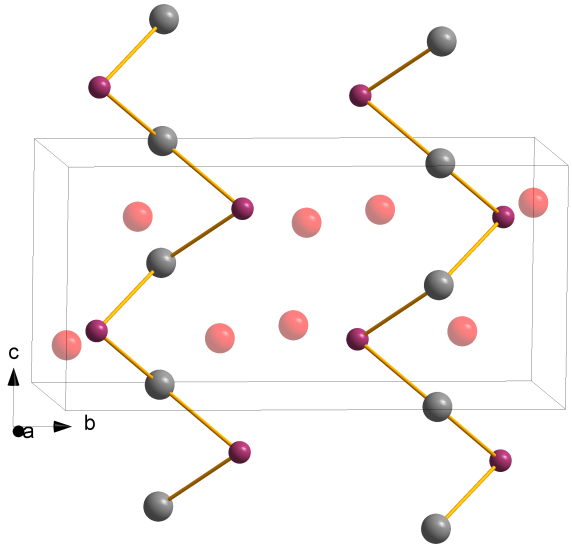

Figure A.186: Crystal structure of K_2SnBi incorporating Sn-Bi zig-zag chains along b.

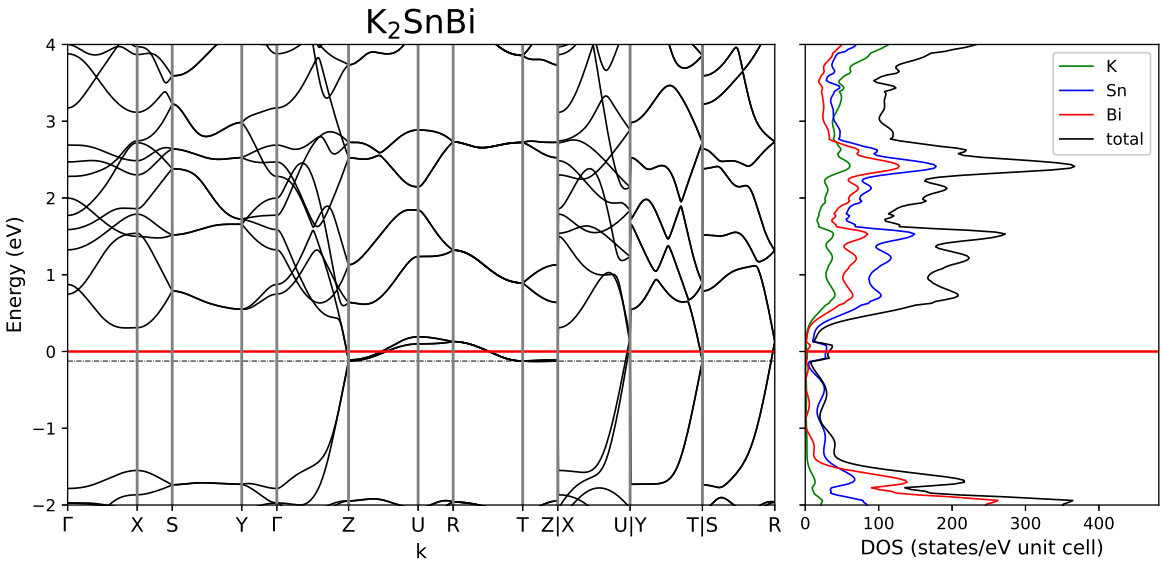

Figure A.187: Band structure and DOS of K_2SnBi.

Table A.303: Overlap population and interatomic distances of K_2SnBi.

Atom A	Atom B	r_{AB} / Å	overlap
K1	Bi1	3.63	0.02
	Bi1	3.632	0.021
	Bi1	3.827	0.015
	Sn1	3.855	0.008
	K2	3.891	0.0
	K1	3.925	0.001
K2	Bi1	3.57	0.013
	Bi1	3.676	0.022
	Sn1	3.794	0.014
	Bi1	3.859	0.017
	K2	3.969	0.001

Atom A	Atom B	r_{AB} / Å	overlap
Sn1	Bi1	3.021	0.19
	Sn1	3.278	0.036

Table A.304: Partial charges for each atom position in K_2SnBi.

Atom	Z	charge	part charge
K1	19	18.24	0.76
K2		18.245	0.755
Sn1	22	22.513	−0.513

Atom	Z	charge	partialcharge
Bi1	23	24.002	−1.002

Since the frequency calculation revealed two imaginary frequencies of $-47.1499\,\mathrm{cm}^2$ and $-45.7958\,\mathrm{cm}^2$ the crystal strcuture was distorted along the first imaginary frequency and re-optimized with lower symmetry in space group $Pmc2_1$ (no. 26). Therein no imaginary frequencies were found.

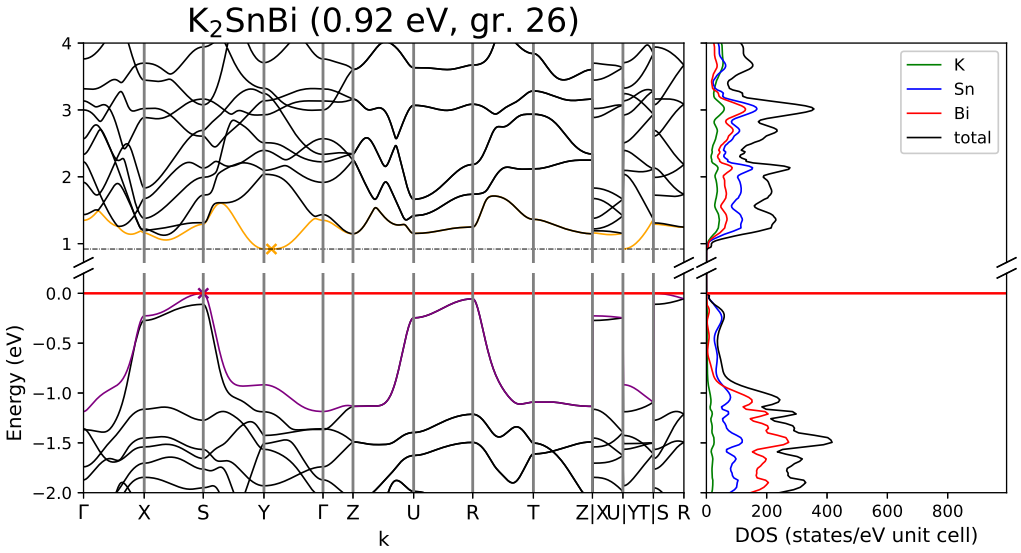

Figure A.188: Band structure and DOS of K_2SnBi (gr. 26).

Table A.305: Partial charges for each atom position in K_2SnBi.

Atom	Z	charge	part charge
K1	19	18.236	0.764
K2		18.239	0.761
K3		18.255	0.745
K4		18.235	0.765

Atom	Z	charge	partialcharge
Sn1	22	22.516	−0.516
Bi1	23	23.971	−0.971
Bi2		24.032	−1.032

Table A.306: Overlap population and interatomic distances of K_2SnBi.

Atom A	Atom B	r_{AB} / Å	overlap
K1	Bi2	3.574	0.019
	Bi2	3.597	0.017
	Sn1	3.836	0.007
	Sn1	3.886	0.006
	Bi1	3.887	0.014
	K4	3.944	0.0
K2	Bi1	3.663	0.023
	Bi1	3.71	0.022
	Bi2	3.787	0.017
	K3	3.85	0.0
	Sn1	3.871	0.008
K3	Bi1	3.592	0.015
	Bi1	3.719	0.022
	Sn1	3.82	0.017
	Bi2	3.897	0.019
	K4	3.97	0.001
K4	Bi2	3.545	0.014
	Bi2	3.615	0.023
	Sn1	3.77	0.01
	Bi1	3.886	0.015
	Sn1	3.948	0.002
Sn1	Sn1	2.999	0.125
	Bi1	3.019	0.21
	Bi2	3.034	0.173
	Sn1	3.599	−0.023

$K_6Sn_3As_5$[32]

$K_6Sn_3As_5$ crystallizes in the orthorhombic space group *Pmmn* (no. 59). The structure is build up by one dimensional chains of consisting of edge-sharing units consisting of two edge-sharing $SnAs_4$ tetrahedra and one $(In-In)As_6$ trigonal prism centred by an Sn-Sn dumbbell. These prism are further connected to a Sn_2As_2 four membered ring which coordinates with its plane vertically.

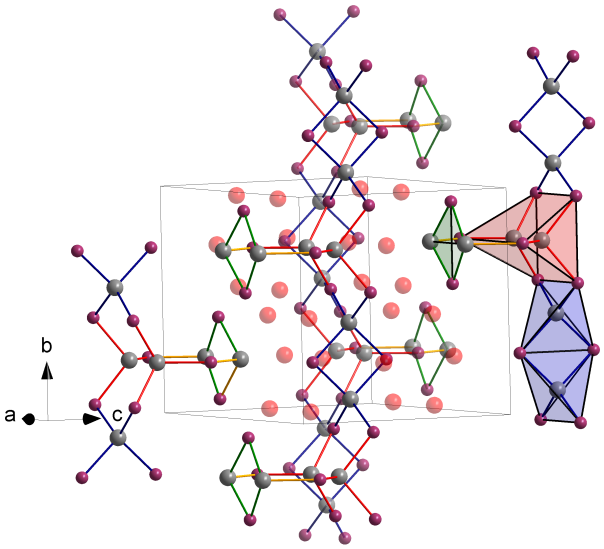

Figure A.189: Crystal structure of $K_6Sn_3As_5$ incorporating linear chains with edge-sharing $SnAs_4$ tetrahedra, $(In-In)Sb_6$ trigonal prisms and square planar four membered rings.

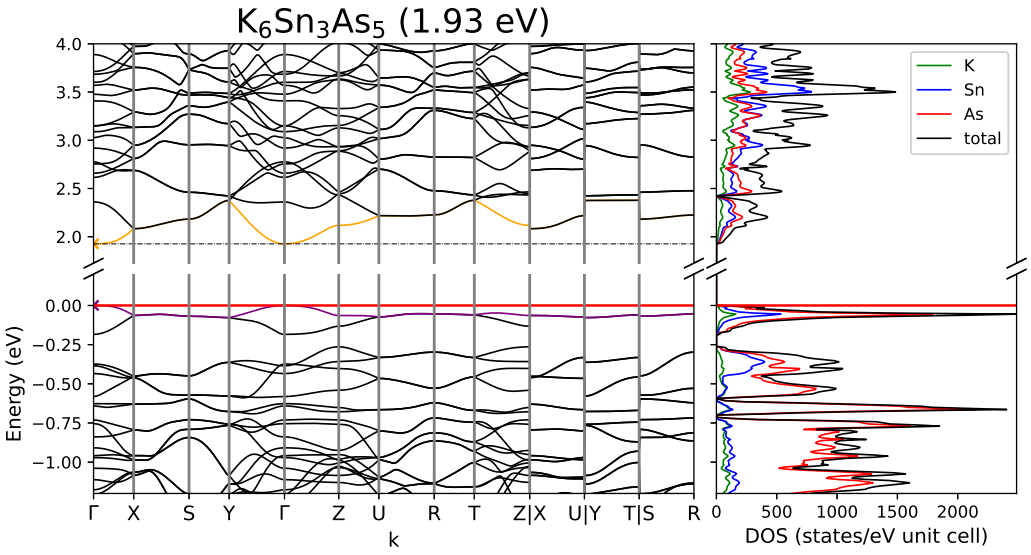

Figure A.190: Band structure and DOS of $K_6Sn_3As_5$.

Table A.307: Overlap population and interatomic distances of $K_6Sn_3As_5$.

Atom A	Atom B	r_{AB} / Å	overlap
K1	As2	3.363	0.019
	As5	3.371	0.016
	As1	3.375	0.021
	As4	3.496	0.016
	As5	3.59	0.023
	Sn3	3.688	−0.006
K2	As4	3.507	0.016
	As4	3.541	0.018
	As3	3.724	0.015
	Sn1	3.742	−0.004
	As2	3.865	0.011
	Sn2	3.888	0.028
K3	As4	3.302	0.019
	As1	3.35	0.03
	As3	3.397	0.02
	As4	3.42	0.017
	As5	3.648	0.026
	Sn2	3.786	0.005
K4	As1	3.447	0.036
	As2	3.494	0.028
	As3	3.61	0.025
	As5	4.043	0.016
K5	As4	3.559	0.018
	Sn2	3.736	0.002
	Sn3	3.835	−0.005
	As1	3.915	0.014
	Sn1	4.131	0.001
Sn1	As4	2.595	0.292
	As2	2.65	0.268
	As3	2.655	0.274
	Sn1	3.642	−0.05
Sn2	As1	2.698	0.244
	As5	2.745	0.2
	Sn2	3.768	−0.039
Sn3	As4	2.645	0.277
	As5	2.664	0.28
	Sn3	2.992	0.219
As1	As1	3.846	−0.029
As2	As3	3.858	−0.041
	As4	4.437	−0.021
As3	As4	4.328	−0.016

Table A.308: Partial charges for each atom position in $K_6Sn_3As_5$.

Atom	Z	charge	part charge
K1	19	18.249	0.751
K2		18.256	0.744
K3		18.276	0.724
K4		18.314	0.686
K5		18.242	0.758
Sn1	22	21.767	0.233
Sn2		22.221	−0.221
Sn3		21.812	0.188
As1	33	33.98	−0.98
As2		33.916	−0.916
As3		33.92	−0.92
As4		33.874	−0.874
As5		33.972	−0.972

Rb_4SnSb_6[182]

Rb_4SnSb_6 crystallizes in the trigonal space group $P\bar{3}$ (no. 147). Its anionic sub structure consists of isolated $SnSb_6^{4-}$ clusters.

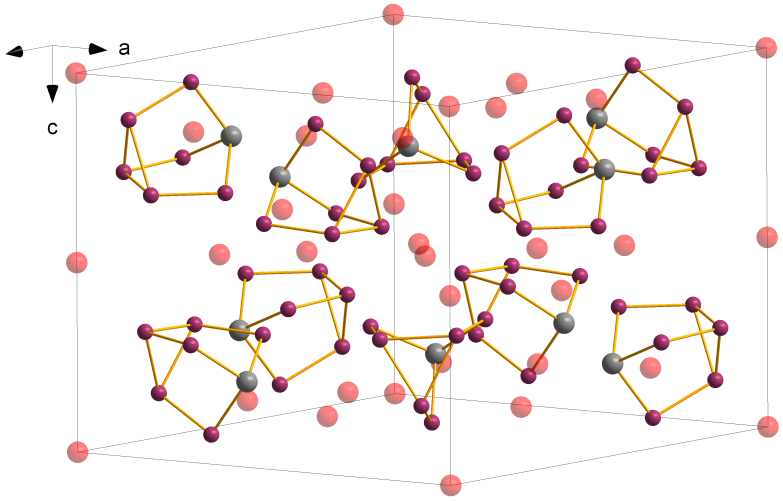

Figure A.191: Crystal structure of Rb_4SnSb_6 with isolated $SnSb_6^{4-}$ clusters.

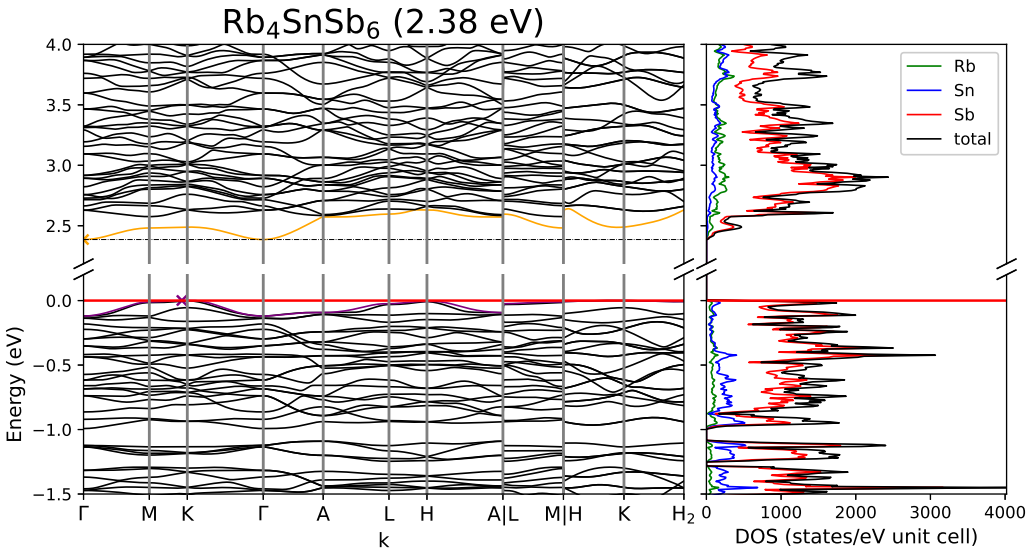

Figure A.192: Band structure and DOS of Rb_4SnSb_6.

Table A.309: Overlap population and interatomic distances of Rb_4SnSb_6.

Atom A	Atom B	r_{AB} / Å	overlap
Rb1	Sb1	3.632	0.018
	Sb2	3.858	0.02
	Rb7	4.307	0.0
	Rb2	4.406	0.001
	Sb5	4.746	0.001
	Rb2	5.172	0.0
Rb2	Sb2	3.827	0.022
	Sb5	3.83	0.014
	Sb2	3.852	0.018
	Sb1	3.945	0.021
	Rb2	3.967	0.0
	Sb5	3.979	0.005
Rb3	Sb3	3.696	0.023
	Sb2	3.771	0.021
	Sb6	3.782	0.003
	Sb4	3.783	0.003
	Sb3	3.801	0.023
	Sn1	3.993	0.017
Rb4	Sb3	3.755	0.028
	Sb5	3.765	0.004
	Sb1	3.778	0.023
	Sb1	3.821	0.02
	Sb3	3.895	0.026
	Sb4	3.907	0.005
Rb5	Sb4	3.957	0.02
	Sb3	5.296	0.001
	Sb6	6.066	0.0
	Sb5	6.651	0.0
Rb6	Sb6	3.85	0.016
	Sb5	5.146	0.0
	Sb4	5.555	0.0
	Sb2	6.28	0.0
Rb7	Sb2	3.702	0.018
	Sn1	3.883	0.009
	Sb3	5.33	0.001
Sn1	Sb3	2.827	0.282
	Sb1	2.834	0.256
	Sb2	2.857	0.255
Sb1	Sb5	2.747	0.293
Sb2	Sb6	2.748	0.303
Sb3	Sb4	2.754	0.295
Sb4	Sb6	2.902	0.193
	Sb5	2.912	0.163
Sb5	Sb6	2.883	0.178

Table A.310: Partial charges for each atom position in Rb_4SnSb_6.

Atom	Z	charge	part charge
Rb1	9	8.295	0.705
Rb2		8.277	0.723
Rb3		8.285	0.715
Rb4		8.289	0.711
Rb5		8.242	0.758
Rb6		8.222	0.778
Rb7		8.25	0.75
Sn1	22	22.341	−0.341
Sb1	23	23.521	−0.521
Sb2		23.653	−0.653
Sb3		23.622	−0.622
Sb4		23.296	−0.296
Sb5		23.244	−0.244
Sb6		23.212	−0.212

$Cs_5In_3As_4$[183]

$Cs_5In_3As_4$ $P2_1/c$ (no. 14). The compound shows two independent structural motives. $InAs_4$ edge-sharing tetrahedra form one dimensional chains along b. The chains incorporate additional bridging In atoms. $(in-In)As_6$ octahedra, which are centred by In-In dumbbells also form edge-sharing chains, which are further connected by edge-sharing tetrahedra dimers, from two dimensional layers in the bc plane.

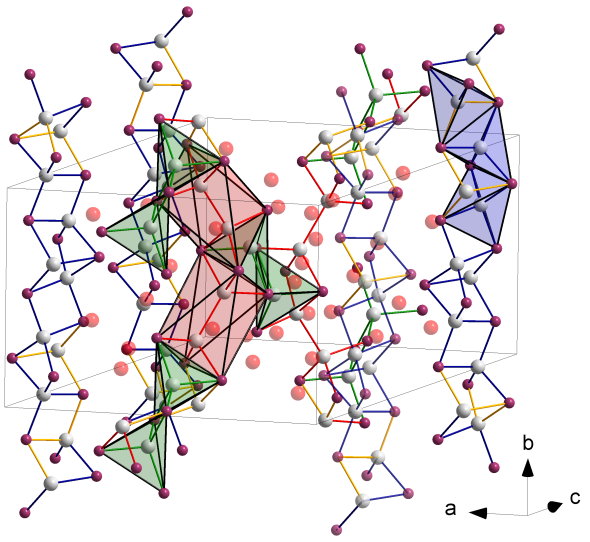

Figure A.193: Crystal structure of $Cs_5In_3As_4$ incorporating one dimensional chains of edge-sharing $InAs_4$ and layers of edge-sharing $(In-In)As_6$ chains connected by dimeric units of edge-sharing$InSb_4$.

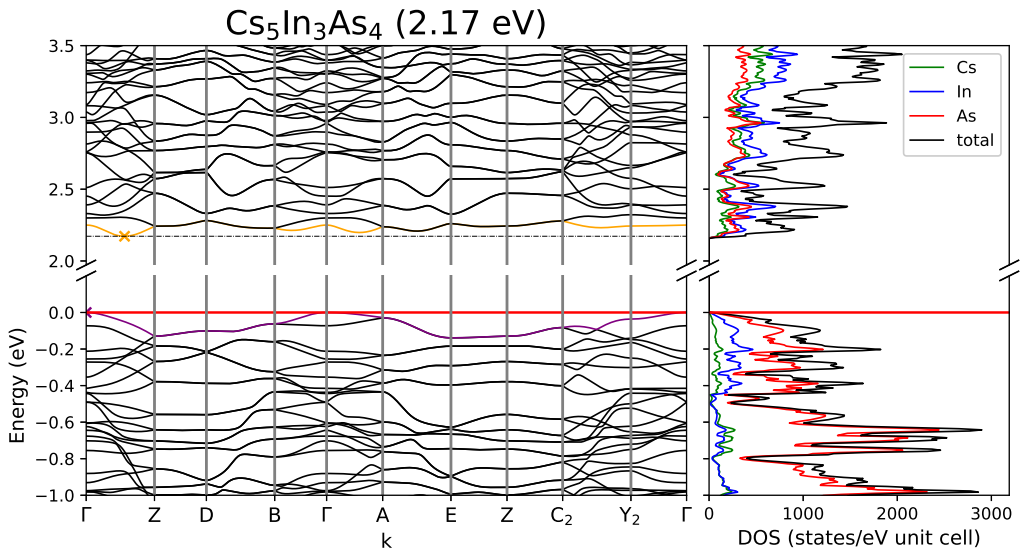

Figure A.194: Band structure and DOS of $Cs_5In_3As_4$.

Table A.311: Partial charges for each atom position in $Cs_5In_3As_4$.

Atom	Z	charge	part charge
Cs1	9	8.233	0.767
Cs2		8.259	0.741
Cs3		8.246	0.754
Cs4		8.289	0.711
Cs5		8.236	0.764
Cs6		8.261	0.739
Cs7		8.259	0.741
Cs8		8.244	0.756
Cs9		8.28	0.72
Cs10		8.271	0.729
In1	21	20.833	0.167
In2		21.033	−0.033
In3		21.078	−0.078
In4		20.815	0.185
In5		20.81	0.19
In6		21.494	−0.494
As1	33	33.857	−0.857
As2		34.037	−1.037
As3		33.837	−0.837
As4		34.012	−1.012
As5		33.943	−0.943
As6		33.799	−0.799
As7		34.057	−1.057
As8		33.817	−0.817

Table A.312: Overlap population and interatomic distances of $Cs_5In_3As_4$.

Atom A	Atom B	r_{AB} / Å	overlap
Cs1	In1	3.656	−0.004
	In3	3.676	−0.016
	As4	3.718	0.023
	As1	3.739	0.01
	As7	3.759	0.028
	As3	3.771	−0.003
Cs2	As7	3.622	0.025
	As8	3.657	0.011
	As7	3.796	0.02
	Cs2	3.952	0.006
	Cs9	3.962	0.007
	As5	3.968	0.015
Cs3	As5	3.595	0.01
	In4	3.633	−0.006
	In6	3.689	−0.011
	As2	3.701	0.031
	As8	3.793	0.013
	Cs8	3.812	0.007
Cs4	As3	3.556	0.009
	As8	3.599	0.012
	As6	3.647	0.013
	As2	3.71	0.015
	As4	3.727	0.018
Cs5	As3	3.585	0.022
	In6	3.667	−0.011
	As5	3.689	0.012
	In5	3.693	−0.004
	As7	3.782	0.015
	As1	3.878	0.018
Cs6	As6	3.739	0.019
	As6	3.741	0.011
	As8	3.741	0.018
	As7	3.801	0.019
	In6	3.864	−0.005
Cs7	As4	3.693	0.024
	As3	3.854	0.018
	As2	3.912	0.023
	As1	3.933	0.012
	In2	3.954	−0.005
	In3	3.955	−0.005
Cs8	As2	3.558	0.018
	As4	3.607	0.026
	As1	3.705	0.015
	In2	3.748	−0.013
Cs9	As3	3.71	0.023
	As6	3.753	0.026
	As5	3.837	0.023
	In3	3.879	−0.005
	As1	3.982	0.022
Cs10	In2	3.781	−0.005
	As8	3.794	0.026
	As5	3.804	0.025
	As2	3.846	0.02
In1	As2	2.686	0.273
	As3	2.729	0.231
	As3	2.732	0.252
	As1	2.775	0.217
	In2	3.365	−0.065
	In3	3.482	−0.035
In2	As4	2.738	0.261
	As2	2.753	0.261
	As1	2.789	0.229
	In3	3.094	0.271
	In3	3.568	−0.046
In3	As4	2.735	0.272
	As1	2.801	0.221
	As3	2.859	0.214
In4	As6	2.683	0.273
	As7	2.715	0.259
	As5	2.726	0.235
	As8	2.746	0.228
	In5	3.211	−0.066
	In5	3.545	−0.068
In5	As8	2.684	0.266
	As7	2.696	0.264
	As6	2.737	0.228
	As5	2.756	0.229
In6	As8	2.866	0.19
	As6	2.876	0.19
	As5	2.973	0.154

$Cs_7In_4Bi_6$[184]

$Cs_{14}In_8Bi_{12}$ crystallizes in the triclinic space group $P\bar{1}$ (no. 2). The compound is build up buy one dimensional chains of edge-sharing $InBi_4$ tetrahedra. Along the chains additional bridging In atoms are located.

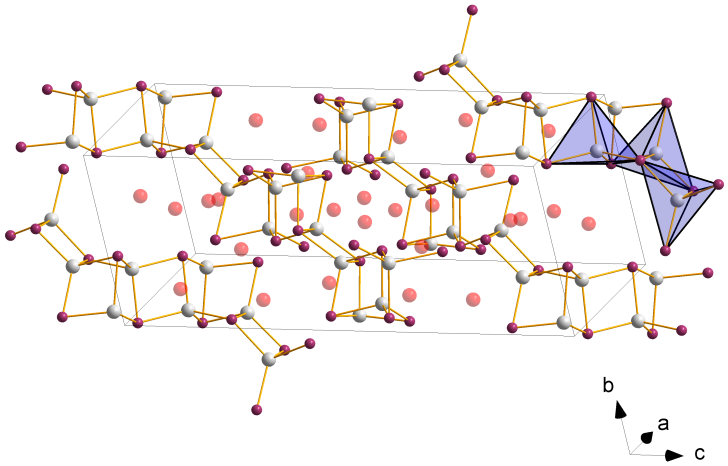

Figure A.195: Crystal structure of $Cs_{14}In_8Bi_{12}$ incorporating one dimensional chains of edge-sharing $InBi_4$ tetrahedra.

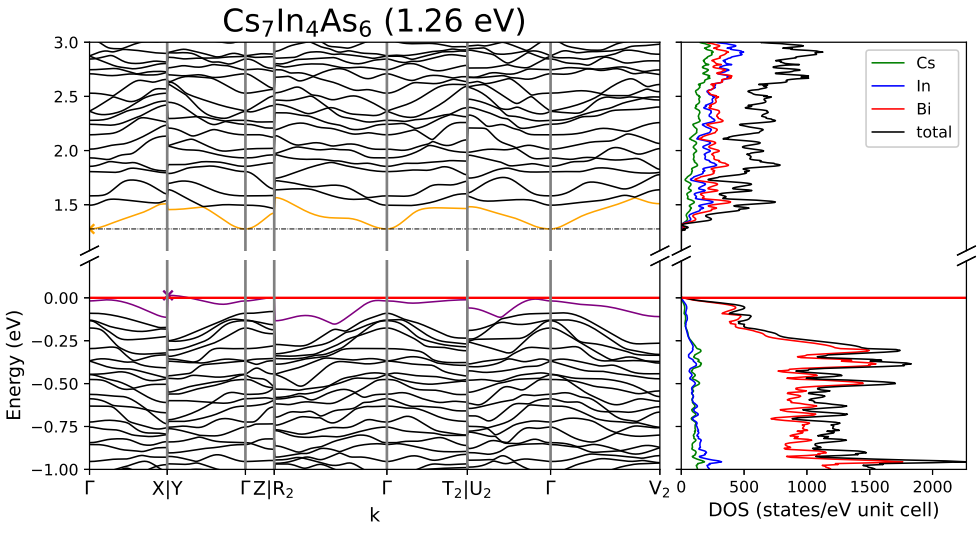

Figure A.196: Band structure and DOS of $Cs_7In_4Bi_6$.

Table A.313: Overlap population and interatomic distances of $Cs_7In_4Bi_3$.

Atom A	Atom B	r_{AB} / Å	overlap
Cs1	In1	3.853	−0.007
	Bi1	3.88	0.003
	Bi11	3.885	0.027
	In5	3.904	−0.006
	Bi5	3.905	0.012
	Bi8	3.923	0.014
Cs2	Bi6	3.852	0.011
	In4	3.874	−0.006
	Bi7	3.887	0.016
	Bi9	3.917	0.005
	In7	3.94	−0.005
	Bi10	3.969	0.026
Cs3	In2	3.786	−0.009
	Bi3	3.805	0.014
	Bi11	3.947	0.026
	Bi8	3.954	0.022
	Cs13	4.031	0.005
	Bi7	4.039	0.011
Cs4	In6	3.749	−0.008
	Bi12	3.879	0.017
	Bi9	3.916	0.009
	Bi10	4.085	0.016
	In2	4.098	−0.002
	Bi4	4.103	0.014
Cs5	Bi3	3.993	0.023
	Bi2	4.003	0.018
	In5	4.152	0.0
	Bi11	4.179	0.026
	Bi8	4.194	0.017
Cs6	Bi3	3.801	0.009
	Bi5	3.854	0.011
	Bi2	3.858	0.013
	Bi4	3.902	0.016
	Bi11	4.14	0.023
	Cs14	4.148	0.005
Cs7	Bi8	3.96	0.018
	Bi5	4.019	0.011
	Bi2	4.071	0.017
	In5	4.082	−0.002
	Cs9	4.139	0.006
	Bi1	4.208	0.012
Cs8	Bi10	3.796	0.018
	In8	3.854	−0.004
	Bi4	3.952	0.02
	Cs12	4.101	0.006
	In6	4.105	0.002
	Bi8	4.134	0.012
Cs9	In3	3.835	−0.005
	Bi1	3.855	0.007
	Bi11	3.875	0.021
	Bi2	3.975	0.019
	In1	4.112	0.001
	Bi3	4.136	0.01
Cs10	Bi4	3.851	0.026
	Bi12	3.942	0.018
	In7	4.088	−0.002
	Bi9	4.092	0.02
	Bi7	4.127	0.019
Cs11	Bi7	3.963	0.021
	Bi12	4.04	0.018
	In7	4.052	−0.002
	Bi6	4.053	0.016
	Bi9	4.184	0.012
Cs12	Bi11	3.857	0.028
	Bi3	4.031	0.015
	In3	4.058	0.002
	Bi6	4.063	0.02
	Bi8	4.241	0.018
Cs13	Bi4	3.863	0.014
	Bi10	3.889	0.015
	Bi12	3.965	0.014
	Bi6	3.987	0.014
	Bi11	4.022	0.021
Cs14	Bi5	3.783	0.018
	Bi10	4.03	0.023
	Bi7	4.063	0.024
	Bi4	4.065	0.023
In1	Bi5	2.965	0.253
	Bi2	3.0	0.239
	Bi2	3.004	0.244
	Bi1	3.05	0.216
	In8	3.494	−0.015
	In5	3.796	−0.011
In2	Bi4	2.919	0.286
	Bi7	2.947	0.279
	Bi9	3.045	0.202
	Bi6	3.057	0.222
	In4	3.514	−0.005
	In7	3.714	−0.024
In3	Bi11	2.901	0.335
	Bi10	3.045	0.235
	Bi5	3.068	0.22
	Bi3	3.106	0.192
	In6	3.4	−0.003
In4	Bi6	2.991	0.242
	Bi12	3.003	0.247
	Bi12	3.003	0.238
	Bi9	3.038	0.218
	In7	3.765	−0.009
In5	Bi8	3.003	0.263
	In5	3.023	0.272
	Bi1	3.052	0.222
	Bi2	3.11	0.215
	In8	3.719	−0.026
In6	Bi10	2.958	0.264
	Bi4	2.961	0.277
	Bi3	3.001	0.229
	Bi6	3.037	0.22
In7	Bi7	2.972	0.274
	In7	2.983	0.261
	Bi9	3.071	0.219
	Bi12	3.088	0.212
In8	Bi8	2.937	0.274
	Bi3	2.97	0.261
	Bi5	2.995	0.233
	Bi1	3.027	0.216

Table A.314: Partial charges for each atom position in $Cs_7In_4Bi_3$.

Atom	Z	charge	part charge
Cs1	9	8.212	0.788
Cs2		8.214	0.786
Cs3		8.259	0.741
Cs4		8.223	0.777
Cs5		8.252	0.748
Cs6		8.268	0.732
Cs7		8.242	0.758
Cs8		8.23	0.77
Cs9		8.229	0.771
Cs10		8.255	0.745
Cs11		8.232	0.768
Cs12		8.26	0.74
Cs13		8.274	0.726
Cs14		8.286	0.714
In1	21	21.11	−0.11
In2		21.011	−0.011
In3		21.052	−0.052
In4		21.112	−0.112
In5		21.138	−0.138
In6		21.103	−0.103
In7		21.135	−0.135
In8		21.03	−0.03
Bi1	23	23.788	−0.788
Bi2		23.661	−0.661
Bi3		23.693	−0.693
Bi4		23.871	−0.871
Bi5		23.677	−0.677
Bi6		23.708	−0.708
Bi7		23.902	−0.902
Bi8		23.902	−0.902
Bi9		23.813	−0.813
Bi10		23.982	−0.982
Bi11		24.23	−1.23
Bi12		23.643	−0.643

References

(1) Sato, K. S. K.; Katayama-Yoshida, H. K.-Y. H. *Japanese Journal of Applied Physics* **2000**, *39*, L555.

(2) Hosono, H. *Journal of non-crystalline solids* **2006**, *352*, 851–858.

(3) Wan, J.; Xu, X.; Zhang, G.; Li, Y.; Feng, K.; Peng, Q. *Energy & Environmental Science* **2017**, *10*, 1739–1745.

(4) Todorov, T.; Gershon, T.; Gunawan, O.; Lee, Y. S.; Sturdevant, C.; Chang, L.-Y.; Guha, S. *Advanced Energy Materials* **2015**, *5*.

(5) Mehta, A.; Mishra, A.; Basu, S.; Shetti, N. P.; Reddy, K. R.; Saleh, T. A.; Aminabhavi, T. M. *Journal of environmental management* **2019**, *250*, 109486.

(6) Rühle, S. *Solar energy* **2016**, *130*, 139–147.

(7) Shockley, W.; Queisser, H. In *Renewable energy*; Routledge: 2018, Vol2_35–Vol2_54.

(8) Andreani, L. C.; Bozzola, A.; Kowalczewski, P.; Liscidini, M.; Redorici, L. *Advances in Physics: X* **2019**, *4*, 1548305.

(9) Wang, A; Zhao, J; Green, M. *Applied physics letters* **1990**, *57*, 602–604.

(10) Kim, J. Y.; Lee, J.-W.; Jung, H. S.; Shin, H.; Park, N.-G. *Chemical reviews* **2020**, *120*, 7867–7918.

(11) Dimroth, F. *physica status solidi c* **2006**, *3*, 373–379.

(12) Atkins, P. W.; De Paula, J.; Keeler, J., *Atkins' physical chemistry*; Oxford university press: 2023.

(13) Holleman, A. F., *Lehrbuch der anorganischen Chemie*; Walter de Gruyter GmbH & Co KG: 2019.

(14) Sevov, S. C. *Intermetallic Compounds-Principles and Practice: Progress* **2002**, *3*, 113–132.

(15) Laves, F. *Die Naturwissenschaften* **1941**, 244–256.

(16) Simon, A.; Borrmann, H.; Horakh, J. *Chemische Berichte* **1997**, *130*, 1235–1240.

(17) Okudera, H.; Dinnebier, R. E.; Simon, A. *Zeitschrift für Kristallographie-Crystalline Materials* **2005**, *220*, 259–264.

(18) Imai, Y.; Watanabe, A. *Journal of alloys and compounds* **2009**, *478*, 754–757.

(19) Wade, K. In *Advances in inorganic chemistry and radiochemistry*; Elsevier: 1976; Vol. 18, pp 1–66.

(20) Mingos, D. M. P. *Accounts of Chemical Research* **1984**, *17*, 311–319.

(21) Scharfe, S.; Kraus, F.; Stegmaier, S.; Schier, A.; Fässler, T. F. *Angewandte Chemie International Edition* **2011**, *50*, 3630–3670.

(22) Wilson, R. J.; Weinert, B.; Dehnen, S. *Dalton Transactions* **2018**, *47*, 14861–14869.

(23) Wallach, C; Mayer, K; Henneberger, T; Klein, W; Fässler, T. *Dalton Transactions* **2020**, *49*, 6191–6198.

(24) Van IJzendoorn, B.; Albawardi, S. F.; Vitorica-Yrezabal, I. J.; Whitehead, G. F.; McGrady, J. E.; Mehta, M. *Journal of the American Chemical Society* **2022**, *144*, 21213–21223.

(25) Liebau, F. *Reviews in Mineralogy and Geochemistry* **1980**, *5*, 1–24.

(26) Zeitz, S.; Kuznetsova, Y.; Fässler, T. F. *Molecules* **2024**, *29*, 4087.

(27) Restle, T. M.; Dums, J. V.; Raudaschl-Sieber, G.; Fässler, T. F. *Chemistry–A European Journal* **2020**, *26*, 6812–6819.

(28) Restle, T. M.; Deringer, V. L.; Meyer, J.; Raudaschl-Sieber, G.; Fässler, T. F. *Chemical Science* **2021**, *12*, 1278–1285.

(29) Ohse, L.; Somer, M.; Blase, W.; Cordier, G. *Zeitschrift für Naturforschung B* **1993**, *48*, 1027–1034.

(30) Blase, W; Cordier, G; Somer, M *Zeitschrift für Kristallographie-Crystalline Materials* **1991**, *195*, 119–120.

(31) Somer, M; Carrillo-Cabrera, W; Peters, E.-M.; Peters, K; Schnering, H. v. *Zeitschrift für Kristallographie-New Crystal Structures* **1998**, *213*, 5–6.

(32) Klein, J; Eisenmann, B *Materials research bulletin* **1988**, *23*, 587–594.

(33) Feng, K.; Kang, L.; Yin, W.; Hao, W.; Lin, Z.; Yao, J.; Wu, Y. *Journal of Solid State Chemistry* **2013**, *205*, 129–133.

(34) Haffner, A.; Hatz, A.-K.; Moudrakovski, I.; Lotsch, B. V.; Johrendt, D. *Angewandte Chemie* **2018**, *130*, 6263–6268.

(35) Cordier, G; Ochmann, H *Zeitschrift für Kristallographie-Crystalline Materials* **1991**, *195*, 308–309.

(36) Fässler, T. F.; Hoffmann, S. *Inorganic chemistry* **2003**, *42*, 5474–5476.

(37) Khatun, M.; Stoyko, S. S.; Mar, A. *Journal of Solid State Chemistry* **2016**, *238*, 229–235.

(38) WinXPOW, S. *Darmstadt, Germany* **2011**, *298*.

(39) Rodríguez-Carvajal, J. *Physica B: Condensed Matter* **1993**, *192*, 55–69.

(40) Sheldrick, G. *University of Göttingen, Germany* **2014**.

(41) Sheldrick, G. *Universität of Göttingen: Göttingen, Germany* **2014**.

(42) Koziskova, J.; Hahn, F.; Richter, J.; Kožíšek, J. *Acta Chimica Slovaca* **2016**, *9*, 136–140.

(43) Gomez, A; Dina, G; Kycia, S *Review of Scientific Instruments* **2018**, *89*.

(44) Toby, B. H.; Von Dreele, R. B. *Journal of Applied Crystallography* **2013**, *46*, 544–549.

(45) NIST **2000**.

(46) WiRe, version 4.2, Gloucestershire: Renishaw plc, 2002.

(47) Dovesi, R.; Erba, A.; Orlando, R.; Zicovich-Wilson, C. M.; Civalleri, B.; Maschio, L.; Rérat, M.; Casassa, S.; Baima, J.; Salustro, S., et al. *Wiley Interdisciplinary Reviews: Computational Molecular Science* **2018**, *8*, e1360.

(48) Dovesi, R; Saunders, V.; Roetti, C; Orlando, R; Zicovich-Wilson, C.; Pascale, F; Civalleri, B; Doll, K; Harrison, N.; Bush, I., et al. **2017**.

(49) Restle, T. M.; Dums, J. V.; Raudaschl-Sieber, G.; Fässler, T. F. *Chemistry–A European Journal* **2020**, *26*, 6812–6819.

(50) Wylezich, T.; Valois, R.; Suta, M.; Mutschke, A.; Ritter, C.; Meijerink, A.; Karttunen, A. J.; Kunkel, N. *Chemistry–A European Journal* **2020**, *26*, 11742–11750.

(51) Sansone, G.; Maschio, L.; Usvyat, D.; Schütz, M.; Karttunen, A. *The journal of physical chemistry letters* **2016**, *7*, 131–136.

(52) Stene, R. E.; Scheibe, B.; Karttunen, A. J.; Petry, W.; Kraus, F. *European Journal of Inorganic Chemistry* **2019**, *2019*, 3672–3682.

(53) Scheibe, B.; Karttunen, A. J.; Weigend, F.; Kraus, F. *Chemistry–A European Journal* **2021**, *27*, 2381–2392.

(54) Ivlev, S. I.; Soltner, T.; Karttunen, A. J.; Mühlbauer, M. J.; Kornath, A. J.; Kraus, F. *Zeitschrift für anorganische und allgemeine Chemie* **2017**, *643*, 1436–1443.

(55) Restle, T. M.; Zeitz, S.; Meyer, J.; Klein, W.; Raudaschl-Sieber, G.; Karttunen, A. J.; Fässler, T. F. *Zeitschrift für anorganische und allgemeine Chemie* **2021**, *647*, 1804–1814.

(56) Restle, T. M.; Zeitz, S.; Stanley, P. M.; Karttunen, A. J.; Meyer, J.; Raudaschl-Sieber, G.; Klein, W.; Fässler, T. F. *Chemistry–A European Journal* **2024**, e202304097.

(57) Scheibe, B.; Haiges, R.; Ivlev, S. I.; Karttunen, A. J.; Müller, U.; Christe, K. O.; Kraus, F. *European Journal of Inorganic Chemistry* **2020**, *2020*, 4483–4496.

(58) Scheibe, B.; Ivlev, S. I.; Karttunen, A. J.; Kraus, F. *European Journal of Inorganic Chemistry* **2020**, *2020*, 1319–1324.

(59) Karttunen, A. J.; Fässler, T. F.; Linnolahti, M.; Pakkanen, T. A. *Inorganic Chemistry* **2011**, *50*, 1733–1742.

(60) Kuklin, M. S.; Eklund, K.; Linnera, J.; Ropponen, A.; Tolvanen, N.; Karttunen, A. J. *Molecules* **2022**, *27*, 874.

(61) Scherf, L. M.; Karttunen, A. J.; Pecher, O.; Magusin, P. C.; Grey, C. P.; Fässler, T. F. *Angewandte Chemie International Edition* **2016**, *55*, 1075–1079.

(62) Karttunen, A. J.; Fässler, T. F. *Chemistry–A European Journal* **2014**, *20*, 6693–6698.

(63) Perdew, J. P.; Yang, W.; Burke, K.; Yang, Z.; Gross, E. K.; Scheffler, M.; Scuseria, G. E.; Henderson, T. M.; Zhang, I. Y.; Ruzsinszky, A., et al. *Proceedings of the national academy of sciences* **2017**, *114*, 2801–2806.

(64) Zagorac, D.; Müller, H; Ruehl, S; Zagorac, J; Rehme, S. *Journal of applied crystallography* **2019**, *52*, 918–925.

(65) Diamond - Crystal and Molecular Structure Visualization, version 3.0, Bonn: Crystal Impact - Dr. H. Putz & Dr. K. Brandenburg GbR, 2014.

(66) Hinuma, Y.; Pizzi, G.; Kumagai, Y.; Oba, F.; Tanaka, I. *Computational Materials Science* **2017**, *128*, 140–184.

(67) Mulliken, R. S. *The Journal of chemical physics* **1955**, *23*, 1841–1846.

(68) Jmol: an open-source Java viewer for chemical structures in 3D, version 14.14.1.

(69) Zeitz, S.; Antoniuk, H.; Hlukhyy, V.; Fässler, T. F. *Chemistry–A European Journal* **2024**, *30*, e202400002.

(70) Botta, M.; Zeitz, S.; Klein, W.; Raudaschl-Sieber, G.; Fässler, T. F. *Inorganic Chemistry* **2024**.

(71) Botta, M.; Zeitz, S.; Fässler, T. F. *Zeitschrift für anorganische und allgemeine Chemie* **2023**, *649*, e202300166.

(72) Restle, T. M.; Zeitz, S.; Stanley, P. M.; Karttunen, A. J.; Meyer, J.; Raudaschl-Sieber, G.; Klein, W.; Fässler, T. F. *Chemistry–A European Journal* **2024**, e202304097.

(73) Daiber, V.; Zeitz, S.; Hlukhyy, V.; Dankert, D.; Fässler, T. F. *Zeitschrift für anorganische und allgemeine Chemie* **2024**, *650*, e202300244.

(74) Restle, T. M.; Zeitz, S.; Meyer, J.; Klein, W.; Raudaschl-Sieber, G.; Karttunen, A. J.; Fässler, T. F. *Zeitschrift für anorganische und allgemeine Chemie* **2021**, *647*, 1804–1814.

(75) Urusov, V.; Nadezhina, T. *Journal of Structural Chemistry* **2009**, *50*, 22–37.

(76) Eickhoff, H.; Toffoletti, L.; Klein, W.; Raudaschl-Sieber, G.; Fässler, T. F. *Inorganic chemistry* **2017**, *56*, 6688–6694.

(77) Juza, R.; Schulz, W. *Zeitschrift für anorganische und allgemeine Chemie* **1954**, *275*, 65–78.

(78) El Maslout, A.; Motte, J.-P.; Gleitzer, C. *Journal of Solid State Chemistry* **1973**, *7*, 250–254.

(79) Eisenmann, B; Somer, M *Zeitschrift für Naturforschung. Teil b, Anorganische Chemie, organische Chemie* **1985**, *40*, 886–890.

(80) Eisenmann, B; Klein, J; Somer, M *Zeitschrift für Kristallographie-Crystalline Materials* **1991**, *197*, 265–266.

(81) Eisenmann, B; Klein, J; Somer, M *Zeitschrift für Kristallographie-Crystalline Materials* **1991**, *197*, 269–270.

(82) Eisenmann, B; Klein, J *Zeitschrift für Kristallographie-Crystalline Materials* **1991**, *197*, 263–264.

(83) Eisenmann, B.; Klein, J.; Somer, M. *Angewandte Chemie* **1990**, *102*, 92–93.

(84) Power, P. P. *Chemical reviews* **1999**, *99*, 3463–3504.

(85) Eisenmann, B; Klein, J; Somer, M *Zeitschrift für Kristallographie-Crystalline Materials* **1991**, *197*, 267–268.

(86) Klein, J.; Eisenmann, B. *Zeitschrift für Kristallographie-Crystalline Materials* **1991**, *196*, 213–230.

(87) Eisenmann, B; Rössler, U *Zeitschrift für Kristallographie-New Crystal Structures* **2000**, *215*, 347–348.

(88) Eisenmann, B; Klein, J; Somer, M *Zeitschrift für Kristallographie-Crystalline Materials* **1991**, *197*, 273–274.

(89) Blase, W; Cordier, G; Somer, M *Zeitschrift für Kristallographie* **1992**, *199*, 279–280.

(90) Schnering, H. v.; Somer, M; Peters, K; Blase, W; Cordier, G *Zeitschrift für Kristallographie-Crystalline Materials* **1990**, *193*, 283–284.

(91) Cordier, G; Blase, W *Zeitschrift für Kristallographie-Crystalline Materials* **1992**, *199*, 277–278.

(92) Blase, W; Cordier, G; Somer, M *Zeitschrift für Kristallographie-Crystalline Materials* **1991**, *195*, 117–118.

(93) Blase, W; Cordier, G; Somer, M *Zeitschrift für Kristallographie-Crystalline Materials* **1991**, *195*, 121–122.

(94) Blase, W; Cordier, G; Somer, M *Zeitschrift für Kristallographie-Crystalline Materials* **1993**, *206*, 141–142.

(95) Blase, W; Cordier, G; Somer, M *Zeitschrift für Kristallographie-Crystalline Materials* **1993**, *206*, 145–146.

(96) Blase, W; Cordier, G; Somer, M *Zeitschrift für Kristallographie-Crystalline Materials* **1993**, *206*, 143–144.

(97) Restle, T. M.; Zeitz, S.; Stanley, P. M.; Karttunen, A. J.; Meyer, J.; Raudaschl-Sieber, G.; Klein, W.; Fässler, T. F. *Chemistry–A European Journal* **2024**, *30*, e202304097.

(98) Wegner, F.; Kamm, F.; Pielnhofer, F.; Pfitzner, A. *Zeitschrift für anorganische und allgemeine Chemie* **2022**, *649*, e202200330.

(99) Cordier, G; Ochmann, H *Zeitschrift für Naturforschung. B, A journal of chemical sciences* **1988**, *43*, 1538–1540.

(100) Cordier, G; Ochmann, H *Zeitschrift für Kristallographie-Crystalline Materials* **1991**, *195*, 105–106.

(101) Cordier, G; Ochmann, H *Zeitschrift für Kristallographie-Crystalline Materials* **1991**, *195*, 107–108.

(102) Bobev, S.; Sevov, S. C. *Journal of Solid State Chemistry* **2002**, *163*, 436–448.

(103) Somer, M; Walz, L; Peters, K; Schnering, H. v. *Zeitschrift für Kristallographie-Crystalline Materials* **1990**, *193*, 301–302.

(104) Boyko, M.; Hlukhyy, V.; Fässler, T. F. *Zeitschrift für anorganische und allgemeine Chemie* **2023**, *649*, e202300164.

(105) Von Schnering, H.; Somer, M; Walz, L; Peters, K; Cordier, G; Blase, W *Zeitschrift für Kristallographie-Crystalline Materials* **1990**, *193*, 299–300.

(106) Somer, M; Walz, L; Thiery, D; Schnering, H. v. *Zeitschrift für Kristallographie-Crystalline Materials* **1990**, *193*, 303–304.

(107) Somer, M; Thiery, D; Hartweg, M; Walz, L; Peters, K; von Schnering, H. *Zeitschrift für Kristallographie-Crystalline Materials* **1990**, *193*, 287–288.

(108) Somer, M; Thiery, D; Hartweg, M; Walz, L; Popp, T; Peters, K; von Schnering, H. *Zeitschrift für Kristallographie* **1990**, *192*, 269–270.

(109) Somer, M; Peters, K; Popp, T; Schnering, H. v. *Zeitschrift für Kristallographie-Crystalline Materials* **1990**, *192*, 273–274.

(110) Büssem, W; Fischer, H; Gruner, E *Naturwissenschaften* **1935**, *23*, 740–740.

(111) Toffoletti, L.; Kirchhain, H.; Landesfeind, J.; Klein, W.; van Wüllen, L.; Gasteiger, H. A.; Fässler, T. F. *Chemistry–A European Journal* **2016**, *22*, 17635–17645.

(112) Asbrand, M.; Eisenmann, B. *Zeitschrift für Naturforschung B* **1993**, *48*, 452–456.

(113) Haffner, A.; Hatz, A.-K.; Hoch, C.; Lotsch, B. V.; Johrendt, D. *European Journal of Inorganic Chemistry* **2020**, *2020*, 617–621.

(114) Eisenmann, B.; Somer, M. *Zeitschrift für Naturforschung B* **1984**, *39*, 736–738.

(115) Eisenmann, B.; Klein, J. *Journal of the Less Common Metals* **1991**, *175*, 109–117.

(116) Hurng, W. M.; Peterson, E. S.; Corbett, J. D. *Inorganic Chemistry* **1989**, *28*, 4177–4180.

(117) Eisenmann, B.; Klein, J. *Zeitschrift für anorganische und allgemeine Chemie* **1991**, *598*, 93–102.

(118) Eisenmann, B; Rößler, U *Zeitschrift für Kristallographie-New Crystal Structures* **1998**, *213*, 28–28.

(119) Ochs, A. M.; Gorai, P.; Wang, Y.; Scudder, M. R.; Koster, K.; Moore, C. E.; Stevanovic, V.; Heremans, J. P.; Windl, W.; Toberer, E. S., et al. *Chemistry of Materials* **2021**, *33*, 946–951.

(120) Eickhoff, H.; Sedlmeier, C.; Klein, W.; Raudaschl-Sieber, G.; Gasteiger, H. A.; Fässler, T. F. *Zeitschrift für anorganische und allgemeine Chemie* **2020**, *646*, 95–102.

(121) Feng, K.; Yin, W.; He, R.; Lin, Z.; Jin, S.; Yao, J.; Fu, P.; Wu, Y. *Dalton Transactions* **2012**, *41*, 484–489.

(122) Hurng, W. M.; Corbett, J. D.; Wang, S. L.; Jacobson, R. A. *Inorganic Chemistry* **1987**, *26*, 2392–2395.

(123) Blase, W; Cordier, G; Somer, M *Zeitschrift für Kristallographie-Crystalline Materials* **1991**, *195*, 115–116.

(124) Cordier, G; Ochmann, H *Zeitschrift für Kristallographie-Crystalline Materials* **1991**, *195*, 111–112.

(125) Cordier, G.; Ochmann, H.; Schäfer, H. *Journal of the Less Common Metals* **1986**, *119*, 291–296.

(126) Cordier, G; Ochmann, H *Zeitschrift für Kristallographie* **1991**, *195*, 113–114.

(127) Cordier, G; Ochmann, H *Zeitschrift für Kristallographie-Crystalline Materials* **1991**, *195*, 125–126.

(128) Cordier, G; Ochmann, H *Zeitschrift für Kristallographie-Crystalline Materials* **1991**, *195*, 310–311.

(129) Cordier, G; Ochmann, H *Zeitschrift für Kristallographie-Crystalline Materials* **1991**, *197*, 283–284.

(130) Cordier, G; Ochmann, H; Schäfer, H *Revue de chimie minérale* **1984**, *21*, 282–291.

(131) Cordier, G; Ochmann, H *Zeitschrift für Kristallographie-Crystalline Materials* **1991**, *197*, 285–286.

(132) Cordier, G; Ochmann, H *Zeitschrift für Kristallographie-Crystalline Materials* **1991**, *197*, 281–282.

(133) Cordier, G; Ochmann, H *Zeitschrift für Kristallographie-Crystalline Materials* **1991**, *197*, 287–288.

(134) Cordier, G; Ochmann, H *Zeitschrift für Kristallographie-Crystalline Materials* **1991**, *197*, 289–290.

(135) Cordier, G; Ochmann, H *Zeitschrift für Kristallographie-Crystalline Materials* **1991**, *197*, 293–294.

(136) Cordier, G; Ochmann, H *Zeitschrift für Kristallographie-Crystalline Materials* **1991**, *197*, 291–292.

(137) Gourdon, O.; Boucher, F.; Gareh, J.; Evain, M.; O'Connor, C.; Jin-Seung, J. *Acta Crystallographica Section C: Crystal Structure Communications* **1996**, *52*, 2963–2964.

(138) Blase, W; Cordier, G; Poth, L; Weil, K. *Zeitschrift für Kristallographie-Crystalline Materials* **1995**, *210*, 60–60.

(139) Boyko, M. Polar Intermetallics at the Border Between Hume-Rothery and Zintl Phases: Investigations in the Systems Alkali Metal–Tin with Late Transition and p-Block Metals, Ph.D. Thesis, Technische Universität München, 2019.

(140) Ponou, S. Germanides, Germanide-Tungstate Double Salts and Substitution Effects in Zintl Phases, Ph.D. Thesis, Technische Universität München, 2006.

(141) Vaughey, J.; Corbett, J. D. *Inorganic chemistry* **1997**, *36*, 4316–4320.

(142) Evers, J. *Journal of Solid State Chemistry* **1979**, *28*, 369–377.

(143) Cultrara, N. D.; Wang, Y.; Arguilla, M. Q.; Scudder, M. R.; Jiang, S.; Windl, W.; Bobev, S.; Goldberger, J. E. *Chemistry of Materials* **2018**, *30*, 1335–1343.

(144) Janzon, K.; Schäfer, H.; Weiss, A. *Zeitschrift für Naturforschung B* **1968**, *23*, 1544–1544.

(145) Nedumkandathil, R.; Benson, D. E.; Grins, J.; Spektor, K.; Häussermann, U. *Journal of Solid State Chemistry* **2015**, *222*, 18–24.

(146) Bordet, P; Affronte, M.; Sanfilippo, S; Nunez-Regueiro, M; Laborde, O; Olcese, G.; Palenzona, A; LeFloch, S.; Levy, D.; Hanfland, M *Physical Review B* **2000**, *62*, 11392.

(147) Slonczewski, J.; Weiss, P. *Physical review* **1958**, *109*, 272.

(148) Asbrand, M; Eisenmann, B *Zeitschrift für Kristallographie-Crystalline Materials* **1993**, *205*, 323–324.

(149) Eisenmann, B.; Klein, J. *Zeitschrift für Naturforschung B* **1988**, *43*, 1156–1160.

(150) Somer, M; Hartweg, M; Peters, K; Schnering, H. v. *Zeitschrift für Kristallographie-Crystalline Materials* **1990**, *191*, 311–312.

(151) Somer, M; Carrillo-Cabrera, W; Peters, E.-M.; Peters, K; von Schnering, H. *Zeitschrift für Kristallographie-Crystalline Materials* **1995**, *210*, 779–780.

(152) Somer, M; Popp, T; Peters, K; von Schnering, H. *Zeitschrift für Kristallographie-Crystalline Materials* **1990**, *193*, 297–298.

(153) Somer, M; Hartweg, M; Peters, K; von Schnering, H. *Zeitschrift für Kristallographie-Crystalline Materials* **1990**, *191*, 313–314.

(154) Somer, M; Popp, T; Peters, K; von Schnering, H. *Zeitschrift für Kristallographie-Crystalline Materials* **1990**, *193*, 295–296.

(155) Somer, M; Popp, T; Peters, K; Schnering, H. v. *Zeitschrift für Kristallographie-Crystalline Materials* **1990**, *193*, 281–282.

(156) Blase, W; Cordier, G; Somer, M *Zeitschrift für Kristallographie-Crystalline Materials* **1991**, *195*, 123–124.

(157) Somer, M; Peters, K; Thiery, D; von Schnering, H. *Zeitschrift für Kristallographie* **1990**, *192*, 271–272.

(158) Wolf, J.; Weber, D.; Schnering, H.-G. v. *Zeitschrift für Naturforschung B* **1986**, *41*, 731–735.

(159) Cordier, G; Ochmann, H; Schäfer, H *Materials research bulletin* **1986**, *21*, 331–336.

(160) Eickhoff, H.; Hlukhyy, V.; Fässler, T. F. *Zeitschrift für anorganische und allgemeine Chemie* **2020**, *646*, 1834–1838.

(161) Eulenstein, A. R.; Bogdanovski, D.; Reinhardt, H.; Miß, V.; Roling, B.; Hampp, N.; Dronskowski, R.; Dehnen, S. *Chemistry of Materials* **2019**, *31*, 8839–8849.

(162) CORDIER, G; OCHMANN, H; SCHÄFER, H *Revue de chimie minérale* **1985**, *22*, 58–63.

(163) Cordier, G; Ochmann, H *Zeitschrift für Kristallographie-Crystalline Materials* **1991**, *197*, 295–296.

(164) Botta, M. Experimental crystal strcuture of Na2Ge2P3, unpublished, N.D.

(165) Eickhoff, H.; Strangmüller, S.; Klein, W.; Kirchhain, H.; Dietrich, C.; Zeier, W. G.; van Wüllen, L.; Fässler, T. F. *Chemistry of Materials* **2018**, *30*, 6440–6448.

(166) Strangmüller, S.; Eickhoff, H.; Klein, W.; Raudaschl-Sieber, G.; Kirchhain, H.; Kutsch, T.; Baran, V.; Senyshyn, A.; van Wüllen, L.; Gasteiger, H. A., et al. *Journal of Materials Chemistry A* **2021**, *9*, 15254–15268.

(167) Müller, D. Experimental crystal strcuture of Li8TiP4, unpublished, N.D.

(168) Botta, M. Experimental crystal strcuture of Na8SnP4, unpublished, N.D.

(169) Eisenmann, B.; Klein, J. *Zeitschrift für Naturforschung B* **1988**, *43*, 69–71.

(170) Merk, S. Experimental crystal strcuture of Li7TaP4, unpublished, N.D.

(171) Restle, T. M.; Sedlmeier, C.; Kirchhain, H.; Klein, W.; Raudaschl-Sieber, G.; Deringer, V. L.; van Wüllen, L.; Gasteiger, H. A.; Fässler, T. F. *Angewandte Chemie International Edition* **2020**, *59*, 5665–5674.

(172) Meyer, J. Experimental crystal strcuture of Na9InSb4, unpublished, N.D.

(173) Ortiz, B. R.; Gorai, P.; Stevanovic, V.; Toberer, E. S. *Chemistry of Materials* **2017**, *29*, 4523–4534.

(174) Ortiz, B. R.; Gorai, P.; Braden, T.; Bensen, E. A.; Wilson, S. D.; Stevanovic, V.; Toberer, E. S. *ACS Applied Energy Materials* **2020**, *3*, 2182–2191.

(175) Cordier, G; Ochmann, H *Zeitschrift für Kristallographie-Crystalline Materials* **1991**, *197*, 297–298.

(176) Wang, J.; Owens-Baird, B.; Kovnir, K. *Inorganic Chemistry* **2021**, *61*, 533–541.

(177) Asbrand, M; Eisenmann, B; Klein, J *Zeitschrift für anorganische und allgemeine Chemie* **1995**, *621*, 576–582.

(178) Cordier, G.; Ochmann, H.; Schäfer, H. *Zeitschrift für anorganische und allgemeine Chemie* **1984**, *517*, 118–124.

(179) Khatun, M.; Mar, A. *Zeitschrift für Naturforschung B* **2016**, *71*, 375–380.

(180) Blase, W; Cordier, G; Somer, M *Zeitschrift für Kristallographie-Crystalline Materials* **1993**, *203*, 146–147.

(181) Eisenmann, B; Asbrand, M *Zeitschrift für Kristallographie-Crystalline Materials* **1992**, *198*, 283–284.

(182) Asbrand, M; Eisenmann, B *Zeitschrift für Kristallographie-Crystalline Materials* **1992**, *198*, 309–310.

(183) Gascoin, F.; Sevov, S. C. *Inorganic Chemistry* **2001**, *40*, 6254–6257.

(184) Bobev, S.; Sevov, S. C. *Inorganic Chemistry* **1999**, *38*, 2672–2675.

B Additional Tables

Table B.1: Electronegativity values for all alkali metals, triels, tertrels and pnictogens.[13]

alkali metal	EN	triel/tetrel	EN	pnictogen	EN
Li	0.98	B	2.04	P	2.19
Na	0.93	Al	1.61	As	2.18
K	0.82	Ga	1.81	Sb	2.05
Rb	0.82	In	1.78	Bi	2.02
Cs	0.97	Si	1.9		
		Ge	2.01		
		Sn	1.96		

C List of Publications and Manuscripts

Publications:

Sabine Zeitz, Hanna Antoniuk, Viktor Hlukhyy, T. F. Fässler, Electronic Structure Analysis of the *A*10*Tt*2P6 System (*A* = Li Cs; *Tt* = Si, Ge, Sn) and Synthesis of the Direct Band Gap Semiconductor K10Sn2P, *Chemistry — A European Journal* **2024**, *30*, e202400002.

Sabine Zeitz, Yulia Kuznetsova, and T. F. Fässler, Large Number of Direct or Pseudo-Direct Band Gap Semiconductors among A_3TrPn_2 Compounds with *A* = Li, Na, K, Rb, Cs; *Tr* = Al, Ga, In; *Pn* = P, As, *Molecules* **2024**, *29*, 4087.

S. Zeitz, M. Boyko, S. Ponou, V. Hlukhyy, T.F. Fässler, Open Sn Framework Structure Hosting Bi Guest atoms – Synthesis, Crystal and Electronic Structure of Na13Sn26Bi, *Chemistry – A European journal* **2024**, e202403592.

Manuscripts:

Sabine Zeitz, Hanna Antoniuk, Thomas F. Fässler, Electronic structure analysis of A_6TrPn_3 compounds with *A* = Rb, Cs; *Tr* = Al, Ga, In and *Pn* = As, Sb, *manuscript for publication*.

Sabine Zeitz, Zoe Listmann, Thomas F. Fässler, Electronic structure analysis of the $A_2Tr/TtPn_2$ system with *A* = Li-Cs; *Tr* = Al-In; *Tt* = Si-Sn; *Pn* = P-Sb, *manuscript for publication*.

Sabine Zeitz, Thomas F. Fässler, Electronic property calculation of *A*Sn*Pn* compounds with *A* = Na, K and *Pn* = P, As, Sb, *manuscript for publication*.

Sabine Zeitz, Yulia Kuznetsova, Thomas F. Fässler, Electronic structure analysis of the ATt_3Pn_3 system with *A* = Li-Cs; *Tr* = Al-In; *Tt* = Si-Sn; *Pn* = P-Sb, *manuscript for publication*.

Sabine Zeitz, Zoe Listmann, Thomas F. Fässler, Electronic structure analysis of $A_2Tr_2Pn_3$ compounds with *A* = Na Cs; *Tr* = Al, Ga, In; *Pn* = As, Sb, *manuscript for publication*.

S. Zeitz, A. Mutschke, T.F. Fässler, CaSi2–xGe*x* , solid solution and analysis of ordered structures, *manuscript for publication*.

Publications as Co-Author:

M. Botta, S. Zeitz, W. Klein, G. Raudaschl-Sieber, T. F. Fässler, $Na_3Ge_2P_3$: A Zintl Phase Featuring [P3Ge–GeP3] Dimers as Building Blocks, *Inorganic Chemistry* **2024**, *63*, 20108–20116.

M. Botta, S. Zeitz, T. F. Fässler, Synthesis, Structure and Physical Properties of the Sodium-Rich Phosphidogermanate Na_8GeP_4, *Zeitschrift für anorganische und allgemeine Chemie* **2023**, *649*, e202300166.

T. M. F. Restle, S. Zeitz, P. M. Stanley, A. J. Karttunen, J. Meyer, G. Raudaschl-Sieber, W. Klein, T. F. Fässler, Direct Band Gap Semiconductors with Two-and Three-Dimensional Triel-Phosphide Frameworks (Triel= Al, Ga, In), *Chemistry–A European Journal* **2024**, *30*, e202304097.

V. Daiber, S. Zeitz, V. Hlukhyy, D. Dankert, T. F. Fässler, Synthesis, Crystal structure, electronic structure, and Raman spectra of $Li_4Sr_2SiP_4$, *Zeitschrift für anorganische und allgemeine Chemie* **2024**, *650*, e202300244.

T. M. F. Restle, S. Zeitz, J. Meyer, W. Klein, G. Raudaschl-Sieber, A. J. Karttunen, T. F. Fässler, Aliovalent substitution in phosphide-based materials–Crystal structures of $Na_{10}AlTaP_6$ and Na_3GaP_2 featuring edge-sharing EP_4 tetrahedra (*E*= Al/Ta and Ga), *Zeitschrift für anorganische und allgemeine Chemie* **2021**, *647*, 1804-1814.

List of Tables

List of Figures